# PHOTOCATALYSIS STUDIES USING MESOPOROUS MODIFIED V-MCM-48 STOBER SYNTHESIS: ACETALDEHYDE, CARBON MONOXIDE, ETHANOL, ACETONE, 2-PROPANOL, & ACETONITRILE

by

LUTHER JAMES MAHONEY

A.S., Herkimer County Community College, 2003
B.S., State University of New York, College of Oneonta, 2005

A THESIS

submitted in partial fulfillment of the requirements for the degree

MASTER OF SCIENCE

Department of Chemistry
College of Arts and Sciences

KANSAS STATE UNIVERSITY
Manhattan, Kansas

2010

Approved by:

Major Professor
Kenneth J. Klabunde

# Copyright

# Abstract

Although Degussia-Huls P-25 $TiO_2$ semiconductor photocatalyst has high photodegradation rate for organic molecules, it works only under ultra-violet (UV) light. Mesoporous metal doped V-MCM-48 silica was synthesized under ambient conditions for use as a visible-light photocatalyst to convert toxic probe molecules to innocuous products: $CO_2 + H_2O$. The synthesis employed a modified Stober metal doped MCM-48 silica method. Powder X-ray diffraction (XRD), diffuse-reflectance-ultra-violet-visible (DR-UV-vis) spectroscopy, and $N_2$ adsorption-desorpton analysis characterization methods were completed on V-MCM-48 mesoporous material. These characterization methods indicate V-MCM-48 structure had formed with visible light absorption and mesoporous properties. Photocatalysis studies were completed with V-MCM-48 under dark, visible, and UV-light illumination conditions for the following probe molecules: acetaldehyde, carbon monoxide, ethanol, acetone, 2-propanol, and acetonitrile. Acetaldehyde over V-MCM-48 was converted to $CO_2$ under dark, visible, and UV-light conditions. Carbon monoxide photooxidation occurred over V-MCM-48 under visible and UV-light. Ethanol and acetonitrile had smaller photodegradation activity over V-MCM-48. Acetone and 2-propanol had no activity photocatalytically. Under dark and visible light illumination, V-MCM-48 consumed approximately one-half acetaldehyde and produced one-third $CO_2$ concentration as compared with the P-25 $TiO_2$ under UV-light. V-MCM-48 produced two-thirds of the amount of $CO_2$ in comparison to nanoparticle Au/ZnO catalyst under UV-light. The results infer V-MCM-48 might be useful in gas and liquid phase photocatalysis including water-splitting due to a high oxidation state ($V^{5+}$), visible light absorption, and high surface area. In conclusion, an extended literature review has been completed and literature employed extensively throughout the thesis with potential methods to further the research on V-MCM-48/Si-MCM-48 in catalysis, chromatography, adsorption/gas separation, and solar collection/water-splitting.

# Table of Contents

# List of Figures

# List of Tables

# Acknowledgements

My first chemistry course was at Herkimer County Community College (HCCC) with Professor John Hawes. I was planning to use the elementary chemistry course to fulfill one of the science requirements and pursue a degree in environmental science focused on forestry; however, due to many career combined with mentally challenging opportunities in the chemical research field presented by Professor Hawes, this beginning course led to several more chemistry courses climaxing with the full-blown self-taught year long organic chemistry (with laboratory) course concurrent with general chemistry course work. Professor Hawes excitement for organic chemistry and his encouragement led to change of plans and pursue of chemistry as my life's career. Therefore, I would like to express my sincere appreciation for his honesty on careers with greatest potential for gainful employment after obtainment of various college degrees. Finally, much of my thinking of how chemistry occurs began with Professor Hawes.

As a transfer student from a community college, my former undergraduate advisor Professor Dr. Joseph F. Chiang presented similar attitude of the vast exciting opportunities in the world of physical sciences when I first met him in July, 2003 at State University of New York (SUNY), College of Oneonta student transfer day. Over the next two years, Dr. Chiang expressed interest in what I was learning in the various chemistry courses. He presented how physical chemistry could be employed throughout all areas of chemistry and emphasized its use in nanotechnology. When no other chemistry faculty member could not provide research opportunity for me so I could obtain American Chemical Society (ACS) certified Bachelor of Science degree upon completion, Dr. Chiang gave me the opportunity to synthesize transition metal doped feldspar ceramics. You have done so much for me, above and beyond the call of duty-thank you (you treated me like your own son!). In conclusion, the graduate research in materials science chemistry was due to your excitement conveyed to me.

I would like to express deep appreciation to Professor Emeritus Dr. John C. Kotz and Professor Emeritus Dr. Harry E. Pence for their dedication in teaching inorganic chemistry and equipping me for graduate studies in chemistry through exciting class lectures and related course work. They accepted where I was at in communication skills from HCCC but did not leave me there and challenged me to excel in scientific writing and presentations. Similarly, Dr. Kotz and Dr. Pence introduced and reinforced the different types of bonding in inorganic materials in contrast to bonds commonly seen in organic chemistry.

In analytical chemistry with Professor Dr. John C. Schaumloffel I learned how to complete analysis on both simple and more complex materials using various analytical instruments. He presented through lecture and laboratory the importance of accuracy and precision in measurements in real world applications. Through Dr. Schaumloffel and Dr. Kotz belief in my improving abilities in chemistry and desire to see me excel beyond SUNY Oneonta, they encouraged me to apply as a National Science Foundation Research Education Undergraduate (NSF REU) student position at Kansas State University (KSU) in summer, 2004. This help went beyond the classroom with Dr. Schaumloffel encouraging me to write a travel grant proposal to present undergraduate research project on metal doped ceramics at the National ACS meeting in San Diego, California and reviewing it, which I obtained. There-

fore, I would like to extend deepest gratitude to Dr. Schaumloffel and Dr. Kotz. To the other chemistry and biochemistry faculty at SUNY Oneonta, Professor Dr. Lawrence W. Armstrong, Professor Emeritus Dr. William B. Dixon, Professor Emeritus Paul V. Koehn, and Dr. Dick Mahlangu, thank you for increasing my knowledge in the areas of organic chemistry, biochemistry, and biophysical chemistry. In conclusion, I would like to express deep appreciation to the chemistry and biochemistry department at SUNY Oneonta for preparing me for further graduate studies as the first step toward becoming a research chemist: this was quite evident when Dr. Chiang, Dr. Schaumloffel, and Dr. Pence took time out of their schedules to teach graduate chemistry courses for me in the fall, 2007, so I could obtain a few additional graduate credit hours to graduate with the master's degree in materials chemistry from KSU and recently with Dr. Chiang reviewing my master's thesis.

At KSU, in the summer of 2004, as an NSF REU student, I would like to express deep gratitude to Professor Dr. Kenneth J. Klabunde for providing the opportunity to complete research in his laboratory in nanoparticle chemistry of metal doped oxide materials. In addition, I would like to extend deep appreciation to post-doctoral fellows in the Klabunde research group: Dr. Shalini Rodrigues, Dr. Ranjit T. Koodali, Dr. Uma Sitharaman, and Dr. Jeevanandam Pethaiyan. Dr. Shalini Rodrigues provided instruction and guidance on how scientific research completed in solid state chemistry in regards to synthesis, characterization, application, and scientific writing. She held a high standard for research that I employ daily. Dr. Koodali shared and discussed the differences of mesoporous silica materials M41S and SBA family of molecular sieves to provide background on these intriguing materials. Dr. Sitharaman and Dr. Pethaiyan answered my many questions related to the chemistry of nanoparticles. As an undergraduate and graduate chemistry student in the Klabunde research group, I would like to thank the graduate students/colleagues for their help in learning how to use the various instruments and related activities in the laboratory: Dr. Dambar Hamal, Dr. Dmytro V. Demydov, Dr. Johanna A. Haggstrom, Dr. Alexander B. Smetana, Dr. Xiangxin Yang, Sreeram Cingarapu, Erin Beavers, Dr. Igor Martyanov, Dr. David Heroux, and Dr. Zhiqiang (Aaron) Yang.

I would like to express deepest gratitude to my graduate chemistry advisor Professor Dr. Kenneth J. Klabunde for giving me the opportunity to work under his leadership in synthesis and characterization of nanomaterials for use in environmental/green energy applications. Also, I would like to thank the graduate committee members for their service and review of the thesis: Professor Chistopher M. Sorensen, Professor Viktor Chikan, and Professor Daniel A. Higgins. I would also like to thank Earline Dikeman and Brenda Luther for providing opportunities to improve my chemistry teaching skills. Also, I would like to express deep gratitude to Besty Edwards for helping me navigate the master's thesis template. In addition, I would like to express appreciation to the many chemistry faculty members that taught graduate courses I completed for their dedication in teaching chemistry. The financial support as an NSF REU and graduate student was provided by the MURI grant through Department of Defense and National Science Foundation plus additional funding provided by the KSU Chemistry Department. In conclusion, I would like to express deep gratitude to the many professors at these three academic institutions for preparing me for additional graduate education as I pursue a Ph.D. in materials science chemistry.

# Dedication

I would like to dedicate this research work to my parents Daniel & Ann Mahoney. I am indented to my parents for providing me with a loving atmosphere based on the Word of God, The Bible, as I grew up in childhood and beyond into young adulthood. You did more than simply talk about the content of the Bible; you lived the Bible in front of me through a personal relationship with Jesus Christ. As the oldest of eight children, you provided me many opportunities to learn responsible living and hard work on a daily basis by treating my brothers and sisters with love and respect: Hannah M. Mahoney, Jessica H. Mahoney, Luke J. Mahoney, Nathaniel B. I. Mahoney, Lydia J. Mahoney, Rachael-Lillian Mahoney, and Graham E. Mahoney. To my family, thank you for encouraging me through my academic course work. Finally, I appreciate Dad and Mom making the below Bible verse the basis for our ability to overcome life's obstacles:

Philippians 4: 13-"I can do all things through Christ that gives me the strength." (New International Version-NIV)

# Preface

This thesis was written as an overview of the mentally exciting/challenging field of solid state chemistry; in particular, metal doped mesoporous silica materials employed in catalytic reactions within the wider field of nanotechnology. The theme of nanotechnology translated into use of metal oxide nanoparticles in environmental remediation of toxic organic molecules under visible light illumination as an alternative to ultra-violet (UV)-light active Degussia-Huls P-25 $TiO_2$ standard. Importance of structure was noted throughout the thesis between two major M41S silica structures: MCM-41 and MCM-48. Variables that determine if unidirectional pore (p6m) or bicontinuous (Ia3d) structure formed corresponding to MCM-41 and MCM-48 materials was extensively reviewed.

The audience of readers was assumed to include the following: (1) individuals that had little chemistry knowledge but desire to learn about solid state chemistry and nanotechnology; (2) chemistry undergraduate students with little understanding of solid state chemistry and desires to gain knowledge in nanochemistry; (3) graduate students in materials science chemistry; and (4) researchers attempting to gain different perspectives on mesoporous metal doped silica materials vs. microporous crystalline zeolite structures. This far reaching audience goal was facilitated beginning in Chapter 1-Introduction, where the problem of toxic probe molecules as a major environmental remediation nascence with potentially an alternative visible light active photocatalyst presented as the solution. The extensive literature review continues the theme of chemistry affected by the structure exhibited from the example between graphite to diamond bonding plus physical properties of zeolites and attempts to develop larger silica structures to handle bulky molecules concluding with MCM-41 and MCM-48.

The following features were employed throughout the thesis as an aid to the reader: (1) expanded explanations with accompanying drawings/figures to facilitate visualization at a deeper level corresponding to enhanced understanding of many variables at work in the synthesis, characterization, and application of V-MCM-48 in environmental remediation setting, which translated into both black and white plus color drawings; and (2) full length references given at the end of each chapter for greater ease of retrieval in further study. In addition, extensive use of previous research results employed throughout the whole thesis including the appendices to help illustrate the value of metal doped mesoporous silica in environmental remediation applications. Critical understanding was paramount in the thesis; for example, concepts of charge density matching, surfactant packing parameter and effects anions plus calcination were explored further. The thesis departed from standard format in two ways: lengthened literature and discussion chapters coupled with extensive use of scientific artwork on areas that needed visual representations to relate the physical quantities.

This past eighteen plus months preparing the thesis have taught me that the majority of the published literature assumes greater background knowledge then would be commonly found among entering chemistry graduate students; therefore, the literature review was central to laying a foundation for the arguments presented in the discussion section: potential applications-merits-challenges that lie ahead for metal doped MCM-48/Si-MCM-48. My fascination was on the mechanism of Si-MCM-48/V-MCM-48 and how to produce hydrothermally stable, photocatalytically active materials in environmental/green energy applications. One would see this in the literature and dis-

cussion chapters. In conclusion, the author hopes that the thesis will meet a need in materials science field of silica chemistry

Luther James Mahoney July, 2009

To those that read this document and would like to comment, please send me an e-mail:

luther.mahoney@yahoo.com

## Quote to think about:

*"Study the unusually successful people you know, and you will find them imbued with enthusiasm for their work which is contagious. Not only are they themselves excited about what they are doing, but they also get you excited."* -Paul W. Ivey

# Chapter 1 –Introduction

## Relevance of Photocatalysis and metal doped MCM-48 silica to environmental remediation

## 1. Background knowledge to the problem

Photocatalysis was started in the 1970's to remediate both air plus groundwater. The first widespread use of a photocatalyst was $TiO_2$ [1]; however, the problem with $TiO_2$ would be that it works in the UV-light wavelength (< 400 nm) range. Modifications of $TiO_2$ were employed by implanting different metal ions into the crystal lattice. [1-5] This enabled $TiO_2$ to absorb in the visible light (> 400 nm) range, thereby making the $TiO_2$ visible light active and causing recombination centers. [2] However, these recombination centers lower the photocatalytic ability of $TiO_2$, so another catalyst was attempted. After experimenting with transition metal doped zeolites and reaching the pore size limit, the researchers started to look for and develop a heterogeneous catalyst that would have larger pore diameter to accommodate larger organic molecules. Then, in 1992, the Mobil Oil Corporation researchers discovered a molecular sieve that had larger pores in comparison to microporous sieves used, which became known as Mobil Composition of Matter, abbreviated as MCM-41, MCM-48, and MCM-50. [6] The MCM-41 was the most stable and easiest to synthesize in comparison to MCM-48 [7,8]; therefore, there has been many applications of the MCM-41 hexagonal unidirectional pore structure. [9-11]

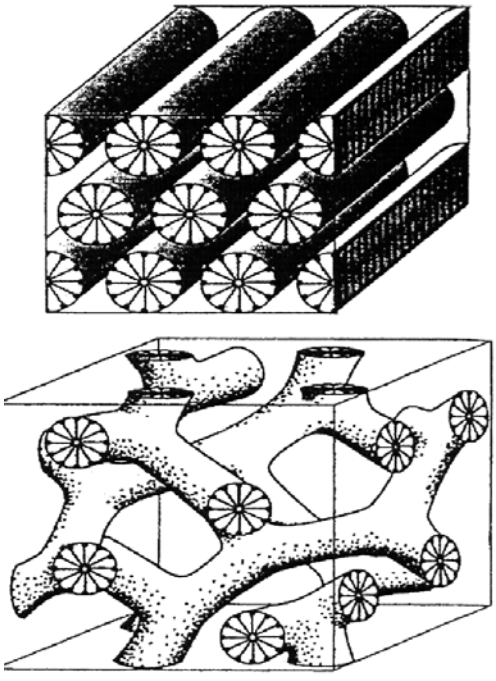

**Figure 1:1 Above MCM-41 and below MCM-48.**

**Supplemental text to Figure 1:1**-As seen in the upper portion, the MCM-41 structure has p6m space group hexagonal one-dimensional pore structure; whereas, the MCM-48 in the lower portion has a bicontinuous cubic three-dimensional Ia3d space group. [11] Schumacher, K. *et al*., *Langmuir* **2000**, *16*, 4648-4654; **DOI:** 10.1021/la991595i Permission granted by American Chemical Society Copyright 2000 ©

The structure of the two most popular M41S materials would be MCM-41 and MCM-48. These two structures have been shown above (previous page) in Figure 1:1. [11] The MCM-41 structure has a honeycomb arrangement of the pore structure; whereas, the MCM-48 structure in the bottom portion has a gyroid minimal surface shape. The MCM-41 has a unidirectional pore structure, which allows reactants and products to flow only in one-dimension, as seen in the upper image in Figure 1:1. In contrast, the MCM-48 structure has a three-dimensional pore unit that permits reactants and products to flow in three-dimensions. The synthesis of MCM-48 requires long periods of time [8,12-17] and has had the problem of irreproducibility of synthetic methods. [18,19]

## 2. Alternative research completed to address the problem

With this introduction on the problem of doped semiconductor materials like $TiO_2$, the research team led by Professor Dr. Kenneth J. Klabunde set out to develop a visible light catalyst that would convert the following probe molecules to carbon dioxide and water: acetaldehyde, carbon monoxide, ethanol, acetone, 2-propanol, and acetonitrile. A novel metal doped synthesis based on the silica sphere Stober synthetic method was applied from literature to produce various compositions of vanadium doped MCM-48 (V-MCM-48). [11,20-22] The master's thesis content that follows would be an exhaustive literature review on both MCM-41 & MCM-48 followed by the research conducted on V-MCM-48 at Kansas State University. The results and discussion sections will provide in depth analysis how this research completed in photocatalysis has led to a novel catalyst that could potentially be employed to split water. The reader would be encouraged to review the table of contents for a particular section of knowledge needed: there would be no need to read the complete literature review. However, the individual that has no or little knowledge of the material listed in the table of contents would benefit tremendously; since, the literature review condenses only the highlights of the numerous research papers used: the reader would be saved from reading several hundred pages of research material!

## References


1. Linsebigler, A. L.; Lu, G.; Yates, Jr. J. T. "*Photocatalysis on $TiO_2$ Surfaces: Principles, Mechanisms, and Selected Results*," *Chemical Reviews* **1995**, *95*, 735-758 (Review article)

2. Yamashita, H.; Takeuchi, M.; Anpo, M. "*Visible-Light-Sensitive Photocatalysts*," *Encyclopedia of Nanoscience and Nanotechnology* (Editor: Nalwa, H. S.), American Scientific Publishers, Stevenson Ranch, California **2004**, *10*, 639-654 (Review article)

3. Tayade, R. J.; Kulkarni, R. G.; Jasra, R. V. "*Transition Metal Ion Impregnated Mesoporous $TiO_2$ for Photocatalytic Degradation of Organic Contaminants in Water*," *Industrial &Engineering Chemistry Research* **2006**, *45*, 5231-5238 (Research article)

4. Martin, S. T.; Morrison, C. L.; Hoffmann, M. R. "*Photochemical Mechanism of Size-Quantized Vanadium-Doped $TiO_2$ Particles*," *Journal of Physical Chemistry* **1994**, *98*, 13695-13704 (Research article)

5. Serpone, N.; Lawless, D. "*Spectroscopic, Photoconductivity, and Photocatalytic Studies of $TiO_2$ Colloids: Naked and with the Lattice Doped with $Cr^{3+}$, $Fe^{3+}$, and $V^{5+}$ Cations*," *Langmuir* **1994**, *10*, 643-652 (Research article)

6. Kresge, C. T.; Leonowicz, M. E.; Roth, W. J.; Vartuli, J. C.; Beck, J. S. "*Ordered mesoporous molecular sieves synthesized by a liquid-crystal template mechanism*," *Nature* **1992**, *359*, 710-712 (Research article)

7. Solberg, S. M.; Kumar, D.; Landry, C. C. "*Synthesis, Structure, and Reactivity of a New Ti-Containing Microporous/Mesoporous Material*," *Journal of Physical Chemistry B* **2005**, *109*, 24331-24337 (Research article)

8. Kruk, M.; Jaroniec, M. "*Characterization of High-Quality MCM-48 and SBA-1 Mesoporous Silicas*," *Chemistry of Materials* **1999**, *11*, 2568-2572 (Research article)

9. Lim, S.; Haller, G. L. "*Preparation of Highly Ordered Vanadium-Substituted MCM-41: Stability and Acidic Properties*," *Journal of Physical Chemistry B* **2002**, *106*, 8437-8448 (Research article)

10. Selvam, P.; Bhatia, S. K.; Sonwane, C. G. "*Recent Advances in Processing and Characterization of Periodic Mesoporous MCM-41 Silicate Molecular Sieves*," *Industrial & Engineering Chemistry Research* **2001**, *40*, 3237-3261 (Review article)

11. Schumacher, K.; Ravikovitch, P. I.; Du Chesne, A.; Neimark, A. V.; Unger, K. K. "*Characterization of MCM-48 Materials*," *Langmuir* **2000**, *16*, 4648-4654 (Research article)

12. Gomez, S.; Giraldo, O.; Javier Garces, L.; Villegas, J.; Suib, S. L. "*New Synthetic Route for the Incorporation of Manganese Species into the Pores of MCM-48*," *Chemistry of Materials* **2004**, *16*, 2411-2417 (Research article)

13. Kruk, M.; Jaroniec, M. "*Characterization of MCM-48 Silicas with Tailored Pore Sizes Synthesized via a Highly Efficient Procedure*," *Chemistry of Materials* **2000**, *12*, 1414-1421 (Research article)

14. Vartuli, J. C.; Schmitt, K. D.; Kresge, C. T.; Roth, W. J.; Leonowicz, M. E.; McCullen, S. B.; Hellring, S. D.; Beck, J. S.; Schlenker, J. L.; Olson, D. H.; Sheppard, E. W. "*Effect of Surfactant/Silica Molar Ratios on the Formation of Mesoporous Molecular Sieves: Inorganic Mimicry of Surfactant Liquid-Crystal Phases and Mechanistic Implications*," *Chemistry of Materials* **1994**, *6*, 2317-2326 (Research article)

15. Huo, Q.; Margolese, D. I.; Stucky, G. D. "*Surfactant Control of Phases in the Synthesis of Mesoporous Silica-Based Materials*," *Chemistry of Materials* **1996**, *8*, 1147-1160 (Research article)

16. Van Der Voort, P.; Morey, M.; Stucky, G. D.; Mathieu, M.; Vansant, E. F. "*Creation of $VO_x$ Surface Species on Pure Silica MCM-48 Using Gas-Phase Modification with $VO(acac)_2$*," *Journal of Physical Chemistry B* **1998**, *102*, 585-590 (Research article)

17. Morey, M. S.; O'Brien, S.; Schwarz, S.; Stucky, G. D. "*Hydrothermal and Postsynthesis Surface Modification of Cubic, MCM-48, and Ultralarge Pore SBA-15 Mesoporous Silica with Titanium*," *Chemistry of Materials* **2000**, *12*, 898-911 (Research article)

18. Xu, J.; Luan, Z.; Hartmann, M.; Kevan, L. "*Synthesis and Characterization of Mn-Containing Cubic Mesoporous MCM-48 and AlMCM-48 Molecular Sieves*," *Chemistry of Materials* **1999**, *11*, 2928-2936 (Research article)

19. Mathieu, M.; Van Der Voort, P.; Weckhuysen, B. M.; Rao, R. R.; Catana, G.; Schoonheydt, R. A.; Vansant, E. F. "*Vanadium-Incorporated MCM-48 Materials: Optimization of the Synthesis Procedure and in Situ Spectroscopic Study of the Vanadium Species*," *Journal of Physical Chemistry B* **2001**, *105*, 3393-3399 (Research article)

20. Schumacher, K.; Grun, M.; *Unger, K. K. "Novel synthesis of spherical MCM-48*," *Microporous and Mesoporous Materials* **1999**, *27*, 201-206 (research article)

21. Schumacher, K.; Hohensche, d. F. v. C.; Unger, K. K.; Ulrich, R.; Chesne, D. A.; Wiesner, U.; Spiess, H. W. "*The Synthesis of Spherical Mesoporous Molecular Sieves MCM-48 with Heteroatoms Incorporated into the Silica Framework*," *Advanced Materials* **1999**, *11*, 1194-1198 (Research article)

22. Stober, W.; Fink, A.; Bohn, E. "*Controlled Growth of Monodisperse Silica Spheres in the Micron Size Range*," *Journal of Colloid and Interface Science* **1968**, *26*, 62-69 (Research article)

# Chapter 2 -Literature Review of M41S Mesoporous Silica Materials

## Section One: Fundamentals of Structure in Relation to Catalysis

## 2.1 Introduction

This literature review will primarily focus on the mesoporous silica MCM-41 and MCM-48 structures; since, they would have many potential and future applications. The three-dimensional (3-D) bicontinuous Ia3d space group MCM-48 structure, as shown in Figure 2:1, would have the most potential application in comparison to one-dimensional (1-D) MCM-41 pore structure shown in Figure 1:1 (page 1). This difference in pore geometry would directly affect the manner and number of collisions that occur with the probe molecules. From a review of the MCM-41 and MCM-48 pore structures, it would apparent that the 3-D bicontinuous Ia3d structure would have greater probability of more interactions with the probe molecules and surface. Section one opens with the value of structure between two carbon based materials followed by importance of recombination centers related to photocatalysis. The difference of structure theme continues with descriptions of microporous and mesoporous materials. Section two provides detailed overview of the mechanism and how various components of the mesoporous M41S silica synthesis affect the final structure. Section three notes the different effects of various treatments on the mesoporous silica structure. Finally, section four provides additional knowledge on subtle effects that determine the stability on the final structure of MCM-48/metal doped MCM-48.

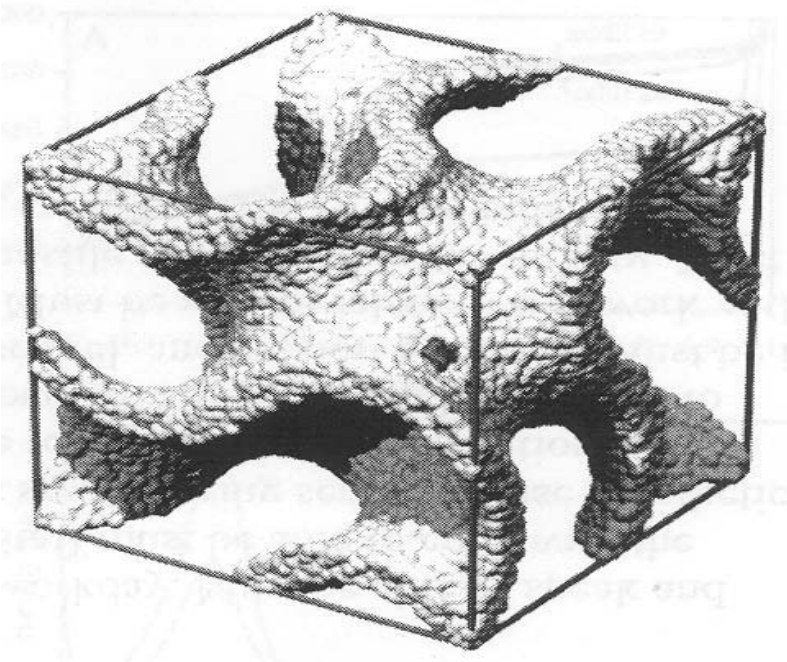

**Figure 2:1 The MCM-48 Mesoporous Silica Bicontinuous Ia3d Cubic Structure.**

**Supplemental text for Figure 2:1**-As seen above in MCM-48 graphic, the structure exhibits both a concave up and concave down wall sections with a curved surface, which means more reaction collisions on the surface that could potentially cause formation of more desired product. [1] Placing transition metal ions on the surface and in the framework of MCM-48 commonly induces catalytic activity. Collart.O. *et al*., *Journal of Physical Chemistry B*

**2004**, *108*, 13905-13912; **DOI:** 10.1021/jp049837x Permission granted by American Chemical Society Copyright 2004 ©

## 2.2 Crystal Lattice Structure Characteristics

The crystal lattice of a structure has a major effect on the resulting material properties. [2] For example, the simple arrangement of carbon atoms in diamond and graphite produce different properties. Graphite has the following characteristics: black, soft, and a lubricant. The diamond properties include transparence and strength. The softness of graphite would be created by the carbon atoms forming sheets. These atoms allow for easy sheet separation; since, they slide on top of each other. In contrast, diamond would be an excellent material for use as a cutting tool. The carbon atom bonding must be strong so that carbon atoms do not shift position. The stronger bonding in the diamond would be due to the three-dimensional arrangement of carbon atoms, which makes it chemically inert while the weakly bound carbon bonded graphite material has the ability to absorb + catalyze reactions. The major difference in chemical reactivity in these materials would be linked to the fact that diamond carbon atoms would be bound in tetrahedral $sp^3$ hybridization arrangement with covalent bonding in a three-dimensional environment: this prevents other atoms from entering the crystal lattice. The graphite material would be comprised of $sp^2$ hybridization arrangement of hexagonal rings in sheets held together with van der Waals forces. The catalytic properties of graphite would be due to both the hexagonal rings and the plane in between in the sheets.

Although the difference in the structure of M41S mesoporous silica materials have similar bonding structures, the exact structure taken determines if the reactants and products flow in only certain directions. MCM-41 has unidirectional hexagonal pore structure that permits reactants and products to flow through the pore channels in one-dimension. The MCM-48 structure with its three-dimensional pore system allows reactants and products to flow in three-dimensions. Therefore, one could conclude from this example that the structure determines the rate of flow of reactants and products. In MCM-50, the structure causes stability problems making it useless as a catalyst support. In conclusion, the types of lattice structure taken with determine chemical reactivity, as noted in the carbon and silica examples listed above and shown in Figures 2:2. [3]

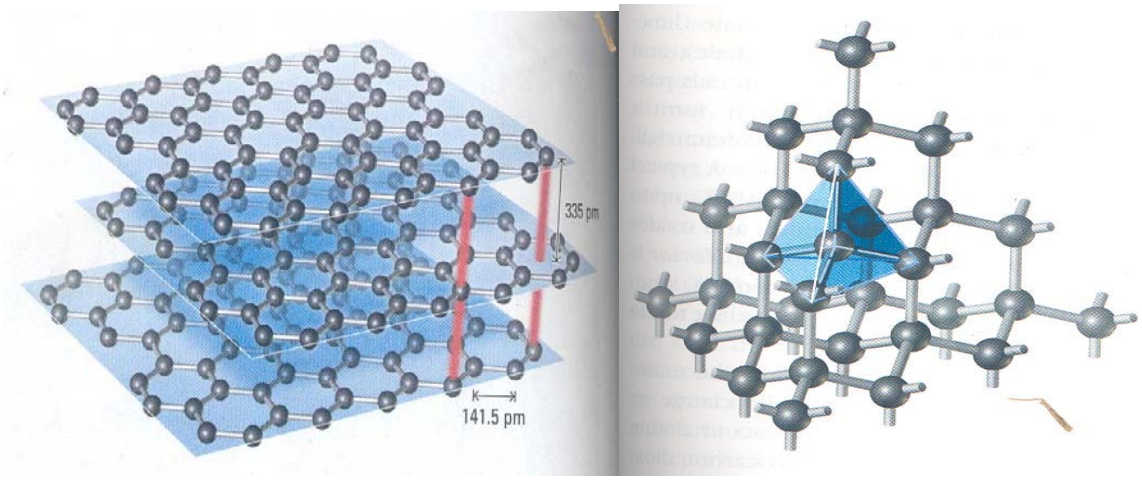


**Figure 2:2 Graphite Structure to the above left and Diamond Structure to the above right.**

**Supplemental text to Figure 2:2**-As seen above in the graphite structure, [3] the major differences would the $sp^2$ hybridization bonding and weak van der Waals forces that hold the lamellar aromatic ring system together in contrast

to the diamond structure, which has stronger covalent bonding. Moore, J. W. *et al*., "*Chemistry The Molecular Science*," **First Edition**, Chapter 11, pages 500-501 Permission granted by Thomson Learning Brooks/Cole Publishing Company, a part of Cengage Learning, Inc. (www.cengage.com/permissions) Copyright 2002 ©

## 2.3 What Recombination Centers cause in semiconductor like materials

Trap sites and recombination centers would be energy levels located in the forbidden region, otherwise known as the bandgap, as shown in Figure 2:3. [4,5] A trap center would be a site where an electron resides for a time period before being thermally ejected into the band. [6] If a hole passes into one of the traps and was not able to be thermally ejected into the band, then, this would be considered a recombination center. Eventually an electron would enter this area and cause recombination or annihiliation of charge carriers (both $h^+ + e^-$) to eventually combine. [6-9] Recombination centers would be important due to the shortening of the lifetime of the electron and hole. The impurities open up energy surface states in the forbidden region of the bandgap, which usually act as recombination centers. [4,5] These recombination centers would significantly lower the photocatalytic ability of the resulting catalyst material allowing heat and light to be given off instead of the desired catalytic reaction. [8-10] In a high surface area material the recombination process would be very important due to the many surface states. [4,5] The recombination velocity would be effected by sample thickness; thus, a thinner sample should have a higher recombination velocity, and surface states would have a certain energetic position.

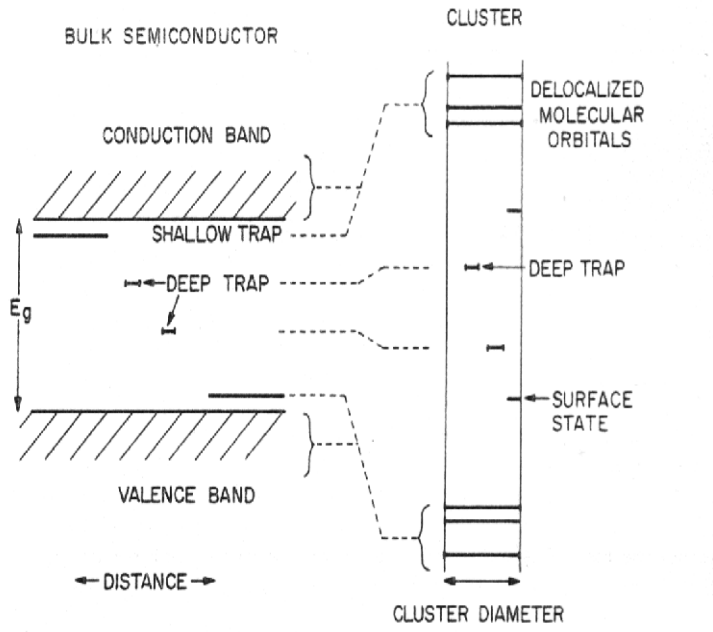


**Figure 2:3 Diagram of trap sites in bulk and cluster semiconductor systems.**

**Supplemental text to Figure 2:3**-The above diagram shows the traps sites that would be possible for a bulk and cluster system. [4] These various trap states have the potential to function either as trap states where an electron or hole could be held for a period of time before being thermally ejected into the band, or the trap sites could work as recombination centers. The major difference between the bulk and cluster structures would be the number of trap states, which generally would be larger in the cluster system of semiconductor particles. Therefore, if it were possible to use the majority of these charge trapping sites for holding a charge particle (be it an electron or hole), it would also be possible to design a semiconductor particle that has excellent photocatalytic properties: this would be the hope of using these small cluster semiconductor particles could potentially have desired photocatalysis properties in

comparison to the bulk member ones'. Finally, the above diagram could potentially explain why one notes higher yields of desired product(s) from using small semiconductor particle, otherwise known as semiconductor nanoparticles. Brus, L., *Journal of Physical Chemistry* **1986**, *90*, 2555-2560; **DOI:** 10.1021/j100403a003 Permission granted by the American Chemical Society Copyright 1986 ©

## 2.4 History of Photocatalysis

In 1921, the first reported use of photo-reactivity was with compounds. The field of gas-solid heterogeneous photocatalysis began in 1971 with the work of Teicher and Stone. [11] The uses of gas-solid application include the following: partial oxidation of organic compounds, the formation of gaseous fuels, the removal of $NO_x$ from power plant exhaust, and the oxidation conversion of building and factory contaminants from air. Although there have been many studies of photocatalytic water treatment, there have been few gas-phase heterogeneous photocatalysis studies completed. There has been increased interest in gas-phase photocatalysis for the remediation of contaminants in the air of confined spaces, such as: aircraft, spacecraft, office buildings, and factories. The conversion of many organics at room temperature has been found to be thermodynamically favorable for the production of $CO_2$ and $H_2O$.

## 2.5 The Importance of Photocatalysis

Gas-phase heterogeneous photocatalysis could be a technique used to improve air quality through the oxidation of contaminated air. [11] Photocatalysis would be applicable where air quality levels would be lower than several hundred ppm; moreover, it would not be economical for the operation of a high temperature oxidation cleaning system at low air pollution concentrations. There would be a need for a material that completely oxidizes catalytically low concentration of pollutants at ambient temperature. The exposure levels range would be from 1-500 ppm in air according to the set Occupational Safety Health Administration (OSHA) work place for Time Weighted Average Permissible Exposure Limits (TWA-PEL). The air quality problem could be at or near the threshold limit values (TLV). The TLV standard would be the level at which, the workers would not be adversely affected by exposure to the airborne substance. Another benefit of photocatalysis oxidation in the removal of pollutants over air purifiers would be the elimination of sorption material that needs disposal. [12] Air purification using photocatalysis could be important in confined air spaces, such as: office building, factories, homes, cars, and spacecraft.

## 2.6 History of Zeolites

In 1756, Swedish scientist Cronstedt discovered zeolite while heating an unidentified silicate which fused readily and exhibited fluorescence. [13] McBain named chabazite a molecular sieve due to its selective absorption of molecules smaller than 5 Å in diameter. However, it was not until the emergence of crystalline aluminosilicates that zeolites and molecular sieve had particular meaning. A need to process larger molecules led to the growing interest in mesoporous materials ranging from 20-500 Å in diameter. Many researchers attempted to make materials with zeolite properties and larger pore diameter. In 1982, a molecular sieve with larger pores was synthesized through an adjustment of the synthesis gel mixture. [13, 14] The structure $AlPO_4$-8 contained 14 member rings, breaking the 12 member ring barrier. Then, VPI-5, cloverrite, and JDF-20 structures were synthesized by various research groups. None of these molecular sieves had any major applications due to low stability. The research team led by Chiola discovered the synthesis of low-bulk density silica, and Yanagisawa et al. found that they could make a hexagonal mesoporous material by placing cationic surfactants between the various layers of kanemite using high pH condi-

tions. [15] In 1992, Mobil Oil Corporation researchers discovered the M41S family of mesoporous aluminosilicate molecular sieve materials with very large uniform pores. [13, 14] With synthesis of the M41S family, the templating system went from a single, pivotal organic molecule to self-assembled surfactant molecules. Hexagonal, cubic, and lamellar were the three types of mesoporous material in this family.

## 2.7 Difference between Microporous and Mesoporous Materials

The synthesis of M41S family of mesoporous materials has similarities to the zeolite synthesis; however, the M41S synthesis uses a surfactant ( a charge organic species) as a template in contrast to single molecules in zeolite synthesis. [16] The M41S synthesis occurs at temperatures generally less than 120°C in a mild environment with an anionic, cationic, Gemini, or neutral surfactant in either basic or acidic solution. [17] Furthermore, with continued investigation of the M41S family, the researchers were able to manipulate the reaction parameters to cause the formation of pores ranging in size from 20 to 100Å in diameter (mesoporous range > 2.0 nm —20 Å). [16-19] This was a major breakthrough in materials chemistry with heterogeneous catalysis; since, the traditional zeolite structures had pore sizes from 20Å and below. [16, 19] The three members of this mesoporous family would include MCM-41, MCM-48, and MCM-50, where MCM represents Mobil Composition of Matter. [19] The MCM-41 material would be an one-dimensional pore structure that has hexagonal packing [19, 20, 23-25]; the MCM-48 material has a cubic structure indexed to the la3d space group that exhibits a bicontinuous three-dimensional pore structure [19]; and MCM-50 has an unstable lamellar structure: these structures could be shown in Figure 2:4. [26] The MCM-48 structure has been shown to exhibit large specific area as high as 1600 $m^2/g$ and pore volume up to 1.2 $cm^3/g$ coupled with a high thermal stability. [27]

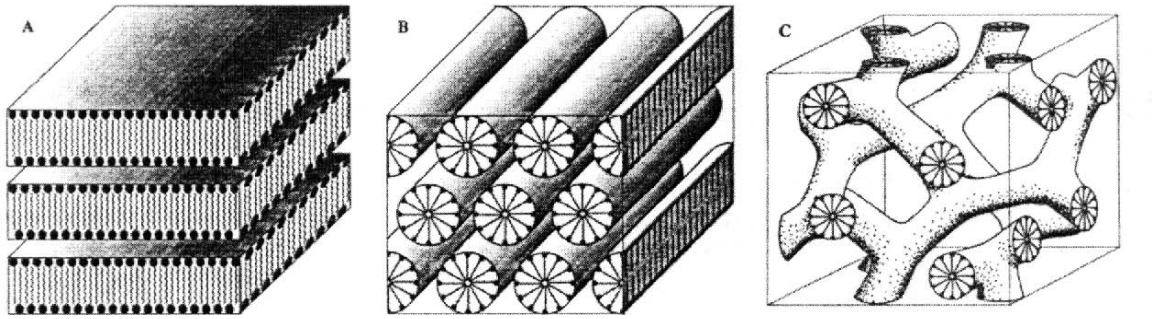


**Figure 2:4 Mesoporous Silica Structures (A) MCM-50; (B) MCM-41; and (C) MCM-48.**

**Supplemental text for Figure 2:4**-As seen in the above Figure 2:4, MCM-50 has a lamellar structure with no structural members to hold up the sheets of silica, thereby making it thermally unstable surfactant template removal; MCM-41 would have unidirectional pore construction; and MCM-48 would have three-dimensional bicontinuous cubic structure. [26] The MCM-50 has in-plane construction similar to the graphite structure in Figure 2:2; however, the removal of the template surfactant molecules leads to collapse of the resulting structure. Hexagonal MCM-41 pore structure allows only for the reactants and products to flow in one-dimension, and cubic MCM-48 permits both reactants coupled with products to flow in three-dimensions, thereby causing it to be the potentially most useful catalyst support considering mass transfer kinetics. Fyfe, C. A.; Fu, G., *Journal of the American Chemical Society* **1995**, *117*, 9709-9714; **DOI:** 10.1021/ja00143a014 Permission granted by American Chemical Society Copyright 1995 ©

Before the discovery of the M41S family of mesoporous materials, bulky organic molecules were not easily oxidized with the microporous materials due to the small kinetic diameter. [17,28] With MCM-41 material, the pore size could be varied from 15 to 100 Å. [28] Even with this advance, the vanadium centers in the MCM-41 mesopor-

ous material lacked stability. Both the V-zeolite and V-mesoporous materials have excellent properties of catalysis of organic molecules using $H_2O_2$ as an oxidant. [29] These mesoporous materials also usually have a very small pore-size range that could be used to increase the selectivity of the catalyst and consequently produce only the desired product. The V-mesoporous materials have great potential in the production of fine chemicals where bulky organic molecules would be common and traditional zeolites would not be useful due to a small kinetic pore diameter. [19, 29] The large surface area of the internal pores in mesoporous materials like MCM-41 & MCM-48 allow for many active sites (otherwise known as metal ions) to be spread out over the catalyst support. [30] For example, the titanium version of M41S family of mesoporous sieves would be an excellent catalyst for the mild selective oxidation of organic molecules using aqueous $H_2O_2$. This was also found with other metal doped MCM-48 materials under varied reaction conditions in organic synthesis. [31-43] Joshi and co-workers in the solvent-free reaction with methyl trimethylsilyl dimethylketene acetal + benzaldehyde had a 100% formation of the β-hydroxyl-ester at a 70% yield operating at 373 K over Sn-MCM-48. [31] In contrast to the larger pore materials, the Ti-zeolites would be limited by size of the molecules that could enter the pore system, which would be approximately 6.5 Å; therefore, it would be expected that the activity decreases progressively from alkanes to branched alkanes, thereby would cause these mesoporous materials to be of great interest. [30] Moreover, most of the metal incorporation has occurred with MCM-41, which this structure only has one-dimensional pores that could be easily plugged. In contrast, the metal incorporated MCM-48 structure would be useful in catalytic reactions of bulky molecules in fine chemical applications due to the three-dimensional pore structure that does not easily get plugged in chemical reactions. [23,34,39,40] Finally, the mesoporous molecular sieves MCM-41, MCM-48, FSM-16 (Folded Sheet Mesoporous Materials and 16 the number of carbon atoms in the alkyl portion of surfactant chain-mesoporous silica similar to MCM-41)44, and HMS (Hexagonal Mesoporous Silica-thicker silica was but not as ordered as MCM-41) [20,45] have received much attention in their synthesis coupled with potential applications due to the following characteristics: an internal large surface area, uniform pore channels, and a narrow pore size distribution that could be easily tuned to the desired structure size. [17,44-46]

The use of molecular silica sieves has attracted much attention due to the following potential areas of use: catalyst supports, absorbents, placement of large molecules in host matrix, and molecular sieves. [17,44-47] All of these potential uses of mesoporous silica molecular sieves would be linked to a large pore size in contrast to the microporous zeolites. The M41S family of mesoporous materials have large regular pores that range in size from 1.5-7.0 nm (15-70 Å); moreover, these materials have a small pore size range, relatively large range order, greater surface areas compared to crystalline zeolites, and possess stability after calcination (process where one heats a sample up to remove the organic templating groups.). [39,48] The larger pore sizes in the M41S molecular sieves allows for the processing of bulky molecules, and a greater amount of catalytically active species spread out evenly over the large surface area; in contrast, the microporous materials do not possess these useful properties and a reaction could take place only on the surface of the catalyst. [39,41,49-51] For vanadium catalysts, the vanadium loading and the nature of the oxide support has a profound effect on the structure of the vanadium species plus the degree (or amount) that the vanadium active sites would be spread out over the catalyst (substrate-support). [50] The catalytic effects of vanadium species on a substrate has been linked to the coordination environment. The incorporation of transition metal oxides

into the mesoporous material while still retaining structural ordering coupled with high surface area of mesoporous sieves remains a challenge. Likewise, the mesoporous molecular sieves, such as MCM-41 and MCM-48, possess channel arrangement that would be crystalline; however, the atomic arrangement of these mesoporous molecular sieves exhibit disorder similar to amorphous silica. [52,53]

Due to the ultra-large pore structure of the mesoporous molecular sieve MCM-41, there has been much attention attracted to this material from its potential use in both absorption separations and catalysis of bulky molecules. [54] However, the MCM-48 three-dimensional pore system would be more useful for industrial applications due to its interwoven coupled with branched structure that allows for reactants and products to pass throughout the pore system with less chance of pore blockage, as shown in Figure 2:4. [31,34,39,41,55] This permits for enhanced mass transfer kinetics in catalytic plus separation applications. [27,31,34,39] Due to the wide pore size range of synthesized $SiO_2$ and $TiO_2$ membranes, there would be a large demand of mesoporous membrane materials that exhibited greater pore control for use in high-performance applications. [56] Likewise, the demand for alkylated aromatic ring systems comprised of two to four rings has attracted much attention due to use in high-performance engineering plastics that have good thermal plus mechanical strength. [14] However, the larger aromatic ringed structures like pyrene could not enter these microporous cavities of the zeolite due to size restrictions. Again, the mesoporous materials work very well on these larger ringed structures where only a surface reaction could occur with the traditional zeolite. Nonetheless, using the typical hydrothermal synthesis of MCM-48 requires longer synthetic reaction time period to obtain quality pore structure in comparison to the shorter reaction time needed to make MCM-41. [34,39,55]

In the microporous metallosilicate molecular sieves, the incorporation of lanthanide, such as Ce, instead of $Si^{4+}$ ions lead to large bond strain due to the longer Si-O-Ce bonds; therefore, the size compatibility for the incorporation of Ce into a micorporous molecular sieve would be very challenging. [20] In contrast, the substitution of Ce into the MCM-41 framework should be easier due to the greater flexibility exhibited in this mesoporous material, and could be expected to bring both heterogeneous acid coupled with redox catalysis activity to the M41S structures. The research, therefore, has focused on heteroatom being substituted into the MCM-48 framework, thereby imparting oxidation catalysis activity to the MCM-48 structure, which would have little catalytic activity alone. [25,57] The relatively easy access of the active sites in the doped MCM-48 results in enhanced reactivity. [22] The use of Ce in the MCM-48 structure could also be expected to give both as a heterogeneous acid coupled with redox catalyst, and the incorporation of $Fe^{3+}$ ions into the MCM-48 framework potentially leading to an oxidation catalyst. One of the main advantages of MCM-48 would be the fact that it has greater stability under mechanical pressure in comparison to MCM-41. [49] Finally, the substitution of transition metal ions into the Si-MCM-48 framework has the potential to increase electron transfer efficiency of dye molecules, like rhodamine B (RhB), in a solid framework due to a larger absorption coefficient coupled with large fluorescence yield in collecting plus utilizing photo-energy. [58]

## 2.8 Describe what makes MCM-41 so easy to make + more stable

As an example of the flexibility [59-62] of the MCM-41 structure, it can be made in a large number of pore sizes even without organic additives like ethanol, which would be needed for MCM-48 synthesis. [48] A low surfactant to Si ratio would favor the formation of MCM-41, as noted in Figure 2:5 plot of various concentrations of sur-

factant in the micelle system. Lower reaction temperature favored the formation of MCM-41. For example, when the synthesis temperature was from 60 to 100°C in a three day reaction time, this led to the formation of the MCM-41 structure: the reason for this happening would be related to the temperature effecting the surfactant packing parameter, g, where $g = V/a_0l$, of the mesoporous structure. The g-value for a temperature from 60-100°C would be lower using ($CTA^+$) surfactant ions in comparison to a temperature range of 135-150°C, which generated the MCM-48 structure. With the use of alkytimethylammonium halides as surfactants in a reaction synthesis, this usually led to the formation of hexagonal or lamellar phases over the cubic MCM-48 structure. [63]

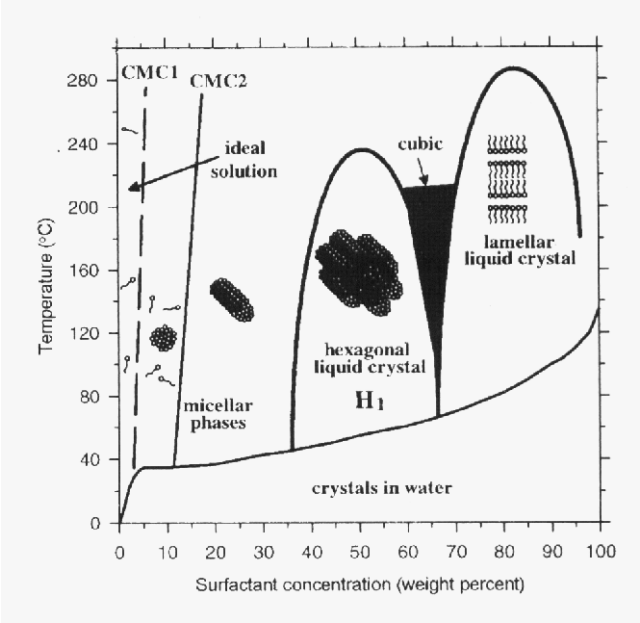


**Figure 2:5 Critical Micelle Concentration as function of temperature and surfactant concentration.**

**Supplemental text for Figure 2:5**-the above plot illustrates the critical micelle concentration (CMC) for the 16 carbon length cetyltrimethylammonium bromide ($C_{16}$TMABr) surfactant in water. [64] In the lower left section of the graph would be the CMC1 where it would be free surfactant molecules; on the right would be CMC2 where the free surfactant molecules begin forming clusters of micelles (structures that would be spherical or elongated); then, these elongated structures start to form hexagonal liquid crystal ($H_1$) in a relatively wide synthesis range; with slightly more surfactant concentration in the water, this causes the hexagonal phase ($H_1$) to convert to cubic micelle structure. Finally, as additional amounts of surfactants were added to the water, the cubic structure converts over to the lamellar phase, as shown in the right portion of the plot. The cubic phase would be in a narrow thin section of the surfactant concentration plot, thereby inferring that a relatively precise amount of surfactant would have to be added to produce the cubic structure and the smallest deviation would cause the formation of either the $H_1$ or lamellar phase. Therefore, the critical packing parameter (CPP) must be in a narrow range to produce the desired cubic structure. Raman, N. K. *et al*., *Chemistry of Materials* **1996**, *8*, 1682-1701; **DOI:** 10.1021/cm960138+ Permission granted by the American Chemical Society Copyright 1996 ©

## 2.9 A description of MCM-48

The M41S family of mesoporous materials has for the first time the potential to oxidize bulky molecules; since, the traditional Ti-zeolites were microporous and only allow for small organic molecules to enter their pores. [65] The MCM-48 material has a three-dimensional pore structure, as shown in Figure 2:6 of different viewpoints, which permits reactants and products to flow in three-dimensions and could prevent pore blockage; in contrast, the MCM-41 material only has unidirectional pore channel system, thereby causing the potential for pore blockage to occur. [18,23,27,31,34,39,41,55-59,65,66] Therefore, MCM-48 would be more useful as a support in catalytic reactions, where pore

blockage could be a concern. [23,57,65,67] The MCM-41 and MCM-48 would be characterized as having the following favorable characteristics: large surface area, narrow pore size distribution, and relatively uniform shape. [67,68] In contrast, to zeolites, these mesoporous molecular sieves have pore diameter between 20 to 100 Å [16,18,20,27,28,54] Although there has been much research completed on the MCM-41 structure, there has been little published results for Si-MCM-48 coupled with influences that substitution of needed metal ions in the framework has on the MCM-48 structure. [67,68] Even though the MCM-41 and MCM-48 structures show thermal stability [27,47] up to 1173 K in dry air and also have stability in air saturated with distilled water vapor to 1073K, however, these structures disintegrate in distilled water [25] and aqueous solutions in contrast to zeolite A, Y, and ZSM-5. [47] As shown in Figure 2:6 of the Si-MCM-48 structure, one could imagine the deterioration of the pore walls beginning with the silanol groups (Si-OH) on the outer thin amorphous silica wall surface participating in hydrolysis of the siloxane (Si-O-Si) bonds, thereby leading to leading to collapse cubic structure. [69] The increased stability hydrothermally of mesoporous silica molecular sieves would be a major break-through in commercialization of this material especially when used as a catalyst or absorbent. [24] Hartmann and Bischof also note the importance of large quantities needed for commercial use. [24] They have been to develop a MCM-48 synthesis that could be scaled up to 150 grams and still be high quality cubic structure; however, care must be taken to carefully shape the pellets to not unduly lower the pore volume of the structure, which could be related to a decrease the channels diameter in Figure 2:6 and reduction in unit cell length (size).

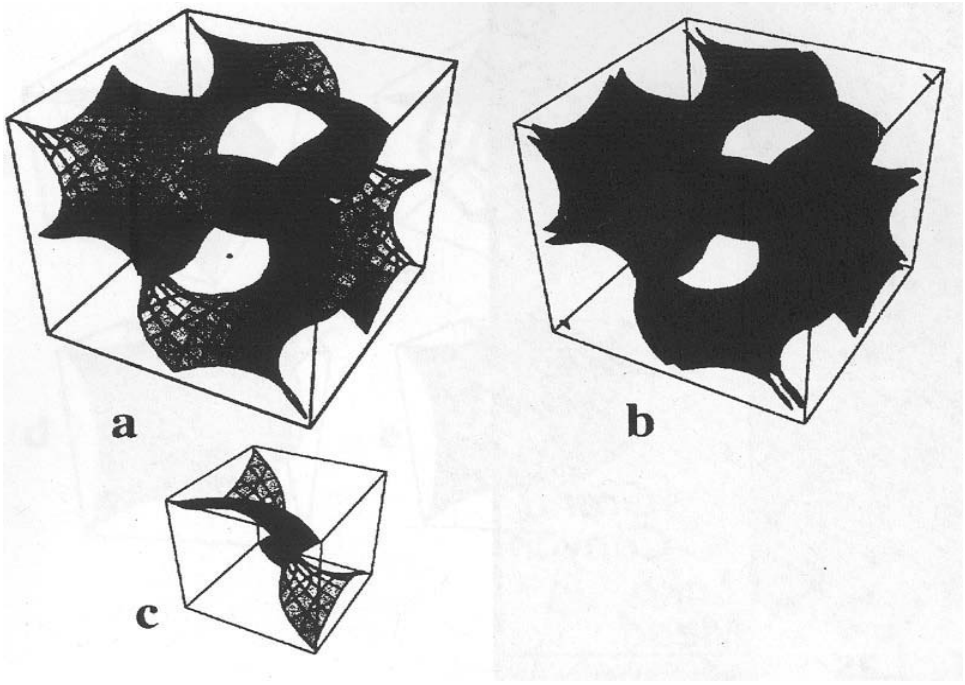


**Figure 2:6 Different views of the bicontinuous Ia3d MCM-48 mesoporous silica structure in a unit cell.**

**Supplemental text for Figure 2:6**-As seen in the above images of MCM-48, the walls appear to be relatively thin and have high curvature with minimal surface area point where the structure twisted into two opposite directions. [69] In part (a) the equation for an approximate gyroid structure was plotted, and in part (b) the solution shown of the thickness of the pore walls of 4.3Å assuming the cubic unit cell was 97 Å in size, which would be in the range of experimentally synthesized Si-MCM-48. As viewed in part (b) focusing on the corners of the unit cell, one could note the close distance between the equation and solution value of the pore wall. This thin pore wall means that

there would only be a few $SiO_4$ units that comprise wall thickness value. In part (c) would be one-eight of the unit cell of part (a) bottom left portion. The view clearly shows that the walls twist in two different directions in a complex manner. Therefore, the highly strained silica framework coupled with thin walls would the opportunity for the cubic structure to collapse under harsh reaction conditions common in industrial applications. Anderson, M. W., *Zeolites* **1997**, *19*, 220-227; **DOI:** 10.1016/S0144-2449(97)00061-4 Permission granted by Elsevier Scientific Publishing, Inc. Copyright 1997 ©

## 2.10 For MCM-48, explain why MCM-48 is difficult to synthesize + irreproducible

The reason for hexagonal MCM-41 [55] obtaining the widespread research interest would be linked to a rather easy synthesis scheme. [22] In contrast, the cubic MCM-48 structure has received much less research interest due to the difficult synthesis conditions that lead to poor reproducibility of MCM-48 structure. [18,39] The majority of studies on improving the structural hydrothermal stability of MCM-48 would be for pure silica, not the heteroatom substituted MCM-48. [25] Moreover, there have been few published papers on heteroatom substituted MCM-48. To deal with this synthesis problem of MCM-48, several different synthesis routes have been developed. [17,27,59,62,70-85] This kinetic control synthesis of MCM-48 was noted to be one of the main reasons for the poor reproducibility of the cubic structure. Moreover, the formation of MCM-48 was determined by an extremely narrow margin of error, thereby leading to poor reproducibility using alkyltrimethylammonium halides surfactants. [63] The research group headed by Stucky and co-workers reasoned that the cubic structure could be formed using select surfactants. [86] This method of synthesis development used the surfactant packing parameter for an amphophilic liquid crystal display: $g = V/ a_0 l$. [48,63,86] The volume (V) refers to the total volume that the alkyl tail groups takes up; the ($a_0$ ) symbol represents the micelle surface that the effective head-group area has on it; and the kinetic length comprising the alkyl chain would be the (l) symbol. [63,86]

## 2.11 Why M41S Materials breakdown/deteriorate in boiling $H_2O$ lacking catalytic activity

Both the MCM-41 and MCM-48 structures exhibit low hydrothermal stability [67] in an aqueous solution environment, thereby making there usefulness in many applications not profitable. [55] To deal with the stability issue, research has been conducted mainly on MCM-41 in the following areas: pore wall thickening, silylation, stabilization using the salt effect, and hydrothermal restructuring process. Likewise, the limiting factor of the M41S family of mesoporous molecular sieves in implementation in most of these various applications would be the low stability of the pore wall structure to water vapor plus mechanical compression. [46,56] The past research, [56] where MCM-48 structure was exposed to water vapor over a long period of time, the result was the collapse of the pore wall structure: this occurred with the MCM-41 structure collapsing in just 2 days of boiling in water. [46,56] To deal with this problem of pore wall structure disintegration upon exposure to moisture, the application of trimethylsilylation to the pores of MCM-48 was completed, and the result was an improvement in stability against water vapor and compression tests. [56] The researchers indicated the trimethyl group in the silylation process capped the chemically reactive hydrophilic silanol groups, thereby preventing attack of nearby Si-O-Si bonds from hydrolysis. [46,56] In the reaction of Al-MCM-41in aqueous conditions, it was determined that a thicker pore wall would improve stability of the structure from local hydrolysis of the Si-O-Si bond. [46] The researchers concluded, if the silicate bond could be protected from hydrolysis, then, the resulting structure would be stable.

Due to a lack of acidic sites and limited ion-exchange capacity, therefore, the Si-MCM-48 structure would be of limited value as a catalyst. [87,88] There has been research conducted on the isomorphous substitution of metal

ions into the silicate MCM-48 framework in order to induce catalytic activity. [1,31-43,87-94] The higher metal content in the MCM-48 structure usually leads to lower XRD peak intensity, thereby inferring a loss of order. [1,31,39,41,90,93,95,96] The opposite of breakdown of the structure would be the formation of oxide bonds from inorganic members, which cause the resulting material to be thermally stable. [60]

Hydrothermal stability was determined by boiling the sample in water for 12 hours. [25] This process was conducted on the Si-MCM-48, Ce-MCM-48, and Fe-MCM-48 structures. The Si-MCM-48 structure was completely destroyed in the hydrothermal test, which reaffirmed previous research. When there was a relatively low amount of Ce incorporated into the MCM-48 structure, the structural integrity was partially retained according to X-ray diffraction (XRD) analysis before and after boiling the Ce-MCM-48 sample, but, when the Si/Ce ratio was increased, (i.e. lower ratio value) the hydrothermal stability enhancement seen for the lower Ce content was destroyed. Research on Al-MCM-48 produced similar results. [87,90]; likewise, addition of increasing chromium ion in MCM-48 led to lower hydrothermal stability. [97]

Hydrothermal stability trend for Ce-MCM-48 indicates that the Ce incorporation in the MCM-48 structure has the Si-O-Ce bonds that have enhanced resistance to attack from water in comparison to the Si-O-Si bonds. [25] The Ce species that would be on the pore wall surface as extra framework species have the ability to act as further protection against water attack; however, when the Ce content would be high in MCM-48 structure, the result indicated a major decline in the ordering of the pore structure, thereby causing decreased hydrothermal stability. These results on the Ce-MCM-48 samples imply that a careful adjustment of the metal content in the MCM-48 would be important for improving the hydrothermal stability. The researchers concluded that the Si/Ce ratio of 100 to 50 improved the hydrothermal stability of the structure, according to XRD analysis in Figure 2:7.

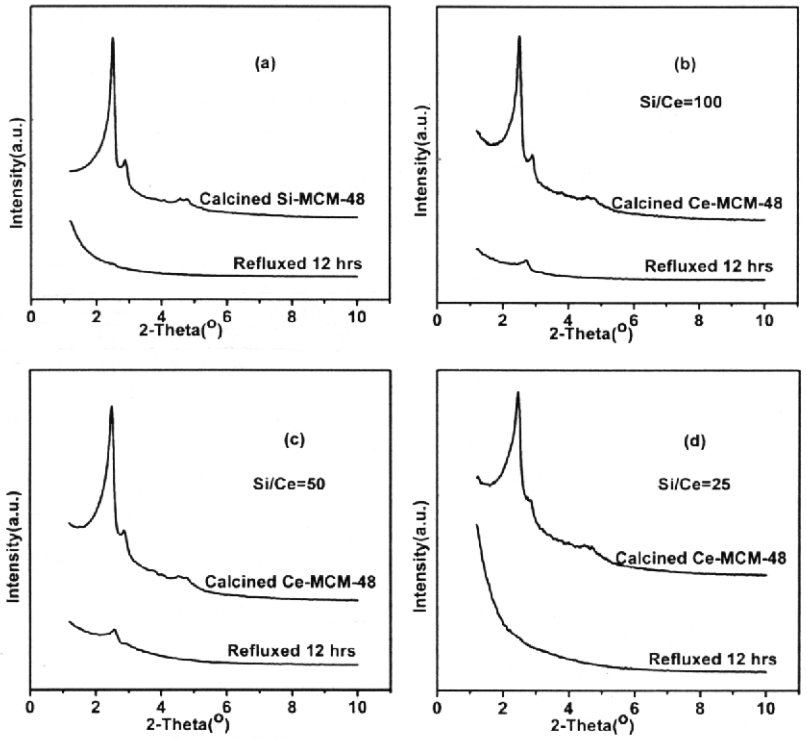


**Figure 2:7 Powder XRD plots under reflux conditions with various amounts of Ce ion.**

**Supplemental text for Figure 2:7**- the XRD plots shown to the above left would be of Si-MCM-48 and Ce-MCM-48, where Si/Ce concentration ratios would be 100, 50, and 25. [25] As seen to the far upper left XRD plot of Si-MCM-48 both after calcination and after 12 hours of boiling in water, the structure was destroyed with refluxing conditions in plot (a); whereas, in plots (b) and (c) of Si/Ce 100 and 50, there was still a small peak after boiling the Ce-MCM-48 sample in boiling water for 12 hours. In plot (d), the over-use of $Ce^{4+}$ ion in the MCM-48 structure produces the same effect as no $Ce^{4+}$ ion in the cubic structure. Therefore, it would be clear that the optimal amount of $Ce^{4+}$ ion would produce the desired structure that could withstand the harsh 12 hour refluxing conditions. Shao, Y. *et al*., *Journal of Physical Chemistry B* **2005**, *109*, 20835-20841; **DOI:** 10.1021/jp054024+ Permission granted by American Chemical Society Copyright 2005 ©

The use of $F^-$ ion in the synthesis of Ce-MCM-48 not only increased the structural long range ordering but also increased the hydrothermal stability of the Ce-MCM-48 against water attack in boiling conditions, as shown in Figure 2:8 of the XRD plots. [25] The use of $F^-$ ion enhanced stability hydrothermally to the point of Si/Ce = 50; however, the increased Ce content caused more disordered structural characteristics at this higher loading of Si/Ce = 25 that could not be compensated for with fluoridization, as shown in Figure 2:8. These results would infer that there would be an optimal amount of Ce in the MCM-48 structure for enhanced hydrothermal stability. Similar results were found for the Fe-MCM-48 structure with exception that the Fe-O-Si bond and non-structural Fe members exhibited low resistance to hydrothermal water attack in contrast with Ce-O-Si bond. The use of NaF in the Fe-MCM-48 structure leads to greater hydrothermal stability similar to Ce-MCM-48. The above results could be due to the $F^-$ ion affecting the silicate species to further increase polymerization of the MCM-48 structure leading to greater hydrothermal stability of the resulting structure. The incorporation of Fe into the MCM-48 framework did not lead to any remarkable improvement in hydrothermal stability.

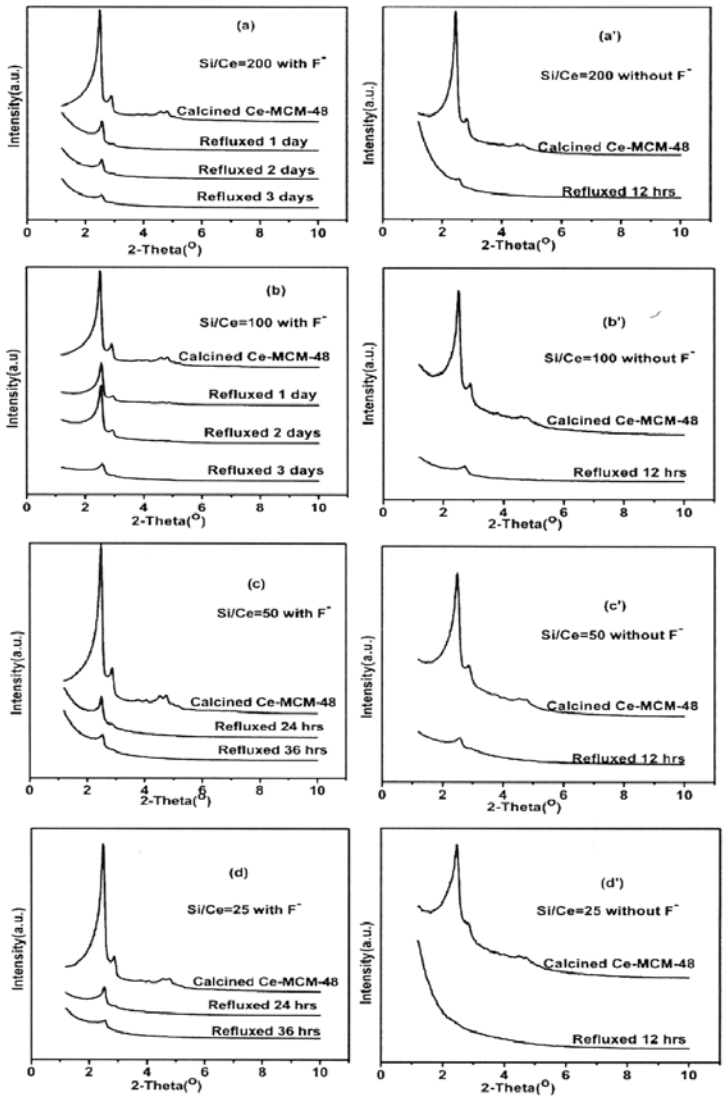


**Figure 2:8 Powder XRD plots with various amounts of Ce ion and fluoride ion.**

**Supplemental text for Figure 2:8**-the above XRD plots would be of Ce-MCM-48 synthesized with $F^-$ anion and without $F^-$ anion at Si/Ce concentration of 200, 100, 50, and 25 (note: a lower ratio number means higher concentration of $Ce^{4+}$ ion in the MCM-48 structure.). [25] In graphs on the left hand (a-d), the F- anion helps increase the structural integrity to Si/Ce = 50; then, at Si/Ce = 25, the concentration of $Ce^{4+}$ ion causes more disorder that could not be corrected with more $F^-$ ion. Finally, the right hand portion (a'-d') without the $F^-$ anion shows practically complete destruction in just 12 hours of refluxing in water in comparison to several days in the same Si/Ce Ce-MCM-48 concentration. Shao, Y. *et al*., *Journal of Physical Chemistry B* **2005**, *109*, 20835-20841; **DOI:** 10.1021/jp054024+ Permission granted by American Chemical Society Copyright 2005 ©

## Section Two: Fundamentals in Synthesis of MCM-48 Structure: Formation Variables

### 2:12 Two mechanisms of synthesizing M41S mesoporous materials

The following mechanisms have been proposed for the formation of the hexagonal phase (MCM-41): liquid crystal templating mechanism, rod mechanism, and layer mechanism. [26,98,99] The liquid crystal templating mechanism employs the concept of the surfactant acting as a template for silicate species to mold around the resulting micelle structure. [26,98-100] Similar to the liquid crystal templating mechanism, the rod mechanism tenants has the tubu-

lar silica wrap around the outer surface of the micelles; then, the structure forms spontaneously into rod-like members in a hexagonal arrangement. [26] Finally, the layer mechanism employs the concept of the lamellar structure converting to hexagonal phase through a transformation process.

The researchers, Stucky and co-workers, have noted that the electrostatic interaction between the surfactant-silicate species would be governed by charge density matching in the cooperative assembly of these mesoporous materials. [26,86] The adjustment of the charge density at the interface of the micelle-silicate has to be carefully controlled of the electrostatic interactions to obtain the desired structure.

The first synthesis mechanism used to explain the construction of the M41S mesoporous materials was the liquid crystal templating model due to the similarity of the phases that occurred in the formation of the material. [16,26,98-100] However, recent research indicates that the M41S mesoporous materials form through cooperative self-assembly mechanism that in the presence of charged surfactants the electrostatic interaction that occurs in between the inorganic member and surfactant leads to determining the resulting structure. [16,18,61,86] The model involves three steps: (1) initially there would be the formation of ion pairs that occurs between the surfactant coupled with the polydentate and polycharged inorganic members; following this first step that mainly occurs due to electrostatic interactions, then, the ion pairs pass into a self-organization phase, which usually gives the liquid crystal structure: hexagonal, cubic, or lamellar. [16] The research on the factors that effect the formation of the M41S family of mesoporous materials would be components that comprise the reaction mixture, pH, and temperature [18] that the reaction takes place. [16] The past research on surfactant-inorganic silicate interaction revealed two important observations: the binding of the multidentate silicate oligomers to the positively charged surfactant species coupled with charge density matching that occurs between the surfactant and silicate members would be major parts of the templating assembly of these two key components. [64]

A theory explaining the micelle structure was developed using the geometry coupled with space that the hydrophilic + hydrophobic groups in the micelle occupy: this value would be called the critical packing parameter (CPP) [$CPP = V_H/a_0l_c$]. [64,86] The variable, $V_H$, would be the volume that the optimal head-group space area used by the micelle. The variable, $l_c$, would be the critical length that the hydrophobic tail uses in spaces dimensions. The $l_c$ value varies with the length of the alkyl chain in the surfactant. The value of CPP indicates what will likely be the structure that the micelle adopts from the surfactant in solution. The larger that the value of CPP has would determine the amount of curvature that micelles aggregate into, as shown in Figure 2:5. For example, with single chain surfactant, such as cetytrimethylammonium bromide (CTAB), would have a low CPP value, while surfactants that have double alkyl chains would have large CPP value. The greater the CPP value leads to lamellar meso-structure, as noted in table one below. [64]

| CPP | types of surfactants | expected aggregate structure |
|---|---|---|
| <0.33 | single chain, relatively large heads | spherical or ellipsoidal micelles |
| 0.33-0.5 | simple surfactants with relatively small head | relatively large cylindrical or rod shaped micelles |
| 0.5-1.0 | double chains with large heads | vesicles or bilayer structures |

**Table 2:1 CPP values commonly found for various types of micllar structures.**

**Supplemental text for Table 2:1**-these critical packing parameter values would commonly occur with as follows: < 0.33 surfactant like CTAB with less alkyl carbon tail; 0.33-0.5 range would include surfactant such as CTAB; and 0.5-1.0 value range occurs with CTAB with addition of an alcohol such as ethanol. [64] More heat and ethanol would increase the critical packing parameter value of a given cationic surfactant, such as CTAB. Raman, N. K. *et al*., *Chemistry of Materials* **1996**, *8*, 1682-1701; **DOI:** 10.1021/cm960138+ Permission granted by American Chemical Society Copyright 1996 ©

The first type of synthesis route involves the direct co-condensation of the anionic inorganic (silicate) member coupled to a cationic surfactant ($S^+I^-$). [101] This synthesis route was used to produce MCM-41 & MCM-48 structures. Stucky and co-workers discovered another synthesis route for the production of non-silica periodic tabular structures that use cooperative condensation of the cationic inorganic member bonded to an anionic surfactant ($S^-I^+$). [101] The third and fourth synthesis avenues determined involved the condensation of ionic inorganic member with closely related charged surfactant species, and these reaction pathways would be regulated by the use of counter-ions of opposite charged species ($S^+X^-I^+$), where $X^- = Cl^-$, $Br^-$, or ($S^-M^+I^-$) where $M^+ = Na^+$, $K^+$. In the synthesis route above, the adjustment of the pH would cause the charge density to be varied, which would allow for other production of oxides that were not $SiO_2$. The researchers found that the cubic antimony(V) oxide could be produced in the pH range of 6.5-7.0, and the hexagonal structure formed at a slightly more acidic range (pH = 6.0-6.5). The use of a more acidic species than silicic acid would allow for the cooperative biphase templating to be completed at these lower pH values, which permits a better match of the charge density of the corresponding oxide to the surfactant.

## 2.13 Detailed Later Explanations of How M41S Mesoporous Materials Form

Since the research completed on M41S materials by Mobil Oil researchers in 1992, [98,99] several synthetic mechanisms have been proposed to account in detail how these mesoporous silica materials form and related phase transitions from silica structure to another. [102-107] Stucky and co-workers reported data that pointed to a cooperative assembly mechanism operated between the surfactant-silicate species according to electrostatic intermolecular forces. 102 They discovered through freeze dry kinetics with low cetyltrimethylammonium chloride (CTACl) surfactant concentration and temperature between 30°C to 100°C that initial lamellar structure forms; then, it converts to hexagonal shape under hydrothermal reaction conditions over a ten day period. From the change in formation of lamellar structure to hexagonal coupled with $Q^3/Q^4$ decrease, these researchers indicate Coulombic charge interactions in the aqueous interface between the surfactant-micelle cationic head-group-area and silica precursor domains determine type of mesoporous structure forms and related structural properties: thermal, mechanical, and degree of hydrophilicity/hydrophobocity.

Due to the many types of ions present in aqueous solution, Stucky and co-workers were able to delineate the particular ones' predominantly important in the formation mechanism by comparison of similar silica systems from literature. [102] It was discovered that multidentate silica oligomers of three to seven Si atoms in length with various negative charges and degree of polymerization in high pH (12-14) aqueous solution had binding constants in the range of two orders of magnitude ($\approx 1 \times 10^2$) higher than monovalent anions. These silica oligomers were noted to be more acidic with $pK_a \approx 6.5$ vs. $pK_a$ of 9.8 and 10.7 for monomer ($Si(OH)_3O^-$)and dimer ($Si(OH)_2(O)_2^-$). In contrast to little to no energy advantage for $Si(OH)_3O^-$ monomer to bind to the surfactant cationic head-group-area in comparison to other counter-ions (such as $Cl^-$) in aqueous solution, these small silica oligomers would be able to bind over more of the positive head group area, thereby lower the interfacial energy and increasing the stability of the surfactant-micelles in solution. Interfacial energy would be considered the repulsion between the positively charged head-groups on the surfactant. Multidentate silica oligomers binding in contrast to the chloride counter-ion in CTACl would screen/shield the positive charge more effectively, which means the surfactant molecules were able to pack in tighter resulting in phase transformation. Finally, the binding occurring at the surfactant-silicate interface would lead to enhanced ordering over a lengthen time period as more silica oligomers attempt to shield the positive charge from surfactant head group area.

Although the electrostatic multidentate binding initiates the formation of M41S mesoporous materials, the resulting material would be essentially worthless from an application point of view structurally due to large $Q^3/Q^4$ ratio noted in Stucky and co-workers research findings. [102] Formation of a stable solid precipitate would require the many silanol groups ($Q^3$ etc.) to condense into stable siloxane (Si-O-Si) ($Q^4$) bonds under hydrothermal conditions, which provide energy over the activation energy barrier. [102,108] Stucky and co-workers note polymerization would be slow and require energy. [102] This would be expected due to the movement of surfactant head-group needs to occur. [102,108] Finally, it was discovered that room temperature synthesized vs. high temperature hydrothermal M41S synthesis led to inferior vs. strong, stable porous material, as shown in powder XRD analysis of Si-MCM-41 and Si-MCM-48 under different hydrothermal synthesis temperatures in Figure 2:9 and Figure 2:10. [102,108-111]

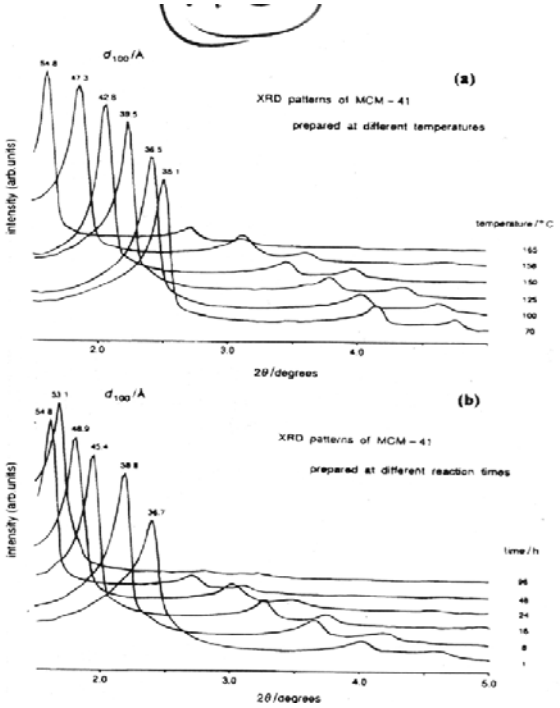


**Figure 2:9 Degree of Condensation of Si-MCM-41 as Function of Hydrothermal Temperature and Time.**

**Supplemental text for Figure 2:9**-As seen in the above powder XRD diffractograms, the higher the synthesis temperature leads to thicker MCM-41 pore walls, as noted in part (a) upper plot. [110] In part (b) at 165°C synthesis temperature the heating period of 48 hours had the largest shift the left coupled with increased peak intensity. The shift to the left means pore walls further condensing into thicker walls and increase in peak intensity infers greater pore wall uniformity. [110] The extended heating to 96 hours causes the undesirable creation of silanol defects, which could be from the reverse reaction occurring in an attempt to release the excess thermal energy. The higher synthesis temperature in the calcinated Si-MCM-41 samples led to unit cell expansion. Cheng, C-F. *et al*., *Journal of the Chemical Society, Faraday Transactions* **1997**, *93*, 359-363; **DOI:** 10.1039/a605136g Permission granted by Royal Society of Chemistry Copyright 1997 ©

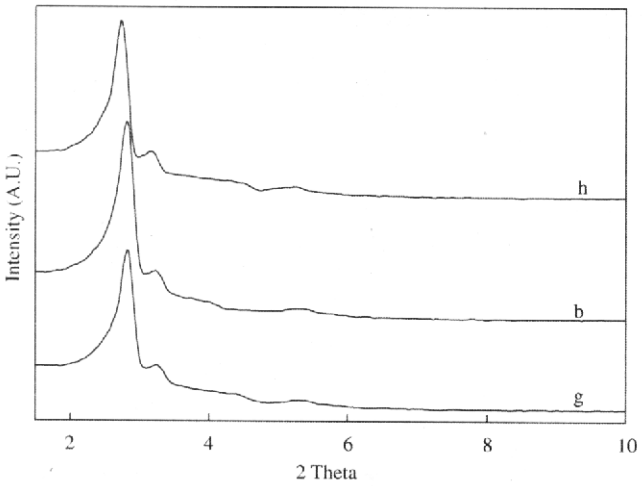


**Figure 2:10 Influence of Hydrothermal Synthesis Temperature on Si-MCM-48 Material.**

**Supplemental text for Figure 2:10**-As seen in the above powder XRD diffractograms, the gradual shift with higher synthesis temperature from lower plot (b) to upper (h) implies an increase in the pore wall thickness. [111] The slight reduction in XRD peak intensity from plot (b) to (h) could mean the synthesis time might need to be reduced at the

higher temperature, according to the proposal put forth in Figure 2:9. The hydrothermal synthesis heating temperature follows: plot (g) 388 K; plot (b) 408 K; and plot (g) 423 K. Si-MCM-48 made at 388 K had the large contraction of 15.38%; whereas, at 423K the Si-MCM-48 had the least amount of unit cell contraction upon calcination of 14.36%. The hydrothermal synthesis time was 24 hours at 388 K vs. 6 hours with 423 K synthesis. The thicker pore walls in Si-MCM-48 plot (g) cause a reduction in the surface area and unit cell, which the MCM-48 structure could be viewed in Figure 2:6; one could conclude that the thicker walls require more space so less walls could fit in the same volume. The reduction in unit cell a0 value could be due to the increased condensation of structure, thereby shortening the Si-O bond in the $SiO_4$ units. Taralkar, U. S. *et al*., *Journal of Physics and Chemistry of Solids* **2008**, *69*, 2075-2081; **DOI:** 10.1016/j.jpcs.2008.03.004 Permission granted by Elsevier Scientific Publishing, Inc. Copyright 2008 ©

The multidenatate silica oligomers binding to surfactant cationic head-group-area results coupled with hydrothermal conditions needed to produce stable mesoporous structure inferred to Stucky and co-workers that interfacial surfactant-silicate region would largely determine the structure formed and related phase changes from freeze dry kinetic experiments. [102] To obtain the most energetically stable head-group-area (A) confirmation value ($A_0$), it was proposed to be affected by balance between electrostatic interactions in the head-group region and optimal hydrophobic alkyl surfactant tail packing. From the steric interfacial energy requirements of the surfactant-silicate system, Stucky and co-workers developed a mathematical model as follows: Gibbs free energy value in relation to head-group-area (A) value would need to be minimized to obtain optimal conformational energy arrangements, as shown in Equation 2:1 and Equation 2:2.

$$A_0 \rightarrow (\partial G/\partial A) = 0$$

**Equation 2:1 Optimal Head-Group Area Partial Derivative of Gribb's free energy with respect to area.**

**Supplemental text for Equation 2:1**-As seen in the above equation, the optimal head-group area would need to be close to the partial Gribb's free energy with respect to partial of area of zero. [102] This implies that the area must increase with the free remaining constant. This would occur if the area increased entropy value was approximately constant.

$$G(A, \rho) = G_{intra}(A) + G_{wall}(\rho) + G_{inter}(A,\rho) + G_{sol}$$

**Equation 2:2 Gibb's free energy as a function of Area and Charge Density.**

**Supplemental text for Equation 2:2**-As seen in the equation, there would be four variables that control the total free energy. [102] $G_{inter}$ and $G_{sol}$ would be of less importance; since, they would stay approximately constant over the synthesis. $G_{wall}$ and $G_{inter}$ have a predominant influence on the total Gribb's free energy value due to change in charge density ($\rho$) and area (A) as the synthesis occurs in the head-group region.

From the above two equations, two conditions would stand out: (1) $A_0$ value would be maximized when partial Gibbs free energy with respect to partial of head-group-area equal zero; and (2) Gibbs free energy would be a function of head-group-area and compositions of individual species within the silica wall. [102] The terms of equation (2) follows: $G_{intra}$ = van der Waals forces + conformational energy of alkyl tail region van der Waals + electrostatic interactions that occur within one micelle in head-group region; $G_{wall}$ = polysilicate free energy of structural formation, which includes solvent, counter-ion, and intermolecular van der Waals + electrostatic forces in the silicate framework (wall); $G_{inter}$ = van der Waals + electrostatic forces due to wall-micelle + micelle-micelle interactions; $G_{sol}$ = composition of solution; and $\rho$ = compositions of different species within the silica wall. $G_{intra}$ variable term determines surfactant-micelle shape adopted corresponding to head-group-area (A) value obtained from equation one; also, the effect of swelling agent employed in synthesis, such as trimethylbenzene (TMB) would be included in this term. Wall polymerization would be governed by the term $G_{wall}$, which would include the multidentate binding value/interaction term responsible for surfactant-silicate/micelle interface. Relationship between the head-group-

area (A) and compositions of species in wall (ρ) would be comprised in the $G_{inter}$ term. $G_{sol}$ would be term for composition of solution related to chemical potential. Interfacial interactions would primarily be electrostatic from the silicate wall and positive charge from head-groups of surfactant-molecules. This interaction between the silicate wall and head-groups of surfactants would comprise the term $\rho_\varepsilon$ known as charge density. Charge density would increase in charge according to 1/A. When the head-group-area (A) would be large, the charge density would spread out over large portion of the negatively charged silica wall leading to lower charge density. Therefore, charge density matching "coined-term" would be optimal electrostatic value $A_0$ from equation (1) with $\rho_\varepsilon$ charge density wall term. These two terms would be interdependent from electrostatic energy interactions. For example, an energetically favorable $A_0$ value of head-group-area (A) would lead to larger charge density matching value $\rho_\varepsilon$ (i.e. smaller $A_0$ value-assume-optimal-would mean 1/A where $A \approx A_0$ leads to larger charge per unit silica wall area-not as spread-out). Stucky and co-workers note from this charge density model of $A_0$ and $\rho_\varepsilon$ would affect unit cell spacing (*d*-spacing) in the final silica product. [102] They claim as further proof of similar mechanism of self-replication mica-type silicates, as noted in literature.

Phase transition from lamellar to hexagonal would be governed by the $G_{wall}$ term which in-turn strongly effected by charge density of the silica wall $\rho_\varepsilon$ term, according to the model of charge density matching presented by Stucky and co-workers. [102] Optimal $A_0$ head-group-area value in the initial early silica oligomers-surfactant stage would be high charge density (i.e. 1/A where $A \approx A_0$ and small $A_0$ value = 1/small value = large charge density) due to large number of negatively charged silica oligomers. In essence, the large charge density of the positive head-group-area (A) would equal negative charges from the silica oligomers for phase transitions to occur. As polymerization of the silica oligomers occurs, the $A_0$ value would increase leading to small charge density matching from the forming wall with less negatively charged silanol groups. This would lead to attempt for the cationic head-group to expand out from tightly pack micelles to try to satisfy the positive charge. Further polymerization/condensation of the resulting silica wall would lead to decrease in initial thickness of wall due to silanol groups only on surface of wall. This wall thickness reduction would not need energy due to less dipole-dipole repulsive forces between the opposite forming silica walls. The resulting silica wall structure would exhibit little condensation, which would permit the head-group-area (A) value to approach optimal $A_0$ head-group-area value. Lamellar-to-hexagonal transition would enable these values (A, $A_0$) to be close numerically. Wall thickness would continue to decrease in order to enable $CTA^+/SiO_2$ volume to stay constant. Finally, the resulting wall thickness for hexagonal phase approximates 8 to 9 Å vs. 10 to 11 Å for lamellar phases.

Double-layer potential at the interface of the cationic head-group-area of the surfactant and silicate oligomers species could be linked to the final wall thickness; since, the amount of silica oligomers at the surfactant head-group-area would be tied to charge compensation, which infers only needed number of silica oligomers at the surfactant-silica interface, according to the charge density matching model. [102] These researchers note that high electrostatic repulsion from the many silanol groups on the silica oligomers at pH = 12 or higher would prevent polymerization, thereby stopping the thickening of the silica wall structure. As shown in Figure 2:10, the charge density matching mechanism would occur as noted above; however, one other possible way would for the surfactant alkyl

tails to tilt at the same time maintaining the planar structure, which would not be favorable from entropy point of view.

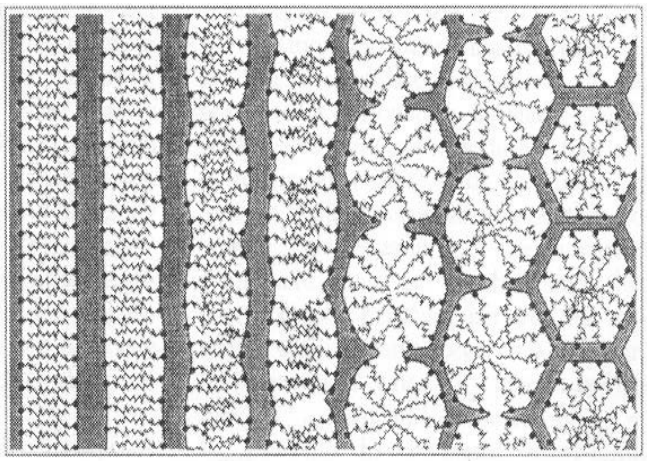

**Figure 2:11 Effects of Charge Density Matching.**

**Supplemental text for Figure 2:11**- As seen in the above image, the charge density matching changes from an initial relatively high value on the right with many silica species to increased condensation with less of the cationic headgroups of surfactant such as CTAB able to find negatively charged silanol (Si-OH) to bind to satisfy the cationic headgroup positive charge. [102] This leads to causing the micelles to attempt a tail-to-tail circular geometry, which causes the hexagonal pore wall to separate. When this occurs, the charge density matching between the silica fragmented was increases due to more Si-OH dangling bonds, instead to $SiO_4$ units. The outcome on the left would be the formation of lamellar planes of silica wall held together by surfactant molecule. The key driving force would be the hydrophobic-hydrophilic interactions between the alkyl tail portion and cationic headgroup. From this line of thinking, one could conclude that use of other species in solution would affect how various structures form and if there were any intermediate phases, such as the metaphase MCM-48. Monnier, A. *et al*., *Science* **1993**, *261*, 1299-1303; **DOI:** 10.1126/science.261.5126.1299 Permission granted by the American Association Advancement of Science Copyright 1993 ©

Stucky and co-workers propose that the $G_{intra}$ and $G_{inter}$ terms determine the surfactant-silica mesoporous structure formed. [102] $A_0$ value would be determined by silicate wall coupled with reaction conditions. High pH caused formation of lamellar structure while low pH caused hexagonal phase. Also, NaCl at high concentrations was found to affect the double-layer potential at the interface of surfactant-silicate, although not significantly up to 0.1 M.

Li and co-workers applied the mathematical charge density model to explain why TEOS was the optimal silica precursor for forming Fe-MCM-48. [112] They noted that too fast or slow condensation rate would have adverse effect on forming Fe-MCM-48, according to the thermodynamic model by Stucky and co-workers. [102,112] As noted earlier, $G_{inter}(A, \rho)$ would be a function of cationic head-group-area and composition of wall variables while $G_{wall}(\rho)$ term comprised of composition of wall. [102] Li and co-workers note $G_{intra}$ and $G_{sol}$ from equation (2) of less importance when reviewing the effects of Si precursors on final product formed. [112] As noted earlier with equation (1), when the head-group-area (A) approaches the optimal $A_0$ value, the $A \approx A_0$ would be related to charge density interaction between silica oligomers and head-group region ($\rho_\varepsilon$). [102] Further $A_0$ value would vary by type of synthesis, which controls morphology of final product. The binding that occurs with larger multidentate ligands as the small silica oligomers condense does not easily occur with fumed silica due to mostly condensed $SiO_4$ units, as noted in Figure 2:11; therefore, the optimal $A_0$ value decreases due to silicate anions forming before attachment to head-group region. This causes lamellar MCM-50 structure to form. In contrast, silica oligomers from TEOS condense

quicker, which will cause formation of larger multidentate silica oligomers that could bind to several cationic head-groups, thereby reducing the head-group-area ($a_0$) value in surfactant packing equation ($g = V/a_0l_c$) leading to phase transition to Ia3d bicontinuous MCM-48 structure. [112] {**Drawing of the effect of different g-values found in Appendix A-A:1-A:13**} Water glass condenses so quickly that needed interaction with surfactant head-group to adopt shape does not occur on the order of structure, thereby leading to poorly ordered structure, as shown in Figure 2:13 synthesized and calcinated Fe-MCM-48 with different silica precursors with $Fe_2(SO_4)_3 \bullet xH_2O$ metal source.

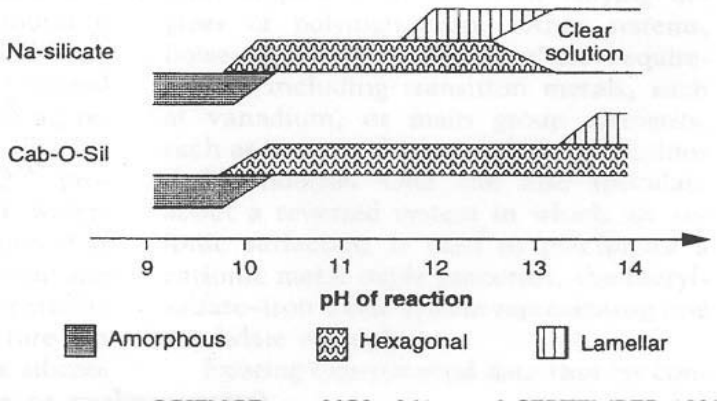


**Figure 2:12 Effect of pH value of two common silica sources as function of the amount condensed $SiO_4$ units.**

**Supplemental text to Figure 2:12**-As seen in the above image, the Cab-O-Sil fumed silica comprised of mostly fully condensed $SiO_4$ units would retain structure up to approximately pH of 13; whereas, sodium silicate initially converts to another structure between pH of 11-12 and as monomers starting at pH of 12.5. [102] This clearly shows that the degree of fully condensed $SiO_4$ units will profoundly effect the charge density matching and phase conversion, which means intermediate structures such as MCM-48 would more easily be made with sodium silicate due to less harsh reaction conditions needed. Also, the affect of pH as function of the degree of fully condensed $SiO_4$ units determine the stability of M41S materials. Monnier, A. *et al*., *Science* **1993**, *261*, 1299-1303; **DOI:** 10.1126/science.261.5126.1299 Permission granted by American Association Advancement of Science Copyright 1993 ©

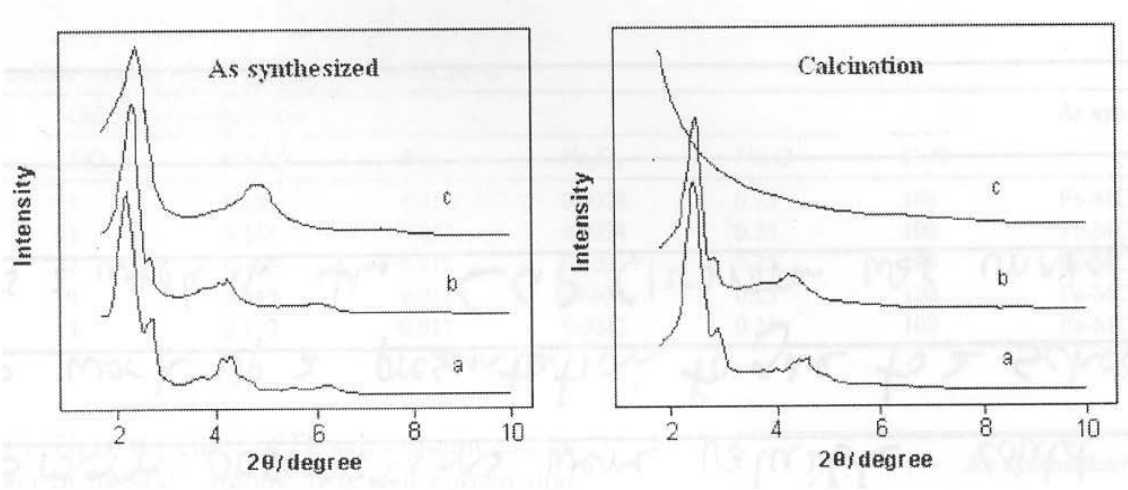


**Figure 2:13 Effect of Different Silica Precursors as a function of $Fe_2(SO_4)_3 \bullet xH_2O$ in Fe-MCM-48.**

**Supplemental text for Figure 2:13**-As seen in the above powder XRD diffractograms of various silica precursors with use of $Fe_2(SO_4)_3 \cdot xH_2O$ metal precursor. [112] In both above plots the following silica precursors listed in letters: (a) TEOS; (b) water glass; and (c) fumed silica. TEOS forms monomers silica species, which condense into silica

oligomers upon hydrolysis in basic solution. Water glass would mainly be comprised of the silica oligomers. Fumed silica made of fully condensed silica $SiO_4$ units. This difference in ease of hydrolysis and formation of silica oligomers that bind to the headgroup region of the surfactant determine if the desired Fe-MCM-48 structure forms and the degree of condensation. Referring back to Figure 2:12 above, the needed harsh reaction conditions would increase the probability of passing the MCM-48 metaphase, which would be seen in both powder XRD plots in Figure 2:13. When the charge density matching was not optimal, as seen in both powder XRD diffractograms above in (b) and (c), the formed structure has poor primary and secondary characteristics. In (a) the powder XRD diffractogram of TEOS prepared Fe-MCM-48 has a few distinct secondary peaks at 4-5° 2θ, which means greater number of fully condensed $SiO_4$ units. Zhao, W. *et al*., *Microporous and Mesoporous Materials* **2007**, *100*, 111-117; **DOI:** 10.1016/j.micromeso.2006.10.020 Permission granted by Elsevier Scientific Publishing, Inc. Copyright 2006 ©

Research completed later on by Stucky and co-workers $^2H$ NMR analysis revealed that double-four-ring (D4R) (cubic octamer) was the main silica species that initiates formation of silica meso-structure at high pH = 13, as shown in Figure 2:14. [103] Silica D4R oligomers possess greater favorability vs. other negatively charged silica species; since, the D4R silica oligomer unit has on each face four oxygen atoms that could bind to the surfactant cationic head-group-area similar to a traditional multidentate ligand. This enhanced binding interactions between the D4R silica oligomers and surfactant cationic head-group-area further enhances Coulombic charge interaction, thereby leading to two-to-three cetyltrimethylammonium ($CTA^+$) ions attaching to the D4R unit. Counter-ions would affect the Gouy-Chapman-Stern double-layer through reduction of repulsion between the individual surfactant cationic head-groups due to the screening/shielding ability of various guest anions toward the positive charges. Guest anion concentration above the threshold value in aqueous solution cause changes in at the interface occurring between the forming silica structure and surfactant molecules, which directly increase the electrostatic component over other intermolecular forces: van der Waals, and hydrophobic. Therefore, the final morphology acquired by the mesoporous silica material would be dominated by the guest anion concentration. Finally, cooperative assembly mechanism proposed by Stucky and co-workers indicates at the surfactant-silicate interface charge density matching and surfactant packing parameter g-value determines if a phase transition will readily occur in M41S synthesis. [102,103] [Note: charge density matching and surfactant packing parameter would be directly related by activation energy barrier with high charge density, partially polymerized silica structure, able to facilitate enhanced structural rearrangement. Surfactant packing parameter equation reveals that the (V) volume variable derived from surfactant volume and of alkyl tail region and cationic head-group-area ($a_0$) strongly effect the g-value with alkyl length of surfactant approximating constant through various phase transitions: $g = V/a_0l_c$.]

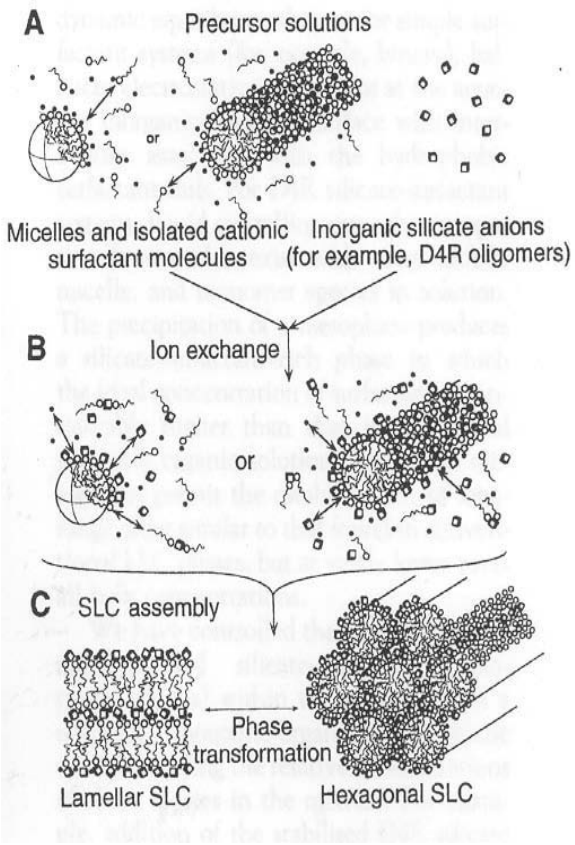


**Figure 2:14 Charge Density Matching mechanism as it occurs with predominantly D4R Silica Oligomers.**

**Supplemental text for Figure 2:14**-As seen in the reaction diagram, the silica oligomers, such as double-four-ringed (D4R) units bond initially to the forming surfactant micelle in part (A) above. [103] When the charge density changes within the forming silica structure, surfactant molecules would be expelled with counter-ion, such as bromide ion in CTAB in part (B). Due to continuing change with the charge density matching between condensing silica oligomers, the hexagonal formed structure could convert to lamellar if there were lengthen reaction conditions with the silica wall lacking silanol groups and surfactant headgroups attempting to satisfy the charge imbalance in part (C). Firouzi, A. *et al*., *Science* **1995**, *267*, 1138-1143; **DOI:** 10.1126/science.7855591 Permission granted by American Association Advancement of Science Copyright 1995 ©

Previous research primarily by Stucky and co-workers led to understanding of thermodynamic and kinetic components of charge density matching plus application of surfactant packing parameter in phase transitions in mesoporous silica materials [56,102,103]; nevertheless, data to conclusively report how charge density matching and surfactant packing parameter function, and which has greater influence, in the M41S mesoporous silica phase transitions was still neeeded. In situ X-ray diffraction analysis employed, by Stucky and co-workers to monitor the phase transitions between hexagonal MCM-41 and lamellar MCM-50, indicated lamellar-to-hexagonal had lower phase transition activation energy barrier; whereas, the hexagonal-to-lamellar transition required greater energy to over-come the phase transition barrier, as shown in Figure 2:15. [104] Lengthen hydrothermal heating periods were shown to increase the complete polymerization to stable $SiO_4$ units in previous research by Stucky and co-workers. [103] Therefore, the increased hydrothermal reaction time of 5.5 hours for synthesis of MCM-50 vs. MCM-41 of 30 minutes facilitates greater $SiO_4$ units in the former material. [104] From an thermodynamic point of view, the increased activation energy barrier of highly polymerized material leads to more energy input to cause phase transition, so MCM-50

to MCM-41 lower energy requirement meant another variable was functioning in the phase transition. These researchers proposed charge density matching occurring at the surfactant-silicate interface could be the reason for enhanced phase transition in MCM-50 to MCM-41. As noted earlier, charge density matching includes $A_0$ optimal electrostatic value of surfactant cationic head-group-area plus interaction of silica wall with these cationic species to form the charge density term $\rho_\varepsilon$. Further evaluation of how to obtain optimal $A_0$ values would indicate the following: partial deferential calculus $(\partial G/\partial A) = \Delta G/\Delta A$, and $\Delta G = \Delta H - T\Delta S$. Due to no bond breaking/forming in optimization of head-group-area electrostatic interactions $A_0$ value occurs, change in enthalpy, $\Delta H$, would be zero ($\Delta H = 0$). Assume the temperature for optimizing the $A_0$ value stays constant (this means the value stays the same throughout the process), then, change in entropy term, $\Delta S$, would be the variable to control optimal head-group-area $A_0$ value. This means change in conformation of molecules, in essence, would be the degree of disorder that determines the idea $A_0$ head-group value. When the change in area, $\Delta A$, value increases with only small changes in entropy, where $\Delta G = \Delta S$, this value obtained from $\Delta G/\Delta A$ equation would approximate a small number close to zero. Closer inspection of charge density $\rho_\varepsilon$ term in the charge density matching concept indicates inverse relationship of $1/A$, which approximates $A_0$ optimal value close to zero. This means charge density $\rho_\varepsilon$ = [(cationic electrostatic charge interactions/area)/(space of interface of surfactant-silicate wall)] Assuming the electrostatic charge approximates constant and a larger silica wall area covered due to greater polymerization to $SiO_4$ units, this would lead to reduced charge density $\rho_\varepsilon$ value. Therefore, one could conclude larger silica wall area with equal to or less cationic charge from the surfactant head-groups leads to lower charge density matching. In practice this would mean phase transition for lamellar (high charge density) to hexagonal (lower charge density) occurs with greater energy input, as proposed by Stucky and co-workers, to increase the change in area value ($\Delta A$) and force some surfactant out of the structure. [104] As shown in Figure 2:15 lamellar to hexagonal transition actually needed less energy. The opposite behavior exhibited might be due to electrostatic binding interaction between surfactant-silicate species not as large of value. Lower energy value would mean reduced activation energy barrier assuming the lamellar structure was not completely condensed into stable $SiO_4$ units. Reapportion of surfactant in the phase transition would require additional energy while the phase has greater favorability when little surfactant needs to be moved in or out of the forming meso-structure. One could conclude that the lamellar structure had intermediate degree of condensation. A combination of increased electrostatic repulsion between cationic head-groups with charge density increasing and stable siloxane bonds would be the reason for the higher activation energy in hexagonal to lamellar transition, as shown in Figures 2:15 and Figure 2:16 Higher electrostatic charge repulsion of surfactant cationic head-groups would require additional energy to cause phase transition, as shown in pictorial form in Figure 2:16 Finally, the degree of condensation, not just charge density matching, would explain the above phase transition results; the hexagonal structure would need less synthesis time due to lower energy barrier from reduced surfactant cationic head-group-area repulsion, thereby leading to less energy need to obtain idea $A_0$ value and form desired structure.

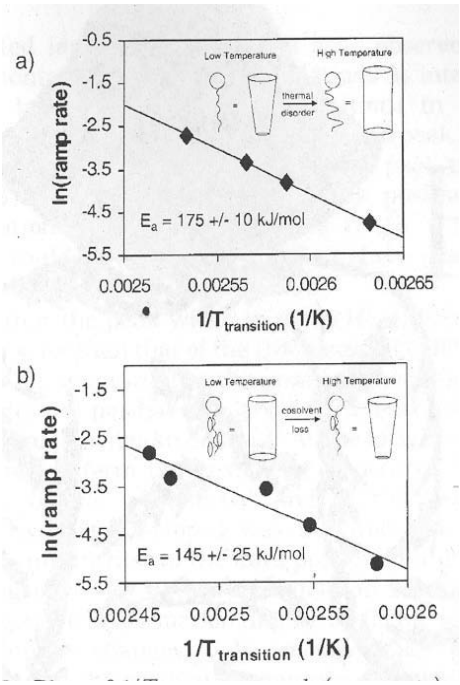


**Figure 2:15 Transformation Activation Energy Plots as Function Reaction Temperature.**

**Supplemental text for Figure 2:15**-As seen in the plot (a), the activation energy needed for a phase transformation from hexagonal MCM-41 to lamellar MCM-50 would be greater than in plot (b) of lamellar to hexagonal, according to Ozawa mathematical relationship. [104] [ln(ramp rate) = $-E_a/RT_{transition}$ + c, Ozawa relationship] In the inset of each of these above plots would be the effect of solvent + surfactant with phase transformation with addition of thermal energy, which changes the surfactant packing parameter. However, the opposite occurred with lamellar-to-hexagonal requiring more heat, thereby infers that charge density matching would be the variable that controls the relative ease of phase transformation: this again shows why the charge density matching must be optimal to form high quality MCM-48. Tolbert, S. H. *et al*., *Chemistry of Materials* **2001**, *13*, 2247-2256; **DOI:** 10.1021/cm0003727 Permission granted by American Chemical Society Copyright 2001 ©

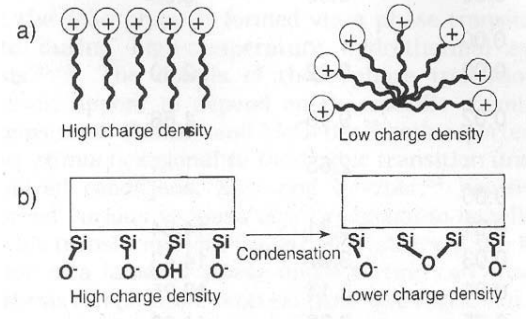


**Figure 2:16 Effects of Both High and Low Charge Density.**

**Supplemental text for Figure 2:16**-As seen in part (a), the high charge density occurs in the headgroups close together due energy advantage to satisfy the charge imbalance between the cationic and anionic silica fragments. [104] With condensation proceeding, the charge density decreases with the headgroups spreading out to find compensating negative charge. If the charge density matching was optimized, intermediate structure, such as MCM-48, would form as stable product. Tolbert, S. H. *et al*., *Chemistry of Materials* **2001**, *13*, 2247-2256; **DOI:** 10.1021/cm0003727 Permission granted by American Chemical Society Copyright 2001 ©

Previous M41S mechanism studies had focused on cooperative mechanism due to charge density matching, major silica oligomers responsible for forming final structure, and related lamellar MCM-50 to hexagonal MCM-41 phase transitions. [102-104] However, phase transition from MCM-41 to MCM-48 had not been delineated in previous

studies. From the introduction of M41S mesoporous silica materials by Mobil Oil researchers in 1992, [98,99] the three-dimensional Ia3d bicontinuous MCM-48 structure appeared to have the largest number of potential applications. Kinetically MCM-48 would be considered metastable (in between two other phases kinetically more stable), although thermodynamically favored. [64] Gallis and Landry earlier had shown that the phase transition from MCM-41 to MCM-48 was driven by introduction of ethanol to the reaction mixture due to increase in the surfactant packing parameter from ethanol entering into the surfactant tail and increasing the volume (V) variable. [18] In situ X-ray diffraction analysis was completed by Stucky and co-workers to delineate how portions/sections of p6m MCM-41 transformed to Ia3d MCM-48. [105] They proposed two transformation models to explain why certain parts of MCM-41 wall structure dissolve and reform in a different plane. Similar to Tolbert *et al.* work on MCM-50 to MCM-41 phase transitions, [104] MCM-41 transformations to MCM-48 has an activation energy barrier, which increases as greater polymerization occurs with more stable siloxane bond formation in MCM-41 to MCM-48. When the mesostructure has partial polymerized framework, the activation energy barrier would be lower with charge density matching and surfactant packing parameter working synergistically together. Tolbert and co-workers found that less polymerized mesoporous silica would convert to another form at lower reaction temperatures. [108] A three hour polymerization period was employed in MCM-41 synthesis followed by hydrothermal heating slowly to 150°C in the MCM-41 to MCM-48 phase study. [105] Research results indicated that only a few siloxane (Si-O-Si) bonds controlled phase transformation, according to smooth transformation in situ X-ray analysis. This means phase transition would require a small amount of energy to increase the surfactant packing parameter volume (V) value and form MCM-48, which explains why too much energy easily cause the surfactant to re-orientate to higher energy conformation to form lamellar phase due to formation of more partially charged wall species. This phase transition occurs smoothly as hydrothermal temperature was increased slowly with MCM-41 (10) and (20) reflections forming (211) and (422) MCM-48 reflections in the beginning stages of structural transformation process, as shown pictorially in Figure 2:17 viewing down [111] direction.

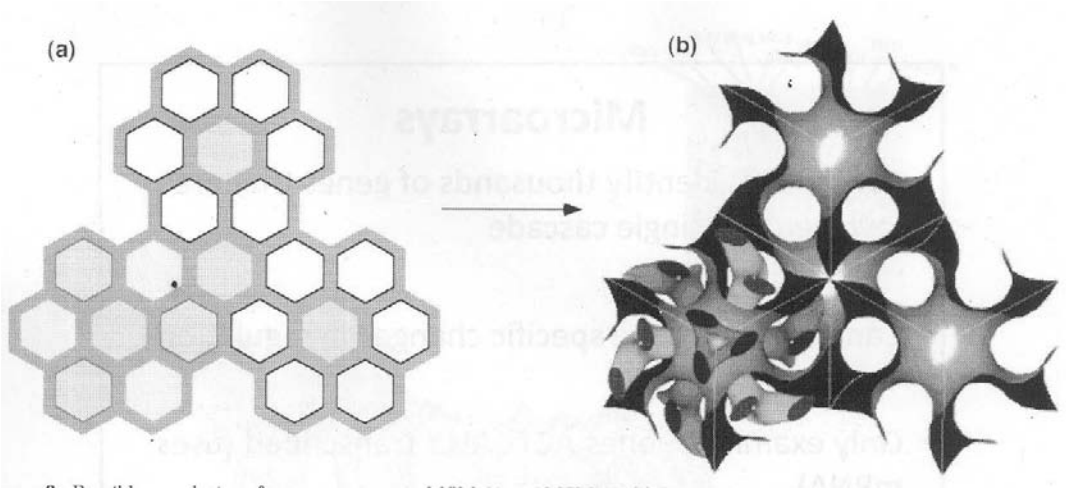


**Figure 2:17 Visual Representation of MCM-41 to MCM-48 Transformation.**

**Supplemental text of Figure 2:17**-As seen in the above image, the transformation process would require the hexagonal MCM-41 pores to twist lengthwise starting from the center. [105] The resulting pore structure would resemble Figure 1:1, Figure 2:1, Figure 2:4, and Figure 2:6 which show the needed curvature to form Ia3d bicontinuous

MCM-48 structure. It would seem from the above view that the level of energy input would be small depending on the degree (amount) of formation of $SiO_4$ units in MCM-41 structure. Landry, C.C. *et al*., *Chemistry of Materials* **2001**, *13*, 1600-1608; **DOI:** 10.1021/cm000373z Permission granted by American Chemical Society Copyright 2001 ©

Stucky and co-workers observe only approximately eight minutes needed at 150°C for hexagonal to cubic formation to occur, which could infer similar structural positions common in both MCM-41 and MCM-48 coupled with close activation energy barriers of formation. [105] The surfactant packing parameter value would decrease in the transformation without a continuous distortion of the MCM-41 structure so that the final position of the silica wall rests on a minimal energy surface. This might explain why the transformation process must occur exactly for MCM-48 to form. The surfactant packing parameter could be increased through formation of one larger cylinder from two small ones in MCM-41, otherwise known as the cylinder merging mechanism. Structural fluctuations in forming the MCM-48 structure would lead to one central cylinder surrounded by six merging to form six sub-sections in the other cylinders, as noted to be the branching monkey towers mechanism. These two MCM-48 formation mechanisms, as shown in Figure 2:18, would mainly be different by the number of bonding reallocation and related activation energy barriers. Transformation would be favorable kinetically in central larger central cylinder formation from less bond re-arrangement in comparison to the branching mechanism. Due to the interconnected bonds between the six sections in the branching monkey tower mechanism, it would have enhanced thermodynamic favorability. Stucky and co-workers results indicate both mechanisms would be at work in forming MCM-48. [105]

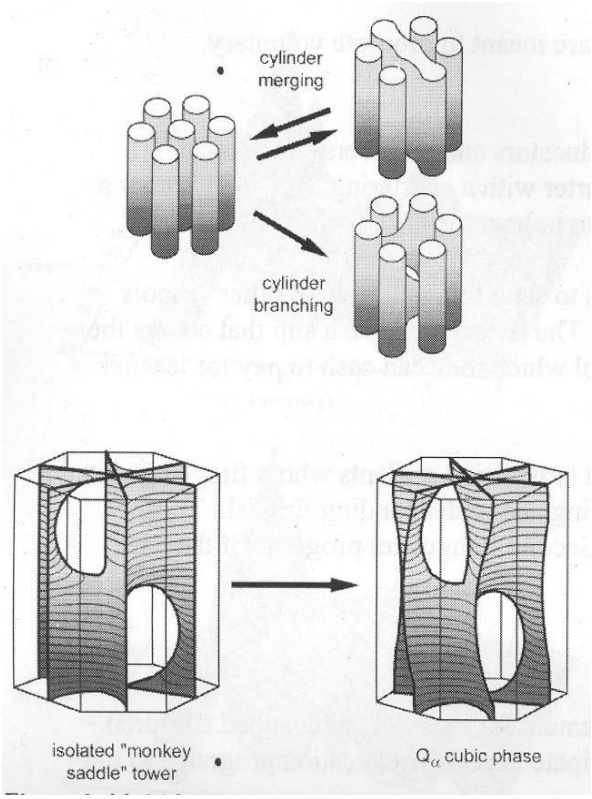


**Figure 2:18 MCM-41 to MCM-48 Transformation Visual Models.**

**Supplemental text for Figure 2:18**-As seen in the above two transformation models of how MCM-41 converts over to MCM-48, the major differences would be the elimination of the central cylinder pore in MCM-41 with cylinder merging mechanism to form a larger pore. [105] Branching mechanism would occur where the central pore dis-

solve and reform at adjacent walls. From a kinetic point of view, cylinder merging would be more favorable then the cylinder branching mechanism; since, the branching mechanism requires more bond breaking and reforming. However, the formation of more stable bonds in the branching mechanism causes this mechanism to occur form a thermodynamic viewpoint. In the bottom images would be a comparison of the similarilies between the "monkey saddle" tower and cubic Ia3d space group. The main difference would be the curved surface known in the Ia3d space group. Landry, C. C. *et al*., *Chemistry of Materials* **2001**, *13*, 1600-1608; **DOI:** 10.1021/cm000373z Permission granted by American Chemical Society Copyright 2001 ©

Previous research by Stucky and co-workers layed the foundation for cooperative assembly mechanism, charge density matching concept, and application of surfactant packing parameter in M41S synthesis. [86,102-105,113] These various studies revealed kinetic, thermodynamic, and activation energy barrier directly determine the final product morphology. [102-105] Practically, this meant the degree of polymerization of the initial silica structure would determine how easily phase transitions occurred both from kinetic and thermodynamic point of view. Tolbert *et al.* work on MCM-50 to MCM-41 and Landry *et al.* results demonstrated the importance of both rates and energy stability barriers in bond reallocation in phase transformations. [104,105] Interfacial interactions studied by Stucky and co-workers facilitated deepen understanding of initial silica structure formation from charge density matching and surfactant packing parameter coupled with discovery of the major silica oligomers responsible for multidentate binding. [102,103] Monnier *et al.* indicated that the electrolyte concentration below 0.1 M using NaCl did not have a major influence on formation of meso-strructure. [102] Firouzo *et al.* noted guest anions from addition of electrolyte would effect the phase transitions. [103] Finally, neither of these earlier or later studies by Stucky and co-workers delineated exactly how guest ions would effect phase transitions and long-range order of silica M41S mesoporous materials. [102-106]

Through the use of various instrumental analysis methods, Bonneviot and co-workers presented a model of slight mismatch of charge density matching needed to form stable, highly ordered Si-MCM-48. [107] This model complements the work of Stucky and co-workers [102,103] with needed modification for electrolyte effects related to formation of cubic phase. [107] Results with various guest ions indicates that the simple $\{S^+, I^-\}$ synthetic model, where $S^+$ = cationic surfactant; $I^-$ = negatively charged silica oligomers, would be better explained with addition of electrolytes in the following formula: $\{(1\text{-}p)S^+, pC^+, mH_2O, xX^-, (1\text{-}n)I^-\}$, where p = cations; m = number of water molecules (concentration); n = anions in Helmholtz planes. As noted in Anpo and co-workers work on the synthesis of MCM-48, 114 at high concentrations, (usually at or above 0.1 M) these guest ions complete with surfactant cationic head-group and negatively charged silica oligomers in formation of Si-MCM-48. [107] Guest ions ability to effect the polymerization of Si-MCM-48 would be due to mediation of electrical balance of charges with slight charge imbalance at the forming silica wall and surfactant cationic head-group region, which causes noted interface curvature.

Introduction of guest ions occurred in synthesis of Si-MCM-48 through pH modification with following acids: HCl, $HNO_3$, and $H_2SO_4$. [107] As shown in Figure 2:19 the pH directly effected when certain M41S phases occurred, with all other variables constant, one could observe that the $H_2SO_4$ addition led to best formed Si-MCM-48. Similar result was discovered in Anpo and co-workers research with the same anions: $Cl^-$, $NO_3^-$, and $SO_4^{2-}$. [114] In addition, previous research found that the pH was a critical parameter in Si-MCM-41 and Si-MCM-48 synthesis, which could be due to charge density matching from degree of negative charge on the silanoate (silica oligomers) groups, as noted by Monnier *et al.* [102,114,115] Low pH value appeared to favor Si-MCM-41 in this research work, [107] thereby increasing the activation energy barrier, as noted in Tolbert *et al.* work on phase transitions. [104] Referring to

Table 2:2, one could view that $H_2SO_4$ used led to least (smaller) $H_2O$/Si ratio in solid silica; whereas, $NO_3^-$, and $Cl^-$ anions cause greater retaination of water in solid material. [107] Trends from the initial synthesis of M41S materials, as a function of pH, shows the following: lower the pH value, the less guest ions and related water molecules in the material; $NO_3^-$ and $H_2SO_4$ acid led to enhanced hydrophobicity of silica wall, in contrast to HCl use; silianoate concentration decreased with pH but not as much with the counter-ions employed; and both guest cations and anions would be located in the surfactant-silicate interface region. To test the importance of pH, $NaNO_3$ was used in one synthesis at pH ≈ 11 with poorly formed MCM-48, which upon calcination structure deteriorated.

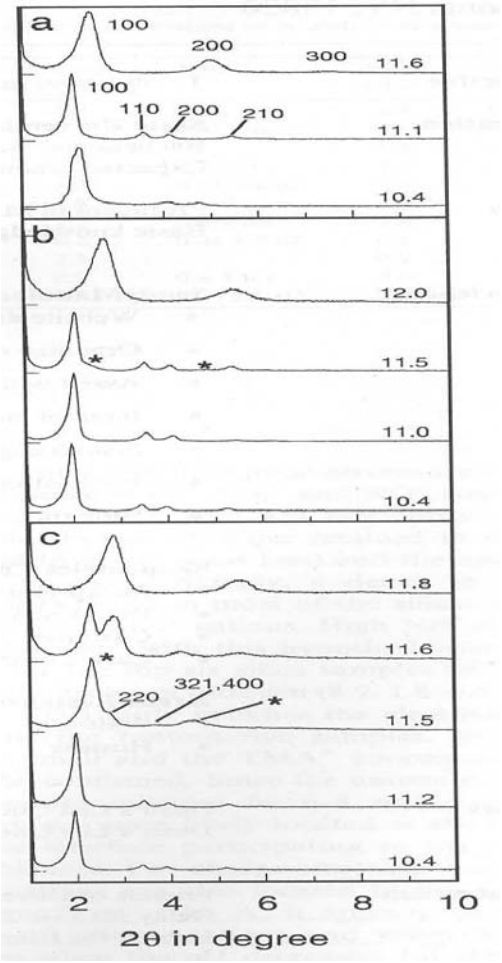


**Figure 2:19 Effect of pH and Counter-ion in formation of MCM-48.**

**Supplemental text for Figure 2:19**-As seen in above powder XRD diffractograms, the pH value and counter-ion (anion) would directly have an effect of determining if MCM-48 forms. [107] Clearly, in a-c plots above, the pH value would be critical for forming MCM-48, as noted previously in literature. [17] The following anions in solution were as follows: (a) $Cl^-$; (b) $NO_3^-$; and (c) $SO_4^{2-}$. The chloride anion does not form MCM-48; whereas, nitrate anion has traces of MCM-48 at pH of 11.5. [107] With use of sulfate anion at pH of 11.5, MCM-48 forms with a few secondary peaks in 4-5° 2θ range. The reason why sulfate anion would be superior for forming MCM-48 would be due to ability to effectively remove water molecules from the surfactant cationic headgroup region, which permits optimal surfactant parking parameter value. In addition, the larger negative charge facilitates the better charge density matching interactions (lower energy configuration), thereby allows the MCM-48 formation with relative ease. Echchahed, B. *et al*., *Microporous and Mesoporous Materials* **2001**, *44-45*, 53-63; **DOI:** 10.1016/S1387-1811(01)00168-8 Permission granted by Elsevier Scientific Publishing, Inc. Copyright 2001 ©

Chemical analyses and XRD characteristics of as-synthesized silica mesophases of series A obtained with acidification using various mineral acids[a]

| Acid | pH ±0.1 | Phases[b] | $d_{hkl}$[c] ±(1 Å) | FWHM-±0.005 | $CTMA^+$/Si ±0.1% | $SiO^-$/Si ±0.1% | $Cl^-$/Si ±0.1% | X/Si % | $\Delta\Sigma^{\pm}$[d] ±0.4% | $H_2O$/Si[e] ±0.5% |
|---|---|---|---|---|---|---|---|---|---|---|
| $HNO_3$ | 12.0 | L | 33 | 0.575 | 17.5 | 23.9 | 2.3 | 0.2 ± 0.1 | 8.9 | 139.0 |
| $H_2SO_4$ | 11.8 | L | 34 | 0.520 | 21.5 | 22.5 | 0.7 | 0.04 ± 0.02 | 2.5 | 106.0 |
| HCl | 11.6 | L | 36 | 0.470 | 21.2 | 24.0 | 9.1 | – | 11.5 | 200.0 |
| $HNO_3$ | 11.5 | H (+C)[f] | 43 | 0.220 | 16.8 | 17 | 3.2 | 0.7 ± 0.1 | 4.1 | 69.0 |
| $H_2SO_4$ | 11.6 | C | 38 | 0.340 | 16.0 | 16.9 | 3.0 | 0.09 ± 0.02 | 3.9 | 86.5 |
| HCl | 11.1 | H | 42 | 0.220 | 18.9 | 19.0 | 1.5 | – | 1.6 | 60.8 |
| $HNO_3$ | 11.0 | H | 44 | 0.210 | 16.6 | 16.4 | 2.2 | 0.6 ± 0.1 | 2.6 | 56.5 |
| $H_2SO_4$ | 11.2 | H | 45 | 0.195 | 15.3 | 15.6 | 0.4 | 0.04 ± 0.02 | 0.8 | 34.3 |
| HCl | 10.4 | H | 40 | 0.320 | 10.6 | 9.2 | 2.3 | – | 0.9 | 11.4 |
| $HNO_3$ | 10.4 | H | 45 | 0.200 | 13.6 | 14.9 | 0.9 | 0.4 ± 0.1 | 3.0 | 44.8 |
| $H_2SO_4$ | 10.4 | H | 46 | 0.205 | 13.9 | 14.5 | 0.2 | 0.04 ± 0.02 | 0.9 | 62.6 |

[a] 1 g of silica washed twice with 200 ml of water at 25°C.
[b] L = lamellar, H = hexagonal and C = cubic.
[c] 100 for lamellar and hexagonal and 211 for cubic.
[d] Charge deficit (missing positive charges per Si).
[e] Obtained from fire mass loss taking into account that only $SiO_2$ is left after calcination.
[f] Contains traces of cubic phase.

**Table 2:2 The effects of various mineral acids on retention of water in silica structure.**

**Supplemental text for Table 2:2**-As seen in the column label acid, use of sulfuric acid was the only anion that formed cubic MCM-48 at pH of 11.6 silanoate concentration of $SiO^-$/Si = 16.9 vs. 17 for nitric acid. [107] Focusing on the $H_2O$/Si ratio, the use of sulfuric acid at pH of 11.8 had the lowest water retention. Clearly, this infers that the sulfate anion effectively pulls water molecules away from the headgroup-silicate region. Echchahed, B. *et al*., *Microporous and Mesoporous Materials* **2001**, *44-45*, 53-63; **DOI:** 10.1016/S1387-1811(01)00168-8 Permission granted by Elsevier Scientific Publishing, Inc. Copyright 2001 ©

Anpo and co-workers reasoned why $SO_4^{2-}$ anion caused the most stable MCM-48 structure was due to sulfate ion's large hydration energy vs. $NO_3^-$ and $Cl^-$ ions. [114] Bonneviot and co-workers report that these guest anions would be solvated by six-to-eight $H_2O$ molecules [107]; however, Anpo and co-workers indicate sulfate anion would have greater self-hydration vs. nitrate or chloride anions. [114] They further expressed that sulfate ion's ability to dehydrate would include the surfactant-silicate interface where hydrated cationic head-group-area and silanoate species interact. Bonneviot and co-workers reasoned that the large dielectric constant of water and therefore its ability to lower electrostatic interactions leads to dissociation of electrolyte. [107] If $H_2SO_4$ completely dissolves, this would lead to the opportunity for sulfate anion to dehydrate the surfactant-silicate interface, which Bonneviot and co-workers indicate would increase the interfacial energy between the positive charged cationic head-groups of $CTA^+$ and multidentate negatively charged silanoate groups, thereby leads to increased long-range order of M41S material, as noted in Table 2:2 under FWHM column. The trend of enhanced hydrophobicity with larger hydration energy of guest anions could be viewed in Table 2:2 with lower silanol group concentration and therefore more stable $SiO_4$ units formed ($SiO^-$/Si) column. This ability to self-hydrate would explain the result of sulfate ion present research and others' work on Si-MCM-48 & Al-MCM-48. [107,114,116] Sulfate ion would enhance the charge density matching and also reduce the hydration of cationic head group area, $a_0$, value in the surfactant packing parameter: $g = V/a_0 l_c$. This proposal by Bonneviot and co-workers [107] that higher interfacial energy leads to longer range order contrasts Wan and Zhao proposal that the reduced interfacial energy would determine the final structure formed. [17] Zhao and co-workers indicate the mesoporous structure formed would be determined by Gribb's free energy of formation ($\Delta G$); however, the surface free energy ($F$) that was involved in the second stage of forming the colloidal particle

would be in competition with Gribb's free energy. [117] The outcome of this interchange between these two energies would determine the type of structure formed. These steps in the colloidal phase separation mechanism shown in Figure 2:20.

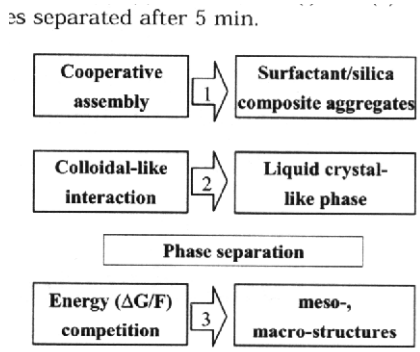


**Figure 2:20 Colloidal Separation Phase Mechanism Flow Diagram.**

**Supplemental text for Figure 2:20**-As viewed in the above flow diagram, the colloidal phase separation mechanism has three steps: cooperative assembly, colloidal interactions, and competition between Gribbs free energy and surface free energy. [117] Cooperative assembly would be based on charge density matching between silicate-surfactant interface, as noted throughout this section. [102-107] Colloidal interactions would be where smaller particles form into larger ones. [117] Competition occurring in the final step between Gribbs and surface free energies determines the resulting structure and morphology. Support for this mechanism would be from scanning electron microscopy (SEM) images taken at different time intervals that show the growth of the colloidal particle. Yu, C. *et al.*, *Chemistry of Materials* **2004**, *16*, 889-898; **DOI:** 10.1021/cm035011g Permission granted by American Chemical Society Copyright 2004 ©

The interface between surfactant cationic head-group-area and negatively charged silanol groups could be represented as a double-layer of two Helmholtz planes with anions on one side and cations on another side. [107] When the guest anion affinity would be large, such as $SO_4^{2-}$ ion, or higher concentration as the $NO_3^-$ and $Cl^-$ anions, the result would be a decrease in Helmholtz planes due to enhanced screening of positive charges, thereby permits surfactant cationic ammonium head-groups to move in closer together with less repulsion. Practically, this means an increased surfactant packing parameter g-value with smooth transition from MCM-41 to MCM-48, and the over-all curvature would be modulated more precisely with guest anions, as noted in high quality Si-MCM-48 production by Anpo and co-workers. [114] Any other guest cations, such as $Na^+$ or trimethylammonium-$TMA^+$, in this synthesis would effect surfactant cation head-groups interface with negatively charged silicate species. [107] Fluctuations of charge density from slight mismatch in Helmholtz planes periodically leads to the curvature noted in Ia3d bicontinuous three-dimensional structure. The pH would affect the silanoate group density, thereby affect appearance of concave or convex curvature, as shown in Figure 2:21. The reason for this would be due to different average distances between guest anions and cations in perspective Helmholtz planes. Slight fluctuations by pH and guest ions would lead to concave/convex-cavity-spheres. In contrast to the proposal put forth by Stucky and co-workers in earlier research on charge density matching M41S mechanism, [102] when the charge density was exactly the same for both Helmholtz planes, the formation of lamellar structure would occur instead of needed slight local imbalance of charges to generate the bicontinuous three-dimensions cubic structure. [107]

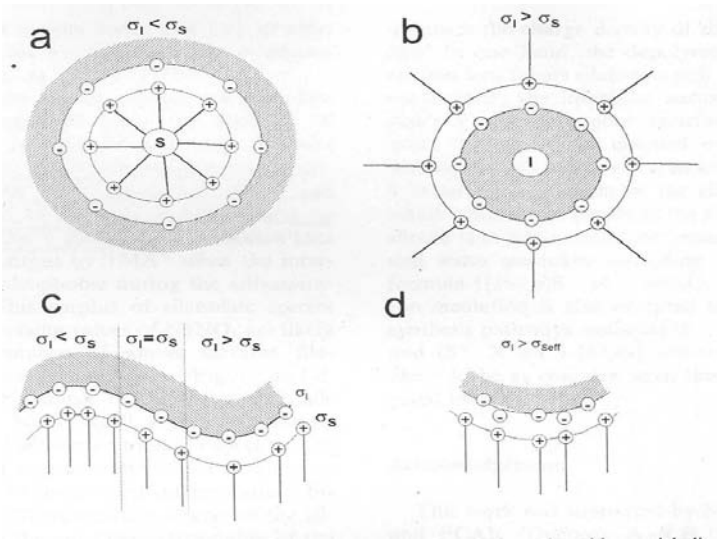


**Figure 2:21 Guest Anion effects on MCM-48 structural formation.**

**Supplemental text of Figure 2:21**-As seen in the above image, (a) and (b) would have a concentration of anions approximately the same leading to convex shape. [107] When there would be a slight imbalance in the Helmholtz planes in (c) and (d), the formation of the concave curvature would occur. Charge density would be σ symbol and subscript s and i would stand for surfactant and inorganic species ($\sigma_s$ and $\sigma_i$) of the Helmholtz planes. Echchahed, B. *et al*., *Microporous and Mesoporous Materials* **2001**, *44-45*, 53-63; **DOI:** 10.1016/S1387-1811(01)00168-8 Permission granted by Elsevier Scientific Publishing, Inc. Copyright 2001 ©

Sulfate anion would be especially important as polymerization occurred; since, the silanolate groups would have reduced negative charge similar to $OH^-$. [107] The larger valence charge of sulfate anion would enhance screening of cationic head-group-area, thereby permits smaller $a_0$ value. Smaller $a_0$ value would allow phase transition to occur earlier before significant polymerization had occurred. Bonnoviet and co-workers [107] reasoned the guest anions populated areas of the interface, where charge density was not optimal (high), to form flat/convex surface, which was also proposed put forth by Li and co-workers [112] as the reason why TEOS in transition metal doped MCM-48 worked so effectively. Vansant and co-workers propose that the formation of MCM-48 initially occurs in the high alcohol solution common in Stober spherical sphere synthesis, but the ethanol cause the micelles to form close pack structure, which results in radial hexagonal tubes building on the faces of the truncated octahedron. [118] Due to the polarity of ethanol, water also associates with ethanol in the reaction mixture; therefore, removal of water from the interface restores the higher charge density needed for MCM-48 formation, as shown in Figure 2:22 spherical particle model depiction. Concave surface forms as the guest anions leave the interfacial area, while guest cations would have highest concentration in the concave region. Formation of convex surfaces would be effected by both anions and cations concentration at Helmholtz planes, as shown in Figure 2:21. [107] Sodium ion in basic solution prevents the formation of stable $SiO_4$ units by forming $SiO^-Na^+$ pairs, which explains why $Na^+$ would have so negative impact on M41S silica synthesis. In conclusion, the model put forth, by Bonnoviet and co-workers, [107] would explain the results of Anpo and co-workers [114] work on different guest anion on Si-MCM-48 and metal doped MCM-48. [112]

(b) and for those spots produced by the cylindrical radial

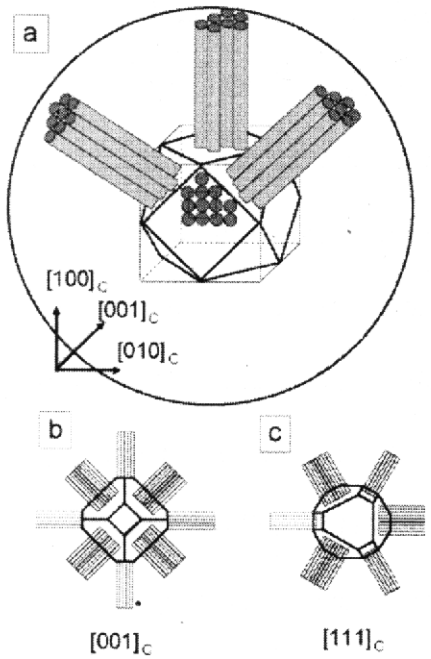


**Figure 2:22 Spherical MCM-48 particle formation model in Stober synthesis.**

**Supplemental text for Figure 2:22**-As seen in the above representation of a spherical silica particle, the truncated octahedral MCM-48 crystal initially grows; however, due to the high alcohol reaction conditions, the charge density matching would be disturbed and surfactant packing parameter value would change. [118] The final result would be cylindrical tubes growing out on the faces of the crystal, as seen in part (a). These tubes would grow in a consistent manner in the $[100]_c$ and $[001]_c$ directions. Part (b) shows the growth of the tubes on the crystal faces of MCM-48 in the $[001]_c$. Part (c) provides another projection from the [111]c direction of the tube growth. Support for this model would be from transmission electron microscopy (TEM) and high resolution electron microscopy (HREM) at different angles, thereby able to develop a crystallographic pattern. Lebedev, O, I. *et al*., *Solid State Sciences* **2004**, *6*, 489-498; **DOI:** 10.1016/j.solidstatesciences.2004.01.013 Permission granted by Elsevier Scientific Publishing, Inc. Copyright 2004 ©

In summary, the model/results presented in this mechanism section would attempt to clarify how various phase transitions occur and how to manipulate synthesis variables to produce highly ordered structure, such as MCM-48. The effects of metal ions might have similar effect on Helmholtz planes, such as $Na^+$, $TMA^+$ cations, but with larger charge, increased polarization would occur, thereby favoring either hexagonal or lamellar phases over MCM-48 if not enough counter-ions like $SO_4^{2-}$ were available to mediate the large positive charge. [107] The imprecise charge balance would explain random nature of placement of metal ions throughout structure affected by hydrolysis of silica precursor, as noted in Co-MCM-41 and Co-MCM-48 with TEOS. [91,92,94] Finally, Vralstad and co-workers discovered that the charge density matching was significantly enhanced with use of $CoSO_4 \cdot 7H_2O$ vs. $CoCl_2 \cdot 2H_2O$ precursors due to the sulfate anions positive effects, which enabled them to increased the metal loading and still form Co-MCM-48. [93]

## 2.14 What comprises the surfactant packing parameter value

The previous research on the effect of ethanol and the self-assembly modeled by the surfactant packing value $g = V/a_0l$ showed that ethanol going into the "tail" portion of the surfactant/micelle led to a larger volume, V, value. [18] The research from Stucky and co-workers showed that alcohols less than four carbon-chains long had the

tendency to be in the outer-shell of the surfactant-micelle. [86,119,120] Gallis and Landry found this research by Stucky *et al.* to be true with alcohol or co-solvent passing into the tail region of the surfactant-micelle, and thereby causing the value of g to increase. [18,86,119,120] Therefore, ethanol used in the hexagonal phase would be expected to form the cubic phase under optimal conditions. [18] The head-group area of the surfactant would comprise the $a_0$ value, and this variable has a major influence on formation of desired structure due to change in degree of hydration. [121] The (l) variable would represent the length of the surfactant alkyl portion, which stays approximately same in various reaction conditions.

## 2.15 The value of ethanol in the reaction synthesis of MCM-48

It has been believed that the formation of the MCM-48 structure needs polar additives in the reaction mixture with the use of cetyltrimethylammonium ion ($CTA^+$) surfactant as a structure directing species. [48] The use of tetraorthosilicate (TEOS) would be used as a silica source; since, it provides ethanol with hydrolysis of the TEOS. This would be important due to the fact that the MCM-41 structure would be produced when no polar additive had been added. [27,48] Ethanol increases the volume of the tail region of the micelle and consequently causes the packing parameter to increase into the desired range for forming the MCM-48 structure. [48] When sodium silicate and fumed silica were used with a 2 hour/4 hour heating procedure that had produced the MCM-48 structure, the result was only the formation of the MCM-41 material; however, with the addition of ethanol at three mole equivalent to $SiO_2$ prior to heating conversion to the MCM-48 structure occurred. [18] Kevan and co-workers [122] note without ethanol no phase transformation from MCM-41 to MCM-48 occurred, which reinforces Gallis and Landry results. [18] The researchers found also that the stirring rate and beaker size had a major effect on the phase produced. When methanol was used as the polar organic additive, from the hydrolysis of tetramethylorthosilicate (TMOS), the result was the formation of MCM-41 not MCM-48. This was linked to higher polarity and hydrophilicity, which could not penetrate the micelle surface. [67] The researchers, then, used two-thirds of the amount of methanol and claim formed MCM-48 structure. They also claim that with the addition of NaCl salt to Si-MCM-48 structure could be made resistant to boiling water conditions, as shown in the powder XRD plot in Figure 2:23. Moreover, other higher alcohols formed the MCM-48 structure with similar surface area values, but with less X-ray diffraction peak resolution in comparison to ethanol and methanol. If too much alcohol was added to the reaction mixture, the result would be the formation of a lamellar structure, which would support previous proposal of how MCM-48 silica spheres formed with radial tubes on the MCM-48 truncated octahedral faces. [118] Therefore, the optimal amount of alcohol would be needed. [67]

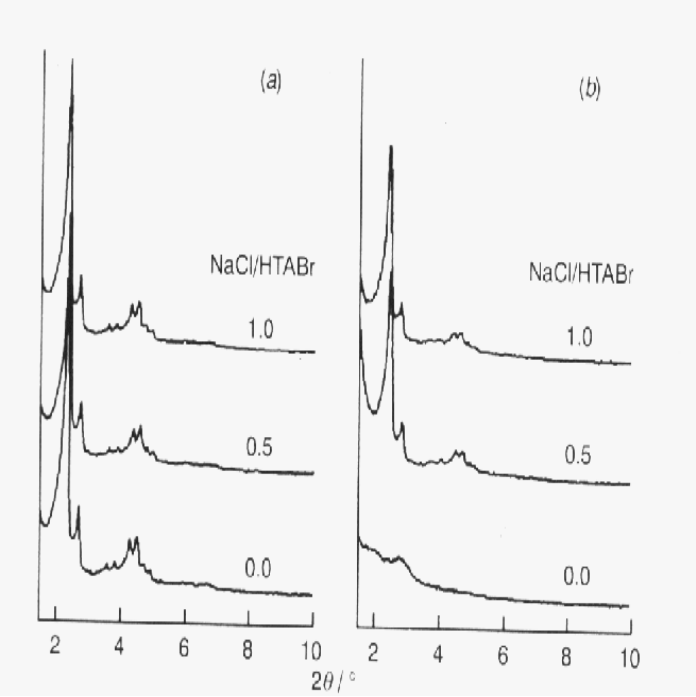


**Figure 2:23 Powder XRD Diffractograms with NaCl under various conditions.**

**Supplemental text for Figure 2:23**-As seen in the above powder XRD plots, left side (a) shows the effect of various molar ratio concentrations of NaCl after calcination. [67] After use of NaCl, the effect under 12 hours of boiling water in plot (b). Clearly, one could see that the use of NaCl improved the structure of Si-MCM-48 and prevented it from major destruction in boiling water conditions in plot (b). Kim, J. M. *et al*., *Chemical Communications* **1998**, 259-260; **DOI:** 10.1039/a707677k Permission granted by the Royal Society of Chemistry Copyright 1998 ©
The increase in ethanol used in the synthesis also led to higher specific surface areas and pore volumes; the same effect was noted for the use of aqueous ammonia up to 0.20 moles. [27] Likewise, the researchers noted that ethanol in the reaction mixture would be a key member in the transformation process due to both the increase in surfactant packing parameter, g, coupled with incompletely polymerized silicate framework causes the conversion from MCM-41 to MCM-48. [55] Tolbert and co-workers note partially polymerized mesoporous silica would have enhanced phase transformation from hexagonal to lamellar phase due to lower activation energy barrier coupled with increased kinetic rate. [108]

## 2.16 Importance of stirring + heating period

For the MCM-48 structure, the reaction temperature coupled with the crystallization time would determine to be the major variables that control pore diameter. [48] Longer hydrothermal synthesis time eventually leads first to the pore swelling and then conversion to the lamellar phase, as seen in the X-ray diffraction plot in Figure 2:24. According to the authors, a lower reaction temperature favored MCM-41. For example, at a synthesis temperature of 60 to 100°C for three days of reaction time led to the generation of MCM-41 structure. The temperature may affect the packing parameter g ($g = V/a_0 l$) of the mesoporous structure. V in the above equation would be the surfactant tail volume, l would be the length of the surfactant chain, and $a_0$ would be the effective head-group area at micelle surface. The packing parameter (g) for 60 to 100°C temperature would be lower using cetyltrimethylammonium ($CTA^+$) surfactant ions in comparison to 135 to 150°C temperature, which generate the MCM-48 structure.

Mokaya and co-workers, however, discovered that a longer hydrothermal synthesis time of four days led to much higher quality Si-MCM-48 at 135°C without polar additives and only CTAOH + fumed silica. [123] Corma and co-workers [78] note the narrow synthesis range with use of CTAOH, and Sayari [124] found that the temperature had to be exactly 132°C to form high quality MCM-48 for a day. Pinnavaia *et al.* [125] have been able to synthesis high quality Si-MCM-48 form sodium silicate under exact synthesis conditions. This shows that the g-value could be increased with heat, although it must be precisely administered.

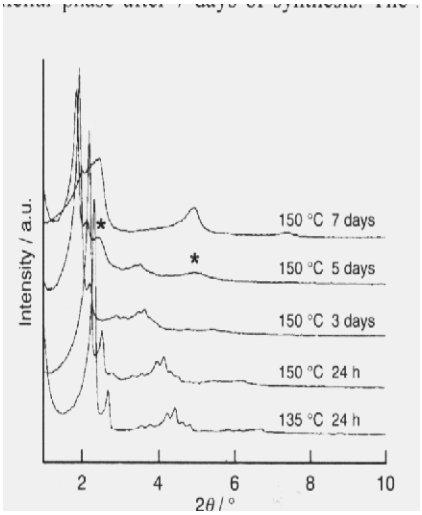


**Figure 2:24 Powder XRD Diffractograms Shows MCM-48 Formation with Elevated Temperatures.**

**Supplemental text in Figure 2:24**-As seen in the above powder XRD plot, the cubic MCM-48 structure formed in 24 hours at 135°C and 150°C; however, with continue reaction time from three to seven days, this leads to a structural transformation to the lamellar phase beginning in five days, as noted with the asterisk in the above XRD. [48] Corma, A. *et al*., *Chemical Communications* **1998**, 579-580; **DOI:** 10.1039/a709093e Permission granted by Royal Society of Chemistry Copyright 1998 ©

Gallis and Landry tried heating the reaction mixture up to 40-50°C in the two hour stirring period to vaporize the ethanol produced from hydrolysis of TEOS: the result was the formation of the MCM-41 structure even with a 4- hour heating period at 150°C. [18] This shows that both the heating temperature and the ethanol effect the packing parameter. Moreover, the researchers found that both stirring time and heating periods were needed to form the MCM-48 structure. The use of various stirring and heating times revealed a trend when the reaction mixture had been stirred for 2-3 hours to allow silicate polymerization and consequently produce well developed structure emerged. The structure at this point shows a structural resemblance to the desired phase, but could also undergo structural distortion. The synthesis temperature must be carefully adjusted with the needed reaction time to form the MCM-48 structure. Russo *et al.* found with the room temperature synthesis of Al-MCM-48 that the synthesis time was important for particular aluminum precursors. [126] However, Koodali and co-workers [127] found a similar trend to Gallis and Landry [18] where the stirring rate and reaction time controlled the degree of quality exhibited in the cubic Si-MCM-48 from the modified Stober synthesis. [27,127-129] High rate of stirring led to poorly formed mesostructure; likewise, the time of the solution-mixture was aged statically significantly increased the structural order, as noted with larger primary powder XRD peak intensity coupled with formation of secondary peaks. [127] When no aging period was completed, the formation of Si-MCM-48 required four hours; otherwise, poorly formed Si-MCM-48 formed. The aging period shorten the length of synthesis time needed to produce high quality Si-MCM-48 to 30

minutes with a 20 minute aging period. In other research on Cr-MCM-41, higher synthesis temperature leads to less contraction of unit cell when calcinated. [130]

## 2.17 Effect of temperature on the amount of contraction at calcination step

The calcinations step caused the as-synthesized Si-MCM-48 sample to decrease in unit-cell size, which would be expected; since, the large organic cations would be removed and protons would take their place coupled with silanol groups' condensating to form a stronger structure. [19,30,67] Therefore, the smaller unit cell for the cetyltrimethylammonium bromide (CTAB) prepared MCM-48 sample at 85.3 Å in comparison to the sample made with chloride ion at 92.5 Å would have less condensation of the pore wall structure. [19] More contraction in the unit cell, upon calcination, would imply larger amount of condensation of the resulting material. Consequently, the material should have a higher thermal stability. The researchers note that the CTAB prepared sample would be expected to give a more thermally stable structure. Kevan and co-workers note that CTAB prepared Si-MCM-48 had larger powder XRD peak intensity vs. CTACl made Si-MCM-48, which infers higher quality for CTAB produced Si-MCM-48. [122] The researchers also found that the Ti-MCM-48 material converted to an amorphous structure after being stored under ambient environment for 6 months. [30]

## 2.18 Effect of Calcination Process on M41S Mesoporous Silica Structures

Although little emphasis in literature given on the structural effect of various calcination ramping and peak temperature (temperature rate to peak followed by plateau) methods chosen on M41S mesoporous materials, the calcination process would determine the formation level of strained siloxane (Si-O-Si) and concentration of silanol (Si-OH) groups in calcinated material. [131] In the modified Stober Si-MCM-48 silica synthesis [27,128,129] Koodali and co-workers reported that ramping temperature of 5°C/minute to 550°C caused the collapse of the material. [127] Unger and co-workers used 1°C/minute ramping rate to 550°C plateau and noted high quality Si-MCM-48 formed. [27,128] This gradual ramping of as-synthesized Si-MCM-48 could reduce number of strained siloxane bonds, which would be vulnerable to hydrolysis, due to less probability of the surfactant decomposing too quickly, thereby causing change of pressure from gaseous release of total oxidation product: $CO_2$. Schuth and co-workers [132] employing the modified Stober synthesis by Unger and co-workers [129,133] for Si-MCM-41 reported two different decomposition mechanisms depending on what type of surfactant used: cetyltrimethylammonium bromide (CTAB), or cetylpyridinium chloride (CPCl). These researchers note with CTAB two powder XRD *d*-spacing changes from 250-300°C and 500°C to 550°C in the first hour at peak temperature. Figure 2:25 and Figure 2:26 provide visual representation of MCM-48 bicontinuous Ia3d structure, as an aid to visualize the effect of calcination process from two different viewpoints with assignment of what comprises the unit cell $\mathbf{a_0}$, pore diameter **D**, and pore wall thickness **t**. [69,131,134] The CPCl prepared Si-MCM-41 material had little change up to 250°C in powder XRD intensities followed by significant increase in peak intensity, up to 550°C plateau, as shown in Figure 2:27. [132]

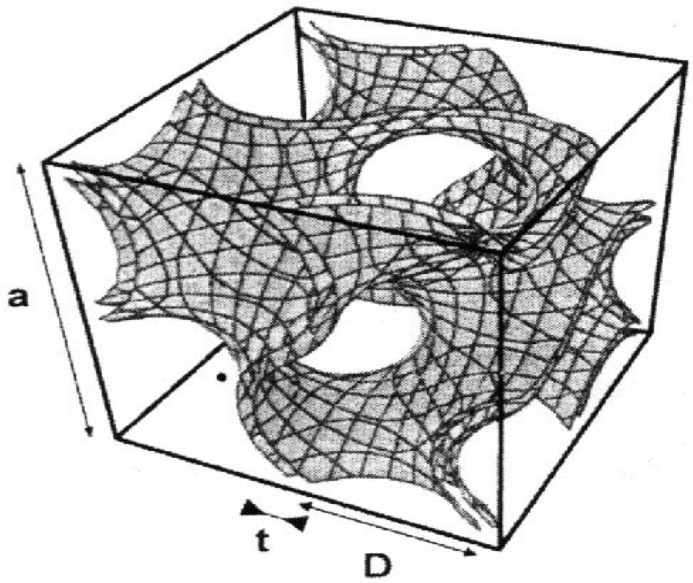


**Figure 2:25Three-Dimensional MCM-48 Image as a unit cell.**

**Supplemental text to Figure 2:25**-As seen in the above figure of MCM-48, **a** letter on the side would be the dimension of the cubic unit cell; **t** would be the average thickness of the MCM-48 wall; and **D** diameter of the pore channel. [69,131] The relationship of the *d*-spacing would be with the unit cell, a, value, which could be separated into smaller sections, otherwise, known as the *d*-spacing in powder XRD. Galarneau, A. *et al*., *Microporous and Mesoporous Materials* **2005**, *83*, 172-180; **DOI:** 10.1016/j.micromeso.2005.03.020 Permission granted by Elsevier Scientific Publishing, Inc. Copyright 2005 © Anderson, M. W., *Zeolites* **1997**, *19*, 220-227 **DOI:** 10.1016/S0144-2449(97)00061-4 Permission granted by Elsevier Scientific Publishing, Inc. Copyright 1997©

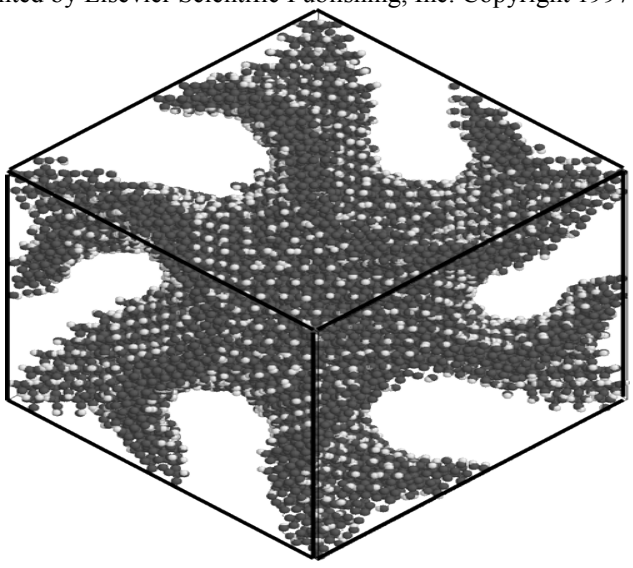

**Figure 2:26 Atomistic Model of Si-MCM-48 in a unit cell.**

**Supplemental text for Figure 2:26**-As seen in the above figure of Si-MCM-48, one noted the twisted bicontinuous structure; however, unlike the other images of MCM-48, this representation shows the oxygen atoms as grey spheres and white spheres for the hydrogen atoms. [134] The view on sees of the structure would be in the [111] direction. The oxygen atoms would be bonded to the silicon atoms not shown for clarity sake. The hydrogen atoms would be from the silanol (Si-OH) bonds on the surface of MCM-48. Silanol groups would be considered defects in the Si-MCM-48 structure, which could facilitate hydrolysis of the stable framework $SiO_4$ bonds in aqueous environments.

These defects abound over the Si-MCM-48 structure, as seen in the above image. Calcination process applied with gradual ramping temperature or post-synthesis hydrothermal treatment reduces the chances of the Si-OH species forming strained $SiO_4$ members, which previous shown to hydrolyze readily due to significant reduction in activation energy. [108] Coasne, B. *et al*., *Langmuir* **2006**, *22*, 11097-11105; **DOI:** 10.1021/la0611728h Permission granted by American Chemical Society Copyright 2006 ©

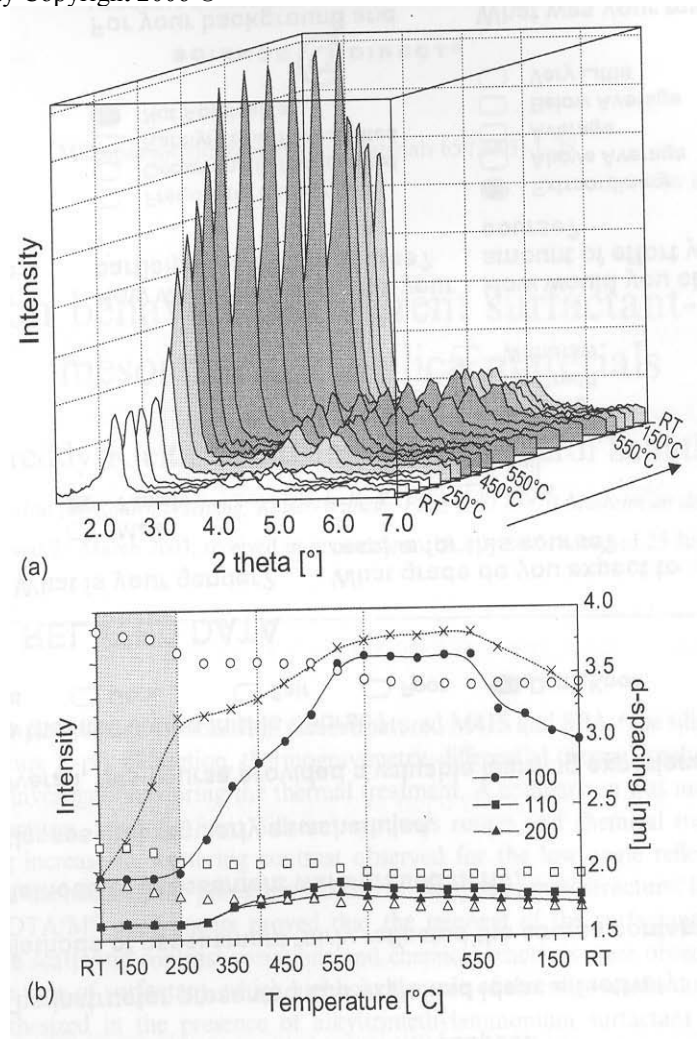


**Figure 2:27 Effect of Calcination Temperature of XRD peak intensity and *d*-spacing for Si-MCM-41.**

**Supplemental text for Figure 2:27**-As seen in above powder XRD plot in part (a), the XRD peak intensity increases as a function of the formation of unit cells with similar consistence with increased temperature up to 550°C. [132] This means that the Si-MCM-41 structure continues to condense into $SiO_4$ units. As the temperature was decreased to room temperature, the Si-MCM-41 structure absorbs water and cause increased disorder throughout the periodic structure. In part (b) a similar trend occurs with the *d*-spacing increasing up to 550°C then decreasing with absorption of water under ambient conditions. Notice the intensity as the x-lines reaches a peak at 550°C and also the primary MCM-48 $d_{100}$ at the same temperature. Little change at low calcination temperature up to 250°C followed by gradual increase in peak intensity could be ascribed to little movement in the pore structure from the CPCl surfactant. The open dot would be the $d_{100}$ intensity peak value as a function of calcination temperature, which shows gradual decrease with increased calcination temperature. Kleitz, F. *et al*., *Microporous and Mesoporous Materials* **2003**, *65*, 1-29; **DOI:** 10.1016/S1387-1811(03)00506-7 Permission granted by Elsevier Scientific Publishing, Inc. Copyright 2003 ©

The fact of little change of powder XRD peak intensity up to 250°C with CPCl made Si-MCM-41 indicates reduced movement of surfactant in pores, as noted in Figure 2:27 above. [132] These researchers employed a ramping

temperature of 5°C/minute for this research, and they noted larger signal-to-noise ratio for the powder XRD reflections coupled with narrower peaks with use of CPCl vs. CTAB in Si-MCM-41 synthesis. This result would be similar to Unger and co-workers Si-MCM-41 prepared material using CPCl surfactant with four sharp, narrow peaks in contrast to three for CTAB made Si-MCM-41. [133] Thermal gravimeteric-digital thermal analysis/mass spectroscopy (TG-DTA/MS) revealed that water would be eliminated first followed by removal CPCl template from ≈ 180°C to 450°C in two stages. [132] The major difference between CPCl decomposition and CTAB would be due to the pyridyl ring, which appears to decompose into two fragments; whereas, CTAB trimethylammonium head-group would convert to decomposition products according to Hofmann elimination reaction. In addition, Schuth and co-workers reported the trends in powder XRD and TG-DTA/MS data would infer CTAB not uniformly spread throughout pores, in contrast to CPCl made Si-MCM-41, which would support claim of two steps in the decomposition of CTAB in Si-MCM-41 synthesis. [132] These researchers discovered similar trend in hydrothermally CTAB prepared Si-MCM-48 for powder XRD intensity increase up to 250°C in the heating process, which could be similar to CPCl prepared Si-MCM-41; otherwise, the decomposition mechanism has been noted to be similar to CTAB made Si-MCM-41. The increase in powder XRD peak intensity $d_{(211)}$ spacing would follow three-steps in creation, as shown in Figure 2:28. In conclusion, the high ramping temperature of 5°C/minute vs. 1°C/minute in CTAB prepared M41S silica mesoporous materials would dramatically affect the amount of strained siloxane bonds formed due to different head-group binding strength to silica framework consequently determining the decomposition mechanism noted between CTAB and CPCl synthesized Si-MCM-41 materials.

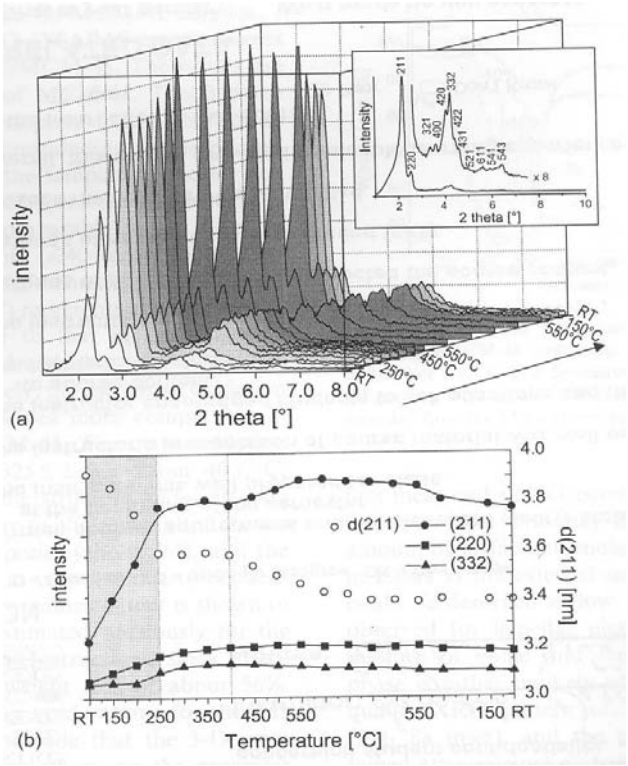


**Figure 2:28 Calcination Behavior of CTAB prepared MCM-48.**

**Supplemental text for Figure 2:28**-As seen in part (a), the powder XRD peak intensity increases dramatically up to 300°C for $d_{211}$ and $d_{220}$ reflections, which could mean movement of the surfactant in the pore channels. [132] After

reaching the plateau of 550°C, the reduction to ambient conditions led to absorption of water, thereby causing some disorder in the pore structure. Part (b) shows the in open dot symbols a significant reduction in $d_{211}$ spacing with calcination temperature, thereby infers a reduction in the unit cell (lattice constant). From a visual point of view, referring to Figure 2:25 and Figure 2:26, the actual unit **a**-value would decrease and corresponding **D**-value reduced in the calcinated Si-MCM-48 structure. This would not be anticipated due to hydrothermal conditions that should produce more stable Si-MCM-48 structure. The researchers report a large lattice constant decrease of 13%, which could mean that the structure not as stable as desired. Kleitz, F. *et al*., *Microporous and Mesoporous Materials* **2003**, *65*, 1-29; **DOI:** 10.1016/S1387-1811(03)00506-7 Permission granted by Elsevier Scientific Publishing, Inc. Copyright 2003 ©

Calcination process would have an even more dramatic effect on as-synthesized M41S materials that had no hydrothermal treatment. [27,127,128,131,132] Schuth and co-workers synthesized Si-MCM-41 using modified Stober synthesis both at room temperature and hydrothermally aged for seven days at 90°C. [132] As shown in Figure 2:29, the Si-MCM-41 sample made at room temperature had lower intensity powder XRD peaks that were broader in contrast to aged one's. Also, the $N_2$ adsorption-desorption isotherm plot showed steep slope coupled with shift to higher $P/P_0$ value before capillary condensation occurred in aged Si-MCM-41 sample. The sharpness of the powder XRD peaks would infer the degree of order in pore structure especially for secondary peaks in 5-6° 2θ range. A shift to larger $N_2$ relative pressure $P/P_0$ (where P = equilibrium vapor pressure and $P_0$ = saturated vapor pressure) would mean larger pore coupled with steeper slope between≈ 0.3 -0.4 $P/P_0$, which means increased pore uniformity. Therefore, the hydrothermally aged Si-MCM-41 sample would be more stable under calcination process due to enhanced structural condensation, noted in Table 2:3 features. [132] Figure 2:30 shows the effect of *d*-spacing and intensity as a function of calcination temperature for CTAB synthesis Si-MCM-41 both at room temperature and hydrothermally aged samples. [132] Hydrothermally aged samples have little decrease in *d*-spacing in contrast to conventional room temperature synthesis. Koodali and co-workers also found that aging the Si-MCM-48 sample had a positive impact on the cubic structure, according to larger powder XRD peak intensity in room temperature synthesis. [127] Galarneau and co-workers complete a study on the effects of post-synthesis treatment hydrothermally for Si-MCM-48. [131] They discovered that Si-MCM-48 hydrothermally post-synthesis treated samples two times had only a reduction of 32% of volume vs. 76% of micellar volume for untreated Si-MCM-48. The powder XRD peaks would be significantly increased with the post-synthesis treatment twice and have large pore volume coupled with steeper capillary condensation slope, as shown in Figure 2:31 and Figure 2:32. Galarneau and co-workers link the higher stability of Si-MCM-48 to enhanced cross-linking (condensation) of silica walls another words more siloxane group condensation before force condensation in calcination process. [131] This conclusion was supported by increased $^{29}$Si MAS NMR $Q^4/Q^3$ ratio values and little change in $N_2$ plot after one year of storage of Si-MCM-48 at ambient conditions, as shown in Figure 2:33. Schuth and co-workers [132] synthesized hydrothermally Si-MCM-48 with eight reflections (considered high quality); however, after calcination, the sample unit cell had contracted by 13%, which would infer more strained siloxane bonds formed during calcination process. As noted in Figure 2:6 of the three viewpoints of Si-MCM-48 by Andersen, [69] the walls of MCM-48 would be thin coupled with twisted structure infers many of the siloxane bonds have wall strain. Adding more strained siloxane bonds would not lead to stronger more resistant structure, rather the wall would hydrolyze at an equal or faster rate, as noted in Tolbert and co-workers research on hexagonal silica transformations. [108] This research shows that even as-synthesized hydrothermally Si-MCM-48 still has substantial loss of volumes upon calcination due to silanol groups on silica walls not

condensed fully, which would anticipated due to the large number of silanol groups in MCM-48 even after calcination, as shown in Figure 2:26, without post-synthesis treatment, as  However, the high ramping temperature of 5°C/minute did not cause collapse of the Si-MCM-48 pore structure as in case of room temperature modified Stober synthesis employed by Koodali and co-workers. [127,132] This would infer that hydrothermally synthesis conditions provide energy needed to over-come the activation energy barrier to cause a few silanol groups to condense, and room temperature modified Stober synthesis would have substantially more silanol groups, which upon quicken ramping temperature conditions lead to destruction of pore network. Schuth and co-workers [132] and Koodali and co-workers [127] both use TEOS, which forms silica monomers upon hydrolysis; whereas, Galarneau and co-workers employed fumed silica comprised of oligomeric silica units. [132,135] Comparison of these research reports reveals that calcination ramping temperature would be pivotal in forming stable Si-MCM-48 structure in room temperature modified Stober synthesis; this temperature heating effect could be still evident with substantial loss in unit cell volume with hydrothermally prepared Si-MCM-48 even for fumed silica made material. [131,132,135] Hydrothermal post-synthesis treatment causes controlled condensation of silanol groups in silica materials by forming thicker silica walls, which Galarneau and co-workers have shown pivotal in thermal treatment experiments to retain large pore volumes. [131,135,136] Horiuchi and co-workers also found similar results with post-synthesis treatment for Si-MCM-41 and Si-MCM-48. [137] However, the improvement of ordering of pore structure was dramatically improved for TEOS made Si-MCM-48, as shown in Figure 2:34. These results show that post-synthesis hydrothermal treatment has a significant positive effect on the structural parameters of M41S mesoporous silica materials. Calcination ramping temperature would be of predominant importance in removal of surfactant in M41S structures not submitted to post-synthesis hydrothermal treatments, as noted in research on Si-MCM-48 with large unit cell contraction. [111,132]

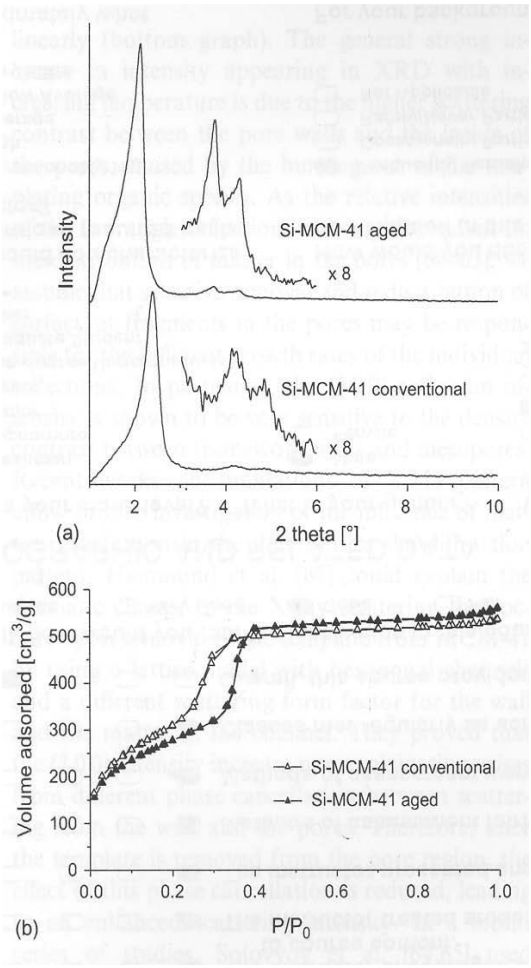


**Figure 2:29 Difference in Calcination Behavior between Aged and Conventional prepared Si-MCM-41.**

**Supplemental text for Figure 2:29**-As seen in part (a), the aged Si-MCM-41 sample for one week exhibits stronger secondary powder XRD peaks; in contrast, the conventional room temperature synthesis using modified Stober synthesis produce weaker XRD peaks, which infers that the aged sample would have greater condensed silica structure. [132] In part (b) the $N_2$ isotherm analysis of the aged Si-MCM-41 prepared sample at 90°C for one week has steeper slope, thereby infers greater pore uniformity. Collectively, this infers that a heating step employed in the synthesis of M41S materials would greatly increase structural characteristics. Kleitz, F. *et al*., *Microporous and Mesoporous Materials* **2003**, *65*, 1-29; **DOI:** 10.1016/S1387-1811(03)00506-7 Permission granted by Elsevier Scientific Publishing, Inc. Copyright 2003 ©

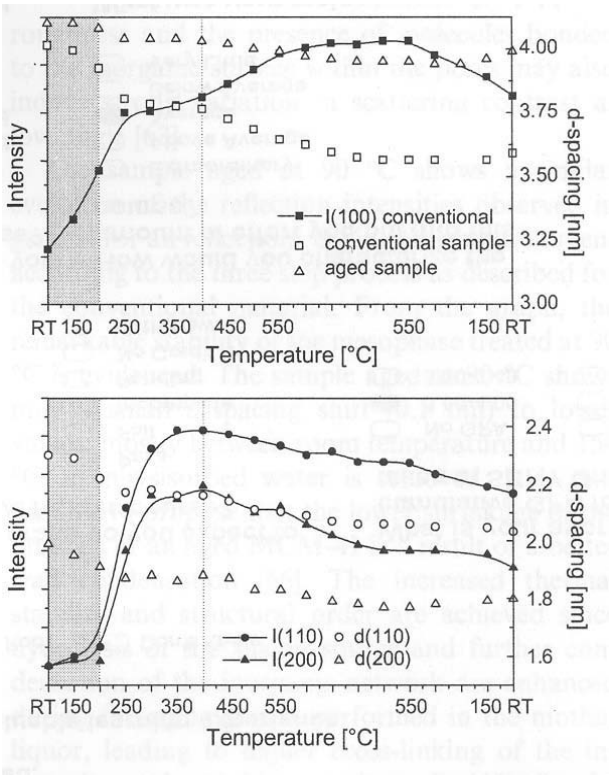


**Figure 2:30 Effect of Synthesis conditions as function of Calcination temperature for Si-MCM-41.**

**Supplemental text for Figure 2:30**-As seen in the top plot, the conventional prepared Si-MCM-41 material from CTAB has major decrease in the d-spacing as a function of calcination temperature. [132] In contrast, the aged Si-MCM-41 sample has little decrease in d-spacing, which would infer more stable and condensed silica framework. The relatively sharp increase in the peak intensity could mean that the poorly condensed Si-MCM-41 structure has forced condensation occurring. In the bottom plot the increase of intensity for the secondary peaks of the aged Si-MCM-41 sample would be less and have less reduction in *d*-spacing in contrast to the conventional prepared Si-MCM-41. This data infers that the aged Si-MCM-41 material would be more stable in comparison to room temperature made Si-MCM-41. Kleitz, F. *et al*., *Microporous and Mesoporous Materials* **2003**, *65*, 1-29; **DOI:** 10.1016/S1387-1811(03)00506-7 Permission granted by Elsevier Scientific Publishing, Inc. Copyright 2003 ©

Physico-chemical parameters observed for the calcined materials, obtained by nitrogen physisorption

| Materials | BET surface area[a] ($m^2/g$) | Total pore volume, $V_p$ ($cm^3/g$) | Pore size, $w_{BJH\,des}$ (nm) | Pore size, $w_d$[b] (nm) | Wall thickness, $b_{BJH}$[c] (nm) | Wall thickness, $b_d$[d] (nm) |
|---|---|---|---|---|---|---|
| C12-MCM-41[e] | 1035 | 0.51 | 2.06 | 2.55 | 1.45 | 0.96 |
| C14-MCM-41 | 1100 | 0.61 | 2.12 | 2.89 | 1.7 | 0.93 |
| C16-MCM-41 | 1130 | 0.78 | 2.47 | 3.31 | 1.7 | 0.85 |
| C18-MCM-41 | 995 | 0.79 | 2.90 | 3.83 | 1.9 | 0.97 |
| C14-MCM-41-aged | 910 | 0.57 | 2.32 | 3.10 | 1.85 | 1.05 |
| C16-MCM-41-aged | 1010 | 0.80 | 2.82 | 3.67 | 1.8 | 0.93 |
| C18-MCM-41-aged | 1015 | 0.85 | 3.62 | 4.16 | 1.55 | 0.99 |
| CPCl/MCM-41 | 995 | 0.58 | 2.24 | 2.96 | 1.7 | 0.99 |
| MCM-48 | 1175 | 0.72 | 2.16 | – | – | – |
| SBA-3[f] | 1470 | 0.65 | 2.04 | 2.86 | 1.7 | 0.87 |
| SBA-15[f] | 737 | $0.67V_{p(meso)}$ $0.13V_{p(micro)}$ | 5.42 | 8.07[g] | 5.10 | 2.45 |

[a] Average BET surface area.
[b] Obtained from the geometrical model with equation $w_d = cd_{100}\left(\frac{V_p\rho}{1+V_p\rho}\right)^{1/2}$, $c = 1.155$ (hexagonal pores) and $\rho = 2.2$ g/cm³.
[c] Wall thickness calculated as $a - w_{BJH}$.
[d] Wall thickness calculated as $a - w_d$.
[e] Limit of the BET equation accuracy.
[f] The presence of microporosity in the silica walls makes the use of the BET equation and the *t*-plot method likely inaccurate resulting in discrepancies.
[g] Obtained from the geometrical model with equation $w_d^{SBA-15} = cd_{100}\left(\frac{V_{p(meso)}}{1/\rho + V_{p(meso)} + V_{p(micro)}}\right)^{1/2}$ $c = 1.213$ (circular pores) and $\rho = 2.2$ g/cm³ [86].

**Table 2:3 The Effects of Different Synthesis Conditions on Calcination Results.**

**Supplemental text for Table 2:3**-As seen (previous page) in the marked items in the left hand column, the conventional Si-MCM-41 has higher surface area at the cost of thinner silica walls as noted in the last two columns on the right in the above table. [132] The thicker walls in the aged Si-MCM-41 would be a major characteristic of more condensed silica materials. Kleitz, F. *et al*., *Microporous and Mesoporous Materials* **2003**, *65*, 1-29; **DOI:** 10.1016/S1387-1811(03)00506-7 Permission granted by Elsevier Scientific Publishing, Inc. Copyright 2003 ©

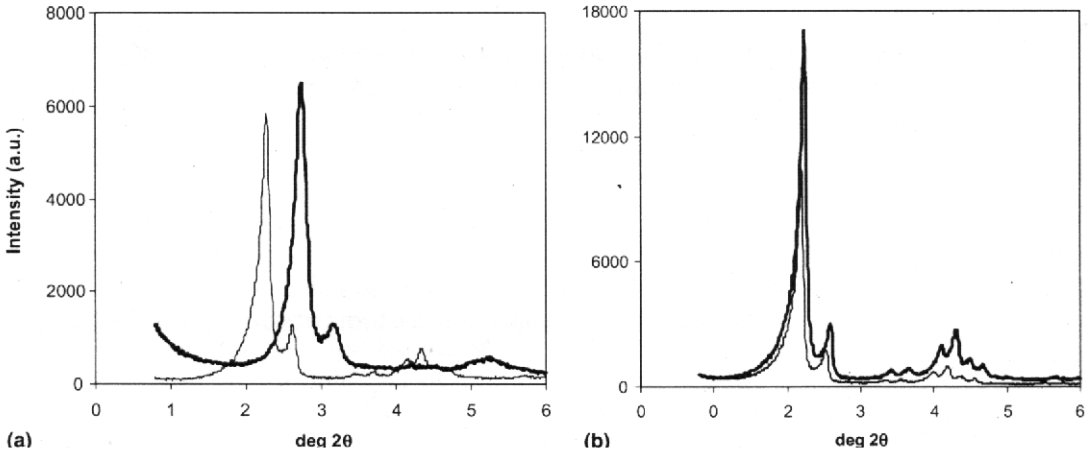


**Figure 2:31 Powder XRD Diffractograms Before and After Post-Synthesis Hydrothermal Treatment.**

**Supplemental text for Figure 2:31**-As seen in the above figure in part (a), the thin line XRD peak in left hand portion would be without post-synthesis hydrothermal treatment and the right one after two hydrothermal post-synthesis treatments. [131] Part (b) in right hand XRD plot shows a similar trend after calcination with the dark thick line the Si-MCM-48 structure that had two post-synthesis hydrothermal treatments vs. thin line of Si-MCM-48 with no post-synthesis treatment. From the above XRD plots, one could conclude that the short hydrothermal post-synthesis treatments effectively increase the formation of stable $SiO_4$ units in Si-MCM-48 through the whole material. Galarneau, A. *et al*., *Microporous and Mesoporous Materials* **2005**, *83*, 172-180; **DOI:** 10.1016/j.micromeso.2005.03.020 Permission granted by Elsevier Scientific Publishing, Inc. Copyright 2005 ©

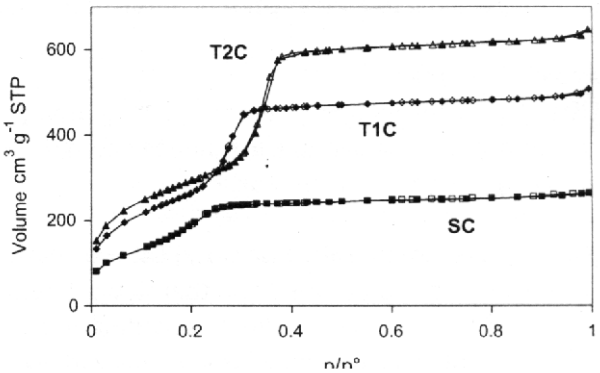


**Figure 2:32 $N_2$ Isotherm Plot Before and After Post-Synthesis Hydrothermal Treatment.**

**Supplemental text for Figure 2:32**-As seen in the above $N_2$ plot of volume (y-axis) vs. relative pressure p/p° (x-axis), one would come to the conclusion that the post-synthesis hydrothermal treatment Si-MCM-48 samples, T2C and T1C, have significantly larger pore volumes and steeper capillary condensation step and a shift to the right in comparison to the Si-MCM-48 sample without post-synthesis hydrothermal treatment, SC. [131] The steeper slope and later on-set of capillary condensation infers greater uniformity of pore diameter and larger pore volume in T2C and T1C samples. Clearly, the T2C Si-MCM-48 sample would be superior from a stability stand-point; however, the increased stability would require the reduction in surface area of approximately 15%. Galarneau, A. *et al*., *Microporous and Mesoporous Materials* **2005**, *83*, 172-180; **DOI:** 10.1016/j.micromeso.2005.03.020 Permission granted by Elsevier Scientific Publishing, Inc. Copyright 2005 ©

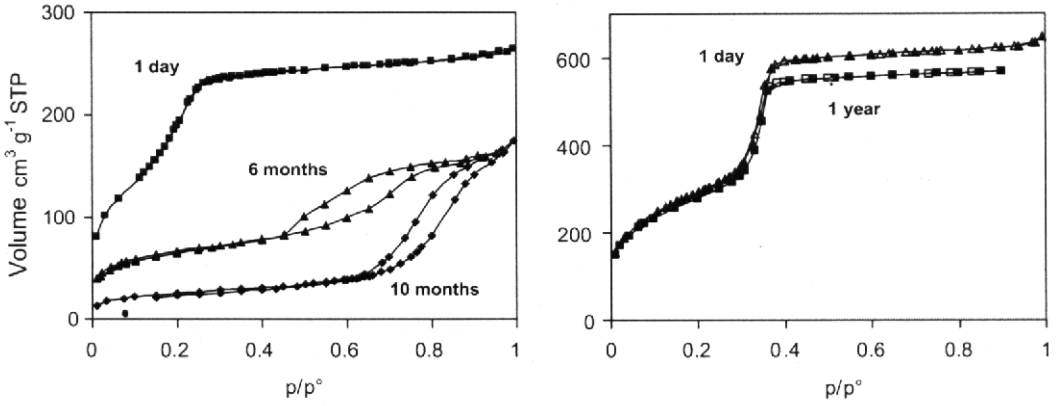


**Figure 2:33 $N_2$ Isotherm Analysis of Calcinated and Post-Synthesis Hydrothermally Treated Si-MCM-48.**

**Supplemental text for Figure 2:33**-As seen in the above nitrogen adsorption-desorption isotherms at 77 K, the left had plot shows the deterioration of pore structure as time increasing from the calcination process with reduction a transformation of the type IV isotherm to type II and type one indicative of amorphous silica and microporous structure at 10 months. [131] In contrast, the nitrogen isotherm for twice hydrothermally treated Si-MCM-48 exhibits little change in the pore volume and the capillary condensation slope appears to be similar to day one when calcinated. Volume of nitrogen absorbed would be a measure of the pore capacity. Increased capillary condensation slope from approximately relative pressure p/p° of 0.3-0.4 infers the degree of uniformity in the pore structure. From a review of these above plots, one could conclude that the absence of the many silanol groups covering Si-MCM-48 without post-synthesis hydrothermal treatment in Figure 2:26 lead to the gradual destruction of the cubic structure due to hydrolysis of the siloxane bond. Clearly, the post-synthesis hydrothermal treatment, T2C, in the right plot has significantly less silanol that could facilitate hydrolysis of the siloxane bonds. Galarneau, A. *et al*., *Microporous and Mesoporous Materials* **2005**, *83*, 172-180; **DOI:** 10.1016/j.micromeso.2005.03.020 Permission granted by Elsevier Scientific Publishing, Inc. Copyright 2005 ©

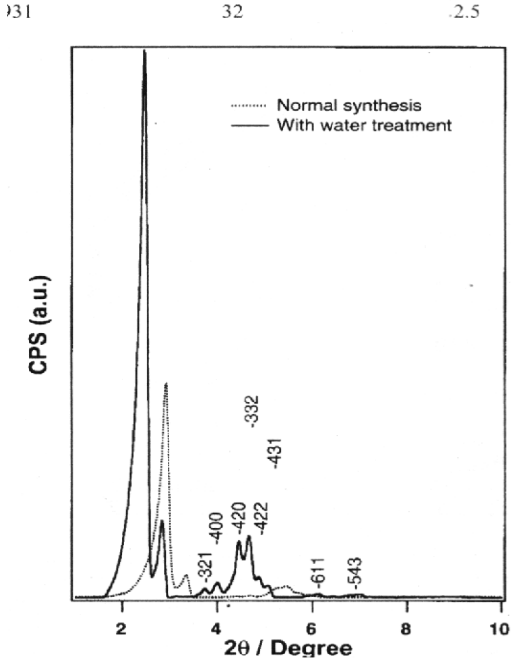


**Figure 2:34 Post-Synthesis Hydrothermal Treatment on TEOS made Si-MCM-48 powder XRD analysis.**

**Supplemental text for Figure 2:34**-As seen in the above powder XRD diffractogram plot, the normal hydrothermal synthesized Si-MCM-48 would be the fine line with substantially lower XRD peak intensity. [137] After post-synthesis hydrothermal treatment, the primary XRD peaks from approximately 2-3° 2θ increase dramatically and the

secondary peaks in the 4-7° 2θ range increase in both intensity and sharpness. This shows that the post-synthesis hydrothermal treatment in water causes the silanol groups to further condense into stable siloxane (Si-O-Si) bonds. The dramatic increase in XRD peak intensity for the TEOS made Si-MCM-48 with post-synthesis treatment would be due to the large number of silanol groups on the walls of Si-MCM-48. Comparison of Figure 2:34 and Figure 2:31 shows that the post-synthesis treated Si-MCM-48 sample made with fumed silica had an increase in XRD peak intensity vs. the standard hydrothermally prepared Si-MCM-48 131; however, the TEOS had significantly large increase in pore uniformity, as noted in increased XRD peak intensity. [137] The reason for why would be due to the silica precursor. TEOS forms monomers while the fumed silica would be primarily made of oligomers silica units. This means that the Si-MCM-48 structure in Figure 2:26 would have significantly less silanol groups adoring the pore wall surfaces using fumed silica. From a review of the above figures, one could conclude that post-synthesis treatment would have major positive effect on all made Si-MCM-48 samples, but the largest effect would be with use of TEOS made samples due to the poorly formed silica walls. Chen, L. *et al.*, *Journal of Physical Chemistry B* **1999**, *103*, 1216-1222; **DOI:** 10.1021/jp983100o Permission granted by American Chemical Society Copyright 1999 ©

Creation of thicker, more condensed, silica walls in M41S materials has been shown to be possible by elevated calcination temperatures up to 760°C. [138] Keene *et al.* employing the modified Stober synthesis had significant pore volume increases up to 760°C, as shown in Figure 2:35. [138] They found 1°C/minute ramping temperature permitted the structure to have enhanced pore volume etc. According to sample control thermal analysis (SCTA), Keeene *et al.* note surfactants present up to 550°C in Si-MCM-41 pores. Condensation of silanol groups would occur from 550°C and 760°C [138]; however, further temperature increase would lead to the Si-MCM-41 structure deteriorating with siloxane bond breaking, as shown in Figure 2:36. Schuth and co-workers [132] research on both Si-MCM-41 room temperature modified Stober synthesis and hydrothermally made Si-MCM-48 with CTAB show water absorption after calcination process, which would infer the structure still exhibits hydrophilic character with silanol groups, as shown in Figure 2:27 and Figure 2:28. This supports Keene *et al.* work that enhanced hydrophobicity would occur at elevated temperatures. [138] In addition, Zhao and Li synthesized nanosize MCM-48 with mixture of CTAB and non-ionic poly(ethylene glycol) monooctylphenyl ether (OP-10). [139] They too note elevated temperature up to 750°C led to increased structural characteristics. Rapid ramping temperature of 15°C/minute to 650°C would appear to have a negative effect on thermal stability! However, Davis and co-workers obtained Si-MCM-41 with large $Q^3/Q^4$ ratio even with 1°C/minute ramping rate to 540°C plateau and poorly condensed structure, as noted in large unit cell contraction. [140] This would confirm the importance of hydrothermal post-synthesis treatment and slow ramping calcination temperature. [131,135,137] In summary, the calcination process would have the most dramatic effect on as-synthesized M41S materials; whereas, post-synthesis hydrothermal conditions would substantially improve hydrophobicity and thicken pore walls, thereby causing them to be more resistant thermally and hydrothermally, which would be important in catalysis applications.

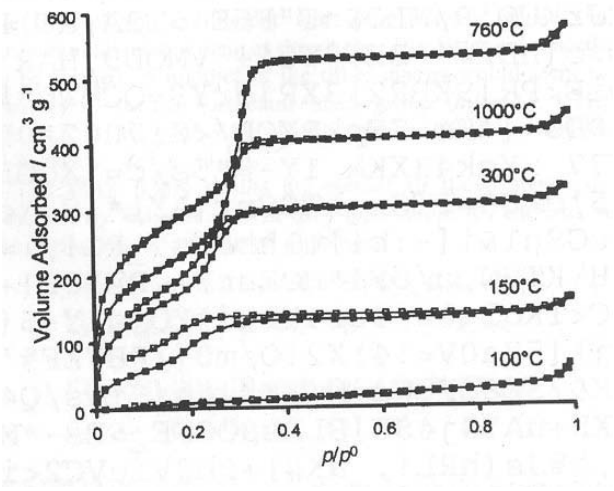


**Figure 2:35 $N_2$ isotherm plot of calcination temperature effect on formation of Si-MCM-41 structure.**

**Supplemental text for Figure 2:35**-As seen in the above $N_2$ isotherm plot of modified Stober prepared Si-MCM-41 material at different calcination temperatures, one could conclude that the gradual increase of ramp temperature of 1°C/minute to 760°C led to enhanced stability in the Si-MCM-41 structure with dramatic increase in pore volume and slope in capillary condensation. [138] This above result infers that the gradual slow increase of calcination temperature permits for slow forced condensation and cross-linking of pore walls, thereby leading to thicker, more polymerized silica walls. As noted in Figure 2:32, the result would mean lower surface area values due to sacrifice of many thinner pore walls for few thicker, larger pore walls. The reason why increased temperature to 1000°C led to decreased structural stability would be due to stable $SiO_4$ units in the wall fragmenting into silanol group species with the thinner walls not reforming easily. Keene, M. T. J. *et al*., *Journal of Materials Chemistry* **1999**, *9*, 2843-2850; **DOI:** 10.1039/a904937a Permission granted by Royal Society of Chemistry Copyright 1999 ©

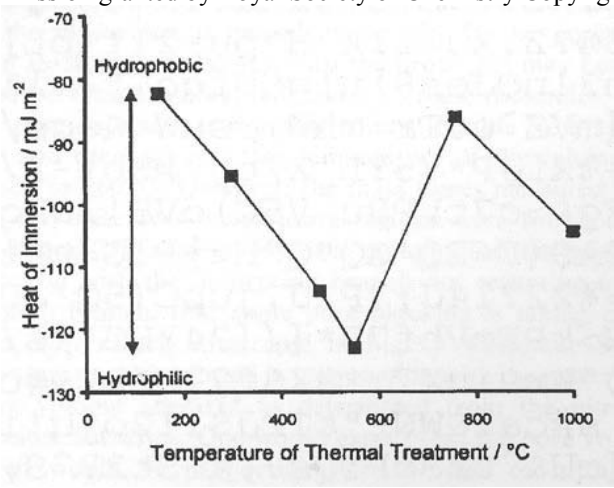


**Figure 2:36 Measurement of Hydrophobicity: Heat of Immersion vs. Calcination Temperature.**

**Supplemental text for Figure 2:36**-As seen in the above figure, the heat of immersion becomes more negative value up to approximately 550°C with increased hydrophilic character for Si-MCM-41, which could be due to the decomposition of CTAB complete leaving behind many surface silanol groups. [138] These wall silanol groups further condense into stable $SiO_4$ units with addition of more heat up to 760°C and reduction in immersion energy negative value. The trend of increased immersion negative value begins to above 760°C and hydrophilic character increases in the silica material. Heat of immersion would be a measure of the energy released as stable $SiO_4$ units for silanol groups. Therefore, one could conclude that gradual elevated temperature of input of thermal energy would lead to formation of more stable siloxane bond formation. Keene, M. T. J. *et al*., *Journal of Materials Chemistry* **1999**, *9*, 2843-2850; **DOI:** 10.1039/a904937a Permission granted by Royal Society of Chemistry Copyright 1999 ©

## 2.19 Effects of Counter-ion on M41S Mesoporous Materials

Although not the focus of early research on M41S mesoporous materials through expressed mechanism/models, [98,99,102,103] later research showed that the counter-ion (anion) has a significantly effect on the charge density matching occurring with surfactant cationic-silicate species in aqueous solution. [93,103,109,112,114,117,141-144] Stucky and co-workers developed cooperative mechanism through $^2H$ NMR instrumental analysis of surfactant-silicate solutions, where double-four-ring (D4R) silica oligomers comprised the primary species binding to the surfactant cationic head-group-area, and the addition of electrolyte through pH adjustment (acid addition) would effect the double layer region between surfactant-silicate interface. [103] Double-layer would be comprised of the outer, Gouy-Chapman, and inner, Stern, layers, as shown in Figure 2:37. [144] Although not studied fully, Stucky and co-workers reported the counter-ion (anion) would effect the outer double-layer, Gouy-Chapman layer, which could lead to reduction in volume needed for surfactant cationic head group. [103] Later research data on synthesis of Si-MCM-48 and Al-MCM-48 cubic bicontinuous phase with various electrolytes of 0.1 M revealed a trend of certain anions, thereby leaving only 4-5 Å thick Stern layers of tightly held ions in Stocker and co-workers work. [116] They further proposed the reason for phase transition would be linked to the surfactant packing parameter $g = V/a_0l_c$ where V = volume of the surfactant micelle; $a_0$ area of hydrated cationic head-group; and $l_c$ length + volume of surfactant alkyl chain. [86,116,121] Assuming the volume (V) of surfactant was constant and $l_c$ value, a decrease in the head-group area would enable a phase change to occur, according to the CTAB surfactant concentration plot in Figure 2:5 earlier in literature review also shown pictorially of corresponding shape taken in Figure 2:38. [144] A review of Stocker and co-workers results indicate $SO_4^{2-}$ ion consistently caused formation of Si-MCM-48 and Al-MCM-48. [116]

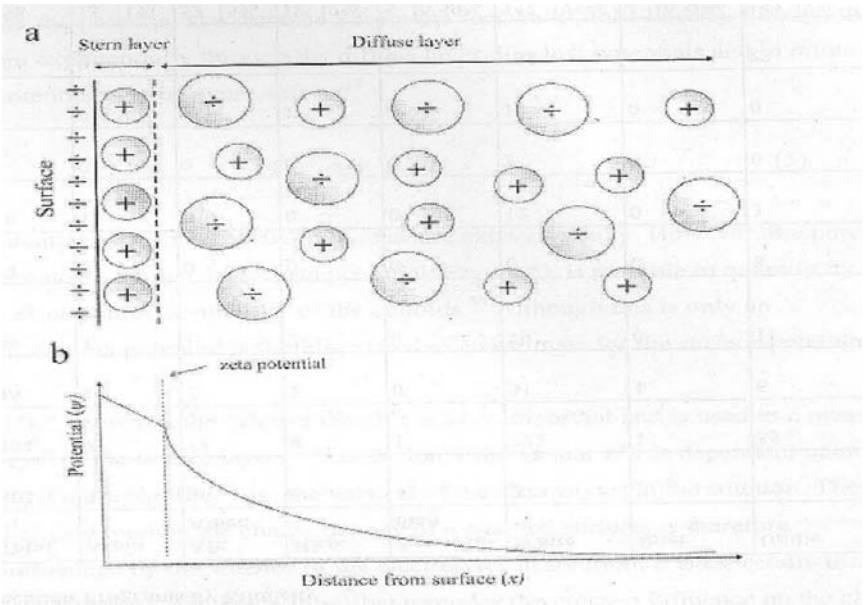


**Figure 2:37 Gouy-Chapman and Stern Counter-ion plot as function of distance.**

**Supplemental text for Figure 2:37**-As seen in the above figure part (a), there would be two outer layers before the surface of the material. [144] The tightly held Stern layer of positively charged cations against the surface and Gouy-Chapman Layer, otherwise known as Diffuse layer, of ions loosely held in the outer layer. In part (b) the zeta potential (ψ) vs distance from surface (x) plot shows a negative exponential slope with increased distance. Collectively, these two plots show that the electrostatic interaction decreases significantly with distance from the surface, which

means the Gouy-Chapman layer of ions could be stripped with a certain counter-ion. Permission granted by author: Dr. Torbjorn Vralstad

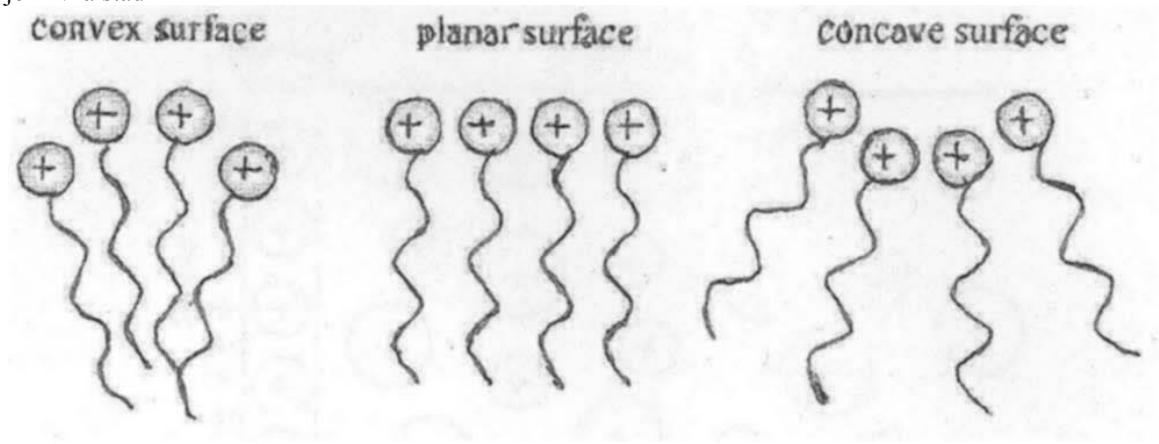


**Figure 2:38 Surfactant Micelle Shapes that Form with various Surfactant Packing Parameter g-value's.**

**Supplemental text for Figure 2:38**-As seen in above figure, [144] the convex surface forms with low g-value; the planar (lamellar) surface forms at large g-value; and the concave surface forms at intermediate surfactant packing parameter values. If the head-group area value, $a_0$, could be reduced with other variables constant, the desired concave surface would form leading to MCM-48 structure. Permission granted by author: Dr. Torbjorn Vralstad.

Further research on electrolyte concentrations revealed differences between anions. Mou and co-workers reported that the induction time for negatively charged silica oligomers to bind to the surfactant cationic portion increased when counter-ion concentration was greater than 0.1 M, which was ascribed to greater completion between the anion and negatively charged silica oligomers for the surfactant cationic head group region. [142] They noted the anion binding to the surfactant cationic head-group followed Hofmeister series with induction time period decreasing from left to right: $ClO_3^->NO_3^->Br^->SO_4^{2-}\sim SO_3^{2-}>Cl^->F^-$. Research completed in post-synthesis under hydrothermal conditions on hexagonal mesoporous silica indicated $Br^-$ anion would cause thicker pore wall formation at expense to ordering of hexagonal structure, which Lin and Mou proposed to be due to stronger binding of bromide ion vs. sulfate ion. [143] They discovered bulk structure trend where thicker pore walls led to decreased pore size and BET surface area, as shown in Figure 2:39. Their research results provided an example of how counter-ion identity directly effect the structural bulk properties. Lin and Mou note that the optimal application of counter-ion and reaction time period provide an avenue to forming the desired structure plus particle morphology. [145] Although these research finding conflicted, [116,142] they illustrated the major role that the counter-ion has on forming a desired structure in contrast to initial research complete in the early 1990s. [98,99,102] Klinowski and co-workers also discovered the counter-ion to CTA+ surfactant with the same silica precursor directly determined the quality of Si-MCM-41 formed, as shown in Figure 2:40. [109] These researchers note that the Br- ion would be harder to solvate and interacts to a greater extent with the CTA+ head-group region in contrast to chloride anion, which Kevan and co-workers also found with Si-MCM-48 prepared from CTAB vs. CTACl. [122] Zhao and co-workers note that the formation of colloidal particle, such as M41S materials, would be directly effected by the concentration of counter-ions, denoted as ionic strength. [117] When the ionic strength was low, the formation of small particles would occur; however, if the concentration of electrolyte was increased, this would facilitate increase particle growth from aggregates, as shown in Figure 2:41. Collart *et al.* [118] studied the mechanism of formation of spherical Si-MCM-48 particles and claim formation occurred on the truncated octahedral faces of radial tubes, as shown in earlier in Figure

2:22. Zhao and co-workers [117] results with Collart *et al.* [118] work appear to indicate that the lack of electrolytes in the Stober spherical particle synthesis [129] coupled with high ethanol concentrations causes the micelles to change shape and charge density matching, which would result in spherical particles over the truncated octahedral Si-MCM-48 crystals. Clearly, the application of sulfate anion could permit formation of larger Si-MCM-48 particles in Stober synthesis due to reduction in induction time, as noted by Zhao and co-workers in formation of SBA-15 with KCl of fifteen minutes with electrolyte vs. 60 minutes without. [117] Galarneau and co-workers [141] found with micelle-templated mesoporous silica structures that the addition of NaCl at a given pH value increase the condensation rate of TEOS, as shown in Figure 2:42. They attribute the trend to the amount of ionization of the silica species. When the silica species exhibits greater degree of ionization, this would facilitate more condensation. The increase condensation rate would permit more of the silica precursor to be formed into stable meso-structures. In conclusion, the appropriate amount of electrolyte could cause the formation of more stable Si-MCM-48 colloidal particles from the Stober sphere synthesis. [129]

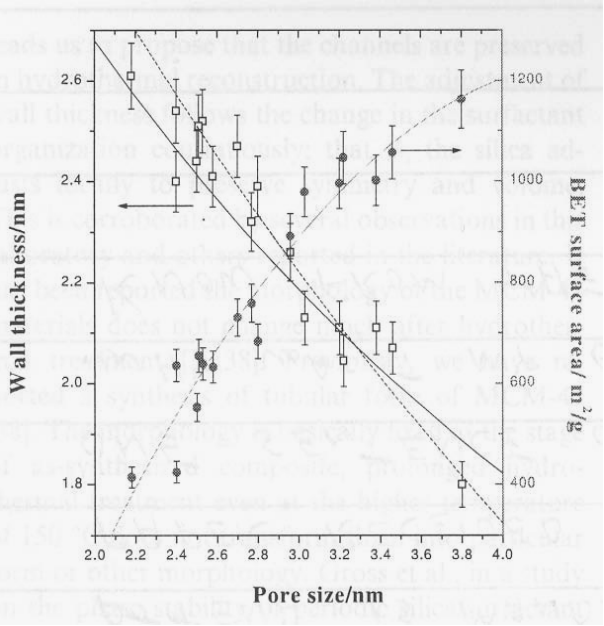


**Figure 2:39 Effect of Counter-ion on Pore wall vs. BET Surface area in Si-MCM-41.**

**Supplemental text for Figure 2:39**-As seen in the above figure, the wall thickness decrease leads to larger BET surface area values. [143] This would occur due to more thinner walls in the sample volume would lead to more surface area. The pore size increases even with more thin pore wall over the same area; since, the thicker pore walls require more area, thereby leading to smaller pore size. The counter-ion (anion) used in this study was bromide anion under three days of hydrothermal synthetic reaction conditions. Lin, H-P.; Mou, C-Y., *Microporous and Mesoporous Materials* **2002**, *55*, 69-80; **DOI:** 10.1016/S1387-1811(02)00407-9 Permission granted by Elsevier Scientific Publishing, Inc. Copyright 2002 ©

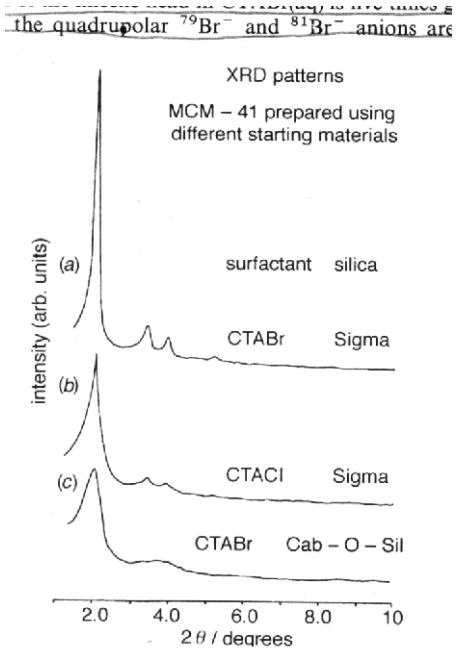


**Figure 2:40 Silica and Counter-ion effect on formation of Si-MCM-41 using powder XRD analysis.**

**Supplemental text for Figure 2:40**-As seen in the above powder XRD diffractogram, the formation of high-quality Si-MCM-41 would be governed by the silica precursor and counter-ion. [109] In the upper XRD diffractogram part (a) the sharp primary peak at approximately 2° 2θ followed by three well-defined secondary peaks in 3-5° 2θ range; whereas, the same silica precursor in part (b), but with use of CTACl vs. CTAB (chloride vs. bromide counter-ion), the structure formed in the same two-theta range would be much weaker and broader. This shows that the anion would not be a mere spectator but has active role in the formation of mesoporous silica structures through modulation of charge density matching. However, in part (c) application of CTAB with Cab-O-Sil brand vs. Sigma brand led to only one poorly formed primary peak, which means less condensation had occurred in the synthesis this Si-MCM-41 sample. Comparison of part (a) and part (c) with same CTAB surfactant but with two silica precursors reveals the subtle effect different types of oligomeric silica species in the Sigma and Cab-O-Sil fumed silica materials. Klinowski and co-workers analyzed the silica precursors with $^{29}$MAS NMR. 109 They found the $Q^3/Q^4$ ratio was higher in Sigma vs. Cab-O-Sil, which means the less polymerized Sigma fumed silica would require less harsh conditions. Cab-O-Sil brand would require more thermal energy and higher pH due to the higher concentration of fully condensed $SiO_4$ units as noted in Figure 2:12. This would explain why Si-MCM-48 has not readily been produced from fumed silica. Clearly, the use of fumed silica vs. TEOS for Si-MCM-48 would be favorable from increased stability as noted in Galarneau and co-workers synthesis of Si-MCM-48. [131,135] Finally, the sample in Figure 2:40 were aged for a time period, which also reinforces Schuth and co-workers results in Si-MCM-41 samples earlier. [132] Cheng, C-F. *et al.*, *Journal of the Chemical Society, Faraday Transactions* **1997**, *93*, 193-197; **DOI:** 10.1039/a605100f Permission granted by Royal Society of Chemistry Copyright 1997 ©

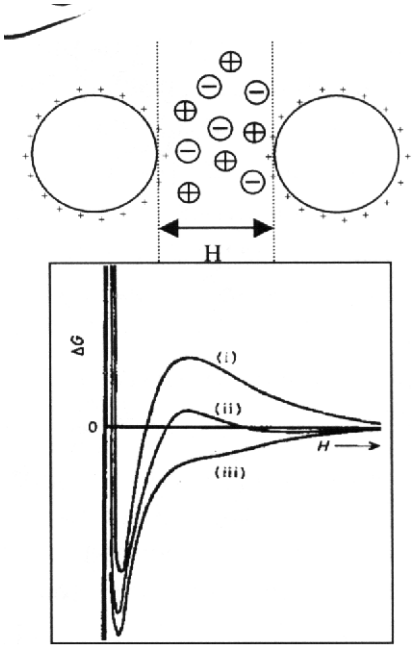


**Figure 2:41 Gibbs free total energy difference for colloidal particles as a function distance + ionic strength.**

**Supplemental text for Figure 2:41**-As seen in the above plot of Gibbs free energy (ΔG) difference between the colloidal particles at different ionic strengths. [117] When the ionic strength would be the lowest (i), the separation distance (*H*) would be the greatest. Higher ionic strength (ii) leads to a smaller gap between the colloidal particles. At much larger concentration of electrolyte, the ionic concentration (iii) would cause the separation distance to be tiny. This would permit the small colloidal particles to form larger particles through aggregation. The result would be a change in morphology of the particle due to reduction in induction time for forming the colloidal particles. Careful application of electrolytes could favorably change the morphology and particle to desired outcome. Yu, C. *et al*., *Chemistry of Materials* **2004**, *16*, 889-898; **DOI:** 10.1021/cm035011g Permission granted by American Chemical Society Copyright 2004 ©

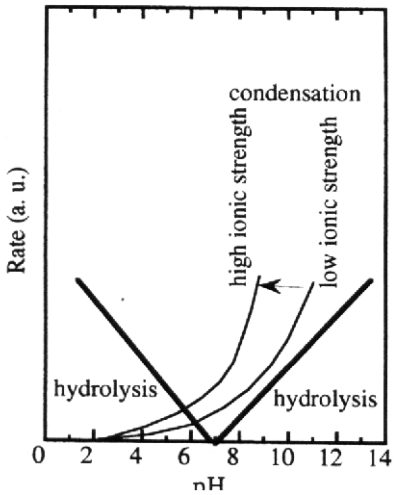


**Figure 2:42 Condensation rate of TEOS as a function of ionic strength and pH value.**

**Supplemental text for Figure 2:42**-As seen in the above plot of condensation rate on y-axis of TEOS as function of pH value on x-axis, one could conclude that the condensation rate initially increases at pH of approximately eight. [141] However, concentration of electrolyte would facilitate increased condensation at a given pH value, such as eight. The difference between low and higher ionic concentration would be in effect a difference in two pH units. Even at

the higher pH value needed in many mesoporous silica metal doped synthesis schemes, careful application of added electrolytes would increase the condensation rate, thereby cause formation of a more condensed silica structure. Di Renzo, F. *et al.*, *Microporous and Mesoporous Materials* **1999**, *28*, 437-446; **DOI:** 10.1016/S1387-1811(98)00315-1 Permission granted by Elsevier Scientific Publishing, Inc. Copyright 1999 ©

Due to the increase recognition of the potential promoting effects of counter-ions, Anpo and co-workers studied the effects of following promoter anions on Si-MCM-48 silica synthesis: $SO_4^{2-}$, $NO_3^-$, and $Cl^-$. [114] The beneficial effects of these promoter anions would be obvious with eight powder XRD reflections in the resulting Si-MCM-48 Ia3d bicontinuous structure, as shown in Figure 2:43. Clearly, $SO_4^{2-}$, $NO_3^-$, and $Cl^-$ anions at concentrations shown in Figure 2:43 have enhanced intensity and ordering of powder XRD peaks coupled with strong secondary reflections in 5-6° 2θ; whereas, the Si-MCM-48 made without these promoter anions lacks the fine structure exhibited by the higher peak intensity and secondary peaks. As shown in Figure 2:44, the pH value would play a central role in charge density matching by effecting the concentration of negatively charged silica oligomers at the interface and surfactant cationic head-group region in Si-MCM-48 even with promoter anions. Adjustment of pH value was found to be $OH^-/Si = 0.5$ best as balance between dissolution of silicate species at higher $OH^-/Si$ ratio and lower $OH^-/Si$ ratio with reduced electrostatic interations. Anpo and co-workers note the wider range of electroyte concentrations for the nitrate ($NO_3^-$) and chloride ($Cl^-$) promoter anions vs. sulfate ($SO_4^{2-}$), which they ascribe to lower valence charge and steric size. [114] Although the synthesis range would be smaller for sulfate ion to form Si-MCM-48, thermal and hydrothermal data indicates sulfate anion would produce greater ordering and polymerization of Si-MCM-48 structure through enhanced electrostatic interactions between surfactant cation head region and negatively charged silica oligomers. In contrast to monovalent $NO_3^-$ and $Cl^-$ anions, $SO_4^{2-}$ anion would be larger both in size and charge and exhibits excellent ability at self-hydrating. Mou and co-workers indicated $SO_4^{2-}$ had a weak affinity for the head group region of surfactant-micelles in comparison to other anions. [142] However, sulfate anion's ability to dehydrate both negatively charged silica oligomers and hydrated cationic head-group region would infer why phase transition and greater polymerization possible with this anion. [114,116] As noted earlier by Stocker and co-workers, [116] the ability to remove the Gouy-Chapman outer layer would permit more surfactant cationic head-groups to be in the same volume, thereby leading to enhanced charge density matching and possible phase transition. Comparison of hydration energies would explain sulfate anion's ability to dehydrate the interfacial region between negatively charged silica oligomers and surfactant cationic head-group, as follows: $SO_4^{2-}$ = -258.1 kilocalorie/mole; $NO_3^-$ = -81.3 kilocalorie/mole; and $Cl^-$ = -71.7 kilocalorie/mole.

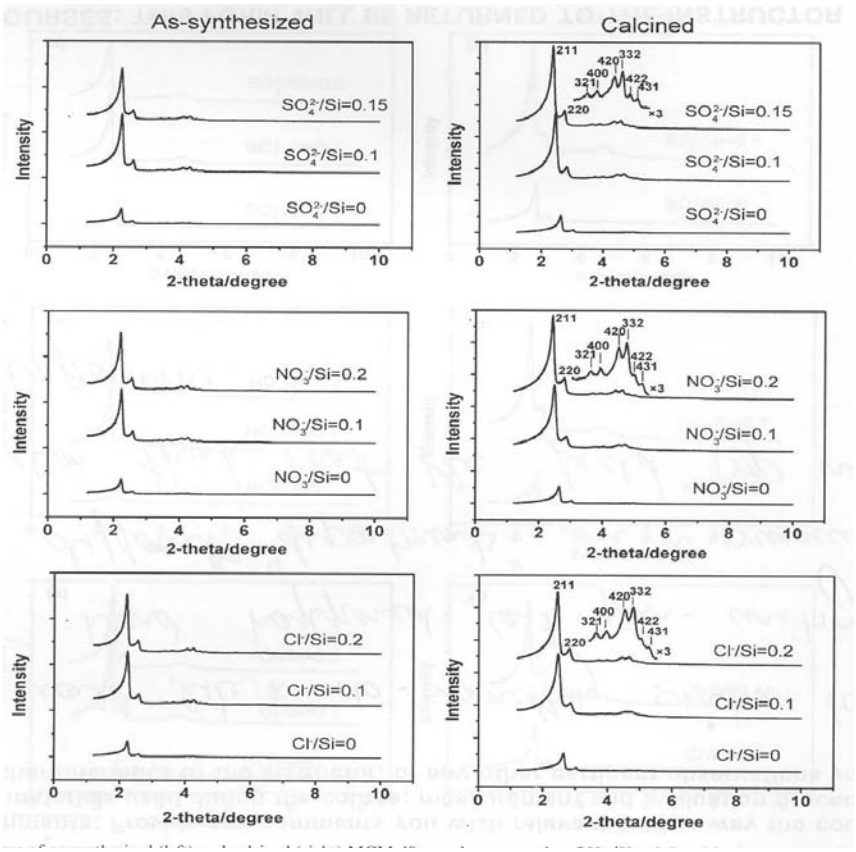


**Figure 2:43 Various counter-ion effects on Si-MCM-48 with powder XRD analysis.**

**Supplemental text for Figure 2:43**-As seen in the above figure, the counter-ion (anion) would have dramatic effect on the formation of hydrothermally stable Si-MCM. [114] The removal of the surfactant with all three anions led to increase in XRD peak intensity; however, the sulfate prepared Si-MCM-48 had greater number of reflections in comparison to nitrate and chloride made Si-MCM-48 viewing from top to bottom. It took less sulfate anion to achieve the desired stable Si-MCM-48 structure; whereas, more monovalent nitrate or chloride anion was needed due to lower charge. This meant that the range of addition of anions was narrower with the sulfate anion while nitrate and chloride ions had a wider synthesis range. Wang, L. *et al*., *Microporous and Mesoporous Materials* **2006**, *95*, 17-25; **DOI:** 10.1016/j.micromeso.2006.04.016 Permission granted by Elsevier Scientific Publishing, Inc. Copyright 2006 ©

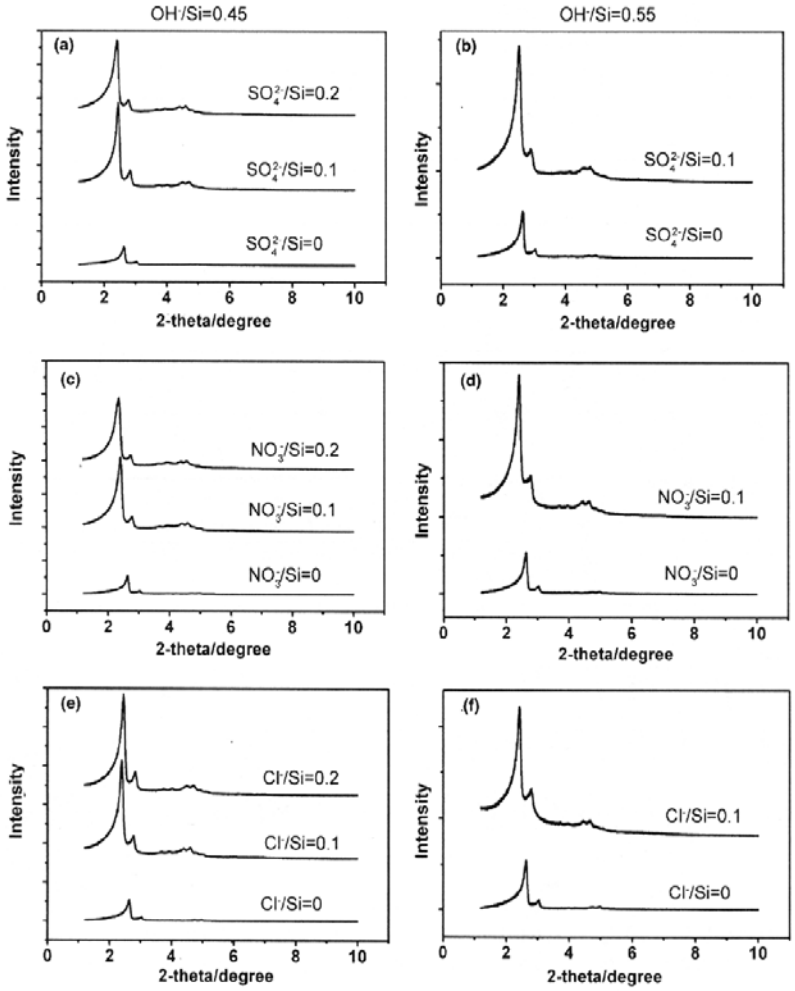


**Figure 2:44 Counter-ion and pH effect on Si-MCM-48 structure formation.**

**Supplemental text for Figure 2:44**-As seen in the above figure, the pH value ($OH^-$/Si) would effect the formation of stable Si-MCM-48 and the optimal anion concentration causing highly ordered Si-MCM-48 to form. [114] Reviewing the top panels (a) and (b) of use of sulfate ion with various $OH^-$/Si ratios, one could conclude that the higher pH value causes the range of anion concentration to be narrower. This would also apply to the middle and bottom panels with nitrate and chloride ion addition. From the above plots, one could note that the pH effect the amount of negatively charged silica oligomers and related charge density matching between the sulfate anion and surfactant head-groups at the interfacial region. This could explain why lower pH value led to larger range for the use of promoter anion vs. narrower in higher pH range. Wang, L. *et al*., *Microporous and Mesoporous Materials* **2006**, *95*, 17-25; **DOI:** 10.1016/j.micromeso.2006.04.016 Permission granted by Elsevier Scientific Publishing, Inc. Copyright 2006 ©

Thermal and hydrothermal study on the use of promoter anions showed that sulfate anion enhanced structural order due to increased polymerization of Si-MCM-48, as shown in Figures 2:45 and 2:46 plus Table 2:4. [114] This data clearly reveals that $SO_4^{2-}$ prepared Si-MCM-48 had least reduction in bulk structural properties, which must be due to the large hydration energy of $SO_4^{2-}$ anion. Table 2:4 shows that the promoter anion had less shrinkage upon calcination with $SO_4^{2-}$ superior at only 3.6%. Figure 2:47 shows that $SO_4^{2-}$ made has the largest BET surface area value compared to $NO_3^-$ and $Cl^-$ anions with slightly wider pore size distribution (PSD) value. This could mean excellent pore connectivity for Si-MCM-48 synthesized promoter anion samples.

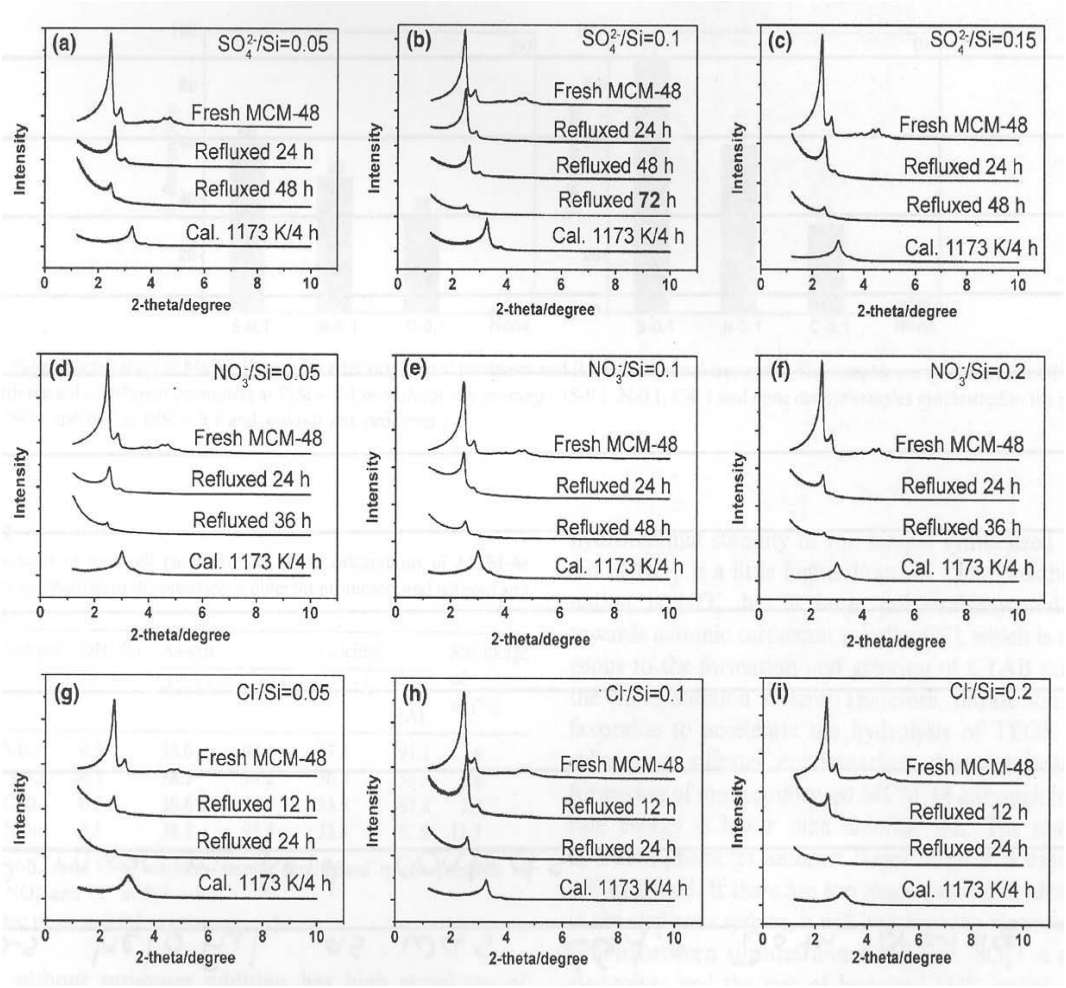


**Figure 2:45 Effect of pH and various counter-ions on the retention of cubic structure under reflux conditions.**

**Supplemental text for Figure 2:45**-As seen in the above figure of the various counter-ions (anions) under reflux (boiling water conditions), the sulfate prepared Si-MCM-48 at $SO_4^{2-}$/Si of 0.1 retained the structure the longest before collapse in comparison to the nitrate and chloride made Si-MCM-48 samples. [114] Clearly, the use of the sulfate promoter anion gave the best stability results for Si-MCM-48. In the above experiment, the $OH^-$/Si ratio was 0.5 in preparing the Si-MCM-48 structures. Wang, L. *et al*., *Microporous and Mesoporous Materials* **2006**, *95*, 17-25; **DOI:** 10.1016/j.micromeso.2006.04.016 Permission granted by Elsevier Scientific Publishing, Inc. Copyright 2006 ©

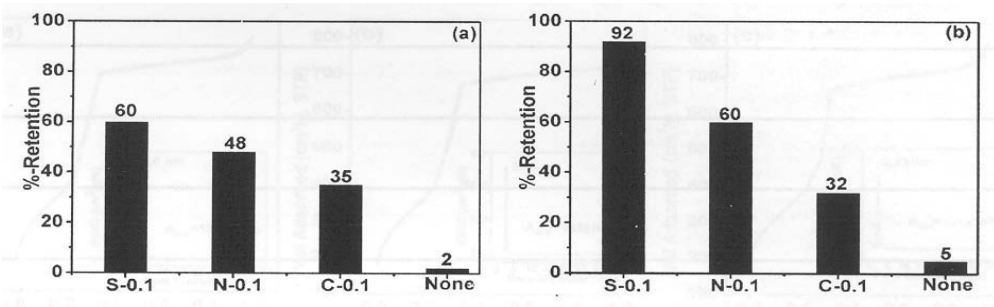


**Figure 2:46 Retention of Cubic Ia3d Structure as a function of Promoter Anions.**

**Supplemental text for Figure 2:46**-As seen in the above figure part (a) under thermal reaction conditions of 1173 K for four hours, the sulfate prepared Si-MCM-48 sample denoted as S-O.1 had the largest retention of structure. [114] Whereas, with nitrate (N-0.1) and chloride (C-0.1) prepared Si-MCM-48 samples structural retention values were

lower. The same held true under hydrothermal conditions of 12 hours of boiling water in part (b). From this data, one could conclude that the use of promoter anions, $SO_4^{2-}$, $NO_3^-$, and $Cl^-$, had a positive major difference on formation on the thermal and hydrothermal stability of Si-MCM-48 structure. The molar ratio of promoter anion was P/Si of 0.1 and these Si-MCM-48 materials synthesized at $OH^-$/Si ratio of 0.5. Wang, L. *et al*., *Microporous and Mesoporous Materials* **2006**, *95*, 17-25; **DOI:** 10.1016/j.micromeso.2006.04.016 Permission granted by Elsevier Scientific Publishing, Inc. Copyright 2006 ©

Contractions of unit cell parameters $a_0$ upon calcinations of MCM-48 samples synthesized in the presence of different promoters and without any promoter

| No. | Sample | $OH^-$/Si | As-syn. | | Calcined | | Shrinkage of $a_0$ (%) |
|---|---|---|---|---|---|---|---|
| | | | $d_{211}$ (Å) | $a_0$[a] (Å) | $d_{211}$ (Å) | $a_0$[a] (Å) | |
| 1 | S-0.1 | 0.5 | 38.6 | 94.5 | 37.2 | 91.1 | 3.6 |
| 2 | N-0.1 | 0.5 | 38.5 | 94.2 | 36.3 | 88.9 | 5.6 |
| 3 | Cl-0.1 | 0.5 | 38.6 | 94.7 | 35.8 | 87.8 | 7.3 |
| 4 | None | 0.5 | 38.2 | 93.5 | 33.8 | 82.9 | 11.3 |

S-0.1, N-0.1 and C-0.1 denote samples synthesized in the presence of $SO_4^{2-}$, $NO_3^-$ and $Cl^-$ at P/Si = 0.1.
[a] Cubic phase unit cell parameters.

**Table 2:4 Effects of Counter-ions on various structural Si-MCM-48 values.**

**Supplemental text for Table 2:4**-As in the above table of values, the sulfate (S-0.1) prepared Si-MCM-48 has the smallest shrinkage value upon calcination in comparison to the nitrate (N-0.1) and chloride (C-0.1) made Si-MCM-48 exhibiting increased shrinkage, as noted in the far right hand column. [114] The same held true for the unit cell $\mathbf{a_0}$-value decreased linearly from sulfate to chloride prepared Si-MCM-48. From a visual point of the view, as seen in Figure 2:25 and Figure 2:26, one could imagine the cubic structure decreasing in size and diameter of the pore channels. The bottom entry of Si-MCM-48 made without no promoter anion had the largest lattice shrinkage, which infers that the promoter anions help facilitate greater condensation of the pore walls. This clearly shows that the simple calcination, such as done in Schuth and co-workers [132] would not be enough to make Si-MCM-48 stable under harsh reaction conditions. Wang, L. *et al*., *Microporous and Mesoporous Materials* **2006**, *95*, 17-25; **DOI:** 10.1016/j.micromeso.2006.04.016 Permission granted by Elsevier Scientific Publishing, Inc. Copyright 2006 ©

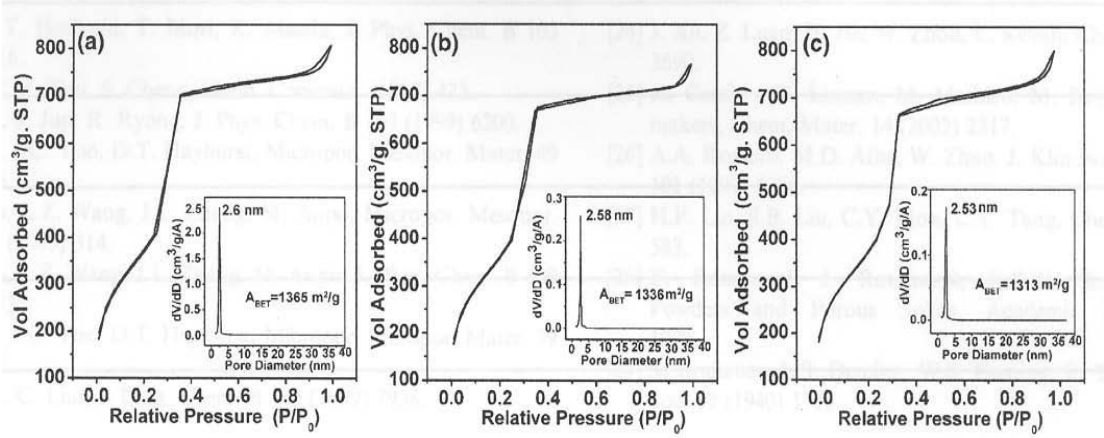


**Figure 2:47 Counter-ions effect with $N_2$ isotherm analysis of Si-MCM-48.**

**Supplemental text for Figure 2:47**-As seen in the above $N_2$ isotherms, the sulfate made Si-MCM-48 would have the highest surface area value in part (a). [114] Nitrate anion would have next largest surface area value in part (b), and chloride anion with the least surface area value in part (c). The pore size distribution (PSD) value was the smallest with use of chloride ion and largest with sulfate anion. The reason for the slightly large PSD value for sulfate anion made Si-MCM-48 might be due to the manner that it has on the charge density matching. With all of these Si-MCM-48 samples, the $OH^-$/Si ratio was 0.5. Wang, L. *et al*., *Microporous and Mesoporous Materials* **2006**, *95*, 17-

25; **DOI:** 10.1016/j.micromeso.2006.04.016 Permission granted by Elsevier Scientific Publishing, Inc. 

Research on metal doped MCM-48 has shown similar results with Ia3d bicontinuous structure forming and similar mechanism proposed for how $SO_4^{2-}$ anion works in aqueous solution. In the synthesis of Fe-MCM-48 Li and co-workers employed several different metal precursors and discovered that $Fe_2(SO_4)_3 \cdot xH_2O$ produced superior product in contrast to $FeCl_3 \cdot 6H_2O$ and $Fe(NO_3)_3 \cdot 9H_2O$. [112] They note reason for this difference due to the counter-ion presence, as shown in Figure 2:48 Vralstad and co-workers discovered that a change from CoCl2 • 2H2O to $CoSO_4$ •$7H_2O$ led to Co-MCM-48 of 2.5 wt% vs. only 1 wt% Co loading with former metal precursor. [93] These researchers attributed increased Co ion content in the MCM-48 framework due to sulfate's anion ability to modify the charge density matching in the surfactant-silicate interfacial region, as shown in Figure 2:49 visual illustration in of the interfacial region with metal cations. Similar to previous research findings, [107,114] they ascribe forming higher quality Fe-MCM-48 to $SO_4^{2-}$ ion ability to reduce the double-layer at the interface between surfactant cationic head-group-area and negatively charged silica oligomers. [112] According to Debye-Huckel theory with diffusion double layer of $1/\kappa$ ($\kappa = 2n_0Z^2e^2/\varepsilon kT)^{1/2}$ where $n_0$: counter-ions concentration, Z: valence state of counter-ions, *e*: the electron charge, ε: in media the dielectric constant, *k*: the Boltzmann constant, and *T*: temperature The guest ions, such as $SO_4^{2-}$, would decrease the double layer with a larger radius and higher valence charge. This higher charge permits $SO_4^{2-}$ ions to bind to $CTA^+$ surfactant cationic head-groups, thereby reducing the head-group area ($a_0$) value in surfactant packing equation $g = V/a_0l_c$. A reduction in $a_0$ value would lead to larger g-value assuming other variable constant, which would favor phase transfer to MCM-48. $NO_3^-$ and $Cl^-$ ability to facilitate binding similar to $SO_4^{2-}$ would be much reduced due to smaller size, reduced valence charge, and less ability to self-hydrate. Li and co-workers propose the surfactant-silica oligomers interface as Helmholtz double electric layers. [112] When there would be unequal distribution of charge, a distortion would occur in the Helmholtz layer at the interface resulting in a curvature. If the sulfate concentration was low, this would favor forming the hexagonal phase due to less negatively charged silica oligomers or $SO_4^{2-}$ ion than cationic $CTA^+$ ions from polymerization of silicate species to balance charges. Bonneeviot and co-workers propose that, when the Helmhotz layer would be equal charge balance from $SO_4^{2-}$ addition, the results would be the formation of lamellar and MCM-48 structure. Therefore, the optimal amount of $SO_4^{2-}$ ion would favor the formation cubic MCM-48, as noted in detailed mechanism of MCM-48 in 2:13 section. Finally, Klabunde and co-workers found that the metal incorporated Al-MCM-41 had lower powder XRD peak intensity vs. Si-MCM-41, which was ascribed to the ionic strength change with metal cationic effecting the template action, thereby shows the effect of both metal cation and counter-ion. [146]

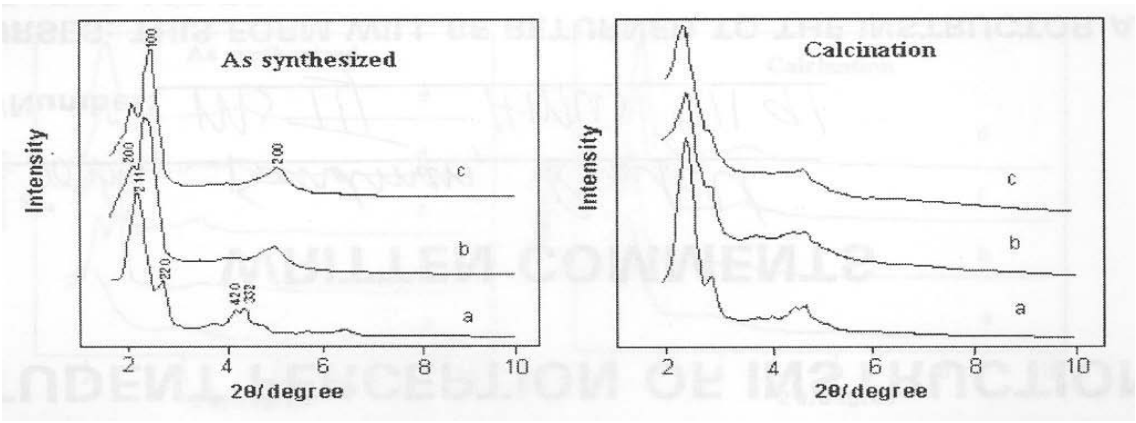


**Figure 2:48 Influences of various counter-ions (anions) in synthesis of Fe-MCM-48.**

**Supplemental text for Figure 2:48**-As seen in the above figure, the anions directly effected if Fe-MCM-48 formed. [112] The iron metal sources employed to form Fe-MCM-48 were as follows: (a) $Fe_2(SO_4)_3 \bullet xH_2O$; (b) $Fe(NO_3)_3 \bullet 9H_2O$; and (c) $FeCl_3 \bullet 6H_2O$. Clearly, the only Fe-MCM-48 structure to form was in (a), which shows the effect of the sulfate anion. The reason for sulfate anion's ability to positively effect the formation of metal doped MCM-48 structure would be linked to the modulation of the charge density matching. The reason for less well defined powder XRD diffractograms of Fe-MCM-48 would be linked to the ionic strength that changes with addition of transition metal cations. This means that the counter-ion must be able to compensate the large cationic charge, which from a charge point of view would infer sulfate as the best choice. Zhao, W. *et al*., *Microporous and Mesoporous Materials* **2007**, *100*, 111-117; **DOI:** 10.1016/j.micromeso.2006.10.020 Permission granted by Elsevier Scientific Publishing, Inc. Copyright 2006 ©

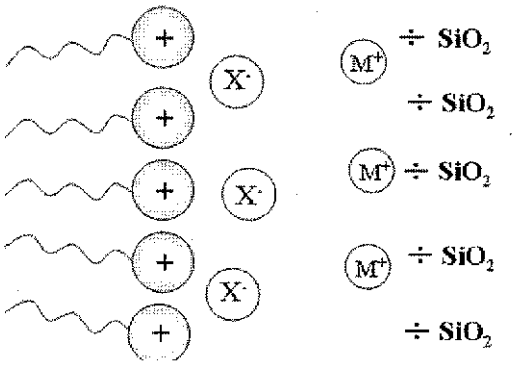


**Figure 2:49 Charge Density Matching Interface with metal cations in metal doped MCM-48 synthesis.**

**Supplemental text in Figure 2:49**-As seen in the above figure, the interfacial region would be comprised of metal cations ($M^+$) and counter-ions ($X^-$). [93] The interaction of $M^+$ and $X^-$ between the surfactant (+) and silica monomers/oligomers ($SiO_2$). The Stern layer in this illustration appears to be dehydrated from the electrolyte. This would facilitate the surfactant-micelle increasing the g-value, thereby forming metal doped MCM-48. The dehydration of the interface would be critical; since, metal cations commonly coordinate waters of hydration, which would affect the surfactant-silicate interface region. Vralstad, T. *et al.*, *Microporous and Mesoporous Materials* **2007**, *104*, 10-17; **DOI:** 10.1016/j.micromeso.2006.06.006 Permission granted by Elsevier Scientific Publishing, Inc. Copyright 2006 ©

## 2.20 Relevance of surfactant to Si ratio

For MCM-48 material, it was determined that the surfactant to Si ratio of 1-1.5 was needed to form the cubic structure. [14,48,62,66,100,147] With the low amount of surfactant in solution, the result was the formation of only the hexagonal MCM-41 structure. [66] As more surfactant was added to the reaction mixture, the hexagonal structure was converted to the cubic one, which would prove the past literature on the formation of liquid crystal phase using ce-

tyltrimethylammonium ($CTAM^+$) component. The cubic phase at higher surfactant ratio would be favored with chloride counter-ion in the solution. The researchers determined that the Si source affected the resulting products.

Previous research on the surfactant/Si (Sur/Si) molar ratio led to the following four categories that caused the formation of the product: the first structure produced a Sur/Si ratio less than one was the hexagonal MCM-41 structure; with increased Sur/Si ratio, the MCM-48 structure was formed at 1-1.5 Sur/Si ratio; even more surfactant in the Sur/Si ratio at 1.2-2 caused the formation of thermally unstable lamellar phase; and with the Sur/Si ratio = 2 led to the development of cubic octamer $[((CTMA)SiO)_{2.5}]_8$. [100] The researchers in the previous work discovered that the phase transformation using tetraorthosilicate (TEOS) hydrolysis rate was effected both by temperature and surfactant concentration. For example, the phase transformation to MCM-48 took place up to the Sur/Si ratio of 1.5 at 4°C; whereas, at ambient temperature of hydrolysis of TEOS, the reaction to form MCM-48 required a lower Sur/Si ratio of only 1.0. The researchers in this previous work indicate that hydrolysis temperature effect on the Sur/Si ratio would be due to the concentration of silicate species available for formation of the MCM-48 structure. The research team headed by Stucky more recently noted a high-to-low curvature phase transformation trend seen for MCM-41 to MCM-48 and beyond to the lamellar structure. [86] The reason for the above trend in phase transformation in hydrothermal setting would be due to condensation followed by reconstruction of the silicate framework. The use of temperature modification caused the phase transformation of MCM-41 to MCM-48, according to Gallis and Landry. [18]

The researchers went on to investigate the Si/P123 (where P123 would be a neutral polymer) ratio, and they found that a ratio between 40-75 for Si/P123 led to the la3d structure. [85] At a Si/P123 ratio of 80, a mixture of the hexagonal p6m and cubic la3d structures were produced, as noted in the X-ray diffraction (XRD) pattern in Figure 2:50. When the Si/P123 ratio was 90, the result was the formation of the hexagonal p6m phase. The researchers also studied the effect of ethanol from the hydrolysis of tetraorthosilicate (TEOS). The researchers fixed the Si/P123 molar ratio at 60 an added 1.27 grams of ethanol to the precursor mixture, which would be equal to a total quantity of ethanol plus Si/P123 molar ratio of 100. The result, according to the XRD pattern in Figure 2:50, was the formation of a highly developed cubic la3d mesoporous material. This would imply that the Si/P123 ratio was the significant variable that controlled the formation of the mesoporous material, and the ethanol from hydrolysis of TEOS only had a small role on the formation of a highly ordered meso-structure.

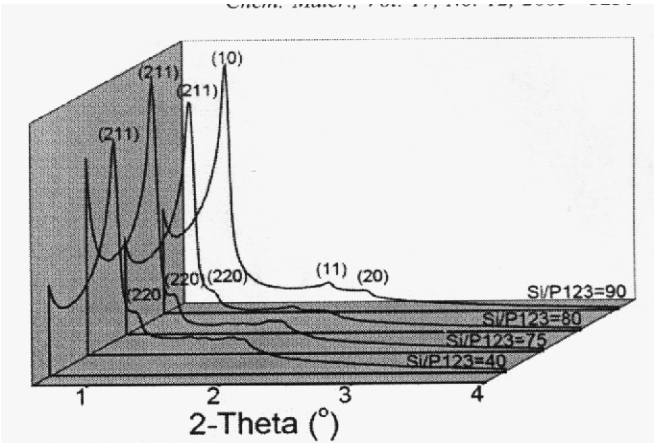


**Figure 2:50 Formation of Cubic Ia3d Si-MCM-48 with non-ionic surfactants.**

**Supplemental text for Figure 2:50**-As seen in the above (previous page) powder XRD plot, the cubic MCM-48 structure was produced between the Si/P123 ratio of 40-75; however, at a higher concentration leads to MCM-48 structure converting to the hexagonal MCM-41 configuration. [85] Chen, D. *et al*., *Chemistry of Materials* **2005**, *17*, 3228-3234; **DOI:** 10.1021/cm50209h Permission granted by American Chemical Society Copyright 2005 ©

## 2.21 Role of surfactant on M41S Mesoporous Materials synthesis

In the M41S synthesis of these mesoporous materials, the surfactant chemistry would be pivotal in the formation of the silica meso-stucture. [19,100,148] The silicate species has an important function with surfactant molecules in determining the resulting structure [56]; in particular, the inorganic silicate and surfactant electrostatic interactions determine the shape that the structure adopts. [19] Figure 2:51 shows the possible type of shape that the surfactants would need to adopt to form MCM-48 Ia3d bicontinuous structure. [38] Three major phases of synthetic organization occur according to solid-state nuclear magnetic resonance (NMR): the first step involves the surfactant converting into a micelle structure (a surfactant that form a spherical or elongated shape in usually aqueous solution phase) coupled with the polydentate and polycharged silica members forming ion pairs; the second step would involve the ion-pairs organizing into a liquid-crystal structure through self-organization, of which the resulting structure would be determined by the mixture composition, pH, temperature, and reaction time period; third and final phase would include the silicate species polycondensating to form a strong, rigid structure. [19] Shown in Figure 2:52 would be the representative micelle structures that could potentially form at different surfactant concentrations. [113]



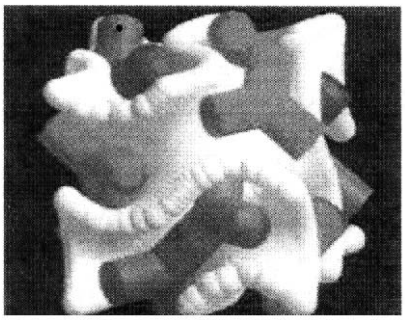

**Figure 2:51 Ideal Surfactant Conformation for forming MCM-48 Mesoporous Silica Structure.**

**Supplemental text for Figure 2:51**-As seen in the above image of MCM-48 structure with surfactants, it would appear the surfactants would need to form conformation head-to-head and tail-to-tail not simply spherical to rod shapes shown in Figure 2:52. [38] The initial steps would follow Figure 2:5 corresponding to Figure 2:52, but clearly the final surfactant shape, as dark color rods, appears to be another shape. The shape taken to form this complex structure might explain why the surfactant/silica ratio must be precisely monitored in addition to other variables. Voort, P. V. D. *et al*., *Catalysis Today* **2001**, *68*, 119-128; **DOI:** 10.1016/S0920-5861(01)00273-3 Permission granted by Elsevier Scientific Publishing, Inc. Copyright 2001 ©

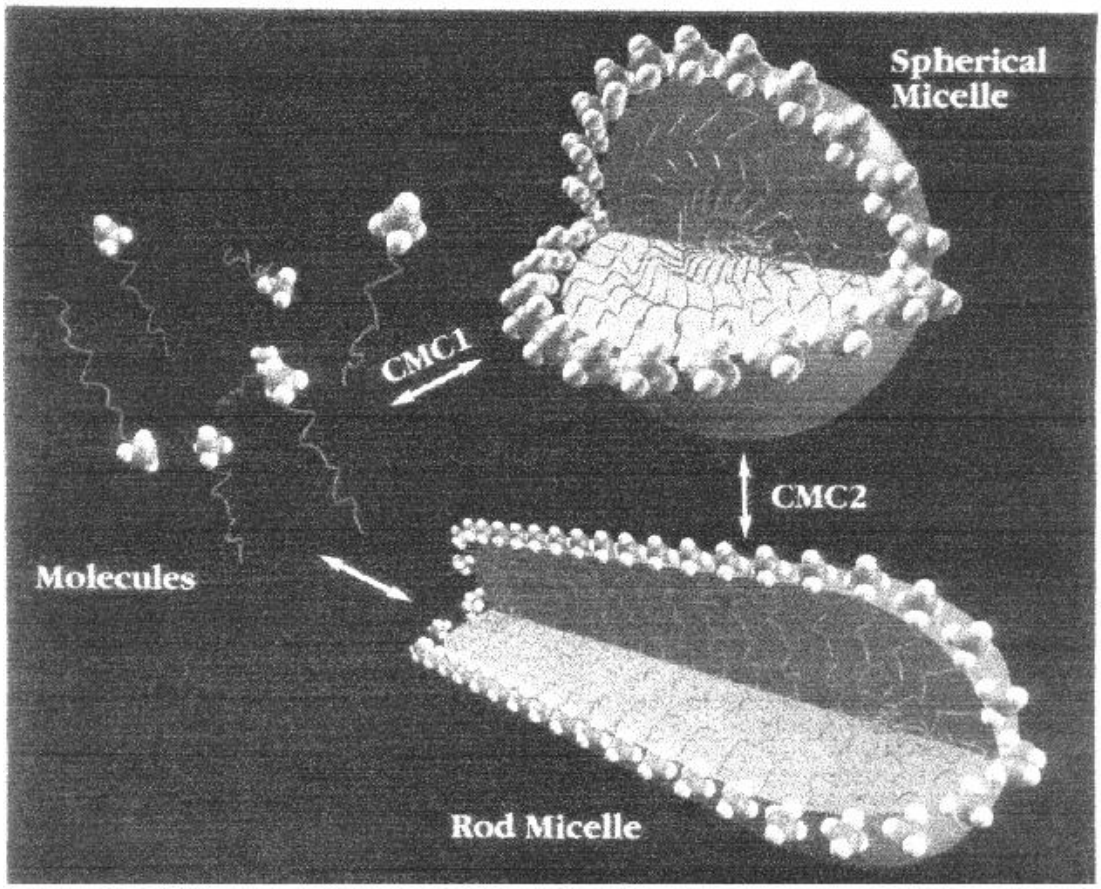


**Figure 2:52 Micelle structures formed at various surfactant concentrations, CMC1 & CMC2.**

**Supplemental text for Figure 2:52**-As seen in the above figure, the micelle structures shown in the above picture provide the conditions needed to form either the spherical or elongated structures. [113] As seen in the above picture, the molecules have to go through two formation steps denoted, as critical micelle concentration 1 & 2 (CMC1 & 2) to form the elongated micelle structure: these CMC steps were noted in Figure 2:5 and related text. It should be noted that the surfactant molecules on the left hand portion of the picture have a polar charged head-group with a long alkyl tail, and the long alkyl tail points inward to lower the repulsion energy of unlike species, which causes the formation of the micelle structure. Huo, Q. *et al*., *Chemistry of Materials* **1994**, *6*, 1176-1191; **DOI:** 10.1021/cm00044a016 Permission granted by American Chemical Society Copyright 1994 ©

As shown in Figure 2:52, surfactants would be considered amphiphiles, which means that they have both a lyphilic (solvent loving) and lyophobic (solvent hating) sections. [64,81,149-153] The cetyltrimethylammonium bromide (CTAB) surfactant in water that forms a micelle with lyophobic tail in the center and the lyphilic head at the outer surface facing the water solvent mixture, as could be viewed in Figure 2:52. [64,81,149,150] Although these synthesis conditions could occur, it causes a competing unfavorable interaction between the head-group and the alkyl tail determine the resulting stability of the micelle in water mixture. This would be one of many reasons for attempting M41S mesoporous silica synthesis using other surfactant combinations of cationic, non-ionic, and anionic surfactants, such as the work of Li and co-workers. [77] They were able to use sodium laurate (SL) and poly(ethylene glycol)-monooctylphenyl (OP-10) coupled with common cationic CTAB to form hollow-shell MCM-48 with this ternary surfactant mixture. As shown in Figure 2:53, the anionic SL species would act similar to other anions, such as sulfate ion, but the tail would be in part way of the alkyl tail region of CTAB micelle. The non-ionic OP-10 alkyl

potion would enter the non-polar section of CTAB. The end result would be large curvature corresponding to MCM-48 structure. In conclusion, the change of the variables V, and $a_0$ in surfactant packing parameter equation would lead to larger g-value and Ia3d MCM-48 structure.

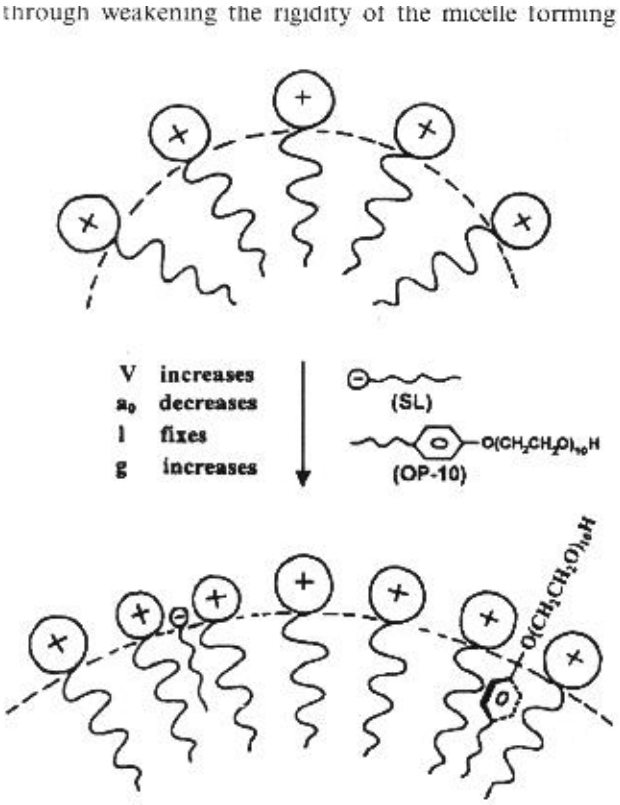


**Figure 2:53 Cationic-Non-ionic-Anionic Ternary Surfactant + Surfactant Packing Parameter Combination.**

**Supplemental text for Figure 2:53**-As seen in the above image of the effect of three types of surfactants, the result would be a reduction in the head-group area, $a_0$, value, thereby permitting the curvature to increase leading to MCM-48 structure conditions favorable for forming Ia3d bicontinuous material. [77] The SL surfactant would accomplish the same goal of reducing the positive charge on the cationic CTAB surfactant head-group, as seen in the upper portion without any other species to reduce the large positive charge. SL would facilitate this by lowering the positive-positive repulsion, as seen in the bottom portion. Non-ionic OP-10 would enter the non-polar tail region and increase the volume variable, V. The final result would be favorable g-value corresponding to Ia3d bicontinuous MCM-48 structure. Kong, L. *et al*., *Microporous and Mesoporous Materials* **2005**, *81*, 251-257; **DOI:** 10.1016/j.micromeso.2005.02.011 Permission granted by Elsevier Scientific Publishing, Inc. Copyright 2005 ©

## 2.22 Effect of short chain surfactant on the formation of pore structure

The pore size may be varied by altering the surfactant chain length. [95] The researchers found that shorter chain length of the surfactant caused pore structure to become more disorganized. [54,127] Further research indicated the pore radius was determined by the total length of the micelle; therefore, this would infer that the pore size could be changed by the surfactant chain length. [63] The use of 6-10 carbon length for the spacer section in the GEMINI surfactant should produce the MCM-41 structure and shorter carbon spacer lengths would cause the formation of lamellar phase. [63,150] To prove that the surfactant was a major variable in the synthesis of the MCM-48 structure, the surfactant/silica ratio and pH (10.5-13) were varied with the MCM-48 structure still forming. [63] The GEM 16-12-16 (number represents carbon chain length for each part of the surfactant) surfactant produced the MCM-48 structure

with the largest intensity while the GEM 18-12-18 gave the highest resolution. The researchers found when they used cetyltrimethylammonium ($CTA^+$) salt the pH has to be carefully adjusted to form the MCM-48 structure: this shows that the surfactant would be a very important component of the synthesis matrix.

## 2.23 Variables that control the size using a surfactant

With MCM-41, it could be made in a large number of pore sizes even without the organic additives; in contrast, the MCM-48 structure would be highly affected by the chain length of the surfactant [21,48,127] and pores greater than 2.8 nm (28 Å) have not been noted in literature. [48] The reason for no need of organic additives would be linked to the fact that volume of the tail region does not need to be as large to form the hexagonal phase of M41S structure. Likewise, the researchers noted that the counter-ion in the surfactant coupled with reaction conditions would affect both the pore size of the resulting product plus relative position of the peaks in the X-ray diffraction (XRD) pattern. [100] The researchers obtained a mean pore diameter of 2.3 nm (23Å) for the MCM-48 material using $C_{16}$TAB surfactant. [24] The pore diameter range was slightly increased, which would mean little pore deformation upon mechanical compression. A decreased pore volume would be an indication that the ordered porous structure has been destroyed in a sample.

## 2.24 Surfactants control what in the reaction mixture

The surfactant concentration controls the following: the amount of micellization, the shape that the micelle adopts, and the degree of aggregation that occurs with the micelles transform to liquid crystals, as shown in Figure 2:5. [64] The surfactant added to the water matrix at low concentration would be present as free molecules, which would be in solution and at the interface. Additional amount of surfactant added to the water cause the formation of the critical micelle concentration (CMC1) where these individual surfactant molecules come together and form tiny spherical aggregates, otherwise known as micelles, as shown in Figure 2:52. With even more surfactant added to the aqueous solution, the point would be reached denoted as (CMC2) in the plot: the spherical micelles coalesce and form elongated cylindrical micelles due to lower amount of solvent between micelles. Still at a higher concentration of surfactant in solution causes the rod-like micelles to aggregate in liquid-crystalline (LC) phases, usually hexagonal close-packed LC spread. A small increase in surfactant concentration causes the formation of cubic bicontinuous LC array of members while even more surfactant in solution leads to the lamellar LC structure. However, at very large concentrations of surfactant in solution, the formation of inverse phases could occur. This occurs in the center of the micelle and causing charged head-groups to point inward, thereby having the alkyl hydrophobic tail on the outside of the micelle.

To explain the observations seen in the $[Si_8O_{20}]^{8-}$ species conversion from one structure to the next, the use of surfactant liquid crystal (SLC) phase systems were employed. [26] The order of the structures begins with the lamellar phase (Lα) at the lowest surfactant concentration, but, with more surfactant, the Lα structure transforms to the cubic MCM-48 structure ($V_1$) followed by the hexagonal one ($H_1$) with more surfactant. Then, the cubic species ($I_1$) forms with additional amounts of surfactant and followed by the formation of micelles. The addition of water to a concentrated Lα SLC system lowers the amount of charge density in the region of the surfactant. This increases volume ratio exhibited between the surfactant polar head region and hydrophobic alkyl region causing an increase in the curvature of the water-surfactant interfaces. The result would be the transformation of the flat bilayers Lα with

zero curvature to the "saddle-splay" curvature $V_1$ followed by the formation of circular cylinders $H_1$; then, the structure sphere base $I_1$ and finally to the spherical micelles with maximum curvature. The researchers indicate that their $[Si_8O_{20}]^{8-}$ system would be governed by a similar pathway to the one listed above on the SLC system.

The acidic vapor treatment causes the silicate anions to be neutralized with protons and lowering the charge density experienced at the silicate region. [26] The result of the lowered charge-density would be the increased head-to-chain volume ratio for the surfactant array. The XRD patterns of the calcinated structures made in the acidic vapor precipate step show that the resulting structure to be stable after removal of template. The silicate-surfactant organization determined by electrostatic interactions would be the main factor in the formation of meso-structures. In conclusion, the size coupled with the charge of oligomeric members would be the most important guideline that needs to be noted with the designing of a mesoporous material, and the ability for the precursor to condense into an extended structure would be very important for the final material exhibiting thermally stable structure.

## 2.25 Instruments describe phase conversion into different structures

As shown in Figure 2:54 of the XRD plot, the MCM-41 structure converts over to the MCM-48 after 11 hours of synthesis time without the addition of NaF, and, after a reaction time of 48 hours, one would expect the formation of lamellar phase. [55] In contrast, with the use of the NaF in the synthesis gel, the formation of MCM-48 occurs after 8 hours converting to a lamellar phase after only 24 hours of reaction time. At higher concentrations above 0.1 N NaF led to the prevention of the MCM-41 converting to MCM-48. With more than 0.1 N NaF in the synthesis gel led to the conversion to MCM-41 directly to the lamellar phase, and, as the reaction time increased, the MCM-41 structure began to collapse, which was noted to be due to the silanol groups on the silicate surface undergoing hydrolysis. Too much $F^-$ ion results in the removal of condensable silicate species in the synthesis gel, thereby forming Si-F bonds in the restructuring process causing an increase in the surfactant to condensable silicate ratio. At a higher surfactant/Si ratio would lead to the direct formation of the lamellar phase, which was exactly what was formed at higher NaF concentrations.

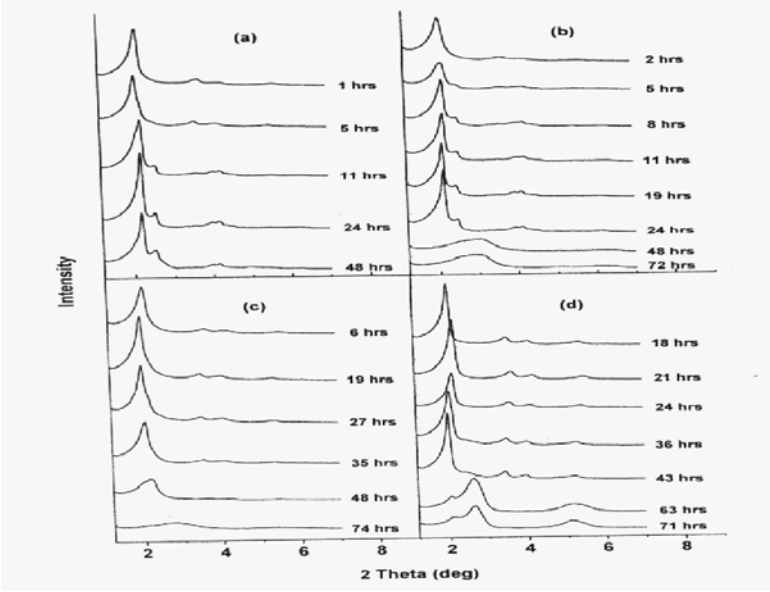


**Figure 2:54 Transformation of MCM-41 to MCM-48 with various concentrations of fluoride anion use.**

**Supplemental text for Figure 2:54**-As seen in the above (previous page) powder XRD plots, the amount of fluoride ion directly determines the length of Si-MCM-48 reaction conversion. [55] The following gel ratio values in (a-d) follows: $SiO_2$-HTACl-0.4$Na_2O$-142$H_2O$-xNaF, where (a) x = 0.0 mole, (b) x = 0.1 mole, (c) x = 0.3 mole, and (d) x = 0.65. As seen in the XRD plot (a), the MCM-48 structure was formed in only 11 hours without NaF; whereas, in plot (b), the MCM-48 structure was formed in 8 hours and after 24 hours begin to convert to lamellar phase. At higher concentration of NaF of x = 0.3 mole and x = 0.65 mole of salt concentration causes the formation only of the hexagonal MCM-41 structure. [Note: HTACl = hexadecyltrimethylammonium chloride.] Kim, W. J. *et al*., *Microporous and Mesoporous Materials* **2002**, *49*, 125-137; **DOI:** 10.1016/S1387-1811(01)00410-3 Permission granted by Elsevier Scientific Publishing, Inc. Copyright 2001 ©

To verify that the NaF was having this effect on the direct transformation to lamellar phase from MCM-41, the researchers reduced the surfactant/Si (Sur/Si) ratio from 1.0 to .67. [55] The result of this reduction coupled with NaF increase in the reaction gel mixture was noted in the XRD analysis of structure in Figure 2:55. Seen in the phase transformation occurred earlier than in previous XRD analysis. This could be due to reduced dissolution oligomeric silicate members in a constant pH. The addition of sodium silicate at a set pH value could cause the suppression of monmeric silicate species increasing the surfactant to condensatable monmeric silicate ratio, thereby creating quicker phase conversion from MCM-41 to MCM-48.

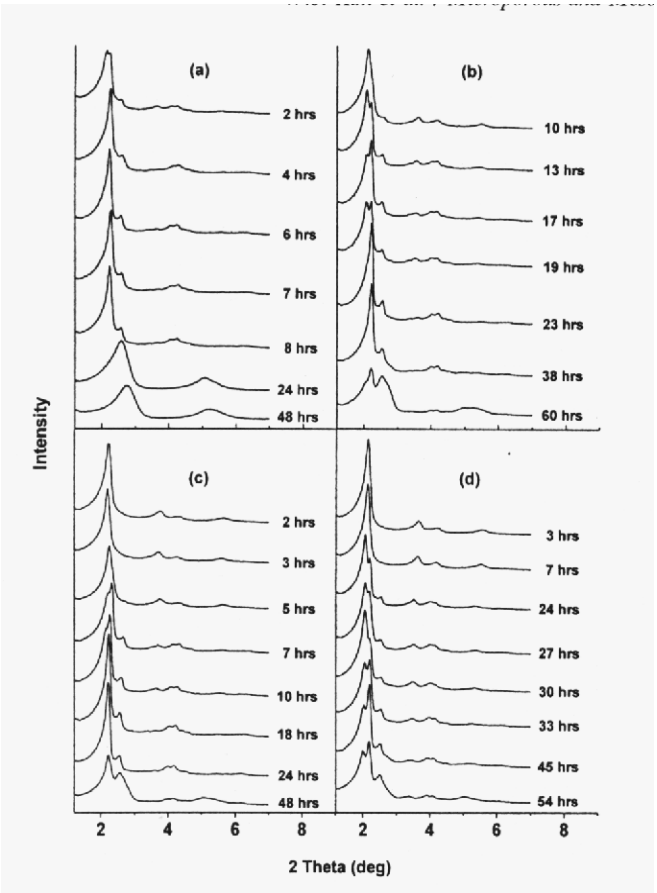


**Figure 2:55 Powder XRD Diffractograms of MCM-41 to MCM-50 lamellar phase transitions.**

**Supplemental text for Figure 2:55**-As seen in figure above, the XRD plots show the effect of reduced Sur/Si ratio coupled with use of NaF salt in the synthesis gel at 1.49$SiO_2$-HTACl-0.4$Na_2O$-142$H_2O$-xNaF, where (a) x = 0.0 mole, (b) x = 0.3 mole, (c) x = 0.5 mole, and (d) x = 0.65 mole. [55] As seen in XRD plot (a), the lower Sur/Si ratio led to shorter synthesis time for forming the MCM-48 structure; likewise, for full formation of MCM-48 characteristics, the concentration of 0.3 mole in XRD plot (b) at 23 hours made the desired cubic structure. With even more

NaF in XRD plot (c), the MCM-48 structure was formed in only 10 hours. A NaF concentration of x = 0.65 mole led to the formation of the lamellar phase. Kim, W. J. *et al*., *Microporous and Mesoporous Materials* **2002**, *49*, 125-137; **DOI:** 10.1016/S1387-1811(01)00410-3 Permission granted by Elsevier Scientific Publishing, Inc. Copyright 2001 ©

Phase transformation occurred after 23 hours of synthesis time with the use of 0.3 mole of NaF. [55] This delay in the formation of the phase conversion would be due to NaF addition effect. The number of silicate members available to condensate had decreased, due to the addition of NaF, through the formation of Si-F bonds in the anion exchange of $OH^-$ ions for $F^-$ ions. The lack of hydroxyl groups in the silicate species to participate in the structural transformation process lengthens the reaction time. The increased of the synthesis time led to the formation both lamellar phase with MCM-48 co-existing, as shown in Figure 2:54 (b).

The increase of NaF to 0.5 mole led to a phase conversion from MCM-41 to MCM-48 at a slower pace than in previous addition of NaF at x = 0 mole, and x = 0.3 mole, as shown in Figure 2:54. [55] With even more NaF addition to the reaction gel led to the elimination of the phase transformation of MCM-41 to MCM-48, instead, at a molar concentration of 0.65 mole NaF, this caused the production of a mixture of MCM-41 and MCM-48, as shonwn in Figure 2:54 (d). This trend seen in various amounts of NaF added to the reaction gel would indicate the following: when the concentration of NaF would be more than the optimal ratio, the residual silanol groups on the silicate species would be removed through anion exchange of $OH^-$ for $F^-$ and consequently lead to the lamellar structure. The above data would support the fact that the amount of surfactant to condensable ratio would be needed to cause the phase transformation of MCM-41 to MCM-48

As seen from Figure 2:54 and Figure 2:55, the use of fluoride anion for increased condensation and replacement of silanol groups would lead to more stable MCM-48 structure. [55] This idea has been extended in later research on Si-MCM-48 to both increase the hydrothermal stability of MCM-48 and reduce the surfactant/Si ratio, thereby causing Si-MCM-48 to have more potential applications. [154-158] Zhang and co-workers found that $F^-$/Si ratio of 0.3 led to a decrease of initial forty hours for crystallization of MCM-48 to only ten hours at 393 K. [154] This may be due to the high electronegativity of fluoride anion attacking the silicon atom and forming Si-F bonds coupled with increasing hydrolysis + condensation rate of TEOS. KF and $NH_4F$ has also the potential to facilitate increased polymerization similar to NaF. These researchers further discovered that introduction of NaF with TEOS before mixing in the surfactant increased hydrothermal stability to reflux conditions of 100°C over three days vs. complete collapse of MCM-48 structure in twelve hours under refluxing conditions at $F^-$/Si 0.1 ratio. 155 Further support was noted with only 1.2% shrinkage of the unit cell with $F^-$ treated sample before addition of surfactant, which the MCM-48 unit cell viewed in Figure 2:25. The hydrothermal synthesis with fluoride anion at 393 K required 24 hours. Additional research revealed that the crystallization time of 36 hours at 393 K with increased F-/Si ratio further increased structural durability under hydrothermal conditions even under four days of reflux conditions. 156 In addition, the pore wall thickness increased from 1.1 nm at 373 K vs. 1.2 nm with fluoride anion plus 393 K reaction temperature. This infers the optimal reaction time and fluoride anion addition would facilitate enhanced hydrothermal stability. Zhang and co-workers were able to reduce the CTAB/Si ratio to 0.1 with increasing amounts of NaF of $F^-$/Si 1.0 ratio. [157] They note the reason why fluoride anion ability to cause the desired results would be due the small size of F- anion, which does not effect the charge interactions between $CTA^+$ and silica oligomers vs. larger anions, such as $SO_4^{2-}$, $NO_3^-$, and $Cl^-$. The Si-MCM-48 structure formed; however, it was not as durable and could

only withstand reflux conditions for 24 hours. Through the increase in crystallization and hydrothermal temperature with use of F-/Si ratio of 0.1 at 423 K for 24 hours, the result was increased stability in the MCM-48 material under reflux environment. [158] In conclusion, Zhang and co-workers were able to decrease the CTAB/Si ratio from 0.65 to 0.1 and increase the stability of Si-MCM-48 with use of fluoride anion to cause further polymerization of silica walls against hydrothermal attack. [154-158]

## 2.26 Alternatives to dealing with the synthesis problem of MCM-48

Although the cetylbenzyldimethylammonium chloride (CBDAC) surfactant was a major step forward in the formation of MCM-48 structure, it was the GEMINI surfactant discovered that caused the consistent formation of the MCM-48 structure. [22,61,63,150] The surfactant has two quaternary nitrogen atoms connected with end methyl/ alkyl groups an adjustable spacer $–CH_2-$ functional group. [61,63,150] The head group area ($a_0$) of this surfactant was noted to change considerably with length of the ($-CH_2-$) spacer functional groups. [63,150] When the $–CH_2-$ group was below 10 carbon atom chain, this section denoted as the spacer was in contact at the air-water interface; however, at carbon value above 10, the increased hydrophobicitiy causes spacer chain to the leave the water and fold into the interface side containing air. This leads to the spacer section of the GEMINI surfactant occupying a region in the hydrophobic area in the micelle, which lowers the effective head-group area variable , $a_0$, while increasing the volume, V, variable. Also, due to the spacer chain connected to the head-group area, it stays in outer section of the micelle.

The researchers found that, when the sodium dodecyl sulfate (SDS) and non-ionic block copolymer 123 (P123) at a SDS/P123 ratio of 2.1 to 2.5, it led to the formation of bicontinuous cubic la3d mesoporous material; on the other hand, if the SDS/P123 ratio was below 2.1, the hexagonal p6m mesoporous material was synthesized. [85] With the SDS/P123 ratio increased to 2.8, the result was formation of a disordered mesoporous material, as concluded from XRD diffraction pattern in Figure 2:56. Therefore, the above synthesis of mesoporous cubic la3d material would indicate a small synthesis range for forming the bicontinuous structure, as shown in previous research with cationic surfactants in phase diagram in Figure 2:5. Studies of micelle interactions between triblock copolymers and anionic mixed surfactants indicated that the SDS molecules would bind to the hydrophobic PPO (poly(propylene oxide)) blocks instead of the copolymers below critical micelle concentration (CMC). [17,85] The result of the low levels of mixed surfactants-PPO blocks would be the existence of an extended conformation shape to lesser/greater degree. Adding more anionic surfactant, after reaching the saturation point of the SDS molecules connected to the copolymers, could cause the conversion of mixed micelles to become smaller aggregates. With the molar ratio of SDS/P123 between 2.1-2.5, a mixed surfactants micelle structure could obtain a larger hydrophobic volume from the SDS molecules binding onto the more hydrophobic PPO blocks, thereby causing the hydrophilic/hydrophobic volume ratio ($V_H/V_L$) to be lowered. [85] The reduced interface curvature exhibited by this surfactant-copolymer interaction would be manipulated in favor of the la3d cubic phase structure. When the molar ratio of the surfactant—copolymer was lower than 2.1, the result was the formation of a hexagonal p6m meso-structure due to the fact that small amount of SDS molecules bound to the PPO blocks could not have a major effect on the solution

over the SDS/P123 ratio of 2.5. A disruption of the self-organization occurring with the block co-polymer occurs, thereby creating a disordered mesoporous material.

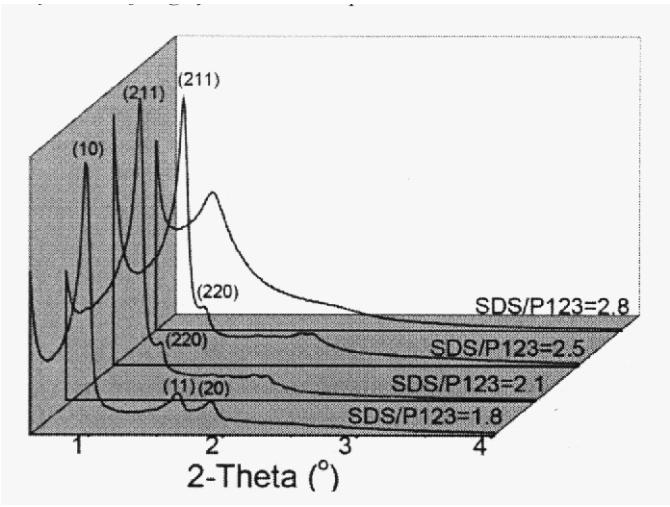


**Figure 2:56 Formation of Si-MCM-48 with optimal amount of anionic/non-ionic surfactants.**

**Supplemental text for Figure 2:56**-As seen in the above figure, the optimal concentration ratio of SDS/P123 was determined to be 2.5 for forming MCM-48. [85] Chen, D. *et al*., *Chemistry of Materials* **2005**, *17*, 3228-3234; **DOI:** 10.1021/cm50309h Permission granted by American Chemical Society Copyright 2005 ©

## Section Three: Fundamentals of MCM-48 Structure Modification

### 2.27 Effect of heteroatom substitution on the unit cell structure

The insertion of a heteroatom usually leads to a larger bond length plus a thickening of the pore wall due to transition metal encouraged cross-linking that occurs in amorphous silica walls. [44,147,159] The combined pore wall thickening coupled with an enlargement of the unit cell would indicate to a first approximation of incorporation of V ions into the structure. [94,147] This belief was supported by $^{29}$Si magic angle spinning nuclear magnetic resonance (MAS-NMR) data. [147,159] The lower intensity of the X-ray diffraction peaks with higher transition metal content infers potentially that partial collapse of cubic structure had occurred with large metal loading in silica framework. [66,128] The research results indicated that the higher metal loading of Mn into MCM-48 structure led to decrease in 2θ angle and consequently large *d*-spacing, as could be viewed in the MCM-48 unit cell in Figure 2:25. [66] The literature confirmed that *d*-spacing [unit cell] increases with transition metal incorporation due to the promotion of cross-linking, which lowers the unit cell contraction in the calcination step. The XRD data indicated a trend of poorer structural ordering as the amount of Al increased with peaks overlapping coupled with lower peak intensity. [100] The expansion of the unit cell would be expected, according to zeolite chemistry; since, the Al-O bond would be 1.75 Å in comparison to the Si-O bond of 1.60Å. However, in the present research, the expected result was the opposite with the substitution of Al into the framework leading to a contraction in the unit cell for both MCM-41 and MCM-48. The use of heteroatoms in place of Si in the framework or as extra framework species opens the possibility of these materials to be used in acidic and redox catalysis capacities. [31-43,53]

### 2.28 Effect of doping on the MCM-48 structure with transition metal ions

The researchers found that the pore radius, pore volume, and surface area decreased with increased vanadium metal incorporation. [22] The lower amount of metal incorporated into the Si framework of MCM-48 indicated

from atomic absorption analysis of the starting gel indicates only part of the elements had been incorporated into the MCM-48 structure. [25] The incorporation of metal ion into the lattice was 80-88% for the hydrothermal synthesis while the novel synthesis had an incorporation rate into the framework of 88-97%. [27] At higher metal concentrations above 18% (w/w), the MCM-48 structure would be destroyed; however, the shape of the particles would still be spherical. The substitution of metal ions in the tetrahedral position has decreased stability with increasing radii of the element in comparison to Si. [68]

## 2.29 Crossing + Lengthening of the bond would mean incorporation of vanadium ions

According to researchers, an increased pore size indicates that the metal ion has been incorporated into the lattice structure. [49] With the connection of the OH (silanol) group to vanadium ion, for example, the binding of the hydroxyl groups to the metal ion causes a contraction of the pore size (volume). However, the result would be an increase in the pore size due to the larger ionic radius of vanadium to Si when the metal ions substitutes for Si.

## 2.30 Three methods for enlarging pore structure

To achieve larger pore sizes in the M41S family of mesoporous materials, three different synthesis modifications were completed. [16] These modifications included: (1) attempt was to adjust the length of the alkyl chain that comprised the surfactant "tail," (2) the use of reagents, such as 1, 3, 5-trimethylbenzene, to enter the hydrophobic section of the micelle and consequently cause the "tail" region to increase in size, and (3) the last method placed the formed sample in the "mother liquor" for extended periods of time at higher temperatures than the synthesis.

## 2.31 Value of post-synthesis have on the structural transformation

The researchers employed the use of hydrothermal post-synthesis to increase the long-range ordering of the pore structure and reduce the synthesis time; since, previous research had shown that the post-treatment increased the pore size. [63] Without this treatment, the resolution of the XRD pattern for the MCM-48 structure had lower quality and peak maxima values at higher 2θ angles, thereby indicating that the cubic structure unit cell was smaller, as shown in Figure 2:57 part A. The results of post-hydrothermal treatment infer that the framework undergoes further condensation coupled with reconstruction, which improves the XRD peak pattern, as shown in Figure 2:57 part B. [18,63] This hydrothermal post-treatment according to thermal gravimetric analysis (TGA) data, shows that the pore walls thicken and additional silica condensates; however, this post-treatment has an optimal number of days, as confirmed by XRD. The treatment leads to the (211) cubic reflection lower diffraction and therefore larger cubic unit cell, as viewed in Figure 2:25. [63,159] The researchers found that optimal hydrothermal + post-synthesis treatment led to the greatest desired structural characteristics, which extended the synthesis. Post-treatment work caused an amorphization of the MCM-48 structure with pore volume remaining relatively constant.

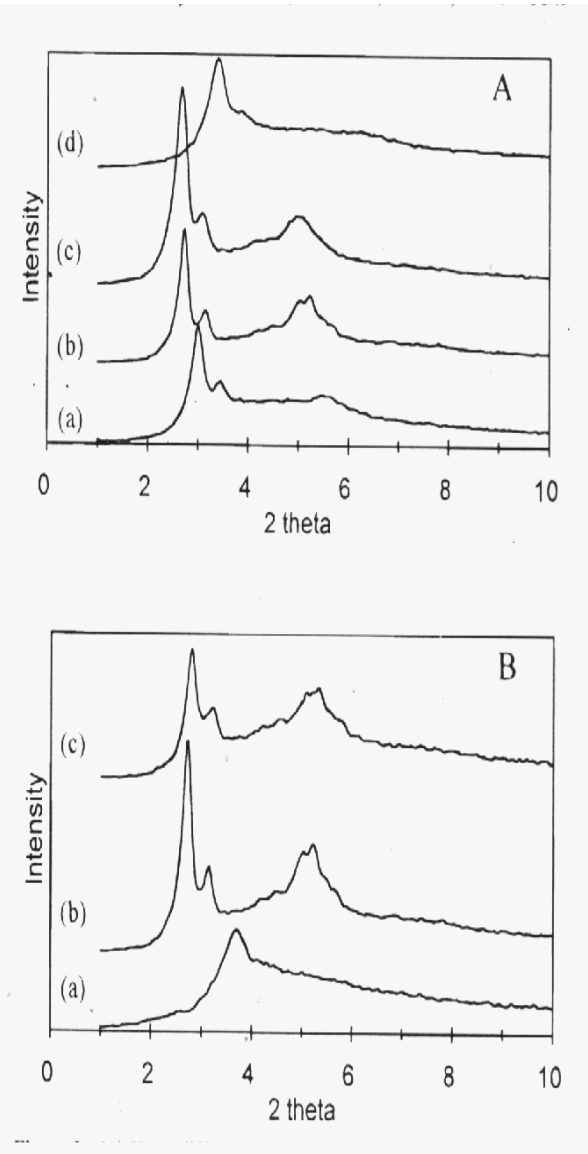


**Figure 2:57 Powder XRD Analysis of Optimal Reaction Conditions for Forming Si-MCM-48.**

**Supplemental text for Figure 2:57**-As seen in the above figure, the XRD plot shows that there would be an optimal synthesis time period, as noted in plot A. [63] In plot A, one could see that XRD diffractogram (b) has the best MCM-48 characteristics with well-defined secondary peak values: this would be with a synthesis time of five days. The other XRD diffractograms in plot A would have the following synthesis times: (a) 1 day, (c) 10 days, and (d) 21 days. The surfactant use for synthesizing these MCM-48 structure would be GEM 16-12-16, where the number represents the number of carbons in each part of the surfactant molecule. A similar set-up was done in XRD plot B with hydrothermal treatment. In (a) would be 1 day of hydrothermal treatment; whereas, in plot (b) would be 3 days of hydrothermal treatment, and in plot (c) would be after 5 days of hydrothermal treatment. Finally, as seen in XRD plot B, the diffractogram (b) would have highest resolution with excellent secondary peaks shown: this clearly reveals the effect of both the synthesis time and hydrothermal treatment in designing and excellent MCM-48 structure. Van Der Voort, P. *et al*., *Journal of Physical Chemistry B* **1998**, *102*, 8847-8851; **DOI:** 10.1021/jp982653w Permission granted by American Chemical Society Copyright 1998 ©

## 2.32 Value of trimethylsilylation

The stability of MCM-48 toward water vapor could be improved dramatically using trimethylsilylation according to previous research results. [22] The large stability noted in both silylated (sil) Si-MCM-48 and MCM-41

would be due to a large amount of hydrophobicity. [16,46,160] Likewise, the stability seen in the (sil) Si-MCM-48 samples was determined to be retained in silylated-calcinated (sil-cal) Si-MCM-48 sample even though the pore walls were no longer hydrophobic from the silylation step. [46] The silylation method used on the Ti-MCM-41 led to a major increase in stability. The sil coated Ti-MCM-41 only absorbed 0.29 mass % $H_2O$ while the Ti-MCM-41 non-sil absorbed 55 mass % $H_2O$. [160] Moreover, the pore volume and surface area were reduced using trimethylsilylation step. For example, the Ti-MCM-48 was only .71 $cm^3/g$ for the pore volume.

The experiment with non-sil Si-MCM-48 with water vapor an aqueous saturated solution of $NH_4Cl$ at room temperature led to a decrease in structure regularity as processed. [46] After 90 days of exposure to the above conditions, the non-sil Si-MCM-48 XRD peak intensities could not be restored by calcinating the sample for 6 hours at 873K: the structure of the non-sil MCM-48 sample had collapsed. This structure destroying process could not be reversed using calcination. The $^{29}Si$ MAS NMR data indicated from the peak ratio that the Si-O-Si bond was being hydrolyzed; since, the products of the hydrolysis were increasing according to the peak ratio. In contrast, the sil Si-MCM-48 retained structural integrity due to little absorption of water indicated from the $^{29}Si$ MAS NMR spectra. The XRD peak intensity of the $d_{211}$ reflection in sil-cal Si-MCM-48 showed little change after a 30 day exposure to moisture treatment, but the $^{29}Si$ MAS-NMR did indicate from the molar ratio a change corresponding to the hydrolysis of the Si-O-Si bond after exposure to a 10 day moisture treatment. The long-range order of the sil-cal Si-MCM-48 was retained even with indication of hydrolytic cleavage of the Si-O-Si bond according to $^{29}Si$ MAS-NMR. The diffraction peak for the $d_{211}$ reflection in the non-sil Si-MCM-48 was considerably decreased with increasing mechanical pressure; moreover, the absorption at $P/P_0 = 0.3$, which usually would be a steep inflection point revealing an ordered mesoporous framework, which decreased with the amount of $N_2$ absorbed. The $N_2$ absorption isotherm for sil Si-MCM-48 showed no change upon compression. However, there was slight decrease in the $d_{211}$ peak height with increasing mechanical stability in comparison to the non-sil Si-MCM-48 sample, which was not expected due to the removal of the methyl groups through calcination.

The researchers indicate that it would be possible for the water absorbed on the silanol group to cause the hydrolysis of the Si-O-Si bond, which would led to the destruction of the ordered mesoporous structure. [46] The capping process employed through the trimethylsilyl groups on the hydrophilic silanol groups cause the Si-O-Si bond to be protected from hydrolysis leading to increased stability of the resulting Si-MCM-48 structure. Finally, the 2 Å thicker wall found in the Si-MCM-48 sample was not noted by researchers as a major reason in structure retention.

## 2.33 Methods to strengthen the pore walls against hydrolysis attack

To deal with this problem of instability in mesoporous molecular sieves, there have been several different methods used in an attempt to strengthen the resulting structure of the M41S family. [47] These methods include (1) increasing thickness of the pore walls, (2) silylation to convert unstable silanol groups, (3) the salt effect to stabilize the mesoporous structure, and (4) the hydrothermal restructuring process. [25, 47] The thickening of the pore wall would appear to be the simplest method of increasing structural stability; however, no synthetic method has been developed to systematically determine the wall thickness. With the silylation method, the silanol groups on the pore walls would be converted to silanes, which would be more durable against hydrothermal conditions. [47] This method allows for systematic control of the silylation technique to consequently increase the hydrophobicity and hydrother-

mal stability of the resulting structure. The silylation method, however, would not be desire-able in applications where one needs hydrophilic pore structure. In contrast to the silylation method, the salt effect structural enhancement technique does not change the amount of silanol group concentration in a calcinated sample, but encourages subtle changes in the structure resulting in an increased stability in the pore structure. The main problem with the salt effect has been poor reproducibility. Researchers found that 10 extra days at 373 K were required for the salt effect to reach the desired result. The researchers also noted two effects that salting had depending on the concentration of salt in the reaction mixture. The first type of salting effect includes branching of the micelles from the hexagonal structure to a disordered worm-like structure: this phase transition would occur at higher salt concentrations. The second step of the salting effect would be due to smaller amount of salt added to the reaction system leading to the reconstruction of local silica structure at a slow pace that in-turns does not show shape changes.

The research from Voegtlin and co-workers on Si-MCM-41 could explain why the above trend with the $F^-$ ion worked to improve the overall pore structure of metal doped MCM-48. [25,161] The $F^-$ ions could be causing the increased polymerization of the silicate species, in a catalytic manner. The $F^-$ ion increases the charge density in the silicate framework, and thereby causes the greater synergistic interaction to occur with the cationic micelles and anionic structure of MCM-48. From the above results of $F^-$ ion use in the synthesis of both Ce-MCM-48 and Fe-MCM-48, it could be concluded that pore structure ordering was increased with the use of fluoride ion. [25] The more metal ion added to the MCM-48 structure caused the framework to be less ordered in the case of Ce incorporation, so both factors of metal incorporation and $F^-$ addition affect the resulting MCM-48 structure.

Using NaF in the reaction mixture appeared to prevent the phase transformation from MCM-41 to MCM-48; instead, the phase conversion from MCM-41 led directly to the lamellar structure. [55] The placement of NaF in gel mixture in initial phase of synthesis of MCM-48 was due to substitution of the hydroxyl group, and thereby leading to fluoride anion replacement of the hydroxyl groups due to its high electronegativity. The removal of the hydroxyl group in the silicate framework with $F^-$ ion leads to increased stability; since, the hydroxyl group would be likely involved in the hydrolysis reaction of the silicate structure when water or an aqueous solution would be present that caused the structure to collapse.

## Section Four: Fundamentals of structure characterization with various analysis techniques

### 2.34 What does X-ray Diffraction data show: Effects of calcination on MCM-48 Structure

The X-ray diffraction pattern by Ryoo and co-workers of the *d*-spacing indicated that the mesoporous structure belonged to the cubic la3d space group made with CTAB-non-ionic surfantant mixture. [19,57] Likewise, the X-ray diffraction (XRD) reflections were more intense for the calcinated MCM-48 sample after 24 hours of heating at 550°C. [19] This increase in peak intensity for the calcinated sample in comparison to the as-synthesized one indicates that the ordering of the structure improved after removing the surfactant. The XRD shows that the I-B30-1.2 [I = synthesis method one; B = cetyltrimethylammonium bromide exchanged with 30% hydroxyl ion; and 1.2 = surfactant to Si ratio: Note: if it was C would = $Cl^-$ type of $CTA^+$ surfactant system.] composition mixture made with cetyltrimethylammonuium bromide (CTAB) was more crystalline in comparison to the I-C40-0.8 sample, which had chloride ion as the anion and a surfactant/Si ratio of 0.8. This result was noted earlier by Kevan and co-workers in synthesis of Si-MCM-48; they found lower quality Si-MCM-48 formed with CTACl vs. CTAB. Klinowski and co-

workers also discovered that the use of CTAB produced higher quality Si-MCM-41 due to the stronger charge bonding interaction in the interfacial region with CTA+ surfactant and silica oligomers, which modulated the effective charge density matching, as noted earlier in Figure 2:40. [109] The lack of XRD peaks above 10° 2θ would mean that the atomic arrangement in the pore walls would be considered disorganized [19,55]; moreover, the structure of the M41S materials would be considered practically amorphous silica both in the pure silica form and metal doped form. [162-165]

## 2.35 Importance of framework condensation

The researchers noted that the samples completed with a longer hydrothermal treatment time period had XRD peaks that were well resolved. [85] The above trend was thought to be from the wall framework condensating more in hydrothermal treatment, thereby causing an increased wall-pore contrast in the resulting material. Likewise, the XRD taken of the synthesis products as the reaction was occurring, as shown in Figure 2:58, reveals a trend involving the amount of neutral surfactant and hydrothermal reaction time and the development of the mesoporous material. [59] For example, at $f_{ns}$ (stands for the amount of neutral surfactant) of 0.05 produced the MCM-41 structure; whereas, when the reaction mixture product was adjusted to $f_{ns} = 0.18$ and four days of hydrothermal reaction time, the resulting product was the same as cubic la3d mesoporous structure, otherwise known as MCM-48. With more heating time using this $f_{ns}$ amount, the MCM-48 structure was converted to the lamellar structure. At $f_{ns}$ ratio of 0.25, the lamellar phase was made in a day independent of reaction time periods.

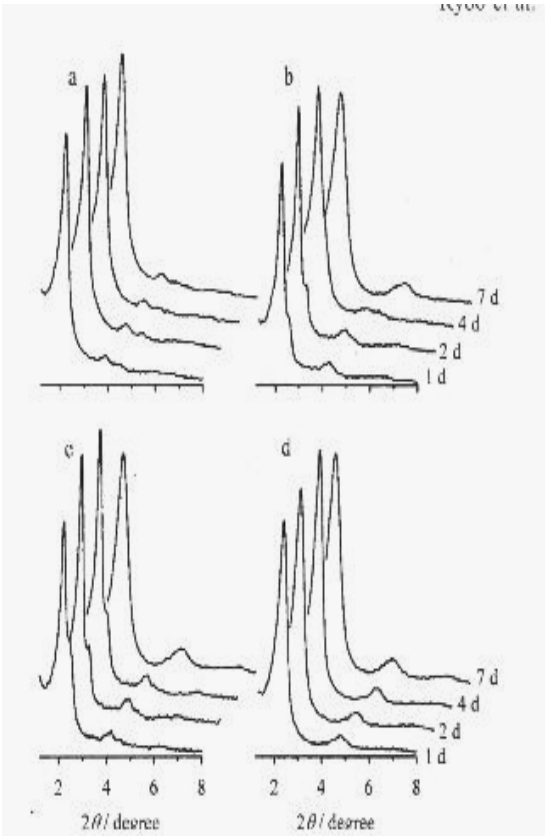


**Figure 2:58 Powder XRD analysis of Si-MCM-48 with cationic-neutral surfactants mixtures employed.**

**Supplemental text for Figure 2:58-**As seen in the above (previous page) figure, the XRD plots show the effect of neutral surfactant and hydrothermal reaction time. [59] The synthesis gel was composed of the following: $5.0SiO_2/1.25Na_2O/f_{ns}C_{12}(EO)_4/(1\text{-}f_{ns})HTMABr/400H_2O$, where $f_{ns}$ = (a) 0.05, (b) 0.11, (c) 0.18, and (d) 0.25. As seen in the XRD plots above, both (a) and (b) plots show mainly hexagonal MCM-41 structure development; whereas, in plot (c) with four days of hydrothermal synthesis leads to the MCM-48 structure. With even more neutral surfactant, the MCM-48 structure converts to the lamellar phase, as seen in plot (d). [Note: HTMABr = n-alkyltrimethylammonium bromide; EO = ethylene oxide.] Ryoo, R. *et al*., *Journal of Physical Chemistry B* **1999**, *103*, 7435-7440; **DOI:** 10.1021/jp9911649 Permission granted by American Chemical Society Copyright 1999 ©

## 2.36 Why does transition metal incorporated MCM-48 show lower XRD peak intensity?

There was a decrease in the intensity of transition metal incorporated MCM-48 material, as shown in XRD plot in Figure 2:59. [23,66] The reasons for the reduction in intensity include: (1) the random placement of transition metal ions in the pores, thereby causes a reduction in periodicity; (2) transition metal ion diluting the silica framework, which would cause the metal ion to absorb X-rays at a higher absorption factor over Si; and (3) partial collapse of the mesoporous structure. [23] The decrease in surface areas and pore volume upon placement of transition metal ions in MCM-48 material would be consistent with ions being incorporated into the pores.

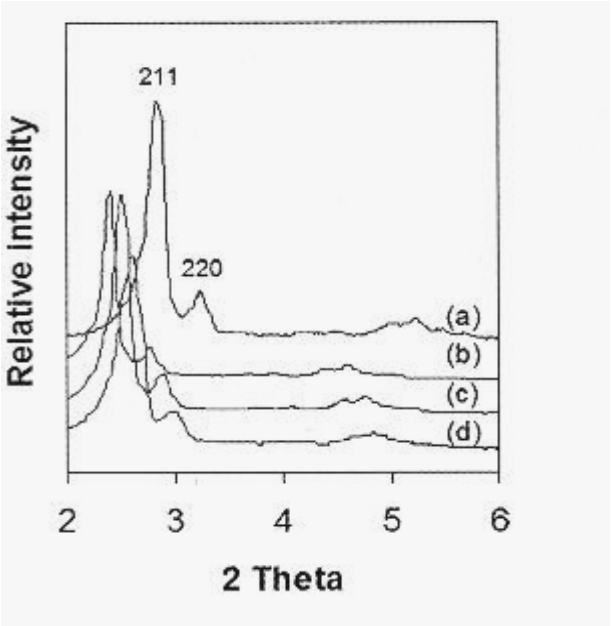


**Figure 2:59 Powder XRD Diffractograms with transition metal ion in cubic Ia3d MCM-48 structure.**

**Supplemental text for Figure 2:59**-As seen in the above figure, the powder XRD peaks shift to lower two theta angles in comparison to Si-MCM-48. [23] The XRD diffractrograms had the following labels: (a) Si-MCM-48; (b) Mn-MCM-48; (c) V-MCM-48; and (d) Cr-MCM-48. As seen in above figure, the XRD peak intensity decreases due to both random placement of transition metal ions in the unit cells that comprise MCM-48 and random placement of these unit cells. Gomez, S. *et al*., *Journal of Catalysis* **2005**, *233*, 60-67; **DOI:** 10.1016/j.cat2005.04.015 Permission granted by Elsevier Scientific Publishing, Inc. Copyright 2005 ©

## 2.37 Effect of Ce incorporation on MCM-48 structure

The XRD analysis of the Ce-MCM-48 showed that, as the Ce content was increased in the MCM-48 structure, the basal diffraction peak position moved to greater 2θ values. [25] Moreover, the incorporation of Ce led to the increase in *d*-values and unit-cell parameter value. This larger unit cell value exhibited in Ce-MCM-48 in comparison to MCM-48 could be due to larger size of $Ce^{4+}$ ion in contrast to the $Si^{4+}$ ion. Therefore, the XRD analysis coupled with the diffuse reflectance ultra-violet-visible (UV-vis) spectroscopy would imply that the Ce ion was par-

tially incorporated into the framework walls of MCM-48; also, previous research indicated that the Ce had been incorporated partially into the framework/pore walls of MCM-48. This trend seen in Ce doped MCM-48 also was evident in $La^{3+}$ ion doped MCM-48. The $La^{3+}$ ion would be larger than the $Si^{4+}$ ion; therefore, upon incorporation of $La^{3+}$ ion into the MCM-48 structure, one would expect the unit cell constant to increase, thereby inferring that the $La^{3+}$ ion had been partially incorporated into the MCM-48 structure. [57] The result was indicated in the cell parameter data. However, the lower intensity for heavily doped La-MCM-48 sample indicated increased disorder in the mesopores. The XRD analysis of the metal doped MCM-48 structure exhibited eight Bragg peaks, which could be indexed to different (hkl) reflections. [58] The presence of all eight reflections would imply the cubic la3d structure with long-range order coupled with no impurity phase. [30,58,85] As the Ce content increases in the MCM-48 structure, the XRD intensity decreased, which would imply that the Ce-MCM-48 introduction of metal ion into the framework had led to decreased uniformity. [58]

## 2.38 Effect of fluoride ion on Ce-MCM-48 structural stability

As the Ce ion amount increased in both the Ce-MCM-48 with fluoride addition and without fluoride in the preparation step, the result was a decreased resolution of the XRD peaks. [25] The intensity exhibited by the (211) diffraction peak was reduced with increased Ce ion in the MCM-48 structure. Lower intensity and the reduced resolution of the peaks with increased Ce ion content were noted in the MCM-48 structure. When using $F^-$ ion and no fluoride ion, reduced structural ordering was noted. This could be from an increased number of defect sites coupled with bond strain, as noted both in a decreased intensity of (211) XRD peaks and at higher angle peaks. Nonetheless, when the Si/Ce ratio was between 200 and 50 synthesized with fluoride ion, the result was the presence of all eight diffraction peaks clearly shown in the XRD indexed to a space group of la3d cubic structure. In contrast, the Ce-MCM-48 made without the fluoride ion secondary peaks were very difficult to distinguish from the base-line. From past research, the identification of secondary peaks in the MCM-48 structure would indicate long range order. Therefore, by comparing the XRD peak diffraction patterns of the Ce-MCM-48 samples made with $F^-$ ion and without $F^-$ ion, one would be able to draw the conclusion that the use of the fluoride ion in the synthesis had a major positive impact on long-range ordering of the resulting Ce-MCM-48 structure. Likewise, the Ce-MCM-48 XRD diffraction peaks for (211) and (220) with various amount of Ce prepared using $F^-$ ion had large XRD peak intensity values, which would indicate higher ordering of the pore structure, as shown in Figure 2:8.

The Fe-MCM-48 structure prepared with fluoride ion exhibited both basal (211) and (220) plus the secondary peaks in the as-synthesized and calcinated samples; in contrast, the Fe-MCM-48 samples made without the $F^-$ ion had only the two basal peaks listed above with no secondary peaks in the as-synthesized or calcinated sample. [25] The XRD intensity was greater in the Fe-MCM-48 sample prepared with $F^-$ ion in comparison to Fe-MCM-48 sample that did not have $F^-$ ion in the synthesis. Again, this would indicate enhanced long-range ordering in the Fe-MCM-48 sample containing the $F^-$ ion.

## 2.39 The effects of compression on MCM-48 structure

When mechanical pressure was applied to the MCM-48 structure, it remained intact up to 400 $N/mm^2$ . [24] The (211) and (220) reflections did not shift. However, at a pressure of 480 $N/mm^2$, the structure of MCM-48 began to deteriorate and structural details were lost. The XRD patterns indicate that a pressure up to 400 $N/mm^2$ led to

intensity close to the uncompressed sample value of MCM-48. Both nitrogen and sub-critical absorption showed a 30% loss in pore volume with compression up to 400 N/mm$^2$. At higher pressures of 600 N/mm$^2$, the pore structure of the pellized MCM-48 material was almost destroyed, as noted by lower intensity of the XRD patterns coupled with a 3-fold reduction in absorption capacity. The pore diameter, however, was not affected by the high compression pressures. The decreased absorption capacity may be due to the destruction of reduced stability of some of the particles. The compression of the MCM-48 powders was determined to be more stable in the shaping process. This would most likely a result both to the three-dimensional pore structure and thicker pore walls of MCM-48.

## 2.40 Transformation behavior using acidic vapor as probe molecule

The researchers conducted experiments on well known polysilicate species using acidic vapor treatment for a set time period control the amount of condensation of the resulting structures, as shown in Figure 2:60. [26] The structure pattern labeled (a) of the cubic silicate species $[Si_8O_{20}]^{8-}$ converts to the MCM-48 structure as the acidic environment causes the controlled condensation of this silicate species: MCM-48 pattern in the XRD was labeled $V_1$. Then, with additional acidic vapor, the la3d cubic MCM-48 structure converts to an intermediate structure labeled (d), which would still be MCM-48, but not as highly ordered. In the XRD labeled (e), the cubic MCM-48 structure has converted to the lamellar phase. With even more acidic vapor, the lamellar structure ($L_1$) transforms to an intermediate between the lamellar and hexagonal phase labeled (f). Finally, the use of more acidic vapor for a long time period leads to hexagonal MCM-41 structure ($H_1$), thereby revealing a pattern of $L_0 \rightarrow V_1 \rightarrow L_1 \rightarrow H_1$.

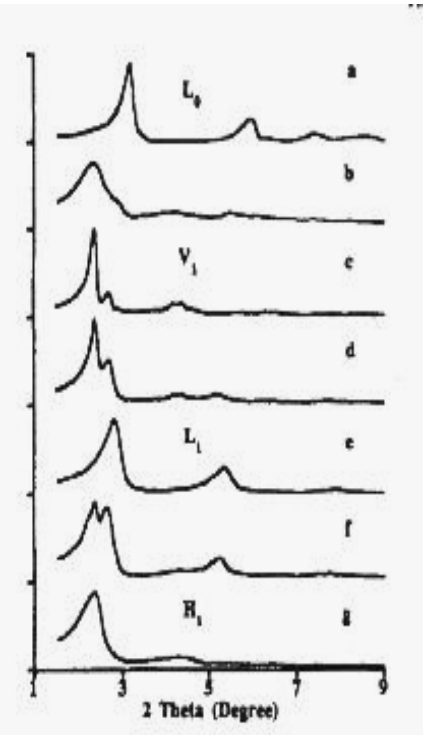


**Figure 2:60 XRD Analysis using acidic vapor as the probe molecule to determine M41S phase transitions.**

**Supplement text for Figure 2:60**-As seen in the above figure, the introduction of acidic vapor to the initial polysilicate species $[Si_8O_{20}]^{8-}$ leads to the formation of M41S mesoporous materials through various phase transitions. [26] The acidic solution used was 0.44% HCl. The initial structure denoted as $L_0$ in the plot (a) was exposed to the acidic vapor for the following number of days at 110°C: 1, 5, and 10 days in (b-d). The plots (e-g) were exposed to the

acidic solution for 8, 12, and 24 days at 130°C. The $V_1$, $L_1$, and $H_1$ would be cubic, lamellar, and hexagonal phases. Fyfe, C. A.; Fu, G., *Journal of the American Chemical Society* **1995**, *117*, 9709-9714: **DOI:** 10.1021/ja00143a014 Permission granted by American Chemical Society Copyright 1995 ©

## 2.41 Ultra-violet-visible (UV-vis) data

The past research has shown that one would expect strong absorptions from the charge-transfer (CT) transitions, as noted to occur with the oxygen ligand transferring an electron to the vanadium ion. [29] These transitions usually would be observed in the UV-vis region. The local structure of the vanadium sites coupled with sizes of the V domains strongly influence and consequently cause the observed electronic CT energy values. [22, 29] For example, with isolated species such as vanadium in the MCM-48 structure, CT transitional energies would be at higher energy value in comparison to polymetic species. This would be due to blue shift phenomena in semi-conductors as a function of size. [29] The researchers indicate that the charge transfer bands give results on the coordination of the $V^{5+}$ ion in the MCM-48 structure. [61] With tetrahedrally coordinated $V^{5+}$ centers, the major absorptions should be in the 240-350 nm region while square pyramidal structure would absorb 350-450 nm section and octahedral complex falls at the 450-600 nm region. [Note: in order to prove that the V-species were isolated, one would need to use FT-IR analysis.]

The Ce-MCM-48 material exhibited a broad absorption from 200-400 nm, and the intensity of the UV-vis absorption increased with the amount of Ce content. [25] The researchers note that the position of the ligand-to-metal charge-transfer band ($O^{2-} \rightarrow Ce^{4+}$) would be governed by the ligand field symmetry of the Ce active centers. [20,25,58] Past research has shown that it takes greater energy wavelength of light to promote an electronic transition from an oxygen ligand to a Ce active center with tetrahedral coordination; whereas, with octahedral coordination, the promotion of an electron from the $O^{2-}$ ligand to the $Ce^{4+}$ ion requires less energy. [25] An absorption at wavelength above 400 nm could indicate [20,25,58] the hexa-coordinated $Ce^{4+}$ member. The broad absorption noted for Ce-MCM-48 sample from 200-400 nm would imply that $Ce^{4+}$ ions have a partial tetrahedral coordination in the pore structure and also same $CeO_2$ particles on the surface of the pore wall. [25] The Fe-MCM-48 has a strong absorption band at 225 nm noted, to be from a CT transition with $Fe^{3+}$ ion in a tetrahedral coordination $Fe(O)_4^-$. [25, 58] Similar to the Ce incorporated into the MCM-48 structure, the La-MCM-48 UV-vis spectra showed two different species with higher energy one considered tetra-coordinated species in the CT $O^{2-} \rightarrow La^{3+}$ transition. [57] The lower energy UV-vis spectra CT transition was indicted to be caused by extra framework hexa-coordinated $La^{3+}$ ion species.

## 2.42 $N_2$ absorption/desorption + $H_2O$ data shows what?: $N_2$ isotherm information

According to the researchers, the $N_2$ absorption isotherms at low temperatures provide the most reliable data on mesoporous structures. [19] The $N_2$ isotherms would be a type IV common to mesoporous materials. [19,20,29,57,66,85,87,127,166] [Note: the $N_2$ absorption-desorption isotherm taken would be at 77 K (liquid nitrogen temperature), unless otherwise stated.] The inflection step range at relative pressures of $P/P_0 = 0.2$-$0.3$ indicates that the mesopores were being filled for the synthesized MCM-48 with cationic-neutral surfactant mixture. [19] The spot where the $P/P_0$ inflection point starts would be related to the pore size; likewise, the degree of sharpness in the inflection step infers the amount of uniformity in pore size system. [19,87] $N_2$ isotherms that has a H3 hystersis loop would be linked to materials that have a slit-shaped pores or plate-like particle morphology, according to IUPAC (International Union of Pure and Applied Chemistry); however, the I-B30-1.2 sample made with cetyltrimethylammonium bro-

mide (CTAB) show no hysteresis between the absorption-desorption cycle from pore condensation. [19] This would indicate small size particles. The MCM-48 structure that has a small hystersis loop would have larger mesopores in between the sample particles. [167] The pore size value for the CTAB prepared sample approximated 28Å, which would be close to our value. [19] The longer period of the synthesis led to thicker walls and a decreased surface area.

The $N_2$ absorption data of the samples show no hysteresis with reversible type IV isotherms. [29] The absorption of monolayer of $N_2$ onto the walls of the mesoporous material would be the first step. The inflection point at $P/P_0 = 0.25$ would imply a large pore volume coupled with a narrow point. The pore size range indicates uniformity of the resulting mesoporous material. The degree of sharpness and height indicates the pore uniformity. [25,29,87] When plotting the internal pore volume verse the pore diameter of the blank MCM-48 material, this produces a sharp peak at 25.7Å and a full width at half maximum (FWHM) of approximately 2.5 Å, which would be cons i-dered to be a small pore size range, as shown in Figure 2:61. [29] The V-MCM-48/0.05 also had a similar pore size range to the blank MCM-48 material. The peak determining the pore size distribution was slightly wider with a FWHM of approximately 4Å. Therefore, the conclusion from the $N_2$ absorption data infers that the V-MCM-48 synthesized material has similar but not identical characteristics to the blank MCM-48 structure.

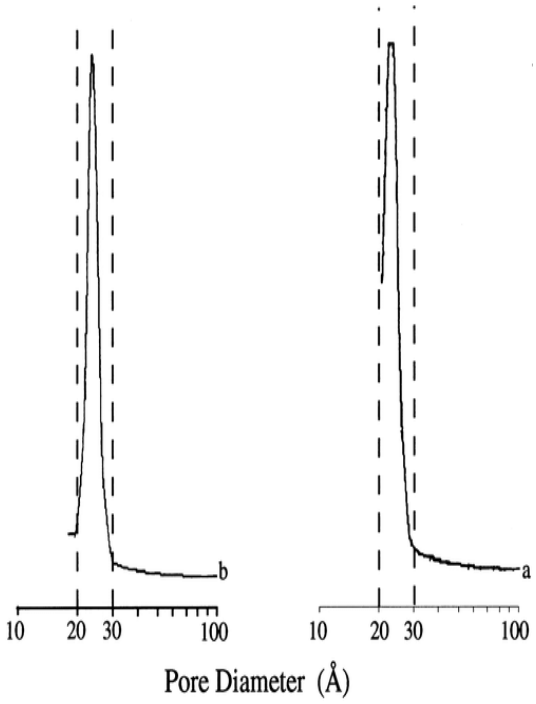


**Figure 2:61 $N_2$ pore size distribution (PSD) analysis of Si-MCM-48 and V-MCM-48/0.05.**

**Supplemental text for Figure 2:61**-As seen in above figure, the peak to the left would be of Si-MCM-48 and the peak to the right would be V-MCM-48/0.05. [29] The Si-MCM-48 peak would have approximately 25.7 Å coupled with a FWHM of 2.5 Å, and the V-MCM-48/0.05 has approximately Å plus a FWHM of 4 Å. From the plot above, one could infer that the blank Si-MCM-48 and V-MCM-48/0.05 had similar specifications. Morey, M. *et al*., *Chemistry of Materials* **1996**, *8*, 486-492; **DOI:** 10.1021/cm950397j Permission granted by American Chemical Society Copyright 1996 ©

## 2.43 $N_2$ absorption-desorption data on M41S materials

The $N_2$ absorption plot showed a sharp increase in the inflection range from ($P/P_0$) 0.3-0.4 and only slightly hysteresis from 0.4-1.0 region ($P/P_0$), as shown in Figure 2:62. [61] The significance of the sharp increase at $P/P_0$ = 0.3-0.4 would infer small pore size range. The discrepancy between the absorption-desorption sections of the isotherm at higher pressure ($P/P_0$ = 0.4-1.0) could be linked to particle-particle porosity or they could be much larger pores then the initial absorption. A sharp pore size range does not occur with particle-to-particle porosity. The perfect M41S material would be free of hysteresis. The sharpness of the inflection range infers a uniform pore size distribution, as shown in the $N_2$ absorption plot of Mn-MCM-48 in Figure 2:62. [66] The $N_2$ absorption data of the sample isotherms would be typical for mesoporous materials, which have type IV isotherms. This inflection range would be considered sharp at relative pressure of 0.2-0.3. The sharp inflection range would indicate capillary condensation of $N_2$ in the pores. [19,23,29,57] The transition metal incorporated MCM-48 samples have reduced surface areas; however, V-MCM-48 has a surface area close to the parent Si-MCM-48 material. [23] The results of $N_2$ absorption data shows that the transition metal incorporated MCM-48 material has high surface area coupled with a small pore size range in comparison to Si-MCM-48.

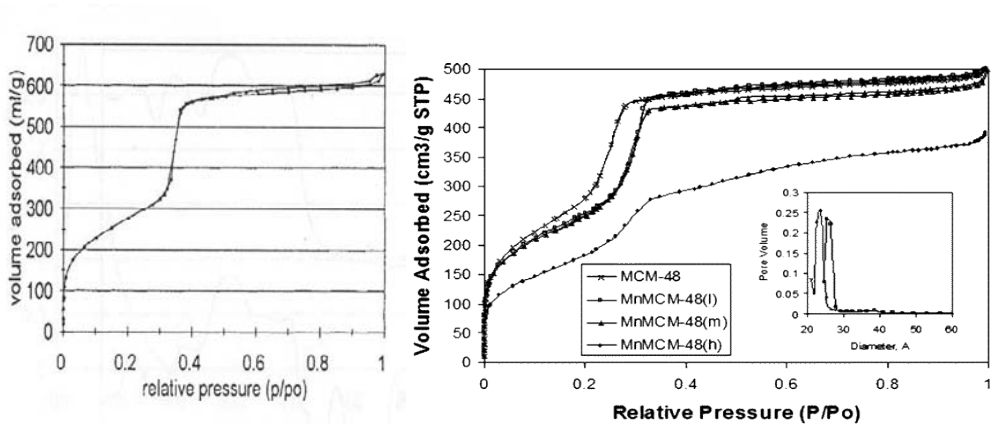


**Figure 2:62 $N_2$ Isotherm Analysis Si-MCM-48 and Mn-MCM-48.**

**Supplemental text for Figure 2:62**-As seen in the above figure, the $N_2$ absorption plot to the left shows a steep increase from the relative range of $P/P_0$ = 0.3-0.4 with a small amount of hysteresis from approximately $P/P_0$ = 0.4-1 for the blank MCM-48 sample [61]; whereas, the Mn-MCM-48 samples $N_2$ absorption plot also show a steep increase from approximately $P/P_0$ = 0.2-0.4 range. [66] This means that the pore structure has a relatively narrow distribution and would be indicated in the plot of pore volume vs. pore diameter in inset. Upper left hand plot: Van Der Voort, P. *et al*., *Journal of Physical Chemistry B* **1998**, *102*, 585-590; **DOI:** 10.1021/jp9727761 Permission granted by American Chemical Society Copyright 1998 © Upper right plot: Gomez, S. *et al*., *Chemistry of Materials* **2004**, *16*, 2411-2417; **DOI:** 10.1021/cm040018z Permission granted by American Chemical Society Copyright 2004 ©

The transition metal MCM-48 materials synthesized by Suib and co-workers all have reversible absorption-desorption isotherms, and the reversibility of the isotherm indicates little obstruction within the pore network. [23] The V-MCM-48 material was found to have various types of vanadium species: isolated, polymeric and framework members. Capillary condensation of nitrogen in the pore structure of MCM-48 would be the reason for the steep step in the relative pressure range of 0.25-0.31. [57] The data collected shows that, as the $La^{3+}$ ion concentration increases, the pore wall thickness increases coupled with both a decrease in BET (Brunauer-Emmett-Teller) surface area and pore volume. Both the Ce-MCM-48 and Fe-MCM-48 at Si/Me = 100 (where Me = Fe, Ce) have common

type IV isotherms and capillary condensation step in the relative pressure $P/P_0$ = 0.2-0.4 range, which would indicate uniform mesopores. [25] The inflection step range would be a major feature of capillary condensation. [71] The steepness and sharpness of the $N_2$ isotherm for both samples would imply good structural ordering of the mesopores coupled with a small pore size range. [22] The incorporation of Ce and Fe elements would not necessarily lead to lower pore uniformity. The trend shows the larger the pore volume, the greater the BET surface area.

## 2.44 Water Absorption Data

The concentration of water absorbed on the non-silylated (non-sil) MCM-48 structure increased with more relative pressure to 400 $cm^3/g$ standard-pressure-temperature (STP) at $P/P_0 = 1$; moreover, this value would be comparable to an absorption of $N_2$ of 500 $cm^3/g$ STP at $P/P_0 = 1$. [56] The indication of the large absorption of water onto the pore surface means that the non-sil MCM-48 was hydrophilic and filled close to completion with water molecules at $P/P_0 = 1$. In contrast, the silylated (sil) MCM-48 either with trimethyl or triethyl silylate groups showed little increase in the amount of water absorbed into the pores at the same relative pressure listed above, at only 20 $cm^3/g$ STP at $P/P_0 = 1$. This infers that the silylation technique had caused the conversion of SiOH to the more stable silyl group on the pore surface, which led to the pore surface having marked increase in hydrophobicity. The pore size range would be smaller with increased NaF added to the synthesis mixture. The $F^-$ ions could further increase long-range order of MCM-48, as shown in Figure 2:55 earlier XRD plot and $N_2$ absorption coupled with pore diameter shown in Figure 2:63. [55] The following material parameters decrease with increased calcination temperature: specific surface area, specific pore volume, and average pore diameter. [27]

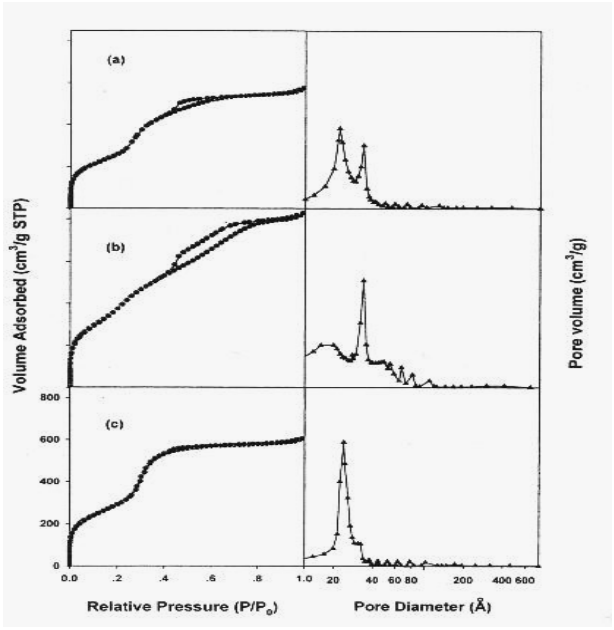


**Figure 2:63 $N_2$ adsorption isotherm of fluoride prepared Si-MCM-48.**

**Supplemental text for Figure 2:63**-As seen in the above figure, the $N_2$ adsorption plots and pore volume vs. pore diameter would be for the following molar synthesis ratio treated hydrothermally with 0.1 N NaF for 48 hours: $1.49SiO_2$-HTACl-$0.4Na_2O$-$142H_2O$-xNaF. [55] The three groups of plots would correspond to NaF salt being added to the synthesis gel: (a) plot x = 0.0 mole; (b) plot x = 0.3 mole; (c) plot x = 0.5 mole. These samples were submitted to calcination and boiling water exposure at 100C for 12 hours. As seen in the plot (c), it has the narrowest pore volume vs. pore diameter plot and little to no hysteresis in the $N_2$ measurement. Therefore, one could conclude that

the $F^-$ ion further increased the structural ordering of the Si-MCM-48 structure. Kim, W. J. *et al*., *Microporous and Mesoporous Materials* **2002**, *49*, 125-137; **DOI:** 10.1016/S1387-1811(01)00410-3 Permission granted by Elsevier Scientific Publishing, Inc. Copyright 2001 ©

## 2.45 Brunauer-Emmett-Teller (BET) or surface area show?

The BET measurements reveal that vanadium in the pores does not lead to blockage, but the BET data also reveals that the main pore size decreased by approximately 10% in comparison to the blank MCM-48 sample. [26] This BET data would most likely be interpretated as the vanadium coating the inside of the pore walls of the MCM-48 material, which occurred with the application of Mn ions. [29,66] The binding of the vanadium with silanol groups on the pore wall to form multiply coordinated Si-O-V bridge could lead to a contraction of the pore wall, as seen in schematic depicting bonding that could take place inside the MCM-48 pores in Figure 2:64. [29]

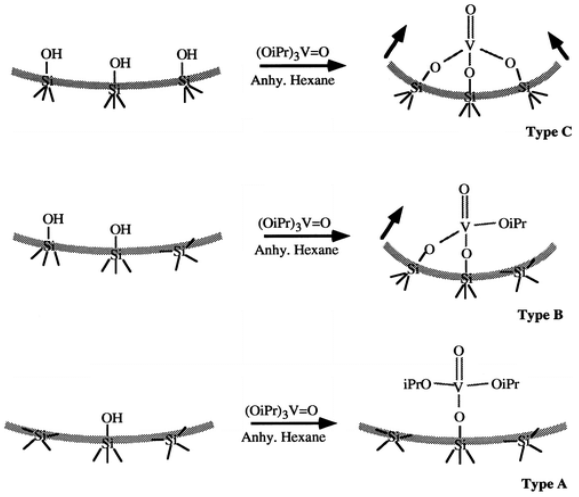


**Figure 2:64 Different types of vanadium grafting routes in the pore channels in V-MCM-48.**

**Supplemental text for Figure 2:64**-As seen in the above figure, there would be three types of vanadium bonds that could form in the pore walls of V-MCM-48 with the silanol groups. [29] The number of silanol groups that bind to the vanadium ion would determine the level of pore constriction. In Type A, only one silanol group would be bound to the vanadium complex; whereas, in Type B, the binding of two silanol groups would still leave a dangling end open for hydrolysis attack in aqueous conditions. Type C would be the desired species in graft metal doped MCM-48. The V-O bond would not be as easily to attack vs. a dangling end, which would lead to loss of active transition metal ions in aqueous solution. Morey, M. *et al*., *Chemistry of Materials* **1996**, *8*, 486-492; **DOI:** 10.1021/cm950397j Permission granted by American Chemical Society Copyright 1996 ©

## 2.46 Reasons for decreased parameter values with mechanical pressure

The tests used on the MCM-48 structure clearly show that it was more stable to shaping compared to MCM-41, which only has a pore volume of 0.2 $cm^3/g$, BET surface area of 330 $m^2/g$ with application of 224 $N/mm^2$. [24] In contrast to the MCM-41 material, the MCM-48 structure pore volume was only reduced to one-quarter of uncompressed value after 600 $N/mm^2$. This higher compression needed to significantly damage the pore structure would be required; since, the MCM-48 structure has a three-dimensional pore structure and thicker walls, which provide more stability. However, the researchers noted that MCM-48 would be inferior in mechanical stability in comparison to zeolites, silica, and alumina due too high porosity and also from a lack of stabilizing crystal structure. The large reduction in surface area indicates that only part of Cr has been incorporated into the crystal structure of MCM-41. [130] The BET surface area values after treatment in boiling water were 927 to 1106 $m^2/g$, which would be

common for MCM-41. [54] The pore volumes would be considered consistent with MCM-41 structure. Finally, the partial adjustment of pH coupled with NaF addition led to enhanced hydrothermal stability of MCM-41 in water.

The use of mesoporous molecular sieves in industrial applications requires the powders made to be shaped to decrease the pressure drop in reactor or absorption columns. [24] The pore volume of the MCM-48 powders decreased by close to 40% with their compression to pellets with BET surface areas only having a reduced value of close to 20% for the MCM-48 compressed to 400 N/mm$^2$ in comparison to the uncompressed sample. The pore diameter of the MCM-48 did not decrease with application of mechanical pressure from palletizing the powder. A related trend seen in the above data for MCM-48 occurred for MCM-41: pressures up to 320 N/mm$^2$ gave similar parameter data. The reduced pressure applied to the MCM-41 structure was noted to be due to the blocking of the pores from other particles of the same material. This led to the overall specific surface area coupled with the pore volume being decrease, and the mean pore diameter staying constant like the MCM-48 material. The pore-blocking model for the MCM-41 material with its one-dimensional pore structure could possibility occur; however, for the MCM-48 structure, this model of pore blocking would be difficult to accept due to the three-dimensional pore structure unless a egg-shell pellet was formed: this would require that the shell of the outer sphere completely blocks the pores in the sphere.

For the MCM-48 structure under pressure in the shaping process, the irreversible destruction of part of the MCM-48 particles would be modeled that better represents what occurs in the palletizing pressure, as shown in Figure 2:65. [24] It should be noted from other research that a lower intensity means increased disorder in the structure. To prove this model for the MCM-48 structure, the researchers milled the MCM-48 pellet compressed to 600 N/mm$^2$ and took the $N_2$ absorption of it. The resultant structural characteristics (pore volume, BET surface area) did not return to uncompressed values. This would imply that particle shaping was irreversible on the MCM-48 sample.

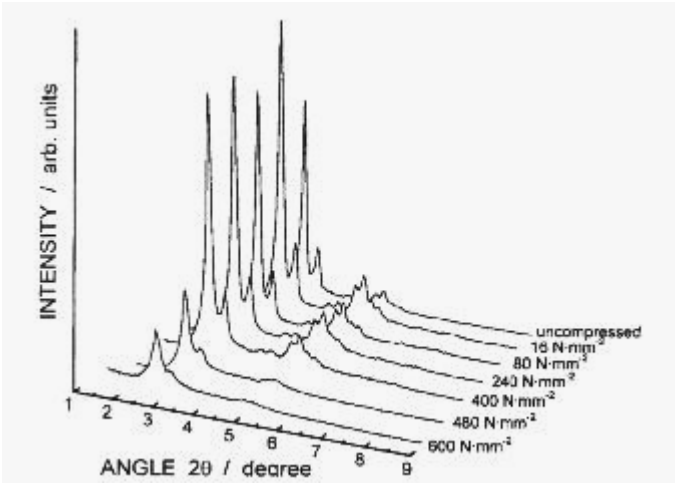


**Figure 2:65 Powder XRD Diffractograms as a function of mechanical pressure.**

**Supplemental text for Figure 2:65**-As seen in the figure of the effect of mechanical pressure on Si-MCM-48, the Si-MCM-48 structure was able to withstand pressure up to 400 N/mm$^2$ without a significant reduction in XRD peak intensity. [24] The gradual loss of peak intensity with increased mechanical pressure meant that the Si-MCM-48 cubic Ia3d framework was giving in to the pressure and pores collapsing. Hartmann, M.; Bischof, C. *Journal of Physical Chemistry B* **1999**, *103*, 6230-6235; **DOI:** 10.1021/jp991103a Permission granted by American Chemical Society Copyright 1999 ©

## 2.47 Catalytic/separation applications of MCM-48

Many potential applications of MCM-48 structure have been explored for potential use in the following areas: (1) environmental remediation/green energy [169-173]; (2) fine organic synthesis [31-43,174-182]; (3) chromatography separations [183-186]; (4) electrode materials [187,188]; (5) composite materials [189-191]; (6) chemical sensor [192]; petroleum cracking [193,194]; and (8) gas separation membranes. [195-206] Pyrolysis of waste plastics to other precursors would help reduce the waster burden in the world; however, the high input of energy causes this method to not currently be used on a large scale. Park and co-workers employed Al-MCM-48 in pyrolysis of polypropylene and were able to generate $C_7$-$C_{10}$ hydrocarbons with the activation energy reduced from approximately 217 kJ/mole to 96 kJ/mole with use of Al-MCM-48 loading of Si/Al of 30. [169] They also found that catalytic performance of Al-MCM-48, due to the three-dimensional pore structure, had little change over five reaction cycles vs. Al-MCM-41 that gradually lost catalytic activity over several reaction cycles. As shown in earlier figures of MCM-48, pyrolysis of plastics reveals the positive effects of bicontinuous three-dimensional MCM-48 structure for handling bulky substrate. Endud and Wong were able to develop Sn-MCM-48 catalyst that was selective for benzyl alcohol to benzaldehyde using *tert*-butyl-hydroperoxide. [174] These researchers found little leaching of the active phase (Sn ions) and conversion rate of approximately 55% over three reaction cycles; whereas, the $SnO_2$ had no activity, which shows the need for the metal ions to be highly dispersed over the support, preferably in the framework, to obtain high catalytic activity. In addition, the catalyst cost substantially less to synthesize; since, it was made from rice hush ash with clump-spherical particle shape, according to field emission-scanning electron microscopy (FE-SEM) analysis. High performance liquid chromatography applications require an open pore network that permits efficient separations of various species. [82-84, 183] Through the use of pseudomorphic synthesis, Galarneau and co-workers have been able to synthesis MCM-41 and MCM-48 with pore size of 4-9 nm using different silica chromatographic supports. [82,84, 183] Unger and co-workers have also been able to synthesize MCM-41 and MCM-48 with spherical shapes using combination of modified Stober silica sphere synthesis and spray drying. [27,128,129,133,184] The initial results from these research reports indicate MCM-48 would be very useful from a mass transfer point of view assuming the particles could be made 1-2 μm and have monodispersity. [82-84,183,184]

Davis and co-workers found that acid functionized MCM-48 had higher proton conductivity in contrast to MCM-41, [187] and Yu and co-workers were able to synthesize nanoporous carbon molecular sieves from silylated MCM-48, [188] which both of these research reports indicate that the resulting material potential use as an electrode, such as direct methanol fuel cells (DMFCs). [187,188] Composite materials could be made of organic polymers in porous materials, such as M41S and SBA family of molecular sieves. [189-191] Mou and co-workers were able to produce elastic macrospheres using TEOS and P123 non-ionic triblock copolymer. [191] The material exhibited high elasticity and was crack free, which could be useful with applications that need high elasticity without deformation. A chemical sensor was made using MCM-48 as the structure to hold Schiff-base Zn complex. [192] The silica framework compatibility in aqueous solution of $Cu^{2+}$ ion permitted complete quenching of the complex fluorescence. The metal doped MCM-48 materials have been employed in cracking applications to produce more valuable light oil products. [14,193,194] The higher diffusion of larger aromatic structures was demonstrated with Al-MCM-48. 193,194 The conversion rate of pyrene was 1.5 times greater for the Al-MCM-48 material in contrast to Al-MCM-41. [14] These

results show the high potential of Al-MCM-48 has at high Si/Al loading of $Al^{3+}$ tetrahedral species in cracking applications of organic molecules. [14,193,194] Gas separation using modified MCM-48 has great potential due to high permeability of the formed membrane using various organic functional groups. [195-206] The major challenges have been surfactant removal and obtaining the desired dispersity of organic functional groups over the walls of MCM-48. These MCM-48 functionalized membranes have been shown to be able to separate various gas mixture, such as $N_2/CO_2$, which would be important for use at power plants to prevent global warming. Finally, the use of mesoporous silica, such as Si-MCM-48, has many potential applications; however, much research still needs to be completed to cause the mesoporous silica to be a reality as commercial products.

## 2.48 Effect of alkali metals on catalytic + structure of transition metal doped MCM-48

Most synthesis of MCM-48 use NaOH to adjust the pH; however, the use of alkali metal ions leads to lower activity of the titanium silicate species. [48] An example of the enhanced reactivity of the Ti-MCM-48 in the epoxidation reaction of cyclohexene using tert-butylhydroperoxide (TBHP) as the oxidant had an initial reaction rate of 1.642 mole/g · h while the Ti-MCM-48 made in the presence of sodium ions only had an initial reaction rate of 0.448 mole/g · h, which would be four times lower in reaction rate at a Si/Ti ratio of 100. On the other hand, the researchers in the present study claim that the use of NaCl increased the crystallinity of the resulting structure of the MCM-48 material. [67] They refer back to the "salt effect" being used successfully on the MCM-41 structure, and therefore it most likely would improve the hydrothermal stability of the MCM-48 structure to water attack. Their XRD of the MCM-48 structure after 12 hours of heating in boiling water appears to confirm their hypothesis, as shown in Figure 2:23. Later research completed by Ryoo and co-workers showed hydrothermal durability increase with various amounts of salts added to Si-MCM-48 in post-synthesis hydrothermal treatment. [207] This would be important from a stability basis for Si-MCM-48; since , Solovyov and co-workers have found through extensive XRD modeling analysis that the pore wall of Si-MCM-48 would only be 0.8 nm (8 Å). [208] Thickening of the pore wall would increase the structure durability toward hydrothermal attack, as noted in literature. [207]

## 2.49 Effect of silanol groups bonded to transition metal ions

The researchers use a novel synthesis to graft active metal oxide species onto the pore walls of MCM-48 using the silanol groups. [22,29,57,144,209-212] The reason for the enhanced reactivity seen in grafted vanadium oxide species in the pore walls of MCM-48 would be linked to strained siloxane bridges. [22] The region around the siloxane bridge would be unsymmetical, thereby leading to one Si atom having less electron density than the other Si atom. This strain in the siloxane bridge causes higher reactivity in comparison to amorphous silica. This allows the $VO(acac)_2$ species (where acac = $CH_3COCHCOCH_3$) to interact with surface chemistry. The liquid exchange of the acac ligand on $VO(acac)_2$ results in the covalently bonded Si-O-VO (acac) species coupled with the formation of Si(acac). However, the problem with these mounted active species in the M41S material would be the fact that they leach rather easily in liquid-phase reactions. [159] Alkylchorosilane have been used to act as a coupling agent for the vanadium and cobalt precursors to bind the partially silylated surface that has silanol groups to bind the metal ions. [144,209,210,212] Through the use of coupling agent, the vanadium leaching was partially eliminated, according to Vansant and co-workers with V- MCM-48. [209,210]

## References


1. Collart, O.; Cool, P.; Voort, P.V.D.; Meynen, V.; Vansant, E. F.; Houthoofd., K.; Grobet, P.J.; Lebedev, O.I.;; Tendeloo, G. V. "*Aluminum Incorporation into MCM-48 toward the Creation of Bronsted Acidity*," *Journal of Physical Chemistry B* **2004**, *108*, 13905-13912 (Research article)

2. http://www.department.kings.edu/Chemlab/animation/index.html (access 3/1/08) (website)

3. Moore, J. W.; Stanitski, C. L.; Jurs, P. C. "Chemistry The Molecular Science," **First Edition**, Chapter 11, pages 500-501 (chemistry textbook)

4. Brus, L. "*Electronic Wave Functions in Semiconductor Clusters: Experiment and Theory*," *Journal of Physical Chemistry* **1986**, *90*, 2555-2560 (Research article)

5. Serpone, N.; Pelizz, E. "*Photocatalysis: Fundamentals and Applications*," **1989 Edition**, Chapters 3, 4, 5 and pages 59, 117, and 130 (Excellent resource field-book)

6. Storchak, V. G.; Eshchenko, D. G.; Brewer, J. H.; Aronzon, B. A.; Cottrell, S. P.; Lichti, R. L.; Savici, A. T.; Uemura, Y. J. "*Deep muonium state in InSb: Recombination center vs. trapping center*," *Physica B* **2006**, *374-375*, 387-389 (Research article)

7. http://www.semiconductorglossary.com (access 3/19/08) (website)

8. Martin, S. T.; Herrmann, H.; Choi, W.; Hoffmann, M. R. "*Time-resolved microwave conductivity. Part 1.-$TiO_2$ photoreactivity and size quantization*," *Journal of the Chemical Society, Faraday Transactions* **1994**, *90*, 3315-3323 (Research article)

9. Martin, S. T.; Herrmann, H.; Hoffmann, M. R. "*Time-resolved microwave conductivity. Part 2.-Quantum-sized $TiO_2$ and the effect of absorbates and light intensity on charge-carrier dynamics*," *Journal of the Chemical Society, Faraday Transactions* **1994**, *90*, 3323-3330 (Research article)

10. Cao, L.; Huang, A.; Spiess, F-J.; Suib, S. L. "*Gas-Phase Oxidation of 1-Butene Using Nanoscale TiO2 Photocatalysts*," *Journal of Catalysis*, **1999**, *188*, 48-57 (Research article)

11. Peral, J.; Domenech, X.; Ollis, D. F. "*Heterogeneous Photocatalysis for Purification, Decontamination and Deodorization of Air*," *Journal of Chemical Technology & Biotechnology* **1997**, *70*, 117-140 (Review article)

12. Zhao, J.; Yang, X. "*Photocatalytic oxidation for indoor air purification: a literature review*," *Building and Environment* **2003**, *38*, 645-654 (Review article)

13. Zhao, X. S.; Lu, G. Q.; Millar, G. J. "*Advances in Mesoporous Molecular Sieve MCM-41*," *Industrial & Engineering Chemistry Research* **1996**, *35*, 2075-2090 (Review article)

14. Pu, S. B.; Kim, J. B.; Seno, M.; Inui, T. "*Isopropylation of polynuclear aromatic hydrocarbons on Al-containing M41S mesoporous catalysts*," *Microporous Materials* **1997**, *10*, 25-33 (Research article)

15. Morey, M. S.; Davidson, A.; Stucky, G. D. "*Silica-Based, Cubic Mesostructures: Synthesis, Characterization and Relevance for Catalysis*," *Journal of Porous Materials* **1998**, *5*, 195-204 (Review article)

16. Sayari, A. "*Catalysis by Crystalline Mesoporous Molecular Sieves*," *Chemistry of Materials* **1996**, *8*, 1840-1852 (Review article)

17. Wan, Y.; Zhao, D. "On the Controllable Soft-Templating Approach to Mesoporous Silicates," Chemical Reviews 2007, 107, 2821-2860 (Review article)

18. Gallis, K. W.; Landry, C. C. "*Synthesis of MCM-48 by a Phase Transformation Process*," *Chemistry of Materials* **1997**, *9*, 2035-2038 (Communication article)

19. Romero, A. A.; Alba, M. D.; Zhou, W.; Klinowski, J. "*Synthesis and Characterization of the Mesoporous Silicate Molecular Sieve MCM-48*," *Journal of Physical Chemistry B* **1997**, *101*, 5294-5300 (Research article)
20. Laha, S. C.; Mukherjee, P.; Sainkar, S. R.; Kumar, R. "*Cerium Containing MCM-41-Type Mesoporous Materials and their Acidic and Redox Catalytic Properties*," *Journal of Catalysis* **2002**, *207*, 213-223 (Research article)

21. Schmidt, R.; Stocker, M.; Akporiaye, D.; Heggelund Torstad, E.; Olsen, A. "*High-resolution electron microscopy and X-ray diffraction studies of MCM-48*," *Microporous Materials* **1995**, *5*, 1-7 (Research article)

22. Baltes, M.; Cassiers, K.; Van Der Voort, P.; Weckhuysen, B. M.; Schoonheydt, R. A.; Vansant, E. F. "*MCM-48-Supported Vanadium Oxide Catalysts, Prepared by the Molecular Designed Dispersion of $VO(acac)_2$: A Detailed Study of the Highly Reactive MCM-48 Surface and the Structure and Activity of the Deposited $VO_x$*," *Journal of Catalysis* **2001**, *197*, 160-171 (Research article)

23. Gomez, S.; Garces, L. J.; Villegas, J.; Ghosh, R.; Giraldo, O.; Suib, S. L. "*Synthesis and characterization of TM-MCM-48 (TM = Mn, V, Cr) and their catalytic activity in the oxidation of styrene*," *Journal of Catalysis* **2005**, *233*, 60-67 (Research article)

24. Hartmann, M.; Bischof, C. "*Mechanical Stability of Mesoporous Molecular Sieve MCM-48 Studied by Absorption of Benzene, n-Heptane, and Cyclohexane*," *Journal of Physical Chemistry B* **1999**, *103*, 6230-6235 (Research article)

25. Shao, Y.; Wang, L.; Zhang, J.; Anpo, M. "*Synthesis of Hydrothermally Stable and Long-Range Ordered Ce-MCM-48 and Fe-MCM-48 Materials*," *Journal of Physical Chemistry B* **2005**, *109*, 20835-20841 (Research article)

26. Fyfe, C. A.; Fu, G. "*Structure Organization of Silicate Polyanions with Surfactants: A New Approach to the Syntheses, Structure Transformations, and Formation Mechanisms of Mesostructural Materials*," *Journal of American Chemical Society* **1995**, *117*, 9709-9714 (Research article)

27. Schumacher, K.; Grun, M.; Unger, K. K. "*Novel synthesis of spherical MCM-48*," *Microporous and Mesoporous Materials* **1999**, *27*, 201-206 (Research article)

28. Chatterjee, M.; Iwasaki, T.; Hayashi, H.; Onodera, Y.; Ebina, T.; Nagase, T. "*Characterization of Tetrahedral Vanadium-Containing MCM-41 Molecular Sieves Synthesized at Room Temperature*," *Chemistry of Materials* **1999**, *11*, 1368-1375 (Research article)

29. Morey, M.; Davidson, A.; Eckert, H.; Stucky, G. "*Pseudotetrahedral $O_{3/2}V{=}O$ Centers Immobilized on the Walls of a Mesoporous, Cubic MCM-48 Support: Preparation, Characterization, and Reactivity toward Water As Investigated by $^{51}V$ NMR and UV-Vis Spectroscopies*," *Chemistry of Materials* **1996**, *8*, 486-492 (Research article)

30. Morey, M.; Davidson, A.; Stucky, G. "*A new step toward transition metal incorporation in cubic mesoporous materials: preparation and characterization of Ti-MCM-48*," *Microporous Materials* **1996**, *6*, 99-104 (Research article)

31. Taralkar, U. S.; Kalita, P.; Kumar, R.; Joshi, P. N. "*Synthesis, characterization and catalytic performance of Sn-MCM-48 in solvent-free Mukaiyama-type aldol condensation reactions*," *Applied Catalysis A: General* **2009**, *358*, 88-94 (Research article)

32. Sakthivel, A.; Dapurkar, S. E.; Selvam, P. "*Mesoporous (Cr)MCM-41 and (Cr)MCM-48 molecular sieves: promising heterogeneous catalysts for liquid phase oxidation reactions*," *Catalysis Letters* **2001**, *77*, 155-158 (Research article)

33. Dapurkar, S. E.; Sakthivel, A.; Selvam, P. "*Novel mesoporous (Cr)MCM-48 molecular sieves: Promising heterogeneous catalysts for selective oxidation reactions*," *New Journal of Chemistry* **2003**, *27*, 1184-1190 (Research article)

34. Dapurkar, S. E.; Selvam, P. "*Mesoporous H-AlMCM-48: highly efficient solid acid catalyst*," *Applied Catalysis A: General* **2003**, *254*, 239-249 (Research article)

35. Pena, M. L.; Dejoz, A.; Fornes, V.; Rey, F.; Vazquez, M. I.; Lopez Nieto, J. M. "*V-containing MCM-41 and MCM-48 catalysts for the selective oxidation of propane in gas phase*," *Applied Catalysis A: General* **2001**, *209*, 155-164 (Research article)

36. Lee, C. W.; Lee, W. J.; Park, Y. K.; Park, S-E. "*Catalytic hydroxylation of benzene over vanadium-containing molecular sieves*," *Catalysis Today* **2000**, *61*, 137-141 (Research article)

37. Bronkema, J. L.; Bell, A. T. "*Mechanistic Studies of Methanol Oxidation to Formaldehyde on Isolated Vanadate Sites Supported on MCM-48*," *Journal of Physical Chemistry C* **2007**, *111*, 420-430 (Research article)

38. Voort, P. V. D.; Baltes, M.; Vansant, E. F. "*Stabilized MCM-48/$VO_x$ catalysts: synthesis, characterization and catalytic activity*," *Catalysis Today* **2001**, *68*, 119-128 (Research article)

39. Selvam, P.; Dapurkar, S. E. "*Catalytic activity of highly ordered mesoporous VMCM-48*," *Applied Catalysis A: General* **2004**, *276*, 257-265 (Research article)

40. Li, H.; Wang, S.; Ling, F.; Li, J. "*Studies on MCM-48 supported cobalt catalyst for Fisher-Tropsch synthesis*," *Journal of Molecular Catalysis A: Chemical* **2006**, *244*, 33-40 (Research article)

41. Samuel, P. P.; Shylesh, S.; Singh, A. P. "*Catalytic properties of tin-containing mesoporous molecular sieves in the selective reduction of carbonyl compounds (Meerwein-Ponndorf-Verley (MPV) reaction*," *Journal of Molecular Catalysis A: Chemical* **2007**, *266*, 11-20 (Research article)

42. Wangcheng, Z.; Guanzhong, L.; Yanglong, G.; Yun, G.; Yanqin, W.; Yunsong, W.; Zhigang, Z.; Xiaohui, L. "*Synthesis of cerium-doped MCM-48 molecular sieves and its catalytic performance for selective oxidation of cyclohexane*, " *Journal of Rare Earths* **2008**, *26*, 515-522 (Research article)

43. Zhan, W.; Guo, Y.; Wang, Y.; Guo, Y.; Liu, X.; Wang, Y. Zhang, Z.; Lu, G. "*Study of Higher Selectivity to Styrene Oxide in the Epoxidation of Styene with Hydrogen Peroxide over La-Doped MCM-48 Catalyst*," *Journal of Physical Chemistry C* **2009**, *113*, 7181-7185 (Research article)

44. Ciesla, U.; Schuth, F. "*Ordered mesoporous materials*," *Microporous and Mesoporous Materials* **1999**, *27*, 131-149 (Review article)

45. Corma, A. "*From Microporous to Mesoporous Molecular Sieve Materials and Their Use in Catalysis*," *Chemical Reviews* **1997**, *97*, 2373-2419 (Review article)

46. Koyano, K. A.; Tatsumi, T.; Tanaka, Y.; Nakata, S. "*Stabilization of Mesoporous Molecular Sieves by Trimethylsilylation*," *Journal of Physical Chemistry B* **1997**, *101*, 9436-9440 (Research article)

47. Kim, J. M.; Jun, S.; Ryoo, R. "*Improvement of Hydrothermal Stability of Mesoporous Silica Using Salts: Reinvestigation for Time-Dependent Effects*," *Journal of Physical Chemistry B* **1999**, *103*, 6200-6205 (Research article)

48. Corma, A.; Kan, Q.; Rey, F. "*Synthesis of Si and Ti-Si-MCM-48 mesoporous materials with controlled pore sizes in the absence of polar additives and alkali metal ions*," *Chemical Communications* **1998**, 579-580 (Communication article)

49. Lim, S.; Haller, G. L. "*Preparation of Highly Ordered Vanadium-Substituted MCM-41: Stability and Acidic Properties*," *Journal of Physical Chemistry B* **2002**, *106*, 8437-8448 (Research article)

50. Yoshitake, H.; Tatsumi, T. "*Vanadium Oxide Incorporated into Mesoporous Titania with a BET Surface Area above 1000* $m^2 \cdot g^{-1}$*: Preparation, Spectroscopic Characterization, and Catalytic Oxidation*," *Chemistry of Materials* **2003**, *15*, 1695-1702 (Research article)

51. Solberg, S. M.; Kumar, D.; Landry, C. C. "*Synthesis, Structure, and Reactivity of a New Ti-Containing Microporous/Mesoporous Material*," *Journal of Physical Chemistry B* **2005**, *109*, 24331-24337 (Research article)

52. Ryoo, R.; Kim, J. M.; Ko, C. H.; Shin, C. H. "*Disordered Molecular Sieve with Branched Mesoporous Channel Network*," *Journal of Physical Chemistry* **1996**, *100*, 17718-17721 (Research article)

53. Echchahed, B.; Moen, A.; Nicholson, D.; Bonneviot, L. "*Iron-Modified MCM-48 Mesoporous Molecular Sieves*," *Chemistry of Materials* **1997**, *9*, 1716-1719 (Communication article)

54. Kim, W. J.; Yoo, J. C.; Hayhurst, D. T. "*Synthesis of hydrothermally stable MCM-41 with initial adjustment of pH and direct addition of NaF*," *Microporous and Mesoporous Materials* **2000**, *39*, 177-186 (Research article)

55. Kim, W. J.; Yoo, J. C.; Hayhurst, D. T. "*Synthesis of MCM-48 via phase transformation with direct addition of NaF and enhancement of hydrothermal stability by post-treatment in NaF solution*," *Microporous and Mesoporous Materials* **2002**, *49*, 125-137 (Research article)

56. Park, D-H.; Nishiyama, N.; Egashira, Y.; Ueyama, K. "*Enhancement of Hydrothermal Stability and Hydrophobicity of a Silica MCM-48 Membrane by Silylation*," *Industrial & Engineering Chemistry Research* **2001**, *40*, 6105-6110 (Research article)

57. Zhan, W.; Guo, Y.; Wang, Y.; Liu, X.; Guo, Y.; Wang, Y.; Zhang, Z.; Lu, G. "*Synthesis of Lanthanum-Doped MCM-48 Molecular Sieves and Its Catalytic Performance for the Oxidation of Styrene*," *Journal of Physical Chemistry B* **2007**, *111*, 12103-12110 (Research article)

58. Shao, Y.; Wang, L.; Zhang, J.; Anpo, M. "*The photoluminescence of rhodamine B encapsulated in mesoporous Si-MCM-48, Ce-MCM-48, Fe-MCM-48 and Cr-MCM-48 molecular sieves*," *Journal of Photochemistry and Photobiology A: Chemistry* **2006**, *180*, 59-64 (Research article)

59. Ryoo, R.; Joo, S. H.; Kim, J. M. "*Energetically Favored Formation of MCM-48 from Cationic-Neutral Surfactant Mixtures*," *Journal of Physical Chemistry B* **1999**, *103*, 7435-7440 (Research article)

60. Kruk, M.; Jaroniec, M.; Ryoo, R.; Kim, J. M. "*Characterization of High-Quality MCM-48 and SBA-1 Mesoporous Silicas*," *Chemistry of Materials* **1999**, *11*, 2568-2572 (Research article)

61. Van Der Voort, P.; Morey, M.; Stucky, G. D.; Mathieu, M.; Vansant, E. F. "*Creation of* $VO_x$ *Surface Species on Pure Silica MCM-48 Using Gas-Phase Modification with* $VO(acac)_2$," *Journal of Physical Chemistry B* **1998**, *102*, 585-590 (Research article)

62. Chen, F.; Huang, L.; Li, Q. "*Synthesis of MCM-48 Using Mixed Cationic-Anionic Surfactants as Templates*," *Chemistry of Materials* **1997**, *9*, 2685-2686 (Communication article)

63. Van Der Voort, P.; Mathieu, M.; Mees, F.; Vansant, E. F. "*Synthesis of High Quality MCM-48 and MCM-41 by Means of the GEMINI Surfactant Method*," *Journal of Physical Chemistry B* **1998**, *102*, 8847-8851 (Research article)

64. Raman, N. K.; Anderson, M. T.; Brinker, C. J. "*Template-Based Approaches to the Preparation of Amorphous, Nanoporous Silicas*," *Chemistry of Materials* **1996**, *8*, 1682-1701 (Review article)

65. Koyano, K. A.; Tatsumi, T. "*Synthesis of titanium-containing mesoporous molecular sieves with a cubic structure*," *Chemical Communications* **1996**, 145-146 (Communication article)

66. Gomez, S.; Giraldo, O.; Garces, L. J.; Villegas, J.; Suib, S. L. "*New Synthetic Route for the Incorporation of Manganese Species into the Pores of MCM-48*," *Chemistry of Materials* **2004**, *16*, 2411-2417 (Research article)

67. Kim, J. M.; Kim, S. K.; Ryoo, R. "*Synthesis of MCM-48 single crystals*," *Chemical Communications* **1998**, 259-260 (Communication article)

68. Kosslick, H.; Lischke, G.; Landmesser, H.; Parlitz, B.; Storek, W.; Fricke, R. "*Acidity and Catalytic Behavior of Substituted MCM-48*," *Journal of Catalysis* **1998**, *176*, 102-114 (Research article)

69. Anderson, M. W. "*Simplified description of MCM-48*," *Zeolites* **1997**, *19*, 220-227 (Research article)

70. Song, M-G.; Kim, J-Y.; Cho, S-H.; Kim, J-D. "*Rapid Synthesis of Mesoporous Silica by an Accelerated Microwave Radiation Method*," *Korean Journal of Chemical Engineering* **2004**, *21*, 1224-1230 (Research article)

71. Bandyopadhyay, M.; Gies, H. "*Synthesis of MCM-48 by microwave-hydrothermal process*," *Comptes Rendus Chimie* **2005**, *8*, 621-626 (Research article)

72. Czechura, K.; Sayari, A. "*Synthesis of MCM-48 Silica Using a Gemini Surfactant with a Rigid Spacer*," *Chemistry of Materials* **2006**, *18*, 4147-4150 (Research article)

73. Zhai, S-R.; Zheng, J-L.; Zou, J.; Wu, D.; Sun, Y-H. "*Mixed Cationic-Nonionic Surfactants Route to MCM-48: Effect of the Nonionic Surfactant on the Structural Properties*," *Journal of Sol-Gel Science and Technology* **2004**, *30*, 149-155 (Research article)

74. Zhao, W.; Luo, Y.; Deng, P.; Li, Q. "*Synthesis of Fe-MCM-48 and its catalytic performance in phenol hydroxylation*," *Catalysis Letters* **2001**, *73*, 199-202 (Research article)

75. Yu, J.; Shi, J-L.; Wang, L-Z.; Gao, J-H.; Yan, D-S. "*Synthesis of MCM-48 under low surfactant/silicon molar ratio conditions*," *Journal of Materials Science Letters* **2000**, *19*, 1461-1464 (Research article)

76. Chen, F.; Song, F.; Li, Q. "*Mixed cationic-anionic templating route to Al-MCM-48," Microporous and Mesoporous Materials* **1999**, *29*, 305-310 (Research article)

77. Kong, L.; Liu, S.; Yan, X.; Li, Q.; He, H. "*Synthesis of hollow-shell MCM-48 using the ternary surfactant templating method*," *Microporous and Mesoporous Materials* **2005**, *81*, 251-257 (Research article)

78. Pena, M. L.; Kan, Q.; Corma, A.; Rey, F. "*Synthesis of cubic mesoporous MCM-48 materials from the system $SiO_2$:CTAOH/Br:$H_2O$*," *Microporous and Mesoporous Materials* **2001**, *44-45*, 9-16 (Research article)

79. Xia, Y.; Mokaya, R. "*Facile and high yield synthesis of mesostructured MCM-48 silica crystals*," *Journal of Materials Chemistry* **2001**, *13*, 657-659 (Communication article)

80. Zhao, W.; Hao, Z.; Hu, C. "*Synthesis of MCM-48 with a high thermal and hydro-thermal stability*," *Materials Research Bulletin* **2005**, *40*, 1775-1780 (Communication article)

81. Edler, K. J. "*Soap and sand: construction tools for nanotechnology*," *Philosophical Transactions of the Royal Society A: Mathematical, Physical & Engineering Sciences* **2004**, *362*, 2635-2651 (Review article)

82. Petitto, C.; Galarneau, A.; Driole, M-F.; Chiche, B.; Alonso, B.; Di Renzo, F.; Fajula, F. "*Synthesis of Discrete Micrometer-Sized Spherical Particles of MCM-48*," *Chemistry of Materials* **2005**, *17*, 2120-2130 (Research article)

83. Galarneau, A.; Iapichella, J.; Bonhomme, K.; Di Renzo, F.; Kooyman, P.; Terasaki, O.; Fajula, F. "*Controlling the Morphology of Mesostructured Silicas by Pseudomorphic Transformation: A Route Towards Applications*," *Advanced Functional Materials* **2006**, *16*, 1657-1667 (Research article)

84. Galarneau, A.; Iapichella, J.; Brunel, D.; Fajula, F.; Bayram-Hahn, Z.; Unger, K.; Puy, G.; Demesmay, C.; Rocca, J-L. "*Spherical ordered mesoporous silicas and silica monoliths as stationary phases for liquid chromatography*," *Journal of Separation Science* **2006**, *29*, 844-855 (Research article)

85. Chen, D.; Li, Z.; Yu, C.; Shi, Y.; Zhang, Z.; Tu, B.; Zhao, D. "*Nonionic Block Copolymer and Anionic Mixed Surfactants Directed Synthesis of Highly Ordered Mesoporous Silica with Bicontinuous Cubic Structure*," *Chemistry of Materials* **2005**, *17*, 3228-3234 (Research article)

86. Huo, Q.; Margolese, D. I.; Stucky, G. D. "*Surfactant Control of Phases in the Synthesis of Mesoporous Silica-Based Materials*," *Chemistry of Materials* **1996**, *8*, 1147-1160 (Review article)

87. Romero, A. A.; Alba, M. D.; Klinowski, J. "*Aluminosilicate Mesoporous Molecular Sieve MCM-48*," *Journal of Physical Chemistry B* **1998**, *102*, 123-128 (Research article)

88. Schmidt, R.; Junggreen, H.; Stocker, M. "*Synthesis of a mesoporous MCM-48 material containing only tetrahedral aluminium*," *Chemical Communications* **1996**, 875-876 (Communication article)

89. Xia, Y.; Mokaya, R. "*Aluminosilicate MCM-48 materials with enhanced stability via simple post-synthesis treatment in water*," *Microporous and Mesoporous Materials* **2004**, *68*, 1-10 (Research article)

90. Xia, Y.; Mokaya, R. "*On the Hydrothermal Stability of Mesoporous Aluminosilicate MCM-48 Materials*," *Journal of Physical Chemistry B* **2003**, *107*, 6954-6960 (Research article)

91. Vralstad, T.; Oye, G.; Ronning, M.; Glomm, W. R.; Stocker, M.; Sjoblom, J. "*Interfacial chemistry of cobalt(II) during sol-gel synthesis of cobalt-containing mesoporous materials*," *Microporous and Mesoporous Materials* **2005**, *80*, 291-300 (Research article)

92. Vrlstad, T.; Glomm, W. R.; Ronning, M.; Dathe, H.; Jentys, A.; Lercher, J. A.; Oye, G.; Stocker, M.; Sjoblom, J. "*Spectroscopic Characterization of Cobalt-Containing Mesoporous Materials*," *Journal of Physical Chemistry B* **2006**, *110*, 5386-5394 (Research aticle)

93. Vralstad, T.; Oye, G.; Stocker, M.; Sjoblom, J. "*Synthesis of comparable Co-MCM-48 and Co-MCM-41 materials containing high cobalt contents*," *Microporous and Mesoporous Materials* **2007**, *104*, 10-17 (Research article)

94. Glomm, W. R.; Vralstad, T.; Oye, G.; Sjoblom, J.; Stocker, M. "*A Direct Sol-Gel Synthesis Method for Incorporation of Transition Metals into the Framework of Ordered Mesoporous Materials*," *Journal of Dispersion Science and Technology* **2005**, *26*, 95-104 (Research article)

95. Wei, D.; Wang, H.; Feng, X.; Chuch, W-T.; Ravikovitch, P.; Lyubovsky, M.; Li, C.; Takeguchi, T.; Haller, G. L. "*Synthesis and Characterization of Vanadium-Substituted Mesoporous Molecular Sieves*," *Journal of Physical Chemistry B* **1999**, *103*, 2113-2121 (Research article)

96. Huang, L.; Huang, Q.; Xiao, H.; Eic, M. "*Al-MCM-48 as a potential hydrotreating catalyst support: I-Synthesis and adsorption study*," *Microporous and Mesoporous Materials* **2008**, *111*, 404-410 (Research article)

97. Shao, Y.; Wang, L.; Zhang, J.; Anpo, M. "*Synthesis and characterization of high hydrothermally stable Cr-MCM-48*," *Microporous and Mesoporous Materials* **2008**, *109*, 271-277 (Research article)

98. Kresge, C. T.; Leonowicz, M. E.; Roth, W. J.; Vartuli, J. C.; Beck, J. S. "*Ordered mesoporous molecular sieves synthesized by a liquid-crystal template mechanism*," *Nature* **1992**, *359*, 710-712 (Research article)

99. Beck, J. S.; Vartuli, J. C.; Roth, W. J.; Leonowicz, M. E.; Kresge, C. T.; Schmitt, K. D.; Chu, C. T-W.; Olson, D. H.; Sheppard, E. W.; McCullen, S. B.; Higgins, J. B.; Schlenker, J. L. "*A New Family of Mesoporous Molecular Sieves Prepared with Liquid Crystal Templates*," *Journal of the American Chemical Society* **1992**, *114*, 10834-10843 (Research article)

100. Vartuli, J. C.; Schmitt, K. D.; Kresge, C. T.; Roth, W. J.; Leonowicz, M. E.; McCullen, S. B.; Hellring, S. D.; Beck, J. S.; Schlenker, J. L.; Olson, D. H.; Sheppard, E. W. "*Effect of Surfactant/Silica Molar Ratios on the Formation of Mesoporous Molecular Sieves: Inorganic Mimicry of Surfactant Liquid-Crystal Phases and Mechanistic Implications*," *Chemistry of Materials* **1994**, *6*, 2317-2326 (Research article)

101. Huo, Q.; Margolese, D. I.; Ciesia, U.; Feng, P.; Gler, T. E.; Sieger, P.; Leon, R.; Petroff, P. M.; Schuth, F.; Stucky, G. D. "*Generalized synthesis of periodic surfactant/inorganic composite materials*," *Nature* **1994**, *368*, 317-321 (Research article)

102. Monnier, A.; Schuth, F.; Huo, Q.; Kumar, D.; Margolese, D.; Maxwell, R. S.; Stucky, G. D.; Krishnamurty, M.; Petroff, P.; Firouzi, A.; Janicke, M.; Chmelka, B. F. "*Cooperative Formation of Inorganic-Organic Interfaces in the Synthesis of Silicate Mesostructures*," *Science* **1993**, *261*, 1299-1303 (Research article)

103. Firouzi, A.; Kumar, D.; Bull, L. M.; Besier, T.; Sieger, P.; Huo, Q.; Walker, S. A.; Zasadzinski, J. A.; Glinka, C.; Nicol, J.; Margolese, D.; Stucky, G. D.; Chmelka, B. F. "*Cooperative Organization of Inorganic-Surfactant and Biomimetic Assemblies*," *Science* **1995**, *267*, 1138-1143 (Research article)

104. Tolbert, S. H.; Landry, C. C.; Stucky, G. D.; Chmelka, B. F.; Norby, P.; Hanson, J. C.; Monnier, A. "*Phase Transitions in Mesostructured Silica/Surfactant Composites: Surfactant Packing and the Role of Charge Density Matching*," *Chemistry of Materials* **2001**, *13*, 2247-2256 (Research article)

105. Landry, C. C.; Tolbert, S. H.; Gallis, K. W.; Monnier, A.; Stucky, G. D.; Norby, P.; Hanson, J. C. "*Phase Transformations in Mesostructured Silica/Surfactant Composites. Mechanisms for Change and Applications to Materials Synthesis*," *Chemistry of Materials* **2001**, *13*, 1600-1608 (Research article)

106. Stucky, G. D.; Zhao, D.; Yang, P.; Lukens, W.; Melosh, **(Fix);** Chmelka, B. F. "*Using the inorganic-organic interface to define pore and macroscale structure*," *Studies in Surface Science and Catalysis* **1998**, *117*, 1-12 (Review article)

107. Echchahed, B.; Morin, M.; Blais, S.; Badiei, A-R.; Berhault, G.; Bonneviot, L. "*Ion mediation and surface charge density in phase transformation of micelle templated silica*," *Microporous and Mesoporous Materials* **2001**, *44-45*, 53-63 (Research article)

108. Gross, A. F.; Ruiz, J.; Tolbert, S. H. "*Effect of Framework Polymerization on the Phase Stability of Periodic Silica/Surfactant Nanostructured Composites*," *Journal of Physical Chemistry B* **2000**, *104*, 5448-5461 (Research article)

109. Cheng, C-F.; Park, D. H.; Klinowski, J. "*Optimal parameters for the synthesis of the mesoporous molecular sieve [Si]-MCM-41*," *Journal of the Chemical Society, Faraday Transactions* **1997**, *93*, 193-197 (Research article)

110. Cheng, C-F.; Zhou, W.; Park, D. H.; Klinowski, J.; Hargreaves, M.; Gladden, L. F. "*Controlling the channel diameter of the mesoporous molecular sieve MCM-41*," *Journal of the Chemical Society, Faraday Transactions* **1997**, *93*, 359-363 (Research article)

111. Taralkar, U. S.; Kasture, M. W.; Joshi, P. N. "*Influence of synthesis conditions on structural properties of MCM-48*," *Journal of Physics and Chemistry of Solids* **2008**, *69*, 2075-2081 (Research article)

112. Zhao, W.; Kong, L.; Luo, Y.; Li, Q. "*Study of the influence factors on the synthesis of Fe-MCM-48 with binary mixed cationic and anionic surfactants*," *Microporous and Mesoporous Materials* **2007**, *100*, 111-117 (Research article)

113. Huo, Q.; Margolese, D. I.; Ciesla, U.; Demuth, D. G.; Feng, P.; Gier, T. E.; Sieger, P.; Firouzi, A.; Chmelka, B. F.; Schuth, F.; Stucky, G. D. "*Organization of Organic Molecules with Inorganic Molecular Species into Nanocomposite Biphase Arrays*," *Chemistry of Materials* **1994**, *6*, 1176-1191 (Review article)

114. Wang, L.; Shao, Y.; Zhang, J.; Anpo, M. "*Synthesis of MCM-48 mesoporous molecular sieve with thermal and hydrothermal stability with the aid of promoter anions*," *Microporous and Mesoporous Materials* **2006**, *95*, 17-25 (Research article)

115. Edler, K. J.; White, J. W. "*Further Improvements in the Long-Range Order of MCM-41 Materials*," *Chemistry of Materials* **1997**, *9*, 1226-1233 (Research article)

116. Oye, G.; Sjoblom, J.; Stocker, M. "*Synthesis and characterization of siliceous and aluminum-containing mesoporous materials from different surfactant solutions*," *Microporous and Mesoporous Materials* **1999**, *27*, 171-180 (Research article)

117. Yu, C.; Fan, J.; Tian, B.; Zhao, D. "*Morphology Development of Mesoporous Materials: a Colloidal Phase Separation Mechanism*," *Chemistry of Materials* **2004**, *16*, 889-898 (Research article)

118. Lebedev, O. I.; Tendeloo, G. V.; Collart, O.; Cool, P.; Vansant, E. F. "*Structure and microstructure of nanoscale mesoporous silica spheres*," *Solid State Sciences* **2004**, *6*, 489-498 (Research article)

119. Huo, Q.; Leon, R.; Petroff, P. M.; Stucky, G. D. "*Mesostructure Design with Gemini Surfactants: Supercage Formation in a Three-Dimensional Hexagonal Array*," *Science* **1995**, *268*, 1324-1327 (Research article)

120. Huo, Q.; Feng, J.; Schuth, F.; Stucky, G. D. "*Preparation of Hard Mesoporous Silica Spheres*," *Chemistry of Materials* **1997**, *9*, 14-17 (Communications article)

121. Israelachvili, J. N.; Mitchell, D. J.; Ninham, B. W. "*Theory of self-assembly of hydrocarbon amphipilies into micelles and bilayers*," *Journal of the Chemical Society, Faraday Transactions II* **1976**, *92*, 1525-1568 (Research article)

122. Xu, J.; Luan, Z.; He, H.; Zhou, W.; Kevan, L. "*A Reliable Synthesis of Cubic Mesoporous MCM-48 Molecular Sieve*," *Chemistry of Materials* **1998**, *10*, 3690-3698 (Research article)

123. Xia, Y.; Mokaya, R.; Titman, J. J. "*Formation of Molecularly Ordered Layered Mesoporous Silica via Phase Transformation of Silicate-Surfactant Composites*," *Journal of Physical Chemistry B* **2004**, *108*, 11361-11367 (Research article)

124. Sayari, A. "*Novel Synthesis of High-Quality MCM-48 Silica*," *Journal of the American Chemical Society* **2000**, *122*, 6504-6505 (Communications article)

125. Liu, Y.; Karkamkar, A.; Pinnavaia, T. J. "*Redirecting the assembly of hexagonal MCM-41 into cubic MCM-48 from sodium silicate without the use of an organic structure modifier*," *Chemical Communications* **2001**, 1822-1823 (Communications article)

126. Russo, P. A.; Ribeiro Carrott, M. M. L.; Carrott, P. J. M.; Lopes, J. M.; Ramoa Ribeiro, F.; Rocha, J. "*Structure and catalytic activity of Al-MCM-48 materials synthesized at room temperature: Influence of the*

*aluminum source and calcination conditions*," *Microporous and Mesoporous Materials* **2008**, *114*, 293-302 (Research article)

127. Boote, B.; Subramanian, H.; Koodali, R. T. "*Rapid and facile synthesis of siliceous MCM-48 mesoporous materials*," *Chemical Communications* **2007**, 4543-4545 (Communications article)

128. Schumacher, K.; Hohensche, d. F. v. C.; Unger, K. K.; Ulrich, R.; Chesne, D. A.; Wiesner, U.; Spiess, H. W. "*The Synthesis of Spherical Mesoporous Molecular Sieves MCM-48 with Heteroatoms Incorporated into the Silica Framework*," *Advanced Materials* **1999**, *11*, 1194-1198 (Research article)

129. Stober, W.; Fink, A.; Bohn, E. "*Controlled Growth of Monodisperse Silica Spheres in the Micron Size Range*," *Journal of Colloid and Interface Science* **1968**, *26*, 62-69 (Research article)

130. Zhu, Z.; Chang, Z.; Kevan, L. "*Synthesis and Characterization of Mesoporous Chromium-Containing Silica Tube Molecular Sieves CrMCM-41*," *Journal of Physical Chemistry B* **1999**, *103*, 2680-2688 (Research article)

131. Galarneau, A.; Driole, M-F.; Petitto, C.; Chiche, B.; Bonelli, B.; Armandi, M.; Onida, B.; Garrone, E.; Di Renzo, F.; Fajula, F. "*Effect of post-synthesis treatment on the stability and surface properties of MCM-48 silica*," *Microporous and Mesoporous Materials* **2005**, *83*, 172-180 (Research article)

132. Kleitz, F.; Schmidt, W.; Schuth, F. "*Calcination behavior of different surfactant-templated mesostructured silica materials*," *Microporous and Mesoporous Materials* **2003**, *65*, 1-29 (Research article)

133. Grun, M.; Lauer, I.; Unger, K. K. "*The Synthesis of Micrometer-and Submicrometer-Size Spheres of Ordered Mesoporous Oxide MCM-41*," *Advanced Materials* **1997**, *9*, 254-257 (Research article)

134. Coasne, B.; Galarneau, A.; Di Renzo, F.; Pellenq, R. J. M. "*Gas Adsorption in Mesoporous Micelle-Templated Silicas: MCM-41, MCM-48, and SBA-15*," *Langmuir* **2006**, *22*, 11097-11105 (Research article)

135. Collart, O.; Voort, P. Van Der.; Vansant, E. F.; Despantier, D.; Galarneau, A.; Di Renzo, F.; Fajula, F. "*A High-Yield Reproducible Synthesis of MCM-48 Starting from Fumed Silica*," *Journal of Physical Chemistry B* **2001**, *105*, 12771-12777 (Research article)

136. Galarneau, A.; Desplaniter-Giscard, D.; Di Renzo, F.; Fajula, F. "*Thermal and mechanical stability of micelle-templated silica supports for catalysis*," *Catalysis Today* **2001**, *68*, 191-200 (Research article)

137. Chen, L.; Horiuchi, T.; Mori, T.; Maeda, K. "*Postsynthesis Hydrothemal Restructuring of M41S Mesoporous Molecular Sieves in Water*," *Journal of Physical Chemistry B* **1999**, *103*, 1216-1222 (Research article)

138. Keene, M. T. J.; Gougeon, R. D. M.; Denoyel, R.; Harris, R. K.; Rouquerol, J.; Llewellyn, P. L. "*Calcination of the MCM-41 mesophase: mechanism of surfactant thermal degradation and evolution of the porosity*," *Journal of Materials Chemistry* **1999**, *9*, 2843-2850 (Research article)

139. Zhao, W.; Li, Q. "*Synthesis of Nanosize MCM-48 with High Thermal Stability*," *Chemistry of Materials* **2003**, *15*, 4160-4162 (Communications article)

140. Chen, C-Y.; Li, H-X.; Davis, M. E. "*Studies on mesoporous materials I: Synthesis and characterization of MCM-41*," *Microporous Materials* **1993**, *2*, 17-26 (Research article)

141. Di Renzo, F.; Testa, F.; Chen, J. D.; Cambon, H.; Galarneau, A.; Plee, D.; Fajula, F. "*Textual control of micelle-templated mesoporous silicates: the effects of co-surfactants and alkalinity*," *Microporous and Mesoporous Materials* **1999**, *28*, 437-446 (Research article)

142. Lin, H-P.; Kao, C-P.; Mou, C-Y. "*Counterion and alcohol effect in the formation of mesoporous silica*," *Microporous and Mesoporous Materials* **2001**, *48*, 135-141 (Research article)

143. Lin, H-P.; Mou, C-Y. "*Salt effect in post-synthesis hydrothermal treatment of MCM-41*," *Microporous and Mesoporous Materials* **2002**, *55*, 69-80 (Research article)

144. Vralstad, T. "Synthesis and characterization of cobalt-containing mesoporous model catalysts," Ph.D. Thesis, December, 2005 Norwegian University of Science and Technology http://www.chemeng.ntnu.no/research/polymer/ugelstadlab/thesis/tyralstad.pdf (accessed 12/12/08)

145. Lin, H-P.; Mou, C-Y. "*Structural and Morphological Control of Cationic Surfactant-Templated Mesoporous Silica*," *Accounts of Chemical Research* **2002**, *35*, 927-935 (Review article)

146. Rodrigues, S.; Uma, S.; Martyanov, I. N.; Klabunde, K. J. "*Visible light induced photocatalytic activity for degradation of acetaldehyde using transition metal incorporated Al-MCM-41 (aluminum doped silica zeolitic material)*," *Journal of Photochemistry and Photobiology A: Chemistry* **2004**, *165*, 51-58 (Research article)

147. Zhang, W.; Pinnavaia, T. J. "*Transition metal substituted derivatives of cubic MCM-48 mesoporous molecular sieves*," *Catalysis Letters* **1996**, *38*, 261-265 (Research article)

148. Alfredsson, V.; Anderson, M. W.; Ohsuna, T.; Terasaki, O.; Jacob, M.; Bojrup, M. "*Cubosome Description of the Inorganic Mesoporous Structure MCM-48*," *Chemistry of Materials* **1997**, *9*, 2066-2070 (Communication article)

149. Moulik, S. P. "*Micelles: Self-organized surfactant assemblies*," *Current Science* **1996**, *71*, 368-376 (Review article)

150. Hait, S. K.; Moulik, S. P. "*Gemini surfactants: A distinct class of self-assembling molecules*," *Current Science* **2002**, *82*, 1101-1111 (Review article)

151. Foster, S.; Antonietti, M. "*Amphiphilic Block Copolymers in Structure-Controlled Nanomaterials Hybrids*," *Advanced Materials* **1998**, *10*, 195-217 (Review article)

152. Jeffrey Brinker, C.; Lu, Y.; Sellinger, A.; Fan, H. "*Evaporation-Induced Self-Assembly: Nanostructures Made Easy*," *Advanced Materials* **1999**, *11*, 579-585 (Review article)

153. Kume, G.; Gallotti, M.; Nunes, G. "*Review on Anionic/Cationic Surfactant Mixtures*," *Journal of Surfactant and Detergents* **2008**, *11*, 1-11 (Review article)

154. Wang, L.; Shao, Y.; Zhang, J. "*Short-time formation of well-ordered cubic mesoporous MCM-48 molecular sieve with the aid of fluoride ions*," *Materials Letters* **2005**, *59*, 3604-3607 (Communications article)

155. Shao, Y.; Wang, L.; Zhang, J.; Anpo, M. "*Novel synthesis of high hydrothermal stability and long-range order MCM-48 with a convenient method*," *Microporous and Mesoporous Materials* **2005**, *86*, 314-322 (Research article)

156. Wang, L.; Shao, Y.; Zhang, J.; Anpo, M. "*Cooperative effect of crystallization temperature and NaF addition in the formation process and hydrothermal stability of MCM-48 mesoporous molecular sieve*," *Microporous and Mesoporous Materials* **2007**, *100*, 241-249 (Research article)

157. Wang, L.; Zhang, J.; Chen, F.; Anpo, M. "*Fluoride-Induced Reduction of CTAB Template Amount for the Formation of MCM-48 Mesoporous Molecular Sieve*," *Journal of Physical Chemistry C* **2007**, *111*, 13648-13651 (Research article)

158. Wang, L.; Zhang, J.; Chen, F. "*Synthesis of hydrothermally stable MCM-48 mesoporous molecular sieve at low cost of CTAB surfactant*," *Microporous and Mesoporous Materials* **2009**, *122*, 229-233 (Research article)

159. Mathieu, M.; Van Der Voort, P.; Wechkhuysen, B. M.; Rao, R. R.; Catana, G.; Schoonheydt, R. A.; Vansant, E. F. "*Vanadium-Incorporated MCM-48 Materials: Optimization of the Synthesis Procedure and an in Situ Spectroscopic Study of the Vanadium Species*," *Journal of Physical Chemistry B* **2001**, *105*, 3393-3399 (Research article)

160. Tatsumi, T.; Koyano, K. A.; Igarashi, N. "*Remarkable activity enhancement by trimethylsilylation in oxidation of alkenes and alkanes with $H_2O_2$ catalyzed by titanium-containing mesoporous molecular sieves*," *Chemical Communications* **1998**, 325-326 (Communication article)

161. Voegtlin, A. C.; Ruch, F.; Guth, J. L.; Patarin, J.; Huve, L. "*$F^-$ mediated synthesis of mesoporous silica with ionic- and non-ionic surfactants. A new templating pathway*," *Microporous Materials* **1997**, *9*, 95-105 (Research article)

162. Ko, C. H.; Ryoo, R. "*Imaging the channels in mesoporous molecular sieves with platinum*," *Chemical Communications* **1996**, 2467-2468 (Communication article)

163. Alfredsson, V.; Anderson, M. W. "*Structure of MCM-48 Revealed by Transmission Electron Microscopy*," *Chemistry of Materials* **1996**, *8*, 1141-1146 (Research article)

164. Xu, W.; Aydin, M.; Zakia, S.; Akins, D. L. "*Aggregation of Thionine within AlMCM-48*," *Journal of Physical Chemistry B* **2004**, *108*, 5588-5593 (Research article)

165. Hartmann, M.; Racouchot, S.; Bischof, C. "*Synthesis and redox properties of MCM-48 containing copper and zinc*," *Chemical Communications* **1997**, 2367-2368 (Communication article)

166. Yong, G-p.; Jin, Z-x.; Tong, H-w.; Yan, X-y.; Li, G-s.; Liu, S-m. "*Selective reduction of bulky polycyclic aromatic hydrocarbons from mainstream smoke of cigarettes by mesoporous materials*," *Microporous and Mesoporous Materials* **2006**, *91*, 238-243 (Research article)

167. Schulz-Ekloff, G.; Rathousky, J.; Zukal, A. "*Controlling of morphology and characterization of pore structure of ordered mesoporous silicas*," *Microporous and Mesoporous Materials* **1999**, *27*, 273-285 (Research article)

168. Kruk, M.; Jaroniec, M.; Ryoo, R.; Joo, S. H. "*Characterization of MCM-48 Silicas with Tailored Pore Sizes Synthesized via a Highly Efficient Procedure*," *Chemistry of Materials* **2000**, *12*, 1414-1421 (Research article)

169. Park, H. J.; Yim, J-H.; Jeon, J-K.; Kim, J. M.; Yoo, K-S.; Park, Y-K. "*Pyrolysis of polypropylene over mesoporous MCM-48 material*," *Journal of Physics and Chemistry of Solids* **2008**, *69*, 1125-1128 (Research article)

170. Anpo, M.; Yamashita, H.; Ikeue, K.; Fujii, Y.; Zhang, S. G.; Ichihashi, Y.; Park, D. R.; Koyano, K.; Tatsumi, T. "*Photocatalyic reduction of $CO_2$ with $H_2O$ on Ti-MCM-41 and Ti-MCM-48 mesoporous zeolite catalysts*," *Catalysis Today* **1998**, *44*, 327-332 (Research article)

171. Krishna, V.; Kamble, V. S.; Gupta, N. M.; Selvam, P. "*Heterogeneous Photocatalytic Degradation of Methanol over Uranyl-Anchored Nanoporous MCM-41 and MCM-48*," *Journal of Nanoscience and Nanotechnology* **2006**, *6*, 1811-1814 (Research article)

172. Bandyopadhyay, B.; Birkner, A.; van der Berg, M. W. E.; Klementiev, K. V.; Schmidt, W.; Grunert, W.; Gies, H. "*Synthesis and Characterization of Mesoporous MCM-48 Containing $TiO_2$ Nanoparticle*," *Chemistry of Materials* **2005**, *17*, 3820-3829 (Research article)

173. Rodrigues, S.; Koodali, R. T.; Uma, S.; Martyanov, I. N.; Kenneth, K. J. "*Single-Step Synthesis of a Highly Active Visible-Light Photocatalyst for Oxidation of a Common Indoor Air Pollutant: Acetaldehyde*," *Advanced Materials* **2005**, *17*, 2467-2471 (Research article)

174. Endud, S.; Wong, K-L. "*Mesoporous silica MCM-48 molecular sieve modified with $SnCl_2$ in alkaline medium for selective oxidation of alcohol*," *Microporous and Mesoporous Materials* **2007**, *101*, 256-263 (Research article)

175. Kutrowski, P.; Chmielarz, L.; Surman, J.; Bidzisha, E.; Dziembaj, R.; Cool, P.; Vansant, E. F. "*Catalytic Activity of MCM-48-, SBA-15-, MCF-, and MSU-Type Mesoporous Silicas Modified with Fe Species in the Oxidative Dehydrogenation of Ethylbenzene in the Presence of $N_2O$*," *Journal of Physical Chemistry A* **2005**, *109*, 9808-9815 (Research article)

176. Sakthivel, A.; Komura, K.; Sugi, Y. "*MCM-48 Supported Tungstophosphoric Acid: An Efficient Catalyst for the Esterification of Long-Chain Fatty Acids and Alcohols in Supercritical Carbon Dioxide*," *Industrial & Engineering Chemistry Research* **2008**, *47*, 2538-2544 (Research article)

177. Mukhopadhyay, K.; Sarkar, B. R.; Chaudhari, R. V. "*Anchored Pd Complex in MCM-41 and MCM-48: Novel Heterogeneous Catalysts for Hydrocarboxylation of Aryl Olefins and Alcohols*," *Journal of the American Chemical Society* **2002**, *124*, 9692-9693 (Communications article)

178. Eswaramoorthy, M.; Neeraj,; Rao, C. N. R. "*High catalytic efficiency of transition metal complexes encapsulated in a cubic mesoporous phase*," *Chemical Communications* **1998**, 615-616 (Communications article)

179. Pirouzmand, M.; Amini, M. M.; Safari, N. "*Immobilization of iron tetrasulfophthaloxyanine on functionalized MCM-48 and MCM-41 mesoporous silicas: Catalysts for oxidation of styrene*," *Journal of Colloid and Interface Science* **2008**, *319*, 199-205 (Research article)

180. Koo, D. H.; Kim, M.; Chang, S. "*$WO_3$ Nanoparticles on MCM-48 as a Highly Selective and Versatile Heterogeneous Catalyst for the Oxidation of Olefins, Sulfide, and Cyclic Ketones*, " *Organic Letters* **2005**, *7*, 5015-5018 (Research article)

181. Zhao, W.; Hao, Z.; Hu, C.; Li, J.; Xu, X. "*The expoxidation of allyl alcohol on Ti-complex/MCM-48 catalyst*," *Microporous and Mesoporous Materials* **2008**, *112*, 133-137 (Research article)

182. Yuan, S.; Shi, L.; Mori, K.; Yamashita, H. "*Synthesis of Ti-containing MCM-48 by using $TiF_4$ as titanium source*," *Materials Letters* **2008**, *62*, 3028-3030 (Communications article)

183. Galarneau, A.; Iapichella, J.; Petitto, C.; Di Renzo, F.; Fajula, F. "*Hierarachical Porous Silicas for Chromatographic Applications Obtained by Pseudomorphic Synthesis*," *Materials Research Society Symposium Proceedings* **2005**, *847*, 345 (**EE** *12.3.1*)

184. Lind, A.; du Fresne von Hohenesche, C.; Smatt, J-H.; Linden, M.; Unger, K. K. "*Spherical silica agglomerates possessing hierarchical porosity prepared by spray drying of MCM-41 and MCM-48 nanospheres*," *Microporous and Mesoporous Materials* **2003**, *66*, 219-227 (Research article)

185. Giraldo, L. F.; Lopez, B. L.; Perez, L.; Urrego, S.; Sierra, L.; Mesa, M. "*Mesoporous Silica Applications*," *Macromolecular Symposia* **2007**, *258*, 129-141 (Review article)

186. Daehler, A.; Boskovic, S.; Gee, M. L.; Separovic, F.; Stevens, G. W.; O'Connor, A. J. "*Postsynthesis Vapor-Phase Functionalization of MCM-48 with Hexamethyldisilazane and 3-Aminopropyldimethylethoxylsilane for Bioseparation Applications*," *Journal of Physical Chemistry B* **2005**, *109*, 16263-16271 (Research article)

187. McKeen, J. C.; Yan, Y. S.; Davis, M. E. "*Proton Conductivity of Acid-Functionalized Zeolite Beta, MCM-41, and MCM-48: Effect of Acid Strength*," *Chemistry of Materials* **2008**, *20*, 5122-5124 (Communications article)

188. Yoon, S. B.; Kim, J. Y.; Yu, J-S. "*Synthesis of highly ordered nanoporous carbon molecular sieves from silylated MCM-48 using devinylbenzene as precursor*," *Chemical Communications* **2001**, 599-560 (Communications article)

189. He, J.; Shen, Y.; Evans, D. G. "*A nanocomposite structure based on modified MCM-48 and polystyrene*," *Microporous and Mesoporous Materials* **2008**, *109*, 73-79 (Research article)

190. He, J.; Shen, Y.; Evans, D. G.; Duan, X. "*Tailoring the performance of polymer composites via altering the properties of the intrapore polymers of MCM-48 nanocomposites as fillers*," *Composites Part A: applied science and manufacturing* **2006**, *37*, 379-384 (Research article)

191. Kao, C-P.; Lin, H-P.; Mou, C-Y. "*Synthesis of elastic macrospheres of silica-surfactant nanocomposites*," *Journal of Physics and Chemistry of Solids* **2001**, *62*, 1555-1559 (Research article)

192. Zhang, H.; Zhang, P.; Ye, K.; Sun, Y.; Jiang, S.; Wang, Y.; Pang, W. "*Mesoporous material grafted with luminescent molecules for the design of selective metal ion chemosensor*," *Journal of Luminescence* **2006**, *117*, 68-74 (Research article)

193. Huang, L.; Huang, Q.; Xiao, H.; Eic, M. "*Al-MCM-48 as a potential hydrotreating catalyst support: II-Diffusion property study*," *Microporous and Mesoporous Materials* **2008**, *114*, 121-128 (Research article)

194. Hussaini, M.; Song, S-K.; Lee, J-H.; Ihm, S-K. "*Characteristics of CoMo Catalysts Supported on Modified MCM-41 and MCM-48 Materials for Thiophene Hydrodesulfurization*," *Industrial & Engineering Chemistry Research* **2006**, *45*, 536-543 (Research article)

195. Kim, S. "*Modified Ordered Mesoporous Silica for $CO_2$-$N_2$ Separation*," MS thesis November, 2003 University of Cincinnati http://www.ohiolink.edu/etd/send-pdf.cgi?ucin1070484926 (accessed 5/1/09)

196. Kumar, P. "Inclusion Chemistry in Periodic Mesoporous Hosts: Growth of Quantum-Confined Materials and Gas Separation Membranes," Ph.D. thesis May, 2007 University of Cincinnati http://www.ohiolink.edu/etd/send=pdf.cgi/KUMAR%20PARVEEN.pdf?acc_num=ucin1186772727 (accessed 5/1/09)

197. Nishiyama, N.; Koide, A.; Egashira, Y.; Ueyama, K. "*Mesoporous MCM-48 membrane synthesized on a porous stainless steel support*," *Chemical Communications* **1998**, 2147-2148 (Communications article)

198. Nishiyama, N.; Park, D. H.; Koide, A.; Egashira, Y.; Ueyama, K. "*A mesoporous silica (MCM-48) membrane: preparation and characterization*," *Journal of Membrane Science* **2001**, *182*, 235-244 (Research article)

199. Huang, H. Y.; Yang, R. T.; Chinn, D.; Munson, C. L. "*Amine-Grafted MCM-48 and Silica Xerogel as Superior Sorbents for Acidic Gas Removal from Natural Gas*," *Industrial & Engineering Chemistry Research* **2003**, *42*, 2427-2433 (Research article)

200. Kim, S.; Ida, J.; Guliants, V. V.; Lin, Y. S. "*Tailoring Pore Properties of MCM-48 Silica for Selective Adsorption of $CO_2$*," *Journal of Physical Chemistry B* **2005**, *109*, 6287-6293 (Research article)

201. Iglesia, O. de la; Pedernera, M.; Mallada, R.; Lin, Z.; Rocha, J.; Coronas, J.; Santamaria, J. "*Synthesis and characterization of MCM-48 tubular membranes*," *Journal of Membrane Science* **2006**, *280*, 867-875 (Research article)

202. Kumar, P.; Ida, J.; Guliants, V. V. "*High flux mesoporous MCM-48 membranes: Effects of support and synthesis conditions on membrane permeance and quality*," *Microporous and Mesoporous Materials* **2008**, *110*, 595-599 (Communications article)

203. Wu, S.; Yang, J.; Lu, J.; Zhou, Z.; Kong, C.; Wang, J. "*Synthesis of thin and compact mesoporous MCM-48 membrane on vacuum-coated α-$Al_2O_3$ tube*," *Journal of Membrane Science* **2008**, *319*, 231-237 (Research article)

204. Kumar, P.; Kim, S.; Ida, J.; Guliants, V. V. "*Polyethyleneimine-Modified MCM-48 Membranes: Effect of Water Vapor and Feed Concentration on $N_2/CO_2$ Selectivity*," *Industrial & Engineering Chemistry Research* **2008**, *47*, 201-208 (Research article)

205. Ji, H.; Fan, Y.; Jin, W.; Chen, C.; Xu, N. "*Synthesis of Si-MCM-48 membrane by solvent extraction of the surfactant template*," *Journal of Non-Crystalline Solids* **2008**, *354*, 2010-2016 (Research article)

206. Pedernera, M.; Iglesia, O. de la; Mallada, R.; Lin, Z.; Rocha, J.; Coronas, J.; Santamaria, J. "*Preparation of stable MCM-48 tubular membranes*," *Journal of Membrane Science* **2009**, *326*, 137-144 (Research article)

207. Jun, S.; Kim, J. M.; Ryoo, R.; Ahn, Y-S.; Han, M-H. "*Hydrothermal stability of MCM-48 improved by post-synthesis restructuring in salt solution*," *Microporous and Mesoporous Materials* **2000**, *41*, 119-127 (Research article)

208. Solovyov, L. A.; Belousov, O. V.; Dinnebier, R. E.; Shmakov, A. N.; Kirik, S. D. "*X-ray Diffraction Structure Analysis of MCM-48 Mesoporous Silica*," *Journal of Physical Chemistry B* **2005**, *109*, 3233-3237 (Research article)

209. Voort, P. Van Der; Vansant, E. F. "*The synthesis of stable, hydrophobic MCM-48/$VO_x$ catalysts, using alkylchlorosilianes as coupling agents for the molecular designed dispersion of $VO(acac)_2$*," *Microporous and Mesoporous Materials* **2000**, *38*, 385-390 (Research article)

210. Voort, P. Van Der; Baltes, M.; Vansant, E. F. "*Synthesis of Stable, Hydrophobic MCM-48/$VO_x$ Catalysts Using Alkylchlorosilanes as Coupling Agents for the Molecular Designed Dispersion of $VO(acac)_2$*," *Journal of Physical Chemistry B* **1999**, *103*, 10102-10108 (Research article)

211. Vralstad, T.; Glomm, W. R.; Oye, G.; Sjoblom, J. "*Cobalt Functionalization of Mesoporous Silica by Incipicent Wetness Impregnation and Co-precipitation*," *Journal of Dispersion Science and Technology* **2005**, *26*, 87-94 (Research article)

212. Vralstad, T.; Oye, G.; Sjoblom, J. "*Cobalt Functionalization of Mesoporous Silica by Organosilane Grafting*," *Journal of Dispersion Science and Technology* **2006**, *27*, 489-496 (Research article)

# Chapter 3 –V-MCM-48 Synthesis & Methods

## 3.1 Brief background literature

The following procedure on the synthesis, characterization, and photocatalytic studies of V-MCM-48 with probe molecules involved the following sub-sections: materials, synthesis, characterization, and photocatalysis probe molecule studies. The synthesis implemented to make V-MCM-48 was adopted and modified from literature research. [1-3] The characterization procedure and photocatalytic experiments were completed according to Klabunde and co-workers. [4] In addition, the experimental synthesis, characterization methods, and photocatalytic studies results were compared to literature to gain the true scientific relevance of this research in the discussion section.

## 3.2 Reagents & Materials

*Materials*: the materials used to synthesize V-MCM-48 without further purification follows: (1) 18.5 Ω Nanopure water, (2) absolute ethanol (AAPER Alcohol & Chemical Company), (3) N-hexadecyltrimethylammonium bromide (CTAB) (Alfa Aesar), (4) aqueous $NH_4OH$ (33 volume %) (Fisher Scientific), (5) $NH_4VO_3$ (Sigma-Aldrich) or $VOSO_4 \cdot 3H_2O$ (Alfa Aesar), and (6) tetraethoxysilane (TEOS) (Sigma-Alrich).

## 3.3 Synthesis of V(x)-MCM-48 Scheme

(1) A volume of 90.0 mL of 18.5 Ω Nanopure water with an appropriate size Teflon stir bar was placed into a 250 mL polypropylene plastic container followed by adjustment or stir plate to the mid-range speed value (~ 400-600 rpm). (Stir plate-Fisher-Scientific brand)

(2) Next, 50.0 mL of absolute ethanol was placed in the mixing water.

(3) Then, 2.40 grams of CTAB surfactant was added to the aqueous medium.

(4) Amount of 12.0 mL of concentrated (~ 14.5 M) $NH_4OH$ was added to this aqueous-surfactant medium.

(5) After the surfactant had dissolved in the aqueous solution, the aqueous vanadium precursor solution (metal precursor dissolved in 10.0 mL of 18.5 Ω Nanopure water) was added to the reaction mixture. The exact amount of vanadium precursor to dissolve was determined by the following: [0.016 moles of Si (3.60 mL of TEOS)]/x moles of vanadium ion = Si/V ratio = 1, 5, 10 etc. From the x moles of vanadium ion one could use unit analysis and the molecular weight of $NH_4VO_3$ or $VOSO_4 \cdot 3H_2O$ to obtain the grams of metal precursor needed for a particular Si/V ratio.

(6) The silica precursor of 3.60 mL of TEOS was poured rapidly into the solution mixture and tightly covered for 24 hours under room temperature stirring conditions.

## 3.4 Preparation of As-Synthesized V-MCM-48 for Calcination

The resulting white powder was recovered through filtration using a Buchner funnel with Whatman 100 filter paper, washed with 3 liters of distilled $H_2O$ followed by 3 liters of 18.5 Ω Nanopure water, dried for approximately 5 hours at 373 K. The template was removed through calcination in air. The process involved crushing the white powder between two sheets of weighting paper using a mortar and pestle to fine dust followed by placing in a half-oblong quartz crucible. The crucible was placed in the tube furnace and temperature programmed in ramping mode at 1 K/minute to 823 K (550°C) followed by holding for 6 hours at 823 K; then, the calcinated powder was

brought back to room temperature at 1 K/minute. After removing the room temperature powder from the tube furnace, it was again crushed between two sheets of weighting paper using a mortar and pestle. The next step was to characterize the structural ordering of the powder employing X-ray diffraction (XRD). [Note: the parent Si-MCM-48 mesoporous material was made under identical reaction conditions with the exception of the use of a metal precursor.]

## 3.5 Characterization Techniques applied to Calcinated V-MCM-48

The characterization of V(x)-MCM-48 involved following analytical instruments in order: (1) powder X-ray diffraction (XRD), (2) Diffuse Reflectance Ultra-Violet-Visible (DR-UV-vis) light spectroscopy, and (3) $N_2$ adsorption-desorption isotherm measurements. The powder XRD measurements were conducted on a Bruker D8 diffractometer with Cu-Kα radiation of 1.5418 Å wavelength. The V(x) -MCM-48 powders were analyzed from 1-10° 2θ in step size of 0.01° to determine the crystallinity of the powder samples. The diffuse-reflectance UV-vis spectra of the V(x)-MCM-48 powders were analyzed on a Cary 500 Scan UV-VIS NIR spectrophotometer using an integrating sphere attachment scanned from 200-800 nm range. The standard reference powder used Teflon. The $N_2$ adsorption-desorption isotherms were measured at 77 K, liquid nitrogen temperature, on a NOVA 1000 Series apparatus (Quantachrome Corporation, Boynton Beach, Florida, USA) using calibrated numbered glass cells. Approximately 100 milligrams of the sample under study was placed in the glass cell and degassed at 423 K for 1 hour before measurements were conducted.

## 3.6 Photocatalysis Studies of Six Probe Molecules under UV, Visible, and Dark Conditions

*The following six probe molecules studied follows using V(x)-MCM-48: $CH_3CHO$, CO, $CH_3COCH_3$, $CH_3CH_2OH$, $CH_3CHOHCH_3$, and $CH_3CN$.* The results of photocatalysis studies with V(x)-MCM-48 were compared with nano-particle gold (CO) and Degussia-Huls P-25 $TiO_2$ for acetaldehyde. The photocatalytic gas-phase experiments were conducted in a cylindrical air-filled static reactor that has a total volume of 305 mL. The light reactor has a quartz window and rest of photocatalytic reactor made of glass. After flushing the light reactor for minimally 20 minutes with air, on a circular glass dish was placed 150 milligrams of the catalyst (be it V(x)-MCM-48, nano-Au, P-25 $TiO_2$ Degussia-Huls etc.) in an uniform manner followed by placing in the light reactor. The temperature of the light reactor was maintained throughout the photocatalytic experiment at 298 K (25.0°C) for the acetaldehyde degradation and CO photooxidation analysis: the other probe molecules ($CH_3CHO$, $CH_3COCH_3$, $CH_3CH_2OH$, & $CH_3CN$) degradation light reactions were conducted at 40.0°C in an attempt to cause them to proceed from liquid to gas-phase. All of the gas-phase experiments were conducted under constant stirring using magnetic Teflon coated stir bar. In the acetaldehyde degradation analysis 100.0 μL of reagent grade acetaldehyde (Sigma-Aldrich) was placed on the inside of the light reactor wall after catalyst dish with sample was in place; then, the light reactor cover was tighten followed by equilibrium of liquid to gas-phase reaction for 20 minutes. The sample procedure was applied to the other probe molecules ($CH_3COCH_3$, $CH_3CH_2OH$, $CH_3CHOHCH_3$, & $CH_3CN$) studied. After equilibration (the liquid acetaldehyde given time to vaporize and reach a gas phase-liquid equilibrium in light reactor) for 20 minutes, the light (be it visible or UV) was shined on the catalyst dish. The resulting gaseous mixture of acetaldehyde and $CO_2$ were extracted in 35 μL aliquots using a gas-tight Hamilton glass syringe (Reno, Nevada USA) usually every 10 minutes to have 15 data points in a 140 minute gas-phase analysis. The injected gaseous sample was analyzed on a

gas-chromatograph-mass-spectrometer (GC-MS) (Shimadzu GC-MS-QP5000). The injection port on the GC-MS was maintained at 473 K (200°C) and column temperature of 313 K (40°C). The carrier was ultra-high purity $N_2$ (99.99999) (Air Gas Company, Manhattan, Kansas USA) at 100 pounds per square inch (psi). The gas-chromatograph column was a Resik 4000 capillary column (What's the column made of, pore size, diameter, and length?) The products of the photocatalytic reactions of acetaldehyde were identified through comparison of experimental and reference mass spectra using the characteristic masses, retention times of products, and retention times of pure probe molecule. [Note: the other five probe molecules photocatalytic analysis of products were conducted in a similar manner with two exceptions: (1) an average 1.0 mL of liquid probe molecule was added to light reactor ($CH_3COCH_3$, $CH_3CHOHCH_3$, $CH_3CH_2OH$, & $CH_3CN$) or 1.0-50.0 mL of gaseous CO was added (amount of CO added to light reactor noted in all plots shown in results section), and (2), due to the lack of calibration curve, plotted peak area vs. time and $CO_2$ concentration (mM).]

The UV-light source for the photocatalytic experiments was 1000 Watt high-pressure mercury arc lamp (Oriel Corporation-now Newport Corporation, Stratford, Connecticut USA). The use of light cut-off filters were employed to provide 300-400 nm UV-light range, and visible light experiments used two cut-off filters to provide from >420 nm: filters Oriel-57346 & Oriel 59680.

## References


(1) Stober, W.; Fink, A. Bohn, E. "*Controlled growth of monodisperse silica spheres in microns size range*," *Journal of Colloid and Interface Science* **1968**, *26*, 62-69 (Research article)

(2) Schumacher, K.; Hohensche, d. F. v. C.; Unger, K. K.; Ulrich, R.; Chesne, D. A.; Wiesner, U.; Spiess, H. W. "*The Synthesis of Spherical Mesoporous Molecular Sieves MCM-48 with Heteroatoms Incorporated into the Silica Framework*," *Advanced Materials* **1999**, *11*, 1194-1198 (Research article)

(3) Schumacher, K.; Grun, M.; Unger, K. K. "*Novel synthesis of spherical MCM-48*," *Microporous & Mesoporous Materials* **1999**, *27*, 201-206 (Research article)

(4) Rodrigues, S.; Koodali, R. T.; Uma, S.; Martyanov, I. M.; Klabunde, K. J. "*Single-Step Synthesis of a Highly Active Visible-Light Photocatalyst for Oxidation of a Common Indoor Air Pollutant: Acetaldehyde*," *Advanced Materials* **2005**, *17*, 2467-2471 (Research article)

# Chapter 4 –V-MCM-48 Characterization and Photocatalysis Studies Results

## 4.1 Introduction

The results of following sections illustrate the three types of characterization completed on experimentally synthesized mesoporous V-MCM-48 material. The first characterization method employed used powder X-ray diffraction (XRD) to determine that the Ia3d space group corresponding to the MCM-48 structure had formed after the synthesis and calcination transformation processes. Next, the light absorption patterns of V-MCM-48 mesoporous materials were elucidated to provide potentially the type of coordination geometry (sphere) of the vanadium transition metal ion from diffuse reflectance ultra-violet-visible (DR-UV-vis) absorption patterns. Finally, the surfaces of the V-MCM-48 internal structures, with various amounts of $V^{5+}$ ions, were characterized with use of $N_2$ absorption-desorption, which provides the following data: surface area, pore diameter, and pore volume.

## 4.2 Powder X-ray Diffraction of Si-MCM-48 & V-MCM-48

Powder XRD diffractograms illustrate the effect of various concentrations of vanadium transition metal ion in vanadium doped MCM-48 structure vs. non-transition metal doped Si-MCM-48 framework, as shown in Figure 4:1. Figure 4:1 plot exhibits the differences in intensity (vertical height) reduction of the XRD peaks with higher vanadium metal loaded MCM-48. The three reasons why the V-MCM-48 material has lower XRD peak intensity with increased vanadium metal ion concentration could be linked to the following: (1) the random placement of transition metal ions in the pores, thereby causes a reduction in periodicity; (2) transition metal ion diluting the silica framework, which could cause the metal ion to absorb X-rays at a higher absorption factor over Si; and (3) partial collapse of the mesoporous structure. [1,2] Also, defect sites created through the doping process of $Ce^{4+}$ and $Fe^{3+}$ metal ions were found to lower the intensity of the XRD peak. [1] To eliminate the third possibility (structural collapse of mesoporous framework from incorporation of metal ion), one would need to use high resolution transmission electron microscopy (HR-TEM) analysis to determine structural integrity. [1,2] Besides the intensity values obtained from XRD peak analysis, the peak location and number of peaks infer that the MCM-48 structure has formed. [1-20] For example, if there was one large main peak with a few (2-3 tiny peaks) secondary peaks in the 2θ at 2-4° angle range, this would indicate formation of the unidirectional hexagonal pore structure of MCM-41. [13, 15, 18, 21-27] Only one large peak in the XRD diffractogram at low angles (2-4°) 2θ means less ordered, thicker walled hexagonal mesoporous material (HMS) had formed. [13, 18, 26]

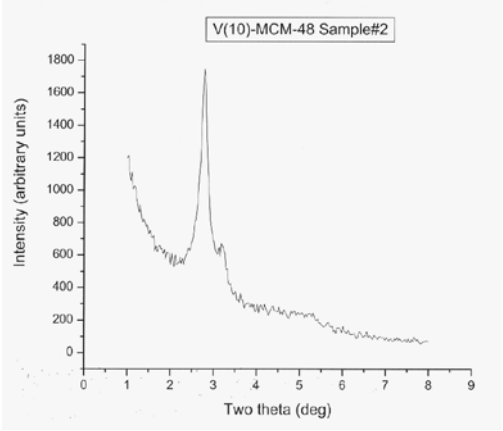


**Figure 4:1 A**: V(10)-MCM-48 experimental diffractogram.

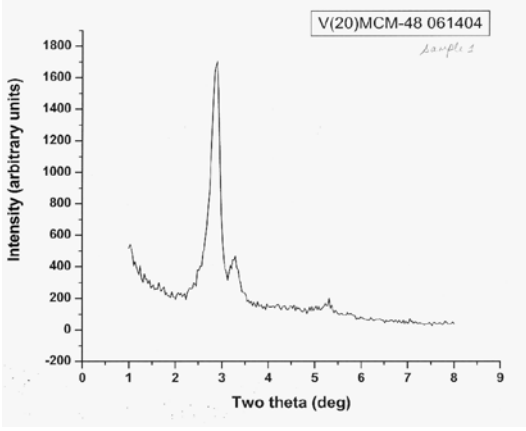


**Figure 4:1 B**: V(20)-MCM-48 experimental diffractogram.

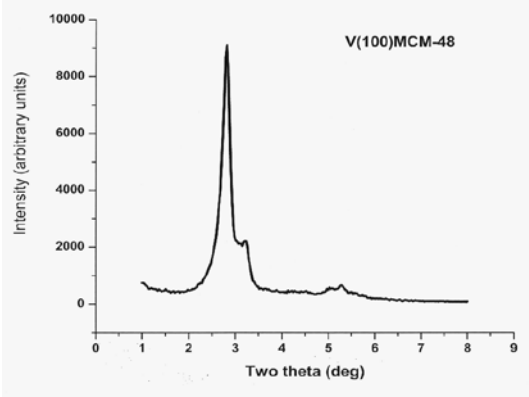


**Figure 4:1 C**: V(100)-MCM-48 experimental diffractogram.

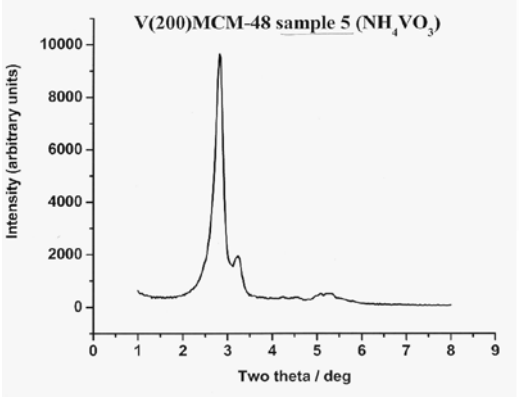


**Figure 4:1 D**: V(200)-MCM-48 experimental diffractogram.

**Figure 4:1 Experimental Powder XRD Diffractograms of Calcinated V(x)-MCM-48.**

**Supplemental text for Figure 4:1**- the above experimental XRD powder diffractograms show the characteristic reflections at low angles 2θ of 2-4° of main peak proceeded by smaller shoulder peak and tiny secondary peaks in 5-6° range, as noted in literature research. [1-20] The experimental powder XRD diffractograms above in Figure 4:1 A would have the lowest peak intensity at V(10)-MCM-48 (largest vanadium metal loading in MCM-48), and Figure 4: 1 D V(200)-MCM-48 (least amount of vanadium metal in MCM-48 structure) experimental powder XRD has the largest peak intensity. Note: the number in parentheses, for example V(10)-MCM-48, would mean the Si/V ratio, where this ratio would indicate Si/V = 10. The Si-MCM-48 structure without vanadium metal was not included in the above diffractograms; since, I could not find it: the peak position and intensity were similar to the V(200)-MCM-48.

When a large main peak followed by a smaller shoulder peak in the 2θ 2-4° of powder XRD diffractogram, this could indicate the formation of the desired MCM-48 structure. [1-20] The amount of shift in the two primary peaks (the large peak followed by smaller shoulder peak) determines the thickness of the walls of MCM-48, and the number of secondary smaller peaks reveals the amount of crystallinity in the MCM-48 structure. [2, 5, 7, 9, 14, 16, 18, 19, 22, 26] Finally, as shown in the experimental powder XRD diffractograms in figure 1 A-D of V-MCM-48, the V-MCM-48 structures had similar crystallinity to the parent Si-MCM-48 material, but still atomically would have amorphous

structure similar to silica, [5, 6, 22, 28-32] and have comparable pore structure to the hydrothermal synthesis result. [2, 5, 7, 9, 14, 16, 18, 19, 22, 26]

## 4.3 Diffuse Reflectance Ultra-Violet-Visible (DR-UV-vis) Light Spectroscopy of V-MCM-48

The DR-UV-vis experimental absorption vs. wavelength plot, as shown in Figure 4:2, shows various amounts of vanadium ion in the MCM-48 mesoporous material. As the concentration of vanadium ion in MCM-48 increases, the peak absorption areas also increase from lowest concentration to greater vanadium ion loading. The coordination geometry of the vanadium species in V-MCM-48 would indicate tetrahedral, square-pyramidal, and octahedral by comparison of literature values. [1, 3, 6, 19, 33, 34] To conclusively differentiate the several vanadium coordination species, the use of both Fourier Transform-Infrared Radiation (FT-IR) and Kubelka-Munk (K-M) function vs. wavelength plot would need to be completed on the experimentally prepared V-MCM-48 and the comparison between the literature values. [19, 33-35] The higher energy wavelength absorption peak (centered at approximately 250 nm) could be the tetrahedral coordinated $VO_4$ species, and the lower energy broader peak (centered at 375 nm) could be a combination of square-pyramidal plus octahedral vanadium species, according to literature position that transition metal ions surrounded by oxide (oxo) ligands produce characteristic values irrespective of the type of metal ion in the MCM-48 matrix. [3, 4, 19, 33] The likelihood of polymeric vanadium species could not be ruled out at especially higher transition metal loading in MCM-48 structure, such as Si/V = 10 (~ 8. 33 wt% vanadium ion loading in MCM-48); since, previous research from literature has shown to have formed polymeric V-O-V units on MCM-48 at approximately 6.7 wt% [1, 33] vanadium ion loading, and silica ($V_2O_5/SiO_2$) at approximately 5 wt% vanadium ion loading on silica. [33, 34]

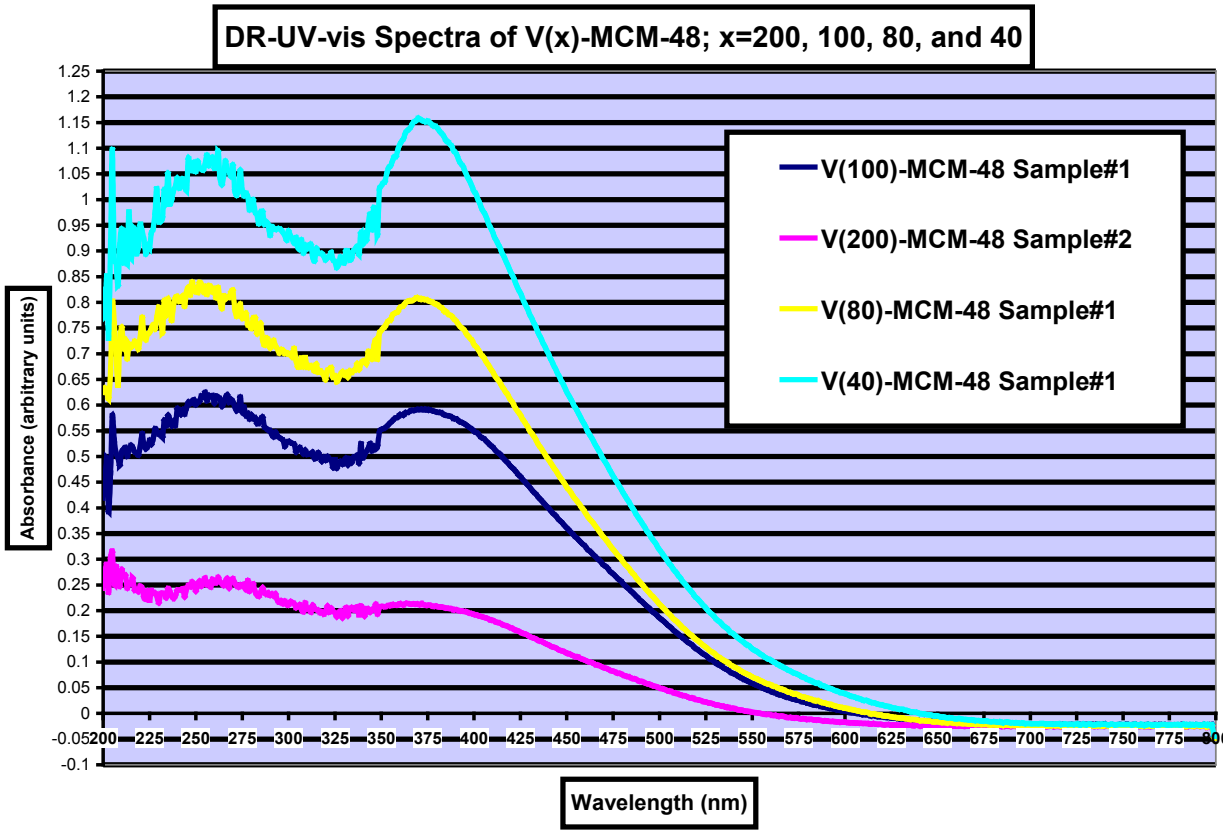


**Figure 4:2 Experimental DR-UV-vis Spectra of Various Concentration of Vanadium cation in V(x)-MCM-48.**

**Supplemental text for Figure 4:2**- the above experimental UV-vis spectra analysis of V(x)-MCM-48 powder, where x = Si/V = 200, 100, 80, and 40, revealed a trend of higher metal loading led to increased light absorption. The absorption peak values approximately centered at 250 nm and 375 nm with a shoulder extending from 420-575 nm in visible light range. The higher vanadium ion loading concentrations (Si/V = 10, 20) in MCM-48 led to absorption values many times greater than the scale on the UV-vis instrument reconfirming the trend of higher transition metal content in MCM-48 causes greater light absorption property. Finally, Klabunde and co-workers reported in previous research on transition metal doped Al-MCM-41that light absorption would only be a prerequisite to developing a photocatalyst; since, in their research of Mn-Al-MCM-41 it had the highest absorption value although the lowest production value of products, and also with $Co/TiO_2$ had visible light absorption band but no photocatalytic activity ($\lambda > 420$ nm). [36,37]

## 4.4 $N_2$ Adsorption-Desorption Analysis of Si-MCM-48 & V-MCM-48: BET, and BJH

The $N_2$ absorption-desorption isotherms (line of constant temperature) were conducted at 77 K, the liquid nitrogen temperature, for both Si-MCM-48 and V-MCM-48, which would appear to have little hysteresis, as shown in the experimental plot in Appendix B-B.1. Characteristics of mesoporous materials would exhibit a type IV reversible isotherm (opposite of hysteresis), according to International Union of Pure & Applied Chemistry (IUPAC), and a sharp inflection from relative pressure ($P/P_0$) of 0.2 to 0.4 would be common for the mesoporous materials, such as M41S and similar analogs (HMS, FSM-16), due to capillary condensation in the mesopores. [4, 5, 7, 10, 12, 19, 21, 22, 24, 38, 39] [Note: HMS stands for *H*exagonal *M*esoporous *S*ilica-thicker walled less organized then M41S mesoporous materials; FSM-16 would stand for *F*olded *S*heet *M*esoporous *M*aterials and 16 would be the number of carbon atoms in the alkyl chain of surfactant used.] The similarity of the hysteresis loops for Si-MCM-48 and V-MCM-48 could infer that the mesoporous structure has little to no microporsity. [2, 19, 21, 22, 24] With increased transition metal

loading of the MCM-48, for example Si/V = 10, there was an increase in the amount of hysteresis due to bond strain caused by substitution of $Si^{4+}$ for $V^{5+}$ ion from the larger ionic radii size of $V^{5+}$ ion, as shown in Appendix B-B.1, the experimental $N_2$ absorption-desorption plot. [23, 40] The experimentally derived pore diameter and volume values, as shown in Table 4:1, would be comparable to literature ones': the difference could be due to greater condensation of pore walls, thereby causing a smaller pore volume. [1, 5] In conclusion, the $N_2$ absorption-desorption plot, as shown in Appendix B-B:1, could indicate that the $V^{5+}$ ion has been successfully substituted in MCM-48 structure in place of $Si^{4+}$ ion due to retention of mesoporous structural surface characteristics, as indicated in previous literature research with Cr, Ce, Mn, Fe with MCM-48 material. [1, 4, 10]

**BET TABLE of Mean Values**

| V(x)-MCM-48 | Surface Area ($m^2/g$) | Pore Volume (cc/g) | Pore Size (A) |
|---|---|---|---|
| X=200 | 1300 | .69 | 22 |
| X=100 | 1500 | .79 | 22 |
| X=80 | 1300 | .71 | 22 |
| X=40 | 1200 | .67 | 22 |
| X=20 | 590 | .34 | 23 |
| X=10 | 1100 | .64 | 24 |

**Table 4:1 Experimental Structure Mean Values for V(x)-MCM-48 Mesoporous Metal Doped Material.**

**Supplemental text for Table 4:1**- the BET experimental set of values above would be within a 10% error margin. Surface area decreases as expected with the exception at X = 20. Potential reason(s) for the anomalies seen in the above table of textural properties (surface area, pore volume, and pore diameter) will be reviewed in the discussion section.

## 4.5 V-MCM-48 Catalytic Photooxidation Properties Studied with Six Probe Molecules

The probe molecules studied for photooxidation reaction with V-MCM-48 were as follows: acetaldehyde, carbon monoxide, acetone, ethanol, 2-propanol, and acetonitrile. All of these probe molecules have importance from an environmental point of view due to wide production (use) in modern life and/or part of the molecule found in toxic compounds, which causes them to be listed as major toxic air pollutants in an indoor environment. [41-55] Moreover, acetaldehyde, carbon monoxide, acetone, ethanol, and 2-propanol in urban surroundings contribute to decreased overall air quality and act as molecules in smog (mixture of toxic partially oxidized organic compounds) production in air. [55-58] The type of products formed in a particular reaction with various probe molecules provides insight into the strength and density of Lewis acid (accepts electrons readily) and/or Bronsted acid sites (donor of $H^+$ species) in a given material, such as metal doped MCM-48. [1, 4, 11, 22, 33, 34, 60, 61] Finally, comparison of the results of the products formed at ambient reaction conditions (25°C standard-pressure-temperature (STP)) in dark, visible, and ultra-violet (UV) light with V-MCM-48 and standards P-25 $TiO_2$ Degussia-Huls (a mixture of ~ 70% anatase and ~ 30% rutile phases, as shown in Appendix B-B:2**)** plus nano gold/different types of supports were completed.

## 4.6 $CH_3CHO$ Photodegradation Reaction over V-MCM-48 & P-25 $TiO_2$ Standard

As noted in the above paragraph, acetaldehyde ($CH_3CHO$) would be considered a common toxic air pollutant and detrimental to indoor air quality from carpets, cigarette smoke, adhesives, and nail polish. [10, 45, 53, 62, 63] The

below experimental results on the photooxidation of $CH_3CHO$ over V-MCM-48 had both partial and total oxidation products in the dark, visible, and UV light range; in contrast, as expected for a UV-light active semiconductor photocatalyst, P-25 $TiO_2$ exhibited activity only under UV-light illumination due to the large bandgap between conduction and valence bands in this type of semiconductor, as indicated in literature. [62-70] [Refer to Appendix B-B:3 for plots of wide-bandgap semiconductors.] The experimental trend in oxidation of acetaldehyde to $CO_2$ + other products for the dark and visible light was more $V^{5+}$ ion in the MCM-48 structure created higher number catalytic active sites, which cause greater number of redox (oxidation-reduction) reactions. The experimental UV-light photooxidation work led to the resulting trend of a medium $V^{5+}$ ion loading in MCM-48 produced the largest amount of $CO_2$ , as shown in Figure 4:7 . The experimental plots of dark and visible light photodegradation in Figures 4:3 to Figure 4:6, Table 4:2 and Table 4:3 show a general trend of more $V^{5+}$ ion led to increased formation of products; however, use of the higher metal loading of Si/V = 1 produced little $CO_2$ product: other higher loading vanadium levels in MCM-48 degradation plots would be listed in the Appendix B-B:4 & B:5. As a comparison of the V-MCM-48 photocatalyst to a standard, P-25 $TiO_2$ was employed under UV-light irradiation and produced more than twice $CO_2$ concentration compared with V(20)-MCM-48, as shown in Figure 4:8 and Table 4:4.

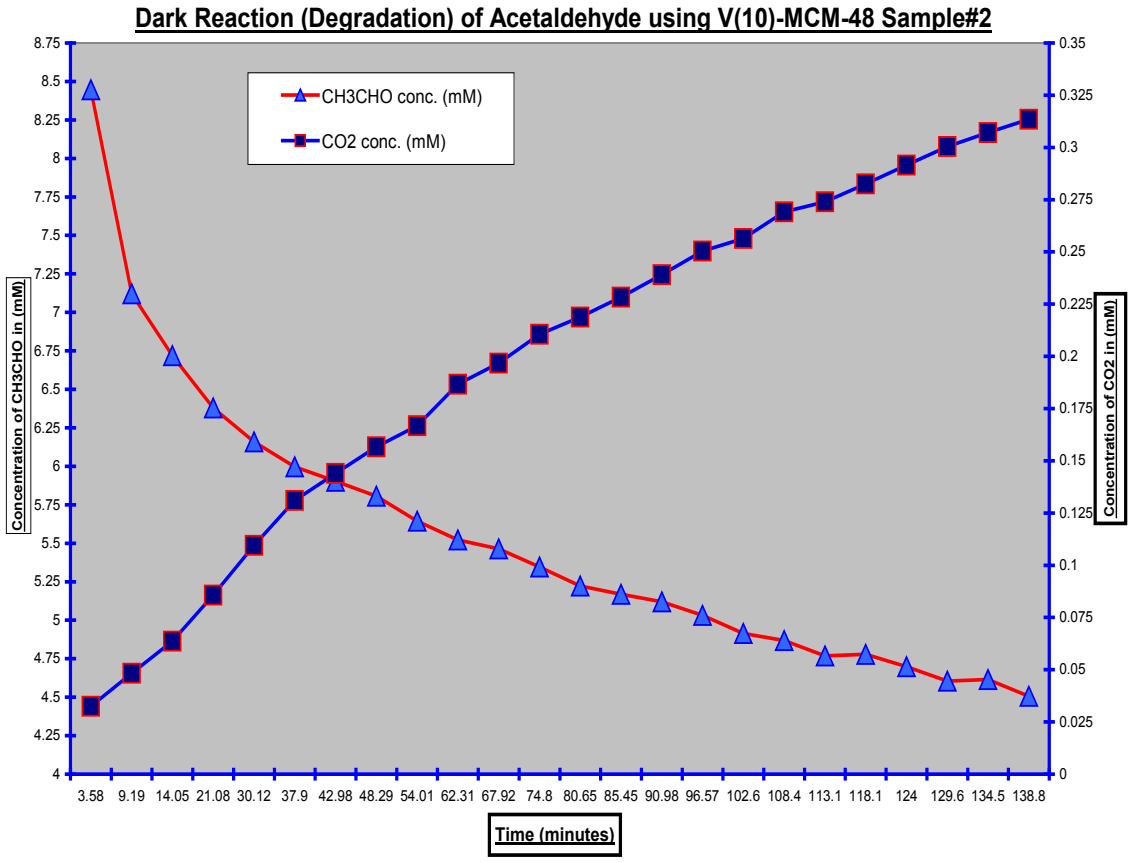


**Figure 4:3 Dark Reaction (Degradation) Acetaldehyde using V(10)-MCM-48 for 140 minutes.**

**Supplemental text for Figure 4:3**- the above experimental photooxiation plot of acetaldehyde over V(10)-MCM-48 Sample # 2 using dark reaction conditions (only room light) produced the following amounts of consumption of toxic pollutant probe molecule and total oxidation product: acetaldehyde consumed 3.9 mM, and produced .28 mM $CO_2$.

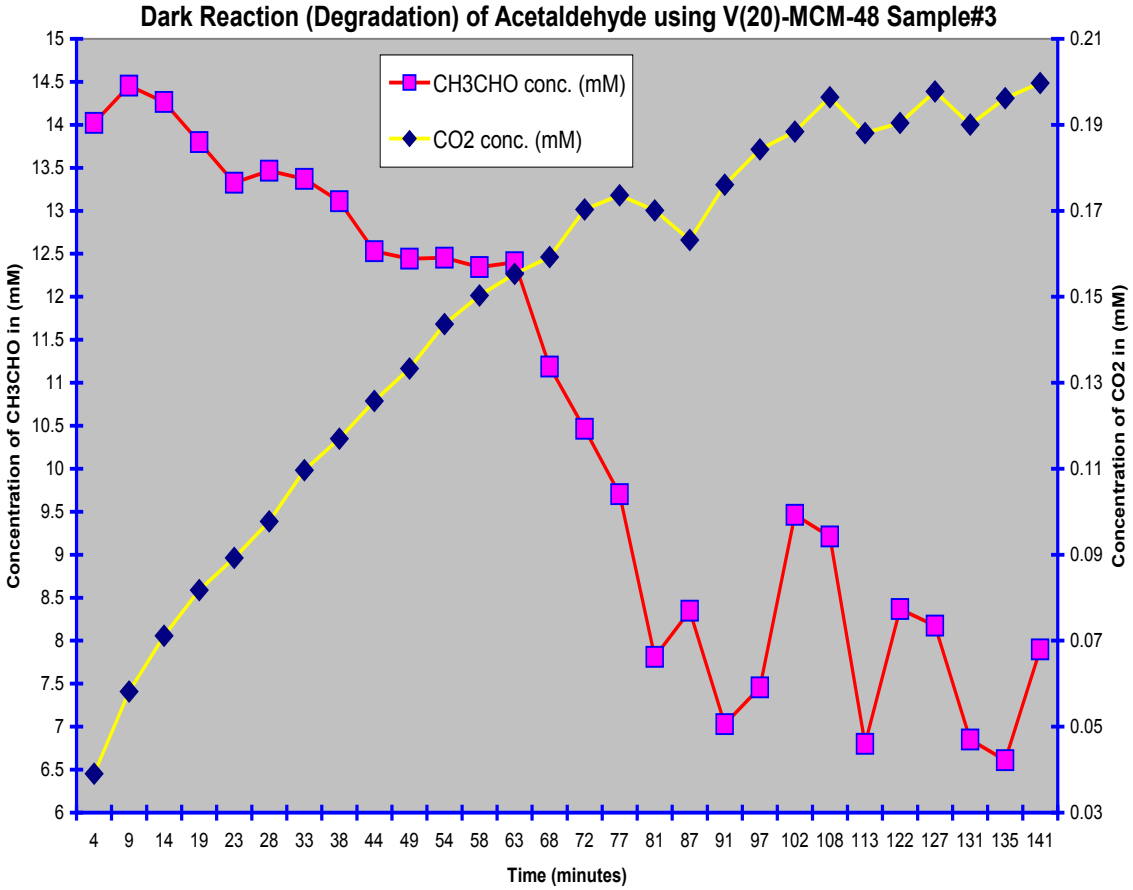


**Figure 4:4 Dark Reaction (Degradation) of Acetaldehyde over V(20)-MCM-48 for 140 minutes.**

**Supplemental text for Figure 4:4**- the above experimental photooxidation plot of toxic pollutant probe molecule acetaldehyde over V(20)-MCM-48 Sample # 3 in dark illumination conditions (only room light) had the following relevant results: consumption of $CH_3CHO$ of 6.1 mM and production of $CO_2$ of .16 mM.

| Dark Reaction Degradation of Acetaldehyde ($CH_3CHO$) over V(x)-MCM-48 in Dark Illumination Conditions | | |
|---|---|---|
| **V(x)-MCM-48** | **$CO_2$ produced in GC-MS analysis (mM)** | **$CH_3CHO$ consumed in GC-MS analysis (mM)** |
| **X = 200** | **0.041** | **3.7** |
| **X =100** | **0.037** | **1.7** |
| **X = 80** | **0.10** | **5.1** |
| **X = 40** | **0.11** | **4.3** |
| **X = 20** | **0.16** | **6.1** |
| **X = 10** | **0.28** | **3.9** |

**Table 4:2 Dark Illumination Acetaldehyde Degradation Results over V(x)-MCM-48.**

**Supplemental text for Table 4:2**- the above experimental dark reaction acetaldehyde degradation data has a clear trend of increased vanadium ion led to greater concentrations of $CO_2$ produced. The Si-MCM-48 structure without vanadium ion has no photocatalytic activity, as shown in Appendix B-B:6**.**

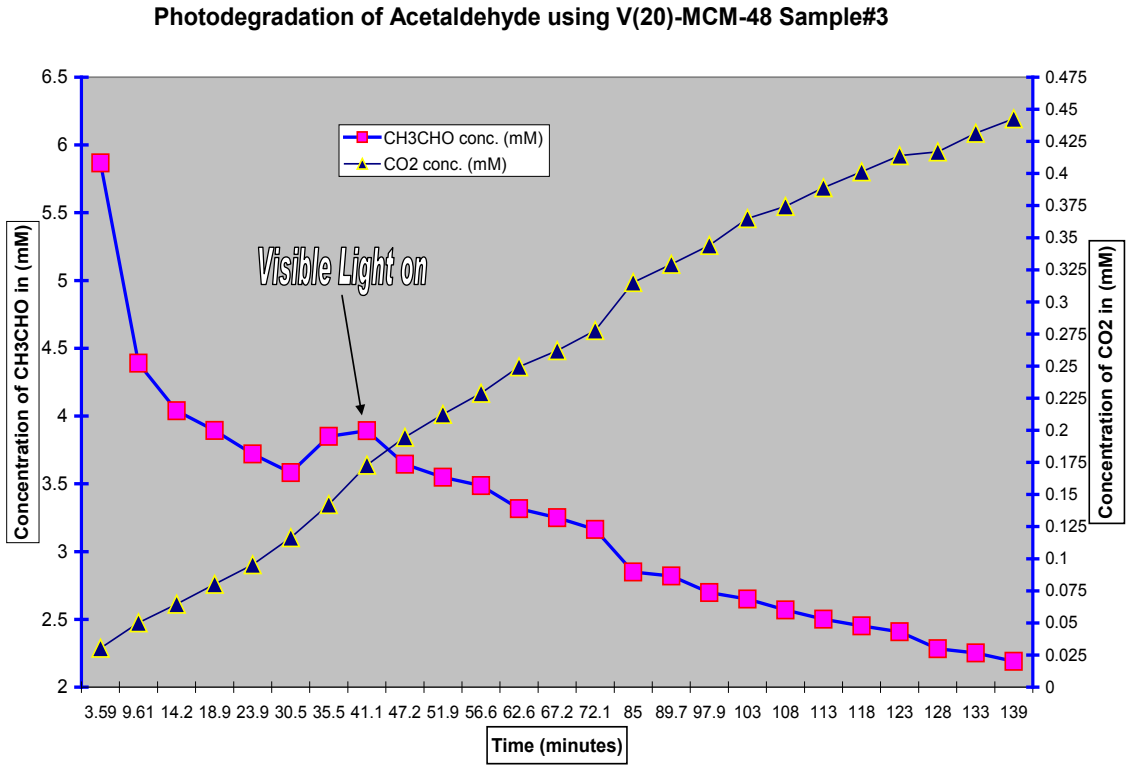


**Figure 4:5 Visible Light Photodegradation of Acetaldehyde over V(20)-MCM-48 for 140 minutes.**

**Supplemental text for Figure 4:5**- the above experimental photodegradation of toxic pollutant probe molecule acetaldehyde using V(20)-MCM-48 Sample # 3 under visible light ($\lambda > 420$ nm) illumination gave the following results: consumption of $CH_3CHO$ of 3.7 mM and production of .41 mM of $CO_2$.

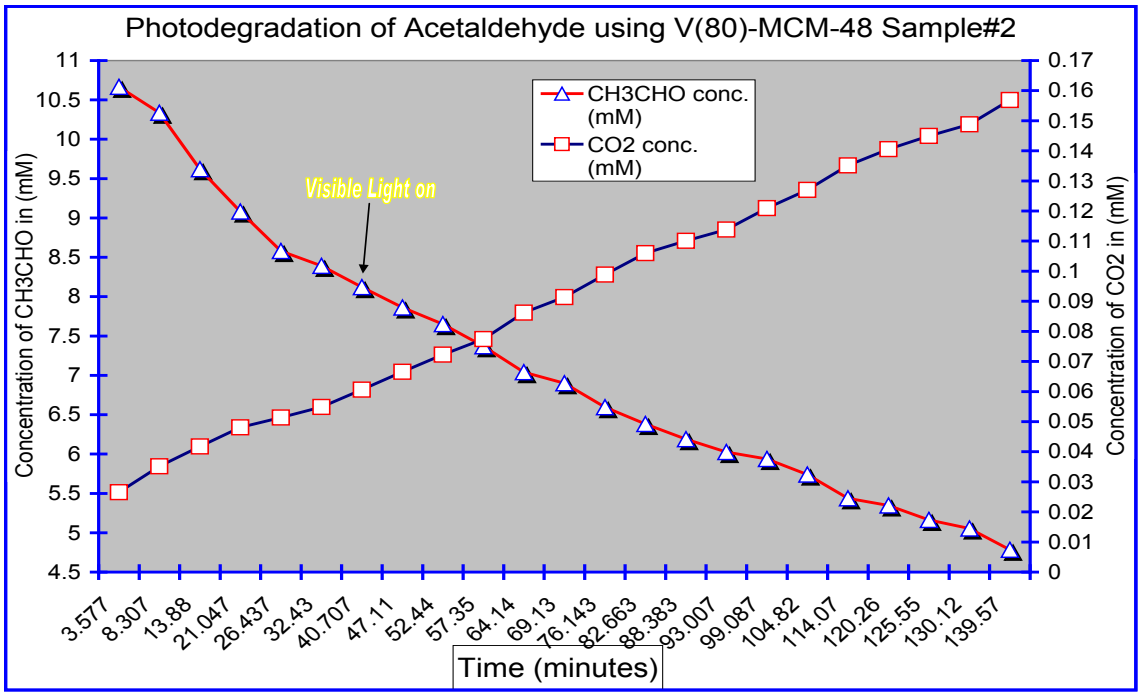


**Figure 4:6 Visible Light Photodegradation of Acetaldehyde over V(80)-MCM-48 for 140 minutes.**

**Supplemental text for Figure 4:6**- the above (previous page) experimental photodegradation plot of the toxic pollutant probe molecule acetaldehyde using V(80)-MCM-48 Sample # 2 under visible light (λ > 420 nm) illumination resulted in the following data highlights: consumption of $CH_3CHO$ of 5.9 mM and production of .13 mM of $CO_2$.

| Visible Light (λ > 420 nm) Photodegradation of Acetaldehyde ($CH_3CHO$) using V(x)-MCM-48 Mean Data | | |
|---|---|---|
| **V(x)-MCM-48** | **$CO_2$ produced in GC-MS analysis (mM)** | **$CH_3CO$ consumed in GC-MS analysis (mM)** |
| **X = 200** | **0.069** | **3.6** |
| **X = 100** | **0.084** | **3,3** |
| **X = 80** | **$0.13_6$** | **5.7** |
| **X = 40** | **$0.14_0$** | **3.9** |
| **X = 20** | **$0.38_0$** | **4.2** |

**Table 4:3 Visible Light Acetaldehyde Photodegradation Results over V(x)-MCM-48 for 140 minute analysis.**

**Supplemental text for Table 4:3**- similar to the trend seen in the experimental dark illumination reaction production of $CO_2$ from acetaldehyde conversion in Table 4:2, the above experimental visible light data shows a trend of increased vanadium ion concentration led to higher amount of $CO_2$ produced up to the point of V(20)-MCM-48: this result, therefore, reveals that too much vanadium ion will lead to lower photocatalytic activity, as would be the case with use of V(10)-MCM-48 which produced only 0.35 mM of $CO_2$ and only consumed 2.9 mM of $CH_3CHO$, as shown in Appendix B-B:7.

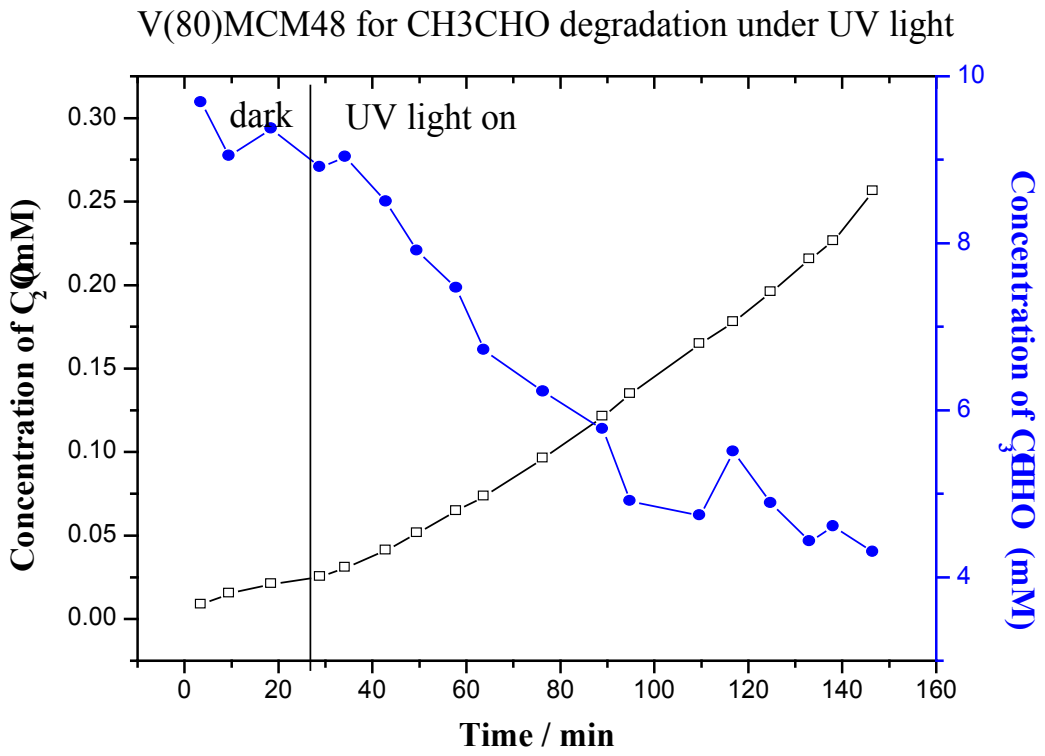


**Figure 4:7 UV-Light Initiated Acetaldehyde Photodegradation over V(80)-MCM-48 for 140 minutes.**

**Supplemental text for Figure 4:7**- the above experimental photooxidation reaction of acetaldehyde over V(80)-MCM-48 under UV-light illumination (320-400 nm cut-off filter) had approximately 5.4 mM consumption of $CH_3CHO$ and $CO_2$ production of close to 0.25 mM. This result would appear to indicate that less vanadium ion was need in MCM-48 structure to have a photocatalytic out-come.

| UV-Light (λ = 320-400 nm) Photodegradation of Acetaldehyde using V(x)-MCM-48 Powders | | |
|---|---|---|
| **V(x)-MCM-48** | **$CO_2$ produced in GC-MS analysis (mM)** | **$CH_3CHO$ consumed in GC-MS analysis (mM)** |
| **X = 200** | **0.075** | **2.8** |
| **X = 100** | **0.094** | **1.0** |
| **X = 80** | **$0.25_0$** | **5.4** |
| **X = 40** | **$0.18_0$** | **4.6** |

**Table 4:4 UV-Light Acetaldehyde Photodegradation Results for V(x)-MCM-48 in 140 minutes.**

**Supplemental text for Table 4:4**-as seen in the above experimental values of acetaldehyde degradation using V(x)-MCM-48 under UV-light illumination, the medium concentration of vanadium ion of V(80)-MCM-48 would produce the most $CO_2$ and consumed the greatest amount of $CH_3CHO$. This data would be in stark contrast to the dark and visible-light data collected on the V(x)-MCM-48 catalysts.

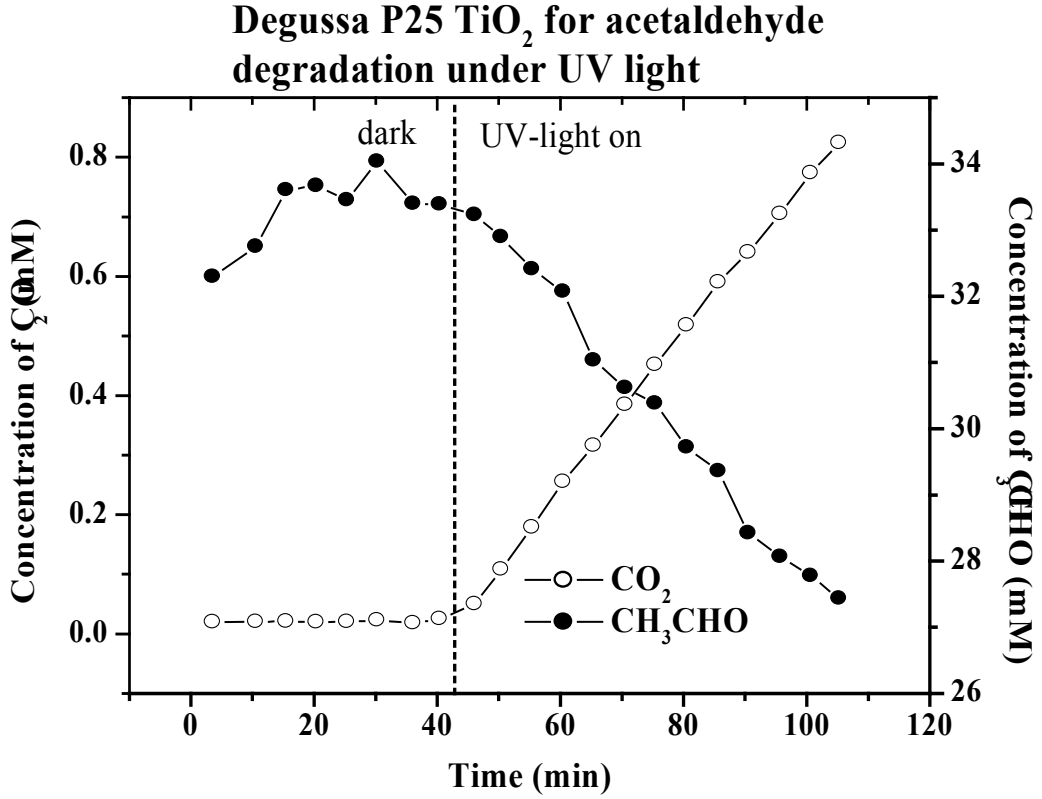


**Figure 4:8 UV-Light Acetaldehyde Photodegradation over Degussa-Huls P-25 $TiO_2$ Standard.**

**Supplemental text for Figure 4:8**- the above experimental plot of acetaldehyde degradation under UV-light illumination using P-25 Degussa-Huls $TiO_2$ photocatalytic standard for comparison of other potential materials photocatalysts showed high activity as expected from an UV-light active catalyst. Although the reaction was not completed for the common procedure 140 minute analysis, but instead for 110 minutes of reaction time, the P-25 semiconductor photocatalyst produced more than double the amount of $CO_2$ of approximately 0.9 mM with the V(20)-MCM-48 visible light catalyst producing 0.41 mM. The amount of $CH_3CHO$ consumed was close to 7 mM. The reason for this much higher photocatalytic activity would be linked to the large charge separation of the charge carriers ($h^+ + e^-$) common in wide-bandgap semiconductors, such as $TiO_2$, ZnO, etc. [62-70]

## 4.7 CO Photooxidation Reaction over V(x)-MCM-41, V(x)-MCM-48, & Nanosize Gold

The below experimental results, as shown in Figures 4:9-4:14 and Table 4:5, using V(x)-MCM-41 & V(x)-MCM-48 in CO photooxidation reveal two trends: (1) less vanadium ion in MCM-48 structure led to increased $CO_2$ production; (2) type of structure with same vanadium metal loading effected the concentration and initial rate of CO photooxidation; and (3) UV-light irradiation more than doubled the initial CO photooxidation reaction rate and increased the CO conversion rate to several times of visible light rate. The low vanadium ion concentration needed for CO photooxidation reaction would be in contrast to the acetaldehyde photodegradation results previously presented in the last section, which will be discussed in the following chapter as to potentially the reason for the contradiction in data. The reason for enhanced photochemistry with UV-light irradiation of V(20)-MCM-48 could infer that certain types of vanadium ion active centers were highly active: these possible vanadium species will be discussed in the next chapter. The experimental work completed on the various nanoparticle Au carbon monoxide catalysts illustrated the following trends, as seen in Figures 4:15-4:29 and Table 4:6-4:9: (1) higher volume of CO used in photooxidation reaction led to larger initial reaction rate (value determined from the slope of the illuminated portion of the plot); (2) the support had a major effect on the reactivity of the nanosize Au from either/or both active/inactive effects, dispersion of nanoparticle Au, and size constrains enforced by support on Au nanoparticles; (3) the little to non-existent visible light oxidative ability of certain nanoparticle Au with different support types; (4) few nanosize gold catalysts had substantial visible light photocatalytic CO oxidation reaction activity; (5) increased CO oxidation activity using nanoparticle Au catalysts under UV-light illumination; and (6) CO oxidation activity dramatically increased with use of nanosize Au on active support (nanosize ZnO) under UV-light irradiation. The gauge of the activity of the V(x)-MCM-41, V(x)-MCM-48, & various nanosize Au catalysts as standards would evaluate the ability to oxidize CO to $CO_2$ by both the concentration of $CO_2$ produced and initial rate (the steepness of the slope) in the linear equation form $y = mx + b$. Due to the fact various amounts of CO were employed in the initial steps of the investigation of V(x)-MCM-41, V(x)-MCM-48, & many types of nanosize Au CO oxidation standards, the volume of CO gas sample used would be noted in all of the captions assuming standard-temperature-pressure [25°C + 1atm] (STP). Also, the percent of $CO_2$ produced in the photooxidation reactions would follow the Ideal Gas Law: $PV = nRT$. [Refer to Appendix B-B:8-B:12 for example calculations.] Note: two replicates completed on standards. Tables 4:6-4:9 shows the percent carbon dioxide made under dark, visible, and ultra-violet illumination conditions with different types of nanosize Au catalyst standards. Finally, the results presented in this chapter will be discussed with potential future ramifications in the next chapter.

### 4.7.1. CO Photooxidation with V(x)-MCM-41 & V(x)-MCM-48 in Visible and UV-light

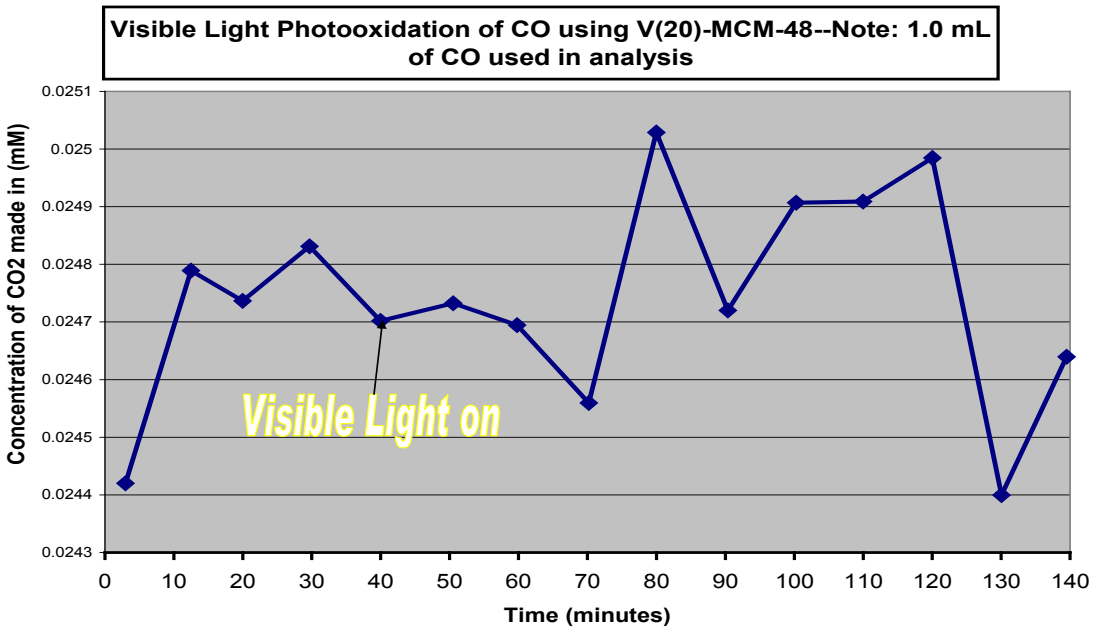


**Figure 4:9 Visible Light Carbon Monoxide Photooxidation over V(20)-MCM-48 for 140 minutes.**

**Supplemental text for Figure 4:9**- the above experimental plot of CO photooxidation over V(20)-MCM-48 under visible light ($\lambda > 420$ nm) with 1.0 mL of CO gave data spread out, as noted by the very low $R^2$ value which indicates the amount of linearity of data. [Initial rate plot in Appendix B-B:13.]

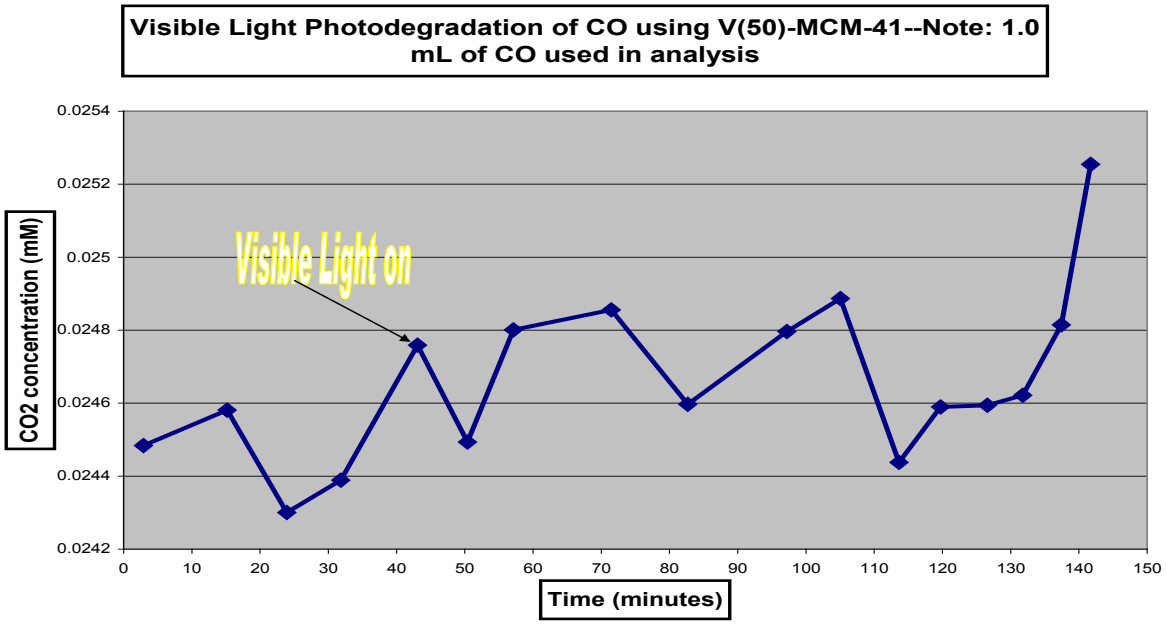


**Figure 4:10 Visible Light Carbon Monoxide Photooxidation over V(50)-MCM-41 for 140 minutes.**

**Supplemental text for Figure 4:10**-the above experimental plot of CO photooxidation with V(50)-MCM-41 under visible light ($\lambda > 420$ nm), and use of 1.0 mL of CO, would have slightly more meaningful data potentially a reaction occurring due to enhanced initial reaction rate and increased $R^2$ value. The amount of $CO_2$ produced was 0.000770 mM and percent $CO_2$ formed would be .58%. [In Appendix B-B:14 initial rate plot.]

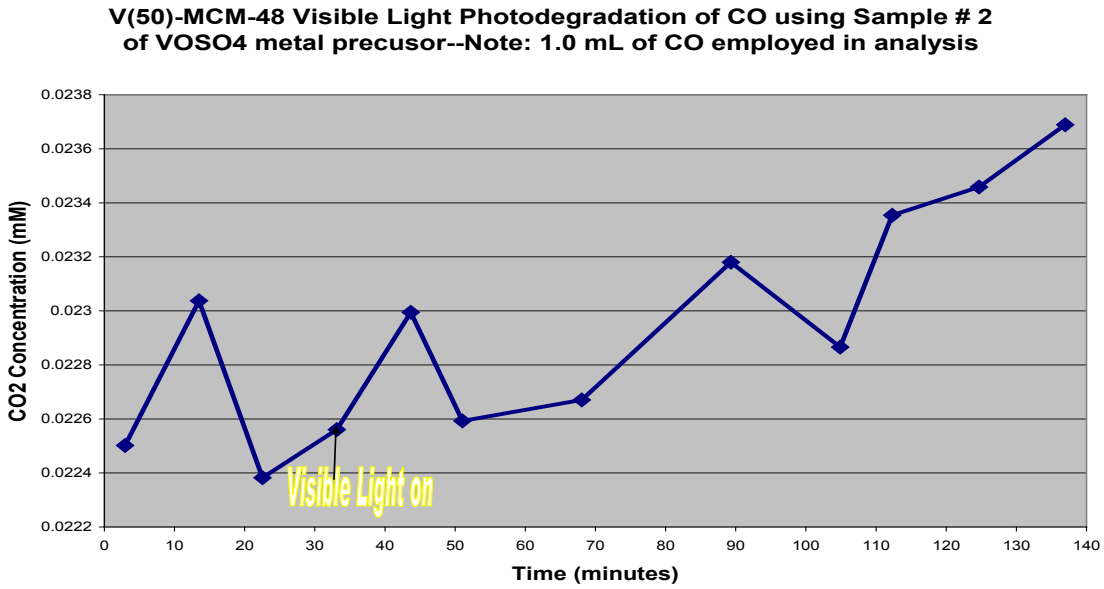


**Figure 4:11 Visible Light Carbon Monoxide Photooxidation over V(50)-MCM-48 for 140 minutes.**

**Supplemental text for Figure 4:11**-seen in the above experimental plot of CO photooxidation over V(50)-MCM-48 using visible light ($\lambda > 420$ nm) and 1.0 mL injected into the light reactor, the concentration of $CO_2$ produced continues to increased with lower vanadium content and use of three-dimensional pore network, as noted by the following enhanced values: more than double slope value, higher $R^2$ value, $CO_2$ made 0.0012 mM, and percent $CO_2$ of .886%. [Initial rate plot in Appendix B-B:15.]

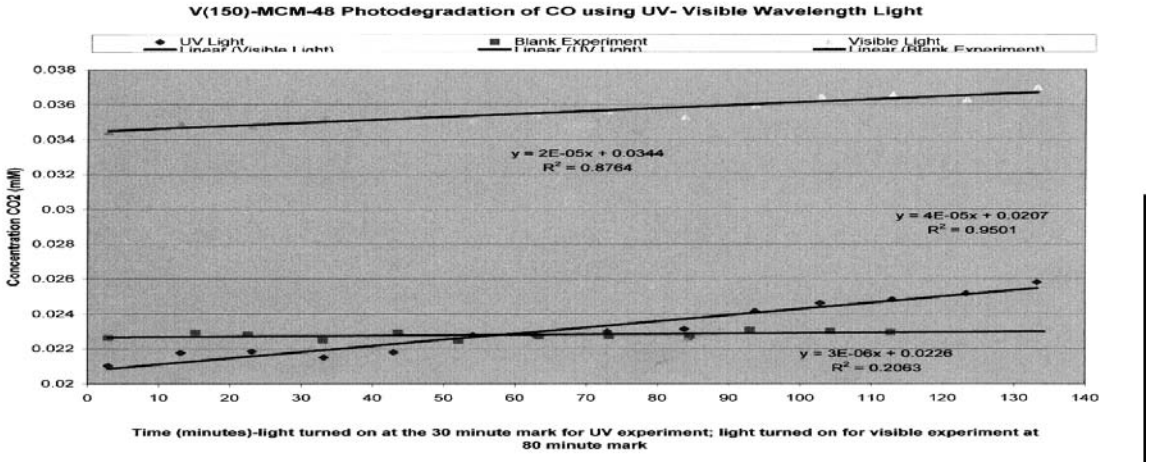


**Figure 4:12 Carbon Monoxide Photooxidation over V(150)-MCM-48 as a function of light conditions.**

**Supplemental text for Figure 4:12**-a comparison of experimental data for V(150)-MCM-48 that shows that the UV-light slope value (4.00E-5) would be double of the visible light one (2.00E-5); whereas, the blank value had only slope value of 3.0E-6. The visible and UV-light $R^2$ plot values continue to improve (.88 and .95). The amount of $CO_2$ created would be 0.0044 mM for UV and visible light of 0.0027 mM: this would result in ~3.3% $CO_2$ made in UV and ~2.0% for visible. 1.0 mL of CO was used in the above analysis with V(150)-MCM-48.

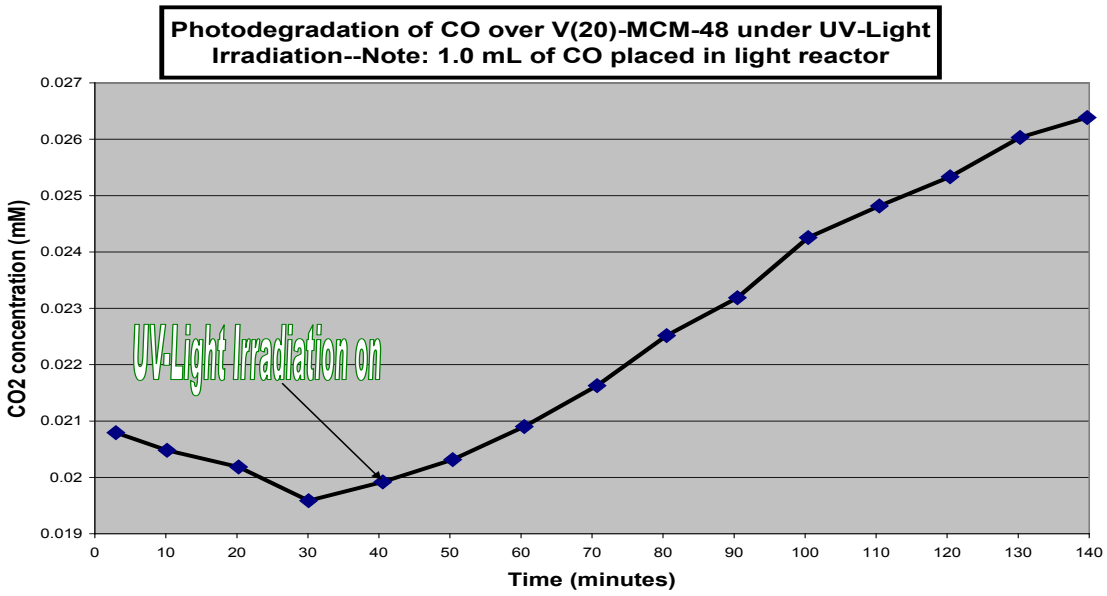


**Figure 4:13 UV-Light Carbon Monoxide Photooxidation over V(20)-MCM-48 for 140 minutes.**

**Supplemental text for Figure 4:13**-the above UV-light irradiation experiment with V(20)-MCM-48 showed that certain type(s) of vanadium ion species were activated by the more intense light energy. The concentration of $CO_2$ produced was 0.0056 mM; the $R^2$ value approached unity of one (noted in below initial rate plot in Figure 4:14); and percent of $CO_2$ produced was 4.1 % using only 1.0 mL of CO. These values would infer that the V(20)-MCM-48 mesoporous material has the potential to be a UV-light CO photooxidation catalyst: this result will be discussed in the next chapter to provide direction for future research.

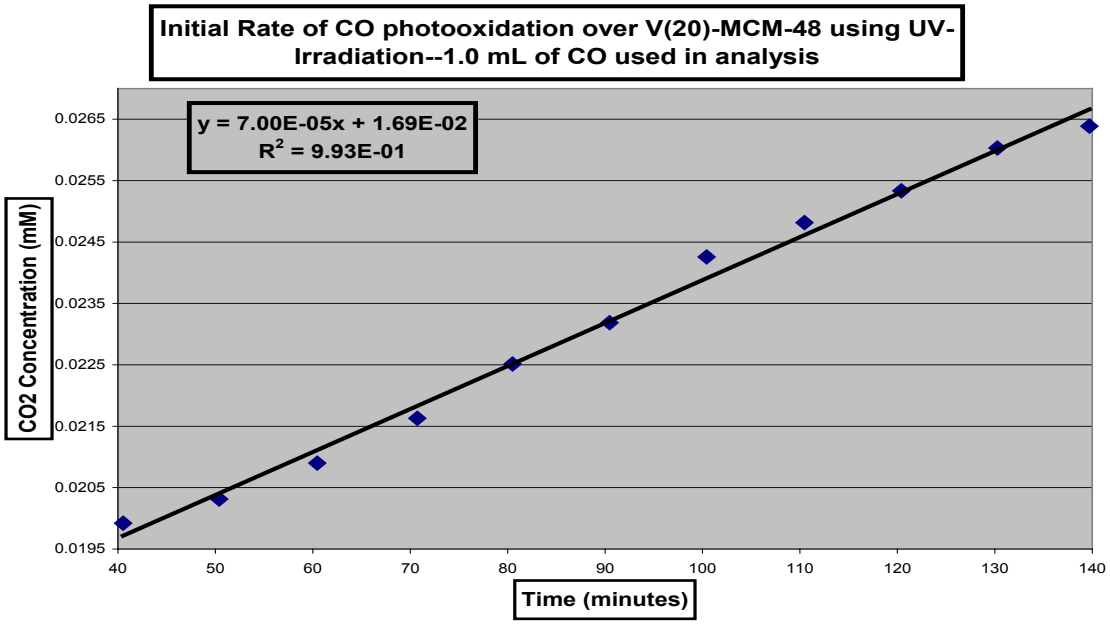


**Figure 4:14 UV-Light Carbon Monoxide Photooxidation Initial Reaction Rate over V(20)-MCM-48.**

**Supplemental text for Figure 4:14**-the above experimental initial reaction rate plot of the UV-light irradiated plot showed enhanced slope value (7.0E-5), and near unity $R^2$ value (0.99) of one. These results will be compared to the nanosize Au catalyst standard in below section and following chapter. Note: this result was complete with only 1.0 mL of CO gas.

| CO Photooxidation with V(x)-MCM-41 & V(x)-MCM-48 under Visible & UV-Light Illumination: 1.0 mL carbon monoxide added in light reactor | | | | | |
|---|---|---|---|---|---|
| **Type of vanadium mesoporous silica structure** | **Slope (Initial Reaction Rate Value)** | **$R^2$ Value** | **$CO_2$ amount made (mM)** | **Percent $CO_2$ made ($CO_2$%)** | **Light Illumination** |
| V-(20)-MCM-48 | -5.8E-07 | 0.008 | 0.00022 | 0.16 | Visible |
| V-(50)-MCM-41 | 1.8E-06 | 0.064 | 0.00077 | 0.56 | Visible |
| V(50)-MCM-48 | 1.3E-05 | 0.84 | 0.0012 | 0.89 | Visible |
| V(150)-MCM-48 Blank | ~3.0E-6 | 0.21 | ~0.00033 | ~0.25 | Visible |
| V(150)-MCM-48 | ~2.0E-5 | 0.88 | ~0.0027 | ~2.0 | Visible |
| V(150)-MCM-48 | ~4.0E-5 | 0.95 | ~0.0044 | ~3.3 | Visible |
| V(20)-MCM-48 | 7.0E-05 | 0.99 | 0.0056 | 4.1 | UV-light |

**Table 4:5 Carbon Monoxide Photooxidation over V(x)-MCM-41 & V(x)-MCM-48 with Visible and UV-light.**

**Supplemental text for Table 4:5**-the above experimental values reveal a general trend of increased slope values, $R^2$ values, $CO_2$ production, and percent $CO_2$ made. In particular, the slope value increases with less vanadium ion content in mesoporous structure with use of visible light, and use of UV-light irradiation led to V(20)-MCM-48 close double the slope value for in comparison to V(150)-MCM-48 under same conditions. The reason why V(20)-MCM-48 under UV-light irradiation had a larger slope value would be linked to the type of vanadium species in the MCM-48 matrix, as will be discussed in next chapter. The $R^2$ values increase from high to low vanadium loading in visible light illuminated mesoporous samples, and UV-light irradiated V(x)-MCM-48 samples show a larger $R^2$ value with more vanadium ion in MCM-48 matrix. Clearly, the amount of $CO_2$ made and percent $CO_2$ values increase with lower vanadium loading in mesoporous materials with UV-light use dramatically causing the activation of certain vanadium centers.

## 4.7.2. CO Oxidation over Nanoparticle Gold Catalysts under Dark Illumination

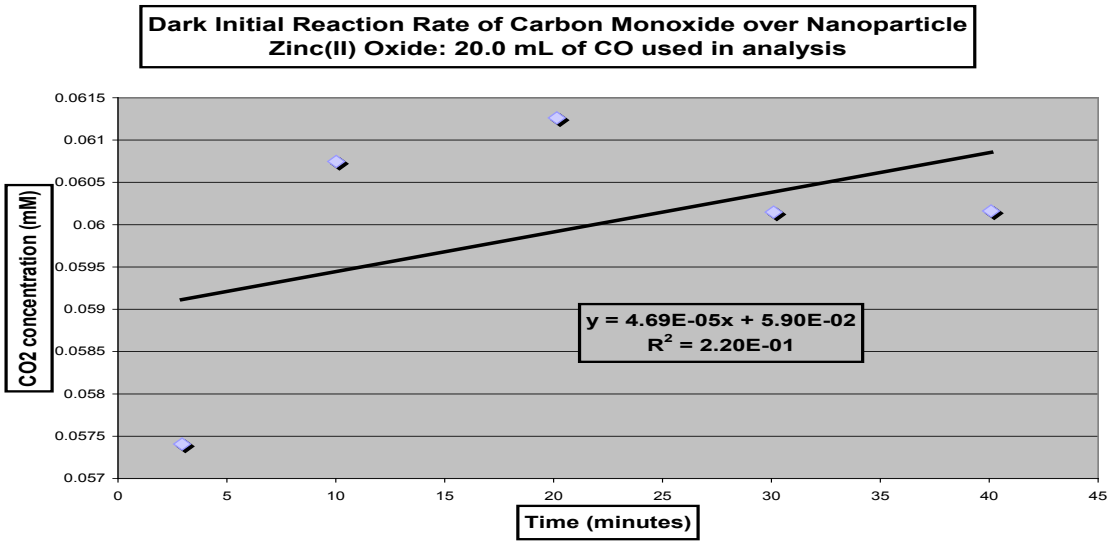


**Figure 4:15 Carbon Monoxide Oxidation Initial Reaction Rate over Nanoparticle ZnO for 40 minutes.**

**Supplemental text for Figure 4:15**-the above experimental plot appears to reveal the slight activity of nanoparticle ZnO in dark (room light) conditions; however, two other experimental results contradict the above work, as seen in the appendix.

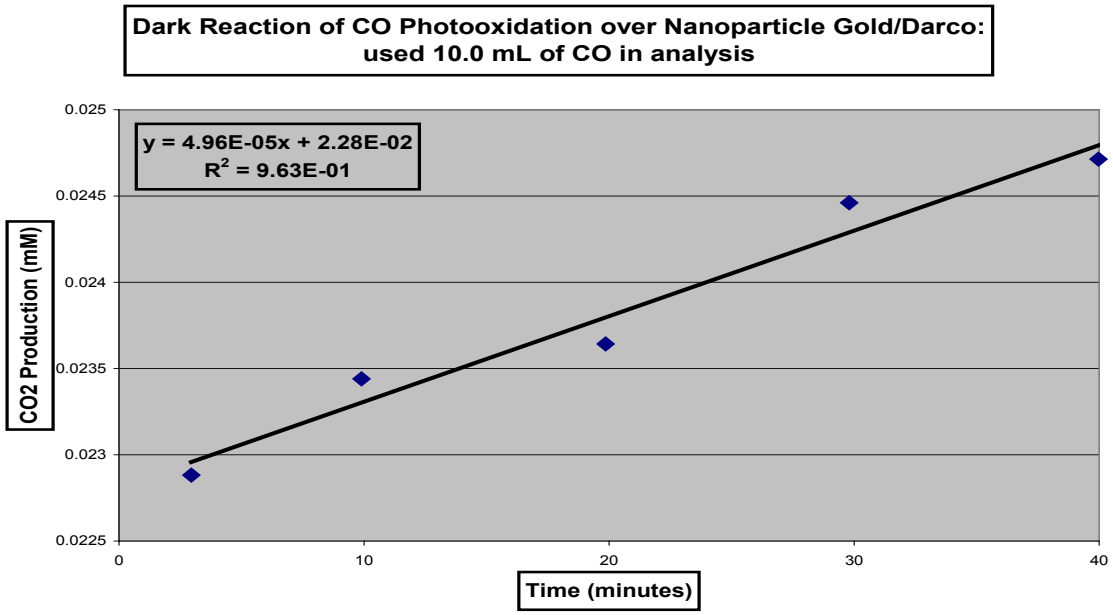


**Figure 4:16 Carbon Monoxide Oxidation Initial Reaction Rate over Nanoparticle Gold/Darco for 40 minutes.**

**Supplemental text for Figure 4:16**-the above experimental plot shows increased slope value in comparison to the nanoparticle ZnO in dark (room light) conditions.

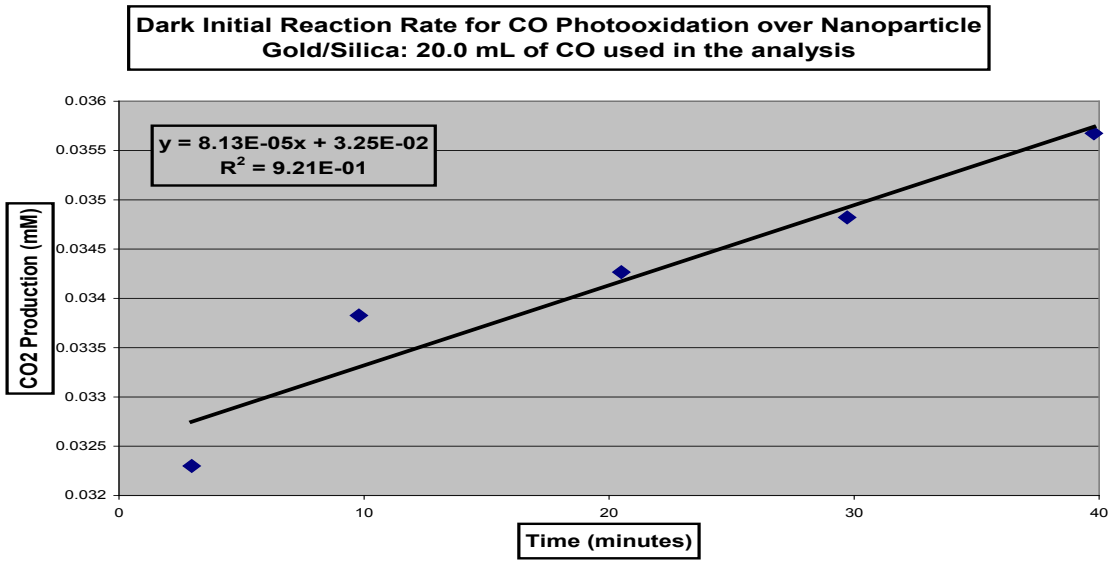


**Figure 4:17 Carbon Monoxide Oxidation Initial Reaction Rate over Nanoparticle Gold/Silica for 40 minutes.**

**Supplemental text for Figure 4:17**-the above experimental plot of nanoparticle gold/silica would appear to increase relatively in a linear manner. Although the slope value of 8.13E-5would be less than the next few other nanoparticle gold catalysts, this catalyst converted more CO to $CO_2$ even though there was less CO injected into the light reactor; therefore, this catalyst has increased untapped potential as a CO oxidation catalyst.

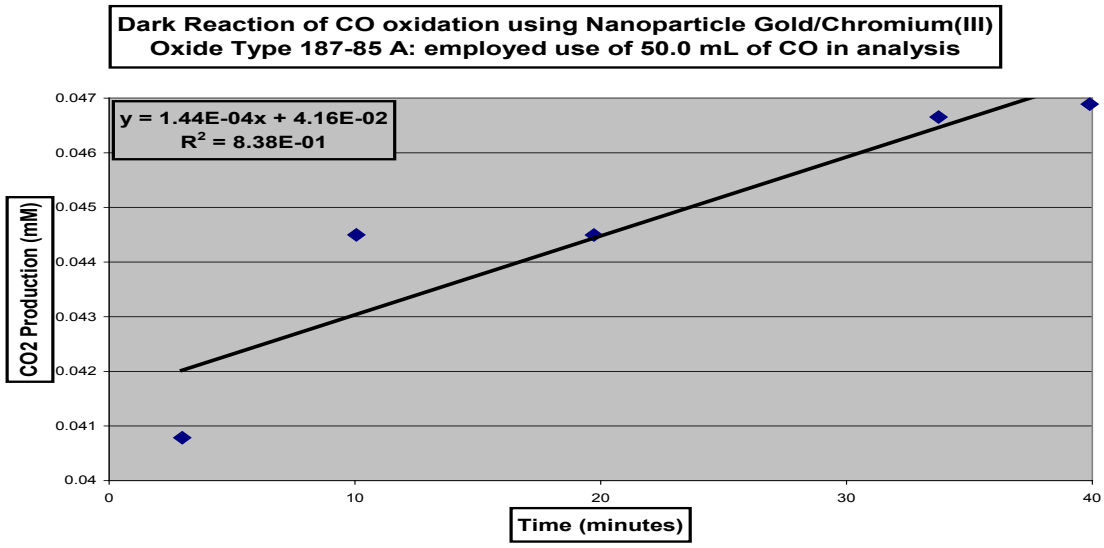


**Figure 4:18 Carbon Monoxide Oxidation Initial Rate over Nanoparticle Gold/Chromium(III) Oxide.**

**Supplemental text for Figure 4:18**-the above experimental plot of nanoparticle gold/chromium(III) oxide had a slope value that increased substantially from the previous plot above. This could be due to the enhanced effect of the chromium(III) oxide support: these possible effects will be discussed in the next chapter.

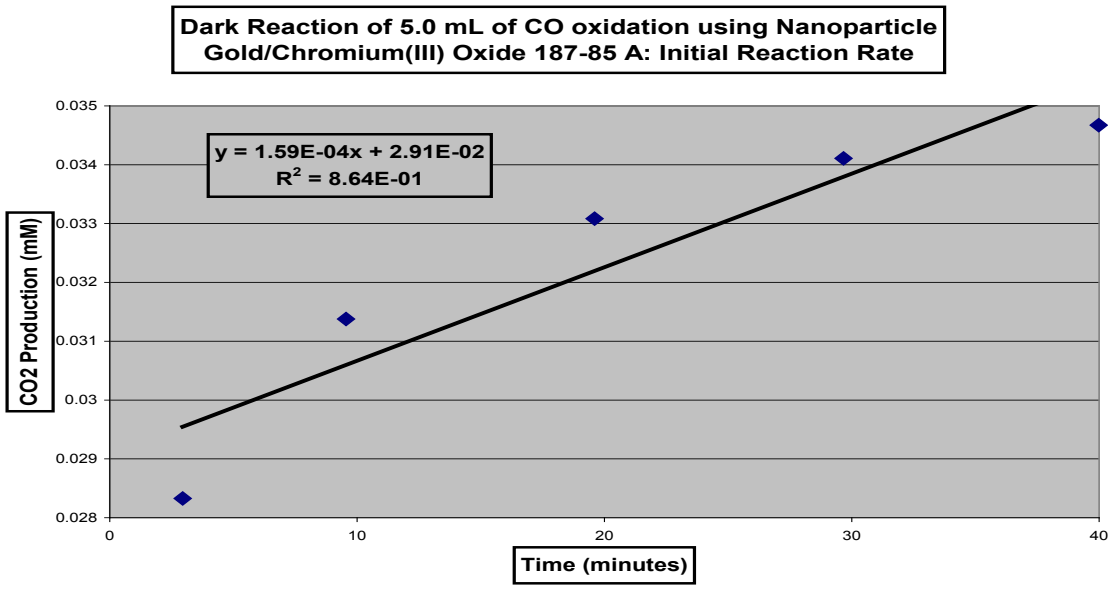


**Figure 4:19 Carbon Monoxide Oxidation Initial Rate over Nanoparticle Gold/Chromium(III) Oxide.**

**Supplemental text for Figure 4:19**-the above experimental plot would be of the identical nanoparticle gold/chromium(III) oxide material employed in the CO oxidation reaction; however, the major difference would the amount of CO injected into the light reactor. At least for the nanoparticle gold/chromium(III) oxide material in the CO oxidation reaction, there would be increased activity with certain amounts of CO. The possible reasons for optimal CO oxidation process occurring will be discussed in the next chapter.

| Comparison of Slope and $R^2$ Values for the Dark Reaction of Nanoparticle Gold Standards with Different Volumes of CO used in the Oxidation Studies in First 40 minutes of oxidation reaction | | | |
|---|---|---|---|
| **Type of Catalyst** | **Volume of CO (mL)** | **Slope Value** | **$R^2$ Value (linearity)** |
| **ZnO** | **20.** | **4.7E-05** | **0.22** |
| **Au/Darco** | **10.** | **5.0E-05** | **0.96** |
| **$Au/SiO_2$** | **20.** | **8.1E-05** | **0.92** |
| **$Au/Cr_2O_3$** | **50.** | **1.4E-04** | **0.84** |
| **$Au/Cr_2O_3$** | **5.0** | **1.6E-04** | **0.86** |

**Table 4:6 Comparisons of Slope and $R^2$ Value for Gold Standards under Dark Conditions.**

**Supplemental text for Table 4:6**-the above experimental dark reaction values reveal three trends: (1) even for higher performing catalysts, less volume of CO led to greater $CO_2$ production in dark reaction; (2) slope values increased with less CO volume; and (3) $R^2$ values show a partial trend toward unity with larger slope values.

## 4.7.3 CO Photooxidation with Nanoparticle Gold Catalysts under Visible Light Conditions.

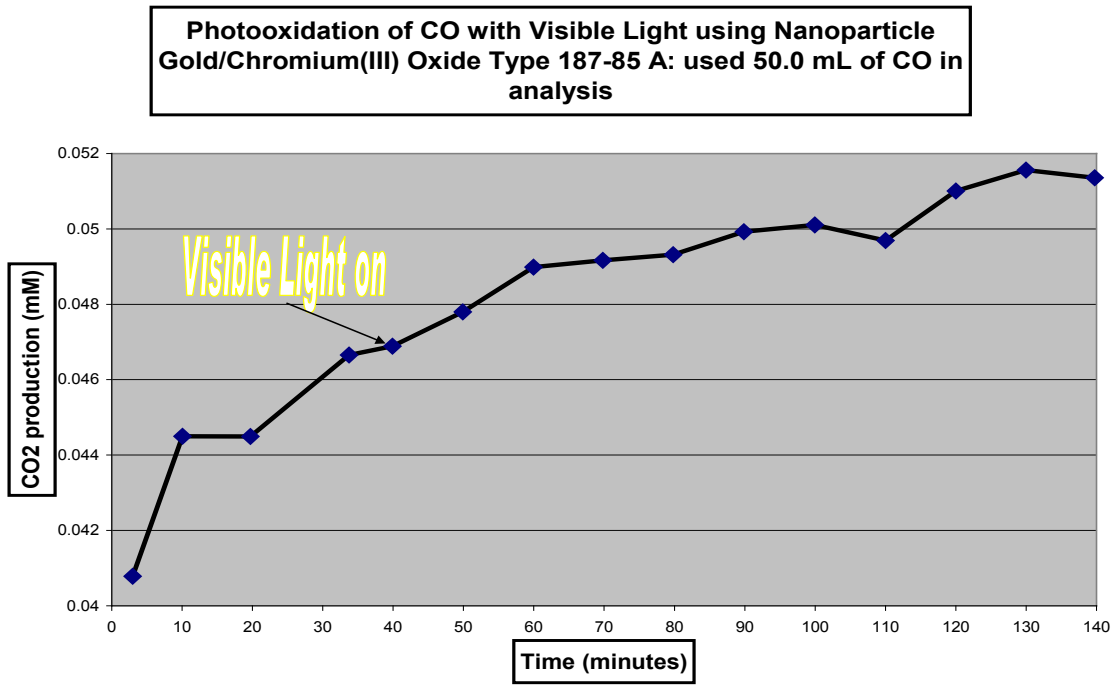


**Figure 4:20 Visible Light Carbon Monoxide Photooxidation over Nanoparticle Gold/Chromium(III) Oxide.**

**Supplemental text for Figure 4:20**-the above experimental plot CO oxidation using nanoparticle $Au/Cr_2O_3$ with 50.0 mL of CO has both a dark reaction and visible light reaction. From a $CO_2$ concentration point of view, this would be the third most active CO oxidation catalyst in dark and visible light conditions. Refer to next chapter for discussion of potentially why this catalyst has room for increased $CO_2$ production. Also, view the visible light initial rate plot in Appendix B-B:16.

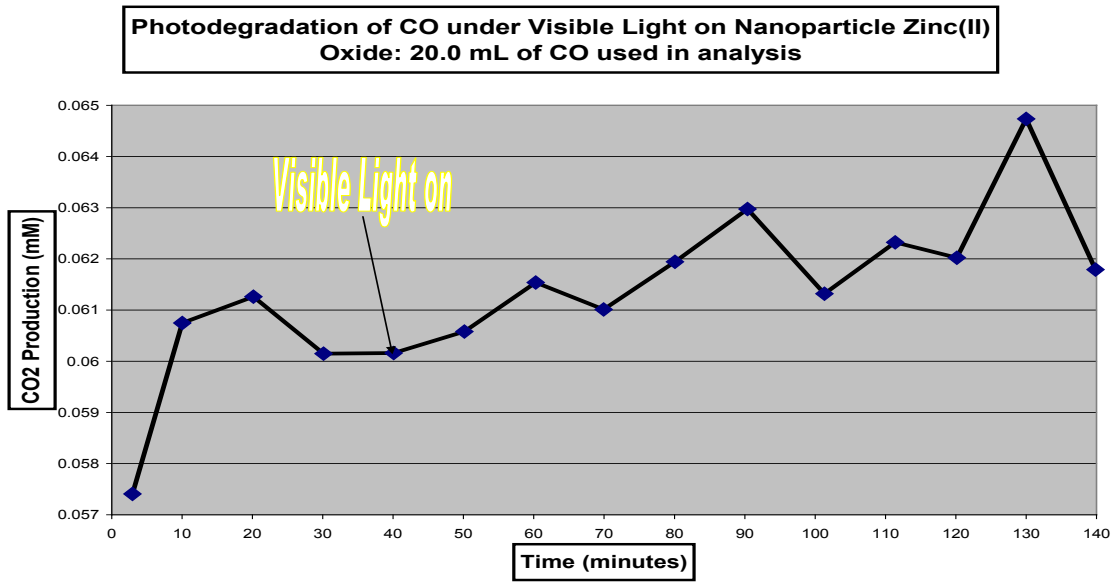


**Figure 4:21 Visible Light Carbon Monoxide Photooxidation over Nanoparticle ZnO.**

**Supplemental text for Figure 4:21**-the above experimental plot appears to reveal slight visible light photooxidation activity with $CO_2$ production value close to the lowest in the class of nanoparticle catalyst standards depending if the last data point would be include or not: refer to Appendix B-B:17 for viewing of the visible light initial rate plots.

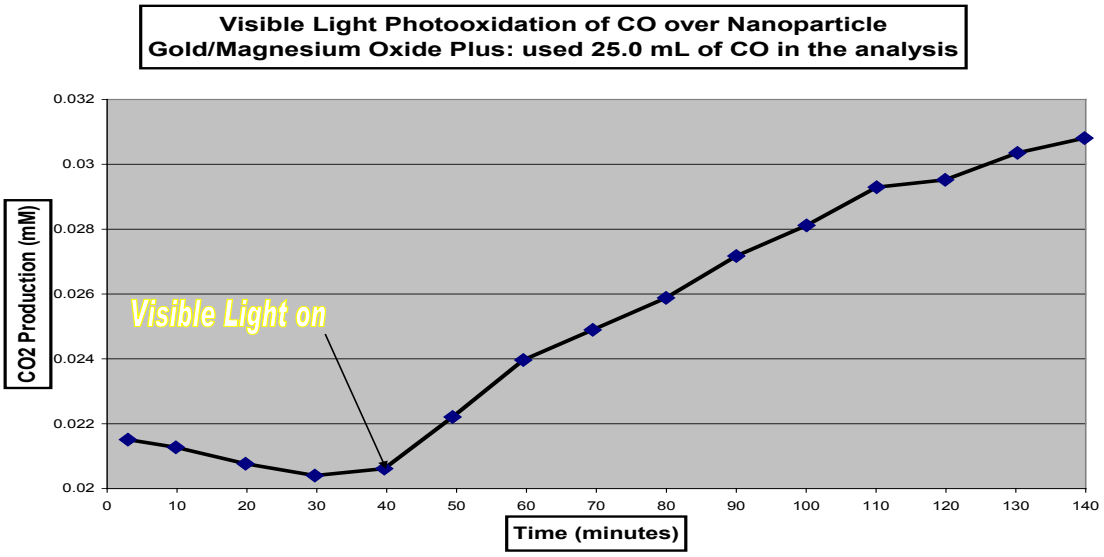


**Figure 4:22 Visible Light Carbon Monoxide Photooxidation over Nanoparticle Gold/Magnesium Oxide Plus.**

**Supplemental text for Figure 4:22**-the above experimental plot of photooxidation of CO over nanoparticle Au/MgO Plus using visible light shows that this catalytic reaction precedes only in the visible light. The concentration of $CO_2$ produced would fifth in this visible series of catalysts. The reason for the lower photodegradation activity could be due to too much CO in the light reactor. A comparison of the initial rates of the catalysts would be provided in the Appendix B-B:18.

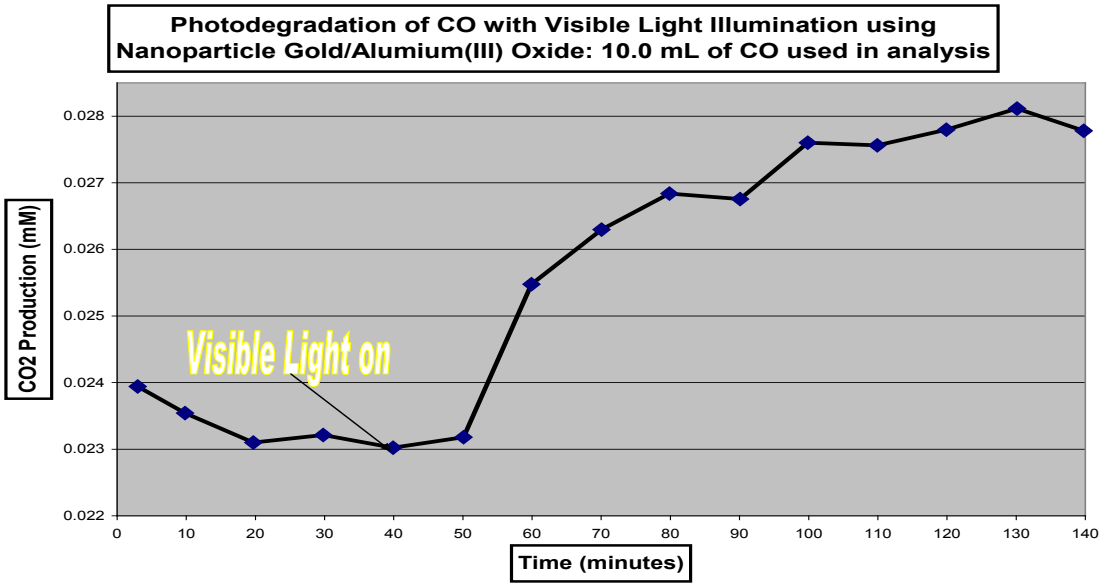


**Figure 4:23 Visible Light Carbon Monoxide Photooxidation over Nanoparticle Gold/Aluminum(III) Oxide.**

**Supplemental text for Figure 4:23**-the above experimental photodegradation CO plot over nanoparticle $Au/Al_2O_3$ using visible light illumination shows that essentially all photooxidation activity due to use of visible light. Concentration $CO_2$ value for the use of this catalyst would be sixth in the visible light nanoparticle catalyst standard series. Refer to Appendix B-B:19.

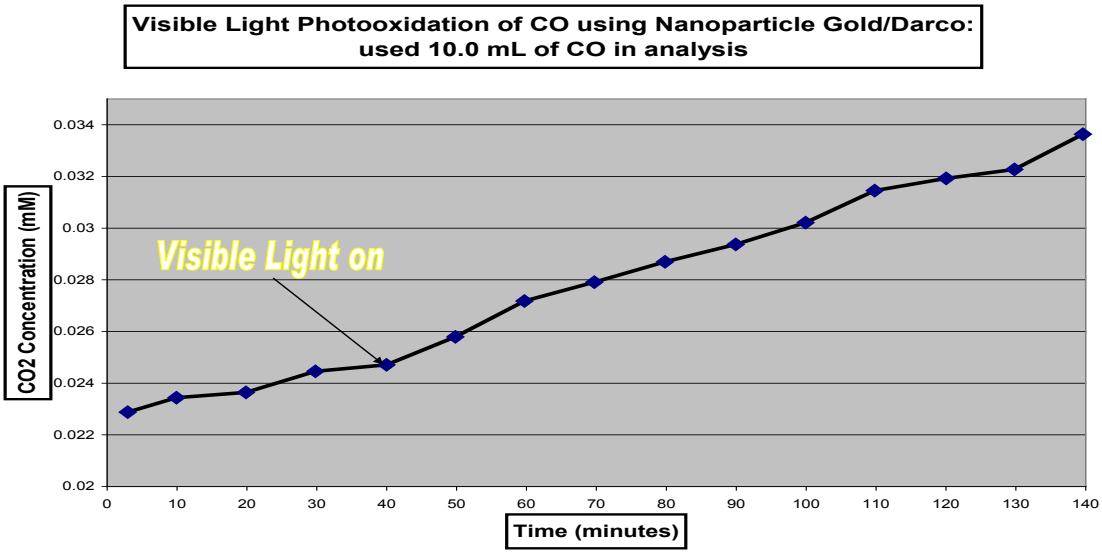


**Figure 4:24 Visible Light Carbon Monoxide Photooxidation over Nanoparticle Gold/Darco.**

**Supplemental text for Figure 4:24**-the above experimental CO photooxidation over nanoparticle Au/Darco plot using visible light shows both a dark and visible light reaction occurring. The combined $CO_2$ production from dark and visible light reactions would place this CO photooxidation catalyst in fourth position in the catalyst standards series. Refer to Appendix B-B:20 for viewing of the initial rate plots.

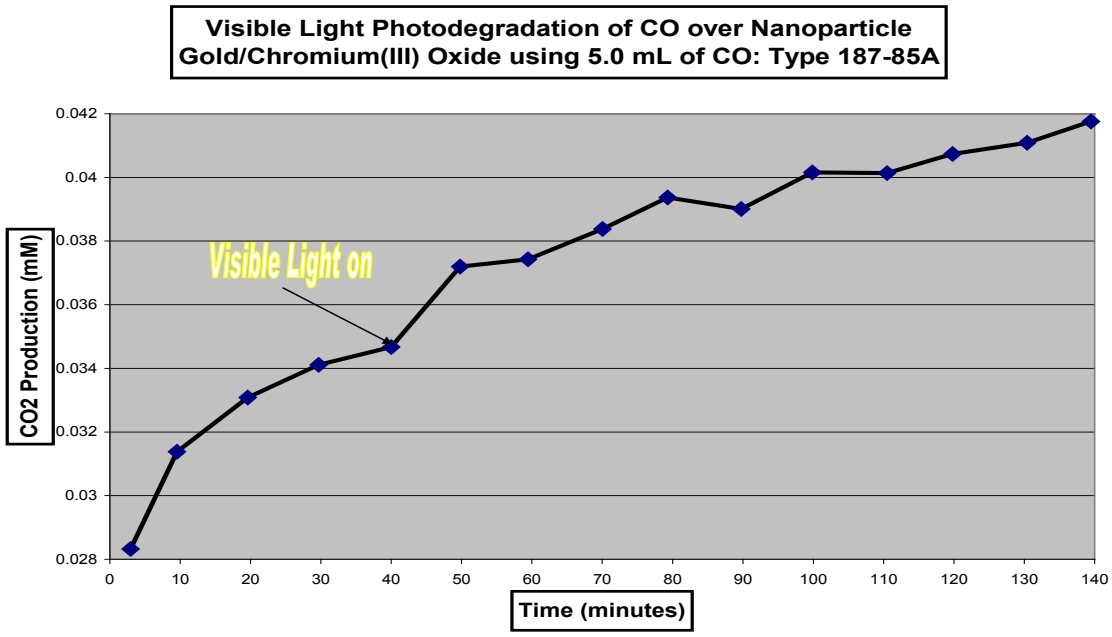


**Figure 4:25 Visible Light Carbon Monoxide Photooxidation over Nanoparticle Gold/Chromium(III) Oxide.**

**Supplemental text for Figure 4:25**-the above experimental CO oxidation plot over nanoparticle $Au/Cr_2O_3$ with 5.0 mL of CO has both a dark and visible light reactions occurring. The total concentration from this catalyst at the given volume of CO would place it in second place as a visible light photooxidation catalyst. Refer to Appendix B-B:21 for initial rate plots.

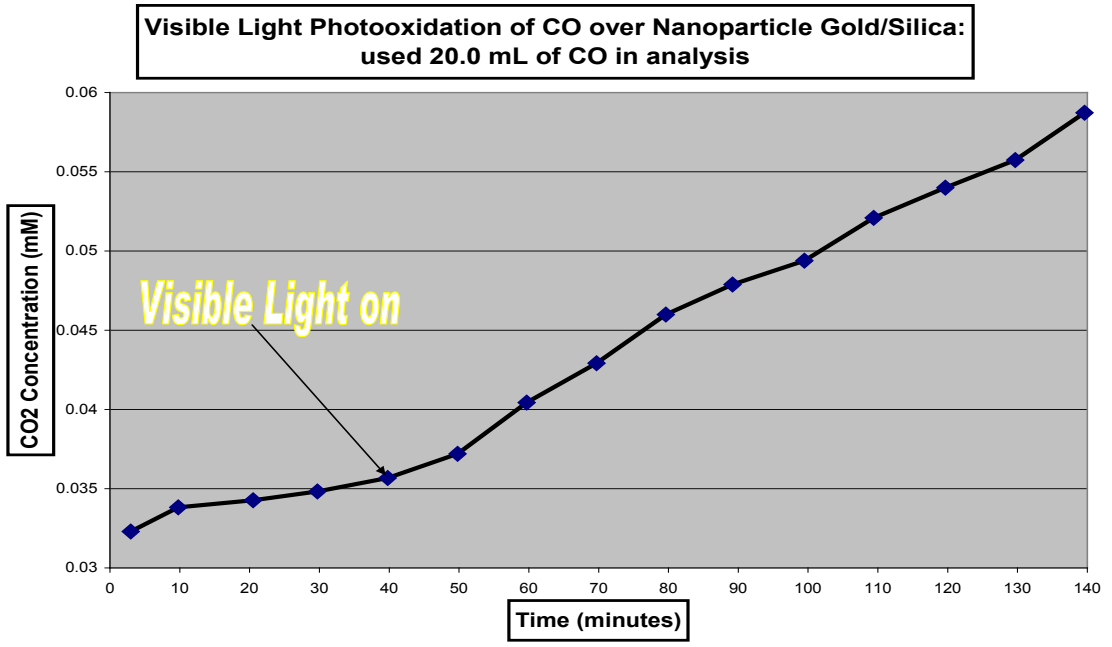


**Figure 4:26 Visible Light Carbon Monoxide Photooxidation over Nanoparticle Gold/Silica.**

**Supplemental text for Figure 4:26**-the above experimental plot of nanoparticle $Au/SiO_2$ in the CO oxidation reactions in both dark and visible light conditions shows high photooxidation activity in the visible light portion of the plot. The total combined concentration of $CO_2$ from dark and visible light reactions would make this catalyst the highest performing catalyst in the catalyst series. Refer to Appendix B-B:22 for initial rate plots.

| Visible Light Carbon Monoxide Photooxidation Comparison of Gold Standards | | | |
|---|---|---|---|
| **Type of Catalyst** | **Volume of CO (mL)** | **Experimental $CO_2$ (mM)** | **Percent $CO_2$ made (%)** |
| **$Au/Cr_2O_3$** | **50.** | **0.011** | **0.16** |
| **ZnO** | **20.** | **0.0044** | **0.16** |
| **Au/MgO Plus** | **25.** | **0.0093** | **0.28** |
| **$Au/Al_2O_3$** | **10.** | **0.0038** | **0.29** |
| **Au/Darco** | **10.** | **0.011** | **0.80** |
| **$Au/Cr_2O_3$** | **5.0** | **0.013** | **2.0** |
| **$Au/SiO_2$** | **20.** | **0.026** | **2.6** |

**Table 4:7 Visible Light Carbon Monoxide Photooxidation Comparisons of Various Gold Catalysts Standards.**

**Supplemental text for Table 4:7**-the above series of experimental CO photooxidation values reveal two trends: (1) the volume of CO injected into the light reactor directly impacts the percent yield of $CO_2$ made; and (2) the highest concentration $CO_2$ production yields were with use of lower volumes of CO. The first trend would be exemplified with the same nanoparticle $Au/Cr_2O_3$ with 50.0 mL and 5.0 mL of CO used in the reactions. Reviewing the $CO_2$ concentration column lower portion shows a general trend of lower amounts of CO used led to increased $CO_2$ production. Refer to the next chapter for potential reasons for the observations seen in the above chapter. Also, review the experimental initial reaction rate plots in Appendix B-B:16-B:22.

| Dark & Visible Light Carbon Monoxide Photooxidation Comparisons of Nanoparticle Gold Standard Results | | | | | | |
|---|---|---|---|---|---|---|
| **Type of Catalyst** | **Volume of CO (mL)** | **Dark Value $CO_2$ (%)** | **$CO_2$ Fraction Concentration in Dark (mM)** | **Visible Light Value $CO_2$ (%)** | **$CO_2$ Fraction Concentration in Visible Light (mM)** | **Total (Dark + Visible Light) Concentration value (mM)** |
| **ZnO** | **20.** | **63** | **0.0028** | **37** | **0.0016** | **0.0044** |
| **$Au/Cr_2O_3$** | **50.** | **58** | **0.0061** | **42** | **0.0045** | **0.011** |
| **$Au/Cr_2O_3$** | **5.0** | **47** | **0.0063** | **53** | **0.0071** | **0.013** |
| **Au/Darco** | **10.** | **17** | **0.0018** | **83** | **0.0089** | **0.011** |
| **$Au/SiO_2$** | **20.** | **13** | **0.0034** | **87** | **0.023** | **0.026** |

**Table 4:8 Dark & Visible Light Carbon Monoxide Photooxidation Results with Nanoparticle Gold Standards.**

**Supplemental text for Table 4:8**-the experimental dark and visible light data above shows two trends: (1) excluding the ZnO values in the table, the dark $CO_2$ production activity decreased with less volumes of CO in the light reactor (i.e. directly proportional) viewing the 2-4$^{th}$ columns top to bottom; (2) the use of less CO in the analysis of visible light photooxidation led to increased $CO_2$ concentration, as viewed in columns 5-7; and (3) the total dark plus visible light fractions added together show a increased $CO_2$ concentration at lower CO volumes. For example, viewing the identical $Au/Cr_2O_3$ nanoparticle catalyst at 50.0 mL and 5.0 mL of CO clearly show total increased $CO_2$ production, and comparison of 50.0 mL of CO over $Au/Cr_2O_3$ with 20.0 mL of CO using $Au/SiO_2$ also shows a major $CO_2$ production increase. Refer to the next chapter for potential ramifications of these above experimental results. Also, as shown in the Appendix B-B:16-B:22 of experimental initial reaction rate plots, the slope values and percent $CO_2$ yield increase directly with the above experimental findings.

### 4.7.4 CO Photooxidation with Au/ZnO & ZnO under UV-light Irradiation

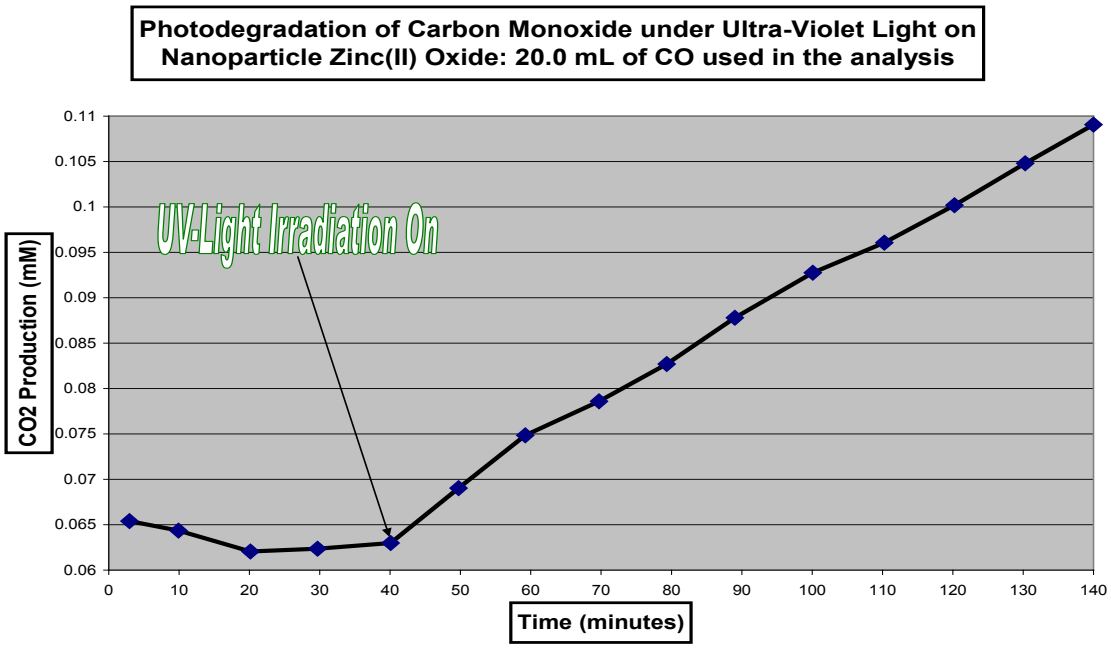


**Figure 4:27 UV-Light Carbon Monoxide Photooxidation over Nanoparticle ZnO.**

**Supplemental text for Figure 4:27**-the above experimental plot of CO photooxidation over nanoparticle ZnO shows no dark reaction activity from 0-40 minute mark; then, $CO_2$ production concentration greatly increases with use of UV-light irradiation. This result clearly would infer that ZnO photocatalytic activity would be in the UV-light wavelength spectrum, which would contradict the earlier questionable result of dark and visible light activity from the ZnO catalyst.

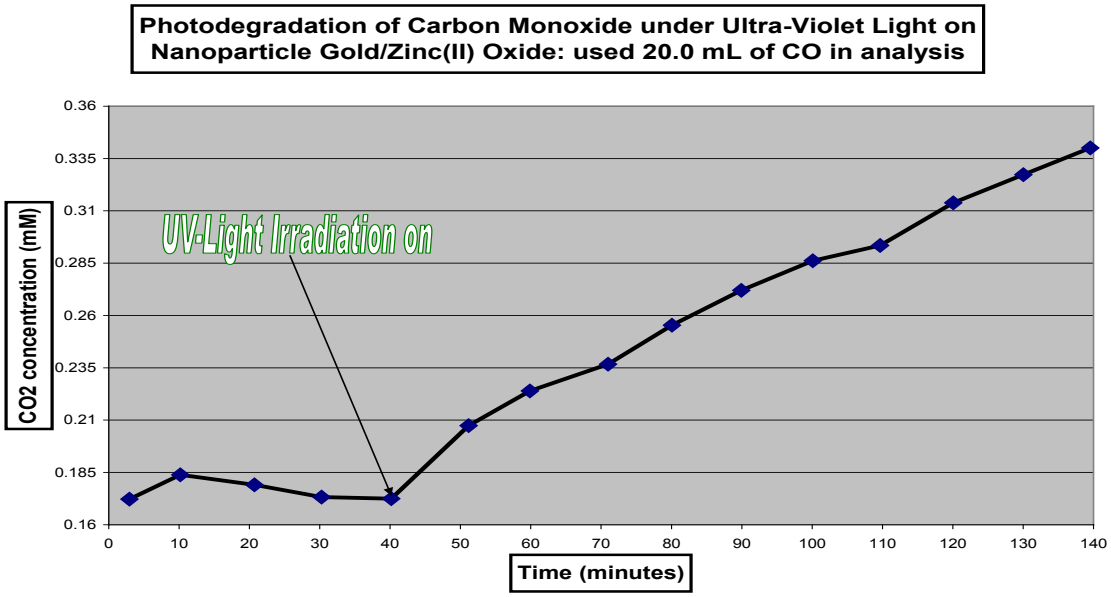


**Figure 4:28 UV-Light Carbon Monoxide Photooxidation over Nanoparticle Gold/ZnO.**

**Supplemental text for Figure 4:28**-the above experimental UV-light irradiation CO photooxidation over nanoparticle Au/ZnO reveals no dark reaction from 1-40 minute marks. Upon use of UV-light, the $CO_2$ production dramati-

cally increases from 40-140 minute marks. This clearly shows the synergistic effect of both use nanosize gold on nanosize zinc(II) oxide.

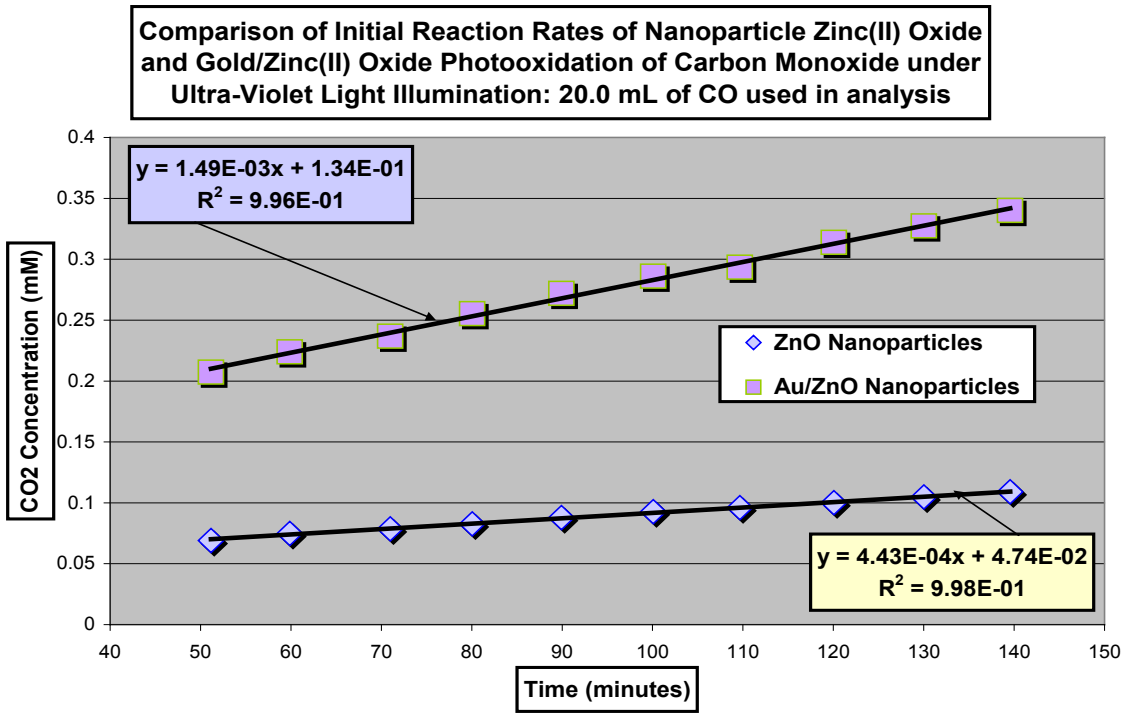


**Figure 4:29 UV-Light Carbon Monoxide Photooxidation Initial Rate of Nanoparticle An/ZnO & ZnO.**

**Supplemental of text for Figure 4:29**-the above experimental comparison plot of nanoparticle ZnO and Au/ZnO in UV-light initiated photooxidation of CO shows the both greater $CO_2$ production and larger slope value. This comparison plot would the second replicate of the original photooxidation CO experiments on ZnO and Au/ZnO. The first experiments showed only slightly higher $CO_2$ concentration and slope values, as seen in the appendix; therefore, this result would need to be completed once to determine if the nanoparticle gold indeed had a synergistic effect coupled with nanoparticle ZnO. The above results will be discussed in the next chapter.

| UV-Light Carbon Monoxide Photooxidation Results with Nanoparticle Zinc(II) Oxide & Gold/Zinc(II) Oxide | | | | | | |
|---|---|---|---|---|---|---|
| **Type of Catalyst** | **Volume of CO (mL)** | **Experimental $CO_2$ (mM)** | **Theoretical $CO_2$ (mM)** | **Percent $CO_2$ yield (%)** | **Slope of Reaction** | **$R^2$ linearity** |
| **ZnO** | **20.** | **0.044** | **2.7** | **1.6** | **4.3E-04** | **1.0** |
| **Au/ZnO** | **20.** | **0.17** | **2.7** | **6.3** | **1.4E-03** | **1.0** |

**Table 4:9 UV-Light Carbon Monoxide Photooxidation Results with Nanoparticle ZnO & Au/ZnO.**

**Supplemental text for Table 4:9**-the above experimental results of CO UV-light photooxidation over nanoparticle ZnO and Au/ZnO show the trend of increased photocatalytic activity combining nanoparticle gold with nanoparticle zinc(II) oxide. It should be noted that the original experiments of these catalysts on CO photooxidation gave similar values.

## 4.8 $CH_3COCH_3$ Photodegradation over V(x)-MCM-48 under Visible Light Illumination

The reason for the poor activity would likely be from inadequate liquid to vaporization problem. This problem will be dealt with in the sub-section of future research and potential application of the discussion section.

## 4.9 $CH_3CH_2OH$ Photodegradation over V(x)-MCM-48 under Visible Light Illumination

The below plot, as shown in Figure 4:30, of ethanol photodegradation over V(20)-MCM-48 would appear to have difficulty with ethanol entering gaseous state from liquid phase. Even with this problem, there was some total oxidation activity occurring and the slope values were comparable to the CO photooxidation ones'. Finally, the next chapter will attempt to address laboratory procedural methods that might cause the ethanol to enter gaseous state using literature references.

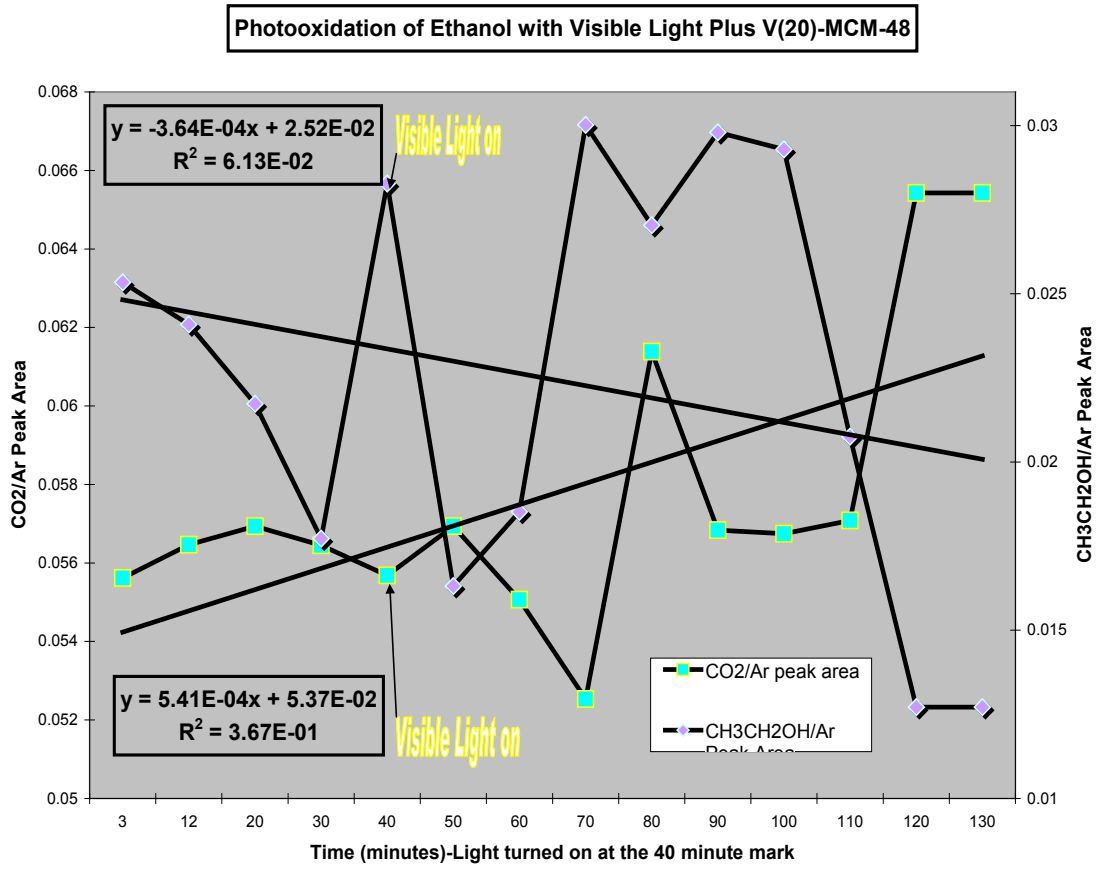


**Figure 4:30 Visible Light Ethanol Photodegradation over V(20)-MCM-48.**

**Supplemental text for Figure 4:30**-the above experimental plot appears to show ethanol degradation to $CO_2$, as noted in slope and concentration values.

## 4.10 $CH_3CHOHCH_3$ Photodegradation over V(20)-MCM-48 under Visible Light

Similar to the situation with the acetone degradation experimental results, the 2-propanol photooxidation reaction had low activity photocatalytically. The low activity would be linked to poor vaporization of the alcohol. This problem will be discussed in the next chapter under future research and potential applications sub-section..

## 4.11 $CH_3CN$ Photodegradation over V(5)-MCM-48 (?) under UV-Light Irradiation

With the use of UV-light, the V(5)-MCM-48 (structure needs to be confirmed?) was relatively active for the production of $CO_2$, as shown below in Figure 4:31. The $CO_2$ activity seen in this reaction might infer the type(s) of vanadium ion species in MCM-48 that would be responsible for the photooxidation occurring. The initial reaction rate plot of acetonitrile under UV-light, as shown below in Figure 4:32, clearly shows photodegradation activity

and has a slope value plus $R^2$ value comparable to many nanoparticle CO oxidation gold catalysts seen above. Methods to improve this reaction results will be discussed in the next chapter.

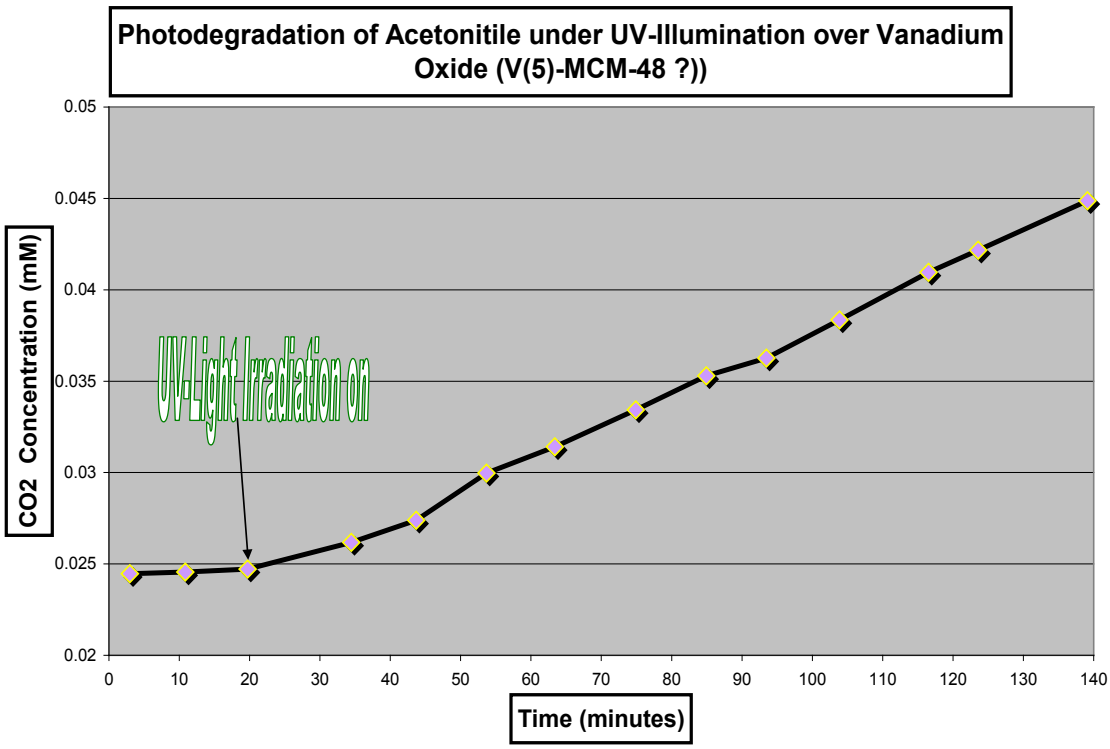


**Figure 4:31 UV-Light Acetonitile Photodegradation over Vanadium Oxide (V(5)-MCM-48 ?).**

**Supplemental text for Figure 4:31**-the above experimental plot of acetonitrile photodegradation occurs with use of V(5)-MCM-48 (structure needs to be confirmed?) under UV-light irradiation clearly shows dramatic increasing photocatalytic activity with use of ultra-violet light energy.

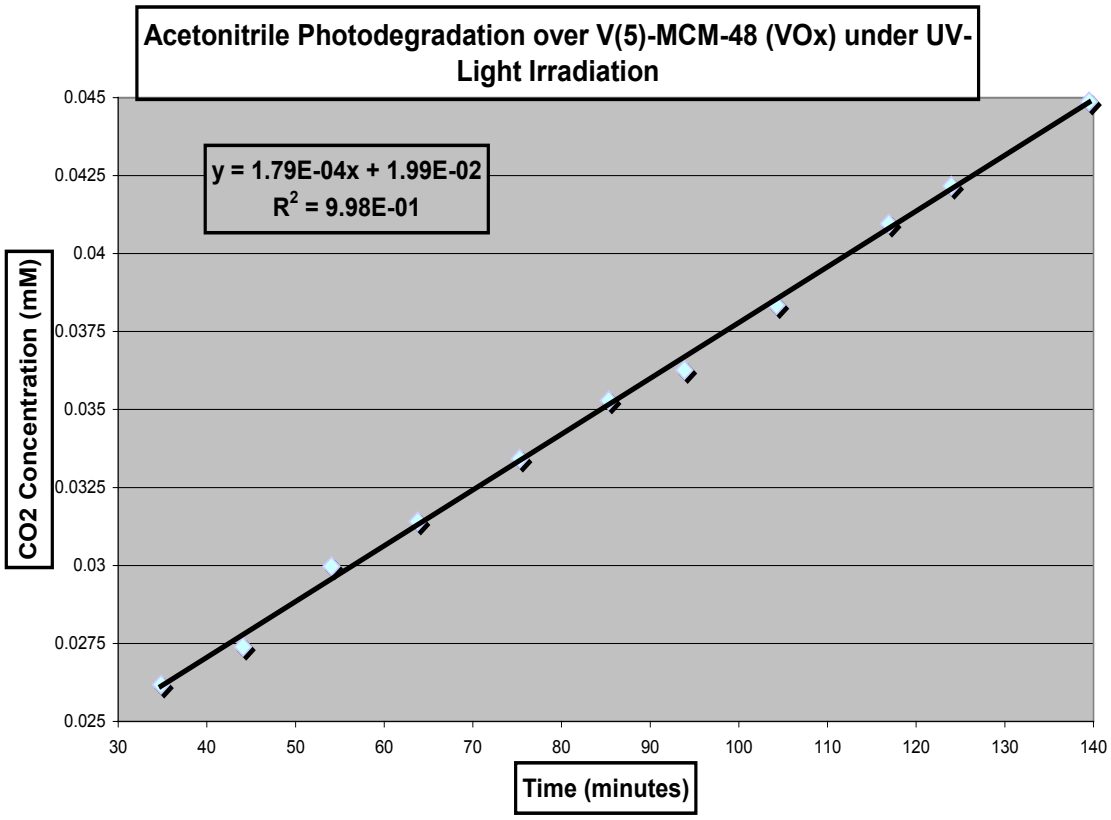


**Figure 4:32 UV-Light Acetonitile Photodegradation Initial Reaction Rate over V(5)-MCM-48 (VOx).**

**Supplemental text for Figure 4:32**-the above experimental initial reaction rate plot of acetonitrile degradation over V(5)-MCM-48 (structure needs to be confirmed?) reveals a direct photooxidation reaction with use of UV-light irradiation energy. The $R^2$ value, which would be a measure of the linearity of the fit data, clearly would be comparable to the best nanoparticle CO oxidation gold catalysts, as seen earlier in this chapter. The concentration of $CO_2$ would be 0.0204 mM: this value will be discussed in the next chapter in comparison to literature data.

## References


1. Gomez, S.; Garces, L. J.; Villegas, J.; Ghosh, R.; Giraldo, O.; Suib, S. L. "*Synthesis and characterization of TM-MCM-48 (TM = Mn, V, Cr) and their catalytic activity in the oxidation of styrene*," *Journal of Catalysis* **2005**, *233*, 60-67 (Research article)

2. Gomez, S.; Giraldo, O.; Garces, L. J.; Villegas, J.; Suib, S. L. "*New Synthetic Route for the Incorporation of Manganese Species into the Pores of MCM-48*," *Chemistry of Materials* **2004**, *16*, 2411-2417 (Research article)

3. Morey, M.; Davidson, A.; Eckert, H.; Stucky, G. "*Pseudotetrahedral $O_{3/2}V{=}O$ Centers Immobilized on the Walls of a Mesoporous, Cubic MCM-48 Support: Preparation, Characterization, and Reactivity toward Water As Investigated by $^{51}V$ NMR and UV-vis Spectroscopies*," Chemistry of Materials **1996**, *8*, 486-492 (Research article)

4. Zhan, W.; Guo, Y.; Wang, Y.; Liu, X.; Guo, Y.; Wang, Y.; Zhang, Z.; Lu, G. "*Synthesis of Lanthanum-Doped MCM-48 Molecular Sieves and Its Catalytic Performance for the Oxidation of Styrene*," *Journal of Physical Chemistry B* **2007**, *111*, 12103-12110 (Research article)

5. Romero, A. A.; Alba, M. D.; Zhou, W.; Klinowski, J. "*Synthesis and Characterization of the Mesoporous Silicate Molecular Sieves MCM-48*," *Journal of Physical Chemistry B* **1997**, *101*, 5294-5300 (Research article)

6. Shao, Y.; Wang, L.; Zhang, J.; Anpo, M. "*Synthesis of Hydrothermally Stable and Long-Range Ordered Ce-MCM-48 and Fe-MCM-48 Materials*," *Journal of Physical Chemistry B* **2005**, *109*, 20835-20841 (Research article)

7. Gallis, K. W.; Landry, C. C. "*Synthesis of MCM-48 by a Phase Transformation Process*," *Chemistry of Materials* **1997**, *9*, 2035-2038 (Communication article)

8. Kim, W. J.; Yoo, J. C.; Hayhurst, D. T. "*Synthesis of MCM-48 via phase transformation with direct addition of NaF and enhancement of hydrothermal stability by post-treatment in NaF solution*," *Microporous and Mesoporous Materials* **2002**, *49*, 125-137 (Research article)

9. Van Der Voort, P.; Mathieu, M.; Mees, F.; Vansant, E. F. "*Synthesis of High Quality MCM-48 and MCM-41 by Means of the GEMINI Surfactant Method*," *Journal of Physical Chemistry B* **1998**, *102*, 8847-8851 (Research article)

10. Rodrigues, S.; Ranjit, K. T.; Uma, S.; Martyanov, I. M.; Klabunde, K. J. "*Single-Step Synthesis of a Highly Active Visible-Light Photocatalyst for Oxidation of a Common Indoor Air Pollutant: Acetaldehyde*," *Advanced Materials* **2005**, *17*, 2467-2471 (Research article)

11. Kosslick, H.; Lischke, G.; Landmesser, H.; Parlitz, B.; Storek, W.; Fricke, R. "*Acidity and Catalytic Behavior of Substituted MCM-48*," *Journal of Catalysis* **1998**, *176*, 102-114 (Research article)

12. Zhang, W.; Pinnavaia, T. J. "*Transition metal substituted derivatives of cubic MCM-48 mesoporous molecular sieves*," Catalysis Letters **1996**, *38*, 261-265 (Research article)

13. Moller, K.; Bein, T.; Fischer, R. X. "*Entrapment of PMMA Polymer Strands in Micro- and Mesoporous Materials*," *Chemistry of Materials* **1998**, *10*, 1841-1852 (Research article)

14. Vartuli, J. C.; Schmitt, K. D.; Kresge, C. T.; Roth, W. J.; Leonowicz, M. E.; McCullen, S. B.; Hellring, S.; Beck, J. S.; Schlenker, J. L.; Olson, D. H.; Sheppard, E. W. "*Effect of Surfactant/Silica Molar Ratios on the Formation of Mesoporous Molecular Sieves: Inorganic Mimicry of Surfactant Liquid-Crystal Phases and Mechanistic Implications*," *Chemistry of Materials* **1994**, *6*, 2317-2326 (Research article)

15. Ryoo, R.; Jun, S.; Kim, J. M.; Kim, M. J. "*Generalised route to the preparation of mesoporous metallosilicates via post-synthetic metal implantation*," *Chemical Communications* **1997**, 2225-2226 (Communications article)

16. Chen, D.; Li. Z.; Yu, C.; Shi, Y.; Zhang, Z.; Tu, B.; Zhao, D. "*Nonionic Block Copolymer and Anionic Mixed Surfactants Directed Synthesis of Highly Ordered Mesoporous Silica with Bicontinuous Cubic Structure*," Chemistry of Materials **2005**, *17*, 3228-3234 (Research article)

17. Kim, J. M.; Kim, S. K.; Ryoo, R. "*Synthesis of MCM-48 single crystals*," *Chemical Communications* **1998**, 259-260 (Communications article)

18. Corma, A. "*From Microporous to Mesoporous Molecular Sieve Materials and Their Use in Catalysis*," *Chemical Reviews* **1997**, *97*, 2373-2419 (Review article)

19. Van Der Voort, P.; Morey, M.; Stucky, G. D.; Mathieu, M.; Vansant, E. F. "*Creation of $VO_x$ Surface Species on Pure Silica MCM-48 Using Gas-Phase Modification with $VO(acac)_2$*," *Journal of Physical Chemistry B* **1998**, *102*, 585-590 (Research article)

20. Echchahed, B.; Moen, A.; Nicholson, D.; Bonneviot, L. "*Iron-Modified MCM-48 Mesoporous Molecular Sieves*," *Chemistry of Materials* **1997**, *9*, 1716-1719 (Communication article)

21. Zhao, X. S.; Lu, G. Q.; Millar, G. J. "*Advances in Mesoporous Molecular Sieve MCM-41*," *Industrial & Engineering Chemistry Research* **1996**, *35*, 2075-2090 (Review article)

22. Ciesla, U.; Schuth, F. "*Ordered mesoporous materials*," *Microporous and Mesoporous Materials* **1999**, *27*, 131-149 (Review article)

23. Lim, S.; Haller, G. L. "*Preparation of Highly Ordered Vanadium-Substituted MCM-41: Stability and Acidic Properties*," *Journal of Physical Chemistry B* **2002**, *106*, 8437-8448 (Research article)

24. Kruk, M.; Jaroniec, M.; Sayari, A. "*Influence of hydrothermal restructuring conditions on structural properties of mesoporous molecular sieves*," *Microporous and Mesoporous Materials* **1999**, *27*, 217-229 (Research article)

25. Vartuli, J. C.; Kresge, C. T.; Leonowicz, M. E.; Chu, A. S.; McCullen, S. B.; Johnson, I. D.; Sheppard, E. W. "*Synthesis of Mesoporous Materials: Liquid-Crystal Templating versus Intercalation of Layered Silicates*," *Chemistry of Materials* **1994**, *6*, 2070-2077 (Research article)

26. Sayari, A. "*Catalysis by Crystalline Mesoporous Molecular Sieves*," *Chemistry of Materials* **1996**, *8*, 1840-1852 (Review article)

27. Beck, J. S.; Vartuli, J. C.; Kennedy, G. J.; Kresge, C. T.; Roth, W. J.; Schramm, S. E. "*Molecular or Supramolecular Templating: Defining the Role of Surfactant Chemistry in the Formation of Microporous and Mesoporous Molecular Sieves*," *Chemistry of Materials* **1994**, *6*, 1816-1821 (Research article)

28. Ryoo, R.; Kim, J. M.; Ko, C. H.; Shin, C. H. "*Disordered Molecular Sieve with Branched Mesoporous Channel Network*," *Journal of Physical Chemistry* **1996**, *100*, 17718-17721 (Research article)

29. Hartmann, M.; Racouchot, S.; Bischof, C. "*Synthesis and redox properties of MCM-48 containing copper and zinc*," *Chemical Communications* **1997**, 2367-2368 (Communication article)

30. Ko, C. H.; Ryoo, R. "*Imaging the channels in mesoporous molecular sieves with platinum*," *Chemical Communications* **1996**, 2467-2468 (Communication article)

31. Alfredsson, V.; Anderson, M. W. "*Structure of MCM-48 Revealed by Transmission Electron Microscopy*," *Chemistry of Materials* **1996**, *8*, 1141-1146 (Research article)

32. Xu, W.; Aydin, M.; Zakia, S.; Akins, D. L. "*Aggregation of Thionine within AlMCM-48*," *Journal of Physical Chemistry B* **2004**, *108*, 5588-5593 (Research article)

33. Baltes, M.; Cassiers, K.; Van Der Voort, P.; Weckhuysen, B. M.; Schoonheydt, R. A. Vansant, E. F. "*MCM-48-Supported Vanadium Oxide Catalysts, Prepared by the Molecular Designed Dispersion of $VO(acac)_2$: A Detailed Study of the Highly Reactive MCM-48 Surface and the Structure and Activity of the Deposited $VO_x$*," *Journal of Catalysis* **2001**, *197*, 160-171 (Research article)

34. Berndt, H.; Martin, A.; Bruckner, A.; Schreier, E.; Muller, D.; Kosslick, H.; Wolf, G.-U.; Lucke, B. "*Structure and Catalytic Properties of $VO_x$/MCM Materials for the Partial Oxidation of Methane to Formaldehyde*," *Journal of Catalysis* **2000**, *191*, 384-400 (Research article)

35. Martyanov, I. M.; Uma, S.; Rodrigues, S.; Klabunde, K. J. "*Structural defects cause $TiO_2$-based photocatalysts to be active in visible light*," *Chemical Communications* **2004**, 2476-2477 (Communication article)

36. Rodrigues, S.; Uma, S.; Martyanov, I. N.; Klabunde, K. J. "*Visible light photocatalytic activity for degradation of acetaldehyde using transition metal incorporated Al-MCM-41 (aluminum doped silica zeolitic material)*," *Journal of Photochemistry and Photobiology A: Chemistry* **2004**, *165*, 51-58 (Research article)

37. Wang, J.; Uma, S.; Klabunde, K. J. "*Visible light photocatalysis in transition metal incorporated titania-silica aerogels*," *Applied Catalysis B: Environmental* **2004**, *48*, 151-154 (Research article)

38. Pak, C.; Haller, G. L. "*Reversible coordination change of chromium in Cr-MCM-41 and Cr-MCM-48 studied by X-ray absorption near edge structure*," *Microporous and Mesoporous Materials* **2001**, *48*, 165-170 (Research article)

39. Gontier, S.; Tuel, A. "*Characterization of vanadium-containing mesoporous silicas*," *Microporous Materials* **1995**, *5*, 161-171 (Research article)

40. Rodgers, G. D. "*Descriptive Inorganic, Coordination, and Solid-State Chemistry*," **Second Edition**, Chapter 7, page 173 (Inorganic chemistry textbook)

41. Martyanov, I. N.; Uma, S.; Rodrigues, S.; Klabunde, K. J. "*Decontamination of Gaseous Acetaldehyde over $CoO_x$-Loaded $SiO_2$ Xerogels under Ambient, Dark Conditions*," *Langmuir* **2005**, *21*, 2273-2280 (Research article)

42. Peral, J.; Ollis, D. F. "*Heterogeneous photocatalytic oxidation of gas-phase organics for air purification: Acetone, 1-butanol, butyraldehyde, formaldehyde, and m-xylene oxidation*," *Journal of Catalysis* **1992**, *136*, 555-565 (Research article)

43. Muggli, D. S.; Larson, S. A.; Falconer, J. L. "*Photocatalytic Oxidation of Ethanol: Isotopic Labeling and Transient Reaction*," *Journal of Physical Chemistry* **1996**, *100*, 15886-15889 (Research article)

44. Pilkenton, S.; Hwang, S-J.; Raftery, D. "*Ethanol Photocatalysis on $TiO_2$-Coated Optical Microfiber, Supported Monolayer, and Powdered Catalysts: An in Situ NMR Study*," *Journal of Physical Chemistry B* **1999**, *103*, 11152-11160 (Research article)

45. Xu, W.; Raftery, D. "*Photocatalytic Oxidation of 2-Propanol on $TiO_2$ Powder and $TiO_2$ Monolayer Catalysts Studied by Solid-State NMR*," *Journal of Physical Chemistry B* **2001**, *105*, 4343-4349 (Research article)

46. Zhuang, J.; Rusu, C. N.; Yates, J. T. Jr. "*Adsorption and Photooxidation of $CH_3CN$ on $TiO_2$*," *Journal of Physical Chemistry B* **1999**, *103*, 6957-6967 (Research article)

47. Sauer, M. L.; Ollis, D. F. "*Photocatalyzed Oxidation of Ethanol and Acetaldehyde in Humidified Air*," *Journal of Catalysis* **1996**, *158*, 570-582 (Research article)

48. Xu, W.; Raftery, D. "*In Situ Solid-State Nuclear Magnetic Resonance Studies of Acetone Photocatalytic Oxidation on Titanium Oxide Surfaces*," *Journal of Catalysis* **2001**, *204*, 110-117 (Research article)

49. El-Maazawi, M.; Finken, A. N.; Nair, A. B.; Grassian, V. H. "*Adsorption and Photocatalytic Oxidation of Acetone on $TiO_2$: An in Situ Transmission FT-IR Study*," *Journal of Catalysis* **2000**, *191*, 138-146 (Research article)

50. Hutchings, G. J.; Rafiq, M.; Siddiqui, H.; Burrows, A.; Kiely, C. J.; Whyman, R. "*High-activity Au/CuO-ZnO catalysts for the oxidation of carbon monoxide at ambient temperature*," *Journal of the Chemical Society, Faraday Transactions* **1997**, *93*, 187-188 (Communication article)

51. Ohko, Y.; Tryk, D. A.; Hashimoto, K.; Fujishima, A. "*Autoxidation of Acetaldehyde Initiated by $TiO_2$ Photocatalysis under Weak UV Illumination*," *Journal of Physical Chemistry B* **1998**, *102*, 2699-2704 (Research article)

52. Huruta, M.; Kobayashi, T.; Sano, H.; Yamada, N. "*Novel Gold Catalysts for the Oxidation of Carbon Monoxide at a Temperature far below 0 °C*," Chemistry Letters **1987**, 405-408 (Communication article)

53. Hwang, S-J.; Raftery, D. "*In situ solid-state NMR studies of ethanol photocatalysis: characterization of surface sites and their reactivities*," Catalysis Today **1999**, *49*, 353-361 (Research article)

54. Muggli, D. S.; Lowery, K. H.; Falconer, J. L. "*Identification of Adsorbed Species during Steady-State Photocatalytic Oxidation of Ethanol on $TiO_2$*," *Journal of Catalysis* **1998**, *180*, 111-122 (Research article)

55. Muggli, D. S.; McCue, J. T.; Falconer, J. L. "*Mechanism of the Photocatalytic Oxidation of Ethanol on $TiO_2$*," *Journal of Catalysis* **1998**, *173*, 470-483 (Research article)

56. Nimlos, M. R.; Wolfrum, E. J.; Brewer, M. L.; Fennell, J. A.; Bintner, G. "*Gas-Phase Heterogeneous Photocatalytic Oxidation of Ethanol: Pathways and Kinetic Modeling*," *Environmental Science & Technology* **1996**, *30*, 3102-3110 (Research article)

57. Henderson, M. A. "*Photooxidation of Acetone on $TiO_2$(110): Conversion to Acetate via Methyl Radical Ejection*," *Journal of Physical Chemistry B* **2005**, *109*, 12062-12070 (Research article)

58. Maye, M. M.; Lou, Y.; Zhong, C-J. "*Core-Shell Gold Nanoparticle Assembly as Novel Electrocatalyst of CO Oxidation*," *Langmuir* **2000**, *16*, 7520-7523 (Research article)

59. Xu, W.; Raftery, D.; Francisco, J. S. "*Effect of Irradiation Sources and Oxygen Concentration on the Photocatalytic Oxidation of 2-Propanol and Acetone Studied by in Situ FTIR*," *Journal of Physical Chemistry B* **2003**, *107*, 4537-4544 (Research article)

60. Rakic, V. M.; Hercigonja, R. V.; Dondur, V. T. "*CO interaction with zeolites studied by TPD and FTIR: transition-metal ion-exchange FAU-type zeolites*," *Microporous and Mesoporous Materials* **1999**, *27*, 27-39 (Research article)

61. Centi, G.; Perathoner, S.; Trifiro, F.; Aboukais, A.; Aissi, C. F.; Guelton, M. "*Physicochemical Characterization of V-Silicalite*," *Journal of Physical Chemistry* **1992**, *96*, 2617-2629 (Research article)

62. Tang, J.; Zou, Z.; Ye, J. "*Efficient Photocatalytic Decomposition of Organic Contaminants over $CaBi_2O_4$ under Visible-Light Irradiation*," *Angewandte Chemie International Edition* **2004**, *43*, 4463-4466 (Research article)

63. Arai, T.; Yanagida, M.; Konishi, Y.; Iwasaki, Y.; Sugihara, H.; Sayama, K. "*Efficient Complete Oxidation of Acetaldehyde into $CO_2$ over $CuBi_2O_4/WO_3$ Composite Photocatalyst under Visible and UV Light Irradiation*," *Journal of Physical Chemistry C* **2007**, *111*, 7574-7577 (Research article)

64. Mills, A.; Le Hunte, S. "*An overview of semiconductor photocatalysis*," *Journal of Photochemistry and Photobiology A: Chemistry* **1997**, *108*, 1-35 (Review article)

65. Gao, B.; Ma, Y.; Cao, Y.; Yang, W.; Yao, J. "*Great Enhancement of Photocatalytic Activity of Nitrogen-Doped Titania by Coupling with Tungsten Oxide*," *Journal of Physical Chemistry B* **2006**, *110*, 14391-14397 (Research article)

66. Linsebigler, A. L.; Lu, G.; Yates, J. T. Jr. "*Photocatalysis on $TiO_2$ Surfaces: Principles, Mechanisms, and Selected Results*," *Chemical Reviews* **1995**, *95*, 735-758 (Review article)

67. Fujishima, A.; Rao, T. N.; Tryk, D. A. "*Titanium dioxide photocatalysis*," *Journal of Photochemistry and Photobiology C: Photochemistry Reviews* **2000**, *1*, 1-21 (Review article)

68. Burda, C.; Lou, Y.; Chen, X.; Samia, A. C. S.; Stout, J.; Gole, J. L. "*Enhanced Nitrogen Doping in $TiO_2$ Nanoparticles*," *Nano Letters* **2003**, *3*, 1049-1051 (Research article)

69. Litter, M. I. "*Heterogeneous photocatalysis Transition metal ions in photocatalytic systems*," *Applied Catalysis B: Environmental* **1999**, *23*, 89-114 (Review article)

70. Hoffman, M. R.; Martin, S. T.; Choi, W.; Bahnemann, D. W. "*Environmental Applications of Semiconductor Photocatalysis*," *Chemical Reviews* **1995**, *95*, 69-96 (Review article)

# Chapter 5 –V-MCM-48 Discussion of Results

## V-MCM-48 Discussion Synthesis: Part I

## 5.1 Introduction

The four sections of the following illustrate the complexity and novelty of the work on V-MCM-48 mesoporous material through: (1) synthesis, (2) characterization methods, (3) photocatalytic studies, and (4) applications plus future research needed. The synthesis outlines the value of each reagent and notes the relative simplicity of the overall synthesis of V-MCM-48 followed by the use of powder X-ray diffraction (XRD), Diffuse Reflectance Ultra-Violet-Visible (DR-UV-vis) spectroscopy, and $N_2$ adsorption-desorption characterization methods. The use of this potential nanoparticle heterogeneous catalyst was explored through the use of environmental remediation using photocatalysis of six probe molecules: $CH_3CHO$, CO, $CH_3COCH_3$, $CH_3CHOHCH_3$, $CH_3CH_2OH$, and $CH_3CN$. The V-MCM-48 was compared to the P-25 $TiO_2$ Degussia-Huls and nanoparticle gold standards to determine photocatalytic ability against published environmental remediation catalysts. From the research results, potential future applications will be outlined coupled with research needed for this material to reach its full potential. Finally, literature references will be employed extensively throughout all areas to aid current and future researchers in the studies of mesoporous-doped transition metal materials characteristics from a synthetic, characterization, and application points of view.

## 5.2 Explanation of Value of Each Reagent in Modified Novel Synthesis of V-MCM-48

The experimental synthesis employed in this research project was a modification of the following literature.[1-3] The modifications completed on the synthesis procedure would be different metal precursors and lengthened reaction time in comparison to Unger and co-workers synthetic synthesis for metal doped MCM-48 materials.[2,3] The synthetic experiments use common reagents added to a small polypropylene container under stirring: (1) deionized water, (2) absolute ethanol, (3) cetytrimethylammonium bromide (CTAB), (4) concentrated $NH_4OH$ (~14.2 M), (5) $NH_4VO_3$ or $VOSO_4 \cdot 3H_2O$, and (6) tetraethylorthosilicate (tetraethoxysilane) (TEOS). After theses reagents had been placed in such order into the plastic container, the screw cap was installed and reaction mixture was stirred for a certain time period. The resulting white precipitate was filtered with both distilled and deionized water. Then, calcination process was used to produce a yellow-orange colored powder consisting of fine granules.

To obtain the desired isomorphically substituted V-MCM-48 product, this required placing the reagents in the order listed above. Deionized water was used for the synthesis to prevent other common metal ions ($Ca^{2+}$, $Mg^{2+}$, $Fe^{3+}$ etc.) from interfering with the formation of the desired product. Absolute ethanol provided the organic species needed for initiating the hydrolysis of TEOS into an ethoxide form (deprotonated ethanol-missing $H^+$ from polar end) coupled with ethanol to fill micelle structure. Use of CTAB surfactant (a long alkyl organic molecule with a polar head group and non-polar tail) provides the structure directing function of Si species in solution from TEOS hydrolysis. Concentrated $NH_4OH$ (aqueous ammonia) was used to increase the pH of the reaction mixture in forming ethoxide species and to catalyze conversion of surfactant molecules to ionic form (release $Br^-$ ion). Dissolved $NH_4VO_3$ or $VOSO_4 \cdot 3H_2O$ aqueous solution added to the reaction mixture provided the needed transition metal ion for potential catalytic activity to the resulting material; since, silica (for example: Si-MCM-48) has little acidic or

ion exchange capability properties needed for catalytic reactions. [4,5] $NH_4^+$ cations from $NH_4OH$ solution produce the common ion effect where $NH_4VO_3$ metal precursor would not dissolve due to the equilibrium shifted to the left (reactants); however, according to powder XRD analysis in the results section, the $NH_4VO_3$ precursor was converted to $V^{5+}$ ion due to the formation of the Ia3d structure, as indicted in literature. [6-25]

When $VOSO_4 \cdot 3H_2O$ precursor was used in the synthesis of V-MCM-48, this would release $SO_4^{2-}$ anion, which would act in a similar manner to the $Br^-$ counter-ion in CTAB and effect condensation of the silica structure, as noted in literature. [10,26] Hydrolyzed TEOS provides the needed $Si^{4+}$ ions/negatively charged fragments (oligomers) for the formation of silica framework of metal-doped MCM-48. Ethoxide ($CH_3CH_2O^-$) species attacks the Si-O bond in TEOS [Si-(O-$CH_2$-$CH_3$)$_4$], and the resulting $Si^{4+}$ ion/negatively charged fragments (oligomers) form around the micelle structure. [3,12,13,22,27] Polymerization occurs with ethanol from hydrolysis of TEOS in solution entering the micelle structure of the surfactant molecules that cluster together to form spherical then rod shaped micellar structure. Silicate and vanadium ion species form around the expanding micelle structure according to electrostatic interactions that governed charge density matching. [12,24,28-31] Drying followed by calcination process removed the surfactant and further increased condensation of the framework both through heat and use of transition metal ion. [10,17,22,32] Gradual increase of the calcination temperature at 1°C/minute (1 K/minute) to 550°C (823 K) prevented resulting structure from collapsing, as noted in powder XRD in literature. [3] Finally, this modified novel synthesis made the finished V-MCM-48 mesoporous material in a two day period of time. [1-3]

## 5.3 Why the Modified Novel Synthesis would be Superior to the Hydrothermal one

The modified synthesis employed to synthesize V-MCM-48 would be simpler in comparison to other synthetic methods due to the decrease of the following: (1) time, (2) financial output, and (3) potential error. In contrast to the hydrothermal synthesis that would take several days to make the desired structure, MCM-41and/or MCM-48, [4,5,6,7,9,10,12,13,16,19,25,27,28,33-84] the modified synthesis from literature [1-3] required only two days to the finished product. Several synthesis routes of mesoporous materials need an average of ten days to produce either MCM-41/or MCM-48 using hydrothermal conditions. [8,14,17,18,23,24,32,85-102] Moreover, this modified synthesis uses common reagents without additional synthetic work, [1-3] unlike other synthesis schemes, which require and/or both purification coupled with additional synthesis of structure directing species: the surfactant. [8,14,24,32,85,86,90,92,95-97,99-101] Many synthetic procedures use several pH adjustments to obtain the desired mesoporous material [23,56,63,72,88,103-105]; whereas, the modified synthetic process employed to produce the V-MCM-48 mesoporous material only requires pH adjustment of reaction mixture once in the beginning of the reaction, [1-3] and it would not need expensive laboratory equipment (autoclave or heating unit, etc) common with the majority of hydrothermal synthesis routes. [4-14,16-19,21-25,27,28,32-140,142-144]

In contrast to the majority of synthesis schemes that produce mesoporous materials use an alkali metal ion containing precursor, such as NaOH, KOH, sodium silicate (various forms), colloidal silica (has $Na^+$ ion in it for stability), [4,6-18,22,24,28,32,37,40-42,44-47,49,51,53-57,60,62-66,69-73,85,86,88-91,94,100,103-107,110-112,115-117,119-122,124-139] the modified novel synthesis [1-3] uses concentrated $NH_4OH$ (aqueous ammonia), which would be a morphology catalyst in silica reaction. [34] Although the exact mechanism for how aqueous ammonia positive effects on the resulting structure has not been completely elucidated, the final product shown in the results section for the modified synthesis clearly reveals

the beneficial properties of aqueous ammonia. The negative effects of alkali metal ions on transition metal containing zeolite/zeolite-silica (M41S mesoporous materials) could not be over-estimated both from stability and catalytic related matters. [27,50,98,107,114,123] Pinnavaia and co-workers studied the effect of $Na^+$ ion on the framework of MCM-41, and caused the deterioration of the local structure due to cation in the framework (even with very small amounts of $Na^+$ ion in the framework!). [107] Nonetheless, Ryoo and Jun reported that the salt (alkali metal containing ion, such $Na^+$ ion) addition effectively increases polymerization of silicate framework through both chemical potential and electrostatic solution variables in the synthesis of mesoporous material, as indicated in $^{29}Si$ NMR larger $Q^4/Q^3$ ratio values (where $Q^4 = SiO_4$ fully condensed unit; $Q^3 = SiO_3OH$ less condensed unit); however, after the calcination process, the $Q^4/Q^3$ ratio was approximately the same as the non-salt treated mesoporous silica material. [72] This result infers the salt effect causes more silanol groups to condense before the calcination process, which would cause the material to have lower concentration of strained siloxane bonds (Si-O-Si) that could easily be attacked in hydrolysis. Even with the positive effects of $Na^+$ ion causing cross-linking and/or change of local pore structure through the application of various salts on the mesoporous structure, as reported in literature, [72,79,80,104,105,131] this could not compensate the negative effect that the sodium ion (or other alkali metal ions) had on the mesoporous structure upon hydrothermal conditions. [107] Coma and co-workers have reported that $Na^+$ ion has a negative effect on the structure and catalytic properties of titanium ion containing zeolites due to formation of crystallites that have little activity. [98] For Ti-MCM-41 and Ti-MCM-48, it was shown that the catalytic rate increased dramatically with the use of silica and base sources, which were absence of $Na^+$ ions. [27,98]

From the incorporation of transition metal heteroatoms into M41S mesoporous materials perspective, the use of alkali metal ions, in particular $Na^+$ ion, would prevent isomorphical substitution into the mesoporous framework, thereby would be needed to produce catalytic properties. [50,114,123] V-MCM-48 modified novel synthesis would require a minimum additional output in time and financial resources to be scaleable, [1-3] so it could be used potentially on an industrial scale if desired. Synthetic scheme developed by Stucky and co-workers/other workers produces high quality Si-MCM-48 + metal doped MCM-48 mesoporous material [8,24,32,86,92,95,96,100]; however, the synthesis requires the production and purification of special surfactant molecule, GEMINI, which adds additional time to the overall synthesis and, most importantly, increased cost. Nevertheless, other synthetic methods that use hydrothermal synthesis, which would not need purification of reagents, have been widely reported in literature. [4-13,16-19,21-23,25,27,33-84,87,89,91,93,94,98,102-126] These hydrothermal synthetic methods also produce mesoporous material, although according to Stucky and co-workers, [95] the GEMINI/CBDAC surfactants would be superior for the reproducibility of MCM-41 and MCM-48. [8,24,32,86,92,95,96,100] [Note: CBDAC would be cetylbenzyl ammonium chloride surfactant.] Repeated pH adjustments to a reaction mixture would require additional time and could potentially cause reduced reproducibility of the desired material, such as metal doped MCM-48, due to likelihood of inconsistent application of aqueous acid to synthesis gel/reaction mixture when not titrated, common in most synthesis strategies that employ pH as a structure enhancement method [50,56,63,72,73,75-79,100,104,107,125,126,131]; whereas, the modified synthesis produced the desired product consistently, as shown in the results section. [1-3] Calcination temperature process employed in the modified metal doped MCM-48 procedure had a gradual increase of 1 1°C/minute heating rate from room temperature (~25°C) to 550°C to enhance controlled condensation of silanol groups to $SiO_4$ units without producing large

numbers of strained siloxane bonds (Si-O-Si); whereas, in literature the calcination step would be completed rather quickly at ramping temperature rates of 2 °C/minute to 5 °C/minute. [62,97,99] Many synthetic methods in literature simply heat the sample up to the final peak value with no gradual temperature increment. [94-96,98,104,135,136] Rapid calcination temperature increase could lead to structural damage and/or collapse of pore channels. In attempt to obtain the maximum mesoporous characteristics of M41S materials, few researchers calcinated their M41S samples at 450°C or lower (723 K). [16,67,101] At this low calcination temperature, the cetyltrimethylammonium positively charged surfactant ($CTA^+$), such as CTAB or CTACl (cetyltrimethylammonium chloride), will not be consumed until approximately 460°C (733 K) according to thermal gravimetric analysis (TGA), which could cause residual surfactant in the pore structure and/or incomplete condensation of silanol groups in the mesoporous material. [145] Finally, only a stir plate and polypropylene container with appropriate size Teflon coated magnetic stir bar would be needed to make several gram qualities: low amount of equipment requirements could cause this modified novel synthesis to reach profitable industry application assuming Si-MCM-48/metal doped MCM-48 had several applications.

## 5.4 Areas that Need Further Improvement in the Modified Novel Synthesis

Certainly, the modified novel synthesis from literature [1-3] would be an excellent synthetic route; however, this synthesis method has a few areas that need further improvement: (1) need greater number of higher order XRD powder reflections, (2) lower cost surfactant + silica source, and (3) higher percent yield of product. In contrast to many hydrothermal synthetic methods that provide higher quality (greater number of higher order reflections) metal doped MCM-48 (or Si-MCM-48), [2-14,17-19,21-25,27,29,32-35,40,41,45,51,53,55,56,64,66,78-82,85-88,91-96,101,106,108,109,111,114-116,122-124,126,128,135-137] such as Stucky and co-workers, [8,24,32,35,86,92,95,96] the modified synthesis [1-3] with vanadium ion had up to five reflections, as shown in results sections of powder XRD diffractograms. [Note: the following powder XRD diffractograms in literature would be similar to ours and have minimally five reflections. [3,65,66,78]] In particular, Stucky and co-workers made Ti-MCM-48 using GEMINI surfactant under hydrothermal conditions to obtain a mesoporous material that had ten reflections. [32] They concluded, that for metal doped MCM-48, it should have minimally eight-to-ten reflections to be considered high quality metal doped MCM-48, and Si-MCM-48 should exhibit thirteen reflections. [86,92] From these literature results, [32,86,92] this would imply that the experimentally derived V-MCM-48 mesoporous material would not be the highest quality. In addition, the modified synthetic method needs further attention in replacement of the ionic surfactant, CTAB, and molecular organic silica precursor: TEOS. Both of these reagents would cost more than non-ionic block co-polymers and several other silica sources used in literature: sodium silicate, ammonium silicate, tetramethylammonium silicate, colloidal silica, and fumed silica. [22,28,33,35,37-39,43,50,55,58,61-66,72,73,75-77,79-81,84,86,88,89,98,100,103-105,107,108,112-129,131,133,135,136,138-140,143,144] $NH_4VO_3$ exhibits insolubility in aqueous phase, thereby prevents complete incorporation of vanadium ion into V-MCM-48: this requires use of a more expensive vanadium metal precursor, $VOSO_4 \cdot 3H_2O$. Finally, the modified synthetic procedure had a percent yield of Si in Si-MCM-48 of only up to 30% with rest of silica as forming negatively charged fragments (oligomers) in solutions phase, according to literature to due to the dilute aqueous reaction conditions employed in the Stober's synthesis [100,121] ; however, the modified novel synthesis has an incorporation of metal ion into framework positions of 88-97% vs. only 80-88% for hydrothermal one. [2,3]

## 5.5 Limitations of Modified Novel Synthesis for V-MCM-48

The major limitations of this modified novel synthesis [1-3] includes pore size increase above the 2-3 nm (20-30 Å) size range typical in CTAB prepared mesoporous materials, lower concentration of fully condensed $SiO_4$ units, and alternative to use of expensive $VOSO_4 \cdot 3H_2O$ metal precursor. [2,3,5,7,9-12,17,22,33-36,39,41,42,44-46,50-53,55,57,58,60,63-67,70,73,75,77-83,89,91,93,102,106-111,113,115,116,118,120-126,129,130,132,133,138-144] Researchers have been able to implement a mesoporous materials synthetic strategy to increase the pore diameter greatly with CTAB surfactant using space-filling molecule, 1,3,5-trimethylbenzene (TMB), under hydrothermal conditions. [119,133,136,143,144] Despite the breakthrough in pore diameter enhancement with use of CTAB + TMB, the resulting mesoporous material would be of lower quality, as indicted with only one broad powder XRD peak for MCM-41and lacks pore structure uniformity. [35,140,145,146]

Stucky and co-workers developed a charge matching and cooperative organization models with surfactant molecules coupled to silica oligomers to produce a larger pore material in comparison to M41S mesoporous materials. [129,147] Despite the pore size limitations of CBCAC, CPCl (cetylpyrdinium chloride) and GEMINI surfactants reported in literature, [8,14,24,32,35,62,85,86,90,95,97,99,148] these researchers were able to increase the pore size through use of GEMINI surfactant and TMB in MCM-41 mesoporous material. [149] Due to the upper pore size limit achieved with use of GEMINI surfactant and TMB, Stucky and co-workers employed the use of non-ionic surfactants in acidic medium to produce mesoporous materials with pore diameter of approximately up to 300Å. [146] This novel mesoporous material was denoted as Santa Barbara Acidic (SBA) with number that indicated type of structure made under acidic conditions. [83,92,112,117,142,146,149-153,155,156] The non-ionic block co-polymers surfactant/anionic surfactant mixtures could be adjusted by the pH value to make the desired pore sizes with relative ease of formation of Ia3d cubic structure. [21,26,88,154] Challenges for non-ionic surfactants to dominate mesoporous/nanostructure materials synthesis include: complete removal of surfactant from host structure, development of materials that have little defect formation, and formation of three-dimensional (3-D) structures of irregular shapes. [157] In addition, the application of non-ionic surfactants in basic (high pH reaction conditions) led to less organized mesoporous structure with use of $NH_4OH$, as reported in literature. [158]

The modified novel synthesis produced spherical shaped metal doped MCM-48 nanoparticles [1-3]; whereas, other synthetic routes made MCM-48 shaped nanoparticles of various geometries: irregular, truncated octahedral, and truncated dodecahedral. [18,22,49,79,96,100,108,114,122,129] Unger and co-workers indicated that aqueous ammonia would be the reason for the formation of spherical shaped particles in room temperature (~25°C) (modified) synthesis [1-3,34]; however, a review of literature appears to show that silica precursor, surfactant, solvent, and heating synthesis period affect the final particle morphology. [18,22,49,79,96,100,108,114,122,129] For example, researchers using CTACl, NaOH, and TEOS under hydrothermal conditions (393 K/3 days and other 368 K/4 days) made truncated octahedron-roundish particles. [18,49] Stucky and co-workers made irregular shaped particles with same reaction variables except use of CTAB and hydrothermal reaction of 383 K/3days. [129] Closer inspection of various literature sources would appear to reveal that aqueous ammonia enhances the formation of uniform, non-agglomerated spherical particles. [2,3,34,100] Galarneau and co-workers made MCM-48 spherical particles from NaOH, TEOS, and GEMINI surfactants under hydrothermal conditions; nevertheless, the particles appear to not be uniform in size, as shown in scanning electron microscopy (SEM) image. [100] They further reported that particle size could be increased through elevated

hydrothermal temperature condition due to Ostward ripening, where larger particles form from smaller ones. Use of fumed silica and sodium silicate with ethanol and various surfactant and/or elevated temperatures (need elevated temperature to increase the g-value in the packing parameter equation $g = V/a_0 l$) plus different bases (NaOH-sodium hydroxide, CTAOH-cetyltrimethylammonium hydroxide, and TMAOH-tetramethylammonium hydroxide) produced truncated rhombic dodecahedral MCM-48 particles. [22,79,108,114,124]

The importance of aqueous ammonia was demonstrated in literature with formation of sub-micron and micron size particles that were both uniform in size and non-agglomerated. [159,160] In an attempt to understand how $NH_4OH$ and CTAB interact to form $Fe_2O_3$ nanoparticles, Oh and co-workers reported $NH_4OH$ effects the shape that CTAB takes by selective absorption onto the particle surface through the modification of hydrolysis and condensation steps of a particular precursor. [161] Therefore, kinetic and thermodynamic parameters were modified in particular formation; since, $NH_4OH$/CTAB version had different particle morphology. Without the $NH_4OH$/CTAB combination, the iron particles formed non-porous solids, but, with use of $NH_4OH$/CTAB, the Brauner-Emitter-Teller (BET) surface area doubled for the iron(III) oxide particles. Zhang and co-workers indicate that $NH_4OH$ might combine with surfactant molecules through enhance hydrogen bonding interactions to form micelles with increased flexibility and length in vanadium and chromium MCM-41. [68]

The modified novel synthesis might have produced a silica material with lower concentration of condensed silanol groups (Si-OH) in comparison to the hydrothermal synthesis of M41S mesoporous materials; since, the hydrothermal conditions cause silanol groups to condensate readily to $SiO_4$ units due to the elevated temperature providing the activation energy to enable rearrangement of silicate bonds, as inferred in literature of greater condensation with increased hydrothermal temperatures. [35,100,121,129] However, the majority of M41S mesoporous materials with transition metal ion incorporation have a reduction in the ordering of the pore structure, [9,11,17,38,62,69,71,162,163] and other literature claims use of CTAB in comparison to CTACl led to increased condensation of silanol groups under hydrothermal conditions, according to $^{29}$Si NMR larger $Q^4/Q^3$ ratio values for CTAB vs. CTACl prepared Si-MCM-48 . [10] Researchers also have reported highly resolved powder XRD diffractogram peaks with use of CTAB vs. CTACl surfactants in M41S mesoporous materials synthesis. [63,113] Finally, use of $VOSO_4 \cdot 3H_2O$ would increase the cost of the modified synthesis, although the desired V-MCM-48 structure consistently formed even at higher metal loading; therefore, the $SO_4^{2-}$ anion would appear to participate in a similar manner to $Br^-$ anion in CTAB in the synthesis: this would be perplexing due to where on the Hofmeister list sulfate and bromide anions fall-direct opposites. [109,113,142,164]

## 5.6 Positive Attributes of V-MCM-48 Modified Novel Synthesis vs. Other Synthetic Routes

Comparison of the modified novel isomorphical substitution of transition metal ion for $Si^{4+}$ ions in silica framework of M41S mesoporous materials would have several positive attributes: (1) transition metal ion locked more firmly to the silica framework, and (2) retention of structural values in comparison to other synthesis methods of doped silica materials. [2,3,17,65,66,70,73,75,93] With vanadium ion in one of the $Si^{4+}$ ion positions bonded to several oxide (oxo) ligands, this would prevent both blocking the pore channels and growth of transition metal crystallites, such as $V_2O_5$. [17,70,73,75,93] In $VO_x/SiO_2$ materials at elevated temperatures the vanadium ion will become mobile on the silica support due to poor acid-base interaction and forms $V_2O_5$ crystallites, especially at higher metal loading.

[165,166] Zhao and Goldfarb determined through Q-band electron pair resonance (EPR) that $Mn^{2+}$ ion in the pores of M41S mesoporous materials would be mobile even after calcination process. [135] Grafting/impregnation of transition metal ions onto the pore surfaces of M41S mesoporous materials using silanol groups would reduce the structural size characteristics (pore diameter, pore volume, and surface area), although researchers claim only slightly. [8,24,42,46,86,90,92,95-97,99] Similar to $VO_x/SiO_2$ material, the use of transition metal ions spread over the surface of M41S materials would cause formation of undesirable metal crystallites. [51,81,91,111] Bischof and co-workers [46] impregnated bare Si-MCM-41 and Si-MCM-48 with copper(II) di(actetato) and obtained metal crystallites with the majority of samples below 220°C (473 K), which would be close to the temperature values employed in calcination of organic-metallic complexes grafted in M41S mesoporous materials. [8,24,42,86,90,92,95-97] This formation of metal crystallites on silica occurs for many transition metal ions on silica support, such as $TiO_2/SiO_2$, $Co_3O_4/SiO_2$, $MgCr_2O_4/SiO_2$, and $CuO/SiO_2$. [98,167] The isomorphical substitution of transition metal ion for $Si^{4+}$ ion in M41S mesoporous materials would have slightly reduced the pore diameter, pore volume, and surface area, as comparison of literature with metal ion in framework vs. metal ion on surface of pore walls. [8,24,38,42,46,60,61,74,76,85,86,90,92-97,99]

Ying *et al*. comments on the difficulty of incorporation of transition metal ions in place of $Si^{4+}$ ion in M41S mesoporous materials [162]; moreover, Stucky and co-workers indicate grafted Zr-MCM-48 would be superior to framework incorporated Zr-MCM-48 due to control of $Zr^{4+}$ ion distribution of species on pore wall surface. [95] Grafting techniques use silanol groups to bind on the pore walls usually through the use of transition metal organic complex in solvent spread over parent M41S mesoporous material and allowed to soak into the pore structure and/or use of gas-phase molecular designed dispersion (MDD), [8,24,42,86,90,92,95-97] which would require an additional calcination step to remove the organic matter from the organometallic complex. The use of MDD produces dispersed transition metal ions in predominantly tetrahedral coordination over porous supports, but only up to 7 wt% metal loading [168]; therefore, the report by Stucky and co-workers would imply the possibility of vanadium ion in polymeric and/or $V_2O_5$ cystallities at even higher metal loading of 8.7 wt%. [24]

Gontier and Tuel found that with increased metal loading of vanadium ion in hexagonal mesoporous material (HMS) and elevated calcination temperature led to significant loss of surface area from ~1000 $m^2/g$ to ~400 $m^2/g$. [169] The greater the calcination temperature and lengthening of heating time would cause the mesoporous material (or any solid porous material) to fuse together with pore channels combining, thereby leads to lower surface area. Additional examples of this would be in solid-state chemistry of ceramic particles made at elevated temperature and lengthen heating period, such as the works of many researchers in the photocatalytic field of water-splitting. [170-205] Reduction of surface area could have the adverse effect of more metal crystallite growth at the same metal loading and/or also a lower catalytic activity due to kinetic and mass transfer factors of the probe molecules only able to interact on the external surface of solid. [23,28,98,206] Researchers studying the dehydrogenation reaction of ethanol over V-MCM-41 at elevated temperatures found that at higher metal loading led to major decrease of desired ethylene product and had a reduced surface area mesoporous catalyst. [38] Kudo and others' in the photocatalytic field of water-splitting indicate greater surface area would increase light absorption area, thereby potentially could cause greater hydrogen and oxygen formation. [207-209] In $WO_3/TiO_2$ and related composite material the lower surface area would be compensated by the increased charge separation of charge carriers ($e^- + h^+$), thereby leading to en-

hanced product formation. [210-216] If charge carrier separation was constant in two metal doped materials, the higher surface area metal mesoporous material would exhibit greater catalytic rates due to large dispersion of catalytically active metal ion species with enhanced opportunities for probe molecules to interact in the pore structure. [23,28,51,98,206] An example of high surface area and enhanced charge separation would be mesoporous $TiO_2$ material that had approximately double the surface area and over two fold increase in photodegradation of acetone ($CH_3COCH_3$). [217]

Researchers have attempted to synthesize and apply transition metal ions to MCM-48 silica support due to greater kinetic and mass transfer characteristics of three-dimensional pore network in comparison to unidirectional metal doped MCM-41 structure. [65,94] Even with slightly higher surface area and increased vanadium ion metal loading in $VO_x$-MCM-48, Lopez Nieto and co-workers found that the framework incorporated vanadium ion in MCM-48 led to the largest catalytic rate gas-phase selective oxidation of propane ($C_3H_8$). [94] Therefore, one could conclude use of a grafting/impregnation of metal ions would cost more financial resources both in time and materials without justified improvement in catalytic activity in mesoporous materials, as reported with large amount of leaching of metal ions in solution phase with exception of Maier and co-workers [118] report of no vanadium ion leaching in MCM-41 liquid phase reaction. [85,96,97,99,118,218,219]

## 5.7 Effects of Isomorphical Substitution of Metal Ions Into Framework of MCM-48

Isomorphical substitution of metal ions into framework both lowers the ordering of the pores and could cause a reduction in durability of resulting structure. [9,51,92] Zhang and Pinnavaia, however, indicate vanadium ion actually increases condensation and cross-linking of the silanol groups, thereby could increase durability of MCM-48 mesoporous materials over parent silica form through increased pore wall thickening, according to $^{29}Si$ NMR $Q^4/Q^3$ ratio value. [17] Lanthanides ($Ce^{4+}$, $La^{3+}$) substituted into the framework increased the durability of the mesoporous material in aqueous phase reactions against hydrolysis. [9,11] The researchers also reported that too great amount of metal ion had an adverse effect and reduced the durability of the mesoporous material due to lattice strain. In many literature reports of framework incorporated metal ions in M41S mesoporous materials, the research finding indicted enhanced pore wall thickness and cross-linking of pores, as found in Zhang and Pinnavaia research results on metal doped MCM-48. [9,11,17,38,62,69,71,138,163] Additionally Stucky and co-workers present a similar case of enhanced stability of SBA mesoporous materials against water attack (hydrolysis) due to thicker pore wall. [149] Stucky and co-worker further indicate that grafting of metal ions to M41S mesoporous material provides additional resistance to hydrolysis in aqueous phase attack due to consumption of silanol groups. [92,96] However, this assumes all of the silanol groups in the M41S mesoporous material were consumed and these researchers' finding that silanol groups still present after application of zirconium(IV) isoproxide solution, according to photoacoustic-fourier-transform-infaraed (PAS-FTIR) analysis. [95] Vansant and co-workers silylated the surface of MCM-48 in an attempt to provide binding sites where water could not attack the siloxane bond and prevent extensive leaching of transition metal ions after $VO_x$ grafting, although the surface area and pore volume decreased significantly (~10%). [97,99]

Reviewing the Brauner-Emitter-Teller (BET) surface area of the mesoporous materials, according to literature, [220] would not provide an accurate description of what effect the metal ion had in the structure. For example, claiming that successful isomorphical substitution of the metal ion in place of $Si^{4+}$ ion had occurred due to retention of large surface areas would not be adequate proof. The reason would be that collapse of the pore walls would still

have relatively high surface areas. Rodrigues *et al*. claims that their Cr-MCM-48/$TiO_2$ samples have successfully incorporated the metal ion into framework position due to retention of high surface area. [15] Researchers found that the surface decreased with more Mn ion loading in MCM-41 framework, thereby infers collapse of pore structure. [132] This difference of what factors constitute substitution of a given metal ion into a framework position from various research groups warrants other characterization methods would be needed to be employed to determine with relative certainty if substitution of metal ion had occurred.

## 5.8 Research Project Goals Met with V-MCM-48 Modified Novel Synthesis

This research project set out to use the modified novel synthetic method [1-3] to make V-MCM-48 and use it in environmental remediation to convert toxic probe molecules to innocuous products: $CO_2 + H_2O$. Klabunde and co-workers were attempting to exploit three major variables related to catalysis work: (1) high surface area, (2) three-dimensional pore networks of MCM-48, and (3) isomorphical incorporation of large quantities of transition metal ions to potentially induce photocatalytic activity. The high surface area permits for more metal ion to be spread over the support without forming less active metal oxide crystallites ($V_2O_5$). For example, only approximately up to 5 wt% vanadium ion could be placed over silica without forming a considerable amount of $VO_x$ species. [221-223] In V-MCM-48 Suib and co-workers found they could incorporate up to approximately 6.7 wt% vanadium ion in MCM-48 with little formation of $VO_x$ species ($V_2O_5$ species etc.). [6] Three-dimensional pore structure of MCM-48 permits probe molecules to flow in three-dimensions, so from a kinetic and mass transfer point of view, this would enable more interaction with active sites (transition metal ions) without causing catalyst/support becoming plugged, such as in the case of unidirectional pore structure of MCM-41. [2,3,6-8,11-14,22,25,27,32,36,44,47,51,66,82,83,86,88,91,93,95,96,100,106,110-112,114,116,120,122,123,125-128,217,224] By incorporation of large quantities of metal ions, in theory, this would lead to greater catalytic activity. In liquid phase reaction of Cr-MCM-48 with various organic molecules, such as ethylbenzene, cyclohexane, and cyclohexane, Selvam and co-workers observed direct increase in product yield with more Cr ion in MCM-48. [66] These researchers came to a similar findings with V-MCM-48 in liquid phase catalysis of cyclohexane oxidation to cyclohexanol. [93] Selvam and co-workers determined through inductively coupled plasma-atomic emission spectroscopy (ICP-AES) analysis of these transition metal doped MCM-48 catalysts had essentially little to no loss of active phase (transition metal ions) after the initial liquid phase reaction, and the product yields from the catalytic reactions continued to be large even after several reaction cycles. [66,93] In conclusion, the goals of developing a photocatalytic mesoporous metal doped material were met with modified novel synthesis. [1-3]

## V-MCM-48 Discussion Characterization: Part II

## 5.9 Introduction

This sub-section will illustrate the value of the three characterization methods employed on experimentally synthesized Si-MCM-48 and V-MCM-48. The initial characterization method to determine whether the desired structure had formed was the powder X-ray diffraction analysis. If a positive outcome resulted, then, the metal doped MCM-48 mesoporous material would be subjected to diffuse reflectance ultra-violet-visible spectroscopy to elucidate both the coordination geometry of $V^{5+}$ ion in matrix and the light absorption properties. Finally, the degree of porosity has been analyzed by nitrogen adsorption-desorption characterization method in Si-MCM-48 and V-MCM-48.

## 5.10 Powder X-ray Diffraction (XRD) Analysis of Parent Si-MCM-48 & V-MCM-48

By the experimental powder XRD diffractograms in the results section of this thesis, as shown in Figure 4:1, it was inferred that the cubic structure corresponding to the Ia3d space group had formed even at large $V^{5+}$ ion loading in comparison to both Si-MCM-48 and metal doped MCM-48 in literature. [2-14,16-19,21-25,27,29,32-35,37,39-41,44,45,47,51-53,55,56,60,64-67,78,81,82,85-89,91-97,99,100,101,106,108,109,111,114-116,121-123,126-129,133,135-137,143] All of the powder XRD diffractograms show the characteristic first two primary peaks assigned to the cubic MCM-48 structure with Miller index of $d_{(200)}$ and $d_{(220)}$. Nonetheless, the powder XRD peak intensity of the individual diffractograms V-MCM-48 compositions had a reduction with increased $V^{5+}$ ion substituted directly into the framework position for $Si^{4+}$ ion. This diffraction peak intensity reduction trend has been extensively indicated throughout literature of transitional metal doped mesoporous materials where direct incorporation synthesis was employed. [4-6,9,11,16,17,32,37,39,45,46,50,52,53,70,73,74,76,78,81,84,91,98,106,132,138,141] Why there was a reduction in peak diffraction intensity could be due to the reasons provided in the results section, according to previous research: (1) random placement of transition metal ions in structure, thereby lower periodic nature of material; (2) transition metal ions have a different absorption factor for X-rays; and (3) potentially partial collapse of mesoporous structure. [6,7,220,225] The random placement of $V^{5+}$ ions/other matter in pores would cause the increase of incoherent scattering in the silica framework due to the fact that the scattering would vary between planes and those with only the structural member $SiO_4$ unit, as shown with lower powder XRD peak diffractograms in literature. [6,7,46,91,92,102,220,225] The effective nuclear charge ($Z_{eff}$) would be less for $V^{5+}$ ion then for $Si^{4+}$ ion, so an electron in the inner shell could be involved in ionization process due to lack of valence electrons, and fact that vanadium ion would give up an electron with longer wavelength X-ray due to larger atomic orbital (Four coordination geometry: $V^{5+}$ =.495 Å vs. $Si^{4+}$ = .40 Å). [226] Finally, partial collapse of mesoporous structure would require the use of another analytical method, as indicated in results section, and future experiment experiments will be proposed in the last portion of the discussion section.

## 5.11 Background Theory of Powder XRD

Powder XRD instrumental analysis mechanism would function through the X-rays knocking off the electrons in both the inner shell and valence orbital of an atom, which produce elastic/coherent and inelastic/incoherent scattering. [227] Tightly held electrons would provide coherent scattering from the inner shell; in contrast, loosely kept valence electrons would produce incoherent scattering. Due to the fact that all free electrons resonate in an identical fashion, this factor could be represented through the intensity peak diffraction value by Thompson equation, which would have dependence components of both angular and polarization. Also, the result of the instrumental X-rays knocking off the loose valence electrons has been given the name Compton scattering to refer to inelastic frequency decay. One could employ the guitar string model analogy to explain why there would be elastic/coherent and inelastic/incoherent decay of frequency from the X-rays ionizing the two types of electrons in an atom: inner shell and valence shell. Imagine two guitar strings: one tightly would and other loosely strung. When both strings were plucked, the string with more tension (amount of resistance) would resonate (vibrate in wave pattern) at a higher frequency; whereas, the loosely wound string would vibrate at a lower frequency value and decay in pitch (amount of amplitude-size of wave) at an increased rate. In a similar manner the tightly held electron from the inner

shell would be expected to resonate at a higher frequency in contrast to the loosely bound electron in valence orbital of an atom. Result of these two process cause both diffraction peak(s) and baseline noise.

Employing the guitar string analogy to explain the angular dependence component of both coherent and incoherent scattering coupled with the Bragg's law, $n\lambda = 2d\sin\theta$, the result would mean that at lower diffraction angles $2\theta$, the free electrons, from ionization with the X-rays, would have shorter wavelength/higher frequency. [227] This relationship could be shown that lower frequency from the inelastic movement of free electrons results in the Compton scattering diffraction peaks at higher $2\theta$ angles. However, as indicated with the guitar string model, the lower frequency that free electrons resonate at would result in many closely spaced tiny peaks, which would be known as the Compton background (noise). Therefore, the relationship of higher frequency and lower $2\theta$ angle, employing the guitar string analogy, would explain why the diffraction peaks at lower $2\theta$ angles have enhanced peak diffraction intensity with little Compton scattering. In summary, the general model of how X-rays interact with isolated atom(s) could be expanded to the unit cell due to the assumption that the X-rays act on the individual atoms' inner and valence shell electrons in an identical fashion, which would provide a link to amplitude (measure of diffraction for the individual planes that comprise the many unit cells) and finally the square of amplitude will give the peak diffraction intensity for individual planes in the material. [Note: the amplitude value squared would be done to eliminate the imaginary portion of the intensity equation, which would provide the real physical intensity value.]

## 5.12 Application of X-ray Diffraction Theory on Metal-Doped MCM-48

From the above review of the mechanism of how X-rays interact on an individual atom, this idea could be expanded to include individual unit cells (collection of atoms) to network of unit cells that could comprise several thousand in a crystallite particle. The unit cell could be cut into planes where the atoms or portions of would lay on these planes. Employing the idea of the guitar string model from literature, [227] coupled with an expansion of the unit cell followed by a collection of unit cells with planes cut through them, one could reason why increased $V^{5+}$ ion content randomly placed in the unit cell would cause a reduction in peak diffraction intensity, such as in V-MCM-48. When the X-rays pass through the unit cell, due to random placement in the unit cell and therefore randomly in certain planes of the material, the $V^{5+}$ metal ion inner shell electrons will have a lower frequency and decay rate, as presented in an earlier. Result would be lower amplitude from the identical unit cell with the exception of $V^{5+}$ in place of $Si^{4+}$ ion. As the number of the unit cells that have $V^{5+}$ metal ion in them increases, the diffraction peaks expected from the $SiO_4$ parent unit all would decrease due to the fact of the cumulative nature of peak diffraction intensity, as the amount of a given plane in a material. [227-229] This would explain why Compton scattering (noise) was increasing in V(10)-MCM-48 (highest $V^{5+}$ metal ion loading in MCM-48) in Figure 4:1 of results section and simultaneously reduction in higher frequency peaks/lower $2\theta$ angle. In conclusion, the reduction of peak diffraction intensity trend with larger amounts of $V^{5+}$ ion loading in MCM-48 coupled with lack of higher angle $2\theta$ diffraction peaks would indicate the mesoporous material was amorphous (lack of consistent number of the same unit cell arrangement). [32,92,228]

Powder XRD peak diffraction shifts could provide clues as to the degree of crystallinity of a material, although M41S mesoporous materials would be considered amorphous from a short-range order view-point; therefore, the uniform pore network in M41S mesoporous materials would be the only component of crystallinity.

[10,11,52,53,89,101,230,231] Thicker walled material of similar atomic structure would have higher resonance frequency, and thereby diffraction peak shift to lower Bragg 2θ angles. [227-229] This would be due to crystal structure/symmetry and macrostrain in the structure. [228] In contrast, thinner walled material would exhibit lower summation of higher frequency resonance due to the fact that the electrons will pass through the thinner material with less obstruction(s), thereby would cause the peak to be shifted to the right in powder XRD diffractograms. [92,227,229] Likewise, the degree of condensation of the structure could be inferred by the amount of the secondary peaks at higher angles; since, this section of the 2θ axis would be dominated by Compton scattering (background noise) from less tightly held electrons in the material, such as: $SiO_3OH$, and $SiO_3O^-$. These secondary peaks would provide a measure of how much of the walls were comprised of fully condensated $SiO_4$ units. [8,24,32,86,92,95,96,100] Secondary powder XRD diffraction peaks would have reduced intensity due to the coherent resonance frequency decay rate, as illustrated earlier with the guitar model and Bragg's law. [227] [One might conclude the 2θ scale in powder XRD was similar to a guitar string with low angles at tightly wound and higher angles having increased string looseness.] Reviewing the experimental powder XRD diffractograms in the results section, the MCM-48 structure formed even at large $V^{5+}$ loading; however, the V-MCM-48 mesoporous material would have little to none of the higher order peaks in the 6-8° 2θ range, as reported in literature of both high quality Si-MCM-48 and framework metal doped MCM-48. [8,24,32,86,92,95,96,100] [Number of higher order powder diffraction peaks and greater intensity would infer the measure of ordering in the M41S structure: this trend would be due to greater condensation structure with $SiO_4$ units and intensity represents the amount of a given phase.] [32,92,227-229]

More of a given component in a material that was uniform would lead to greater peak diffraction intensity, and the larger the crystallite particle size would cause the peaks to increase in sharpness while the smaller sized crystallite particles would exhibit peak broadening. [228,229] Peak broadening would be due to either or both defects in structure of material and/or not enough lattice planes to reduce the incoherent resonance frequency from the loosely held electrons. [227-229] Viewing the experimental V-MCM-48 powder XRD diffractograms in Figure 4:1 in the results section, characteristic assignment of two peaks for cubic Ia3d space group MCM-48 structure appeared to be sharp with perhaps intermediate amount of peak broadening particularly at the base of each of these peaks. [229] Peak broadening would not be common at 1 μm (1000 nm) or above. Stober's synthesis has been reported to make smaller crystallite particle sizes of approximately 650 nm, so it would be thought potentially that the V-MCM-48 particles experimentally made could be of a few hundred nanometers in size. [160] This would explain why small qualities of metal crystallites ($V_2O_5$) could not be detected with powder XRD analysis from peak broadening and low intensity in the baseline of the diffractogram. [228,229] In summary, powder XRD analysis would provide an avenue to determine the long-range order of a given structure with relative ease due to easy sample preparation; however, other analytical methods employing various instruments would yield greater insight into the local environment of V-MCM-48: future research ideas will be provided in the last part of the discussion section.

## 5.13 Diffuse Reflectance Ultra-Violet-Visible (DR-UV-vis) Spectroscopy Analysis

From viewing the experimental DR-UV-vis absorption vs. wavelength plot in Figure 4:2 of results section, one could interpret that increased $V^{5+}$ metal ion in MCM-48 led directly to higher light absorption. This phenomenon would be expected due to many transition metal ions having light absorption properties in UV-vis wavelength.

[81,92] From the comparison of literature values, [24,57,90,93,94] the experimental V-MCM-48 could have the following $V^{5+}$ ion species: tetrahedral, square-pyramidal, and octahedral. It was found from previous research literature $V^{5+}$ ion surround by four oxide (oxo) ligands produced higher energy absorption of approximately 250 nm, which would be close to the experimental value obtained. [24,57,73,90,93,94,232] Followed by the $VO_4$ framework species, the shoulder portion of the broad peak might have a combination of square-pyramidal and octahedral $V^{5+}$ coordination centers on the pore walls of MCM-48 from similar peak positions listed in literature on V-MCM-48. [57,85,90] In addition, the formation of polymeric $V^{5+}$ species could have formed at higher metal loading in MCM-48, such as Si/V = 10 (~8.33 wt%); since, polymeric vanadium species formed at lower loading in MCM-48 in previous literature research. [57,85,90,93] Vansant and co-workers found through DR-UV-vis spectroscopy that only at 3.5 wt% vanadium ion loading in direct incorporation synthesis route in MCM-48 had polymeric $VO_x$ species coupled with several other types with deconvolution of absorption peaks similar to the experimental V-MCM-48 in the results section. [85] Finally, Si-MCM-48 was found to not have any light absorption from 200-800 nm range, as expected according to literature. [81,92]

## 5.14 $N_2$ Adsorption-Desorption Analysis of Si-MCM-48 & V-MCM-48

As seen in the $N_2$ adsorption-desorption isotherm of V-MCM-48 in the Appendix B-B:1, the shape of the isotherm would be considered type IV with a H2 hysteresis loop, after reviewing literature. [3,30,33,140,220,233-240] International Union of Pure and Applied Chemistry (IUPAC) classification of type IV isotherms would belong to mesoporous materials. [241-246] The characteristic that sets apart the type IV isotherm would be its capillary condensation step (inflection range). The size and steepness of the slope would infer the degree of pore uniformity. [30,33,220] Previous research indicated this particular portion of the $N_2$ absorption-desorption isotherm plot to be critical attribute for mesoporous materials. [220,236,244-247] Therefore, reviewing the experimental $N_2$ isotherm reveals the pores would not all be of the same size; since, there was hysteresis (deviation from the adsorption/desorption branches) and the size (length of capillary condensation was longer then usual) of inflection step. [33,220,234,245,247-249] According to IUPAC classification of hysteresis loops, the experimental $N_2$ isotherm hysteresis loop would resemble an H2 one. [245] Comparison of this $N_2$ isotherm with literature of other mesoporous materials in the SBA family would be close in similarities both adsorption-desorption branches. [235,238,239,241,249] The researchers indicate this hysteresis shown would be indicative of ink-bottle pores. IUPAC reference literature report $N_2$ phyisorption analysis of ink-bottle pore characterization has several underlying factors that affect this type of structural formation: (1) capillary, and (2) network. [234,238-241,249]

An explanation of the capillary condensation phenomenon would involve the $N_2$ gas density increasing at the interface more then in the bulk state, and the multilayer addition of $N_2$ molecules on the surface of the pore walls results in the formation of a meniscus (similar to meniscus in the graduated cylinder used in chemistry laboratory). [220,236,245-247] When the equilibrium pressure had been reached in the material of interest, the addition of more adsorbate ($N_2$ gas) would lead to saturation point, which would be completed at high relative pressure ($P/P_0$) with $N_2$ adsorbing at the external surface between the particles. Hysteresis generally occurs when evaporation and condensation rates were not the same. $N_2$ adsorption occurs at approximately $P/P_0 = 0.20\text{-}0.42$ but with a difference leads to a change in desorption slope value vs. adsorption. This would cause the elimination of the meniscus. The effect of

various sized pores in a network porous solid such as MCM-48 would complicate the release of the $N_2$ adsorbate and further increase hysteresis due to one portion of the pore channel releasing $N_2$ faster than other.

An explanation for ink-bottle pore structure formation may be due to the larger transition metal ion size in place of $Si^{4+}$ ion. For example, substitution of $V^{5+}$ ion in four coordination positions as $Si^{4+}$ ion would be 0.495 Å vs. 0.40 Å for $Si^{4+}$ ion. [93,226] Trends in most zeolite chemistry substitution would follow larger bond length with framework incorporation of a larger transition metal ion for $Si^{4+}$ ion with the $Al^{3+}$ ion as the main exception reported in literature. [17,19,85,93] Moreover, the increase in the unit cell has been accepted by researchers to be a first approximation of metal substitution for $Si^{4+}$ ion. [17,85,93] When coupled the random distribution of $V^{5+}$ ion with larger atomic radii and longer bond length, this could explain why the experimentally made V-MCM-48 mesoporous material might have the ink-bottle pore structure. Although the $N_2$ isotherm for Si-MCM-48 could not be located, one could assume with reasonable certainty that both of the literature and experimental Si-MCM-48 structures would have similar texture properties with little to no hysteresis. [24,33,62,249]

## 5.15 What Comprises the Regions of an $N_2$ Adsorption-Desorption Isotherm Plot

Nitrogen physisorption analysis could be used to probe the textual characteristics of a given porous material. [220] The nitrogen isotherm for mesoporous materials, such as M41S structures, may be comprised of five regions. Reviewing the experimental V-MCM-48 $N_2$ adsorption-desorption isotherm plot in the Appendix B-B.1 starting from left at approximately zero relative pressure ($P/P_0$ where P = equilibrium vapor pressure; $P_0$ = saturated vapor pressure), [140,236] the uptake of $N_2$ gas would begin with nitrogen adsorbing in the internal and external surface portions. [220] The large textual properties of M41S mesoporous materials would require increased volumes of $N_2$, as seen in the experimental V-MCM-48 $N_2$ isotherm plot to approximately $P/P_0 = 0.15$. With addition quantities of nitrogen molecules at elevated relative pressures, multilayer formation would occur in the pores of the V-MCM-48 mesoporous material in the range of $P/P_0 = 0.15$-$0.20$. Although this section would only be a few data points in the experimental $N_2$ isotherm plot of V-MCM-48, region two would be employed to calculate Brunauer-Emmett-Teller (BET) surface due to the gradual liner increase of $N_2$ layers in the material. [140,220,236,245]

As the relative pressure continues to increase from $P/P_0 = 0.20$ to 0.30 in the experimental V-MCM-48 nitrogen isotherm plot, the pore network structure would fill simultaneously with nitrogen gas molecules, which results in increased steepness of slope in the $N_2$ isotherm plot. [220] In this section of the $N_2$ isotherm would be attributed to capillary condensation phenomenon. [220,236,245-247] The filling of liquid nitrogen in the capillary condensation region would be expected due to instability of the meniscus at elevated relative pressures. Employing the Kelvin equation permits the pore size of a given material to be determined by the capillary condensation step. [140,220,236,245-247] Pore structure uniformity would be implied by the size and slope of this region. [24,33,220] Therefore, the slope from $P/P_0 = 0.20$-$0.30$ would not be as steep in the experimental V-MCM-48 $N_2$ isotherm in comparison to Si-MCM-48 made coupled with gradual step suggests less uniform pore structure.

Viewing the experimental $N_2$ isotherm plot of V-MCM-48 from $P/P_0 = 0.30$ to 0.90 would comprise region four with multilayer adsorption of $N_2$ molecules on the external surface. [220,245] Reduced slope value of region four in the experimental V-MCM-48 nitrogen isotherm plot infers external particle surface comprised a small portion of the total BET surface area value. [33] Region five with relative pressure of 0.90 to 1.0 in V-MCM-48 experimental nitro-

gen isotherm plot includes $N_2$ molecules fill between the individual particles, and the condensation of nitrogen gas would occur at approximately $P/P_0 = 1$. [220,245] In addition, the experimental V-MCM-48 $N_2$ isotherm show both slight hysteresis and increase in volume, which would be attributed to microporosity; however, in comparison to literature, [140,236] the amount of microporosity would appear to be small in this mesoporous material. Finally, Barrett-Joyner-Halenda (BJH) method was applied to the desorption branch of experimental V-MCM-48 $N_2$ isotherm in region three to determine the pore volume and pore diameter. [220,245]

Referring to the Brunauer-Emmett-Teller (BET) experimental surface area values in the results section, it could be interpreted as a general trend of reduced surface area with increased $V^{5+}$ ion framework incorporation. In addition the substantial decrease of textural values at Si/V = 20 for V-MCM-48 could be due to sintering from imperfect substation of $V^{5+}$ ion for $Si^{4+}$. Literature research on framework incorporated $Sn^{2+}$ ion in MCM-48 had a similar pattern of textural values at Si/Sn = 20 and had higher surface area and pore volume at Si/Sn = 10 (greater metal loading). [234] They indicate that sintering of at the lower metal loading could be due to the poorer bonding interaction, which would allow the Sn-MCM-48 particle to increase in size upon heating. The introduction of transition metal ions into MCM-48 would have caused increased cross-linking and encourage thickening of pore wall, and thereby a reduction in surface area as a general trend with framework incorporation of more metal ion. [17,85,93] Similarly, the pore volume decreases in the experimentally made V-MCM-48 mesoporous material, which would be expected due to the thicker pore walls that occupy more of the volume. [9,11] Pore size diameter stayed approximately constant throughout the higher $V^{5+}$ ion metal loading in the V-MCM-48 structure; this was expected after reviewing literature. [93] One possible reason for the pore diameter value remains relatively constant even at larger vanadium ion loading could be due to the size difference (there would be only ~20% difference) and random placement of $V^{5+}$ ions in the MCM-48 matrix. [226] In conclusion, experimentally synthesized V-MCM-48 would appear to have formed pore structure with various amounts of constriction.

In summary, the experimental results presented in earlier section of this thesis indicates that $V^{5+}$ ion was substituted for $Si^{4+}$ ion in tetrahedral positions in direct synthesis route, as compared with literature. [17,85,93] The powder XRD diffractograms of the V-MCM-48 show the trend of reduced peak intensity with more $V^{5+}$ ion loading, which would be expected in framework substituted mesoporous materials reported in previous research. [6,9,11,39.85] This shows the MCM-48 structure formed even at high $V^{5+}$ ion loading; however, the degree of condensation would appear to be less than the hydrothermal metal doped M41S mesoporous material synthesis. [9,11,129] DR-UV-vis spectroscopy for experimentally made V-MCM-48 appeared to indicate that the $V^{5+}$ ion could have three types of coordination in comparison to literature: tetrahedral, square-pyramidal, and octahedral. [24,57,90,93,94] In addition, V-MCM-48 would have light absorption properties. The research results of Klabunde and co-workers indicate that this would only be a prerequisite step to photocatalytic activity. [59,250] $N_2$ adsorption-desorption analysis of the experiment isotherm infers ink-bottle pore structure due to hysteresis with comparison of literature findings. [234,238] The texture properties of the V-MCM-48 mesoporous materials would be consistent with greater $V^{5+}$ ion framework substitution for $Si^{4+}$ ion in MCM-48 with the use of the literature claim of transition metal ion encouraging pore wall thickening. [17,85,93] All three instrumental method results point to a need for further research to eliminate many uncertainties in

the experimental data, and expand on the analytical methods employed to characterize the local and particle geometry: these potential future experiments will be presented in the last portion of the discussion section.

## V-MCM-48 Discussion Photocatalysis Studies: Part III

## 5.16 Introduction

This sub-section illustrates the application of V-MCM-48. Various nanoparticle gold standards, and Degussia-Huls P-25 $TiO_2$ standard on the remediation of the following four probe molecules: acetaldehyde ($CH_3CHO$), carbon monoxide (CO), ethanol ($CH_3CH_2OH$), and acetonitrile ($CH_3CN$) were presented. In addition, two other probe molecules, acetone ($CH_3COCH_3$) and 2-propanol ($CH_3CHOHCH_3$), were employed to determine the potential photocatalytic ability of V-MCM-48. It will be discussed in the next sub-section due to poor results. Each of these six probe molecules employed in this photocatalytic studies would have environmental importance, as noted in the results section. The acidity of the vanadium coordination sphere in MCM-48 silica could be inferred through the products formed with reactions of the six probe molecules. Finally, the probe molecules noted above provide insight into the electronic states of the vanadium species in MCM-48 silica that induce the desired oxidation reaction.

## 5.17 Acetaldehyde Dark Degradation over V-MCM-48

The application of V-MCM-48 mesoporous material was employed for the conversion of the toxic probe molecule acetaldehyde into innocuous products: $CO_2 + H_2O$. Through the introduction of the $V^{5+}$ ion into the three-dimensional (3-D) MCM-48 silica pore network, Klabunde and co-workers attempted to exploit the oxidation capacity common in transition metal ions in high oxidation states from Lewis acid/base reactions, otherwise known to induce reduction-oxidation (redox) catalysis on the surface. [59,226,250,251,252] The 3-D MCM-48 silica framework served to both lock the $V^{5+}$ ions in place with a desired coordination geometry, increase the mass transfer kinetics of the 3-D network vs. MCM-41 one-dimensional (1-D) structure, and to enhance the separation of individual $V^{5+}$ ions with large surface area, as noted on metal doped mesoporous materials. [8,15,65,66,73,85,93,98,253-255] Electronic transitions in various metal doped materials have been reported based on the ligand-metal-charge-transfer (LMCT) mechanism. [8,24,57,65,73,85,90,93,232,254,256-263] This phenomenon involves promotion of an electron from the ligand orbital at lower energy into metal orbital depending on the wavelength of light energy absorbed by the material. [8,57,260,261,264-266] Ligand and metal orbital electron transfer would depend on the coordination geometry assuming surrounding the metal ion. These orbitals could be categorized into groups according to similar symmetry and energy, which would be known as energy states (levels). [256] Therefore, upon absorption of a photon with certain energy, the electron transfer from a lower state to a higher state would exist in an instance of time permitting photocatalysis to occur. V-MCM-48 has three types of coordination $V^{5+}$ ion-oxide (oxo) spheres, as previously assigned in the DR-UV-vis characterization section: tetrahedral, square-pyramidal, and octahedral. The tetrahedral $V^{5+}$ ion species could be in the framework and on the surface of MCM-48 silica pore walls through silanol (Si-OH) group bonding interactions, as noted in literature and experimental DR-UV-vis spectrum analysis in Figure 4:2 of the results section. [8,24,85,90,93,94] In ambient conditions (moist air) the $V^{5+}$ ion could coordinate one or two aqua ($H_2O$) ligands to form square-pyramidal and octahedral coordination spheres. [8,24,85,93,97,221,267] Vansant and co-workers found that the V-MCM-48 mesoporous material exhibited yellow-orange color after exposure to a few hours of moist air, which was noted to be due to coordination of two aqua ligands to $V^{5+}$ centers. [85] The result of coordination of the aqua ligands gave

color change for V-MCM-48 from white (no electronic transitions due to empty d-orbital too high in energy above non-bonding $1_{tu}$ π oxo electron for visible light absorption (promotion of an electron)-LMCT) [264,266] to yellow-orange and increasing $V^{5+}$ ion concentration in MCM-48 silica would strengthen the intensity of color seen, as noted in literature with mesoporous materials doped with transition metal ions and color change. [24,60,85] This adoption of aqua ligands would cause the $V^{5+}$ centers to have visible light absorption, as noted in Figure 4:2 DR-UV-vis plot in results section peak shoulder from approximately 400 nm-575 nm. Aqua ligands coordinated to transition metal ion oxide (oxo) coordination spheres enable the visible light absorption due to donation of an electron pair from the aqua ligand into the metal orbital, as shown in molecular orbital diagram in Appendix C-C:1-C:3. [265] Earlier reports indicated that vanadium M41S mesoporous materials of coordination aqua ligands led to visible light absorption, as shown in their DR-UV-vis plots. [8,57,65,73,85,93] Finally, the LMCT model for electronic transitions in metal doped materials has been widely proposed in literature as primary reason for intense color and energy state transitions with metal d-d transitions of lower importance due to the selection and symmetry rules of permitted electron transfer from certain orbitals. [8,24,57,73,85,90,93,93,221,232,254,256-263,268,269]

V-MCM-48 mesoporous material was found to degrade the probe molecule acetaldehyde to $CO_2$, $H_2O$, and $CH_3COOH$ under dark illumination conditions (room light-low intensity), as noted in results section Figures 4:3 + 4:4 and Table 4:2. Acetic acid ($CH_3COOH$) was formed as incomplete oxidation by-product of acetaldehyde, as noted at the end of the reaction of a color change from yellow-orange to dark-green, as noted in literature with $CoO_x$ xerogels initial light blue color to final dark green color. [270] A color conversion would be linked to the change of oxidation state of transition metal ion through reduction/oxidation, as occurred in literature with Cr-MCM-41, Cr-MCM-48 and $CoO_x$-loaded xerogels. [60,270] The oxidation state would change from $V^{5+}$ to $V^{4+}$ according to the dark-green color assigned to $V^{4+}$ silica materials. [232,263] [(Note: according to literature, the higher the charge of metal ion in oxo complex to lower energy-therefore lower charge would mean greater energy gap between $1_{tu}$ π non-bonding oxide (oxo) ligand electrons to metal e orbital) [264,271]] Although not common in photochemistry of transition metal doped materials to function under room light, V-MCM-48 degraded acetaldehyde to $CO_2$ + $H_2O$ products. This could be proposed due to the aqua ligands bonded to the $V^{5+}$ ion where the oxygen atom on the aqua ligand donates an electron pair into the empty metal 3d orbital, which causes the aqua ligand oxygen to lack a full stable 2*p*-orbital, as presented in molecular orbital diagram in Appendix C-C:1-C:3. [265] The lack of a stable noble gas configuration (eight valence electrons) in aqua oxygen atom would lead to instability. [252] Vansant and co-workers report with use of Raman spectroscopy aqua ligands cause oxide (V=O) bond to convert to two geminal hydroxyl groups with water coordination due to hydrogen bonding, as shown in diagram in Appendix C-C:4. [272] When gaseous acetaldehyde molecules collide with the $V^{5+}$ coordination sphere in MCM-48, the bridging oxygen between $V^{5+}$ coordination spheres abstracts a hydrogen atom from acetaldehyde, thereby might initiate the reduction-oxidation (redox) reaction, as shown in Appendix C-C:5-C:7. In addition, other literature has noted a decrease of the band-edge energy ($E_g$) with coordination of aqua ligands on V-M41S mesoporous materials. [221,261,273] Finally, the production of $CO_2$ would imply that the vanadium coordination sites were basic; since, previous research on methanol oxidation with V-MCM-41, V-MCM-48, and $VO_x$-MCM-48 reported basic vanadium sites responsible for formation of CO and $CO_2$ products and usually more than one of these sites was needed to complete the oxidation process. [61,90,274,275]

Review of experimental dark degradation reaction data of acetaldehyde with V(10)-MCM-48 and V(20)-MCM-48, Figure 4:3 & 4:4 and Table 4:2 in results section, one might determine that with increased vanadium ion loading in the MCM-48 silica matrix greater concentration of complete oxidation product, $CO_2$, was formed. However, this trend was slightly different for the consumption of acetaldehyde with V(20)-MCM-48 consuming approximately a third more probe molecules, even though its half the vanadium concentration of V(10)-MCM-48 (Si/V = 10). With half the vanadium loading and assumption the $V^{5+}$ ion would have greater dispersion on a higher surface area support, such as MCM-48 silica, these $V^{5+}$ active sites would produce less carbon dioxide due to further distance apart between each of the catalytic sites. In addition, the incomplete degradation of acetaldehyde could cause greater formation of acetic acid, and the 3-D MCM-48 silica matrix with less $V^{5+}$ ion could act as a molecular sieve adsorbent, as noted with zeolite structures in literature. [206] Servam and co-workers found more product formation with increase metal loading of Cr and V ion in MCM-48 catalysts up to Si/Cr =25 and Si/V = 50 in liquid phase catalysis. [65,66,93] Higher loading of metal ion destroyed the MCM-48 silica matrix, thereby lowering catalytic activity. Gas-phase partial oxidation of propane over $V/Al_2O_3$ revealed a trend of greater $CO/CO_2$ production with oxygen as the oxidant to preserve the $V^{5+}$ oxidation state: proof was when $N_2O$ was employed with oxidation state of vanadium decreasing to $V^{3+}/V^{4+}$ with less replenishment of active lattice oxygen responsible for $CO/CO_2$ production. [276] Also, these researchers found higher metal $V^{5+}$ loading on $Al_2O_3$ support produced more $CO/CO_2$ with oxygen as the oxidant. Doornkamp and Ponec noted with Mars and Van Krevelen mechanism, $CO/CO_2$ formation for the active lattice oxide (oxo) ligands would be largest for low metal-oxygen (oxo) bond strength and high exchange of oxygen, such as $V_2O_5$ illustrated in Appendix C-C:8-C:9. [277-280] These finding support Klabunde and co-workers experimental argument that high oxidation state needed to induce photocatalytic oxidation of toxic probe molecules. [250,251] Finally, the molecular sieve adsorbent effect could be seen in Figure 4:3 & 4:4 in the first two data points of a major decrease in acetaldehyde concentration.

## 5.18 Acetaldehyde Visible Light Photodegradation over V-MCM-48

Similar to the LMCT model presented above for the dark reaction, the visible light ($\lambda > 420$ nm) photodegradation reaction potentially works with the wall pseudotetrahedral $V^{5+}$ ion accepts one or two aqua ligands into its coordination sphere. Due to relatively close proximity of these $V^{5+}$ square-pyramidal and octahedral species especially at higher metal loading (Si/V = 10), which could form polymeric $VO_x$ species, the result would be the lower metal energy level receives an electron from the oxide (oxo) non-bonding orbital with visible wavelength light, as shown in molecular orbital diagram in Appendix C-C:1-C:3. [281-284] The energy states (levels) that comprise both the metal and ligand orbitals could have a higher energy separation in comparison to the dark reaction energy levels, which depended on the aqua $V^{5+}$ orbital overlap to form $V^{5+}$ species larger than one. [285]

Referring to acetaldehyde visible light photodegradation data in Figure 4:5 & 4:6 and Table 4:3, one would note that the $CO_2$ production concentration was not the highest with largest $V^{5+}$ ion loading in MCM-48 silica matrix. Instead, Si/V = 20 MCM-48 silica composition had the largest carbon dioxide production. This could be due to formation of polymeric $VO_x$ and/or $V_2O_5$ crystallites that have limited photocatalytic activity due to lack of corners and anionic defect vacancies needed for the $V^{5+}$ coordination sphere (active site) to regenerate after completion of reaction, as noted in literature on large $V^{5+}$ loading on MgO support. [286] Formation of $CO/CO_2$ has been noted in

literature to involve basic sites [90,274,287,288]; therefore, if these Lewis acid sites were too close together, this could prevent the acetaldehyde hydrogen atom from easily abstracted by the bridging oxygen due to change of electron donation from the geminal hydroxyl species to the bridging oxygen, as inferred in literature. [24,255] As noted in literature, [286] $VO_x$ polymeric/$V_2O_5$ crystallites would be packed tightly with no anionic vacancies needed to regenerate the active site, thereby greatly reducing catalytic activity. This research group found with propane oxydehydrogenation reaction with high vanadium loading on MgO the reaction rate decreased steadily, which was attributed to lack of defects: corners and anionic vacancies. Similar to the dark acetaldehyde degradation data discussion above, a lower metal loading concentration at Si/V = 80 consumed the most acetaldehyde, which follow proposed mechanism of degradation to $CO_2$ as in the dark in Appendix C-C:1-C:3. This could be due to the $V^{5+}$ square-pyramidal and octahedral species too far apart for sequential photodegradation reaction to produce $CO_2$, as noted with Sb-V-MgO with propylene oxidation led to $CO_2$ if electrophilic $V^{5+}$ ions where in a sequence, instead of isolated $V^{5+}$ species. [275] Instead, addition quantities of $CH_3COOH$ could have been produced coupled with the molecular sieve capacity of MCM-48 silica similar to zeolites, which would explain larger acetaldehyde consumption rate with still lower $CO_2$ production concentration. [286] Besides these two anomalies in the visible light acetaldehyde photodegradation data with V-MCM-48, the general trend was increased $V^{5+}$ loading produced larger concentration of carbon dioxide. As noted in the above dark reaction section, [65,66,93] larger metal ion loading to a point led to greater formation of products, which could be ascribed to more active sites to react with the probe molecules.

## 5.19 Acetaldehyde Ultra-Violet Light Photodegradation over V-MCM-48

In contrast to the LMCT mechanism explanation given for the dark and visible degradation of acetaldehyde over V-MCM-48 mesoporous material, the ultra-violet (UV) light ($\lambda$ = 320-400 nm) photodegradation reaction appears to occur with activation of both framework and surface $V^{5+}$ species in tetrahedral/pseudotetrahedral coordination geometry. These $V^{5+}$ species would have greater distance between individual metal coordination spheres (active sites), which cause the energy level separation in the states (group of orbitals of correct symmetry and energy) to be further apart from the filled oxide (oxo) ligand ones'. This increase in energy separation of states in greater isolated individual metal coordination spheres has been linked to the blue-shift semiconductor effect, as reported in literature. [8,289] Assignment of these two four coordinate species from literature DR-UV-vis shows higher frequency light needed for promotion of an electron in this type of geometry coupled with evaluation of experimental DR-UV-vis plot in Figure 4:2 results section. [8,24,57,65,73,85,90,93,221,232,257,258,269,281,282,290] The absorption of light for tetrahedral coordination oxide (oxo) $V^{5+}$ species would be from 240-340 nm, according to literature. [24] With the absorption at approximately 250 nm in DR-UV-vis plot in Figure 4:2 of results section, this would infer the $V^{5+}$ tetrahedral species had enhanced distance between the active sites in comparison to other $V^{5+}$ coordination sites involved in acetaldehyde degradation reaction. Under UV-light irradiation oxidation of organic molecules has been proposed to occur with the double bond to $V^{5+}$ (V=O) converting to single oxide (oxo) bond, and the organic molecule would interact with the basal plane orbital of $V^{5+}$ and oxo species lacking an electron. [281,282,291] In addition, the formation of products could occur with one of the single bonds to the support detaching; then, interaction of organic probe molecule interact with the coordination sphere and upon formation of product the oxo bond reforms, as shown in proposed UV-light activated mechanism for CO photooxidation (i.e. Acetaldehyde photodegradation under UV-light irradia-

tion with V(x)-MCM-48 could occur in similar manner to CO photooxidation under same light conditions). [291] Tanaka and co-workers found the lattice oxygen was responsible for forming propylene oxide (PO) on $V_2O_5/SiO_2$ catalyst under UV-light irradiation, and deep oxidation occurred when lattice oxygen was replaced with $O_2$ if PO was not removed as it formed. [260] This last type of LMCT mechanism would involve $V^{5+}$ species on the surface in pseudotetrahedral geometry in pore structure. [281,282,291] An older mechanism ascribes the promotion of an electron into $V^{5+}$ from double bond (V=O) species under UV-light that causes formation of superoxide radical ($O_2^-$), which could cause deep oxidation to $CO_2$. [260,292,293] Framework tetrahedral $V^{5+}$ species in MCM-48 silica would primarily operate with both probe molecules colliding with the metal coordination sphere and electron density from the $1_{tu}$ $\pi$-orbital of oxo ligand promoted to e-orbital of $V^{5+}$ ion to form triplet state, as shown in molecular orbital diagram in Appendix C-C:10-C:14. The energy levels (states) for promotion of the electron would involved the following states, as illustrated in molecular orbital diagram in Appendix C-C:11: $(e)^4(a_2)^2(e^*) \rightarrow (e)^4(a_2)^1(e^*)^1$. [281,282] Photodegradation would occur under UV-light irradiation for framework tetrahedral $V^{5+}$ oxide (oxo) coordination species in redox reaction with these proposed energy states, as shown in molecular orbital diagram in Appendix C-C:15: $(e)^4(a_2)^2(e^*) \rightarrow (e)^4(a_2)^1(e^*)^1$.

In the results section Figure 4:7 and Table 4:4, the V(80)-MCM-48 composition had the largest $CO_2$ production and consumption of acetaldehyde. This contrasts the trends in the dark and visible light acetaldehyde degradation data where the highest $V^{5+}$ loading in MCM-48 silica (Si/V = 10; Si/V = 20) produced the most $CO_2$, and the middle (Si/V = 80) $V^{5+}$ loading consumed the most acetaldehyde. The reason for this difference in data results would be the increasing efficiency of LMCT charge separation similar to semiconductors. The formation of a triplet state in $V^{5+}$ oxide (oxo) coordination sphere would enhance the charge carrier lifetimes, as noted to be the reason for the photocatalytic transition in $V^{5+}$ doped silica material. [281-284] Due to the blue-shift effect of increased isolated $V^{5+}$ coordination spheres in MCM-48 silica from greater surface area, the energy levels (states) in the coordination sphere would have greater charge separation, which would provide enhanced charge carrier lifetimes, as occurs with larger bandgap semiconductors. [217,289,294,295] In turn, recombination rate would be reduced, thereby would enhance the oxidation ability of the active site. Klabunde and co-workers report the enhanced oxidative ability of metal doped ETS-10 (ETS = Engelhard Corporation Titanosilicate) due to the large bandgap in acetaldehyde photodegradation reaction. [296] Also, the distance of the $V^{5+}$ coordination sphere would need to be optimal to produce $CO/CO_2$ due to complete oxidation product requires a series of active sites for consecutive reaction with lattice oxygens, as noted in literature. [38,90,222,274,275,291,297] The enhanced charge carrier separation in LMCT phenomenon could explain why V(80)-MCM-48 in visible light consumed most acetaldehyde probe molecule but not largest $CO_2$ producer, which likely formed incomplete oxidation product $CH_3COOH$. The Degussa-Huls P-25 $TiO_2$ standard for photodegradation of organic molecules was employed for acetaldehyde, as shown in Figure 4:8. Due to the large charge separation of the charge carriers ($e^- + h^+$) in the $TiO_2$ semiconductor material even with much lower surface area, the result was more than double carbon dioxide production of best V-MCM-48 catalyst ((V(10)-MCM-48)) and approximately double acetaldehyde consumption in only 110 minutes not standard 140 minutes reaction time. In conclusion, the number of framework and pseudotetrahedral $V^{5+}$ species would be fewer than the square-pyramidal and octahedral $V^{5+}$ species; since, the higher metal loading led to decreased activity photocatalytically.

## 5.20 Carbon Monoxide Visible Light Photooxidation over V-MCM-48

In contrast to the acetaldehyde degradation with V-MCM-48 under dark light conditions, V-MCM-48 mesoporous material had only CO catalytic activity with visible light ($\lambda > 420$ nm) and ultra-violet (UV) ($\lambda = 320$ nm-400 nm) light irradiation. The reason for no dark reaction could be due to the need for light to cause a promotion of an electron into higher energy level (state), according to the LMCT model, noted in literature. [281-284,298,299] Also, the CO molecule would be able to resist oxidation due to the large bond order of three (triplet bond), which would enhance its stability. [252,264] This enhanced stability with CO would explain why the concentration of $CO_2$ made was lower then with acetaldehyde under similar reaction conditions.

Similar to the assignment of $V^{5+}$ coordination species responsible for acetaldehyde visible light photodegradation, the square-pyramidal and octahedral $V^{5+}$ oxide (oxo) species with one to two aqua ligands to give five or six coordination geometry could be responsible for the oxidation of CO under visible light illumination. For example, in acetaldehyde visible light photocatalysis of metal oxides on silica aerogels, Klabunde and co-workers propose the metal species ($Cr^{6+}$ or $Co^{3+}$) was bound to either tetrahedral or octahedral set of oxide ligands. [251] These square-pyramidal and octahedral $V^{5+}$ species would be on the pore surface of V-MCM-48. The energy levels (states) for CO photocatalysis to occur would be proposed to be the same as acetaldehyde photodegradation ones' due to the fact of same material under identical wavelength of light. The $V^{5+}$ coordination species activated under visible light appeared to need to be further apart to oxidize CO to $CO_2$, in contrast to literature that a series of $V^{5+}$ basic sites were needed for complete oxidation of an organic probe molecule. [90,274,298,299] This would prevent formation of polymeric $VO_x$ species through oxolation reaction on silica surface at increased $V^{5+}$ loading. [221] $VO_x$ polymeric species/$V_2O_5$ crystallites have been shown in literature to have less catalytic potential vs. isolated $V^{5+}$ species due to lack of anionic vacancies/corners and poor charge separation of charge carriers ($e^- + h^+$). [286,300]

Referring to Figures 4:9-4:13 and Table 4:5 in results section, the trend of decreased $V^{5+}$ metal loading in MCM-48 led to increased $CO_2$ under visible light conditions, pore structural change, and enhanced $CO_2$ formation with UV-light irradiation. Figure 4:9 with V(20)-MCM-48 had little CO photooxidation activity from the higher metal loading on MCM-48 silica matrix, which caused a reduction in square-pyramidal and octahedral species coupled with formation of polymeric $VO_x$ chains on the pore wall surface. [24,90] Figure 4:10 shows V(50)-MCM-41 had slightly greater CO photocatalytic activity due to the lower metal loading in MCM-41 silica structure, thereby allowed for more square-pyramidal and octahedral species to be retained as isolated members. Further improvement of $CO_2$ formation rate occurred at the same metal loading in Figure 4:11 with use of the 3-D pore network of MCM-48 silica matrix, which had a larger surface area and more corners + edges. Vralstad studied $NO_x$ remediation over both Co-MCM-41 and Co-MCM-48 and noted that higher $NO_x$ conversion rate with Co-MCM-48 due to 3-D pore network and its concave and convex bicontinuous structure. [256] Previous research has shown that increased surface area led to large photocatalytic production activities. Dagan and Tomkiewicz found that similarly increasing the surface area in photocatalysis of aqueous waste using $TiO_2$ aerogels led to quadruple reduction in salicylic acid in comparison to the lower surface area Degussia-Huls P-25 $TiO_2$ photocatalyst. [301] This may be attributed to higher absorption of probe molecule and enhanced quantum confinement with higher surface area $TiO_2$ aerogels. Likewise, Sun and Klabunde noted that corners and edges permitted for more probe molecule interactions kinetically on ultra-

fine MgO material, thereby higher chlorinated organic product formation rate. [302] Figure 4:12 shows the V(150)-MCM-48 composition under various light conditions with even lower $V^{5+}$ loading in MCM-48 silica structure led to increased CO photooxidation under visible light. This could be due to the square-pyramidal and octahedral species further apart from each other on the MCM-48 silica support pore wall surface, thereby lowering the potential for polymeric $VO_x$ formation. The coordination of CO to $V^{5+}$ ion in MCM-48 could be ruled out due to no color change as occurred in V-MCM-48 acetaldehyde reaction of yellow-orange ($V^{5+}$) to dark-green ($V^{4+}$). In addition, previous researchers reported that CO bonding stability to $V^{5+}$ ion would be essentially non-existent due to poor σ bonding overlap of orbitals. [303,304]

## 5.21 Carbon Monoxide Ultra-Violet Light Photooxidation over V-MCM-48

The UV-light photo-activated V-MCM-48 CO oxidation reaction involved framework tetrahedral and pseudotetrahedral $V^{5+}$ species on the pore surface of MCM-48 silica structure. These active sites need shorter frequency light to promote an electron from ligand level to higher metal energy state according to LMCT model. [8,24,85,90,221,284-284,299,305] This promotion of an electron to a higher energy orbital would enhance the oxidation ability of a photocatalyst, as noted with semiconductor materials in literature. [217,294,296] This would be the reason why longer charge carrier separation lifetime enhances photooxidation activity, which permits more time for destabilization of probe molecule such as CO. Previous literature indicated with isolated $VO_4$ species on pore wall surface that the catalyst reaction occurs in the basal plane of V=O bond with triplet energy state, as shown in Appendix C-C:16 of proposed CO UV-light activated photooxidation mechanism. [281-284,298,299] Framework tetrahedral species could be proposed to operate in a similar manner with few changes. An electron from CO could be accepted by $VO_4^{3-}$ and then form superoxide radial species. [306] Wachs and co-workers found with methanol oxidation over $VO_4^{3-}$ species that the LMCT transitions occurred at higher energy lower intensity for $V^{3+}/V^{4+}$ reduced intensity. [307] Therefore, one could assume feasible for $VO_4^{3-}$ to operate in a similar manner in CO photooxidation; since, methanol oxidation by-products would be CO, which under thermal conditions converts to $CO_2$ with lattice oxygen. [90,274] In Figure 4:12 the use of UV-light significantly increases the photooxidation slope and percent $CO_2$ production value, as noted in Table 4:3 in results section. However, the higher metal loading V(20)-MCM-48 mesoporous material had larger photooxidation $CO_2$ rate and increased slope value due to potentially more of the four coordinate $V^{5+}$ species in MCM-48 silica matrix. Finally, Table 4:5 illustrates the above discussed trends in V-MCM-48 CO photooxidation data in results section.

## 5.22 Five Variables of Carbon Monoxide Oxidation over Nanoparticle Gold Catalysts

In literature five main variables have been reported to affect CO oxidation rates over gold nanoparticle materials: (1) cluster size; (2) coordination number for different portions of individual Au clusters (corners, edges, kinks, and steps); (3) shape of cluster; (4) type of support for the clusters; and (5) type of synthesis Au preparation/activation treatments. [308-319] In addition, other variables that have an effect on the CO oxidation process would include: oxidation state of Au, electronic quantum-size effect, lattice strain, and diffusion of oxygen in the support. [310] Gold cluster size would be the predominant variable that determines the CO oxidation rate; since, the gold cluster size determines if and how CO molecules coordinate to the surface of the material. [310,312,315,316,318] Norskov and co-workers note that 2-4 nm Au vs. 20-30 nm Au particles have greater then two orders of magnitude higher oxida-

tion rate. [312] They note the reason for large CO oxidation rate with tiny Au nanoparticles (clusters) would be linked to coordination sites that have defects, such as: corners, edges, kinks, and steps. The formation of these catalytically active defect sites require that the coordination number (number of atoms at a given defect site) have a low value. [310,312,314,315] Iwasawa and co-workers workers found the $Au/Fe(OH)_3$* catalyst to have enhanced activity of more than three times with coordination number of 7.4-8.0 vs. 12 for bulk gold, according to entended X-ray absorption fine structure (EXAFS) analysis; whereas, larger Au nanoparticles with coordination number of 9.8+/-1.0 had dramatically reduced CO oxidation activity. [315] Janssens and co-workers noted Au(100) and Au(111) surface with coordination number above eight led to repulsion between CO and $O_2$ on the surface, thereby lowering catalytic activity. [310] Infrared studies on CO absorption occur independently of size/thickness of Au nanoparticles; since, CO absorbs on edge/corner sites on Au clusters. When the coordination number was less than eight, more corners/edge sites were exposed with decrease number of Au atoms per a site, which has been found to directly increase CO and $O_2$ absorption followed by more $CO_2$ production, as shown in Appendix C-C:17. [310] Weststrate and co-workers reported that higher CO oxidation activity would occur over their model $Au/CeO_2$ (111) catalyst surface as the coordination number decreased to six-to-seven. [308] They note with these small Au particles greater than 60% of surface gold atoms would have the ideal coordination site for absorbing CO molecules. These researchers report that CO absorbs little at terrace sites; nonetheless, six coordinate kink + corner sites CO absorbs strongly and seven coordination step + edge sites absorption of CO was less according to CO desorption analysis. Larger Au nanoparticles were found to have less of these catalytically active surface atoms. Low Au coordination numbers have been linked to the strength of Au-CO + Au-O bonds due to binding states of gold and oxygen (*d*-states of Au + O 2*p*-orbital). [312] Small Au nanoparticles would have more corners and edges of low coordination number; therefore, these low coordination sites would favor Au *d*-states close in proximity to Femi level, which would provide stronger binding interaction with oxygen to effect $O_2$ dissociation/activation reaction on surface. Absorption energies would be reduced by approximately one eV with absorption on $Au_{10}$ (coordination of four vs. Au(111)-coordination of nine) for oxygen and carbon monoxide, thereby means potentially stronger bonding interactions. Activation energy trends commonly follow binding energy patterns, which would indicate reaction energy barriers were reduced. In conclusion, small Au nanoparticles bind more strongly in contrast to larger Au nanoparticles due to less catalytically active low coordination sites, as illustrated in Appendix C-C:18: corners, kinks, steps, and edges. [312]

Although the Au nanoparticle size and coordination number would have a dramatic impact on CO oxidation rates, Au particle shape, type of support, and synthetic preparation/activation method(s) would have cumulative large effect on the gold nanoparticle CO oxidation catalytic activity. [308,310,312-318] Boccuzzi and co-workers have noted that shape of gold islands from 3-D nanoparticle to 2-D gold cluster of two-to-three Au atoms thick on $TiO_2$ support have enhanced CO oxidation ability due to change of electronic properties from purely metallic character to a bandgap of 0.3-0.8 Volts. [311] Type of support employed for Au nanoparticles have been claimed to affect CO oxidation by many researchers [309,311,313-315,317,318]; however, other researchers claim the support only has secondary effect on CO oxidation. [310,312,316] Schubert and co-workers note that active (reducible) supports, such as: $Fe_2O_3$, $TiO_2$, $NiO_x$, $CoO_x$, form reactive oxygen on surface of support, which could migrate to the support/Au nanoparticle interface where CO would be bound to the surface and initiate $CO_2$ formation, as illustrated in Appendix C-C:19. [314]

Reactive oxygen might form on the oxygen vacancies in active supports. In contrast, inert supports, such as: MgO, $Al_2O_3$, would be irreducible and not provide oxygen to the Au nanoparticle site through activation and/or lattice oxygen. [309,314,320] Corma and co-workers have found that use of nanocystalline $CeO_{2-x}$ support vs. commercial $CeO_2$ support in Au CO oxidation led to enhanced catalytic activity due to formation of $\eta^1$-superoxide and peroxide intermediate species at the defects in the nanocrystalline support, and CO oxidation occurred at this defect/Au nanoparticle interface to form $CO_2$. [320] EXAFS data showed little to no Au-O bonding interaction on $Au/CeO_2$ catalyst: they remark that the little catalytic activity on conventional $CeO_2$ support was due to essentially no oxygen atoms at the gold nanoparticle-support interface, which could interact with CO, as illustrated in Appendix C-C:20. Iwasawa and co-workers note the positive attributes of metal hydroxide active support due to many defect sites that bind Au nanoparticles to the support, thereby preventing formation of larger Au nanoparticles. [315] Lin and Chen synthesized high surface area $Fe_xO_y$ material to serve as a support for Au nanoparticle. [317] In contrast to iron oxide support made through co-precipitation with a low surface area (50 $m^2/g$), $Fe_xO_y$ support with 406 $m^2/g$ surface area used many surface hydroxyl groups to bind/attach Au nanoparticles from growing in size and had enhanced CO oxidation rates, which could be attributed to relationship of highly active tiny Au nanoparticle and defects for activating oxygen for $CO_2$ production. Janssens and co-workers propose that the support effect for active vs. inert would be linked to the shape of Au particles. [310] They illustrate the Au particle size/shape with a model for $TiO_2$, $MgAl_2O_4$, and $Al_2O_3$ supports, as presented in Appendix C-C:17. The active support $TiO_2$ causes formation of more corners and edges, in contrast to inert $MgAl_2O_4$ and $Al_2O_3$. Finally, use of an active support vs. inert one in CO oxidation has been shown to increase catalytic rate by a factor of two-to-four times. [312]

Synthetic preparation/activation methods have been noted to have a significant effect on the resulting CO oxidation catalytic rate. [309,310,315,316] Lin and Chen note to obtain high surface area $Fe_xO_y$ support for Au nanoparticle, one must carefully adjust the pH value, $FeCl_3$ feed rate, and calcination temperature. [317] These researchers tried other metal precursors, such as $FeCl_2$, and $Fe(NO_3)_3$, and obtained lower surface area material. In addition, low drying and calcination temperature prevent hydroxyl surface groups on $Fe_xO_y$ from being eliminated + reduce likelihood of sintering of support material. Use of a chloride containing metal precursor meant that the material must be thoroughly rinsed to remove $Cl^-$ ions from damaging Au nanoparticles. [The $Cl^-$ ion causes agglomeration of Au particle coupled with suppressing Au cation to reduction in $H_2$ activation treatment step.] [318] The actual synthesis of the Au nanoparticles would also be of utmost importance due to formation mechanism, which affects the activity of the resulting material to CO oxidation. [315-317,319,321-323] Huruta *et al.* note co-precipitation led to highly active Au nanoparticle catalysts for CO oxidation; in contrast, impregnation of support with Au precursors led to larger Au particles with the CO oxidation activity even though calcinated at half temperature of co-precipitated Au sample of 200°C. [319,321] These researchers link the reason for growth of large Au nanoparticles (ten nanometers or larger in diameter) to low melting temperature, reduced sublimation energy, and Tamman temperature of very low value (Tamman temperature-when metal atoms become mobile on support). [319] Iwasawa and co-workers note the importance of the precursors employed for synthesizing both gold nanoparticles and support. [315] They show how Au-phosphine complexes that commonly produce large Au nanoparticles upon thermal decomposition; instead, with use of wet metal hydroxide support, the impregnated Au-complex/as-precipitated support under careful calcination pro-

duced dispersed Au nanoparticles with enhanced CO oxidation ability. Zhang and co-workers report the effect of precipitant in the co-precipitation coupled with calcination temperature directly determined the CO oxidation ability of Au/ZnO catalyst. [322] These researchers note that the precipitant effects the formation of small Au nanoparticles and ZnO. They found $Na_2CO_3$ to be the best precipitant, and $Na^+$ ions positively could lower production of carbonate-like species on Au/ZnO catalyst surface, thereby enhancing CO oxidation rate. Huang and co-workers indicate that the $Na_2CO_3$ precipitant vs. $NH_4OH$ (aqueous ammonia-$NH_3$) led to increased stronger bonding interaction between Au/ZnO and silica support, which increased the CO oxidation rate. [323] Finally, researchers report that Au/ZnO material to have catalytic activity and stability under ambient conditions in CO oxidation; in contrast, $Au/TiO_2$, and $Au/ZrO_2$ catalysts deactivate under humid reaction CO oxidation conditions. [322]

Calcination process could affect the size of Au nanoparticles formed in the final material. Boccuzzi and co-workers studied the effect of calcination temperature on $Au/TiO_2$ deposition-precipitation prepared samples at following temperatures: 473 K, 573 K, and 873 K. [311] As the calcination temperature increased, the Au nanoparticle size also becomes larger. At 473 K and 573 K, the Au particle sizes were 2.4 nm and 2.5 nm; however, the Au nanoparticle size dramatically increased to 10.6 nm at 873 K, which could be ascribed to sintering (growth) of the Au particles. The CO oxidation activity was enhanced with the $Au/TiO_2$ prepared samples at 473 K and 573 K; whereas, the large 10.6 nm Au nanoparticles had little activity toward CO oxidation. The authors propose the higher CO oxidation activity for the 2.4 nm and 2.5 nm Au nanoparticles due to formation of step sites over the Au nanoparticles and at the borderline (interface) between Au nanoparticle and support. Due to the negative effects of high calcination temperature, many researchers have employed use of low calcination temperature to reduce the amount of sintering of Au nanoparticle on support. [315,316,322,323] Finally, to reduce the agglomeration of Au nanoparticles on support, Mon and co-workers employed Al-SBA-15 aluminosilicate support to slow Au particle growth due to thick silica walls and $Al^{3+}$ ion lower Au mobility, which produced at 100°C seven nanometer Au nanoparticles in Al-SBA-15 support. [324]

In summary, the major variables outlined above would affect dramatically the CO oxidation rate on Au-nanoparticle support catalyst. [308-319] The other variables, such as oxidation state of Au, quantum size effect, lattice strain, and diffusion oxygen from support have been proposed to effect the CO oxidation rate over Au nanoparticles, although greater understanding of how these various entities effect the catalytic CO oxidation rate need further study. [318] Clearly, the debate over the support effect will continue; since, the oxygen activation step would affect the CO oxidation rate. [325] Finally, other compositions of Au, such as Au-Ag alloy might produce enhanced CO oxidation over wider range of conditions, due to less size related sintering problems encountered with Au nanoparticles. [325-327]

## 5.23 Carbon Monoxide Dark Reaction over Nanoparticle Gold Catalysts

The dark reaction of CO oxidation with nanoparticle gold on various supports and different volumes of CO gas produced the following trend: lower CO volume more $CO_2$ production, the slope value increased with less CO volume, and $R^2$ values had a partial pattern of appropriate unity with increased slope value. Figures 4:15-4:19 and Table 4:6 in results section show the three trends in CO oxidation over nanoparticle gold with the different supports. Figure 4:15 appears to show a small dark reaction with CO and nanoparticle ZnO; however, other data in the Ap-

pendix B casts doubt on this result coupled with small $R^2$ value. According to literature, [293,328] ZnO would be a large bandgap semiconductor like $TiO_2$ and would therefore not be able to function under little light conditions. Figures 4:17-4:18 shows an increase in slope values with relatively low amount of CO. The reason for enhanced oxidation reaction of CO could be linked to high surface area of darco and silica, which would prevent formation of larger gold nanoparticles similar to what occurs in vanadium ions on silica supports, as noted in literature when metal loading increases. [57,65,274,315,317,320,323,329] These larger gold nanoparticles would have higher coordination number with less corners/edges, which have been shown to be important in CO oxidation catalytic studies. [308,310-312,314,315,317,318,320] Therefore, even with inert/active support effect, this could explain the enhanced CO oxidation ability of these gold catalysts. Figures 4:18-4:19 show that both the active $Cr_2O_3$ support and lower CO volume led to increased $CO_2$ production. The active support effect enhances the oxidation ability of the nanoparticle gold clusters due to enhancement of coordination of CO and $O_2$ along edge/corners sites coupled with activation of reactive oxygen similar to $Fe_2O_3$ support material from oxygen vacanies, according to literature. [310-312,314,317,318,320,329] CO volume could affect the absorption of $O_2$ and desorption of $CO_2$ from nanoparticle gold clusters. Too great CO volume would prevent adequate amount of $O_2$ to be on surface of gold nanoparticle to be activated to bond with CO to form $CO_2$, as illustrated in Appendix C-C:21 with CO occupying all coordination sites on $Au/TiO_2$ nanoparticle catalyst. [311] Finally, the above proposal could be supported with larger slope value, which would be an indication of the reaction kinetics of interaction with the gold nanoparticle catalyst.

## 5.24 Visible Light Carbon Monoxide Photooxidation over Nanoparticle Gold Catalysts

The visible light ($\lambda > 420$ nm) photooxidation reaction of CO over various gold nanoparticle catalysts had the following findings, as presented in Figure 4:20-4:26 and Tables 4:7-4:8 in results section: less CO in light reactor more $CO_2$ product, and inert/active support effect on $CO_2$ production. As noted in dark CO oxidation section with gold nanoparticle catalysts, too large CO volume would prevent $O_2$ from being activated on the gold surface due to all coordination sites taken by CO surfaces. [311] Boccuzzi *et al.* model of the $Au/TiO_2$ surface shows that $O_2$ needs to bind to the Au particle in addition to CO, as shown in Appendix C-C:22. [311] Previous investigations have noted the importance of the inert/active support effect in nanoparticle gold catalysts. [310-312,314,317,318,320,329] Janssens and co-workers report $Au/Al_2O_3$ four times lower CO oxidation activity vs. $Au/TiO_2$, which they ascribe to support effects other then reducibility. [310] Figure 4:20 had the lowest $CO_2$ production considering the large amount of CO gas injected into the light reactor, which could be due to complete effect with $O_2$ on the surface of the gold nanoparticle. Likewise, nanoparticle ZnO had little $CO_2$ production, as expected according to literature due to the large bandgap of this semiconductor. [294,328,330] Nanoparticle Au/MgO Plus had the next largest $CO_2$ concentration from visible light photooxidation of CO. A large amount of CO might be part of the reason why coupled with dispersion and inert support effect for low catalytic activity. MgO Plus would have relatively large surface area but not as large in comparison to silica support such as Si-MCM-48. [2] In addition, the MgO support would be considered inert, according to literature. [314,317,318,323,329] This inert support effect could determine the size of the gold nanoparticles on the surface. Janssens and co-workers note the potential at reducible supports such as $TiO_2$ that contain oxygen defects that could function as anchoring sites for Au clusters, and more of these sites would facilitate formation of low-coordination Au atoms. [310] Westrate and co-workers found $Au/CeO_2$ (111) for CO oxidation occurred on low-

coordination sites, such as steps/corners primarily. [308] Figure 4:23 displays the slightly higher activity of $Au/Al_2O_3$ nanoparticle catalyst in CO photooxidation reaction. According to literature on vanadium on $Al_2O_3$ vs. $V/SiO_2$ acid/base bonding characteristics, the $Al_2O_3$ support would be acidic facilitating formation of isolated metal ion species, such as vanadium [218,219,331]; however, the inert effect of $Al_2O_3$ would cause it to effect gold nanoparticle size, thereby amount of gold atoms in the cluster for each catalytic site. Janssens and co-workers propose use of $Al_2O_3$ support effect the intrinsic turn-over-frequency value for CO oxidation due potentially to metalloxide-boundary or electronic effect. [310] Au/Darco nanoparticle catalyst had substantial increase in $CO_2$ production, as shown in Table 4:7 and Figure 4:24. The reason for the higher photooxidation activity of gold/darco nanoparticles could be due to greater surface area, which would permit formation of smaller gold nanoparticles at a given metal loading concentration. Figure 4:25 would illustrate the effect of CO in optimal amount in the photocatalytic oxidation reaction over gold/chromium(III) oxide nanoparticle catalyst. This would also be due to the active support effect of $Cr_2O_3$, thereby would enable formation of smaller gold clusters similar to $TiO_2$ oxygen vacancies anchoring effect. [310] $Au/SiO_2$ nanoparticle had the highest visible light CO photooxidation rate and could be due to large surface area characteristic of silica supports, as noted in literature. [316,323] The high surface area would facilitate greater gold metal loading without forming large size metal clusters, as noted in literature of other metals, such as vanadium. [2,8,24,90] Finally, referring to Table 4:8, one could view the trend of lower CO concentration led to more visible light $CO_2$ photooxidation portion vs. dark reaction, which might be due to enhanced activity of bonding of CO and $O_2$ to conversion to $CO_2$ at a quicken rate.

## 5.25 UV-Light Carbon Monoxide Photooxidation over Nanoparticle ZnO & Au/ZnO

The UV-light ($\lambda$ = 320-400 nm) activated photooxidation of CO over ZnO and Au/ZnO nanoparticles had both significant $CO_2$ production, as shown in Figure 4:27-4:28 and Table 4:9. ZnO nanoparticles had little less $CO_2$ production then $Au/Cr_2O_3$ at 5.0 mL of CO. The reason for the oxidative ability of ZnO would be linked to charge-carrier separation common with large bandgap semiconductor, as noted in literature. [294,330] Combination of the active support ZnO with gold nanoparticle led to the largest $CO_2$ production of 6.3% under UV-light. This synergistic effect has been shown in Figure 4:29; however, the result would only be little over 2 % more $CO_2$ production vs. V(20)-MCM-48 under UV-light. In conclusion, these gold catalysts above results discussed above and in results section contradict literature on gold nanoparticle, [308-319,320-323,332,333] and might be due to the static reactor used in the photooxidation analysis, which has slower kinetic rate vs. flow reactor commonly employed. [334]

## 5.26 Visible & UV-Light Photodegradation of Ethanol + Acetonitrile over V(20)-MCM-48

Visible light ($\lambda$ > 420 nm) photodegradation of ethanol ($CH_3CH_2OH$) preliminary results, as shown in Figure 4:30, indicate a small complete degradation reaction with proposed photodegradation reaction shown in Appendix C-C:23-C:27. The mechanism would involve LMCT with similar energy states at work as with acetaldehyde. Acetonitrile ($CH_3CN$) was tested under UV-light ($\lambda$ = 320-400 nm) due to its enhanced stability similar to CO due to a triple bond. As shown in Figure 4:31 in the results section with application of UV-light, the $CO_2$ production proceeds with a slope value comparable to the Au/ZnO nanoparticle. Although no research was found on the photodegradation of acetonitrile, one could assume that the framework and pseudotetrahedral $V^{5+}$ coordination sites were responsible for the $CO_2$ production, which would indicule same energy states as UV-light initiated CO photooxida-

tion reaction with proposed photodegradation mechanism in Appendix C-C:28-C:33. Although acetone and 2-propanol showed little reaction over V(x)-MCM-48 at 25°C, the proposed photodegradation mechanisms showed in Appendix C-C:34-C:40. Finally, the next sub-section will cover laboratory procedures that might improve the oxidation ability with these probe molecules.

## V-MCM-48 Discussion Future Research & Applications: Part IV

## 5.27 Introduction

This final sub-section in the discussion section of the thesis will provide methods that potentially could resolve the uncertainties in the data collected using V-MCM-48 mesoporous materials, gold standards, Degussia-Huls P-25 $TiO_2$ catalysts in photocatalysis of the following six probe molecules: $CH_3CHO$, CO, $CH_3CH_2OH$, $CH_3CN$, $CH_3COCH_3$, and $CH_3CHOHCH_3$. Several methods have been reported in literature that could enhance the structural integrity of V-MCM-48 in aqueous reaction conditions. Additional instrumental methods have been reported in literature that would further increase knowledge of the type(s) of $V^{5+}$ species in the MCM-48 silica structure. From the review of previous research completed, future research will be proposed for the six probe molecules. A section dedicated to use of alkali-metal-ions has been devoted for understanding how they work over $VO_x/SiO_2$ and potentially used in V(x)-MCM-48 to enhanced $CO_2$ production. Literature indicates metal doped MCM-48 & Si-MCM-48 could be employed in the following categories in addition to photocatalysis of the six probe molecules: liquid/gas-phase catalysis, chromatography, adsorption/separations, & solar collection/water-splitting. Finally, through the extensive use of literature, direction and vision will be given of where V-MCM-48/Si-MCM-48 might be employed to solve various application problems.

## 5.28 Modification of Synthetic Variables/Reaction Conditions for Synthesis of V-MCM-48

As noted earlier in the discussion section, there would be several synthetic variables that could be adjusted to lower the cost of V-MCM-48 production coupled with enhancement of structural characteristics, according to literature. [21,35,48,62,64,77,78,81,86,100,114,116,121,123,133,136,255] Galarneau and co-workers reported that the yield of silica from Stober MCM-48 synthesis with TEOS would be 30% or less due to dilute reaction medium conditions. [100] They propose the use of fumed silica, which cost substantially less than TEOS, and the yield would be approximately 70%. Furthermore, Vansant and co-workers have completed hydrothermal studies on silica precursors TEOS and fumed silica. [62] $N_2$ adsorption-desorption analysis of the Si-MCM48 silica prepared from these precursors before and after hydrothermal reaction conditions showed a marked increase in structural stability in Si-MCM-48 prepared from fumed silica. This was further evident in the calcination of both Si-MCM-48 silica materials made with the two precursors. At elevated temperatures, the TEOS prepared Si-MCM-48 structure surface area was substantially (~80% reduction) reduced with collapse of pore network. Major reason for the enhancement of Si-MCM-48 structure with fumed silica was due to higher condensation of pore walls. Fumed silica would be in oligomeric form (several Si-O-Si units long); whereas, TEOS would hydrolyze in solution to form monomers, which would have to form more bonds to, have the same condensed wall structure as fumed silica. [58,100,113,121,335] Due to entropy change, disorder would be more likely to occur then forming the same number of bonds needed as fumed silica to have the same condensation level. Therefore, monomers of TEOS potentially would form smaller oligomers of silica and condense into thinner silica walls; in contrast, fumed silica would have larger silicate oligomers, so there would be

less need for forming as many siloxane (Si-O-Si) bonds to produce a stable structure. [336] [Analogy: which would be more likely to occur to make a uniform structure: making ten bonds vs. one-hundred bonds?] Although use of fumed silica would produce a more stable, less costly Si-MCM-48 structure, as noted in literature, [100] this would require careful adjustment of synthetic procedure and use of an autoclave plus lengthen the synthesis time for production of Si-MCM-48. Therefore, one might employ a simple addition of dilute acid in a Si-MCM-48 synthesis with TEOS to reduce the pH value, thereby causing more silicate condensation and silica oligomers to precipitate out of solution: pH = 9, 85% yield of silica; pH = 5, 98% silica yield. [337] This reduction of pH might not be favorable for metal doped mesoporous materials, according to literature on framework incorporated Co-MCM-41 silica. [338] These researchers found that an increase in pH of 12 produced the largest powder XRD peak intensity vs. lower pH values, which would infer enhanced siloxane bond formation, as shown in Appendix C-C:41. Vralstad and co-worker note with Co-MCM-41 and Co-MCM-48 syntheses more dilute sulfuric acid led to decreased $Co^{2+}$ ion in the silica framework. [339] Similarly, the reduction of pH value might not be favorable to cause the isomorphical framework substitution of $V^{5+}$ for $Si^{4+}$ in MCM-48; since, the tetrahedral $V^{5+}$ species $VO_4^{3-}$ would only be in this form from pH = 12-14. [255,340] Unger and co-workers report the modified Stober synthesis employed to make Al-MCM-41 with aqueous ammonia ($NH_4OH$) had a pH value of 11.8-12, which would be similar for the V-MCM-48 synthesis (similar reaction conditions). [2,3,341] Through the modification of Stober's silica spherical particle synthesis, [1] Koodali and co-workers were able to facilitate greater condensation rate in the resulting Si-MCM-48 particles, thereby enhancing siloxane bond formation with a silica yield of 81% to 96%. [342] This was accomplished by adjusting the concentrations and stirring rate: TEOS, CTAB, aqueous ammonia ($NH_4OH$), and ethanol. The stirring rate was found to be pivotal in forming the most stable Si-MCM-48 structure. In conclusion, the use of pH adjustment with dilute aqueous acid might be helpful with increasing the stability of Si-MCM-48 and silica yield; however, framework incorporation might be prevented by reducing the pH value, so the modified synthesis by Koodali and co-workers could be easily be employed with little output of resources: use of fumed silica has great potential but would require greater amount of resources and time. [100,342]

Besides the use of TEOS and stability of MCM-48, literature indicates that the cost of CTAB surfactant would cause MCM-48 silica synthesis to beyond the reach of industrial applications. [21,97,99] The main methods applied to lower the surfactant costs for mesoporous silica synthesis include: lowering the surfactant/silica ratio, use of CTAB-anionic mixtures, and cationic-non-ionic surfactant mixtures. Reduction of the amount of CTAB surfactant in the MCM-48 synthesis would be an excellent method to increase the thickness of silica walls and lower synthesis cost. This has been accomplished with synthesis similar to Stober's except it uses NaOH. [343] Later refinement of this synthesis employed fluoride ion to permit lower CTAB/Si ratio for Si-MCM-48 synthesis. [344] Due to the negative effects of $Na^+$ on silica materials, [107,255] one might employ use of $NH_4OH$ instead of NaOH; however, Koodali and co-workers report lower then 0.41 of surfactant/Si ratio led to poor MCM-48 formation. [342] Therefore, the recent synthesis by researchers at surfactant/Si = 0.10 might be accomplished with use of a mixture of non-ionic/anionic surfactants. One of the early attempts at using mixtures of surfactants was by Li and co-workers. [47] They employed use of carboxylate anionic surfactant ($C_nH_{2n+1}COONa$, n = 11, 13, 15, 17) with CTAB to produce MCM-48 silica with pores of approximately 30 Å and pore volume of close to 1.0 g/cm$^3$. Instead of using of the

sodium version of these anionic surfactants, why not exchange with $NH_4^+$ from $NH_4NO_3$ and complete the modified Stober's synthesis with reduced amount of CTAB surfactant? [1] Recently, Li and co-workers have been able to synthesize Al-MCM-48 using mixed surfactant system. [82] Similarly, use the modified Stober synthesis for V-MCM-48 but employ surfactants by Li and co-workers plus $NH_4^+$ ion instead of $Na^+$ ion and $NH_4OH$. [1,47] Furthermore, this modification with use of surfactant mixture could be extended with cationic-non-ionic ones. Sun and co-workers were able to use a CTAB + OP-10 (p-Octyl polyethylene glycol ether) mixture to produce MCM-48. [345] Benefits of this synthesis include: wide surfactant ratio of OP-10/CTAB, lower cost, lower amount of surfactant in interfacial area where silicate anions condense, higher condensation rate, and larger pore size. Modification with $NH_4OH$ might produce MCM-48 silica. In conclusion, the reduction of CTAB surfactant used in the modified Stober synthesis could lower the cost of MCM-48 synthesis and have the potential of increasing the textural properties (pore size, pore volume, and wall thickness).

As noted earlier in the discussion section on the low solubility of $NH_4VO_3$ in aqueous medium, the following methods might cause the increasing solubility of $NH_4VO_3$ in reaction medium: (1) add $H_2SO_4$ to $NH_4VO_3$ to produce $VOSO_4 \cdot xH_2O$; and (2) add aqueous oxalic acid to produce $(NH_4)_2[VO(C_2O_4)_2]$. Vanadium sulfate oxide would be several times more expensive then $NH_4VO_3$; however, if $H_2SO_4$ could be added to produce the desired $VOSO_4 \cdot xH_2O$ precursor, this would enable to use the modified metal doped Stober's synthesis to produce V-MCM-48 at much higher metal loading rate due to enhanced solubility of metal precursor. [1-3] $VOSO_4 \cdot 3H_2O$ has been used in the majority of MCM-48 synthesis schemes that produce V-MCM-48 in framework. [85,93,94] Oxalic acid would be another alternative to cause $NH_4VO_3$ to have increasing solubility in aqueous medium, which has been done to produce $VO_x$ species. [255] Through the modification of $NH_4VO_3$ and other metal precursors, the $V^{5+}$ ion loading could be substantially increased in MCM-48 silica framework, according to Unger and co-workers. [2,3] This in fact occurred with synthesis of Co-MCM-48 from use of $CoCl_2 \cdot 2H_2O$ to $CoSO_4 \cdot 7H_2O$ precursors. [346]

## 5.29 Synthesis Modifications to Enhance Structural Stability of V-MCM-48

The above paragraphs outlined the synthetic methods that could produce Si-MCM-48 and V-MCM-48 at lower cost. The following methods for directly increasing the stability of the MCM-48 silica structure include: (1) fluoride ($F^-$) ion addition; (2) sulfate ($SO_4^{2-}$) ion addition; and (3) short high temperature hydrothermal treatments. Previous research on addition of $F^-$ ion to the synthesis gel of MCM-48 showed that too much prevent phase conversion from MCM-41 to MCM-48 to not occur; moreover, Kim and co-workers found that, at optimal amounts of fluoride ion, it would act as a hydrolysis and condensation catalyst and substitute for $OH^-$ in the silanol (Si-OH) groups in MCM-48. [13] These researchers also found, by boiling the as-synthesized MCM-48 with NaF salt, for a set period of time at 100°C, the $Q^3/Q^4$ ratio decreased significantly according to $^{29}Si$ MAS NMR. Recent research with $NH_4F$ in Al-MCM-48 modified Stober room temperature synthesis showed that the fluoride ion increased the condensation rate of Al-MCM-48 structure coupled with increased acidity of remaining OH groups. [347] The researchers found that careful addition of $NH_4F$ had no effect on the formation of Al-MCM-48 and/or spherical morphology of the metal doped spherical particles. Future research to produce Si-MCM-48 and metal doped MCM-48 silica with increased stability might employ addition of $NH_4F$ in synthesis gel and boil as-synthesized structure in $NH_4F$. If non-ionic surfactant was employed, the pH of the solution could be lower and $F^-$ ion would more effectively cause

condensation to occur in Si-MCM-48. [337,348] Ryoo and co-workers report boiling MCM-48 as-synthesized material in salt solution (example: NaCl) increased the number of $Q^4$ units ($SiO_4$) in silica wall of Si-MCM-48. [79]

The synthetic methods provided below modified from literature have potential to both lower cost of Si-MCM-48 synthesis and produce a more stable structure. Vogetin and co-workers reported that $(NH_4)_2SiF_6$ in pH = 6-7 medium the silica precursor becomes highly soluble and produces an increased polymerized MCM-41 structure at room temperature. [348] Other research reports favorable results with use of TEOS, CTAB/CTAOH and few hours under hydrothermal conditions produce highly ordered Si-MCM-48 silica structure with reduced levels of silanol groups. [349,350] One might combine these three synthesis methods to produce a much more stable Si-MCM-48 product at reduced cost. [348-350] Into a Teflon lined steel bomb following reagents should be added in order covered and heated at 393 K (120°C) for half-hour increments up to ten hours: fumed silica, concentrated $NH_4OH$, CTAB/CTOH, absolute ethanol, and 1/12 $H_2SiF_6$ amount compared to fumed silica. Similarly, Anpo and co-workers were able to reduce the CTAB/Si ratio to 0.1 with $F^-$ ion at 1.0 with use of TEOS as silica precursor. [351] One might attempt fumed silica in this synthesis with $NH_4F$ + $NH_4OH$ and heat under hydrothermal conditions for up to 72 hours at 393 K (120°C). [100,351,352] Also, one might attempt a mixture of non-ionic surfactant with CTAB and $F^-$ ion, which might enhance the hydrolysis/condensation rate of silica due to the "salting out effect" of $F^-$ ion on PEO blocks that complete for water molecules. [353]

Similar to the use of $F^-$ ion to increase condensation of silica, sulfate anion ($SO_4^{2-}$) has been shown to enhance the stability of Si-MCM-48. Anpo and co-workers found that $SO_4^{2-}$ ion, due to large hydration energy that in turn dehydrates the silicate and surfactant species, it causes greater condensation to occur within the pore walls of Si-MCM-48 in comparison to $Cl^-$ and $NO_3^-$ ions. [354] With the modified V-MCM-48 Stober synthesis, [1-3] one could use $VOSO_4 \cdot xH_2O$ + $(NH_4)_2SO_4$ to increase the thickness of the Si-MCM-48 silica pore wall. At high $VOSO_4 \cdot xH_2O$ metal loading, no sulfate ion would be needed. In addition to sulfate ion, use of $V^{5+}$ ion might increase the durability of MCM-48 silica to a point, as noted in previous research with chromium MCM-48. [355] Previous research indicated use of $NH_4Br$ in post-synthesis under hydrothermal conditions cause the silica pore wall to thicken. [356] This might be due to the relative binding of $Br^-$ ion to surfactant, which would permit silicate structure to further condensate. Therefore, one might try $NH_4NO_3$; since, it has the tightest binding to the surfactant head group, such as CTAB, according to the Hofmeister series of anions binding to cations: $NO_3^- > Br^- > Cl^- > SO_4^{2-} \sim F^-$. Further research might be conducted to see which of the ammonium salts of the above series proves the thickest pore wall and therefore most stable silica structure. In conclusion, use of $SO_4^{2-}$ anion, metal ion, and other ammonium salts have the potential to dramatically increase stability of Si-MCM-48 and metal doped MCM-48.

This last structural enhancement method for Si-MCM-48 and metal doped MCM-48 could significantly increase the degree of hydrothermal stability. Galareau and co-workers reported that post-treatment hydrothermally at 403 K (130°C) for two consecutive periods of two hours each led to much greater powder XRD peak intensity and lower amount of unit cell, $a_0$, contraction of Si-MCM-48 structure upon calcination. [116] Previous research has noted the benefits of higher temperature led to increased pore wall condensation and thicker silica walls. [349,356-358] In summary, $F^-$, $SO_4^{2-}$, and use of repeated short hydrothermal treatments would substantially increase the stability of the modified Stober prepared V-MCM-48 product and increase its use in various applications.

## 5.30 Instrumental Methods for Elucidation of V-MCM-48 Characteristics

Fromliterature review, the following methods have provided to further elucidate the structural features of V-MCM-48 using powder XRD, DR-UV-vis spectroscopy, and $N_2$ adsorption-desorption analysis. In addition, other characterization methods will be reviewed to provide a background for future research on metal doped mesoporous materials. Through use of the Scherrer's equation of peak broadness in powder XRD analysis, one could determine the particle size of a material. [359] The monodispersity and particle size would be universally important in various applications, such as: catalysis, chromatography, adsorption/separations, and solar energy collection/water-splitting. Therefore, future researchers could use the knowledge of particle size to modify synthesis/reaction conditions to produce the desired size particle. In addition to determining the particle size of V-MCM-48, one could complete powder XRD analysis of as-synthesized samples, old samples, and used samples. By completion of these addition analysis steps, one could monitor the changes that occur at each stage of synthesis and after calcination process. Previous research revealed that as-synthesized MCM-48 before calcination determined the unit-cell, $a_0$, parameter and after calcination the amount of shrinkage. [116] This value could be compared with other synthesis schemes to infer amount of condensation that had occurred. These researchers were able to compare the calcinated Si-MCM-48 and after one year of storage with two hydrothermal treatments proposed in the above paragraph. [116] They also were able to complete $N_2$ adsorption-desorption analysis, which revealed little change in structure after storage in ambient conditions (25°C + 1 atm + STP= standard-presurre-temperature). In contrast, Stucky and co-workers report for their Ti-MCM-48 sample, after six months of storage at ambient conditions, the conversion to complete amorphous structure. [32] With use of powder XRD analysis completed on spent catalyst, one might be able to design future catalysts to avoid structural defects that rendered the catalyst ineffective. In conclusion, completion of these additional powder XRD analysis treatments on V-MCM-48 would permit comparison to literature and infer the structural quality of the mesoporous material.

Besides the DR-UV-vis spectroscopy work completed on V-MCM-48, completion of K-M plot with vanadium standards, as referenced in results section, would permit both assignment of band-edge ($E_g$) for the various types of $V^{5+}$ species in MCM-48 silica. [273,275,278,360] Likewise, the plot in results section Figure 4:2 could have deconvolution technique applied to determine the percentage of certain $V^{5+}$ species, as done in literature. [85,276] Comparison of dehydrated V-MCM-48 samples could infer the effect of $H_2O$ ligand coordination has on the $V^{5+}$ coordination sphere in MCM-48 silica. Vansant and co-workers reported $H_2O$ coordination caused formation of geminal hydroxyl groups to vanadium-silica supported material, according to FT-Raman spectroscopy analysis. [272] V-MCM-41 has been reported in literature for tetrahedral coordination of isolated $V^{5+}$ species to have a band-edge ($E_g$) of 3.6 eV in dehydrated state vs. 3.3 eV with aqua ligands attached. [261] From completion of these additional methods, one could further ascertain the type of $V^{5+}$ coordination centers at work in photocatalysis of probe molecules. By synthesizing different Si/V compositions of V-MCM-48 with different types of $V^{5+}$ coordination oxide (oxo)/$H_2O$ coordinated-framework vs. wall attachment, one could use the band-edge and deconvolution data to determine what type of $V^{5+}$ coordination species in a series or isolated produce the most product by inference, which would permit the modified synthesis to produce particular $V^{5+}$ species at desire concentration and most desired products from catalytic reactions.

$N_2$ adsorption-desorption analysis techniques could be further expanded to include the pore size distribution (PSD) and t-plot (thickness plot). This would enable comparison of V-MCM-48 mesoporous materials to be compared to literature work. [233-249] PSD value would provide a method for determining the pore size uniformity. This would be important for shape selective catalysis, such as in liquid phase organic chemistry synthesis. [65,66,93,254] The t-plot would be used to determine if there were micropores in the walls of V-MCM-48. In addition, the t-plot extrapolated to the origin could provide the surface area value, which could be compared against BET surface area value. As noted earlier in the discussion section, the ascensions of high surface area does not necessarily mean that partial collapse of pore walls has not occurred with metal introduction into framework. [220] Therefore, these above characterization methods would provide deepen understanding of the pore network in V-MCM-48.

The analysis methods that follow would provide greater certainty of the $V^{5+}$ coordination geometry, pore structure, particle morphology, acidity of $V^{5+}$ spcies, amount of residual surfactant in structure, and metal content in V-MCM-48: $^{51}$V NMR, FT-IR, PAS-FT-IR, XANES, XAFS, XPS, RS, EXAFS, HR-TEM, TEM, SS $^{29}$Si MAS NMR, DRIFT, SAXS, granulometry analysis, SEM, $NH_3$-TPD, pyridine-TPD, microcalometry, TGA, TGA-DTA, EDS, XFA, AA, and ICP-AES. Researchers note that solid-state $^{51}$V NMR could be used to determine the coordination symmetry surrounding vanadium ion; moreover, the degree of vanadium polymeric species ($VO_n$) could be determined with the broadness of the peak due to anisotropy effect. [141] Unger and co-workers report use of solid-state $^{51}$V NMR to find if incorporation of heteroatoms into the MCM-48 silica matrix had occurred, and Reddy and co-workers note solid-state $^{51}$V NMR the best method for finding the level of incorporation of vanadium ion in MCM-41 framework. [2,84] The major limitation of this analytical technique would be if the material had paramagnetic metal ion species, such as $V^{4+}$ ($d^1$). [255] Fourier transform-infrarred (FT-IR) spectroscopy could be used to infer if $V^{5+}$ ion had coordinated in the tetrahedral framework positions in the MCM-48 silica due to the stretching frequency of vanadium-oxygen (oxo) bonds. Sarbam and co-workers synthesized Ce-MCM-41 and employed FT-IR analysis to obtain the stretching vibration frequency, and thereby compare with standards/literature of $Ce^{4+}$ ion had incorporated in MCM-41 silica framework position plus relative amounts of $Ce^{4+}$ ion species. [39] A variation of FT-IR spectroscopy would be photoacoustic (PAS)-FT-IR. Stucky and co-workers report the value of this technique would be enhanced structural elucidation due to prevention of KBr dilution errors and possible structural damage upon pellet formation. [92,96] The frequencies of some of the bands in the metal grafted MCM-48 were larger than in common FT-IR analysis, which was ascribed to structural retention/structural distortion prevention. X-ray absorption near-edge structure (XANES) could be implemented to elucidate the coordination sphere of metal ion in silica matrix, such as Cr-MCM-48. [60] Haller and co-workers employed XANES to determine the coordination of Cr ion in MCM-41 and MCM-48 silica. This was possible due to the shape and position noted for onset of absorption edge, which changed with valence and structure that the Cr ion adopted in the silica matrix. Therefore, it would be possible to tell if framework species were in the silica structure and coordination adopted, such as in metal doped mesoporous materials: Fe-MCM-48, V-MCM-41, Co-MCM-41, and Co-MCM-48. [25,48,361] X-ray absorption fine structure spectroscopy (XAFS) could be used to determine the oxidation state, coordination, quantity, and potentially dispersion of vanadium species in MCM-48 silica. [255] However, the data analysis for XAFS would require additional knowledge to reduce the complexity of analysis. X-ray photoelectron spectroscopy (XPS) would be similar to XAFS in analy-

sis features with exception of lack of ability of determine coordination geometry, and this technique would be only sensitive toward the chemistry of the surface. Raman spectroscopy (RS) could be employed to locate metal ion in the matrix + oxidation state + structure, such as with V-MCM-48. [6] Reddy and co-workers claim RS analysis could be used to tell if $V_2O_5$ clusters in MCM-41 mesoporous material had formed. [84] The major limitation of this method would be its level of sensitivity especially at low vanadium ion loading in mesoporous silica materials. [255] Stucky and co-workers report extended X-ray absorption fluorescence spectroscopy (EXAFS) was able to differentiate the bonding and coordination of $Zr^{4+}$ ion in framework and grafted MCM-48 silica. [95] Similarly, Vrlastad and co-workers found careful EXAFS analysis permitted assignment (differentiation) between both surface and framework incorporated cobalt species. [361] In conclusion, the above methods outlined to differentiate the vanadium species in MCM-48 silica could provide with greater certainty types of $V^{5+}$ coordination geometries.

The following analysis techniques could provide pore structure characterization results on V-MCM-48: HR-TEM, TEM, SS $^{29}$Si MAS NMR, DRIFT, SAXS, and granulometry. High resolution-transmission electron microscopy (HR-TEM) could be employed for defect analysis of pore network in MCM-48. Previous researchers have used HR-TEM to check for defects after incorporation of metal ion in MCM-41. [68] Likewise, other researchers were able to see the distortations of pores with greater incorporation of Mn ion in MCM-41. [132] Transmission electron microscopy (TEM) provides wide view over the pore structure, such as metal doped MCM-41 and MCM-48. [29,39,127,224] Kim and co-workers were able to differentiate the effect of $F^-$ ion on the MCM-48 silica pore wall structure with TEM analysis. [13] Besides a surface view presented by HR-TEM and TEM analysis, solid-state $^{29}$ Si magic angle spinning-nuclear magnetic resonance (MAS-NMR) would provide detailed data on the amount of condensation in the pore structure from the silanol ratios: $Q^1$, $Q^2$, $Q^3$, and full condensed $Q^4$. [12,163] Landry and co-workers employed solid-state $^{29}$Si MAS NMR to monitor the phase transition from MCM-41 to MCM-48 and tell the nature of polymerization of mesoporous silicate. [12]; likewise, research on Mn-MCM-41 with solid-state $^{29}$Si MAS NMR was used to determine if the $Q^4/Q^3$ ratio had changed with Mn ion incorporation. [132] Diffuse reflectance fourier-transform infrared (DRIFT) characterization method could be used to determine silanol groups in mesoporous materials, such as metal doped MCM-48. [163] This characterization technique would be employed in silica support analysis for chromatography. Small angle X-ray scattering (SAXS) and granulometry analysis could be used to tell if pore structure was ordered. [161,224] Finally, the many pore structural characterization methods listed above could be employed to develop a unifying picture of the molecular bonding in V-MCM-48 and related mesoporous silica materials.

The particle morphology of the structure could be investigated with scanning electron microscopy (SEM). Unger and co-workers have used this characterization technique on the modified Stober metal silica sphere synthesis to show that spherical shaped metal doped MCM-48 particles were formed. [1-3] In addition, this characterization method could be used to determine particle size and surface area, which could be compared to powder XRD and $N_2$ adsorption-desorption bulk measurements. [39,224] The acidity of $V^{5+}$ sites in V-MCM-48 and other metal doped mesoporous materials could be elucidated with ammonia-temperature programmed desorption ($NH_3$-TPD), where the higher the temperature of desorption would indicate increase acidity of certain sites on catalyst surface. [6] Haller and co-workers were able to use pyridine-TPD in situ to determine acid strength and kinds of acid sites in frame-

work V-MCM-41. [43] Other researchers used $NH_3$-TPD to determine type of coordination of $La^{3+}$ ion adopted in MCM-48 silica structure coupled with acidity of catalyst. [9] Similar to TPD would be microcalorimetry, which uses probe molecule and heat of chemisorption to determine strength of acid site. This was completed on isomorphous framework substituted Al, Ga, Fe,-MCM-48 mesoporous materials using $NH_3$. [16] Thermal gravimetric analysis (TGA) and thermal gravimetric analysis/differential analysis (TGA/DA) methods have been employed to determine the level of silanol groups and amount of surfantant/$H_2O$ in structure after calcination. [2,39,65,163,224,261] Unger and co-workers employed TGA to determine if any organic matter from the surfactant was left behind from calcination of V-MCM-48. [2]

The characterization methods discussed include: XFA, EDX, EDS, AA, and ICP-AES. All of these methods would be used to determine the metal concentration in the finished product in comparison to metal ion added in synthesis gel. X-ray fluorescence analysis was used by Unger and co-workers to determine what the $V^{5+}$ ion incorporation rate was for the modified Stober metal doped MCM-48 silica sphere in comparison to the hydrothermal one. [2,3] Energy dispersive X-ray (EDX) analysis was used in the synthesis of Al-MCM-48 and Ce-MCM-41 to find the metal loading after calcination. [4,39] Energy dispersive spectroscopy (EDS) with TEM provided concentration/distribution of $Co^{2+}$ species in M41S silica samples made with sodium silicate and TEOS, as noted in the synthesis of Co-MCM-41 and Co-MCM-48. [361] Similarly, atomic absorption (AA) spectroscopy has been used to find the difference in Si/Fe metal loading between initial and final Fe-MCM-48 product. [11,25] Inductively coupled plasma-atomic emission spectroscopy (ICP-AES) would provide a higher amount of accuracy vs. AA spectroscopy due to the fine emission lines given off by particular metal ions even at very low metal concentrations with Al, Ga, and Fe. [16] In summary, the above paragraphs presented characterization methods that could provide a more coherent direction of what comprises V-MCM-48 and other metal doped mesoporous materials.

## 5.31 Future Photocatalysis Research of Six Probe Molecules under Various Conditions

### 5.31.1 $CH_3CHO$

In general, different catalysts have different conversion rates under different reaction conditions. V-MCM-48 has been employed under photocatalytic conditions with l00 μL of liquid acetaldehyde. What would the degradation rate of acetaldehyde be at lower or higher initial concentrations in the static light reactor? From the assignment earlier of $V^{5+}$ species in MCM-48, it was tentatively proposed that complete oxidation to $CO_2$ required a series (several active lattice oxygens) of basic $V^{5+}$ centers, according to literature. [61,90,298,362] Therefore, with a change of metal precursor, it might be possible to use larger metal loading in V-MCM-48 and perfect type of species desired by removing wall species with dilute $H_2SO_4$ similar to what was done with Co-MCM-41 to eliminate $CoO_x$ species on pore wall surfaces. [338] In the synthesis of Co-MCM-48 the change from $CoCl_2 \cdot 2H_2O$ to $CoSO_4 \cdot 7H_2O$ permitted framework incorporation of $Co^{2+}$ ion in MCM-48 silica matrix up to 2.5 wt% vs. only ~ 1 wt% originally. [346] Vralstad and co-workers studied the interfacial chemistry of $Co^{2+}$ ion in M41S metal doped synthesis and noted charge density matching would effect not just by the metal cation but by the anion (counter-ion), such as $SO_4^{2-}$ or $Cl^-$ in precursors. [339] By completing DR-UV-vis analysis after washing with dilute acid, this would remove certain species from V-MCM-48 catalyst to provide an avenue for elucidation the effect of individual $V^{5+}$ species in MCM-48 silica structure similar to aqueous phase removal, according to literature. [85,90,97,99,267] With deconvolution of the peaks in

the DR-UV-vis plot, one may be able to determine if the species active for acetaldehyde were attached to wall surface or framework. [85,90] Re-completion of the acetaldehyde degradation data under dark, visible, and UV would infer the degree of activity of pore wall surface $V^{5+}$ species. With this change of catalytic preparation, deactivation from incomplete oxidation to acetic acid could be determined and reduced. As noted in literature, [363,364] $TiO_2$ deactivates with organic probe molecules, such as acetaldehyde. V-MCM-41 tetrahedral species have been reported with a band-edge ($E_g$) 3.3 to 3.6 eV compared to 3.2 eV band-gap for semiconductor anatase $TiO_2$. [261] It has been noted that the larger the bandgap the greater the oxidative ability of a catalyst, which could help prevent $V^{5+}$ centers in MCM-48 from deactivating easily. [289,359] High oxidation state has been noted to be needed to induce photocatalysis, which could be due to enhanced of charge carrier lifetimes. [250,251,255] Finally, Tanaka and co-workers reported use of $Cs^+$ ion with on $V_2O_5/SiO_2$ greately increased $CO_2$ production from $CH_3CHO$ due to $Cs^+$ ion interaction with vanadium oxide, as discussed further in 5.32. [365]

### 5.31.2 CO

With CO photooxidation using V-MCM-48, a switch in metal precursor and use of a greater metal loading in the MCM-48 mesoporous materials might enhance oxidation rate. Through determination of DR-UV-vis deconvolution of absorption peaks, more metal ion might proceed into the framework positions or on surface of pore walls. Due to the different concentrations of different vanadium species present with a change in metal precursor in MCM-48 silica, visible and UV-light photocatalysis experiments would need to be repeated. Depending on the results, a heavier or lower loading of $V^{5+}$ ion might produce the greatest $CO_2$ production. For the gold catalysts, one would need to repeat the best performing CO photooxidation catalysts under systematic adjustment of the volume of CO gas to find the optimal CO/air mixture. Au clusters have been shown to grow slowly in Al-SBA-15 due to $Al^{3+}$ ion, which reduces the mobility of the Au atoms in the silica matrix. [324] Mou and co-workers report high CO oxidation activity with use of Au-Ag alloy in silica matrix; since, Ag activates $O_2$ to form reactive oxygen, which has been noted to be the rate determining step in CO oxidation reaction. [324-326] One might employ Au-Ag alloy in V-MCM-48 with $V^{5+}$ ion vs. $Al^{3+}$ ion higher charge could lead to even smaller gold cluster size, thereby cause the catalyst to be highly active for CO oxidation reaction. In conclusion, the CO photooxidation rate appears determined by $V^{5+}$ species that had greater isolation vs. acetaldehyde degradation, so the higher metal loading would only work if in the framework.

### 5.31.3 $CH_3CH_2OH$

Ethanol photodegradation occurred only at a small rate over V-MCM-48 under visible light at 25°C. Literature suggested increasing the temperature of the light reactor from 25°C to 80°C in ethanol photodegradation over $TiO_2$ led to major increase in total oxidation product. [366] Ethanol photodegradation reactions that occurred at 25°C had gaseous ethanol injected into the light reactor. [288] One might attempt the photodegradation of ethanol at 80°C over V-MCM-48 under visible light, again. If the total degradation reaction increases significantly, then, complete UV-photodegradation of ethanol with Degussia-Huls P-25 $TiO_2$ at 25°C and see what type of data present. Ethanol boiling point would be 78°C, which might explain the poor data result obtained over V-MCM-48 under visible conditions. As a reference, acetaldehyde boiling point would be 22°C. If the reaction works for V-MCM-48 at 80°C, one might use the catalyst made from different metal precursors and see if any larger photocatalytic activity.

### 5.31.4 $CH_3COCH_3$ + $CH_3CHOHCH_3$

For both acetone and 2-propanol, it would appear that the probe molecules had not converted from liquid to gas-phase for photocatalysis to begin on surface of V-MCM-48. With elevated temperature from the boiling point for each of these reactants, it might permit enough of the reactant to absorb on the surface of the V-MCM-48 mesoporous material for photocatalysis to occur. This would appear likely considering the increased photodegradation rate of $TiO_2$ up to 80°C with ethanol. [366]

### 5.31.5 $CH_3CN$

Although acetonitrile had $CO_2$ production under UV-light at 25°C with its boiling point of 81°C, this photodegradation reaction would be likely would be larger over V-MCM-48 similar to ethanol over $TiO_2$ in literature. [366] The switch of metal precursors and dilute $H_2SO_4$ catalyst washing might lead to more framework $V^{5+}$ species that appear active for acetonitrile photodegradation. $CH_3CN$ degradation reaction like CO could be completed with IR analysis to determine the acid sites in V-MCM-48, as done by Yates and co-workers with acetonitrile over $TiO_2$. [367] In summary, completing ethanol, acetone, 2-propanol, and acetonitrile at elevated temperatures might lead to high photocatalysis activity; moreover, change of light reactor from static (good for monitoring kinetics-slow down reactions) to flow reactor would likely increase the rate of degradation. [334]

## 5.32 Potentially Higher Photocatalytic Activity Using Alkali Metal Ions over V-MCM-48

The experimental results of acetaldehyde indicated major reason for not all probe conversion to carbon dioxide was due to deactivation of the metal center. Tanaka *et al.* [368-379] and Wachs *et al.* [380] found increased conversion of organic probe molecule with use of alkali metal ions over $VO_x/SiO_2$. In environmental remediation with use of cesium ion ($Cs^+$) over $VO_x/SiO_2$ found large increase in acetaldehyde photodegradation rate. [365] The acetaldehyde photodegradation result would be linked to the enhanced basicity exhibited by the $Cs^+$ ion over the monomeric $VO_4^{3-}/SiO_2$ (VS) electronic states, as could be inferred from previous research even with a reduced surface area. [368-380] Basicity could be characterized as the ability to abstract an electrophilic species with excess electron density. This translates usually into the hydrogen species removed from an organic molecule as the initial step in transformation process to other products. The research results with alkali-metal ions over VS indicate activation of C-H bond, instead of fission of C-C organic framework bond, leads to larger reaction conversion activities with substantial increase in $CO_2$ concentration vs. unmodified VS. [368-380] When VS converts an alkene, such as propylene, the insertion of oxygen atoms for the two smaller partially oxidized organic fragments occurs. [375] In turn, the VS catalyst reduces to lower oxidation state and does not re-oxidize to initial $V^{5+}$ state easily, which might explain the lower activity of VS in heterogeneous catalysis due to consumption of one to two oxygen atoms from the active site ($VO_4^{3-}$). In contrast, application of alkali-metal ions strongly reduce the Lewis acidity of the $V^{5+}$ ion coupled with increased basicity of attached oxygen atoms to the transition metal ion. [368,372,374,375,380]

Through diffuse reflectance UV-vis spectroscopy (DR-UV-vis) and vanadium K-edge (V-K-edge) X-ray absorption near-edge absorption spectroscopy (XANES) analysis, Tanaka *et al.* report no coordination of $H_2O$ (aqua) to the $V^{5+}$ center from the spectra shifted to lower wavelength plus reduced absorption in alkali-metal-ion modified VS. [374,375] The DR-UV-vis V-K-edge XANES analysis revealed approximately tetrahedral symmetry in the alkali-metal-ion modified VS; whereas, aqua coordinated to VS forming distorted octahedral geometry and re-

lated red-shifted DR-UV-vis spectra, as shown in Appendix C-C:42. [375] Similarly, the reaction rate of hydrated/dehydrated $Rb^+$-modified VS (Rb-VS) had the identical activity in the conversion of 2-methylpropane to propanone (acetone), methanol, and carbon dioxide, which infers that $H_2O$ was not coordinating to the transition metal center. [372]

Due to the highly basic alkaki-metal hydroxide solution applied over the VS material, the surface area decreases dramatically as the alkali-metal ion/$V^{5+}$ ratio increases, as noted in previous research. [368-380] Even with the drastic reduction in surface area, the reaction activity increases greatly with the application of alkali-metal ions over vanadium oxide on silica + aluminum oxide supports. Tanaka *et al.* employed Rb-VS at Rb/V of 2.5 and had eight-fold increase in propylene conversion ($C_3H_6$) rate vs. unmodified VS, as shown in Appendix C-C:43. [378] Likewise, 2.5Rb-VA (Rb/V = 2.5; $VO_4^{3-}/Al_2O_3$-VA) was three times more active then VA without the alkali-metal-ions. From an environmental viewpoint, propylene photooxidation with alkali-metal-ions led to dramatic increase in $CO_2$ concentration even with the major reduction in surface area, as noted in Appendix C-Table C:1. [378] Clearly, $Rb^+$ ion causes the modification of VS with $CO_2$ concentration of 51% vs. unmodified VS of only 12% at 2.5 wt% $VO_x$ loading and $C_3H_6$ conversion rate of 244 vs. 30. Comparison of carbon dioxide concentration reveals basicity might be the major reason for enhanced $CO_2$ evolution on Rb-2.5VS vs. Rb-2.5VA; since, the surface area values were approximately 10% different, although $CO_2$ concentration was 51% vs. 31% in Rb-2.5 VS and Rb-2.5 VA, respectively. [Note: Rb/V ratio was 1.5 and 2.5 wt% $VO_x$ loading over silica and aluminum oxide supports.] The acidic $Al_2O_3$ support would not be to enhance the active sites oxygen atom's basicity, and the lower reaction conversion rate of 67 vs. 244 in Rb-2.5-VA and Rb-2.5-VS would be linked to the stronger acid-base interaction of nucleophilic (electron rich) olefin propylene to the electrophilic $Al_2O_3$ support. Tanaka *et al.* found that larger rubidium ion loading up to Rb/V of six at 0.5 wt% $V_2O_5$ loading on silica led to 80.1% $CO_2$ selectivity production rate vs. 14.5% $CO_2$ value with conversion rate of 0.02 percent in contrast to .38 percent of propylene, as shown Appendix C-Table C:1. [376] Finally, comparison of higher surface 2.5 wt% VS of 597 $m^2/g$ (0.29 V/$nm^2$) and 2.5 wt% VA of 170 $m^2/g$ (0.97 V/$nm^2$) showed that yield of more than four times of six carbon alcohol and ketone products for VA vs. VS, which reveals highly dispersed $V^{5+}$ ions closer together gave more products from cyclohexane. [381]

Adjacent alkali-metal-ions interact with the $VO_4^{3-}$ cluster on silica by modifying the attached oxygen atoms to the $V^{5+}$ ion, according to previous instrumental results. [374] Tanaka *et al.* reported that V=O bond in VS shifted from 1035 $cm^{-1}$ to 940 $cm^{-1}$ in Raman spectroscopy analysis with application of alkali-metal-ions. The Raman peaks were broad for Rb-VS, which infers that $Rb^+$ ion adjacent and modulating the V=O bond due to no sharp peaks corresponding to rubidium vanadates. This would be expected if the $Rb^+$ was removing electron density from the V=O bond. Fourier-transform (FT)-extended X-ray absorption fine structure (EXAFS) analysis reveals two types of bonds in Rb-VS material, thereby implies $Rb^+$ ion adjacent to $V^{5+}$ ion on silica support as $VO_4^{3-}$ monomeric species. FT-EXAFS analysis completed with inverse function also revealed that the $Rb^+$ ion was adjacent to $V^{5+}$ ion due to the small peak at 3.2 Å in the spectrum. In addition, Rb-VS curve-fitting analysis indicates two types of bonds (1.65 Å & 1.86 Å) with interatomic distances of close match to $V^{5+}$ and $Rb^+$ ions adjacent to each other. Tanaka *et al.* employed ab initio molecular orbital calculations to verify these experimental findings, and the bond lengths + angles support the elongation of V=O and one V-O-Si support bond to form $Rb^+$ $O_1$-V-$O_2$ system with double-bonded

character spread over the three atoms, as proposed in Appendix C-C:44 of Rb-VS model, consistent with the above instrumental results. [374]

The above sections indicate that alkali-metal-ions have a dramatic effect on the electric states of vanadium oxide on silica; however, the application of the photooxidation studies applied by Tanaka *et al.* using glass light filters proved the existence of two types of light activated centers with propane probe molecules: (1) $\lambda$ = 310-390 nm; and (2) $\lambda$ > 390 nm. [369-371] When VS catalyst was exposed to light range of $\lambda$ = 310-380 nm, the activation of V=O from $\pi \rightarrow \pi^*$ transition and/or n $\rightarrow \pi^*$ from lattice oxygen occurred with formation of a singlet-to-triplet excited electronic state, according to previous research. [281,282,298,305,306] These researchers note that the lowest energy triplet ($T_1$) state occurs through intersystem crossing (ISC), and Trans *et al.* indicates other triplet higher energy states possible due to the longer lifetime of the electronic transitions, as shown in Appendix C-C:45 involving $\pi \rightarrow \pi^*$ transitions. [281,282] Anpo *et al.* [305] and Tanaka *et al.* [298,306] both employed carbon monoxide as a probe molecule and noted triplet state inferred as the active one for photocatalysis due to quenching of photoluminescence spectra. Recent research on VA by Tanaka *et al.* indicates that the lowest energy triplet state directly involved in photocatalysis process, as shown in pictorially in Appendix C-C:46. [382] These researchers employed photoluminescent analysis coupled with infrared absorption spectroscopy with detuarated cyclohexane, $C_6D_{12}$. Although the excitation wavelength was not identical to the one used by Trans *et al.* in their analysis and assignment of the energy states in VS, [281,282] the photoluminescent excitation spectrum has similar features as Trans *et al.* one's [281,282] and was assigned the first two transitions as unstable singlet excited states $S_1$ and $S_2$ from charge transfer V=O oxygen to $V^{5+}$ ion through n$\rightarrow \pi^*$ transitions. [382] Additional evidence with infrared absorption spectroscopy showed that the V=O band at 1030 $cm^{-1}$ for VA disappears under various wavelengths of light. The oxygen-deturated hydrogen (OD) stretching band appears with use of $C_6D_{12}$, which proves chemical interaction with V=O bond with the oxygen atom from V=O inserting into the cycloalkane through an alcoxide intermediate form. They indicate that exchange of the $^{16}O$ atom in cyclohexanone exchanges finally with the V=$^{18}O$ bond at the end of the reaction. In addition, Trans *et al.* indicated non-bonding (n) to $\pi^*$ orbital into V=O bond would enhance lifetime of $T_1$ state due to orbital mismatch. [281,282] Similar to the research findings of Tanaka and co-workers with VA and cyclohexane under photooxidation conditions, previous analysis using deturated propane ($C_3D_8$) showed that the activation of the C-H bond as the rate determining step due to a rate constant greater than one with alkali-metal-ion modified VS. [373] Also, it was found that the lowest energy triplet state ($T_1$) was the one active in causing the C-H bond to lengthen and separate. Application of alkali-metal-ions could enhance triplet state due to formation of orbitals of similar energy between $O_1$-V-$O_2$ that scattered the unpaired electron, although Tanaka *et al.* claim reduction of triplet state responsible for forming larger amounts of select partially oxidized organic products + $CO_2$.

Support for alkali-metal-ion modified VS $T_1$ state would be from product yield/distribution results with propane probe molecule photooxidation studies. [369,370] As shown in Appendix C-Tables C:2 & C:3, one could view lower conversion efficiency of VS vs. Rb-VS and enhanced selectivity with use of alkali-metal-ion under UV-light irradiation. [370] Similarly, at $\lambda$ > 390 nm, propane conversion percent improved markablely with use of alkali-metal-ions vs. unmodified VS and product selectivity increased. UV-light activated VS produced several main products from propane: aldehydes, ketones, and $CO_2$. [369,370] Whereas, alkali-metal-ion modified VS species has a narrow

product distribution of mainly propanone (acetone) and carbon dixoxide at $\lambda > 390$ nm. Appendix C-C:47 & C:48 clearly show no activity and little activity catalytically under dark and visible light ($\lambda > 390$ nm) for unmodified VS; in contrast, with use of potassium ion over VS, the visible light induced photooxidation reaction occurs under $\lambda >$ 390 nm wavelength light. [370] As shown in Appendix C-C:47 & C:48 oxygen consumption would be markablely different in these two types of light centers, which might explain the photocatalytic results and longevity of the active centers, $VO_4^{3-}$. Besides the photooxidation studies with different wavelengths of light used, photoluminescence analysis showed the effects of alkali-metal-ions on V=O bond in VS, as shown in Appendix C-C:49-C:52. [370] As shown in Appendix C-C:49, the fine-structure of V=O bond deteriorates with larger alkali-metal-ions, which infers greater interaction of the V=O species with alkali-metal-ions. Further analysis of the spectra by differentiation of the peak intensity, as shown in Appendix C-C:50, reveals the broadening of the oscillatory peaks with increase atomic size of alkali-metal-ions, thereby implying greater interaction between V=O and alkali-metal-ion. Photoluminescence excitation results in Appendix C-C:51 show broad peaks centered at approximately 390 nm, which infers development of a new type of light activated center. Application of 400 nm light led to photoluminescence spectra with increased intensity, as shown in Appendix C-C:52. These results indicate that larger alkali-metal-ions atomic radii leads to greater interaction with the V=O bond in VS. Greater interaction of alkali-metal-ions led to larger conversion activity and formation of products, as shown in Appendix C-Tables C:2 & C:3. [370] Combining this photoluminescence analysis results with DR-UV-vis analysis, EXAFS/XANES, and $k^3$ weighted V-K-edge EXAFS instrumental methods, Tanaka *et al.* experimental data support the ab initio molecular orbital model in Appendix C-C:44 of $Rb^+$ ion adjacent to the $V^{5+}$ metal center and causing elongation of V=O + V-O-Si bonds with double bond character spread over the three atoms: $O_1$-V-$O_2$. [369,370,374,376] Photoluminescence and photooxidation data appears to show a trend of greater interactions electronically with alkali-metal-ion modified VS species, which leads to greater selectivity and higher reaction conversion of organic probe molecules. [369,370,375,378] These trends shown in Appendix C-Tables C:2 & C:3 and C:49-C:52 infer that alkali-metal-ions have a great impact on the electronic structure of $VO_4^{3-}$. [370]

Tanaka *et al.* results indicated that increased basicity with alkali-metal-ion use on VS led to reduced Lewis acidity from $V^{5+}$ metal center. [368-379] These researchers further investigated if coordination of aqua or reduction of the oxidation state of vanadium led to deactivation. [375] Similar to previous research findings, [298,305,306] these researchers found no coordination of aqua ligand and higher energy light needed for activation of $VO_4^{3-}$ without $H_2O$ or alkali-metal-ion modifications to the active center, as shown in Appendix C-C:53 & Table C:4. [375] More importantly, they found that reduction of $V^{5+}$ to $V^{4+}$ deactivated the catalyst with reaction activity diminishing, as shown in Appendix C-C.54. [375] After six hours on steam with propylene probe molecule, the DR-UV-vis spectrum exhibits a tail at approximately 800 nm and elimination of visible absorption from approximately 400 nm to 550 nm, thereby proving deactivation of metal center by reduction of oxidation state leads to low/non-existent photocatalysis activity. In conclusion, this proves Klabunde and co-workers findings that high oxidation state needed to have photocatalysis occur. [250,251]

With $TiO_2$, the formation of a hole and molecular oxygen results in formation of hydroxyl radical that attacks the organic probe molecule [289,294]; however, due to lack of knowledge if lattice oxygen or $O_2$ was responsible

for insertion of oxygen in the organic probe molecule over VS, alkali-metal-ion VS, Tanaka *et al.* employed $^{18}O_2$ isotopic tracer to study further the reaction with propylene, propane, and 2-methylpropane probe molecules. [291,370,371] FT-IR analysis of propylene photooxidation with $^{18}O_2$ showed formation of ethanal inseration of $^{16}O$ into the double bond. [291] As reaction time increased over VS, two new bands increased assigned to $^{18}O$ labeled molecular oxygen. The decrease of $^{16}O$ inseration into propylene over lengthen reaction time infers lattice oxygen consumed initially and replenished with $^{18}O_2$ to re-oxidize the reduced vanadium ion back to $V^{5+}$ state. Results with $^{18}O_2$ isotopic tracer study with propane and Rb-VS showed that lattice oxygen, the active species in formation of actone with $^{18}O/^{16}O$ ratio, gradually increase as the reaction time increased. [370] Appendix C-C:55 shows with increased irradiation time the conversion efficiency reduces, which could be explained due to initially $^{16}O$ lattice oxygen consumed on the active sites followed by lengthen time period where molecular oxygen would act as an reagent to oxidize $V^{5+}$ ion and replace lattice oxygen. The relatively rapid increase of $^{18}O/^{16}O$ ratio in the propanone and propanal products would not be due to exchange between lattice and the organic molecules; since, the rate of exchange would be much slower, as shown in Appendix C-C:56. [370] Moreover, Somorjai *et al.* reported $^{18}O_2$ temperature-programmed isotopic exchange studies with various transition metal ions in ZSM-5 zeolite in oxydehydrogenation of ethane occurs the slowest with $V^{5+}$ ion in the following trend: $Cu^{2+}>Nb^{5+}>Co^{2+}>V^{5+}$. [383] Finally, this result was repeated with 2-methylpropane and labeled $^{18}O_2$ to form $(CH_3)_2C=^{16}O + CH_3{}^{18}OH$, thereby indicates lattice oxygen the active species in VS catalyst system both with and without alkali-metal-ions. [371]

Tanaka *et al.* further studied alkali-metal-ion modified VS species to delineate if lattice oxygen could be the as the role of oxygen supply or if molecular oxygen was needed to replenish the lattice oxygen. [370] As shown in Appendix C-Tables C:2-C:3 & Table C:5 the reaction rate decreases linearly from approximately 40% conversion rate to 20% after five reaction cycles under $\lambda > 390$ nm light. Identical trend occurs for VS with steady decrease after two reaction cycles, as shown in Appendix C-Table C:5. [370] Formation of reduced organic products (olefins-$C_3H_6$-propylene) increases with molecular $O_2$ to replenish the lattice oxygen consumed; however, conversion rate drastically decreases, as shown in Appenxdix C-Tables C:2 & C:3. [370] From this study, one could conclude that there would be two types of light centers and molecular oxygen was needed to replenish/re-oxidize the reduced vanadium metal center. Similar to the deactivation seen for VS in propane photooxidation studies, the color changed from white to dark color like the VS unmodified catalysts inferring reduction of the metal center. Finally, the activity decreased with deactivation of the metal center, as noted previously with reduction in DR-UV-vis spectra intensity with change from $V^{5+}$ to $V^{4+}/V^{3+}$ in analysis by Wachs *et al.* [307], which reinforces the argument presented and related data that high oxidation state would be needed in photooxidation by Klabunde and co-workers. [250,251]

From an environmental remediation approach, propane photooxidation results reveal greater $CO_2$ concentration (selectivity) with larger alkali-metal-ion sizes, as shown in Appendix C-Tables C:2 & C:3. [370] This trend also held with photo-expoxidation of propylene with alkali-metal-ions, which led to increase $CO_2$ production with larger rubidium ion loading over VS catalyst, as shown in Appendix C-Table C:6. [376] From these photooxidation results, [370,376] one could conclude that the alkali-metal-ions selectively activates C-H bond, thereby initiates key step in formation of $CO_2$; since, abstraction of a hydrogen atom from small alkane, such as propane was determined to be the rate determining bearourer, according to deutrated hydrogen propane experiments by Tanaka *et al.*, as previously

discussed earlier. [373] Wachs and co-workers [380] have noted in ethane that the C-H bond has slight electrophilic character, and larger alkali-metal-ions would facilitate increased basicity of attached oxygen atoms to transition metal center due to greater interaction electronically through larger atomic size that enables more efficient transfer of valence electron to the VS species, as proposed by previous researchers. [368-379] Wachs and co-workers indicate, for example, $Cs^+$ ion , would have greater stabilization effect due to larger atomic orbital that mixes to a greater extent vs. smaller alkali-metal-ions, such as $Li^+$. [380] This enhanced electrostatic effect with larger alkali-metal-ion would also be demonstrated in previous research using photoluminescent, Raman spectroscopy, DR-UV-vis spectroscopy, and FT-IR spectroscopy. [368-380] As noted earlier in Appendix C-C:49-C:52 of photoluminescent analysis results, [370] the V=O bond in VS deteriorates as the size of the alkali-metal-ion increases from $Na^+$ to $Rb^+$ ion with broadening peak shape, in contrast to the sharp peak for VS without alkali-metal-ions. [369,370] Tanaka *et al.* attributed the greater electrostatic interaction of larger alkali-metal-ion with V=O as the major reason. [369-372] They also employed Raman spectroscopy and found a shift from 1040 $cm^{-1}$ to 940 $cm^{-1}$ with increase alkali-metal-ion size. Wachs et al. indicate from DR-UV-vis analysis that larger alkali-metal-ions has a small blue shift to lower wavelengths compared to smaller alkali-metal-ions, which would infer larger interaction electronically with VS active center. [380] and potentially smaller VS domain size note with $Cs^+$ modified $V/SiO_2$ vs. $V/SiO_2$ by Zhao *et al.* [384] This blue shift was also confirmed in excitation (emission) spectra in photoluminescent analysis by Tanaka *et al.* with $Na^+$, $K^+$, and $Rb^+$ ions, as shown in Appendix C-C:52. [370] In contrast to Tanaka *et al.* experimental results that showed no alkali-metal-ion vanadates due to broad Raman peaks, [368-379] Wachs *et al.* found, at low vanadium ion loading up to 5 wt% with cesium ion, that different forms of $Cs_3VO_4$ occurred on silica. [380] When the vanadium loading was 0.5 wt% greater on silica, the Raman band for V=O at 1040 $cm^{-1}$ appeared with fixed ratio of Cs:V:Si = 1:x:100, where x = 0.1, 1.0, 2.0, 10.0 and 20.0. This result conflicts with Tanaka *et al.* research that showed shift of V=O bond to 940 $cm^{-1}$ with alkali-metal-ion application to VS. [374,377] FT-IR characterization of alkali-metal-ion modified $V/SiO_2$ revealed both tetrahedral and octahedral $VO_x$ structures; but with larger alkaki-metal-ion loading, the formation of tetrahedral alkali-metal-ion vanadates occurred, according to Wachs and co-workers. [380] Finally, these above results show that alkali-metal-ions with increased size have enhanced effect on the electronic state of VS. [368-380]

Activation of the C-H bond in small alkanes and alkenes to form carbon dioxide would be effected be effected by the reducibility, contact time, and concentration of V-O-V bridging bonds in the catalyst, as noted with use of alkali-metal-ions/basic support with $VO_x$ in literature. [368-379,384-386] Basicity determines the ability to abstract an electrophilic species (usually a hydrogen organic molecule) from a molecule under study; however, reducibility would be the next determining factor in a series of needed reactions to form deep oxidation product: $CO_2$. Blasco *et al.* reported in the oxidative dehydrogenation of *n*-butane that catalytic activity follow hydrogen temperature-programmed reduction ($H_2$-TPR) trend $T_{onset}$: $V/Al_2O_3 \leq V/MgO > V/Sepiolite\ (SEP) \leq V/hydrotalcite\ (HTH)$. [386] $V/Al_2O_3$ had the largest catalytic activity for *n*-butane to $C_4$ alkenes, as shown in Appendix C-Table C:7. [386] V/MgO had second highest catalytic activity with V/HTH and V/SEP having approximately half activity of each, which might be due to, in addition to reducibility, BET surface area value and vanadium oxide loading on the support. Comparison of the surface area values show catalytic activity not directly related; since, V/MgO had surface area of 108 $m^2/g$ while V/HTH was 162 $m^2/g$. From a review of Appendix C-Table C:8, one could determine that the vana-

dium oxide loading would be the determining factor besides reducibility of catalyst/support. The activity trend with vanadium loading equalized for the different catalysts reveals $V/Al_2O_3 > V/MgO \approx V/SEP > V/HTH$. This trend would follow the $H_2$-TPR reducibility trend, thereby infers that the vanadium loading and support determine the catalytic activity. A deeper explanation of the types of $VO_x$-support bonds infers that higher concentrations of MgO and $Al_2O_3$ in V/HTH lower the ability for attached oxygen atoms in the support to liberate as active oxygen species in formation of product(s), as noted in the atomic ratio values in Appendix C-Table C:8. [386] In contrast, V/SEP has a much greater concentration of $SiO_2$ with considerably less acidic $Al_2O_3$, and the fact that silica would be sightly acidic means the MgO concentration, although not as large as V/HTH, would favor enhanced reducibility, which translates into higher catalytic activity, as shown in Appendix C-C:57. [386] Finally, this catalytic activity value would not translate into higher $CO_2$ production, as noted in Appendix C-C:57.

Besides the reducibility, the type of V-O-support bonds would directly affect both reactivity of catalyst and product distribution. [385] V/HTH would have a larger number of $V^{5+}$ tetrahedral species with many types of bridging oxygen atoms, according to $^{51}V$ NMR; whereas, V/SEP would be comprised of V-O-V dimeric $V^{5+}$ species. From an environmental remediation viewpoint, $CO_2$ concentration from *n*-butane oxidative dehydrogenation was the highest for V/MgO and second highest for V/HTH, when comparing the contact time (W/F) of *n*-butane of each catalyst plus $CO_2$ concentration, as shown in Appendix C-C:57. [385] Researchers indicate that basicity and the bridging oxygen between two $V^{5+}$ species on silica to be critical in complete oxidation of diesel soot particles and ethane. [380, 384] $Cs^+$-modified $V/SiO_2$ formed higher concentration of aldehydes from ethane at elevated temperatures; however, when the concentration of $Cs^+$ ion was above 1.0 wt% loading on $V/SiO_2$, the formation of highly basic active sites were formed with enhanced activation of lattice oxygen, which resulted in greater $CO_2$ production from ethane. In addition, the bridging oxygen between tetrahedral $V^{5+}$ species was shown to favor deep oxidation of diesel soot + ethane due to high oxygen mobility. Further enhancement occurred with application of $K^+$ ion to $V/SiO_2$, according to lower $T_{90}$/°C and greater $CO_2$ concentration. [380] [$T_{90}$ = 90%/°C soot consumed-lower temperature-more active.] Larger $K^+$ ion loading led to lower $T_{90}$/°C values, and higher $S_{CO2}$° ($CO_2/CO + CO_2$) concentrations, which showed that both increased basicity and ease of removal of bridging oxygen atom increase $CO_2$ production. This above result was noted by Zhao *et al.* with $Cs^+$-$V/SiO_2$ in ethane oxidation and polymeric V-O-V bonds led to increase $CO_x$. [384] In addition, Irusta *et al.* note lower formaldehyde yield could be due to the longer V-O-V bond in polymeric $VO_x$, which would detach from the support easier then V-O-Si bond, thereby permitting enhanced $CO_2$ production from methane. [385] Finally, higher $CO_2$ concentrations reported by these researchers would indicate that the ease of oxygen atom removal in catalyst would be the major factor in $CO_2$ formation. [380,384,385]

Basicity and reducibility would be major reasons for increased $CO_2$ production of small alkanes due to activation of C-H bond vs. fission of C-C bond, which requires more energy, as noted in results by Tanaka *et al.* with alkali-metal-ion modified VS in Appendix C-Tables C:2 & C:3. [369,370] Nevertheless, branched alkanes, such as 2-methylpropane, and propylene show reduced $CO_2$ production in contrast to propane. [372,375,376] As shown in Appendix C-Table C:9 the conversion percent increased from $Na^+$ to $Rb^+$ ion; however, Na-VS had the highest $CO_2$ concentration with $\lambda$ = 310-390 nm light. [371] Similarly, with $\lambda > 390$ nm light, Na-VS still had greater $CO_2$ production vs. Rb-VS. The reason for why less $CO_2$ made with $Rb^+$ vs. $Na^+$ might be due to steric hinderance, where the $Rb^+$

ion could not interact with $O_1$-V-$O_2$ system as efficiently with the 2-methylpropane molecule in triplet state, even though the basicity would be greater with $Rb^+$ ion vs. $Na^+$ ion. Likewise, propylene conversion rate much lower then propane with Rb-VS. [369,370,376] The reason would be higher basicity of alkali-metal-ion modified VS, thereby favors C-H bond activation, but alkenes would be electron rich, this causes them not to be activated easily, as noted by researchers. [369-379,384]

Photo-epoxidation of propylene with rubidium ion modified VS was 0.86 μmole/minute vs. 0.72 μmole/minute for unmodified VS both at 0.5 wt% $V_2O_5$ loading. [260,376] The key difference would be the selectivity for propylene oxide and $CO_2$ with reduced concentration of partially oxygenated products, as noted in Appendix C-Tables C:6 & C:10. [260,376] Wachs *et al.* research results indicate the enhanced aldehdye formation from ethane in $Cs^+$-V/$SiO_2$, but higher $CO_2$ production with potassium nitrate (K*n*) modified V/$SiO_2$ could be linked to the alkali metal ion precursor. [380] Zhao *et al.* had enhanced $CO_x$ formation for ethane with $Cs^+$ ion at higher $VO_x$ loading and found $Cs^+$ facilitated the formation of $VO_x$ species that favor $CO_x$-polymeric with high basicity. [384] These researchers used alkali nitrates in application over VS. [380,384] Tanaka *et al.* employed alkali hydroxides in their research with $VO_x/SiO_2$. [368-379] They used both KOH and $KNO_3$ to determine if the pH value was critical in forming alkali-metal-ion light activated VS sites. [371] As shown in Appendix C-Table C:11, the K-VS had close to double the conversion rate of 2-methylpropane vs. Kn-VS, which implies that the $K^+$ ion from KOH interacts to a greater extent with VS in contrast to $KNO_3$. Furthermore, photoluminescence analysis of K-VS and Kn-VS shows that VS effected by the $K^+$ ion in both precursors, but KOH prepared VS sample had a much higher intensity, thereby infers greater interaction of $K^+$ ion from KOH prepared VS plus larger number of these dispersed active sites. The interactions electronically of alkali-metal-ion would be much greater, as noted in photoluminescent data with alkali hydroxides and Raman spectroscopy, which showed a shift from 1040 $cm^{-1}$ to 940 $cm^{-1}$ from V=O bond. [374] This contrasts with Wachs *et al.* work where the V=O bond increased with $VO_x$ loading and formation of alkali vanadates [380]; whereas, Tanaka *et al.* noted no formation of alkali vanadates, according to broad Raman peaks instead of sharp peaks for alkali vanadates. [374,377] In conclusion, this explains why Wachs *et al.* [380] , Zhao *et al.* [384] obtained the result of $Cs^+$ ion forming more aldehydes, where the trend by Tanaka *et al.* [369-371] was larger size alkali-metal-ion favor $CO_2$ production due to greater interaction of $Rb^+$ ion with the $O_1$-V-$O_2$ elongation VS electronically, thereby effecting the $T_1$ state.

A deepen understanding of how alkali-metal-ions increase the basicity would be due to donation of electron density to the VS active center, thereby shifts the LUMO approximately 2 eV and HUMO 4 eV higher in energy, which results in less ability to accept electron density from alkenes. [369,372] Molecular orbital diagrams in Appendix C-C:58 & C:59 show both decrease of energy separation with alkali-metal-ions and shift of LUMO and HUMO to higher energy. [368,373] Due to the donation of electron density to the bridging oxygen next to the VS site, the oxygen atom ability to abstract a hydrogen from a alkane increases. [368] Tanaka *et al.* note that increased basicity would be due to promotion of a β-38 electron (unpaired) to the $K^+$-$O_1$-V-$O_2$ π* orbital in the triplet state, which would be highly unstable and reactive, as shown in Appendix C-C:59. [373] The double bond character would be spread over $O_1$-V-$O_2$ atoms, as shown in Appendix C-C:60. [373] This enhances instability due to similar energies for ground state $S_0$ and triplet $T_1$ state, as shown in Appendix C-C:59. [373] This was recently reinforced with use of VA and cyclo-

hexane photooxidation by Tanaka *et al.* [382] In addition, the triplet state permits propane to enter the active site close due to the elongation of $O_1$-V-$O_2$ conditions and therefore larger stabilization energy in contrast to ground state. Donation of an electron to the anti-bonding π* orbital ( n → π*) from alkali-metal-ion stabilized π* orbital of V=O and/or causes instability of non-bonding electron in oxygen of V=O. [374] As shown in Appendix C-C:61 with $Rb^+$ ion, the electron density would enter the metal center with light activation of the triplet state of lowest energy $S_0$ → $T_1$. [377] When the propane molecule C-H bond interacts with the $O_1$-V-$O_2$ site, the $V^{5+}$ oxidation state proceeds to $V^{4+}$, as shown in Appendix C-C:62. [377] The stabilization energy determines, which bond, primary or secondary, hydrogen was abstracted. The secondary hydrogen would be abstracted due to higher stabilization energy, according to Boltzmann distribution of energy.

In summary, alkali-metal-ions over VS enhance conversion activation both partial and total oxidation products. It would appear from an environmental viewpoint that alkali-metal-ions on V-MCM-48 would cause increased $CO_2$ production due to larger surface area and dispersed active sites. $Cs^+$ ion would likely be the best at activation of C-H bond to enhance basicity and the ability to donate plus effect electrostatically the electron state of VS. This was confirmed from the above research results with organic probe molecules. [368-380,384] Tanaka *et al.* showed that use of alkali hydroxide was pivotal in forming highly active light centers in photooxidation. Finally, enhanced $CO_2$ production dramatically increased with use of $Cs^+$ ion over $VO_x/SiO_2$ in acetaldehyde degradation and higher conversion rate of propylene over Rb-2.5VS, as shown in Appendix C-Table C:1. [365,378]

## 5.33 Review of Future Research with Potential Applications for MCM-48 Silica

### 5.33.1 Catalysis

Doping with metal ions K, Al, Cr, and V in MCM-48 silica has led to catalytically active mesoporous materials in liquid-phase catalysis of bulky substrates due to large pore volume and surface area. [65,66,93,253,387,388] For example, Al-MCM-48 was used to convert butyl-ether substitute to a useful product in high yield. [253] Moreover, the leaching problem common in zeolite metal doped catalysts including grafted metal doped M41S mesoporous materials would be essentially non-existent when the transition metal ion was incorporated in the framework positions of MCM-48 silica in aqueous phase. [65,66,85,90,93,97,99,253] The Rare earth ($La^{3+}$, $Ce^{4+}$)-MCM-48 catalysts have been shown to be highly active in epoxidation reactions, such as styrene and cychohexene, due to the 3-D pore network of MCM-48 silica, which permits reactants and products to flow in three dimensions. [9,11,290] V-KIT-6 would be a Ia3d bicontinuous large pore structure similar to MCM-48. [263] With the larger pores of this structure, even larger organic molecules could be converted to make fine organic molecules in fine chemical synthesis. The authors reference the possibility of photocatalysis being employed over V-KIT-6 due to enhanced kinetics. [263] Recently, $V_2O_5/MgF_2$ coupled semiconductor material was synthesized and tried on several probe molecules under visible and UV-light conditions. [300] Generally, these semiconductor catalysts have low surface area; therefore, if coupled with a high surface area support such as MCM-48 silica or KIT-6, the result might be synergistic enhancement of photocatalytic rate. Finally, the synthesis of small nanoparticles could be further decreased by adjustment of the modified Stober synthesis, which would result in more corners and edges shown to increase the catalytic rate of a reaction. [1,250,251,308-319]

### 5.33.2 Chromatography

Si-MCM-48 silica has been proposed as a replacement for monolithic silica support due to its 3-D pore structure, which permits lower diffusion coefficients in HPLC liquid-phase separations. Galareau and co-workers have reported on the pseudomorphic synthesis of MCM-48 form silica supports used in chromatography. [1,133,224] They have been able to produce MCM-48 in only a few hours of hydrothermal synthesis. Also, the product had spherical shape needed for use in chromatography. The Stober synthesis used to produce V-MCM-48 also makes silica spheres; however, according to literature, [1,133,224] the size of the spheres need to be 5-10 μm in diameter and have monodisperse size to be highly effective in liquid-phase chromatography. The Stober synthesis usually will only make up to ~ 1 μm spheres with polydispersity. [1-3] An article recently described formation of 1.5 cm spheres with polymer in them. [389] If surfactant + $NH_4OH$ converted the solid to MCM-48 followed by the techniques proposed to generate a more stable V-MCM-48 structure, it might be possible to use this material as a chromatography support. In conclusion, additional research will likely lead to a 3-D silica support, such as MCM-48 and/or KIT-6, this might replace the monolithic silica material.

### 5.33.3 Adsorption/Gas Separation/Chemical Sensor

Recent work on functionalized MCM-48 has shown with 3-D pore structure effective for separating $CO_2$ from flue gas of power plants. [390] The porosity and ability to diffuse the $CO_2$ through the silica membrane would be key challenge ahead for grafted amine-MCM-48, which entitiles reducing the calculated cost of $CO_2$ separation from $CO_2/N_2$ mixture approximately \$57/ton $CO_2$ to economical level of close to \$10/ton $CO_2$ at power plants. [391] Kim [391] notes that hydration of MCM-48 increased the number of silanol groups; therefore, use of modified Stober synthesis might be highly effective due to production of a large number of silanol groups that could be used as ligands with PEI polymer. [1-3] The density of silanol groups was a determining factor in how many amine function groups could be grafted as ligands on the walls of Si-MCM-48. Through the use of polyethyleneimine (PEI) that has branched amine functional groups, the $CO_2$ adsorption rate substantially increased in the gas separation of $CO_2/N_2$ gas mixture. Kumur notes PEI would be the most efficient ligand for removing $CO_2$ from mixtures of $CO_2$ + $N_2$ with functionalized MCM-48. [392] Size control, number of amine groups over the material determine if high adsorption and separation of $CO_2/N_2$ mixtures occurs, according to Kumar. [392] Similar to Kim's finding, [391] Kumar notes separation ability of the PEI-functionalized MCM-48 membrane doubled under the influence of water vapor due to enhancement of binding of $CO_2$ to amine groups, which might be from increased hydrogen binding. [392] Kim found that use of the amino-proply-modified reagents used commonly in synthesizing gas adsorption + separation materials not effective with $CO_2/N_2$ mixtures encountered at power plants. [391] By increasing the number of amine functional groups in the pores of MCM-48, one could obtain greater selectivity for $CO_2$ in separation of the gas mixture. Combining the basic amine functional groups to the walls of MCM-48 through silanol (Si-OH) group binding, Yang *et al.* have been able to separate $CO_2$ and $H_2S$ acidic gases in sour natural gas in "sweetening" process at lower energy requirements vs. commonly used liquid-solvent approach with monethanolamine (MEA), diethanolamine (DEA), and methyl-diethanolamine (MDEA). [393] They found that moisture and methane had no effect on the separation of the acidic gases, and $CO_2$ adsorption capacity. Growing/applying the silica to the support, such as Kumar work, [392] would be the next step in development of highly efficient gas separation membranes. It would be con-

ceivable that additional progress in functionization of MCM-48 will allow it to be used as a chemical sensor. For example, use of metal doped MCM-48 luminescent would be quenched when place in $Cu^{2+}$ solution. [394]

### 5.33.4 Solar Energy Collection/Water Splitting

V-MCM-48 could be potentially used for solar collection/water spitting due to the $V^{5+}$ oxidation state, which might permit photocatalysis of $H_2O = H_2 + O_2$ to occur. Klabunde and co-workers have noted high oxidation state needed to have high photocatalytic activity for photodegradation of toxic organic molecules. [250,251] It might be that this high oxidation state could induce oxidation of $H_2O$ under visible light? The result recently of taking $V_2O_5$ (2.1 eV) semiconductor and coupling to large bandgap (6.0 eV) $MgF_2$ semiconductor warrants further research [300]; since, other coupling/doping of semiconductors has led to high product formation rates under visible light. [210-213,215,216394-402] The problem with $V_2O_5$ like $Fe_2O_3$, $Cr_2O_3$, and $RuO_2$ would be that they generate electron-hole pairs that essentially recombine instantly. [300] With use of $MgF_2$, the separation of charge carriers occurs more effectively, thereby leading to higher oxidative rates. In similar though, why not combine $VO_x$/MgO with high surface area MCM-48 silica support for water-splitting? Literature reveals $VO_x$/MgO employed in partial oxidation reactions of organic molecules and environmental remediation. [287,398-400] Hamal and Klabunde note with $V_2O_5/TiO_2$ the need to have intimate bonding of $VO_x$ and $TiO_2$ for photocatalytic activity to occur. [359] Paola and co-workers reported similarly mixing of $WO_3/WS_2$ powder had little photocatalytic activity; however, with the formation of $WO_3$ islands with $WS_2$, there was much greater photocatalytic rate. [214] Due to the small bandgap of $V_2O_5$, the $V_2O_5/MgF_2$ catalyst absorbs well into the visible light range, so its potential as a visible light photocatalyst would be highly favorable. [300] The major two variables in solar light collection would be absorption of light and separation of charge carriers. Therefore, the $V_2O_5/MgF_2$ catalyst appears to have high potential in energy applications. [300] Finally, the $V_2O_5/MgF_2$ catalyst works better with very small amount of Pt: future research that could find another non-precious metal would cause this catalyst to reach wide-spread use.

## 5.34 After Thought About What Presented in Discussion Chapter

In summary, the V-MCM-48 catalyst would appear to have a bright future in photocatalysis, liquid-phase catalysis, chromatography, gas separation, and green energy applications; however, for all of these applications to reach wide-spread use of V-MCM-48/MCM-48, it will require intense research both at the basic level of synthesis (Stober's synthesis), of $V^{5+}$ oxide (oxo) transitions in MCM-48 silica, and funding. In closing, it would be the view of the author that the government of America puts too little in research and expects miracles overnight in the science field, and essentially all individuals involved in scientific research spend many years of persistence to reach a positive outcome to advance their certain section of research.

## References


1. Stober, W.; Fink, A.; Bohn, E. "*Controlled Growth of Monodisperse Silica Spheres in the Micron Size Range*," *Journal of Colloid and Interface Science* **1968**, *26*, 62-69 (Research article)

2. Schumacher, K.; Hohensche, d. F. v. C.; Unger, K. K.; Ulrich, R.; Chesne, D. A.; Wiesner, U.; Spiess, H. W. "*The Synthesis of Spherical Mesoporous Molecular Sieves MCM-48 with Heteroatoms Incorporated into the Silica Framework*," *Advanced Materials* **1999**,*11*,1194-1198 (Research article)

3. Schumacher, K.; Grun, M.; Unger, K. K. "*Novel synthesis of spherical MCM-48*," *Microporous and Mesoporous Materials* **1999**,*27*, 201-206 (Research article)

4. Romero, A. A.; Alba, M. D.; Klinowski, J. "*Aluminosilicate Mesoporous Molecular Sieve MCM-48*," *Journal of Physical Chemistry B* **1998**, *102*, 123-128 (Research article)

5. Schmidt, R.; Junggreen, H.; Stocker, M. "*Synthesis of a mesoporous MCM-48 material containing only tetrahedral aluminum*," *Chemical Communications* **1996**, 875-876 (Communication article)

6. Gomez, S.; Garces, L. J.; Villegas, J.; Ghosh, R.; Giraldo, O.; Suib, S. L. "*Synthesis and characterization of TM-MCM-48 (TM = Mn, V, Cr) and their catalytic activity in the oxidation of styrene*," *Journal of Catalysis* **2005**, *233*, 60-67 (Research article)

7. Gomez, S.; Giraldo, O.; Garces, L. J.; Villegas, J.; Suib, S. L. "*New Synthetic Route for the Incorporation of Manganese Species into the Pores of MCM-48*," *Chemistry of Materials* **2004**, *16*, 2411-2417 (Research article)

8. Morey, M.; Davidson, A.; Eckert, H.; Stucky, G. "*Pseudotetrahedral $O_{3/2}V{=}O$ Centers Immobilized on the Walls of a Mesoporous, Cubic MCM-48 Support: Preparation, Characterization, and Reactivity toward Water As Investigated by $^{51}V$ NMR and UV-vis Spectroscopies*," *Chemistry of Materials* **1996**, *8*, 486-492 (Research article)

9. Zhan, W.; Guo, Y.; Wang, Y.; Liu, X.; Guo, Y.; Wang, Y.; Zhang, Z.; Lu, G. "*Synthesis of Lanthanum-Doped MCM-48 Molecular Sieves and Its Catalytic Performance for the Oxidation of Styrene*," *Journal of Physical Chemistry B* **2007**, *111*, 12103-12110 (Research article)

10. Romero, A. A.; Alba, M. D.; Zhou, W.; Klinowski, J. "*Synthesis and Characterization of the Mesoporous Silicate Molecular Sieves MCM-48*," *Journal of Physical Chemistry B* **1997**, *101*, 5294-5300 (Research article)

11. Shao, Y.; Wang, L.; Zhang, J.; Anpo, M. "*Synthesis of Hydrotheramally Stable and Long-Range Ordered Ce-MCM-48 and Fe-MCM-48 Materials*," *Journal of Physical Chemistry B* **2005**, *109*, 20835-20841 (Research article)

12. Gallis, K. W.; Landry, C. C. "*Synthesis of MCM-48 by a Phase Transformation Process*," *Chemistry of Materials* **1997**, *9*, 2035-2038 (Communication article)

13. Kim, W. J.; Yoo, J. C.; Hayhurst, D. T. "*Synthesis of MCM-48 via phase transformation with direct addition of NaF and enhancement of hydrothermal stability by post-treatment in NaF solution*," *Microporous and Mesoporous Materials* **2002**, *49*, 125-137 (Research article)

14. Van Der Voort, P.; Mathieu, M.; Mees, F.; Vansant, E. F. "*Synthesis of High Quality MCM-48 and MCM-41 by Means of the GEMINI Surfactant Method*," *Journal of Physical Chemistry B* **1998**, *102*, 8847-8851 (Research article)

15. Rodriques, S.; Ranjit, K. T.; Uma, S.; Martyanov, I. M.; Klabunde, K. J. "*Single-Step Synthesis of a Highly Active Visible-Light Photocatalyst for Oxidation of a Common Indoor Air Pollutant: Acetaldehyde*," *Advanced Materials* **2005**, *17*, 2467-2471 (Research article)

16. Kosslick, H.; Lischke, G.; Landmesser, H.; Parlitz, B.; Storek, W.; Fricke, R. "*Acidity and Catalytic Behavior of Substituted MCM-48*," *Journal of Catalysis* **1998**, *176*, 102-114 (Research article)

17. Zhang, W.; Pinnavaia, T. J. "*Transition metal substituted derivatives of cubic MCM-48 mesoporous molecular sieves*," *Catalysis Letters* **1996**, *38*, 261-265 (Research article)

18. Moller, K.; Bein, T.; Fisher, R. X. "*Entrapment of PMMA Polymer Strands in Micro- and Mesoporous Materials*," *Chemistry of Materials* **1998**, *10*, 1841-1852 (Research article)

19. Vartuli, J. C.; Schmitt, K. D.; Kresge, C. T.; Roth, W. J.; Leonowicz, M. E.; McCullen, S. B.; Hellring, S.; Beck, J. S.; Schlenker, J. L.; Olson, D. H.; Sheppard, E. W. "*Effect of Surfactant/Silica Molar Ratios on the Formation of Mesoporous Molecular Sieves: Inorganic Mimicry of Surfactant Liquid-Crystal Phases and Mechanistic Implications*," *Chemistry of Materials* **1994**, *6*, 2317-2326 (Research article)

20. Ryoo, R.; Jun, S.; Kim, J. M.; Kim, M. J. "*Generalised route to the preparation of mesoporous metallosilicates via post-synthetic metal implantation*," *Chemical Communications* **1997**, 2225-2226 (Communications article)

21. Chen, D.; Li, Z.; Yu, C.; Shi, Y.; Zhang, Z.; Tu, B.; Zhao, D. "*Nonionic Block Copolymer and Anionic Mixed Surfactants Directed Synthesis of Highly Ordered Mesoporous Silica with Bicontinuous Cubic Structure*," *Chemistry of Materials* **2005**, *17*, 3228-3224 (Research article)

22. Kim, J. M.; Kim, S. K.; Ryoo, R. "*Synthesis of MCM-48 single crystals*," *Chemical Communications* **1998**, 259-260 (Communications article)

23. Corma, A. "*From Microporous to Mesoporous Molecular Sieve Materials and Their Use in Catalysis*," *Chemical Reviews* **1997**, *97*, 2373-2419 (Review article)

24. Van Der Voort, P.; Morey, M.; Stucky, G. D.; Mathieu, M.; Vansant, E. F. "*Creation of $VO_x$ Surface Species on Pure Silica MCM-48 Using Gas-Phase Modification of $VO(acac)_2$*," *Journal of Physical Chemistry B* **1998**, *102*, 585-590 (Research article)

25. Echchahed, B.; Moen, A.; Nicholson, D.; Bonneviot, L. "*Iron-Modified MCM-48 Mesoporous Molecular Sieves*," *Chemistry of Materials* **1997**, *9*, 1716-1719 (Communication article)

26. Tang, J.; Yu, C.; Zhou, X.; Yan, X.; Zhao, D. "*The anion sequence in the phase transformation of mesostructures templated by non-ionic copolymers*," *Chemical Communications* **2004**, 2240-2241 (Communication article)

27. Corma, A.; Kan, Q.; Rey, F. "*Synthesis of Si and Ti-Si-MCM-48 Mesoporous materials with controlled pore sizes in the absence of polar additives and alkali metal ions*," *Chemical Communications* **1998**, 579-580 (Communication article)

28. Sayari, A. "*Catalysis by Crystalline Mesoporous Molecular Sieves*," *Chemistry of Materials* **1996**, *8*, 1840-1852 (Review article)

29. Fyfe, C. A.; Fu, G. "*Structure Organization of Silicate Polyanions with Surfactants: A New Approach to the Synthesis, Structure Transformations, and Formation Mechanisms of Mesostructured Materials*," *Journal of the American Chemical Society* **1995**, *117*, 9709-9714 (Research article)

30. Raman, N. K.; Anderson, M. T.; Brinker, C. J. "*Template-Based Approaches to the Preparation of Amorphous, Nanoporous Silicas*," *Chemistry of Materials* **1996**, *8*, 1682-1701 (Review article)

31. Huo, Q.; Margolese, D. I.; Ciesia, U.; Feng, P.; Gler, T. E.; Sieger, P.; Leon, R.; Petroff, P. M.; Schuth, F.; Stucky, G. D. "*Generalized synthesis of periodic surfactant/inorganic composite materials*," *Nature* **1994**, *368*, 317-321 (Research article)

32. Morey, M.; Davidson, A.; Stucky, G. D. "*A new step toward transition metal incorporation in cubic mesoporous materials: preparation and characterization of Ti-MCM-48*," *Microporous Materials* **1996**, *6*, 99-104 (Research article)

33. Kruk, M.; Jaroniec, M.; Ryoo, R.; Kim, J. M. "*Characterization of High-Quality MCM-48 and SBA-1 Mesoporous Silicas*," *Chemistry of Materials* **1999**, *11*, 2568-2572 (Research article)

34. Schumacher, K.; Ravikovitch, P. I.; Du Chesne, A.; Neimark, A. V.; Unger, K. K. "*Characterization of MCM-48 Materials*," *Langmuir* **2000**, *16*, 45480-4654 (Research article)

35. Huo, Q.; Margolese, D. I.; Stucky, G. D. "*Surfactant Control of Phases in the Synthesis of Mesoporous Silica-Based Materials*," *Chemistry of Materials* **1996**, *8*, 1147-1160 (Research article)

36. Xu, J.; Luan, Z.; Hartmann, M.; Kevan, L. "*Synthesis and Characterization of Mn-Containing Cubic Mesoporous MCM-48 and AlMCM-48 Molecular Sieves*," *Chemistry of Materials* **1999**, *11*, 2928-2936 (Research article)

37. Pu, S.; Kim, J. B.; Seno, M.; Inui, T. "*Isopropylation of polynuclear aromatic hydrocarbons on Al-containing M41S mesoporous catalysts*," *Microporous Materials* **1997**, *10,* 25-33 (Research article)

38. Gucbilmez, Y.; Dogu, T.; Balci, S. "*Ethylene and Acetaldehyde Production by Selective Oxidation of Ethanol Using Mesoporous V-MCM-41 Catalysts*," *Industrial & Engineering Chemistry Research* **2006**, *45*, 3496-3502 (Research article)

39. Laha, S. C.; Mukherjee, P.; Sainkar, S. R.; Kumar, R. "*Cerium Containing MCM-41-Type Mesoporous Materials and their Acidic and Redox Catalytic Properties*," *Journal of Catalysis* **2002**, *207*, 213-222 (Research article)

40. Schmidt, R.; Stocker, M.; Akporiaye, D.; Heggelund Torstad, E.; Olsen, A. "*High-resolution electron microscopy and X-ray diffraction studies of MCM-48*," *Microporous Materials* **1995**, *5*, 1-7 (Research article)

41. Hartmann, M.; Bischof, C. "*Mechanical Stability of Mesoporous Molecular Sieve MCM-48 Studied by Absorption of Benzene, n-Heptane, and Cyclohexane*," *Journal of Physical Chemistry B* **1999**, *103*, 6230-6235 (Research article)

42. Hadjiivanov, K.; Tsoncheva, T.; Dimitrov, M.; Minchev, C.; Knozinger, H. "*Characterization of Cu/MCM-41 and Cu/MCM-48 mesoporous catalysts by FTIR spectroscopy of absorbed CO*," *Applied Catalysis A: General* **2003**, *241*, 331-340 (Research article)

43. Lim, S.; Haller, G. L. "*Preparation of Highly Ordered Vanadium-Substituted MCM-41: Stability and Acidic Properties*," *Journal of Physical Chemistry B* **2002**, *106*, 8437-8448 (Research article)

44. Park, D-H.; Nishiyama, N.; Egashira, Y.; Ueyama, K. "*Enhancement of Hydrothermal Stability and Hydrophobicity of a Silica MCM-48 Membrane by Silylation*," *Industrial & Engineering Chemistry Research* **2001**, *40*, 6105-6110 (Research article)

45. Shao, Y.; Wang, L.; Zhang, J.; Anpo, M. "*The photoluminescence of rhodamine B encapsulated in mesoporous Si-MCM-48, Ce-MCM-48, Fe-MCM-48 and Cr-MCM-48 molecular sieves*," *Journal of Photochemistry and Photobiology A: Chemistry* **2006**, *180*, 59-64 (Research article)

46. Hartmann, M.; Racouchot, S.; Bischof, C. "*Characterization of copper and zinc containing MCM-41 and MCM-48 mesoporous molecular sieves by temperature programmed reduction and carbon monoxide adsorption*," *Microporous and Mesoporous Materials* **1999**, *27*, 309-320 (Research article)

47. Chen, F.; Huang, L.; Li, Q. "*Synthesis of MCM-48 Using Mixed Cationic-Anionic Surfactants as Templates*," *Chemistry of Materials* **1997**, *9*, 2685-2686 (Communication article)

48. Wei, D.; Wang, H.; Feng, X.; Chuch, W-T.; Ravikovitch, P.; Lyubovsky, M.; Li, C.; Takeguchi, T.; Haller, G. L. "*Synthesis and Characterization of Vanadium-Substituted Mesoporous Molecular Sieves*," *Journal of Physical Chemistry B* **1999**, *103*, 2113-2121 (Research article)

49. Alfrdsson, V.; Anderson, M. W.; Ohsuna, T.; Terasaki, O.; Jacob, M.; Bojrup, M. "*Cubosome Description of the Inorganic Mesoporous Structure MCM-48*," *Chemistry of Materials* **1997**, *9*, 2066-2077 (Communication article)

50. Zhu, Z.; Chang, Z.; Kevan, L. "*Synthesis and Characterization of Mesoporous Chromium-Containing Silica Tube Molecular Sieves CrMCM-41*," *Journal of Physical Chemistry B* **1999**, *103*, 2680-2688 (Research article)

51. Kohn, R.; Froba, M. "*Nanoparticles of 3d transition metal oxides in mesoporous MCM-48 silica host structures: Synthesis and characterization*," *Catalysis Today* **2001**, *68*, 227-236 (Research article)

52. Xu, W.; Aydin, M.; Zakin, S.; Akins, D. L. "*Aggregation of Thionine within AlMCM-48*," *Journal of Physical Chemistry B* **2004**, *108*, 5588-5593 (Research article)

53. Hartmann, M.; Racouchot, S.; Bischof, C. "*Synthesis and redox properties of MCM-48 containing copper and zinc*," *Chemical Communications* **1997**, 2367-2368 (Communication article)

54. Yong, G-P.; Jin, Z-X.; Tong, H-W.; Yan, X-Y.; Li, G-S.; Liu, S-M. "*Selective reduction of bulky polycyclic aromatic hydrocarbons from mainstream smoke of cigarettes by mesoporous materials*," *Microporous and Mesoporous Materials* **2006**, *91*, 238-243 (Research article)

55. Schulz-Ekloff, G.; Rathousky, J.; Zukal, A. "*Controlling of morphology and characterization of pore structure of ordered mesoporous silicas*," *Microporous and Mesoporous Materials* **1999**, *27*, 273-285 (Research article)

56. Kruk, M.; Jaroniec, M.; Ryoo, R.; Joo, S. H. "*Characterization of MCM-48 Silicas with Tailored Pore Sizes Synthesized via a Highly Efficient Procedure*," *Chemistry of Materials* **2000**, *12*, 1414-1421 (Research article)

57. Lee, C. W.; Lee, W. J.; Park, Y. K.; Park, S-E. "*Catalytic hydroxylation of benzene over vanadium-containing molecular sieves*," *Catalysis Today* **2000**, *61*, 137-141 (Research article)

58. Mokaya, R. "*Influence of pore wall thickness on the steam stability of Al-grafted MCM-41*," *Chemical Communications* **2001**, 633-634 (Communications article)

59. Rodriques, S.; Uma, S.; Martyanov, I. N.; Klabunde, K. J. "*Visible light photocatalytic activity for degradation of acetaldehyde using transition metal incorporated Al-MCM-41 (aluminum doped silica zeolitic material)*," *Journal of Photochemistry and Photobiology A: Chemistry* **2004**, *165*, 51-58 (Research article)

60. Pak, C.; Haller, G. L. "*Reversible coordination change of chromium in Cr-MCM-41 and Cr-MCM-48 studied by X-ray absorption near edge structure*," *Microporous and Mesoporous Materials* **2001**, *48*, 165-170 (Research article)

61. Lim, S.; Haller, G. L. "*Gas phase methanol oxidation on V-MCM-41*," *Applied Catalysis A: General* **1999**, *188*, 277-286 (Research article)

62. Cassiers, K.; Linssen, T.; Mathieu, M.; Benjelloun, M.; Schrijnemarkers, K.; Van Der Voort, P.; Cool, P.; Vansant, E. F. "*A Detailed Study of Thermal, Hydrothermal, and Mechanical Stabilities of a Wide Range of Surfactant Assembled Mesoporous Silicas*," *Chemistry of Materials* **2002**, *14*, 2317-2324 (Research article)

63. Edler, K. J.; White, J. W. "*Further Improvements in the Long-Range Order of MCM-41 Materials*," *Chemistry of Materials* **1997**, *9*, 1226-1233 (Research article)

64. Xu, J.; Luan, Z.; He, H.; Zhou, W.; Kevan, L. "*A Reliable Synthesis of Cubic Mesoporous MCM-48 Molecular Sieve*," *Chemistry of Materials* **1998**, *10*, 3690-3698 (Research article)

65. Sakthivel, A.; Dapurkar, S. E.; Selvam, P. "*Mesoporous (Cr)MCM-41 and (Cr)MCM-48 molecular sieves: promising heterogeneous catalysts for liquid phase oxidation reactions*," *Catalysis Letters* **2001**, *77*, 155-158 (Research article)

66. Dapurkar, S. E.; Sakthivel, A.; Selvam, P. "*Novel mesoporous (Cr)-MCM-48 molecular sieves: Promising heterogeneous catalysts for selective oxidation reactions*," *New Journal of Chemistry* **2003**, *27*, 1184-1190 (Research article)

67. Landmesser, H.; Kosslick, H.; Storek, W.; Fricke, R. "*Interior surface hydroxyl groups in ordered mesoporous silicates*," *Solid State Ionics* **1997**, *101-103*, 271-277 (Research article)

68. Yuan, Z. Y.; Wang, J. Z.; Zhang, Z. L.; Chen, T. H.; Li, H. X. "*Vanadium- and chromium-containing MCM-41 molecular sieves with hierarchical structure*," *Microporous and Mesoporous Materials* **2001**, *43*, 227-236 (Research article)

69. Kawi, S.; Shen, S.-C. "*Effects of structural and non-structural Al species on the stability of MCM-41 materials in boiling water*," *Materials Letters* **2000**, *42*, 108-112 (Research article)

70. Reddy, E. P.; Davydov, L.; Smirniotis, P. S. "*Characterization of Titania Loaded V-, Fe-, and Cr-Incorporated MCM-41 by XRD, TPR, UV-vis, Raman, and XPS Techniques*," *Journal of Physical Chemistry B* **2002**, *106*, 3394-3401 (Research article)

71. Shen, S. –C.; Kawi, S. "*Understanding of the Effect of Al Substitution on the Hydrothermal Stability of MCM-41*," *Journal of Physical Chemistry B* **1999**, *103*, 8870-8876 (Research article)

72. Ryoo, R.; Jun, S. "*Improvement of Hydrothermal Stability of MCM-41 Using Salt Effects during the Crystallization Process*," *Journal of Physical Chemistry B* **1997**, *9*, 317-320 (Research article)

73. Luan, Z.; Xu, J.; He, H.; Klinowski, J.; Kevan, L. "*Synthesis and Spectroscopic Characterization of Vanadosilicate Mesoporous MCM-41 Molecular Sieves*," *Journal of Physical Chemistry* **1996**, *100*, 19595-19602 (Research article)

74. Chaudhari, K.; Das, T. K.; Rajmohanan, P. R.; Lazar, K.; Sivasanker, S.; Chandwadkar, A. J. "*Synthesis, Characterization, and Catalytic Properties of Mesoporous Tin-Containing Analogs of MCM-41*," *Journal of Catalysis* **1999**, *183*, 281-291 (Research article)

75. Chao, K. J.; Wu, C. N.; Chang, H.; Lee, L. J.; Hu. S-f. "*Incorporation of Vanadium in Mesoporous MCM-41 and Microporous AFI Zeolites*," *Journal of Physical Chemistry B* **1997**, *9*, 6341-6349 (Research article)

76. Cheng, C-F.; He, H.; Zhou, W.; Klinowski, J.; Sousa Goncalves, J. A.; Gladden, L. F. "*Synthesis and Characterization of the Gallosilicate Mesoporous Molecular Sieve MCM-41*," *Journal of Physical Chemistry* **1996**, *100*, 390-396 (Research article)

77. Vidya, K.; Dapurkar, S. E.; Selvam, P.; Badamali, S. K.; Kumar, D.; Gupta, N, M. "*Encapsulation, characterization and catalytic properties of uranyl ions in mesoporous molecular sieves*," *Journal of Molecular Catalysis A: Chemical* **2002**, *181*, 91-97 (Research article)

78. Vidya, K.; Dapurkar, S. E.; Selvam, P.; Badamali, S. K.; Gupta, N. M. "*The entrapment of $UO_2^{2+}$ in mesoporous MCM-41 and MCM-48 molecular sieves*," *Microporous and Mesoporous Materials* **2001**, *50*, 173-179 (Research article)

79. Jun, S.; Kim, J. M.; Ryoo, R.; Ahn, Y-S.; Han, M-H. "*Hydrothermal stability of MCM-48 improved by post-synthesis restructuring in salt solution*," *Microporous and Mesoporous Materials* **2000**, *41*, 119-127 (Research article)

80. Yu, J.; Shi, J-L.; Chen, H-R.; Yan, J-N.; Yan, D-S. "*Effect of inorganic salt addition during synthesis on pore structure and hydrothermal stability of mesoporous silica*," *Microporous and Mesoporous Materials* **2001**, *46*, 153-162 (Research article)

81. Dapurkar, S. E.; Badamali, S. K.; Selvam, P. "*Nanosized metal oxides in the mesopores of MCM-41 and MCM-48 silicates*," *Catalysis Today* **2001**, *68*, 63-68 (Research article)

82. Chen, F.; Song, F.; Li, Q. "*Mixed cationic-anionic templating route to Al-MCM-48*," *Microporous and Mesoporous Materials* **1999**, *29*, 305-310 (Research article)

83. Trofymluk, O.; Levchenko, A. A.; Tolbert, S. H.; Novrotsky, A. "*Energetics of Mesoporous Silica: Investigation into Pore Size and Symmetry*," *Chemistry of Materials* **2005**, *17*, 3772-3783 (Research article)

84. Reddy, K. M.; Moudrakovski, I.; Sayari, A. "*Synthesis of Mesoporous Vanadium Silicate Molecular Sieves*," *Journal of the Chemical Society, Chemical Communications* **1994**, 1059-1060 (Communication article)

85. Mathieu, M.; Van Der Voort, P.; Wechkhuysen, B. M.; Rao, R. R.; Catana, G.; Schoonheydt, R. A.; Vansant, E. F. "*Vanadium-Incorporated MCM-48 Materials: Optimization of the Synthesis Procedure and in Situ Spectroscopic Study of the Vanadium Species*," *Journal of Physical Chemistry B* **2001**, *105*, 3393-3399 (Research article)

86. Morey, M. S.; Davidson, A.; Stucky, G. D. "*Silica-Based, Cubic Mesostructures: Synthesis, Characterization and Relevance for Catalysis*," *Journal of Porous Materials* **1998**, *5*, 195-204 (Review article)

87. Koyano, K. A.; Tatsumi, T.; Tanaka, Y.; Nakata, S. "*Stabilization of Mesoporous Molecular Sieves by Trimethylsilylation*," *Journal of Physical Chemistry B* **1997**, *9*, 9436-9440 (Research article)

88. Ryoo, R.; Joo, S. H.; Kim, J. M. "*Energetically Favored Formation of MCM-48 from Cationic-Neutral Surfactant Mixtures*," *Journal of Physical Chemistry B* **1999**, *103*, 7435-7440 (Research article)

89. Ko, C. H.; Ryoo, R. "*Imaging the channels in mesoporous molecular sieves with platinum*," *Chemical Communications* **1996**, 2467-2468 (Communication article)

90. Baltes, M.; Cassiers, K.; Van Der Voort, P.; Weckhysen, B. M.; Schoonheydt, R. A.; Vansant, E. F. "*MCM-48-Supported Vanadium Oxide Catalysts, Prepared by the Molecular Designed Dispersion of $VO(acac)_2$: A Detailed Study of the Highly Reactive MCM-48 Surface and the Structure and Activity of the Deposited $VO_x$*," *Journal of Catalysis* **2001**, *197*, 160-171 (Research article)

91. Kumar, D.; Pillai, K. T.; Sudersanan, V.; Dey, G. K.; Gupta, N. M. "*Hydrothermal Synthesis and Characterization of Uranium-Containing MCM-48 Samples*," *Chemistry of Materials* **2003**, *15*, 3859-3865 (Research article)

92. Morey, M. S.; O'Bren, S.; Schwarz, S.; Stucky, G. D. "*Hydrothermal and Postsynthesis Surface Modification of Cubic, MCM-48, and Ultralarge Pore SBA-15 Mesoporous Silica with Titanium*," *Chemistry of Materials* **2000**, *12*, 898-911 (Research article)

93. Selvam, P.; Dapurkar, S. E. "*Catalytic activity of highly ordered mesoporous VMCM-48*," *Applied Catalysis A: General* **2004**, *276*, 257-265 (Research article)

94. Pena, M. L.; Dejoz, A.; Fornes, V.; Rey, F.; Vazquez, M. I.; Lopez Nieto, J. M. "*V-containing MCM-41 and MCM-48 catalysts for the selective oxidation of propane in gas phase*," *Applied Catalysis A: General* **2001**, *209*, 155-164 (Research article)

95. Morey, M. S.; Stucky, G. D.; Schwarz, S.; Froba, M. "*Isomorphic Substitution and Postsynthesis Incorporation of Zirconium into MCM-48 Mesoporous Silica*," *Journal of Physical Chemistry B* **1999**, *103*, 2037-2041 (Research article)

96. Morey, M. S.; Bryan, J. D.; Schwarz, S.; Stucky, G. D. "*Pore Surface Functionalization of MCM-48 Mesoporous Silica with Tungsten and Molybdenum Metal Centers: Perspectives on Catalytic Peroxide Activation*," *Chemistry of Materials* **2000**, *12*, 3435-3444 (Research article)

97. Van Der Voort, P.; Baltes, M.; Vansant, E. F. "*Synthesis of Stable, Hydrophobic MCM-48/$VO_x$ Catalysts Using Alkychlorosilanes as Coupling Agents for the Molecular Designed Dispersion of $VO(acac)_2$*," *Journal of Physical Chemistry B* **1999**, *103*, 10102-10108 (Research article)

98. Blasco, T.; Corma, A.; Navarro, M. T.; Perez Pariente, J. "*Synthesis, Characterization, and Catalytic Activity of Ti-MCM-41 Structures*," *Journal of Catalysis* **1995**, *156*, 65-74 (Research article)

99. Van Der Voort, P.; Baltes, M.; Vansant, E. F. "*Stabilized MCM-48/$VO_x$ Catalysts: synthesis, characterization and catalytic activity*," *Catalysis Today* **2001**, *68*, 119-128 (Research article)

100. Collart, O.; Van Der Voort, P.; Vansant, E. F.; Despantier, D.; Galarneau, A.; Di Renzo, F.; Fajula, F. "*A High-Yield Reproducible Synthesis of MCM-48 Starting from Fumed Silica*," *Journal of Physical Chemistry B* **2001**, *105*, 12771-12777 (Research article)

101. Alfredsson, V.; Anderson, M. W. "*Structure of MCM-48 Revealed by Transmission Electron Microscopy*," *Chemistry of Materials* **1996**, *8*, 1141-1146 (Research article)

102. Marler, B.; Oberhagemann, U.; Vortmann, S.; Gies, H. "*Influence of the sorbate type on the XRD peak intensities of loaded MCM-41*," *Microporous Materials* **1996**, *6*, 375-383 (Research article)

103. Kim, W. J.; Yoo, J. C.; Hayhurst, D. T. "*Synthesis of hydrothermally stable MCM-41 with initial adjustment of pH and direct addition of NaF*," *Microporous and Mesoporous Materials* **2000**, *39*, 177-186 (Research article)

104. Ryoo, R.; Kim, J. M. "*Structural Order in MCM-41 controlled by Shifting Silicate Polymerization Equilibrium*," *Journal of the Chemical Society, Chemical Communications* **1995**, 711-712 (Communication article)

105. Kim, J. M.; Jun, S.; Ryoo, R. "*Improvement of Hydrothermal Stability of Mesoporous Silica Using Salts: Reinvestigation for Time-Dependent Effects*," *Journal of Physical Chemistry B 1999*, *103*, 6200-6205 (Research article)

106. Xia, Y.; Mokaya, R. "*On the Hydrothermal Stability of Mesoporous Aluminosilicate MCM-48 Materials*," *Journal of Physical Chemistry B* **2003**, *107*, 6954-6960 (Research article)

107. Pauly, T. R.; Petkov, V.; Liu, Y.; Billinge, S. J. L.; Pinnavaia, T. J. "*Role of Framework Sodium versus Local Framework Structure in Determining the Hydrothermal Stability of MCM-41 Mesostructures*," *Journal of the American Chemical Society* **2002**, *124*, 97-103 (Research article)

108. Sayari, A. "*Novel Synthesis of High-Quality MCM-48 Silica*," *Journal of the American Chemical Society* **2000**, *122*, 6504-6505 (Communication article)

109. Che, S.; Lim, S.; Kaneda, M.; Yoshitake, H.; Terasaki, O.; Tatsumi, T. "*The Effect of the Counteranion on the Formation of Mesoporous Materials under the Acidic Synthesis Process*," *Journal of the American Chemical Society* **2002**, *124*, 13962-13963 (Communication article)

110. Landry, C. C.; Tolbert, S. H.; Gallis, K. W.; Monnier, A.; Stucky, G. D.; Norby, P.; Hanson, J. C. "*Phase Transformation in Mesostructured Silica/Surfactant Composites. Mechanisms for Change and Applications to Materials Synthesis*," *Chemistry of Materials* **2001**, *13*, 1600-1608 (Research article)

111. Froba, M.; Kohn, R.; Bouffaud, G.; Richard, O.; van Tendeloo, G. "*$Fe_2O_3$ Nanoparticles within Mesoporous MCM-48 Silica: In Situ Formation and Characterization*," *Chemistry of Materials* **1999**, *11*, 2858-2865 (Research article)

112. Kim, J. M.; Sakamoto, Y.; Hwang, K. Y.; Kwon, Y-U.; Terasaki, O.; Park, S-E.; Stucky, G. D. "*Structural Design of Mesoporous Silica by Micelle-Packing Control Using Blends of Amphiphilic Block Copolymers*," *Journal of Physical Chemistry B* **2002**, *106*, 2552-2558 (Research article)

113. Cheng, C-F.; Park, D.H.; Klinowski, J. "*Optimal parameters for the synthesis of the mesoporous molecular sieve [Si]-MCM-41*," *Journal of the Chemical Society, Faraday Transactions* **1997**, *93*, 193-197 (Research article)

114. Xia, Y.; Mokaya, R. "*Facile and high yield synthesis of mesostructured MCM-48 silica crystals*," *Journal of Materials Chemistry* **2003**, *13*, 657-659 (Communication article)

115. Chen, L.; Horiuchi, T.; Mori, T.; Maeda, K. "*Postsynthesis Hydrothermal Restructuring of M41S Mesoporous Molecular Sieves in Water*," *Journal of Physical Chemistry B* **1999**, *103*, 1216-1222 (Research article)

116. Galarneau, A.; Driole, M-F.; Petitto, C.; Chiche, B.; Bonelli, B.; Armandi, M.; Onida, B.; Garrone, E.; di Renzo, F.; Fajula, F. "*Effect of Post-synthesis treatment on the stability and surface properties of MCM-48 silica*," *Microporous and Mesoporous Materials* **2005**, *83*, 172-180 (Research article)

117. Morishige, K.; Tateishi, N.; Fukuma, S. "*Capillary Condensation of Nitrogen in MCM-48 and SBA-16*," *Journal of Physical Chemistry B* **2003**, *107*, 5177-5181 (Research article)

118. Oldroyd, R. D.; Sanker, G.; Thomas, J. M.; Hunnius, M.; Maier, W. F. "*Creation, characterisation and performance of vanadyl active sites in Microporous and mesoporous silica-based catalysts for the selective oxidation of hydrocarbons*," *Journal of the Chemical Society, Faraday Transactions* **1998**, *94*, 3177-3182 (Research article)

119. Martin, T.; Galarneau, A.; Di Renzo, F.; Fajula, F.; Plee, D. "*Morphological Control of MCM-41 by Pseudomorphic Synthesis*," *Angewandte Chemie International Edition* **2002**, *41*, 2590-2592 (Research article)

120. Tolbert, S. H.; Landry, C. C.; Stucky, G. D.; Chmelka, B. F.; Norby, P.; Hanson, J. C.; Monnier, A. "*Phase Transitions in Mesostructured Silica/Surfactant Composites: Surfactant Packing and the Role of Charge Density Matching*," *Chemistry of Materials* **2001**, *13*, 2247-2256 (Research article)

121. Petitto, C.; Galarneau, A.; Driole, M-F.; Chiche, B.; Alonso, B.; Di Renzo, F.; Fajula, F. "*Synthesis of Discrete Micrometer-Sized Spherical Particles of MCM-48*," *Chemistry of Materials* **2005**, *17*, 2120-2130 (Research article)

122. Xia, Y.; Mokaya, R. "*Aluminosilicate MCM-48 materials with enhanced stability via simple post-synthesis treatment in water*," *Microporous and Mesoporous Materials* **2004**, *68*, 1-10 (Research article)

123. Pena, M. L.; Kan, Q.; Corma, A.; Rey, F. "*Synthesis of cubic mesoporous MCM-48 materials from the system $SiO_2$:CTAOH/Br:$H_2O$*," *Microporous and Mesoporous Materials* **2001**, *44-45*, 9-16 (Research article)

124. Kaneda, M.; Tsubakiyama, T.; Carlsson, A.; Sakamoto, Y.; Ohsuna, T.; Terasaki, O. "*Structural Study of Mesoporous MCM-48 and Carbon Networks Synthesized in the Spaces of MCM-48 by Electron Crystallography*," *Journal of Physical Chemistry B* **2002**, *106*, 1256-1266 (Research article)

125. Lin, H-P.; Wong, S-T.; Mou, C-Y.; Tang, C-Y. "*Extensive Void Defects in Mesoporous Aluminosilicate MCM-41*," *Journal of Physical Chemistry B* **2000**, *104*, 8967-8975 (Research article)

126. Liu, Y.; Karkamkar, A.; Pinnavaia, T. J. "*Redirecting the assembly of hexagonal MCM-41 into cubic MCM-48 from sodium silicate without the use of an organic structure modifier*," *Chemical Communications* **2001**, 1822-1823 (Communication article)

127. Solberg, S. M.; Kamar, D.; Landry, C. C. "*Synthesis, Structure, and Reactivity of a New Ti-Containing Microporous/Mesoporous Material*," *Journal of Physical Chemistry B* **2005**, *109*, 24331-24337 (Research article)

128. Koyano, K. A.; Tatsumi, T. "*Synthesis of titanium-containing mesoporous molecular sieves with a cubic structure*," *Chemical Communications* **1996**, 145-146 (Communication article)

129. Monnier, A.; Schuth, F.; Huo, Q.; Kumar, D.; Margolese, D.; Maxwell, R. S.; Stucky, G. D.; Krishnamurty, M.; Petroff, P.; Firouzi, A.; Janicke, M.; Chmelka, B. F. "*Cooperative Formation of Inorganic-Organic Interfaces in the Synthesis of Silicate Mesostructures*," *Science* **1993**, *261*, 1299-1303 (Research article)

130. Wang, S.; Li, H. "*Structure directed reversible adsorption of organic dye on mesoporous silica in aqueous solution*," *Microporous and Mesoporous Materials* **2006**, *97*, 21-26 (Research article)

131. Kruk, M.; Jaroniec, M.; Ryoo, R.; Kim, J. M. "*Monitoring of the structure of siliceous mesoporous molecular sieves tailored using different synthesis conditions*," *Microporous Materials* **1997**, *12*, 93-106 (Research article)

132. Wang, L-Z.; Shi, J-L.; Yu, J.; Yan, D-S. "*Synthesis of Nanostructured Mesoporous Silica Materials Containing Manganese*," *Nanostructured Materials* **1998**, *10*, 1289-1299 (Research article)

133. Galarneau, A.; Iapichella, J.; Bonhomme, K.; Di Renzo, F.; Kooyman, P.; Terasaki, O.; Fajula, F. "*Controlling the Morphology of Mesostructured Silicas by Pseudomorphic Transformation: A Route Towards Applications*," *Advanced Functional Materials* **2006**, *16*, 1657-1667 (Research article)

134. Ulagappan, N.; Rao, C. N. R. "*Evidence for supramolecular organization of alkane and surfactant molecules in the process of forming mesoporous silica*," *Chemical Communications* **1996**, 2759-2760 (Communication article)

135. Zhao, D.; Goldfarb, D. "*Synthesis of Mesoporous Manganosilicates: Mn-MCM-41, Mn-MCM-48 and Mn-MCM-L*," *Journal of the Chemical Society, Chemical Communications* **1995**, 875-876 (Communication article)

136. Beck, J. S.; Vartuli, J. C.; Roth, W. J.; Leonowicz, M. E.; Kresge, C. T.; Schmitt, K. D.; Chu, C. T-W.; Olson, D. H.; Sheppard, E. W.; McCullen, S. B.; Higgins, J. B.; Schlenker, J. L. "*A New Family of Mesoporous Molecular Sieves Prepared with Liquid Crystal Templates*," *Journal of the American Chemical Society* **1992**, *114*, 10834-10843 (Research article)

137. Selvam, P.; Bhatia, S. K.; Sonwane, C. G. "*Recent Advances in Processing and Characterization of Periodic Mesoporous MCM-41 Silicate Molecular Sieves*," *Industrial & Engineering Chemistry Research* **2001**, *40*, 3237-3261 (Review article)

138. Zhang, W.; Froba, M.; Wang, J.; Tanev, P. T.; Wong, J.; Pinnavaia, T. J. "*Mesoporous Titanosilicate Molecular Sieves Prepared at Ambient Temperature by Electrostatic ($S^+I^-$, $S^+X^-I^+$) and Neutral ($S^\circ I^\circ$) Assem-*

*bly Pathways: A Comparison of Physical Properties and Catalytic Activity for Peroxide Oxidations*," *Journal of the American Chemical Society* **1996**, *118*, 9164-9171 (Research article)

139. Mokaya, R. "*Improving the Stability of Mesoporous MCM-41 Silica via Thicker More Highly Condensed Pore Walls*," *Journal of Physical Chemistry B* **1999**, *103*, 10204-10208 (Research article)

140. Sayari, A.; Liu, P.; Kruk, M.; Jaroniec, M. "*Characterization of Large-Pore MCM-41 Molecular Sieves Obtained via Hydrothermal Restructuring*," *Chemistry of Materials* **1997**, *9*, 2499-2506 (Research article)

141. Chatterjee, M.; Iwasaki, T.; Hayashi, H.; Onodera, Y; Ebina, T.; Nagase, T. "*Characterization of Tetrahedral Vanadium-Containing MCM-41 Molecular Sieves Synthesized at Room Temperature*," *Chemistry of Materials* **1999**, *11*, 1368-1375 (Research article)

142. Kim, M. J.; Ryoo, R. "*Synthesis and Pore Control of Cubic Mesoporous Silica SBA-1*," *Chemistry of Materials* **1999**, *11*, 487-491 (Research article)

143. Kresge, C. T.; Leonowicz, M. E.; Roth, W. J.; Vartuli, J. C.; Beck, J. S. "*Ordered mesoporous molecular sieves synthesized by a liquid-crystal template mechanism*," *Nature* **1992**, *359*, 710-712 (Research article)

144. Lefevre, B.; Galarneau, A.; Iapichella, J.; Petitto, C.; Di Renzo, F.; Fajula, F. "*Synthesis of Large-Pore Mesostructured Micelle-Templated Silicas as Discrete Spheres*," *Chemistry of Materials* **2005**, *17*, 601-607 (Research article)

145. Huo, Q.; Margolese, D. I.; Ciesla, U.; Demuth, D. G.; Feng, P.; Gier, T. E.; Sieger, P.; Firouzi, A.; Chmelka, B. F.; Schuth, F.; Stucky, G. D. "*Organization of Organic Molecules with Inorganic Molecular Species into Nanocomposite Biphase Arrays*," *Chemistry of Materials* **1994**, *6*, 1176-1191 (Review article)

146. Zhao, D.; Feng, J.; Huo, Q.; Melosh, N.; Fredrickson, G. H.; Chmelka, B. F.; Stucky, G. D. "*Triblock Copolymer Syntheses of Mesoporous Silica with Periodic 50 to 300 Angstrom Pores*," *Science* **1998**, *279*, 548-552 (Research article)

147. Firouzi, A.; Kumar, D.; Bull, L. M.; Besier, T.; Sieger, P.; Huo, Q.; Walker, S. A.; Zasadzinski, J. A.; Glinka, C.; Nicol, J.; Margolese, D.; Stucky, G. D.; Chmelka, B. F. "*Cooperative Organization of Inorganic-Surfactant and Biomimetic Assemblies*," *Science* **1995**,*267*, 1138-1143 (Research article)

148. Khushalani, D.; Kuperman, A.; Coombs, N.; Ozin, G. A. "*Mixed Surfactant Assemblies in the Synthesis of Mesoporous Silicas*," *Chemistry of Materials* **1996**, *8*, 2188-2193 (Research article)

149. Huo, Q.; Leon, R.; Petroff, P. M.; Stucky, G. D. "*Mesostructure Design with Gemini Surfactants: Supercage Formation in a Three-Dimensional Hexagonal Array*," *Science* **1995**, *268*, 1324-1327 (Research article)

150. Luan, Z.; Maes, E. M.; van der Heide, P. A. W.; Zhao, D.; Czernuszewicz, R. S.; Kevan, L. "*Incorporation of Titanium into Mesoporous Silica Molecular Sieve SBA-15*," *Chemistry of Materials* **1999**, *11*, 3680-3686 (Research article)

151. Kruk, M.; Jaroniec, M.; Ko, C. H.; Ryoo, R. "*Characterization of the Porous Structure of SBA-15*," *Chemistry of Materials* **2000**, *12*, 1961-1968 (Research article)

152. Li, Y.; Feng, Z.; Lian, Y.; Sun, K.; Zhang, L.; Jia, G.; Yang, Q.; Li, C. "*Direct synthesis of highly ordered Fe-SBA-15 mesoporous materials under weak acidic conditions*," *Microporous and Mesoporous Materials* **2005**, *84*, 41-49 (Research article)

153. Vradman, L.; Titelman, L.; Herskowitz, M. "*Size effect on SBA-15 microscopy*," *Microporous and Mesoporous Materials* **2006**, *93*, 313-317 (Research article)

154. Liu, X.; Tian, B.; Yu, C.; Gao, F.; Xie, S.; Tu, B.; Che, R.; Peng, L-M.; Zhao, D. "*Room-Temperature Synthesis in Acidic Media of Large-Pore Three-Dimensional Bicontinuous Mesoporous Silica with Ia3d Symmetry*," *Angewandte Chemie International Edition* **2002**, *41*, 3876-3878 (Research article)

155. Zhao, D.; Huo, Q.; Feng, J.; Chmelka, B. F.; Stucky, G. D. "*Nonionic Triblock and Star Diblock Copolymer and Oligomeric Surfactant Syntheses of Highly Ordered, Hydrothermally Stable, Mesoporous Silica Structures*," *Journal of the American Chemical Society* **1998**, *120*, 6024-6036 (Research article)

156. Soler-Illia, G. J. de. A. A.; Sanchez, C.; Lebeau, B.; Patarin, J. "*Chemical Strategies To Design Textured Materials: from Microporous and Mesoporous Oxides to Nanonetworks and Hierarchical Structures*," *Chemical Reviews* **2002**, *102*, 4093-4138 (Review article)

157. Lodge, T. P. "*Block Copolymers: Past Successes and Future Challenges*," *Macromolecular Chemistry and Physics* **2003**, *204*, 265-273 (Review article)

158. Choi, D-G.; Yang, S-M. "*Effect of two-step sol-gel reaction on the mesoporous silica structure*," *Journal of Colloid and Interface Science* **2003**, *261*, 127-132 (Research article)

159. Korusiewicz, B.; Maruszewski, K. "*Organization of silica spherical particles into different shapes on silicon substrates*," *Materials Science-Poland* **2007**, *25*, 835-841 (Research article)

160. Park, J. S.; Hah, H. J.; Koo, S. M.; Lee, Y. S. "*Effect of Alcohol Chain Length on Particle Growth in a Mixed Solved System*," *Journal of Ceramic Processing Research* **2006**, *7*, 83~89 (Research article)

161. Kim, H-G.; Kim, D-W.; Oh, C.; Park, S-H.; Oh, S-G. "*Preparation of rod-type ferric oxyhydroxide particles by forced hydrolysis in the presence of a cationic surfactant*," *Journal of Ceramic Processing Research* **2007**, *8*, 172~176 (Research article)

162. Ying, J. Y.; Mehnert, C. P.; Wong, M. S. "*Synthesis and Applications of Supramolecular-Templated Mesoporous Materials*," *Angewandte Chemie International Edition* **1999**, *38*, 56-77 (Review article)

163. Giraldo, L. F.; Lopez, B. L.; Perez, L.; Urrego, S.; Sierra, L.; Mesa, M. "*Mesoporous Silica Applications*," *Macromolecular Symposia* **2007**, *258*, 129-141 (Review article)

164. Leontidis, E. "*Hofmeister anion effects on surfantant self-assembly and the formation of mesoporous solids*," *Current Opinion in Colloid & Interface Science* **2002**, *7*, 81-91 (Review article)

165. Wachs, I. E.; Briand, L. E.; Jehng, J-M.; Burcham, L.; Gao, X. "*Molecular structure and reactivity of the group V metal oxides*," *Catalysis Today* **2000**, *57*, 323-330 (Review article)

166. Blasco, T.; Lopez Nieto, J. M. "*Oxidative dehydrogenation of short chain alkanes on supported vanadium oxide catalysts*," *Applied Catalysis A: General* **1997**, *157*, 117-142 (Review article)

167. Finocchio, E.; Willey, R. J.; Busca, G.; Lorenzelli, V. "*FTIR studies on the selective oxidation and combustion of light hydrocarbons at metal oxide surfaces*," *Journal of the Chemical Society, Faraday Transactions* **1997**, *93*, 175-180 (Research article)

168. Baltes, M.; Van Der Voort, P.; Collart, O.; Vansant, E. F. "*The Adsorption of $VO(acac)_2$ on a Mesoporous Silica Support by Liquid Phase and Gas Phase Modification to Prepare Supported Vanadium Oxide Catalysts*," *Journal of Porous Materials* **1998**, *5*, 317-324 (Research article)

169. Gontier, S.; Tuel, A. "*Characterization of vanadium-containing mesoporous silicas*," *Microporous Materials* **1995**, *5*, 161-171 (Research article)

170. Tokunaga, S.; Kato, H.; Kudo, A. "*Selective Preparation of Monoclinic and Tetragonal $BiVO_4$ with Scheelite Structure and Their Photocatalytic Properties*," *Chemistry of Materials* **2001**, *13*, 4624-4628 (Research article)

171. Teramura, K.; Maeda, K.; Saito, T.; Takata, T.; Saito, N.; Inoue, Y.; Domen, K. "*Characterization of Ruthenium Oxide Nanocluster as a Cocatalyst with $(Ga_{1-x}Zn_x)(N_{1-x}O_x)$ for Photocatalytic Overall Water Splitting*," *Journal of Physical Chemistry B* **2005**, *109*, 21915-21921 (Research article)

172. Wang, D.; Zou, Z.; Ye, J. "*Photocatalytic Water Splitting with the Cr-Doped $Ba_2In_2O_5/In_2O_3$ Composite Oxide Semiconductors*," Chemistry of Materials 2005, 17, 3255-3261 (Research article)

173. Tang, J.; Zou, Z.; Ye, J. "*Photophysical and Photocatalytic Properties of $AgInW_2O_8$*," *Journal of Physical Chemistry B* **2003**, *107*, 14265-14269 (Research article)

174. Kudo, A.; Omori, K.; Kato, H. "*A Novel Aqueous Process for Preparation of Crystal Form-Controlled and Highly Crystalline $BiVO_4$ Powder from Layered Vanadates at Room Temperature and Its Photocatalytic and Photophysical Properties*," *Journal of the American Chemical Society* **1999**, *121*, 11459-11467 (Research article)

175. Kudo, A.; Kato, H.; Tsuji, I. "*Strategies for the Development of Visible-light driven Photocatalysts for Water Splitting*," *Chemistry Letters* **2004**, 1534-1539 (Communication article)

176. Kudo, A.; Ueda, K.; Kato, H.; Mikami, I. "*Photocatalytic $O_2$ evolution under visible light irradiation on $BiVO_4$ in aqueous $AgNO_3$ solution*," *Catalysis Letters* **1998**, *53*, 229-230 (Research article)

177. Vinke, I. C.; Diepgrond, J.; Boukamp, B. A.; de Vries, K. J.; Burggaraaf, A. J. "*Bulk and electrochemical properties of $BiVO_4$*," *Solid State Ionics* **1992**, *57*, 83-89 (Research article)

178. Liu, H.; Nakamura, R.; Nakato, Y. "*Bismuth-Copper Vanadate $BiCu_2VO_6$ as a Novel Photocatalyst for Efficient Visible-Light-Driven Oxygen Evolution*," *ChemPhysChem* **2005**, *6*, 2499-2502 (Communication article)

179. Kudo, A.; Nakagawa, S.; Kato, H. "*Overall Water Splitting into $H_2$ and $O_2$ under UV Irradiation on NiO-loaded $ZnNb_2O_6$ Photocatalysts Consisting of $d^{10}$ and $d^0$ Ions*," *Chemistry Letters* **1999**, 1197-1198 (Communication article)

180. Yamakata, A.; Ishibashi, T-a.; Kato, H.; Kudo, A.; Onishi, H. "*Photodyamics of $NaTaO_3$ Catalysts for Efficient Water Splitting*," *Journal of Physical Chemistry B* **2003**, *107*, 14383-14387 (Research article)

181. Kato, H.; Kudo, A. "*Energy structure and photocatalytic activity for water splitting of $Sr_2(Ta_{1-x}Nb_x)2O_7$ solid solution*," *Journal of Photochemistry and Photobiology A: Chemistry* **2001**, *145*, 129-133 (Research article)

182. Ko, Y-G.; Lee, W. Y. "*Effects of nickel-loading method on the water-splitting activity of a layered $NiO_x/Sr_4Ti_3O_{10}$ photocatalyst*," *Catalysis Letters* **2002**, *83*, 157-160 (Research article)

183. Takata, T.; Shinohara, K.; Tanaka, A.; Hara, M.; Kondo, J. N.; Domen, K. "*A highly active photocatalyst for overall water splitting with a hydrated layered perovskite structure*," *Journal of Photochemistry and Photobiology A: Chemistry* **1997**, *106*, 45-49 (Research article)

184. Kudo, A. "*Photocatalyst materials for water splitting*," *Catalysis Surveys from Asia* **2003**, *7*, 31-38 (Research article)

185. Kudo, A.; Kato, H.; Nakagawa, S. "*Water Splitting into $H_2$ and $O_2$ on New $Sr_2M_2O_7$ (M = Nb and Ta) Photocatalysts with Layered Perovskite Structures: Factors Affecting the Photocatalytic Activity*," *Journal of Physical Chemistry B* **2000**, *104*, 571-575 (Research article)

186. Zou, Z.; Ye, J. "*Experimental and Theoretical Studies of Photocatalytic Water Splitting on Mixed Oxide Semiconductors*," *Materials Science Forum* **2003**, *423-425*, 475-478 (Research article)

187. Zou, Z.; Arakawa, H. "*Direct water splitting into $H_2$ and $O_2$ under visible light irradiation with a new series of mixed oxide semiconductor photocatalysts*," *Journal of Photochemistry and Photobiology A: Chemistry* **2003**, *158*, 145-162 (Research article)

188. Takata, T.; Tanaka, A.; Hara, M.; Kondo, J. N.; Domen, K. "*Photocatalytic water decomposition by layered perovskites*," *Studies in Surface Science and Catalysis* **2000**, *130*, 1943-1948 (Research article)

189. Hwang, D. W.; Kim, H. G.; Kim, J.; Cha, K. Y.; Kim, Y. G.; Lee, J. S. "*Photocatalytic Water Splitting over Highly Donor-Doped (110) Layered Perovskites*," *Journal of Catalysis* **2000**, 193, 40-48 (Research article)

190. Chung, K-H.; Park, D-C. "*Water photolysis reaction on cerium oxide photocatalysts*," *Catalysis Today* **1996**, *30*, 157-162 (Research article)

191. Ishii, T.; Kato, H.; Kudo, A. "*$H_2$ evolution from an aqueous methanol solution $SrTiO_3$ photocatalysts co-doped with chromium and tantalum ions under visible light irradiation*," *Journal of Photochemistry and Photobiology A: Chemistry* **2004**, *163*, 181-186 (Research article)

192. Luo, J.; Maggard, P. A. "*Hydrothermal Synthesis and Photocatalytic Activities of $SrTiO_3$ Coated $Fe_2O_3$ and $BiFeO_3$*," *Advanced Materials* **2006**, *18*, 514-517 (Research article)

193. Abe, R.; Higashi, M.; Sayama, K.; Abe, Y.; Sugihara, H. "*Photocatalytic Activity of $R_3MO_7$ and $R_2TiO_7$ (R = Y, Gd, La; M = Nb, Ta) for Water Splitting into $H_2$ and $O_2$*," *Journal of Physical Chemistry B* **2006**, *110*, 2219-2226 (Research article)

194. Kim, J.; Hwang, D. W.; Kim, H. G.; Bae, S. W.; Lee, J. S.; Li, W.; Oh, S. H.; "*Highly efficient overall water splitting through optimization of preparation and operation conditions of layered perovskite photocatalysts*," *Topics in Catalysis* **2005**, *35*, 295-303 (Research article)

195. Abe, R.; Sayama, K.; Sugihara, H. "*Development of New Photocatalytic Water Splitting into $H_2$ and $O_2$ using Two Different Semiconductor Photocatalysts and a Shuttle Redox Mediator $IO_3^-/I^-$*," *Journal of Physical Chemistry B* **2005**, *109*, 16052-16061 (Research article)

196. Tsuji, I.; Kato, H.; Kudo, A. "*Visible-Light-Induced $H_2$ Evolution from an Aqueous Solution Containing Sulfide and Sulfite over a $ZnS$-$CuInS_2$-$AgInS_2$ Solid-Solution Photocatalyst*," *Angewandte Chemie International Edition* **2005**, *44*, 3565-3568 (Research article)

197. Tsuji, I.; Kato, H.; Kobayashi, H.; Kudo, A. "*Photocatalytic $H_2$ Evolution under Visible-Light Irradiation over Band-Structure-Controlled $(CuIn)_xZn_{2(1-x)}S_2$ Solid Solutions*," *Journal of Physical Chemistry B* **2005**, *109*, 7323-7329 (Research article)

198. Kato, H.; Hori, M.; Konta, R.; Shimodaira, Y.; Kudo, A. "*Construction of Z-scheme Type Heterogeneous Photocatalysis Systems for Water Splitting into $H_2$ and $O_2$ under Visible Light Irradiation*," *Chemistry Letters* **2004**, 1348-1349 (Research article)

199. Harada, H.; Hosoki, C.; Kudo, A. "*Overall water splitting by sonophotocatalytic reaction: the role of powdered photocatalyst and an attempt to decompose water using a visible-light sensitive photocatalyst*," *Journal of Photochemistry and Photobiology A: Chemistry* **2001**, *141*, 219-224 (Research article)

200. Konta, R.; Kato, H.; Kobayashi, H.; Kudo, A. "*Photophyical properties and photocatalytic activitites under visible light irradiation of silver vanadates*," *Physical Chemistry Chemical Physics* **2003**, *5*, 3061-3065 (Research article)

201. Kato, H.; Kudo, A. "*Photocatalytic water splitting into $H_2$ and $O_2$ over various tantalite photocatalysts*," *Catalysis Today* **2003**, *78*, 561-569 (Research article)

202. Ritterskamp, P.; Kuklya, A.; Wustkamp, M-A.; Kerpen, K.; Weidenthaler, C.; Demuth, M. "*A Titanium Disilicide Derived Semiconducting Catalyst for Water Splitting under Solar Radiation-Reversible Storage of Oxygen and Hydrogen*," *Angewandte Chemie International Edition* **2007**, *46*, 7770-7774 (Research article)

203. Zou, Z.; Ye, J.; Sayama, K.; Arakawa, H. "*Direct splitting of water under visible light irradiation with an oxide semiconductor photocatalyst*," *Nature* **2001**, *414*, 625-627 (Research article)

204. Kato, H.; Asakura, K.; Kudo, A. "*Highly Efficient Water Splitting into $H_2$ and $O_2$ over Lanthanum-Doped $NaTiO_3$ Photocatalysts with High Crystallinity and Surface Nanostructure*," *Journal of the American Chemical Society* **2003**, *125*, 3082-3089 (Research article)

205. Kim, H. G.; Borse, P. H.; Choi, W.; Lee, J. S. "*Photocatalytic Nanodiodes for Visible-Light Photocatalysis*," *Angewandte Chemie International Edition* **2005**, *44*, 4585-4589 (Research article)

206. Zhao, X. S.; Lu, G. Q.; Millar, G. J. "*Advances in Mesoporous Molecular Sieve MCM-41*," *Industrial & Engineering Chemistry Research* **1996**, *35*, 2075-2090 (Review article)

207. Yoshioka, K.; Petrykin, V.; Kakihana, M.; Kato, H.; Kudo, A. "*The relationship between photocatalytic activity and crystal structure in strontium tantalates*," *Journal of Catalysis* **2005**, *232*, 102-107 (Research article)

208. Kim, H. G.; Hwang, D. W.; Bae, S. W.; Jung, J. H.; Lee, J. S. "*Photocatalytic water splitting over $La_2Ti_2O_7$ synthesized by the polymerizable complex method*," *Catalysis Letters* **2003**, *91*, 193-198 (Research article)

209. Zou, Z.; Ye, J.; Arakawa, H. "*Photocatalytic water splitting into $H_2$ and/or $O_2$ under UV and visible light irradiation with a semiconductor photocatalyst*," *International Journal of Hydrogen Energy* **2003**, *28*, 663-669 (Research article)

210. Kwon, Y. T.; Song, K. Y.; Lee, W. I.; Choi, G. J.; Do, Y. R. "*Photocatalytic Behavior of $WO_3$-Loaded $TiO_2$ in an Oxidation Reaction*," *Journal of Catalysis* **2000**, *191*, 192-199 (Research article)

211. Di Paola, A.; Palmisano, L.; Augugliaro, V. "*Photocatalytic behavior of Mixed $WO_3/WS_2$ powders*," *Catalysis Today* **2000**, *58*, 141-149 (Research article)

212. Do, Y. R.; Lee, W.; Dwight, K.; Wold, A. "*The Effect of $WO_3$ on the Photocatalytic Activity of $TiO_2$*," *Journal of Solid State Chemistry* **1994**, *108*, 198-201 (Research article)

213. Li, X. Z.; Li, F. B.; Yang, C. L.; Ge, W. K. "*Photocatalytic activity of $WO_x$-$TiO_2$ under visible light irradiation*," *Journal of Photochemistry and Photobiology A: Chemistry* **2001**, *141*, 209-217 (Research article)

214. Di Paola, A.; Palmisano, L.; Venezia, A. M.; Augugliaro, V. "*Coupled Semiconductor Systems for Photocatalysis. Preparation and Characterization of Polycrystilline Mixed $WO_3/WS_2$ Powders*," *Journal of Physical Chemistry B* **1999**, *103*, 8236-8244 (Research article)

215. Long, M.; Cai, W.; Cai, J.; Zhou, B.; Chai, X.; Wu, Y. "*Efficient Photocatalytic Degradation of Phenol over $CO_3O_4/BiVO_4$ Composite under Visible Light Irradiation*," *Journal of Physical Chemistry B* **2006**, *110*, 20211-20216 (Research article)

216. Bessekhouad, Y.; Robert, D.; Weber, J.-V. "*Photocatalytic activity of $Cu_2O/TiO_2$, $Bi_2O_3/TiO_2$ and $ZnMn_2O_4/TiO_2$ heterojunctions*," *Catalysis Today* **2005**, *101*, 315-321 (Research article)

217. Yu, J. C.; Wang, X.; Fu, X. "*Pore-Wall Chemistry and Photocatalytic Activity of Mesoporous Titania Molecular Sieve Films*," *Chemistry of Materials* **2004**, *16*, 1523-1530 (Research article)

218. Baltes, M.; Van Der Voort, P.; Weckhuysen, B. M.; Ramachandra Rao, R.; Catana, G.; Schoonheydt, R. A.; Vansant, E. F. "*Synthesis and characterization of alumina-supported vanadium oxide catalysts prepared by the molecular designed dispersion of VO(acac)$_2$ complexes*," *Physical Chemistry Chemical Physics* **2000**, *2*, 2673-2680 (Research article)

219. Reddy, J. S.; Liu, P.; Sayari, A. "*Vanadium containing crystalline mesoporous molecular sieves Leaching of vanadium in liquid phase reactions*," *Applied Catalysis A: General* **1996**, *148*, 7-21 (Review article)

220. Lensveld, D. Universiteit Utrecht Ph.D. Dissertation (2003) "*On the Preparation and Characterisation of MCM-41Supported Heterogeneous Nickel and Molybdenum Catalysts*," (focus on chapter # 2): http://igitur-archive.library.uu.nl/dissertations/2003-0325-143241/inhoud.htm (accessed 10/8/2008)

221. Gao, X.; Bare, S. R.; Weckhuysen, B. M.; Wachs, I. E. "*In Situ Spectroscopic Investigation of Molecular Structures of Highly Dispersed Vanadium Oxide on Silica under Various Conditions*," *Journal of Physical Chemistry B* **1998**, *102*, 10842-10852 (Research article)

222. Berndt, H.; Martin, A.; Bruckner, A.; Schreier, E.; Muller, D.; Kosslick, H.; Wolf, G.-U.; Lucke, B. "*Structure and Catalytic Properties of VO$_x$/MCM Materials for the Partial Oxidation of Methane to Formaldehyde*," *Journal of Catalysis* **2000**, *191*, 384-400 (Research article)

223. Hess, C.; Hoefelmeyer, J. D.; Tilley, T. D. "*Spectroscopic Characterization of Highly Dispersed Vanadia Supported on SBA-15*," *Journal of Physical Chemistry B* **2004**, *108*, 9703-9709 (Research article)

224. Galarneau, A.; Iapichella, J.; Brunel, D.; Fajula, F.; Bayram-Hahn, Z.; Unger, K.; Puy, G.; Demesmay, C.; Rocca, J-L. "*Spherical ordered mesoporous silicas and silica monoliths as stationary phases for liquid chromatography*," *Journal of Separation Science* **2006**, *29*, 844-855 (Research article)

225. Hammond, W.; Prouzet, E.; Mahanti, S. D.; Pinnavaia, T. J. "*Structure factor for the periodic walls of mesoporous MCM-41 molecular sieves*," *Microporous and Mesoporous Materials* **1999**, *27*, 19-25 (research article)

226. Rodgers, G. D. "*Descriptive Inorganic, Coordination, and Solid-State Chemistry*," **2002**, *Second Edition*, Chapters 4, 5, 7, 9, pages: 58, 59, 93, 96, 111-115, 118, 119, 173, 217-223 (Inorganic textbook)

227. "*Development of a Model for Diffracted Intensity*," Class Notes: Chapter 4, 2/18/98 http://www.eng.uc.edu/~gbeaucag/Classes/XRD/Chapter4html/Chapter4.html (accessed 1/26/2009)

228. Connolly, J. R. "*Diffraction Basics, Part 2*," epswww.unm.edu/xrd/xrdclass/06-Diffraction-II.pdf (accessed 1/26/2009)

229. Connolly, J. R. "*Introduction Quantitative X-ray Diffraction Methods*," epswww.unm.edu/xrd/xrdclass/09-Quant-intro.pdf (accessed 1/26/2009)

230. Ciesla, U.; Schuth, F. "*Ordered mesoporous materials*," *Microporous and Mesoporous Materials* **1999**, *27*, 131-149 (Review article)

231. Ryoo, R.; Kim, J. M.; Ko, C. H.; Shin, C. H. "*Disordered Molecular Sieve with Branched Mesoporous Channel Network*," *Journal of Physical Chemistry* **1996**, *100*, 17718-17721 (Research article)

232. Kornatowski, J.; Wichterloava, B.; Jirkovsky, J.; Loffler, E.; Pilz, W. "*Spectroscopic studies of vanadium-substituted zeolitic silicates of MFI topology*," *Journal of the Chemical Society, Faraday Transactions* **1996**, *92*, 1067-1078 (Research article)

233. Thommes, M.; Kohn, R.; Froba, M. "*Sorption and Pore Condensation Behavior of Nitrogen, Argon, and Krypton in Mesoporous MCM-48 Silica Materials*," *Journal of Physical Chemistry B* **2000**, *104*, 7932-7943 (research article)

234. Endud, S.; Wong, K-L. "*Mesoporous silica MCM-48 molecular sieve modified with $SnCl_2$ in alkaline medium for selective oxidation of alcohol*," *Microporous and Mesoporous Materials* **2007**, *101*, 256-263 (Research article)

235. Grosman, A.; Ortega, G. "*Nature of Capillary Condensation and Evaporation Processes in Ordered Porous Materials*," *Langmuir* **2005**, *21*, 10515-10521 (Research article)

236. Kruk, M.; Jaroniec, M. "*Gas Adsorption Characterization of Ordered Organic-Inorganic Nanocomposite Materials*," *Chemistry of Materials* **2001**, *13*, 3169-3183 (Review article)

237. Coasne, B.; Grosman, A.; Dupont-Pavlovsky, N.; Ortega, C.; Simon, M. "*Adsorption in an ordered and non-interconnected mesoporous material: Single crystal porous silicon*," *Physical Chemistry Chemical Physics* **2001**, *3*, 1196-1200 (Research article)

238. Miyazawa, K.; Inagaki, S. "*Control of the microporosity within the pore walls of ordered mesoporous silica SBA-15*," *Chemical Communications* **2000**, 2121-2122 (Communications article)

239. Lukens, W. W. Jr.; Schmidt-Winkel, P.; Zhao, D.; Feng, J.; Stucky, G. D. "*Evaluating Pore Sizes in Mesoporous Materials: A Simplified Standard Adsorption Method and a Simplified Broekhoff-de Boer Method*," *Langmuir* **1999**, *15*, 5403-5409 (Research article)

240. Coasne, B.; Gubbins, K. E.; Pellenq, R. J.-M. "*Domain theory for capillary condensation hysteresis*," *Physical Review B* **2005**, *72*, 024304/024304-1—024304-9 (Research article)

241. Tompsett, G. A.; Krogh, L.; Griffin, D. W.; Conner, W. C. "*Hysteresis and Scanning Behavior of Mesoporous Molecular Sieves*," *Langmuir* **2005**, *21*, 8214-8225 (Research article)

242. Aranovich, G.; Donohue, M. "*Analysis of Adsorption Isotherms: Lattice Theory Predictions, Classification of Isotherms for Gas-Solid Equilibria, and Similarities in Gas and Liquid Adsorption Behavior*," *Journal of Colloid and Interface Science* **1998**, *200*, 273-290 (Research article)

243. Donohue, M. D.; Aranovich, G. L. "*Adsorption Hysteresis in Porous Solids*," *Journal of Colloid and Interface Science* **1998**, *205*, 121-130 (Research article)

244. Storck, S.; Bretinger, H.; Maier, W. F. "*Characterization of micro- and mesoporous solids by physisorption methods and pore-size analysis*," *Applied Catalysis A: General* **1998**, *174*, 137-146 (Review article)

245. Sing, K. S. W.; Everett, D. H.; Haul, R. A. W.; Moscou, L.; Pierotti, R. A.; Rouquerol, J.; Siemieniewska, T. "*Reporting Physisorption Data For Gas/Solid Systems with Special Reference to the Determination of Surface Area and Porosity*," *Pure and Applied Chemistry* **1985**, *57*, 603-619 (Research article)

246. Urbonaite, S. Stockholm University (2008)Ph.D. Thesis "*Synthesis and Characterisation of Carbide Derived Carbons*," Focus on chapter # 3: http://urn.kb.se/resolve?urn=urn:nbn:se:su:diva-7423 (Accessed 10/8/2008)

247. Mcnall, M.; Laurence, R. L.; Conner, W. C. "*An experimental approach to test sorption mechanisms in MCM-41*," *Microporous and Mesoporous Materials* **2001**, *44-45*, 709-716 (Research article)

248. Ravikovitch, P. I.; Neimark, A. V. "*Relations between Structural Parameters and Adsorption Characterization of Templated Nanoporous Materials with Cubic Symmetry*," *Langmuir* **2000**, *16*, 2419-2423 (Research article)

249. Thommes, M.; Kohn, R.; Froba, M. "*Sorption and pore condensation behavior of pure fluids in mesoporous MCM-48 silica, MCM-41 silica, SBA-15 silica and controlled-pore glass at temperatures above and below the bulk triple point*," *Applied Surface Science* **2002**, *196*, 239-249 (Research article)

250. Wang, J.; Uma, S.; Klabunde, K. J. "*Visible light photocatalysis in transition metal incorporated titania-silica aerogels*," *Applied Catalysis B: Environmental* **2004**, *48*, 151-154 (Research article)

251. Wang, J.; Uma, S.; Klabunde, K. J. "*Visible light photocatalytic activities of transition metal oxide/silica aerogels*," *Microporous and Mesoporous Materials* **2004**, *75*, 143-147 (Research article)

252. Kotz, J. C.; Treichel, P. M. Jr. "*Chemistry and Chemcial Reactivity*," **2003**, *Fifth Edition*, Chapters 5, 17, 20, 22, pages 168-175; 720-724; 826-879; 935 (Chemistry textbook)

253. Dapurkar, S. E.; Selvam, P. "*Mesoporous H-AlMCM-48: highly efficient solid acid catalyst*," *Applied Catalysis A: General* **2003**, *254*, 239-249 (Research article)

254. Kadgaonkar, M. D.; Laha, S. C.; Pandey, R. K.; Kumar, P.; Mirajkar, S. P.; Kumar, R. "*Cerium-containing MCM-41 materials as selective acylation and alkylation catalysts*," *Catalysis Today* **2004**, *97*, 225-231 (Research article)

255. Weckhuysen, B .M.; Keller, D. E. "*Chemistry, spectroscopy and the role of supported vanadium oxides in heterogeneous catalysis*," *Catalysis Today* **2003**, *78*, 25-46 (Review article)

256. Vralstad, T. "Synthesis and characterization of cobalt-containing mesoporous model catalysts," Ph.D. Thesis, December, 2005 Norwegian University of Science and Technology http://www.chemeng.ntnu.no/research/polymer/ugelstadlab/thesis/tyralstad.pdf (accessed 12/12/08)

257. Centi, G.; Perathoner, S.; Trifiro, F.; Aboukais, A.; Aissi, C. F.; Guelton, M. "*Physicochemical Characterization of V-Silicalite*," *Journal of Physical Chemistry* **1992**, *96*, 2617-2629 (Research article)

258. Moussa, N.; Ghorbel, A. "*UV-vis-DR of $VO_x/SiO_2$ catalysts prepared by sol-gel method*," *Applied Surface Science* **2008**, *255*, 2270-2275 (Research article)

259. Catana, G.; Ramachandra Rao, R.; Weckhuysen, B. M.; Voort, P. V. D.; Vansant, E.; Schoonheydt, R. A. "*Supported Vanadium Oxide Catalysts: Quantitative Spectroscopy, Preferential Adsorption of $V^{4+/5+}$, and $Al_2O_3$ Coating of Zeolite Y*," *Journal of Physical Chemistry B* **1998**, *102*, 8005-8012 (Research article)

260. Amano, F.; Tanaka, T.; Funabiki, T. "*Steady-State Photocatalytic Epoxidation of Propene by $O_2$ over $V_2O_5/SiO_2$ Photocatalysts*," *Langmuir* **2004**, *20*, 4236-4240 (Research article)

261. Shylesh, S.; Singh, A. P. "*Vanadium-containing ethane-silica hybrid periodic mesoporous organosilicas: Synthesis, structural characterization and catalytic applications*," *Microporous and Mesoporous Materials* **2006**, *94*, 127-138 (Research article)

262. Anpo, M.; Zhang, S. G.; Mishima, H.; Matsuoka, M.; Yamashita, H. "*Design of photocatalysts encapsulated within the zeolite framework and cavities for the decomposition of NO into $N_2$ and $O_2$ at normal temperature*," *Catalysis Today* **1997**, *39*, 159-168 (Research article)

263. Jermy, B. R.; Cho, D-R.; Bineesh, K. V.; Kim, S-Y.; Park, D-W. "*Direct synthesis of vanadium incorporated three-dimensional KIT-6: A systematic study in the oxidation of cyclohexane*," *Microporous and Mesoporous Materials* **2008**, *115*, 281-292 (Research article)

264. Miessler, G. L.; Tarr, D. A. "*Inorganic Chemistry*," **2004**, *Third Edition*, Chapter 11, page 407

265. Kettle, S. F. A. "*Physical Inorganic Chemistry: A Coordination Chemistry Approach*," **1996**, *First Edition*, Chapters? Pages? (Inorganic Chemistry textbook)

266. Douglas, B.; McDaniel, D.; Alexander, J. "*Concepts And Models of Inorganic Chemistry*," **1994**, *Third Edition*, Chapters? Pages? (Inorganic Chemistry textbook)

267. Voort, P. Van Der; Vansant, E. F. "*The synthesis of stable, hydrophobic MCM-48/$VO_x$ catalysts, using alkylchlorosilianes as coupling agents for the molecular designed dispersion of $VO(acac)_2$*," *Microporous and Mesoporous Materials* **2000**, *38*, 385-390 (Research article)

268. Ebsworth, E. A. V.; Rankan, D. W. A.; Cradock, J. "*Structural Methods in Inorganic Chemistry*," **1991**, *Second Edition*, Chapter 6, pages: 284-289 (Chemistry Inorganic Analysis Book)

269. Garcia, H.; Lopez Nieto, J. M.; Palomares, E.; Solsona, B. "*Photoluminescence of supported vanadia catalysts: linear correlation between the vanadyl emission wavelength and the isoelectric point of the oxide support*," *Catalysis Letters* **2000**, *69*, 217-222 (Research article)

270. Martyanov, I. N.; Uma, S.; Rodrigues, S.; Klabunde, K. J. "*Decontamination of Gaseous Acetaldehyde over $CoO_x$-Loaded $SiO_2$ Xerogels under Ambient, Dark Conditions*," *Langmuir* **2005**, *21*, 2273-2280 (Research article)

271. Atanasov, M.; Brunold, T. C.; Gdel, H. U.; Daul, C. "*Charge-Transfer Spectra and Bonding in Tetrahedral Mn, Cr, and V and Mn, Cr, and V Oxo Anions*," *Inorganic Chemistry* **1998**, *37*, 4589-4602 (Research article)

272. Van Der Voort, P.; White, M. G.; Mitchell, M. B.; Verberckmoes, A. A.; Vansant, E. F. "*The effect of water on the structure of supported vanadium oxide structures. An FT-RAMAN, in situ DRIFT and in situ UV-VIS diffuse reflectance study*," *Spectrochimica Acta Part A: Molecular and Biomolecular Spectroscopy* **1997**, *53*, 2181-2187 (Research article)

273. Gao, X.; Wachs, I. E. "*Investigation of Surface Structures of Supported Vanadium Oxide Catalysts by UV-vis-NIR Diffuse Reflectance Spectroscopy*," *Journal of Physical Chemistry B* **2000**, *104*, 1261-1268 (Research article)

274. Bronkema, J. L.; Bell, A. T. "*Mechanistic Studies of Methanol Oxidation to Formaldehyde on Isolated Vanadate Sites Supported on MCM-48*," *Journal of Physical Chemistry C* **2007**, *111*, 420-430 (Research article)

275. Michaels, J. N.; Stern, D. L.; Grasselli, R. K. "*Oxydehydrogenation of propane over Mg-V-Sb-oxide catalysts. II. Reaction kinetics and mechanism*," *Catalysis Letters* **1996**, *42*, 139-148 (Research article)

276. Kondratenko, E. V.; Baerns, M. "*Catalytic oxidative dehydrogenation of propane in the presence of $O_2$ and $N_2O$-the role of vanadia distribution and oxidant activation*," *Applied Catalysis A: General* **2001**, *222*, 133-143 (Research article)

277. Doornkamp, C.; Ponec, V. "*The universal character of the Mars and Van Krevelen mechanism*," *Journal of Molecular Catalysis A: Chemical* **2000**, *162*, 19-32 (Review article)

278. Doornkamp, C.; Clement, M.; Ponec, V. "*Activity and selectivity patterns in the oxidation of allyl iodide on the period IV metal oxides: The participation of lattice oxygen in selective and total oxidation reactions*," *Applied Catalysis A: General* **1999**, *188*, 325-336 (Research article)

279. Doornkamp, C.; Clement, M.; Ponec, V. "*The Isotopic Exchange Reaction of Oxygen on Metal Oxides*," *Journal of Catalysis* **1999**, *182*, 390-399 (Research article)

280. Doornkamp, C.; Clement, M.; Gao, X.; Deo, G.; Wachs, I. E.; Ponec, V. "*The Oxygen Isotopic Exchange Reaction on Vanadium Oxide Catalysts*," *Journa of Catalysis* **1999**, *185*, 415-422 (Research article)

281. Tran, K.; Hanning-Lee, M. A.; Biswas, A.; Stiegman, A. E.; Scott, G. W. "*Electronic Structure of Discrete Pseudotetrahedral Oxovanadium Centers Dispersed in a Silica Xerogel Matrix: Implications for Catalysis and Photocatalysis*," *Journal of the American Chemcial Society* **1995**, *117*, 2618-2626 (Research article)

282. Tran, K.; Stiegman, A. E.; Scott, G. W. "*Primary photophysical process of discrete pseudotetrahedral oxovanadium centers dispersed in a silica xerogel matrix*," *Inorganica Chimica Acta* **1996**, *243*, 185-191 (Research article)

283. Belletti, A.; Borromei, R.; Cavalli, E.; Oleari, L. "*The luminescence of $VO_4^{3-}$ ions in $Ca_2PO_4Cl$*," *European Journal of Solid State Inorganic Chemistry* **1998**, *35*, 483-493 (Research article)

284. Morita, M.; Kajiyama, S.; Rau, D.; Sakurai, T.; Iwamura, M. "*Luminescence of closed shell molecular complex centers in nanoporous sol-gel $SiO_2$ glasses*," *Journal of Luminescence* **2003**, *102-103*, 608-613 (Research article)

285. Yoshida, S.; Tanaka, T.; Nishimura, Y.; Mizutani, H.; Funabiki, T. "*The Local Structures of Vanadium Oxide on Silica and γ-Alumina Studied by X-ray Absortion (XANES/EXAFS) Spectroscopy-The Effect of Hydration*," *Proceedings 9th International Congress on Catalysis* **1988**, *3*, 1473-1480 (Conference paper)

286. Pantazidis, A.; Auroux, A.; Herrmann, J.-M.; Mirodatos, C. "*Role of acid-base, redox and structural properties of VMgO catalysts in the oxidative dehydrogenation of propane*," *Catalysis Today* **1996**, *32*, 81-88 (Research article)

287. Bronkema, J. L.; Bell, A. T. "*An Investigation of the Reduction and Reoxidation of Isolated Vanadate Sites Supported on MCM-48*," *Catalysis Letters* **2008**, *122*, 1-8 (Research article)

288. Masih, D.; Yoshitake, H.; Izumi, Y. "*Photo-oxidation of ethanol on mesoporous vanadium-titanium oxide catalysts and the relation to vanadium(IV) and (V) sites*," *Applied Catalysis A: General* **2007**, *325*, 276-282 (Research article)

289. Hoffmann, M. R.; Martin, S. T.; Choi, W.; Bahnemann, D. W. "*Environmental Applications of Semiconductor Photocatalysis*," *Chemcial Reviews* **1995**, *95*, 69-96 (Review article)

290. Wangcheng, Z.; Guanzhong, L.; Yanglong, G.; Yun, G.; Yanqin, W.; Yunsong, W.; Zhigang, Z.; Xiaohui, L. "*Synthesis of cerium-doped MCM-48 molecular sieves and its catalytic performance for selective oxidation of cyclohexane*, " *Journal of Rare Earths* **2008**, *26*, 515-522 (Research article)

291. Amano, F.; Yamaguchi, T.; Tanaka, T. "*Photocatalytic Oxidation of Propylene with Molecular Oxygen over Highly Dispersed Titanium, Vanadium, and Chromium Oxides on Silica*," *Journal of Physical Chemistry B* **2006**, *110*, 281-288 (Research article)

292. Maldotti, A.; Molinari, A.; Amadelli, R. "*Photocatalysis with Organized System for the Oxofunctionalized of Hydrocarbons by $O_2$*," *Chemical Reviews* **2002**, *102*, 3811-3826 (Review article)

293. Krauss, M. "*Electronic structure and spectra of oxovanadium silicate*," *Journal of Molecular Structure (Theochem)* **1999**, *458*, 73-79 (Research article)

294. Linsebigler, A. L.; Lu, G.; Yates, J. T. Jr. "*Photocatalysis on $TiO_2$ Surfaces: Principles, Mechanisms, and Selected Results*," *Chemical Reviews* **1995**, *95*, 735-758 (Review article)

295. Fujishima, A.; Rao, T. N.; Tryk, D. A. "*Titanium dioxide photocatalysis*," *Journal of Photochemistry and Photobiology C: Photochemistry Reviews* **2000**, *1*, 1-21 (Review article)

296. Uma, S.; Rodrigues, S.; Martyanov, I. N.; Klabunde, K. J. "*Exploration of photocatalytic activities of titanosilicate ETS-10 and transition metal incorporated ETS-10*," *Microporous and Mesoporous Materials* **2004**, *67*, 181-187 (Research article)

297. Kondratenko, E. V.; Cherian, M.; Baerns, M.; Su, D.; Schlogl, R.; Wang, X.; Wachs, I. E. "*Oxidative dehydrogenation of propane over V/MCM-41 catalysts: comparison of $O_2$ and $N_2O$ as oxidants*," *Journal of Catalysis* **2005**, *234*, 131-142 (Research article)

298. Yoshida, S.; Matsumura, Y.; Noda, S.; Tunabiki, T. "*Photo-activation of Lattice Oxygen in Vanadium Oxide Support on Silica*," *Journal of the Chemical Society, Faraday Transactions I* **1981**, *77*, 2237-2245 (Research article)

299. Van Tol, J.; Van Hulst, J. A.; Van Der Waals, J. H. "*The luminescent triplet state of $VO_4^{3-}$ in $YPO_4$ I. Polarization of the emission*," *Molecular Physics* **1992**, *76*, 547-566 (Research article)

300. Chen, F.; Wang, J.; Xu, J. Q.; Zhou, X. P. "*Visible light photodegradation of organic compounds over $V_2O_5/MgF_2$ catalyst*," *Applied Catalysis A: General* **2008**, *348*, 54-59 (Research article)

301. Dagan, G.; Tomkiewiez, M. "*$TiO_2$ Aerogels for Photocatalytic Decomination of Aquatic Environments*," *Journal of Physical Chemistry* **1993**, *97*, 12651-12655 (Research article)

302. Sun, N.; Klabunde, K. J. "*Nanocrystal Mixed Oxide-Chlorine Adducts: Selective Catalysts for Chlorination of Alkanes*," *Journal of the American Chemical Society* **1999**, *121*, 5587-5588 (Communication article)

303. Concepcion, P.; Hadjiivanov, K.; Knozinger, H. "*Low-Temperature CO Adsorption on V-Containing Aluminophosphates: An FTIR Study*," *Journal of Catalysis* **1999**, *184*, 172-179 (Research article)

304. Venkov, T. V.; Hess, C.; Jentoft, F. C. "*Redox Properties of Vanadium Ions in SBA-15-Supported Vanadium Oxide: An FTIR Spectroscopic Study*," *Langmuir* **2007**, *23*, 1768-1777 (Research article)

305. Anpo, M.; Tanahashi, I.; Kubokawa, Y. "*Photoluminescence and Photoreduction of $V_2O_5$ Supported on Porous Vycor Glass*," *Journal of Physical Chemistry* **1980**, *84*, 3440-3443 (Research article)

306. Jonson, B.; Rebenstorf, B.; Larsson, R.; Lars, S.; Andersson, T. "*Activity Measurements and Spectroscopic Studies of the Catalytic Oxidation of Toluene over Silica-supported Vanadium Oxides*," *Journal of the Chemical Society, Faraday Transactions I* **1988**, *84*, 1897-1910 (Research article)

307. Burcham, L. J.; Deo, G.; Gao, X.; Wachs, I. E. "*In situ IR, Rama, and UV-Vis DRS spectroscopy of supported vanadium oxide catalysts during methanol oxidation*," *Topics in Catalysis* **2000**, *11-12*, 85-100 (Research article)

308. Weststrate, C. J.; Resta, A.; Westerstrom, R.; Lundgren, E.; Mikkelsen, A.; Andersen, J. N. "*CO Adsorption on a $Au/CeO_2$ (111) Model Catalyst*," *Journal of Physical Chemistry C* **2008**, *112*, 6900-6906 (Research article)

309. Comotti, M.; Li, W-C.; Spliethoff, B.; Schuth, F. "*Support Effect in High Activity Gold Catalysts for CO Oxidation*," *Journal of the American Chemical Society* **2006**, *128*, 917-924 (Research article)

310. Janssens, T. V. W.; Carlsson, A.; Puig-Molina, A.; Clausen, B. S. "*Relation between nanoscale Au particle structure and activity for CO oxidation on supported gold catalysts*," *Journal of Catalysis* **2006**, *240*, 108-113 (Research article)

311. Boccuzzi, F.; Chiorino, A.; Manzoli, M.; Lu, P.; Akita, T.; Ichikawa, S.; Haruta, M. "*$Au/TiO_2$ Nanosized Samples: A Catalytic, TEM, and FTIR Study of the Effect of Calcination Temperature on the CO Oxidation*," *Journal of Catalysis* **2001**, *202*, 256-267 (Research article)

312. Lopez, N.; Janssens, T. V. W.; Clausen, B. S.; Xu, Y.; Mavrikakis, M.; Bligaard, T.; Norskov, J. K. "*On the origin of the catalytic activity of gold nanoparticles for low-temperature CO oxidation*," *Journal of Catalysis* **2004**, *223*, 232-235 (Communication article)

313. Guczi, L.; Peto, G.; Beck, A.; Frey, K.; Geszti, O.; Molnar, G.; Daroczi, C. "*Gold Nanoparticles Deposited on $SiO_2$/Si(100): Correlation between Size, Electron Structure, and Activity in CO Oxidation*," *Journal of the American Chemical Society* **2003**, *125*, 4332-4337 (Research article)

314. Schubert, M. M.; Hackenberg, S.; van Veen, A. C.; Muhler, M.; Plzak, V.; Behm, R. J. "*CO Oxidation over Supported Gold Catalysts-"Inert" and "Active" Support Materials and Their Role for the Oxygen Supply during Reaction*," *Journal of Catalysis* **2001**, *197*, 113-122 (Research article)

315. Kozlov, A. I.; Kozlova, A. P.; Liu, H.; Iwasawa, Y. "*A new approach to active supported Au catalysts*," *Applied Catalysis A: General* **1999**, *182*, 9-28 (Review article)

316. Wolf, A.; Schuth, F. "*A systematic study of the synthesis conditions for the preparation of higly active gold catalysts*," *Applied Catalysis A: General* **2002**, *226*, 1-13 (Review article)

317. Lin, H-Y.; Chen, Y-W. "*Low-Temperature CO Oxidation on Au/$Fe_xO_y$ Catalysts*," *Industrial & Engineering Chemistry Research* **2005**, *44*, 4569-4576 (Research article)

318. Kung, M. C.; Davis, R. J.; Kung, H. H. "*Understanding Au-Catalyzed Low-Temperature CO Oxidation*," *Journal of Physical Chemistry C* **2007**, *111*, 11767-11775 (Review article)

319. Haruta, M.; Yamada, N.; Kobayashi, T.; Iijima, S. "*Gold Catalysts Prepared by Coprecipitation for Low-Temperature Oxidation of Hydrogen and of Carbon Monoxide*," *Journal of Catalysis* **1989**, *115*, 301-309 (Research article)

320. Guzman, J.; Carrettin, S.; Fierro-Gonzalez, J. C.; Hao, Y.; Gates, B. C.; Corma, A. "*CO Oxidation Catalyzed by Supported Gold: Cooperation between Gold and Nanocrystalline Rare-Earth Supports Forms Reactive Surface Superoxide and Peroxide Species*," *Angewandte Chemie Internation Edition* **2005**, *44*, 4778-4781 (Research article)

321. Haruta, M.; Kobayahi, T.; Sano, H.; Yamada, N. "*Novel Gold Catalysts for the Oxidation of Carbon Monoxide at a Temperature far Below 0°C*," *Chemistry Letters* **1987**, *16*, 405-408 (Communication article)

322. Wang, G. Y.; Zhang, W. X.; Lian, H. L.; Jiang, D. Z.; Wu, T. H. "*Effect of calcination temperatures and precipitant on the catalytic performance of Au/ZnO catalysts for CO oxidation at ambient temperature and in humid circumstances*," *Applied Catalysis A: General* **2003**, *239*, 1-10 (Research article)

323. Qian, K.; Huang, W.; Fang, J.; Lv, S.; He, B.; Jiang, Z.; Wei, S. "*Low-temperature CO oxidation over Au/ZnO/$SiO_2$ catalysts: Some mechanism insights*," *Journal of Catalysis* **2008**, *255*, 269-278 (Research article)

324. Chiang, C-W.; Wang, A.; Wan, B-Z.; Mou, C-Y. "*High Catalytic Activity for CO Oxidation of Gold Nanoparticles Confined in Acidic Support Al-SBA-15 at Low Temperature*," *Journal of Physical Chemistry B* **2005**, *109*, 18042-18047 (Research article)

325. Wang, A.; Hsieh, Y-P.; Chen, Y-F.; Mou, C-Y. "*Au-Ag alloy nanoparticle as catalyst for CO oxidation: Effect of Si/Al ratio of mesoporous support*," *Journal of Catalysis* **2006**, *237*, 197-206 (Research article)

326. Wang, A-Q.; Chang, C-M.; Mou, C-Y. "*Evolution of Catalytic Activity of Au-Ag Bimetallic Nanoparticles on Mesoporous Support for CO Oxidation*," *Journal of Physical Chemistry B* **2005**, *109*, 18860-18867 (Research article)

327. Liu, J-H.; Wang, A-Q.; Chi, Y-S.; Lin, H-P.; Mou, C-Y. "*Synergistic Effect in an Au-Ag Alloy Nanocatalyst: CO Oxidation*," *Journal of Physical Chemistry B* **2005**, *109*, 40-43 (Research article)

328. Serpone, N.; Maruthamuthu, P.; Pichat, P.; Pelizzetti, E.; Hidaka, H. "*Exploiting the interparticle electron transfer process in the photocatalysed oxidation of phenol, 2-chlorophenol and pentachlorophenol: chemical evidence for electron and hole transfer between coupled semiconductors*," *Journal of Photochemistry of Photobiology A: Chemistry* **1995**, *85*, 247-255 (Research article)

329. Bandyopadhyay, M.; Korsak, O.; van den Berg, M. W. E.; Grunert, W.; Birkner, A.; Li, W.; Schuth, F.; Gies, H. "*Gold nano-particles stabilized in mesoporous MCM-48 as active CO-oxidation catalyst*," *Microporous and Mesoporous Materials* **2006**, *89*, 158-163 (Research article)

330. Mills, A.; Le Hunte, S. "*An overview of semiconductor photocatalysis*," *Journal of Photochemistry and Photobiology A: Chemistry* **1997**, *108*, 1-35 (Review article)

331. Olthof, B.; Khodakov, A.; Bell, A. T.; Iglesia, E. "*Effects of Support Composition and Pretreatment Conditions on the Structure of Vanadia Dispersed on $SiO_2$, $Al_2O_3$, $TiO_2$, $ZrO_2$, and $HfO_2$*," *Journal of Physical Chemistry B* **2000**, *104*, 1516-1528 (Research article)

332. Bandyopadhyay, M. "*Synthesis of mesoporous MCM-48 with nanodispersed metal and metal oxide particles inside the pore system*," Ph.D. Dissertation October, 2004 Ruhr-Universitat Bochum http://www-brs.ub.ruhr-uni-bochum.de/netahtml/HSS/Diss/BandyopadhyayMahuya/diss.pdf (accessed 7/31/09)

333. Narkhede, V. S.; De Toni, A.; Narkhede, V. V.; Curaya, M.; (Hans) Niemantsverdriet, J. W.; van der Berg, M. W. E.; Grunert, W.; Gies, H. "*Au/$TiO_2$ catalysts encapsulated in the mesopores of siliceous MCM-48-Reproducible synthesis, structural characterization and activity for CO oxidation*," *Microporous and Mesoporous Materials* **2009**, *118*, 52-60 (Research article)

334. Lichtin, N. N.; Avudaithai, M.; Bernan, E.; Dong, J. "*Photocataytic Oxidative Degradation of Vapors of Some Organic Compounds over $TiO_2$*," *Research in Chemical Intermediates* **1994**, *20*, 755-781 (Review article)

335. Hench, L. L.; West, J. K. "*The Sol-Gel Process*," *Chemical Reviews* **1990**, *90*, 33-72 (Review article)

336. Davidson, A. "*Modifying the walls of mesoporous silicas prepared by supramolecular-templating*," *Current Opinion in Colloid & Interface Science* **2002**, *7*, 92-106 (Review article)

337. Wang, S.; Wu, D.; Sun, Y.; Zhong, B. "*The synthesis of MCM-48 with high yields*," *Materials Research Bulletin* **2001**, *36*, 1717-1720 (Communication article)

338. Lim, S.; Ciuparu, D.; Yang, Y.; Du, G.; Pfefferle, L. D.; Haller, G. L. "*Improved synthesis of highly ordered Co-MCM-41*," *Microporous and Mesoporous Materials* **2007**, *101*, 200-206 (Research article)

339. Vralstad, T.; Oye, G.; Ronning, M.; Glomm, W. R.; Stocker, M.; Sjoblom, J. "*Interfacial chemistry of cobalt(II) during sol-gel synthesis of cobalt-containing mesoporous materials*," *Microporous and Mesoporous Materials* **2005**, *80*, 291-300 (Research article)

340. Jolly, W. L. "*Modern Inorganic Chemistry*," **1991**, *Second Edition*, Chapter 14, page 370 (Chemistry Inorganic textbook)

341. Matsumoto, A.; Chen, H.; Tsutsumi, K.; Grun, M.; Unger, K. "*Novel route in the synthesis of MCM-41 containing framework aluminum and its characterization*," *Microporous and Mesoporous Materials* **1999**, *32*, 55-62 (Research article)

342. Boote, B.; Subramanian, H.; Koodali, R. T. "*Rapid and facile synthesis of siliceous MCM-48 mesoporous materials*," *Chemical Communications* **2007**, 4543-4545 (Communications article)

343. Yu, J.; Shi, J-L.; Wang, L-Z.; Gao, J-H.; Yan, D-S. "*Synthesis of MCM-48 under low surfactant/silicon molar ratio conditions*," *Journal of Materials Science Letters* **2000**, *19*, 1461-1464 (Research article)

344. Wang, L.; Zhang, J.; Chen, F. "*Synthesis of hydrothermally stable MCM-48 mesoporous molecular sieve at low cost of CTAB surfactant*," *Microporous and Mesoporous Materials* **2009**, *122*, 229-233 (Research article)

345. Zhai, S-R.; Zheng, J-L.; Zou, J.; Wu, D.; Sun, Y-H. "*Mixed Cationic-Nonionic Surfactants Route to MCM-48: Effect of the Nonionic Surfactant on the Structural Properties*," *Journal of Sol-Gel Science and Technology* **2004**, *30*, 149-155 (Research article)

346. Vralstad, T.; Oye, G.; Stocker, M.; Sjoblom, J. "*Synthesis of comparable Co-MCM-48 and Co-MCM-41 materials containing high cobalt contents*," *Microporous and Mesoporous Materials* **2007**, *104*, 10-17 (Research article)

347. Campelo, J. M.; Luna, D.; Luque, R.; Marinas, J. M.; Romero, A. A.; Calvino, J. J.; Rodriguez-Luque, M. P. "*Synthesis of acidic Al-MCM-48: influence of the Si/Al ratio, degree of the surfactant hydroxyl exchange, and post-treatment in $NH_4F$ solution*," *Journal of Catalysis* **2005**, *230*, 327-338 (Research article)

348. Voegtlin, A. C.; Ruch, F.; Guth, J. L.; Patarin, J.; Huve, L. "*$F^-$ mediated synthesis of mesoporous silica with ionic- and non-ionic surfactants. A new templating pathway*," *Microporous Materials* **1997**, *9*, 95-105 (Research article)

349. Taralkar, U. S.; Kasture, M. W.; Joshi, P. N. "*Influence of synthesis conditions on structural properties of MCM-48*," *Journal of Physics and Chemistry of Solids* **2008**, *69*, 2075-2081 (Research article)

350. Wang, L.; Shao, Y.; Zhang, J. "*Short-time formation of well-ordered cubic mesoporous MCM-48 molecular sieve with the aid of fluoride ions*," *Materials Letters* **2005**, *59*, 3604-3607 (Communications article)

351. Wang, L.; Zhang, J.; Chen, F.; Anpo, M. "*Fluoride-Induced Reduction of CTAB Template Amount for the Formation of MCM-48 Mesoporous Molecular Sieve*," *Journal of Physical Chemistry C* **2007**, *111*, 13648-13651 (Research article)

352. Shao, Y.; Wang, L.; Zhang, J.; Anpo, M. "*Novel synthesis of high hydrothermal stability and long-range order MCM-48 with a convenient method*," *Microporous and Mesoporous Materials* **2005**, *86*, 314-322 (Research article)

353. Soler-Illia, G. J. de A. A.; Crepaldi, E. L.; Grosso, D.; Sanchez, C. "*Block copolymer-templated mesoporous oxide*," *Current Opinion in Colloid and Interface Science* **2003**, *8*, 109-126 (Review article)

354. Wang, L.; Shao, Y.; Zhang, J.; Anpo, M. "*Synthesis of MCM-48 mesoporous molecular sieve with thermal and hydrothermal stability with the aid of promoter anions*," *Microporous and Mesoporous Materials* **2006**, *95*, 17-25 (Research article)

355. Shao, Y.; Wang, L.; Zhang, J.; Anpo, M. "*Synthesis and characterization of high hydrothermally stable Cr-MCM-48*," *Microporous and Mesoporous Materials* **2008**, *109*, 271-277 (Research article)

356. Lin, H-P.; Mou, C-Y. "*Salt effect in post-synthesis hydrothermal treatment of MCM-41*," *Microporous and Mesoporous Materials* **2002**, *55*, 69-80 (Research article)

357. Xia, Y.; Mokaya, R.; Titman, J. J. "*Formation of Molecularly Ordered Layered Mesoporous Silica via Phase Transformation of Silicate-Surfactant Composites*," *Journal of Physical Chemistry B* **2004**, *108*, 11361-11367 (Research article)

358. Mesa, M.; Sierra, L.; Lopez, B.; Ramirez, A.; Guth, J-L. "*Preparation of micron-sized spherical particles of mesoporous silica from a triblock copolymer surfactant, usable as a stationary phase for liquid chromatography*," *Solid State Sciences* **2003**, *5*, 1303-1308 (Research article)

359. Hamal, D.; Klabunde, K. J. "*Synthesis, characterization, and visible light activity of new nanoparticle photocatalysts based on silver, carbon, and sulfur-doped $TiO_2$*," *Journal of Colloid and Interface Science* **2007**, *311*, 514-522 (Research article)

360. Gao, X.; Bare, S. R.; Fierro, J. L. G.; Wachs, I. E. "*Structural Characteristics and Reactivity/Reducibility Properties of Dispersed and Bilayered $V_2O_5/TiO_2/SiO_2$ Catalysts*," *Journal of Physical Chemistry B* **1999**, *103*, 618-629 (Research article)

361. Vrlstad, T.; Glomm, W. R.; Ronning, M.; Dathe, H.; Jentys, A.; Lercher, J. A.; Oye, G.; Stocker, M.; Sjoblom, J. "*Spectroscopic Characterization of Cobalt-Containing Mesoporous Materials*," *Journal of Physical Chemistry B* **2006**, *110*, 5386-5394 (Research aticle)

362. Kondratenko, E. V.; Cherian, M.; Baerns, M. "*Mechanistic aspects of the oxidative dehydrogenation of propane over an alumina-supported $VCrMnWO_x$ mixed oxide catalyst*," *Catalysis Today* **2005**, *99*, 59-67 (Research article)

363. Arana, J.; Dona-Rodriguez, J. M.; Gonzalez, O.; Tello Rendon, E.; Herrera, Melian, J. A.; Colon, G.; Navio, J. A.; Perez, Pena, J. "*Gas-phase ethanol photocatalytic degradation study with $TiO_2$ doped with Fe, Pd and Cu*," *Journal of Molecular Catalysis A: Chemical* **2004**, *215*, 153-160 (Research article)

364. Sauer, M. L.; Ollis, D. F. "*Photocatalyzed Oxidation of Ethanol and Acetaldehyde in Humidified Air*," *Journal of Catalysis* **1996**, *158*, 570-582 (Research article)

365. Tanaka, M.; Amano, F.; Ohtani, B. "*Cesium-Ion-Modified Vanadium Complex on Silica for Photocatalytic Decomposition of Acetaldehyde*," *P28 Note* http://pcat.cathokudai.ac.jp/eiccs/image/abstract/P28tanaka.pdf (accessed 5/18/09)

366. Vorontsov, A. V.; Dubovitskaya, V. P. "*Selectivity of photocatalytic oxidation of gaseous ethanol over pure and modified $TiO_2$*," *Journal of Catalysis* **2004**, *221*, 102-109 (Research article)

367. Zhuang, J.; Rusu, C. N.; Yates, J. T. Jr. "*Adsorption and Photooxidation of $CH_3CN$ on $TiO_2$*," *Journal of Physical Chemistry B* **1999**, *103*, 6957-6967 (Research article)

368. Tanaka, T.; Nishimura, Y.; Kawasaki, S-C.; Ooe, M.; Funabiki, T.; Yoshida, S. "*$V_2O_5/SiO_2$ Catalysts Modifed by $Na^+$ Ions: Surface Characterization by Spectroscopic Methods and Photoassisted Oxidation of 2-Propanol and Propene*," *Journal of Catalysis* **1989**, *118*, 327-338 (Research article)

369. Tananka, T.; Takenaka, S.; Funabiki, T.; Yoshida, S. "*Selective Photoxidation of Propane to Propanone over Alkali-ion-modified Silica-supported Vanadium Oxide*," *Chemistry Letters* **1994**, 1585-1588 (Communication article)

370. Tanenaka, S.; Kuriyama, T.; Tanaka, T.; Funabiki, T.; Yoshida, S. "*Photooxidation of Propane over Alkali-Ion-Modified $V_2O_5/SiO_2$ Catalysts*," *Journal of Catalysis* **1995**, *155*, 196-203 (Research article)

371. Takenaka, S.; Tanaka, T.; Funabiki, T.; Yoshida, S. "*Selective partial oxidation of light alkanes over alkali-ion-modified silica-supported vanadium oxides excited with visible light*," *Catalysis Letters* **1997**, *44*, 67-74 (Research article)

372. Tanaka, T.; Takenaka, S.; Funabiki, T.; Yoshida, S. "*Photo-assisted oxidation of 2-methylpropane over $Rb^+$ modified $V_2O_5/SiO_2$: Formation of 2-methylpropane-3-ol from 2-methylpropane and $O_2$*," *Journal of the Chemical Society, Faraday Transactions* **1996**, *92*, 1975-1979 (Research article)

373. Takenaka, S.; Tanaka, T.; Funabiki, T.; Yoshida, S. "*Reaction mechanism of photooxidation of propane over alkali-ion-modified silica-supported vanadium pentaoxide under irradiation by visible light*," *Journal of the Chemical Society, Faraday Transations* **1997**, *93*, 4151-4158 (Research article)

374. Takenaka, S.; Tanaka, T.; Yamazaki, T.; Funabiki, T.; Yoshida, S. "*Structure of Active Species in Alkali-Ion-Modified Silica-Supported Vanadium Oxide*," *Journal of Physical Chemistry B* **1997**, *101*, 9035-9040 (Research article)

375. Tanaka, T.; Ito, T.; Takenaka, S.; Funabiki, T.; Yoshida, S. "*Photocatalytic oxidation of alkane at a steady rate over alkali-ion-modified vanadium oxide supported on silica*," *Catalysis Today* **2000**, *61*, 109-115 (Research article)

376. Amano, F.; Tanaka, T. "*Modification of photocatalytic center for photo-epoxidation of propylene by rubidium ion addition to $V_2O_5/SiO_2$*," *Catalysis Communications* **2005**, *6*, 269-273 (Research article)

377. Amano, F.; Ito, T.; Takenaka, S.; Tanaka, T. "*Selective Photocatalytic Oxidation of Light Alkanes over Alkali-Ion-Modified $V_2O_5/SiO_2$; Kinetic Study and Reaction Mechanism*," *Journal of Physical Chemistry B* **2005**, *109*, 10973-10977 (Research article)

378. Amano, F.; Yamaguchi, T.; Tanaka, T. "*Effect of alkali-ion-doping on the local structure and the photocatalytic properties of alumina-supported vanadium oxides*," *Catalysis Today* **2007**, *120*, 126-132 (Research article)

379. Yoshida, S.; Takenaka, S.; Tanaka, T. "*Photooxidation of Light Alkanes Over Alkali-Ion-Modified Vanadium Catalysts*," *Research in Chemical Intermediates* **1998**, *24*, 309-327 (Research article)

380. Zhao, Z.; Liu, J.; Duan, A.; Xu, C.; Kobayashi, T.; Wachs, I. E. "*Effects of alkali metal cations on the structures, physico-chemical properties and catalytic behaviors of silica-supported vanadium oxide catalysts for the selective oxidation of ethane and the complete oxidation of diesel soot*," *Topics of Catalysis* **2006**, *38*, 309-325 (Research article)

381. Teramura, K.; Tanaka, T.; Yamamoto, T.; Funabiki, T. "*Photo-oxidation of cyclohexane over alumina-supported vanadium oxide catalyst*," *Journal of Molecular Catalysis A: Chemical* **2001**, *165*, 299-301 (Research article)

382. Teramura, K.; Hosokawa, T.; Ohuchi, T.; Shishido, T.; Tanaka, T. "*Photoactivation mechanism of orthovanadate-like $(V{=}O)O_3$ species*," *Chemical Physics Letters* **2008**, *460*, 478-481 (Research article)

383. Chang, Y.-F.; Somorjai, G. A.; Heinemann, H. "*An $^{18}O_2$ Temperature-Programmed Isotope Exchange Study of Transition-Metal-Containing ZSM-5 Zeolites Used for Oxydehydrogenation of Ethane*," *Journal of Catalysis* **1995**, *154*, 24-32 (Research article)

384. Zhao, Z.; Yamada, Y.; Teng, Y.; Ueda, A.; Nakagawa, K.; Kobayashi, T. "*Selective Oxidation of Ethane to Acetaldehyde and Acrolein over Silica-Supported Vanadium Catalysts Using Oxygen as Oxidant*," *Journal of Catalysis* **2000**, *190*, 215-227 (Research article)

385. Irusta, S.; Marchi, A. J.; Lombardo, E. A.; Miro, E. E. "*Characterization of surface species on $V/SiO_2$ and $V, Na/SiO_2$ and their role in the partial oxidation of methane to formaldehyde*," *Catalysis Letters* **1996**, *40*, 9-16 (Research article)

386. Blasco, T.; Lopez Nieto, J. M.; Dejoz, A.; Vazquer, M. I. "*Influence of the Acid-Base Character of Supported Vanadium Catalysts on Their Catalytic Properties for the Oxidative Dehydrogenation of n-Butane*," *Journal of Catalysis* **1995**, *157*, 271-282 (Research article)

387. Li, Y.; Zhang, Y.; Xue, B.; Guo, Y. "*Synthesis of dipropyl carbonate by transesterification over $KNO_3/MCM$-48*," *Journal of Molecular Catalysis A: Chemical* **2008**, *287*, 9-15 (Research article)

388. Eimer, G. A.; Pierella, L. B.; Monti, G. A.; Anunziata, O. A. "*Synthesis and characterization of Al-MCM-41 and Al-MCM-48 mesoporous materials*," *Catalysis Letters* **2002**, *78*, 65-75 (Research article)

389. Kao, C-P.; Lin, H-P.; Mou, C-Y. "*Synthesis of elastic macrospheres of silica-surfactant nanocomposites*," *Journal of Physics and Chemistry of Solids* **2001**, *62*, 1555-1559 (Research article)

390. Kim, S.; Ida, J.; Guliants, V. V.; Lin, Y. S. "*Tailoring Pore Properties of MCM-48 Silica for Selective Adsorption of $CO_2$*," *Journal of Physical Chemistry B* **2005**, *109*, 6287-6293 (Research article)

391. Kim, S. "*Modified Ordered Mesoporous Silica for $CO_2$-$N_2$ Separation*," MS thesis November, 2003 University of Cincinnati http://www.ohiolink.edu/etd/send-pdf.cgi?ucin1070484926 (accessed 5/1/09)

392. Kumar, P. "Inclusion Chemistry in Periodic Mesoporous Hosts: Growth of Quantum-Confined Materials and Gas Separation Membranes," Ph.D. thesis May, 2007 University of Cincinnati http://www.ohiolink.edu/etd/send=pdf.cgi/KUMAR%20PARVEEN.pdf?acc_num=ucin1186772727 (accessed 5/1/09)

393. Huang, H. Y.; Yang, R. T.; Chinn, D.; Munson, C. L. "*Amine-Grafted MCM-48 and Silica Xerogel as Superior Sorbents for Acidic Gas Removal from Natural Gas*," *Industrial & Engineering Chemistry Research* **2003**, *42*, 2427-2433 (Research article)

394. Zhang, H.; Zhang, P.; Ye, K.; Sun, Y.; Jiang, S.; Wang, Y.; Pang, W. "*Mesoporous material grafted with luminescent molecules for the design of selective metal ion chemosensor*," *Journal of Luminescence* **2006**, *117*, 68-74 (Research article)

395. Vradman, L.; Landau, M. V.; Herskowitz, M.; Ezersky, V.; Talianker, M.; Nikitenko, S.; Koltypin, Y.; Gedanken, A. "*High loading of short $WS_2$ slabs inside SBA-15: promotion with nickel and performance in hydrodesulfurization and hydrogenation*," *Journal of Catalysis* **2003**, *213*, 163-175 (Research article)

396. Sano, T.; Negishi, N.; Uchino, K.; Tanaka, J.; Matsuzawa, S.; Takeuchi, K. "*Photocatalytic degradation of gaseous acetaldehyde on $TiO_2$ with photodeposited metals and metal oxides*," *Journal of Photochemistry and Photobiology A: Chemistry* **2003**, *160*, 93-98 (Research article)

397. D'Elia, L. F.; Rincon, L.; Ortiz, R. "*Test of vanadium pertoxide as anode for the electrooxidation of toluene: A theoretical approach of the electrode process*," *Electrochimica Acta* **2004**, *50*, 217-224 (Research article)

398. Mishakov, I. V.; Vedyagin, A. A.; Bedilo, A. F.; Zaikovskii, V. I.; Klabunde, K. J. "*Aerogel $VO_x$/MgO catalysts for oxidative dehydrogenation of propane*," *Catalysis Today* **2009**, *144*, 278-284 (Research article)

399. Martyanov, I. N.; Klabunde, K. J. "*Decomposition of $CCl_3F$ over vanadium oxides and $[MgV_xO_y]MgO$ shell/core-like particles*," *Journal of Catalysis* **2004**, *224*, 340-346 (Research article)

400. Chesnokov, V. V.; Bedilo, A. F.; Heroux, D. S.; Mishakov, I. V.; Klabunde, K. J. "*Oxidative dehydrogenation of butane over nanocrystalline MgO, $Al_2O_3$, and $VO_x$/MgO catalysts in the presence of small amounts of iodine*," *Journal of Catalysis* **2003**, *218*, 438-446 (Research article)

401. Yang, X.; Cao, C.; Erickson, L.; Hohn, L.; Maghirang, R.; Klabunde, K. "*Synthesis of visible-light-active $TiO_2$-based photocatalysts by carbon and nitrogen doping*," *Journal of Catalysis* **2008**, *260*, 128-133 (Research article)

402. Yang, X.; Cao, C.; Hohn, K.; Erickson, L.; Maghirang, R.; Hamal, D.; Klabunde, K. "*Highly visible-light active C- and V-doped $TiO_2$ for degradation of acetaldehyde*," *Journal of Catalysis* **2007**, *252*, 296-302 (Research article)

# Chapter 6 –V-MCM-48 Conclusion

The research completed involved the modified metal doped Stober silica sphere synthesis, characterization, and photocatalytic studies. [1-3] In contrast to many mesoporous MCM-48 silica syntheses that employ hydrothermal conditions, [5-10] the vanadium doped MCM-48 structure was carried out at room temperature with finished product in two days. This modified Stober synthesis consistently produced V-MCM-48 even at high metal loadings of Si/V = 10 (≈ 8.33 wt%). [1-3] Powder X-ray diffraction (XRD) analysis of the calcinated V-MCM-48 compositions showed the two primary peaks characteristic of bicontinuous Ia3d space group, as reported in literature. [2,3] Reduction in powder XRD peak intensity trend was observed with larger metal ion loading in mesoporous materials, which was reported in literature. [9,11,12] Diffuse-reflectance-ultra-violet-visible (DR-UV-vis) spectroscopy analysis revealed two absorption peaks. These absorption peaks were centered at approximately 250 nm and 375 nm. Comparison of these peak values to literature led to the assignment of three types of vanadium coordination sites in MCM-48 silica matrix. [13-15] $N_2$ adsorption-desorption characterization of the pore structure had type IV isotherm with H2 hysteresis loop, according to literature. [16,17] Type IV isotherm would be assigned to mesoporous materials, and H2 hysteresis loop would be for ink-bottle porous structure. The BET surface area and BJH pore volume values decreased with larger vanadium ion loading in V-MCM-48, which has been reported on other metal doped M41S mesoporous materials. [11,18,19] Photocatalysis studies were completed with V-MCM-48 under dark, visible, and ultra-violet (UV) light illumination conditions on the following six probe molecules: $CH_3CHO$, CO, $CH_3CH_2OH$, $CH_3COCH_3$, $CH_3CHOHCH_3$, and $CH_3CN$. In addition, several types of nanoparticle gold catalysts and Degussia-Huls P-25 $TiO_2$ standards were employed as compared with the V-MCM-48 in photodegradation studies. Formation of carbon dioxide formation occurred over the V-MCM-48 mesoporous material with acetaldehyde, carbon monoxide, ethanol, and acetonitrile. Acetone and 2-propanol had no photodegradation activity at ambient reaction conditions. Gold CO oxidation catalysts formed $CO_2$ at lower than expected rates compared to literature. [20-26] Acetaldehyde UV-light photodegradation with P-25 $TiO_2$ showed significantly larger $CO_2$ production vs. V-MCM-48. Finally, the results indicate V-MCM-48 might be useful in water-splitting due to high oxidation state ($V^{5+}$), visible light absorption, and high surface area-three dimensional pore support structure.

## References


1. Stober, W.; Fink, A.; Bohn, E. "*Controlled Growth of Monodisperse Silica Spheres in the Micron Size Range*,"*Journal of Colloid and Interface Science* **1968**, *26*, 62-69 (Research article)

2 Schumacher, K.; Grun, M.; Unger, K. K. "*Novel synthesis of spherical MCM-48*," *Microporous and Mesoporous Materials* **1999**, *27*, 201-206 (Research article)

3. Schumacher, K.; du Fresne von Hohenesche, C.; Unger, K. K.; Ulrich, R.; Du Chesne, A.; Wiesner, U.; Spiess, H. W. "*The Synthesis of Spherical Mesoporous Molecular Sieves MCM-48 with Heteroatoms Incorporated into the Silica Framework*," *Advanced Materials* **1999**, *11*, 1194-1198 (Research article)

4. Romero, A. A.; Alba, M. D.; Klinowski, J. "*Aluminosilicate Mesoporous Molecular Sieve MCM-48*," *Journal of Physical Chemistry B* **1998**, *102*, 123-128 (Research article)

5 .Schmidt, R.; Junggreen, H.; Stocker, M. "*Synthesis of a mesoporous MCM-48 material containing only tetrahedral aluminum*," *Chemical Communications* **1996**, 875-876 (Communication article)

6. Gomez, S.; Garces, L. J.; Villegas, J.; Ghosh, R.; Giraldo, O.; Suib, S. L. "*Synthesis and characterization of TM-MCM-48 (TM = Mn, V, Cr) and their catalytic activity in the oxidation of styrene*," *Journal of Catalysis* **2005**, *233*, 60-67 (Research article)

7. Gomez, S.; Giraldo, O.; Garces, L. J.; Villegas, J.; Suib, S. L. "*New Synthetic Route for the Incorporation of Manganese Species into the Pores of MCM-48*," *Chemistry of Materials* **2004**, *16*, 2411-2417 (Research article)

8. Romero, A. A.; Alba, M. D.; Zhou, W.; Klinowski, J. "*Synthesis and Characterization of the Mesoporous Silicate Molecular Sieves MCM-48*," *Journal of Physical Chemistry B* **1997**, *101*, 5294-5300 (Research article)

9. Shao, Y.; Wang, L.; Zhang, J.; Anpo, M. "*Synthesis of Hydrotheramally Stable and Long-Range Ordered Ce-MCM-48 and Fe-MCM-48 Materials*," *Journal of Physical Chemistry B* **2005**, *109*, 20835-20841 (Research article)

10. More Citations on hydrothermally prepared M41S mesoporous materials under Discussion section subtitle follows: "**Explanation of Why the Modified Novel Synthesis would be Superior to the Hydrothermal One**."

11. Zhan, W.; Guo, Y.; Wang, Y.; Liu, X.; Guo, Y.; Wang, Y.; Zhang, Z.; Lu, G. "*Synthesis of Lanthanum-Doped MCM-48 Molecular Sieves and Its Catalytic Performance for the Oxidation of Styrene*," *Journal of Physical Chemistry B* **2007**, *111*, 12103-12110 (Research article)

12. Zhang, W.; Pinnavaia, T. J. "*Transition metal substituted derivatives of cubic MCM-48 mesoporous molecular sieves*," *Catalysis Letters* **1996**, *38*, 261-265 (Research article)

13. Van Der Voort, P.; Morey, M.; Stucky, G. D.; Mathieu, M.; Vansant, E. F. "*Creation of $VO_x$ Surface Species on Pure Silica MCM-48 Using Gas-Phase Modification with $VO(acac)_2$*," *Journal of Physical Chemistry B* **1998**, *102*, 585-590 (Research article)

14. Mathieu, M.; Van Der Voort, P.; Weckhuysen, B. M.; Rao, R. R.; Catana, G.; Schoonheydt, R. A.; Vansant, E. F. "*Vanadium-Incorporated MCM-48 Materials: Optimization of the Synthesis Procedure and in Situ Spectroscopic Study of the Vanadium Species*," *Journal of Physical Chemistry B* **2001**, *105*, 3393-3399 (Research article)

15. Morey, M.; Davidson, A.; Eckert, H.; Stucky, G. "*Pseudotetrahedral $O_{3/2}V{=}O$ Centers Immobilized on the Walls of a Mesoporous, Cubic MCM-48 Support: Preparation, Characterization, and Reactivity toward Water As Investigated by $^{51}V$ NMR and UV-Vis Spectroscopies*," *Chemistry of Materials* **1996**, *8*, 486-492 (Research article)

16. Sing, K. S. W.; Everett, D. H.; Haul, R. A. W.; Moscou, L.; Pierotti, R. A.; Routquerol, J.; Siemieniewska, T. "*Reporting Physisorption Data for Gas/Solid Systems with Special Reference to the Determination of Surface Area and Porosity*," *Pure and Applied Chemistry* **1985**, *57*, 603-619 (Research acticle)

17. McNall, M.; Laurence, R. L.; Conner, W. C. "*An experimental approach to test sorption mechanisms in MCM-41*," *Microporous and Mesoporous Materials* **2001**, *44-45*, 709-716 (Research acticle)

18. Kohn, R.; Froba, M. "*Nanoparticles of 3d transition metal oxides in mesoporous MCM-48 silica host structures: Synthesis and characterization*," *Catalysis Today* **2001**, *68*, 227-236 (Research article)

19. Morey, M. S.; O'Bren, S.; Schwarz, S.; Stucky, G. D. "*Hydrothermal and Postsynthesis Surface Modification of Cubic, MCM-48, and Ultralarge Pore SBA-15 Mesoporous Silica with Titanium*," *Chemistry of Materials* **2000**, *12*, 898-911 (Research article)

20. Haruta, M.; Kobayashi, T.; Sano, H.; Yamada, N. "*Novel Gold Catalysts for the Oxidation of Carbon Monoxide at a Temperature far Below 0°C*," *Chemistry Letters* **1987**, 405-408 (Research article)

21. Haruta, M.; Yamada, N.; Kobayashi, T.; Iuima, S. "*Gold Catalysts Prepared by Coprecipitation for Low-Temperature Oxidation of Hydrogen and of Carbon Monoxide*," *Journal of Catalysis* **1989**, *115*, 301-309 (Research article)

22. Iizuka, Y.; Fujiki, H.; Yamauchi, N.; Chijiiwa, T.; Arai, S.; Tsubota, S.; Haruta, M. "*Adsorption of CO on gold supported on $TiO_2$*," *Catalysis Today* **1997**, *36*, 115-123 (Research article)

23. Boccuzzi, F.; Chiorinio, A.; Manzoli, M.; Lu, P.; Akita, T.; Ichikawa, S.; Haruta, M. "*$Au/TiO_2$ Nanosized Samples: A Catalytic, TEM, and FTIR Study of the Effect of Calcination Temperature on the CO Oxidation*," *Journal of Catalysis* **2001**, *202*, 256-267 (Research article)

24. Qian, K.; Huang, W.; Fang, J.; Lv, S.; He, B.; Jiang, Z.; Wei, S. "*Low-temperature CO oxidation over $Au/ZnO/SiO_2$ catalysts: Some mechanism insights*," *Journal of Catalysis* **2008**, *255*, 269-278 (Research acticle)

25. Wang, Y. G.; Zhang, W. X.; Lian, H. L.; Jiang, D. Z.; Wu, T. H. " *Effect of calcination temperatures and precipitant on the catalytic performance of Au/ZnO catalysts for CO oxidation at ambient temperature and in humid circumstances*," *Applied Catalysis A: General* **2003**, *239*, 1-10 (Research article)

26. Comotti, M.; Li, W-C.; Spliethoff, B.; Schuth, F. "*Support Effect in High Activity Gold Catalysts for CO Oxidation*," *Journal of the American Chemical Society* **2006**, *128*, 917-924 (Research article)

# Appendix A - Drawings of Various Surfactant Packing Parameter Values

This appendix represents the drawing of the surfactant packing parameter that control the formation of various mesoporous silica structures, such as MCM-48 discussed throughout the earlier chapters. The initial figures provide visual representation of the species in a given solution: ions, ethanol, water molecules, and surfactant molecules. From this, drawing provided of the surfactant molecule structure formed under various anions and different concentrations of surfactant molecules with and without ethanol. Finally, the optimal concentrations of anions (counter-ions), ethanol in both the hydrothermal and Stober synthesis have been illustrated in formation of MCM-48.

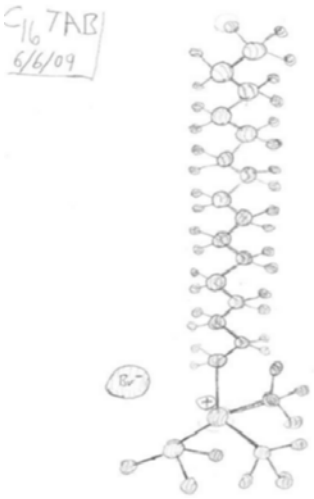


**Figure A:1 CTAB Surfactant Molecule without water molecules.**

**Supplemental text for Appendix A-A:1**-The main parts of the cationic cetyltrimethylammonium bromide (CTAB) surfactant would be the sixteen long carbon alkyl hydrophobic chain and the polar trimethylammonium head-group region with bromide anion as the counter-ion. As will become more appearent throughout the rest of Appendix A, the anion would directly effects the aggregation of the surfactant head-groups.

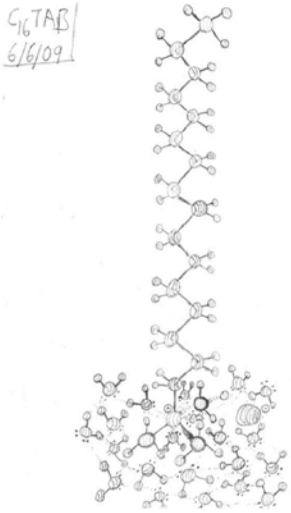


**Figure A:2 CTAB with Water Molecules Solvating the Cationic Head-group.**

**Supplemental text for Appendix A-A:2**-The key portion of the CTAB molecule in polar water would be the cationic trimethylammonium head-group. The degree (or amount) of water solvating the cationic head-group would be determined by the number and type of counter-ions (anions) surrounding the head-group region, thereby directly influences the surfactant packing parameter.

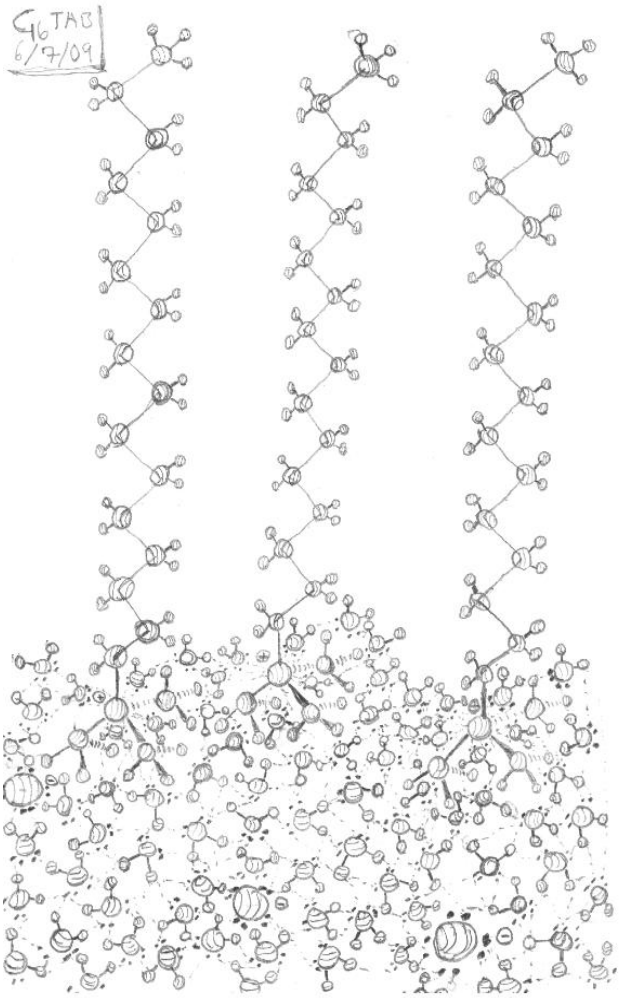


**Figure A:3 Three CTAB molecules with water molecules solvating the cationic head-group region.**

**Supplemental text for Appendix A-A:3**-The key variables to note would be the formation of lamellar structure and water molecules do not pass into the hydrophobic alkyl region, but instead reside in the cationic head-group section. Also, the bromide ($Br^-$) anion would appear to be in the outer region of the head-group area known as the Gouy-Chapman layer, which means the water molecules would attempt to passive the positive nitrogen atom in the trimethylammonium group with lone pair of electrons from oxygen atom in water.

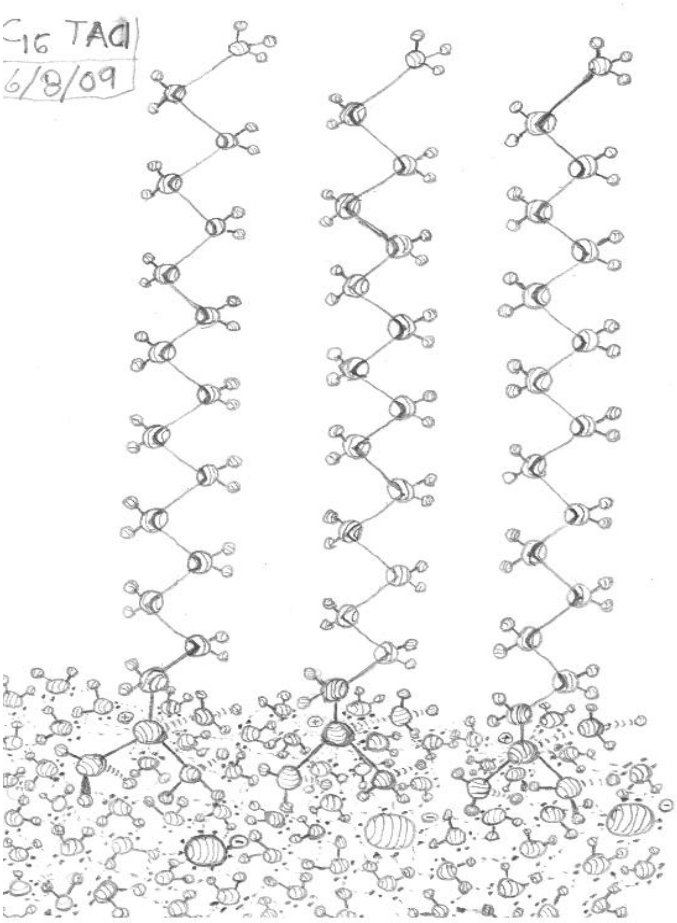


**Figure A:4 Three CTACl Surfactant Molecules Cationic Head-Group Region Solvated with Water Molecules.**

**Supplemental text for Appendix A-A:4**-The key difference between A.3 with $CTA^+$ ions with $Br^-$ counter-ions would be that chloride anion would be the counter-ion. As noted be A.3 and A.4 above, the chloride anion would shield the the cationic cetytrimethylammonium head-group to less extent than bromide anion; therefore, this leads to more water molecules surrounding the positively charged head-group region. In turn, this increases the the g-value in the surfactant packing parameter ($g = V/a_0l_c$) leading to lamellar structure.

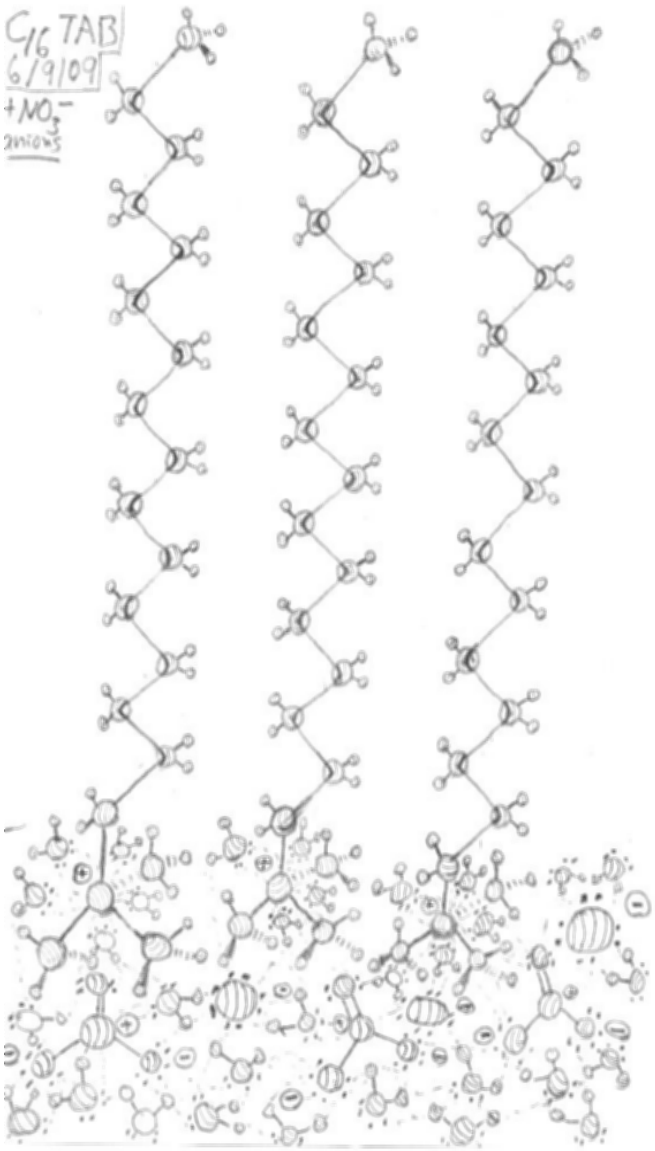


**Figure A:5 CTAB Surfactant Molecules with Nitrate Anion with Water Molecules.**

**Supplemental text for Appendix A-A:5**-The key region to focus on would the the cationic head-group region of $CTA^+$ ion. In comparison to just bromide or chloride anions in the solutions, as noted in A.3 and A.4, the nitrate ($NO_3^-$) anion more effectively solvates the cetytrimethylammonium head-group region, thereby dehydrating the trimethylammonium head-groups. The dehydration of the cationic surfactant head-group region leads to tigher formation of initial micelle. This dehydration of the trimethylammonium head-group would be key to forming intermediate structures, such as MCM-48.

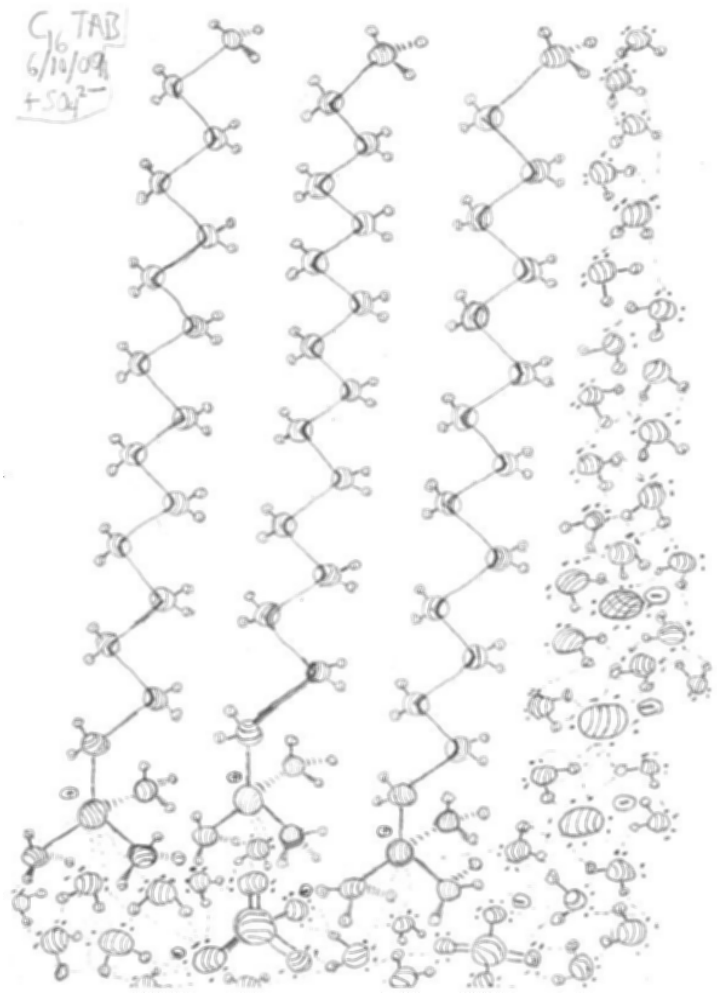


**Figure A:6 Three CTAB Surfactant Molecules with Sulfate Anion in Aqueous Solution.**

**Supplemental text for Appendix A-A:6**-As seen in the above drawing, the sulfate anion ($SO_4^{2-}$) dehydrates the trimethylammonium head-groups, thereby leading to tighter formation the head-groups and resulting micelle shape taken. Besides the effect of sulfate anion, one could note the bromide anion further away from the inner region known as Stein layer. Also, the water molecules on the right hand side would not mixture with the hydrophobic alkyl tail region.

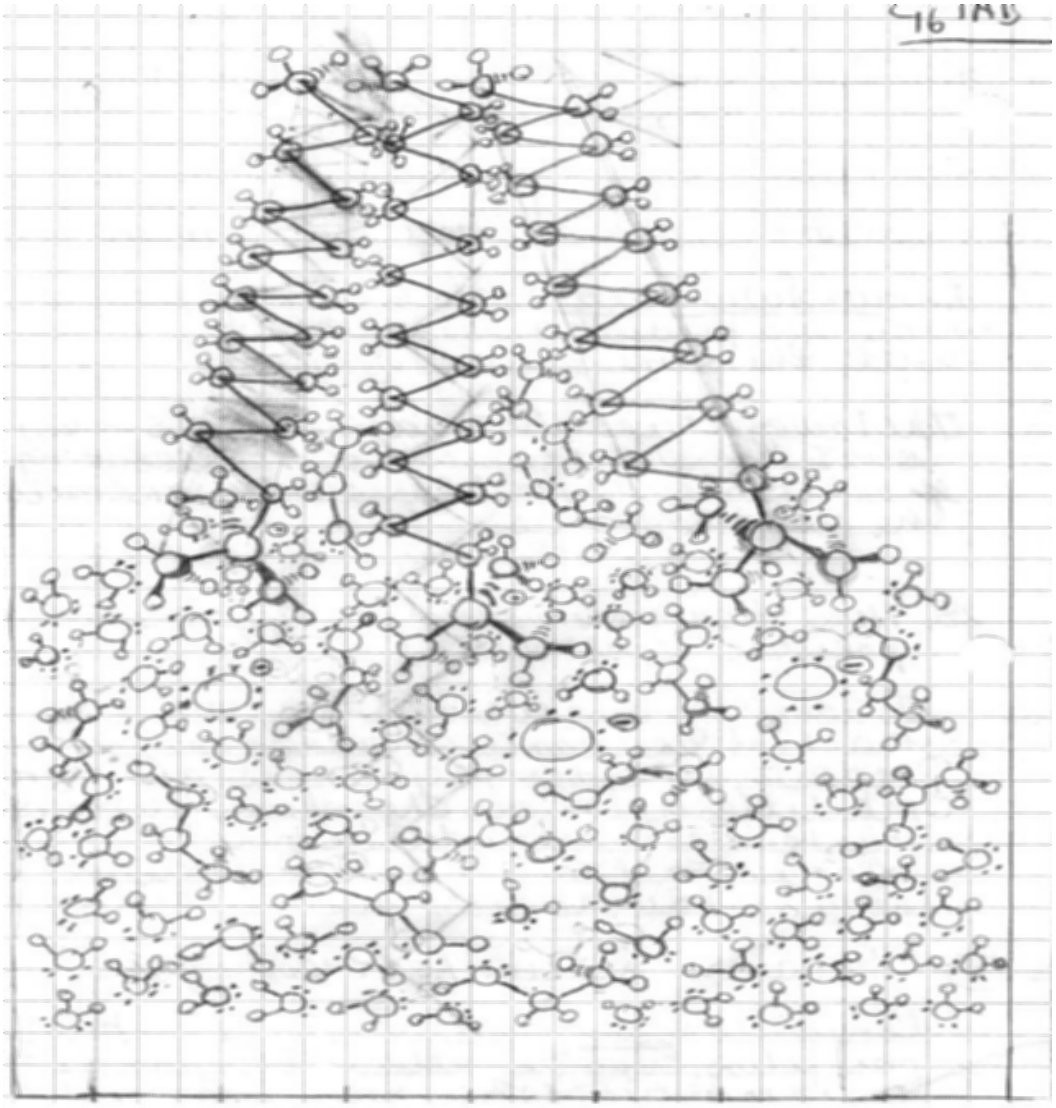

**Figure A:7 CTAB Micelle Formations with Ethanol Corresponding to MCM-41 g-value.**

**Supplemental text for Appendix A-A:7**-As seen in the above drawing, the three CTAB surfactant molecules hydrophobic region aggregates together to reduce the non-polar-polar interactions with the aqueous medium. Due to the polar hydroxyl group and alkyl non-polar portion of ethanol, the ethanol penetrates slightly into the hydrophobic region, although not deep into the alkyl tail region. This causes the change in the volume of the alkyl tail (V) in surfactant packing parameter equation ($g = V/a_0 l_c$), which causes an increase the surfactant packing parameter g-value. The result would be g-value corresponding to ⅓ to ½ for MCM-41 structure. Also, seen in the above drawing, the head-group region appears to be saturated with water molecules donating electron density to the cationic trimethylammonium head-groups, which noted earlier leads to larger head-group value, $a_0$. Additionally, the bromide counter-ions (anions) do not appear to be dehydrating the surface of the $CTA^+$ surfactant ion.

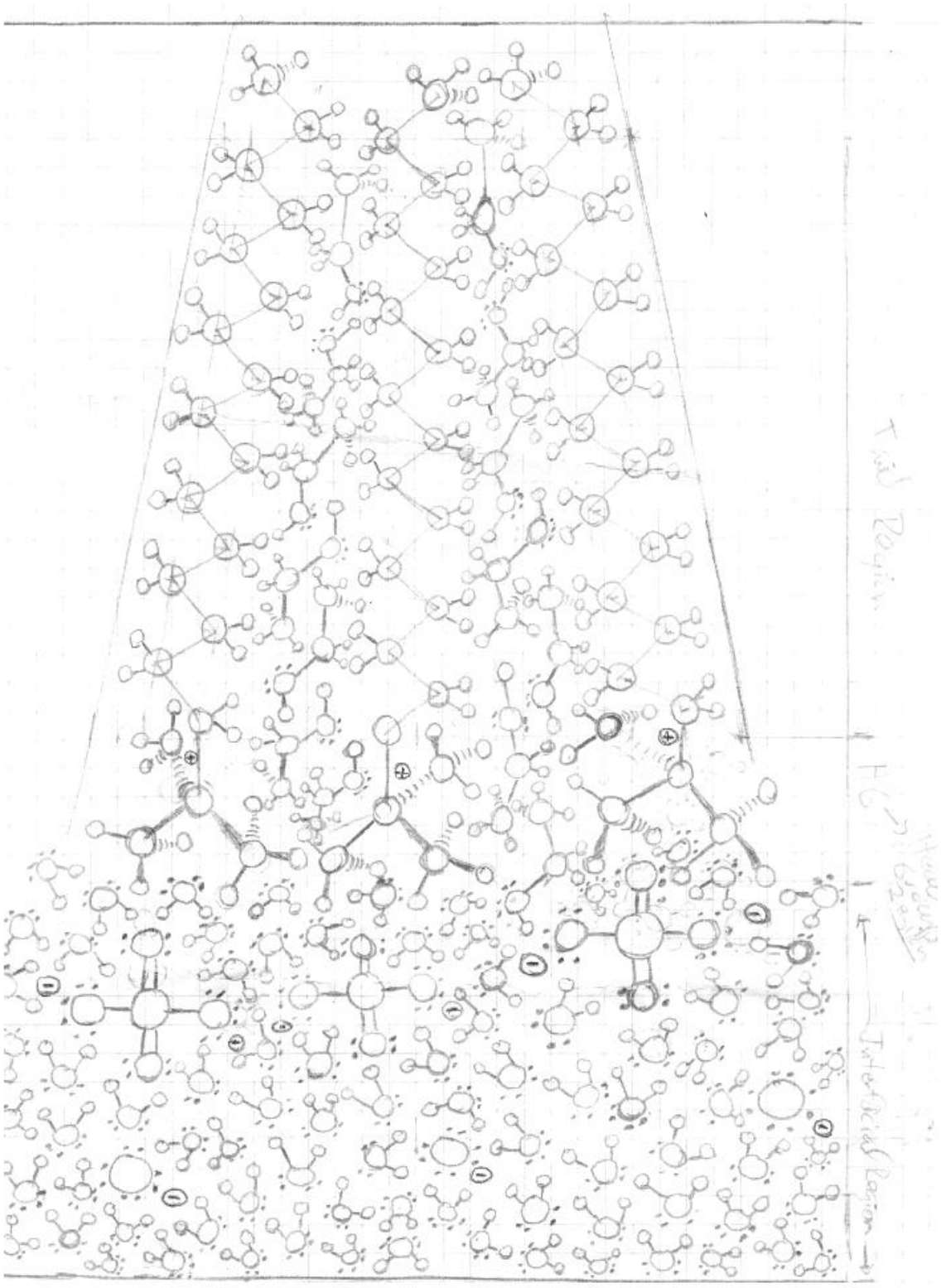

**Figure A:8 Hydrothermal Induced Formation of MCM-48 with Sulfate Anion + Ethanol.**

**Supplemental text for Appendix A-A:8**-The key region to focus on would be the infacial with the cationic head-groups. As seen in the above drawing, the sulfate anion removes most of the water molecules from the cetyltrimethylammonium head-group region. In addition, the ethanol molecules penetrate hydrophobic alkyl chain region of

the $CTA^+$ surfactant ion from the thermal energy imput. Key points would be the reduction in the head-group region, $a_0$, value and increase in the alkyl tail region. This in-turn leds to further increase in surfactant packing parameter g-value ($g = V/a_0l_c$), thereby to the value of ½ to ⅔ coorsponding to MCM-48 structure. Clearly, the contribution of the counter-ion would affect the degree of hydration of the cationic head-groups, which would determine if this tiny region was retained of passed to a larger g-value.

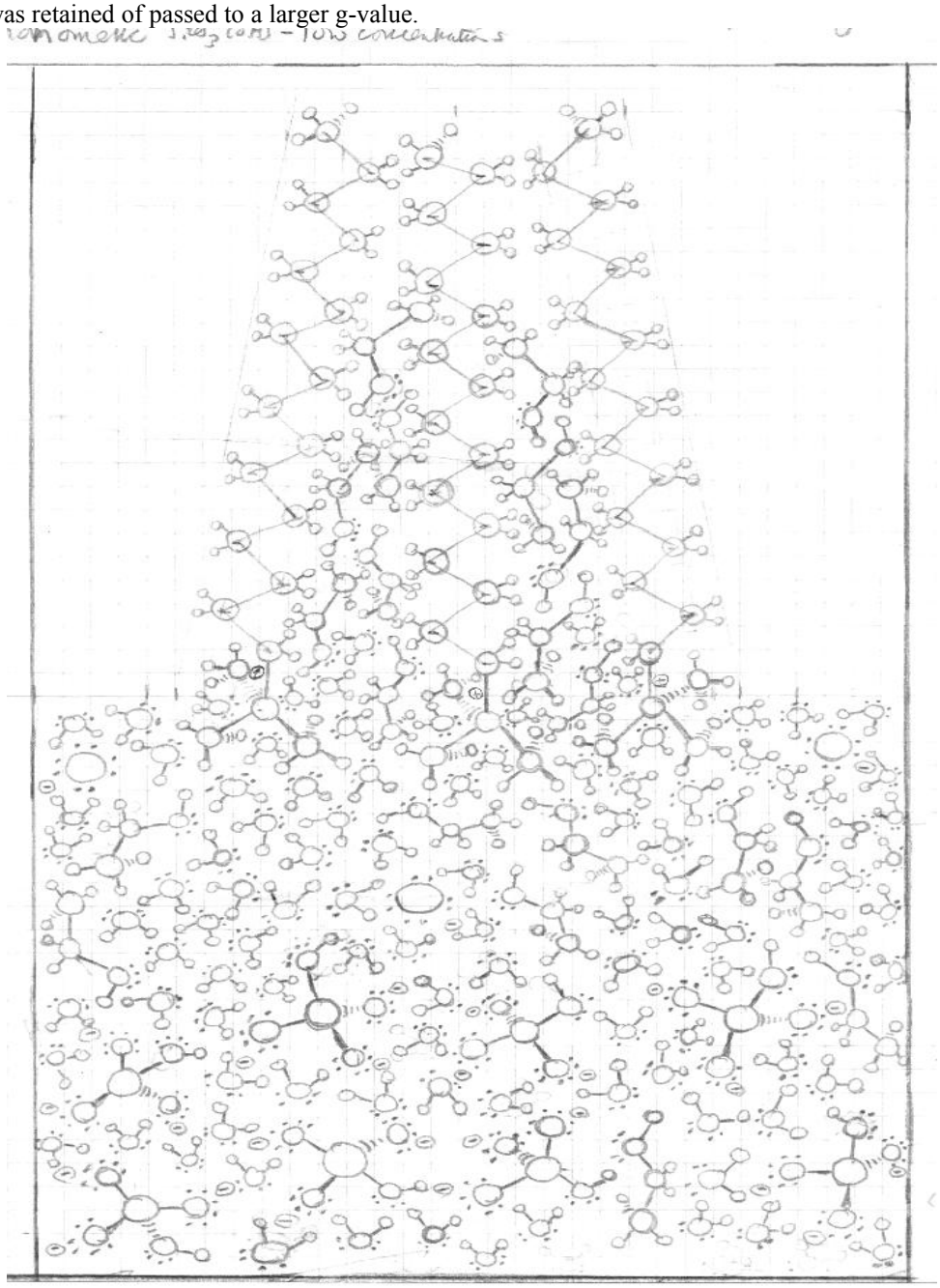

**Figure A:9 Modified Stober MCM-48 Synthesis with Small amount of Silica Monomers.**

**Supplemental text for Appendix A-A:9**-The major difference between the hydrothermal synthesis and the modified Stober synthesis of MCM-48 would be use of excess ethanol and water. The excess ethanol would act in a similar manner to less ethanol under hydrothermal conditions, thereby increasing the alkyl tail volume (V) in the surfactant packing parameter equation ($g = V/a_0l_c$). Key conclusions from the above drawing would be the fact of monomeric silica oligomers not at the interface of the cationic head-groups, but in the Guoy-Chapman outer layer.

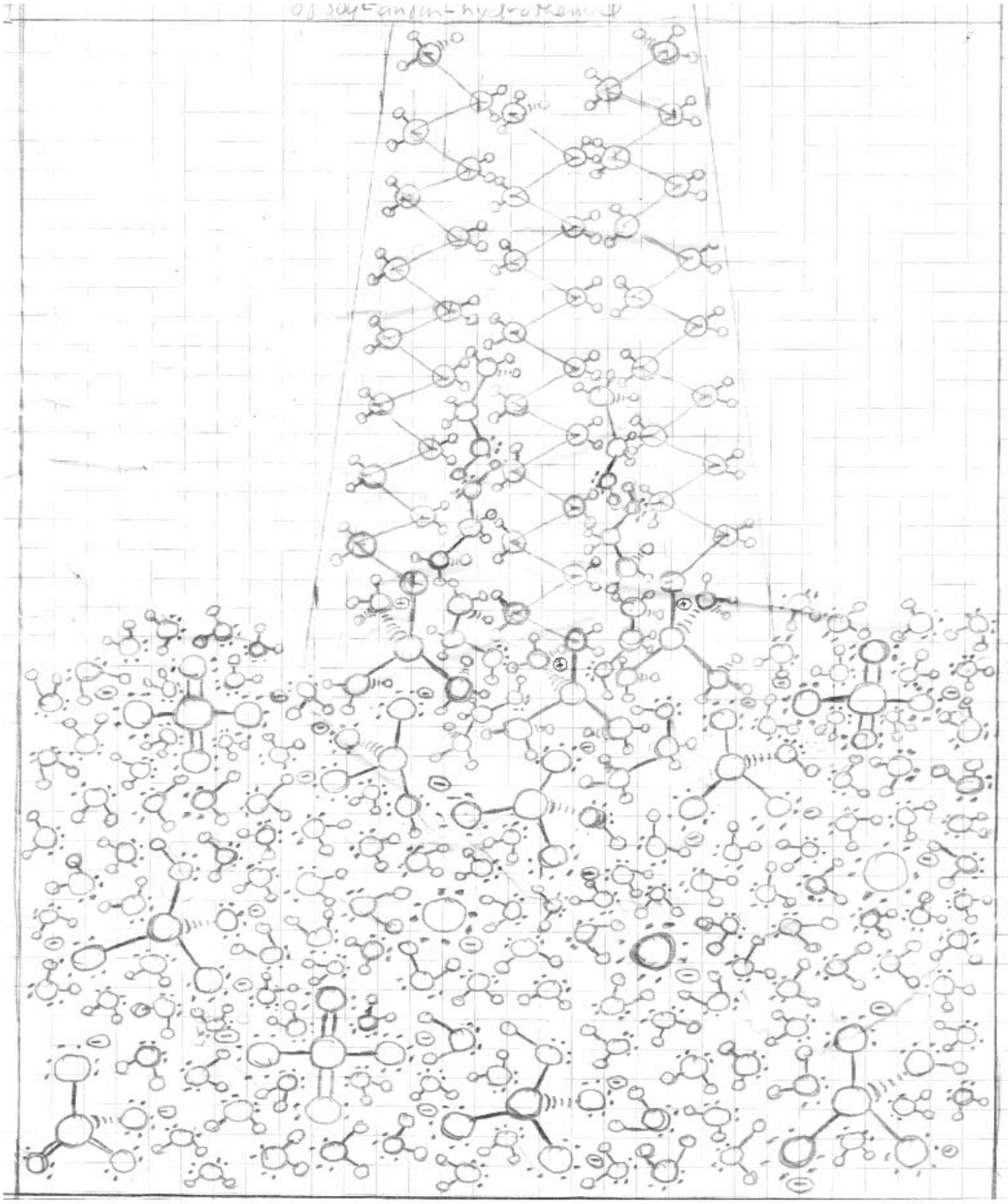

**Figure A:10 Effect of Sulfate Anion Initially with Small Concentration of Silica Monomers for MCM-48.**

**Supplemental text for Appendix A-A:10**-Key variables to look at in the above drawing would be the removal of water molecules from the cationic region due to the highly charged sulfate anion. The silica monmers would be in the Stern layer region. In addition, the ethanol penetrates into the hydrophobic alkyl region. With a reduction in the head-group region, $a_0$, value and the alkyl tail volume (V) and chain length (l) approximately constant, the g-value ($g = V/a_0l_c$) increases into the tiny region corresponding to MCM-48 of g-value ½ to ⅔.

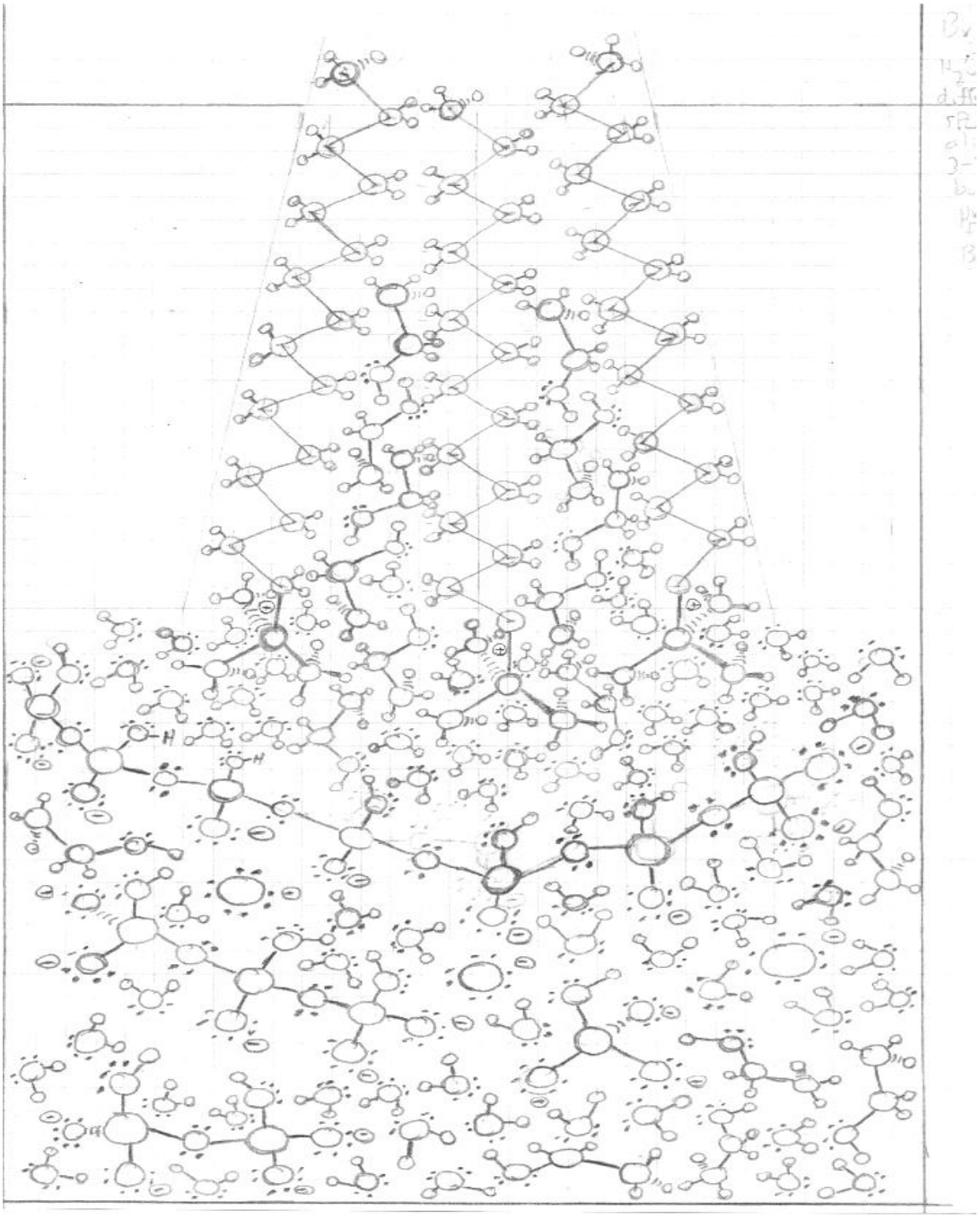

**Figure A:11 Formation of Silica Oligomers in Modified Stober MCM-48.**

**Supplemental text for Appendix A-A:11**-In contrast to the silica monmers not close to the cationic head-groups in A.9, the formation of silica oligomers leads to larger negative charge, which leads to stronger cationic-anionic binding interactions with $CTA^+$ surfactant ions. Similar to previous drawings with ethanol in the reaction mixture, the ethanol penetrates into the hydrophobic tail region of $CTA^+$ surfactant ions.

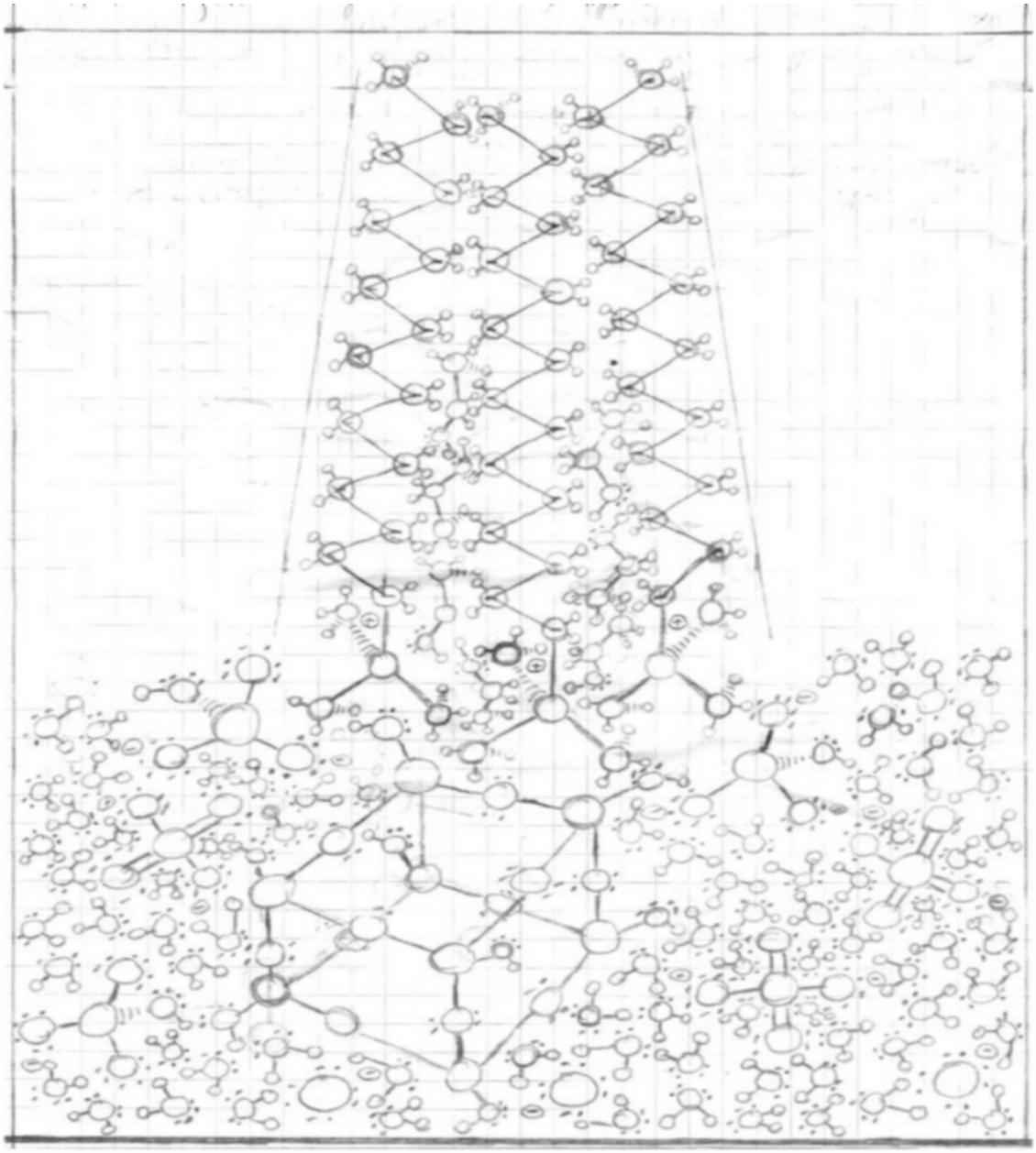

**Figure A:12 Formation of D4R Silica Oligomer Units with Sulfate Anion in MCM-48 Synthesis.**

**Supplemental text for Appendix A-A:12**-At still higher concentrations of silica monomer, these silica monomers form into double four-ring (D4R) octamer silica oligomers. Due to each face of the D4R octamer having four oxygen atoms with lone pairs of electrons, this leads to stronger binding to the cetyltrimethylammonium head-group region. As noted earlier in this appendix, the sulfate anion dehydrates the cationic head-group region, which results in both tighter formation of the surfactant head-group region and greater bonding interaction between the D4R silica oligomer units. The end result would be enhanced formation kinetic rate and creation of the MCM-48 silica structure.

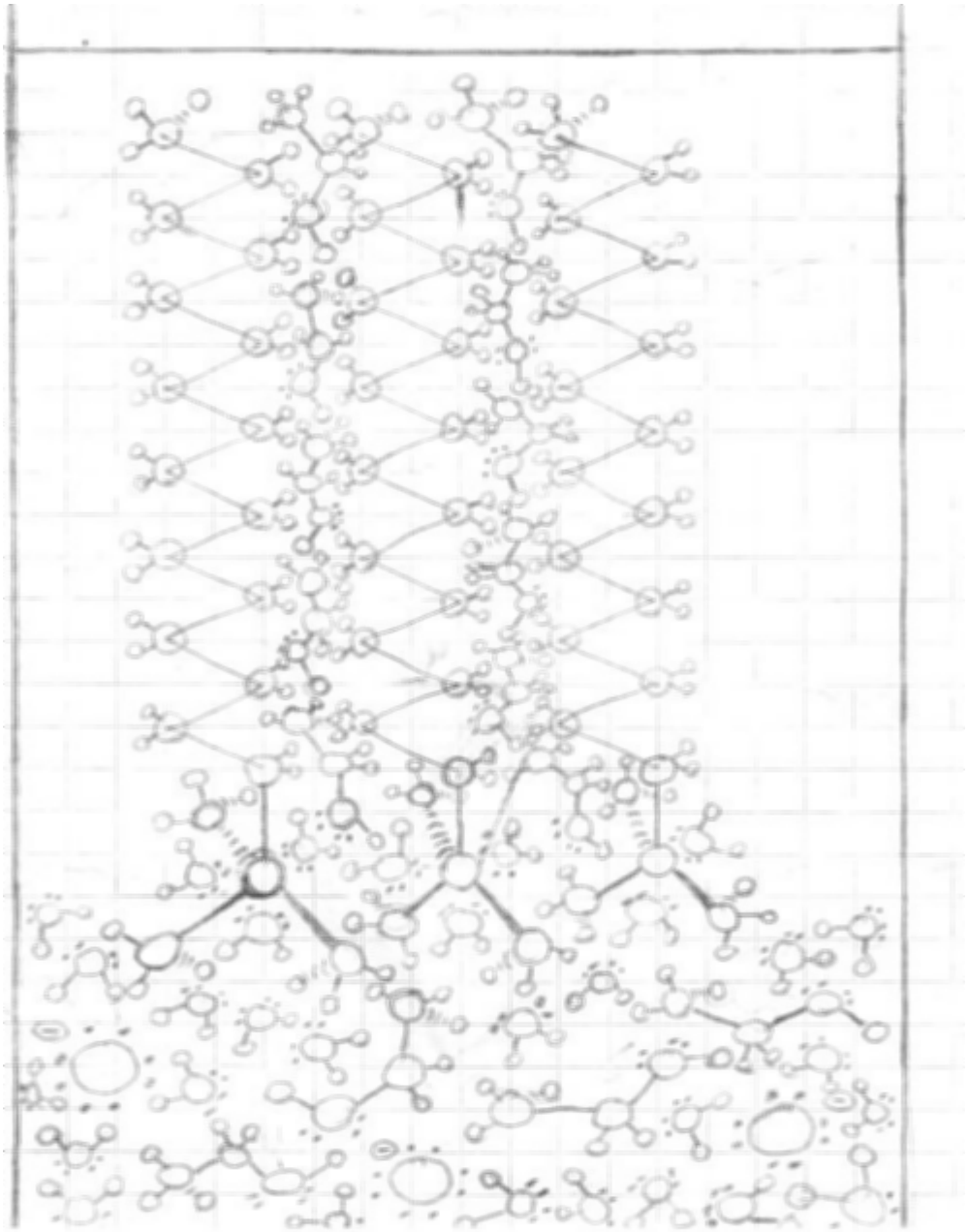

**Figure A:13 Formation of MCM-50 Lamellar Silica Structure at 150°C corresponding to g-value of 1.**

**Supplemental text for Appendix A-A:13**-The formation of unstable lamellar MCM-50 silica structure occurs when large thermal energy forces the ethanol molecule deep into the hydrophobic tail region. This causes the alkyl tail volume (V) to increase with the head-group, $a_0$, and carbon chain length ($l_c$) to approximate constant, thereby leading to a large g-value ($g = V/a_0l_c$) of one. This also could occur with CTAB surfactant in the modified Stober MCM-48 synthesis if the reaction was extended beyond the optimal time.

# Appendix B - Experimental/Literature Supplemental Data/Structures

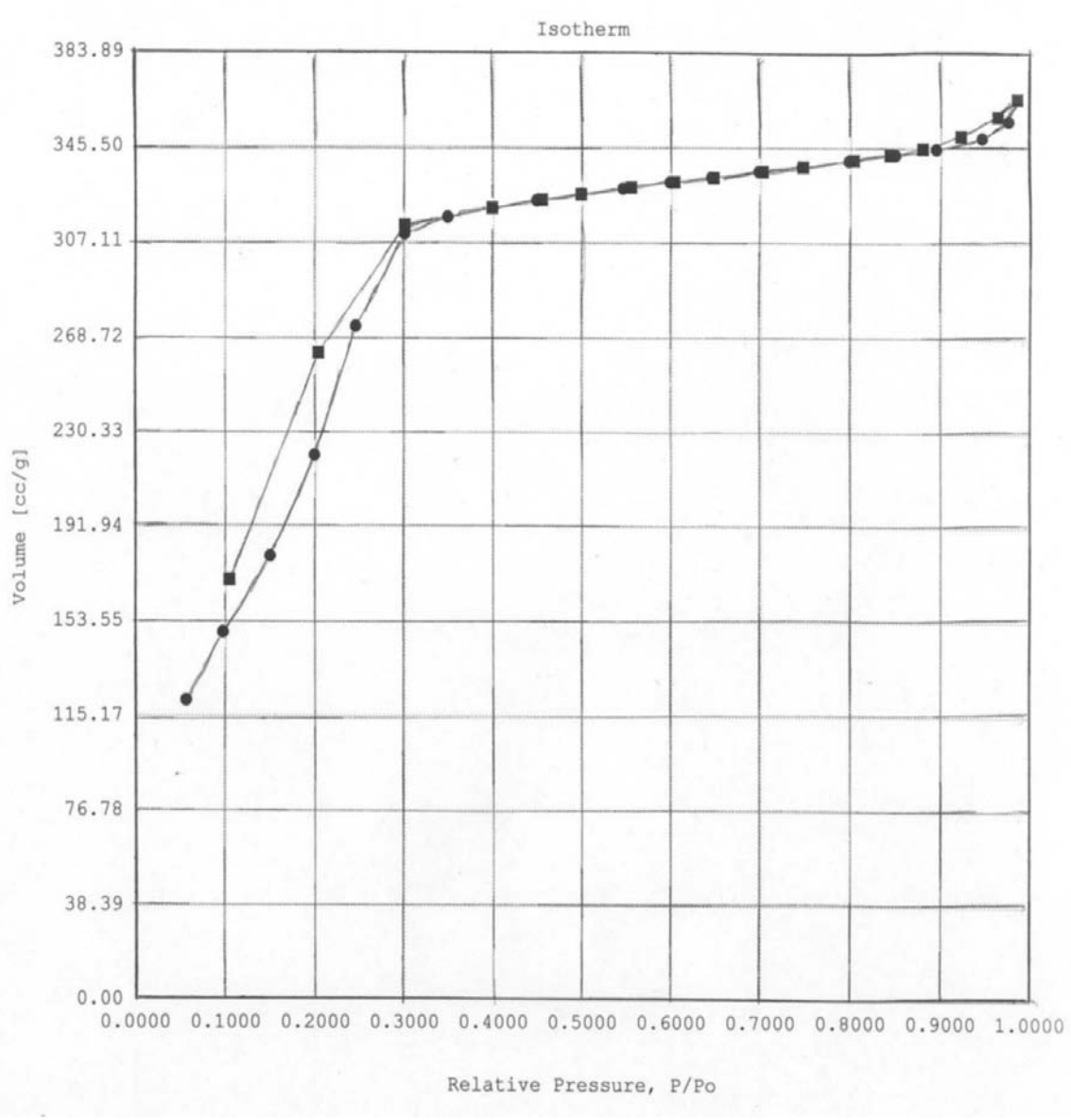


**Figure B:1 V(150)-MCM-48 Experimental $N_2$ Isotherm Adsorption-Desorption Plot.**

**Supplemental text for Appendix B-B:1**-The experimental $N_2$ isotherm plot has five sections. The key sections would be approximately 0.1000 to 0.3000 relative pressure increase led to capillary condensation found in mesoporous solids and 0.9000 to 1.0000 relative pressure where small hysteresis loop found. Both the hysteresis at the capillary step and at end would indicate ink-bottled pore structure. Refer to Chapter 5 Discussion Part II for thorough presentation of each of the five regions commonly seen in mesoporous solids.

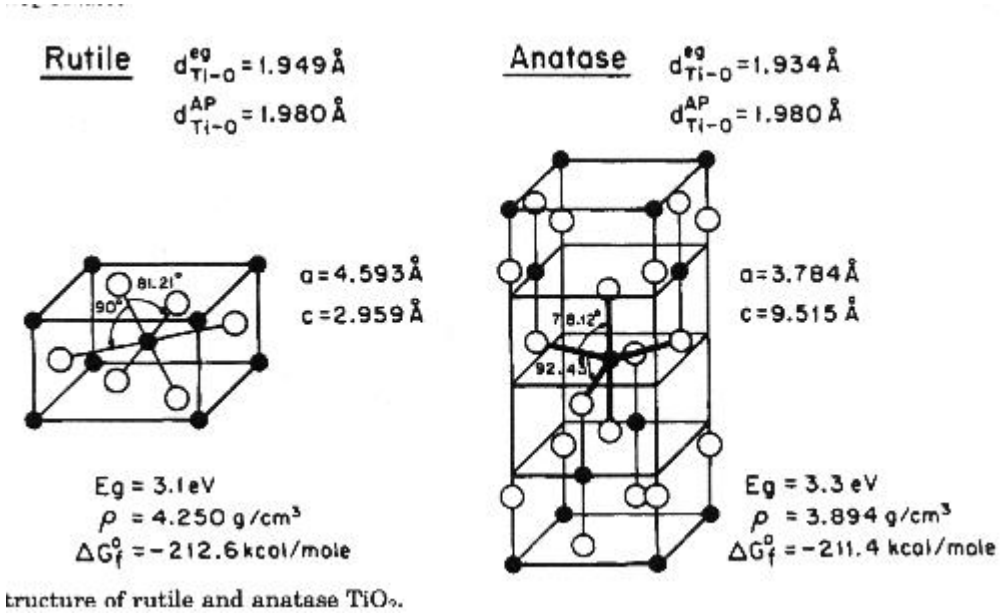


tructure of rutile and anatase $TiO_2$.

**Figure B:2 Structures of $TiO_2$ Rutile and Anatase.**

**Supplemental text for Appendix B-B:2**-As seen in the above image of the rutile and anatase structures of $TiO_2$, the placement of titanium and oxygen atoms determines the coordination number of each atom in the unit cell and reactivity + bandgap of this resulting semiconductor. Linsebigler, A. L. *et al.*, *Chemical Reviews* **1995**, *95*, 735-758 **DOI:** 10.1021/cr00035a13; Permission granted by American Chemical Society Copyright 1995 ©

Linsebigler et al.

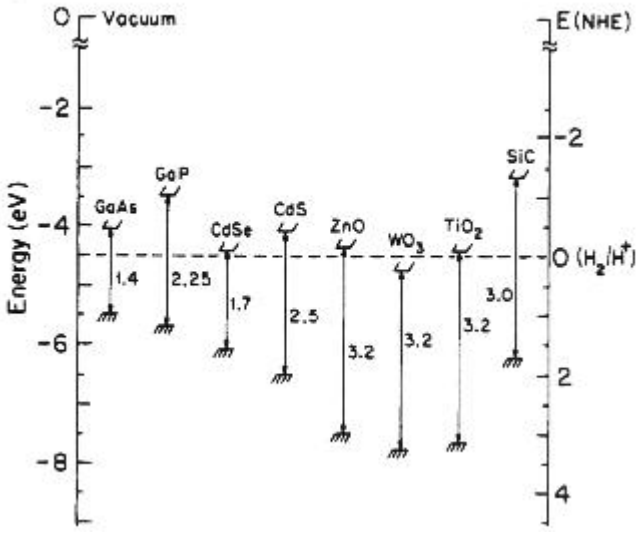


**Figure B:3 Bandgap of Various Semiconductor Materials.**

**Supplemental text for Appendix B-B:3**-The larger the bandgap of a particular semiconductor requires higher frequency light (shorter wavelength light-higher energy) to promote an electron from the HUMO to LUMO orbitals. The p-type semiconductors commonly have smaller bandgaps then the n-type semiconductors, such as $TiO_2$. However, the p-type tends to deteriorate over extended use under photocatalytic conditions; in contrast, larger bandgap semiconductor materials of n-type retain stability under various conditions. Finally, besides the size of the bandgap, the oxidation-reduction potential determines its ability to breakdown probe molecules and converts water to hydrogen and oxygen in water-splitting with light. Linsebigler, A. L. *et al.*, *Chemical Reviews* **1995**, *95*, 735-758 **DOI:** 10.1021/cr00035a13; Permission granted by American Chemical Society Copyright 1995 ©

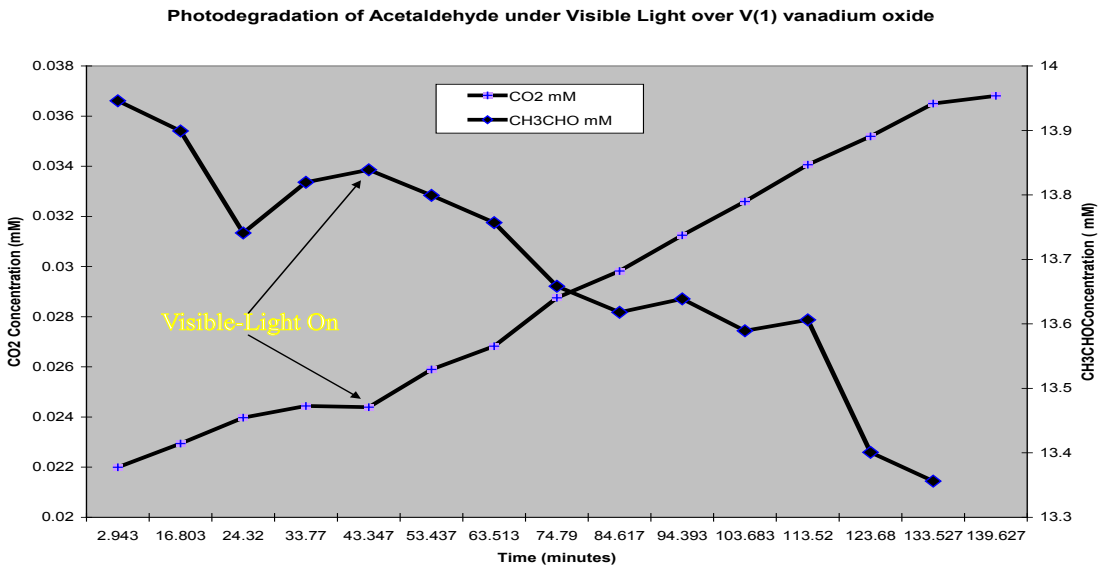


**Figure B:4 Visible-Light Photodegradation of Acetaldehyde over V(1) on Silica ($VO_x/SiO_2$).**

**Supplemental text for Appendix B-B:4**-As seen in the above photodegradation plot of acetaldehyde over V(1)-Si/V molar ratio of 1-had only 0.015 mM of $CO_2$ production and consumption of 0.57 mM of $CH_3CHO$. The structure of this material reflected amorphous silica with no peaks. Clearly, this proves that structure directly effects the photodegradation rate.

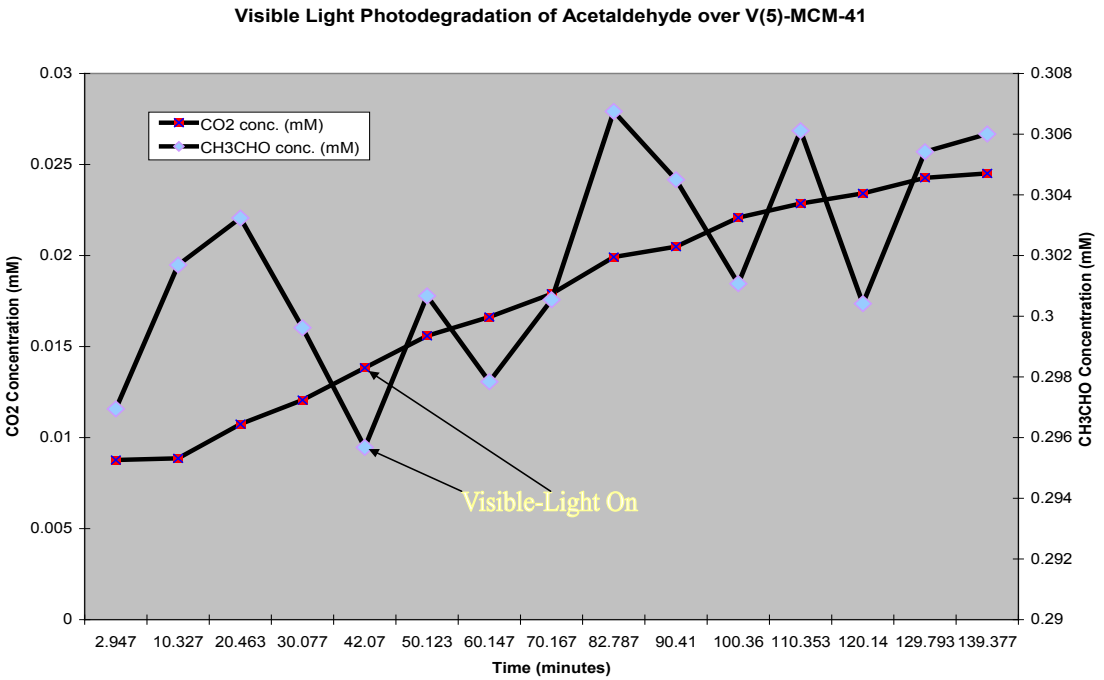


**Figure B:5 Visible-Light Photodegradation of Acetaldehyde over V(5)-MCM-41.**

**Supplemental text for Appendix B-B:5**-As seen the above photodegradation plot, the V(5)-MCM-41 produced 0.016 mM of $CO_2$ with no consumption of acetaldehyde. Clearly, the structure was the reason for the slightly higher $CO_2$ production less vanadium ion in contrast to V(1). The reason for no acetaldehyde consumption has not been determined.

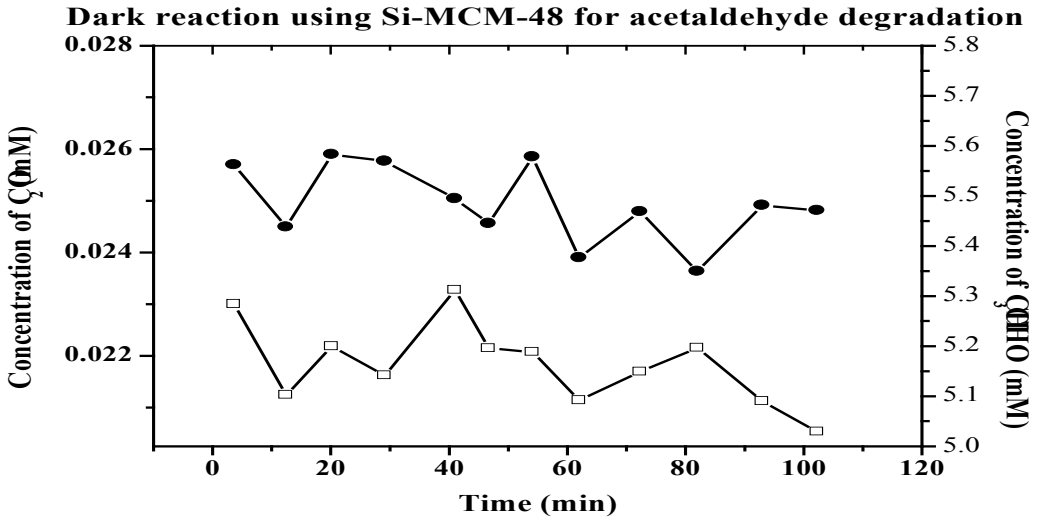


**Figure B:6 Experimental Dark Acetaldehyde Degradation over Si-MCM-48.**

**Supplemental text for Appendix B-B:6-** As seen in the above plot, the Si-MCM-48 material has essentially no photocatalytic activity toward acetaldehyde. The dark circles represent acetaldehyde concentration and open squares would be carbon dioxide concentration. A small amount of acetaldehyde was absorbed onto Si-MCM-48 with no carbon dioxide production.

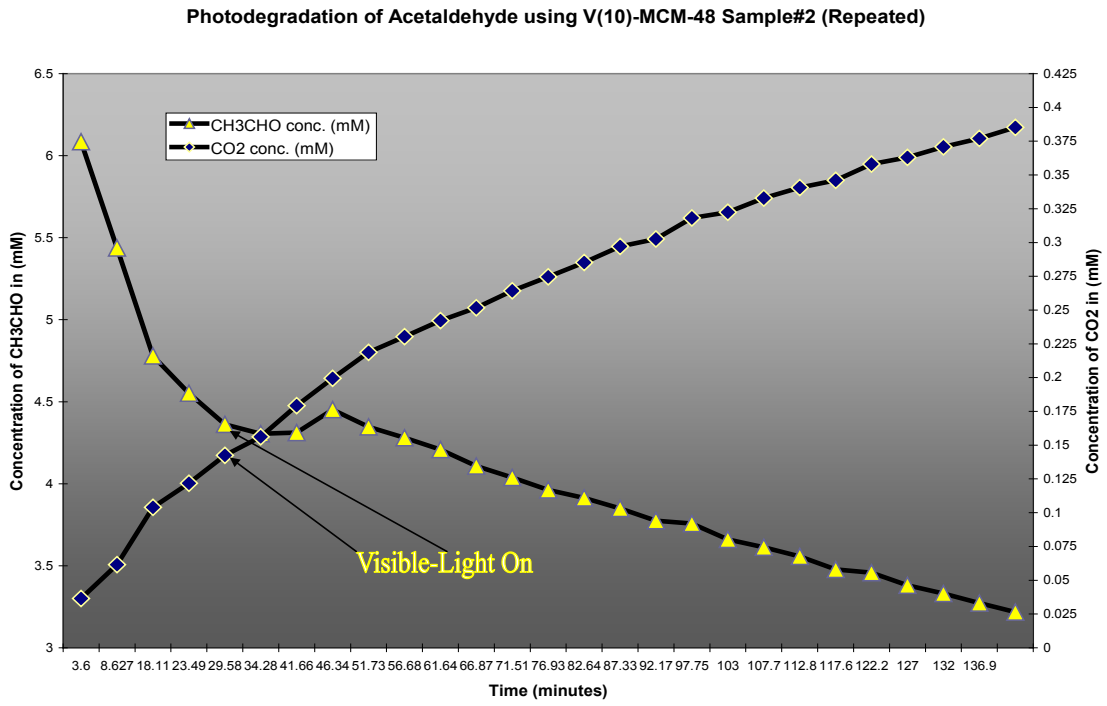


**Figure B:7 Acetaldehyde Visible-Light Photodegradation over V(10)-MCM-48.**

**Supplemental text for Appendix B-B:7-** As seen in the above photodegradation plot, V(10)-MCM-48 had both dark and visible light acetaldehyde degradation reaction to $CO_2$. The consumption of acetaldehyde was 2.9 mM with .35 mM $CO_2$ production.

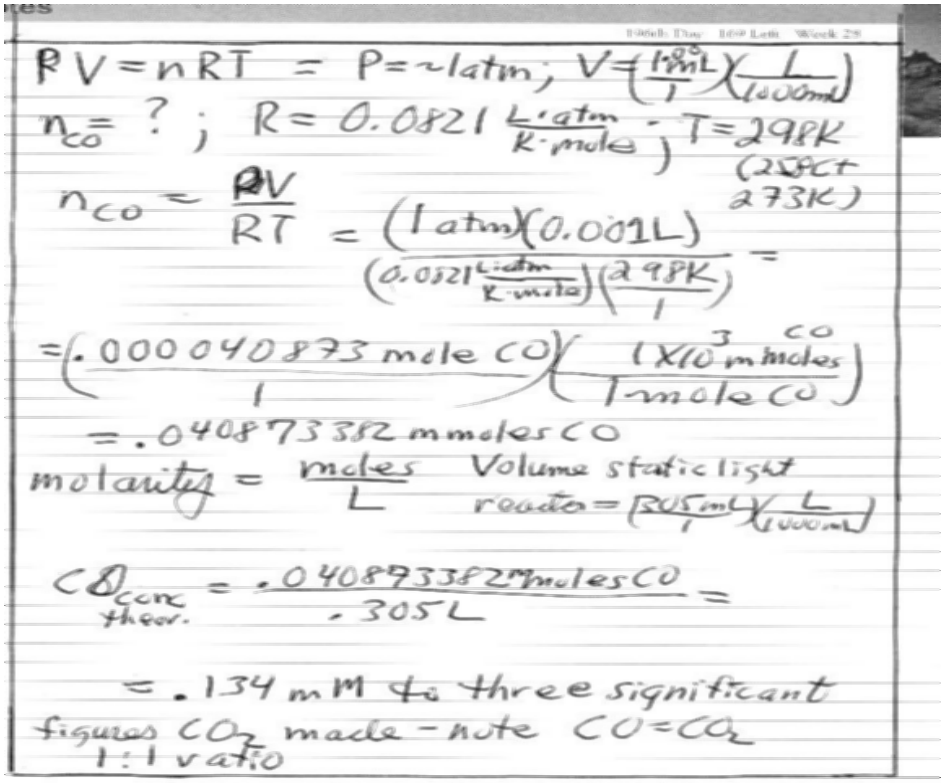


**Figure B:8 Theoretical $CO_2$ Concentration from Ideal Gas Law with 1.00 mL of CO.**

**Supplemental text for Appendix B-B:8**-As seen in the above theoretical calculation of carbon dioxide, the only variable changed in the ideal law equation was the volume of CO with other variables constant throughout CO oxidation experiments. Note: 1:1 molar ratio of CO produces $CO_2$: $CO + \frac{1}{2}O_2 \rightarrow CO_2$.

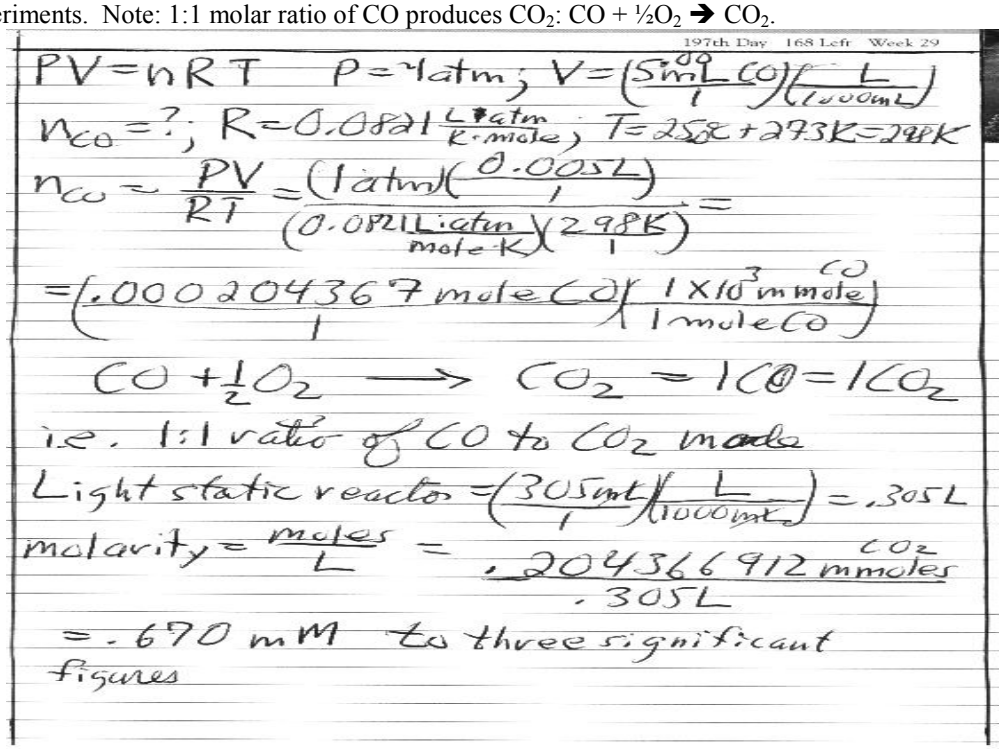


**Figure B:9 Theoretical $CO_2$ Concentration Calculation with 5.00 mL of CO Probe Molecules.**

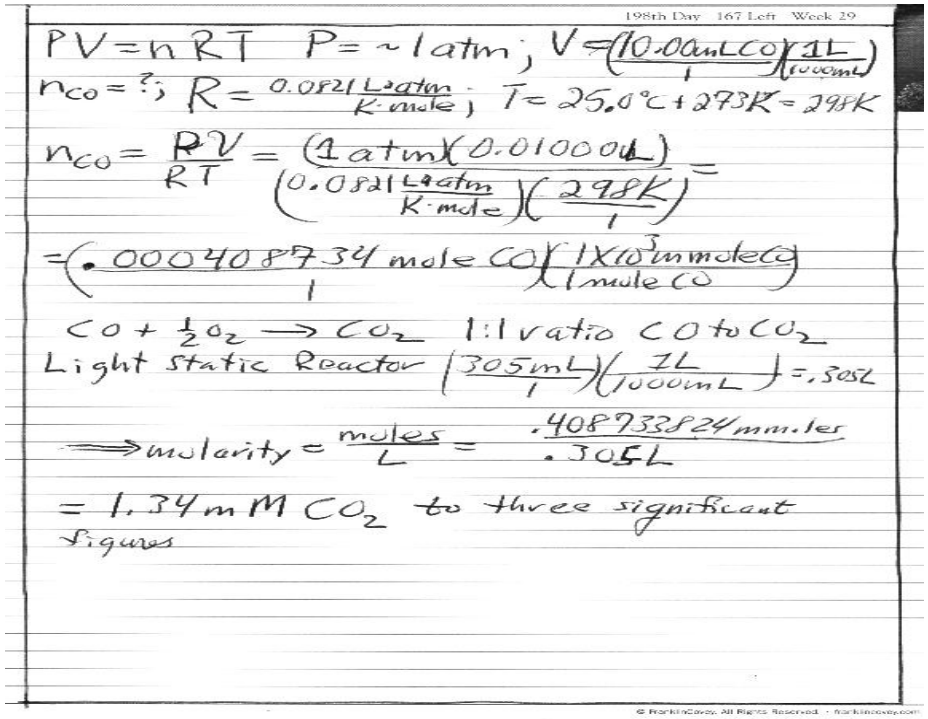


**Figure B:10 Theoretical $CO_2$ Concentration Calculation with 10.00 mL of CO Probe Molecules.**

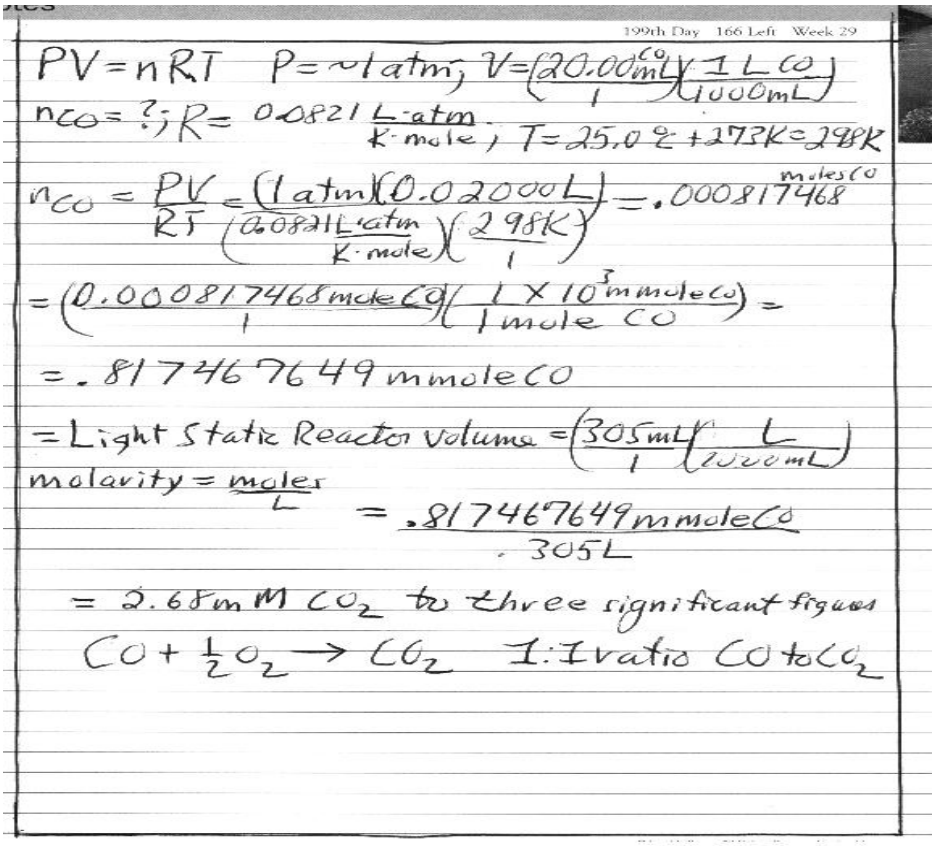


**Figure B:11 Theoretical $CO_2$ Concentration Calculation with 20.00 mL of CO Probe Molecules.**

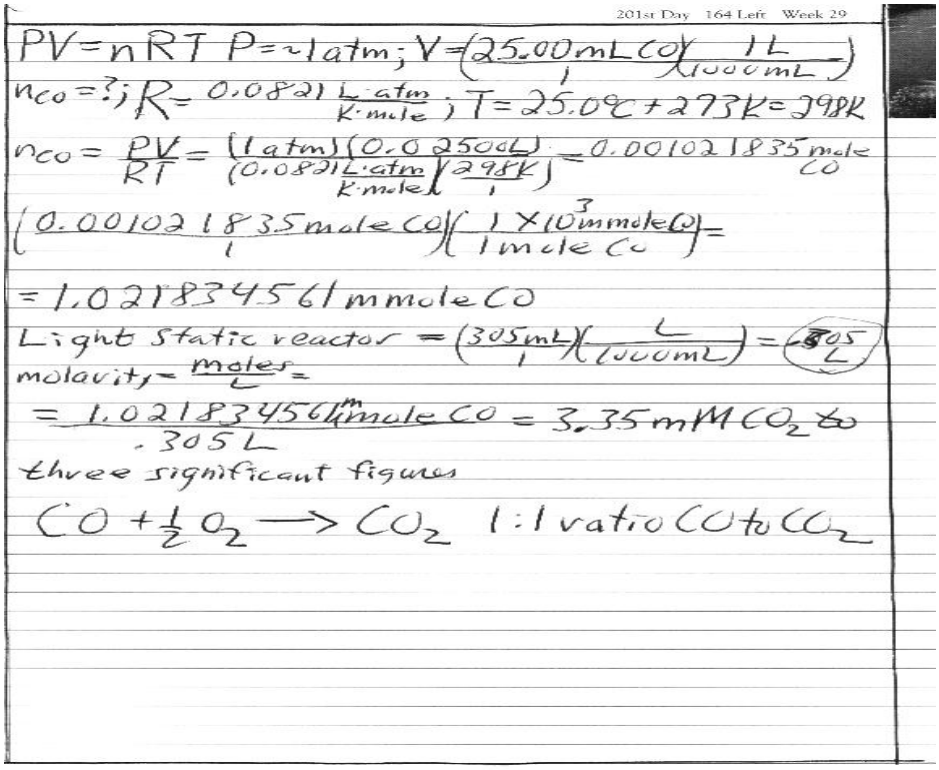


**Figure B:12 Theoretical $CO_2$ Concentration Calculation with 25.00 mL of CO Probe Molecules.**

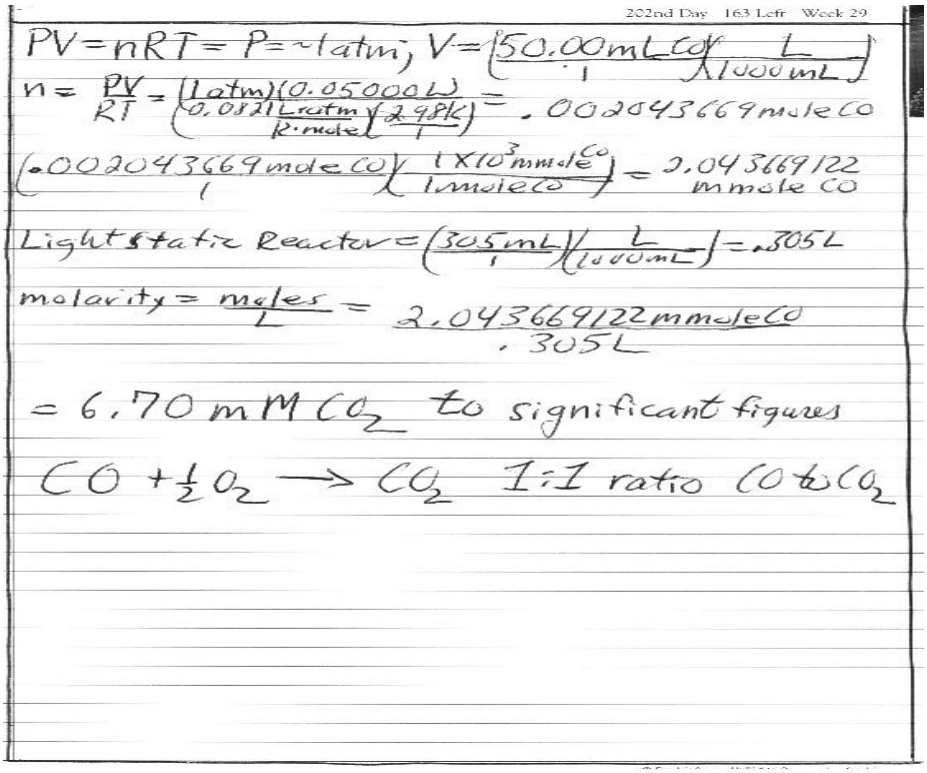


**Figure B:13 Theoretical $CO_2$ Concentration Calculation with 50.00 mL of Probe Molecules.**

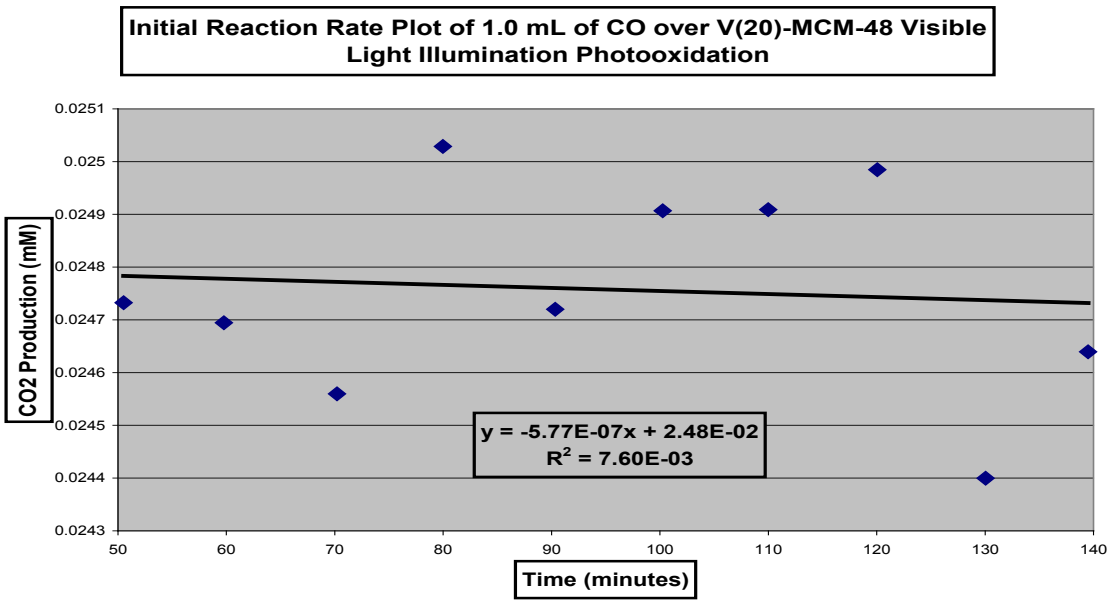


**Figure B:14 Initial Rate Visible Light Photodegradation Plot CO over V(20)-MCM-48.**

**Supplemental text for Appendix B-B:14**-As seen in the above plot, there was essentially no photooxidation reaction over V(20)-MCM-48 with 1.0 mL of carbon monoxide. The type of vanadium centers active in CO photooxidation would appear not to be active under visible light illumination.

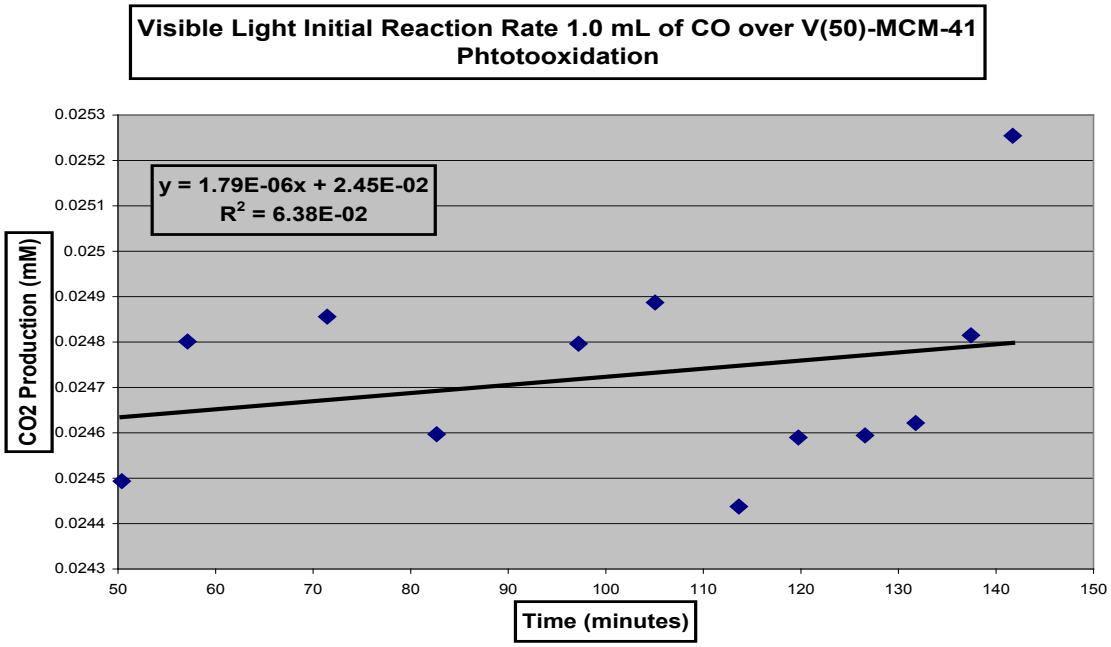


**Figure B:15 Visible-Light CO Photooxidation over V(50)-MCM-41 Initial Reaction Plot.**

**Supplemental text for Appendix B-B:15**-In contrast to B:14 CO photooxidation plot, the V(50)-MCM-41 appears to have some vanadium centers active in the visible light with 1.0 mL of CO due to the slight production of $CO_2$.

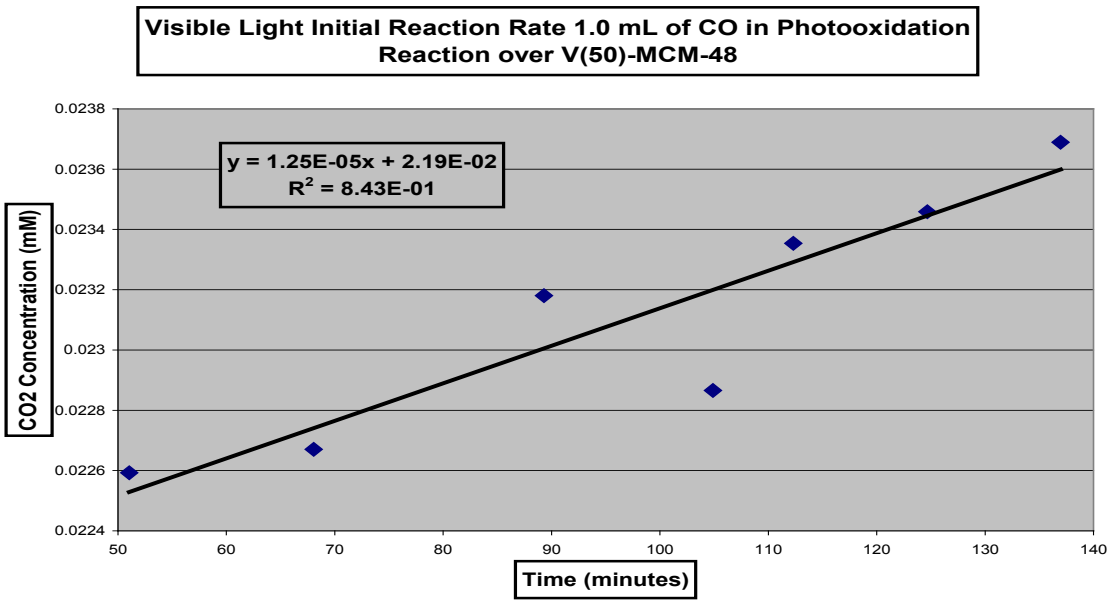


**Figure B:16 Visible-Light CO Photooxidation Initial Reaction Plot over V(50)-MCM-48.**

**Supplemental text for Appendix B-B:16**-The change from unidirectional MCM-41 to three-dimensional MCM-48 with same vanadium loading led to increased $CO_2$ production and slope value with 1.0 mL of CO.

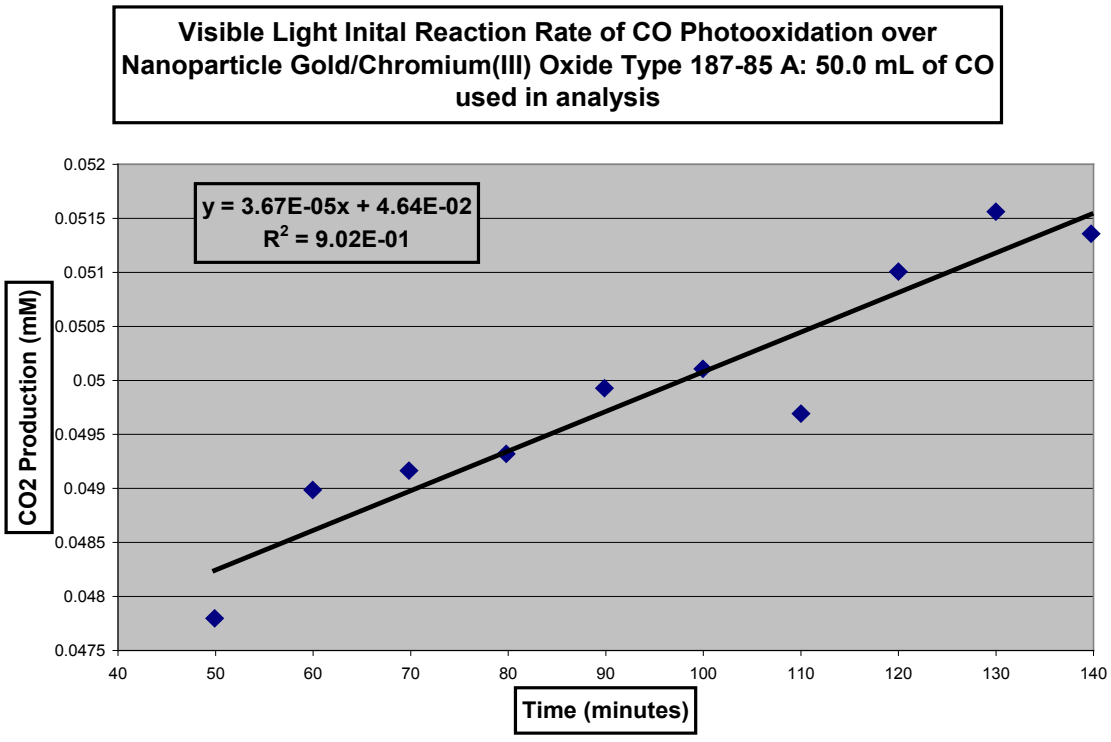


**Figure B:17 Visible-Light Initial Reaction Rate Plot of CO Photooxidation over $Au/Cr_2O_3$ with 50.0 mL CO.**

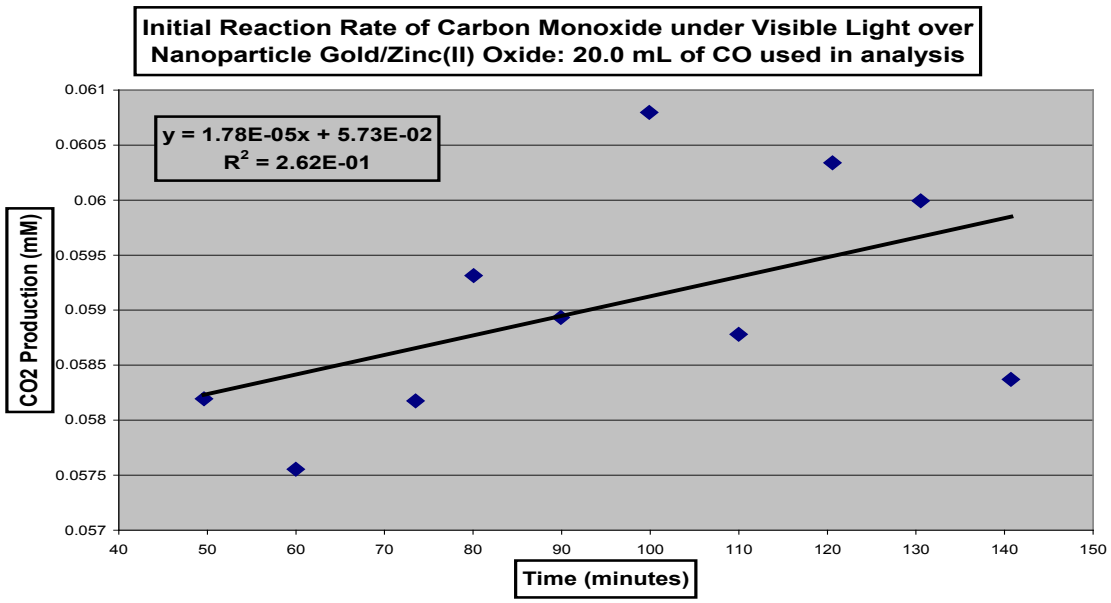


**Figure B:18 Visible-Light CO Photooxidation over ZnO with 20.0 mL of CO.**

**Supplmental text for Appendix B-B:18**-As seen in the above plot of CO visible-light photooxidation over ZnO nanoparticle, the slope value less then B.16 above, which would imply that the photooxidation ZnO with visible light would be minimum similar to V(20)-MCM-48 under visible-light-little CO photooxidation.

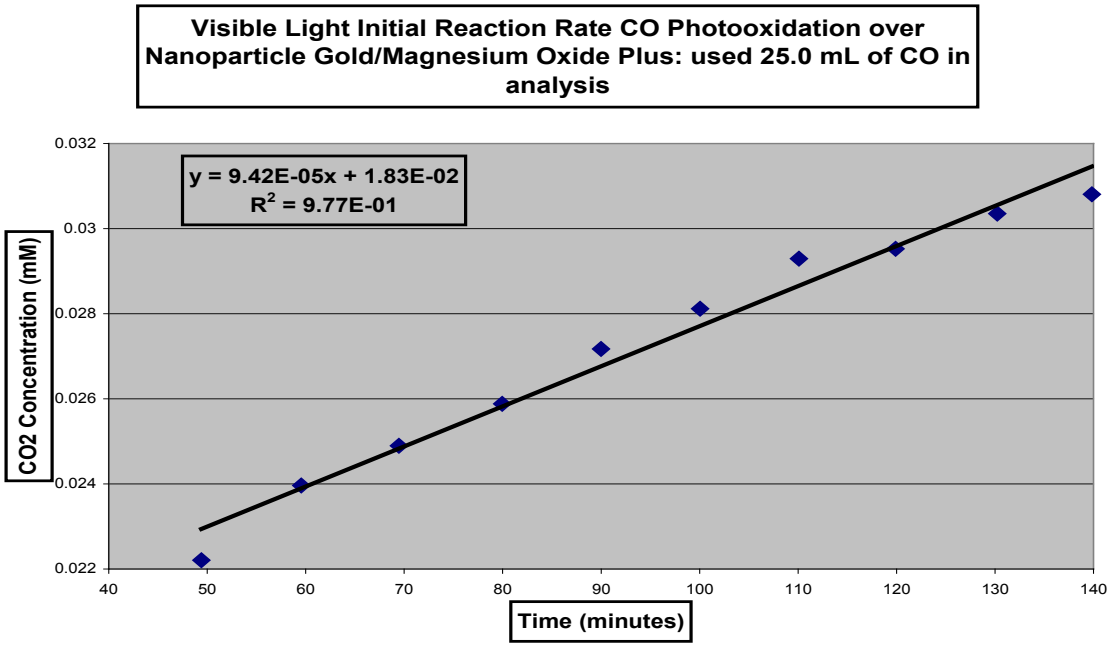


**Figure B:19 Visible-Light Initial Reaction Rate of 25.0 mL of CO over Au/MgO Plus.**

**Supplemental text for Appendix B-B:19**-As seen in the above initial rate plot, the slope increases in a linear fashion with CO photooxidation over Au/MgO Plus, in contrast to ZnO nanoparticle.

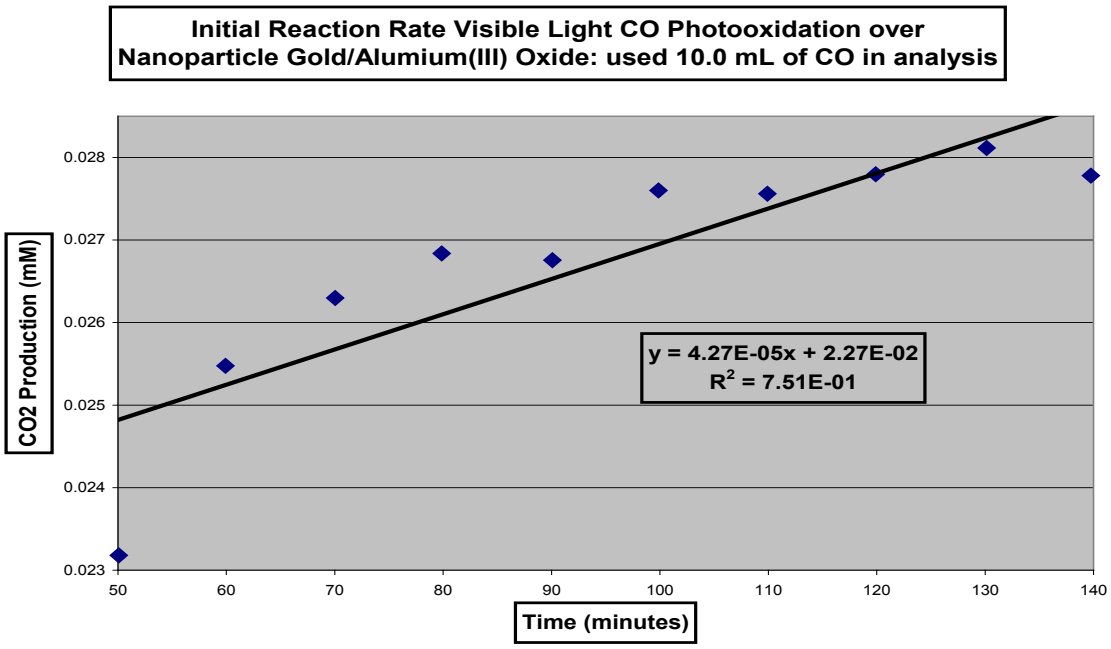


**Figure B:20 Visible-Light CO Photooxidation Initial Reaction Rate over $Au/Al_2O_3$ with 10.0 mL of CO.**

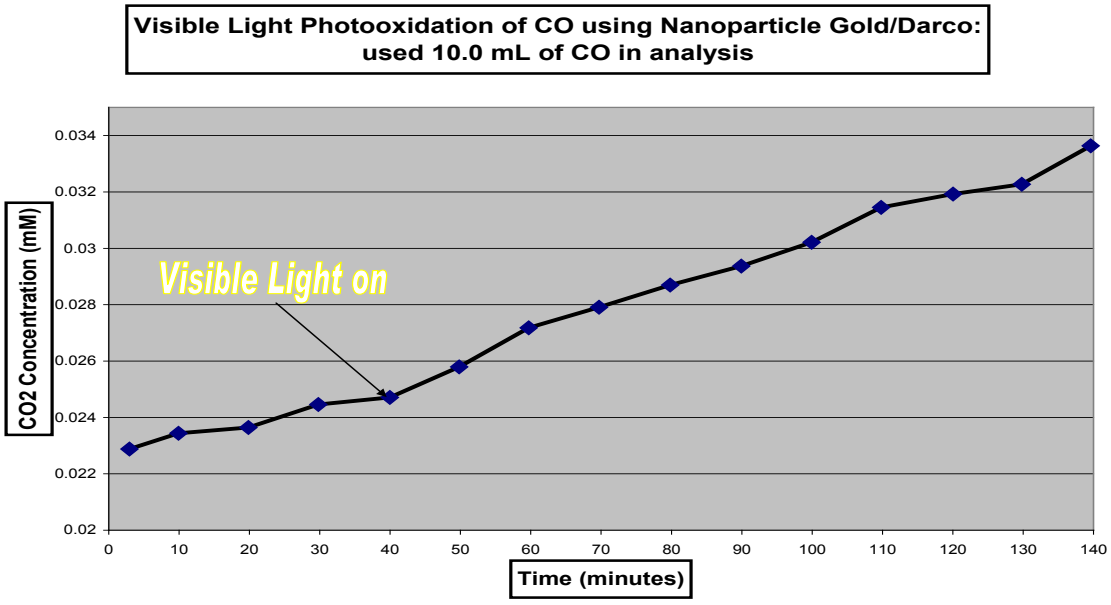


**Figure B:21 Visible-Light CO Photooxidation over Au/Darco with 10.0 mL of CO.**

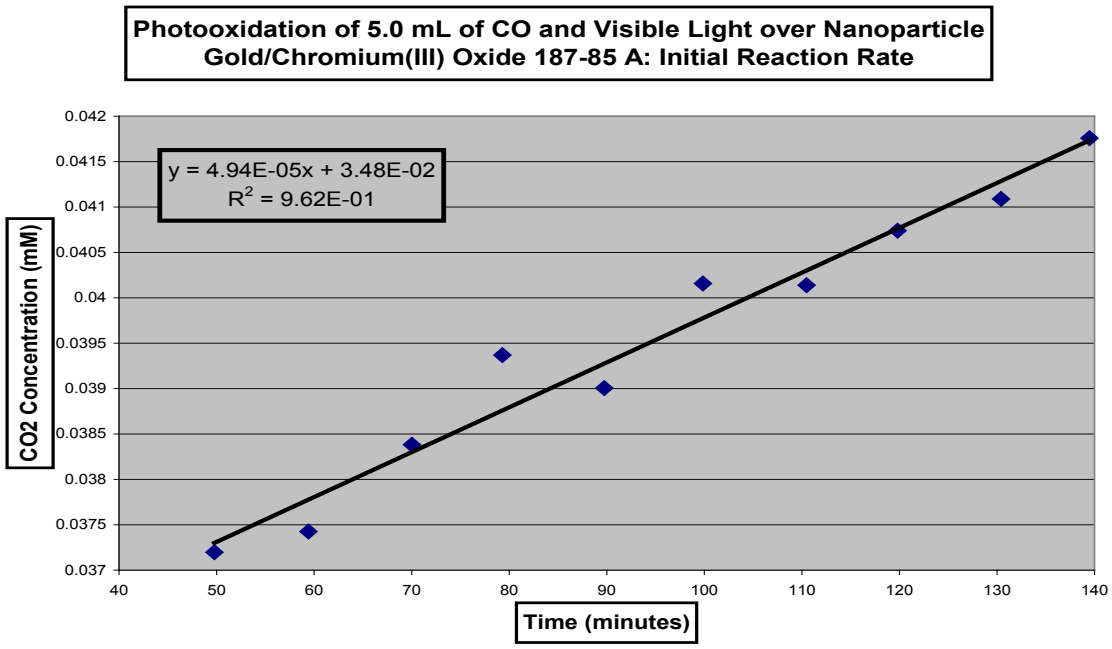


**Figure B:22 Visible-Light CO Photooxidation over $Au/Cr_2O_3$ with 5.0 mL of CO.**

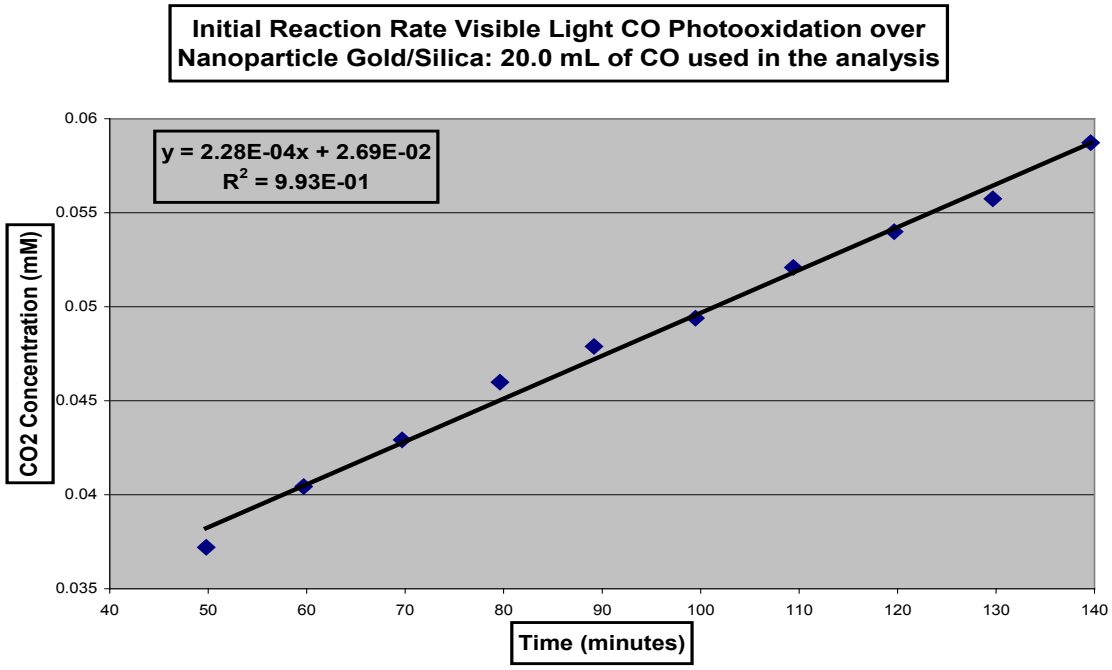


**Figure B:23 Visible-Light CO Photooxidation over $Au/SiO_2$ with 20.0 mL of CO.**

# Appendix C - Proposed V-MCM-48 Degradation Mechanisms

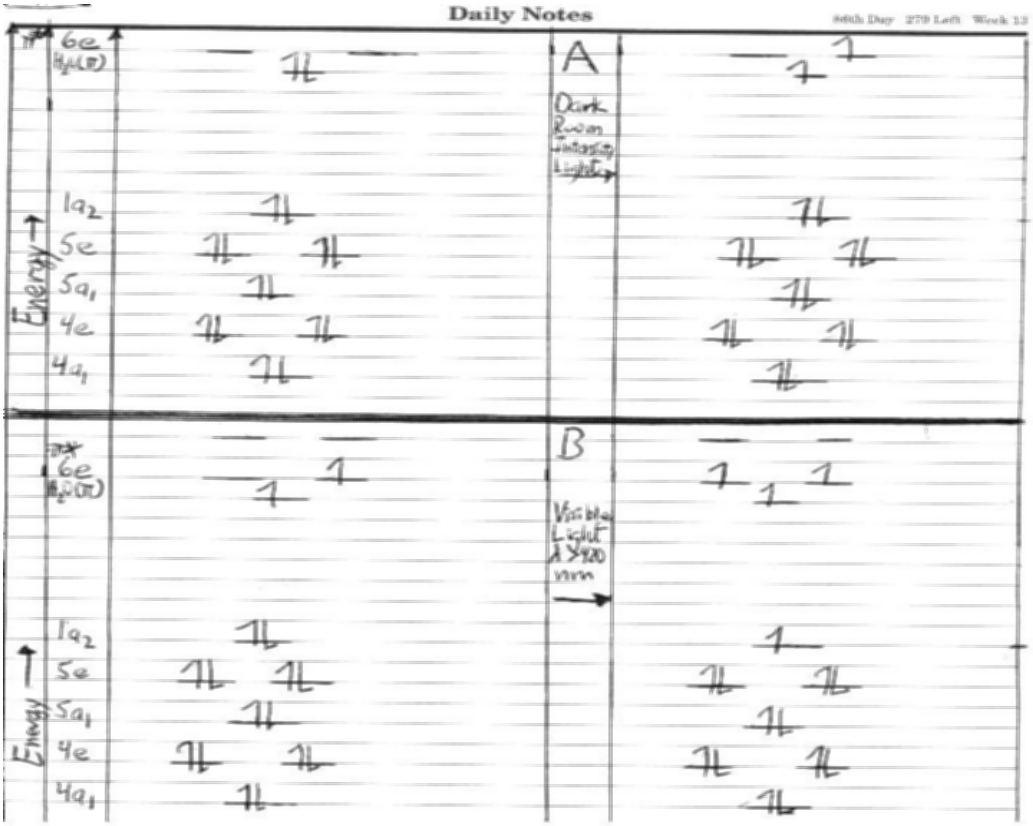


**Figure C:1 Molecular Orbital Digrams with Aqua Donation under Dark and Visible-Light Illumination.**

**Supplemental text for Appendix C-C:1**-In upper molecular orbital diagram labeled A the oxygen atom from aqua ligand donates electron density from the π orbital into 6e empty $V^{5+}$ metal 3d orbital. With addition of visible light in part B, ($\lambda > 420$ nm) one of the non-bonding oxygen electron from $1a_2$ orbital enters into the 6e metal orbital. These above molecular orbital diagrams would be consistent with previous literature on $V^{5+}$ on silica by Tran *et al.* [1,2]


1. Tran, K. *et al.*, *Journal of the American Chemical Society* **1995**, *117*, 2618-2626
2. Tran, K. *et al.*, *Inorganica Chimica Acta* **1996**, *243*, 185-191

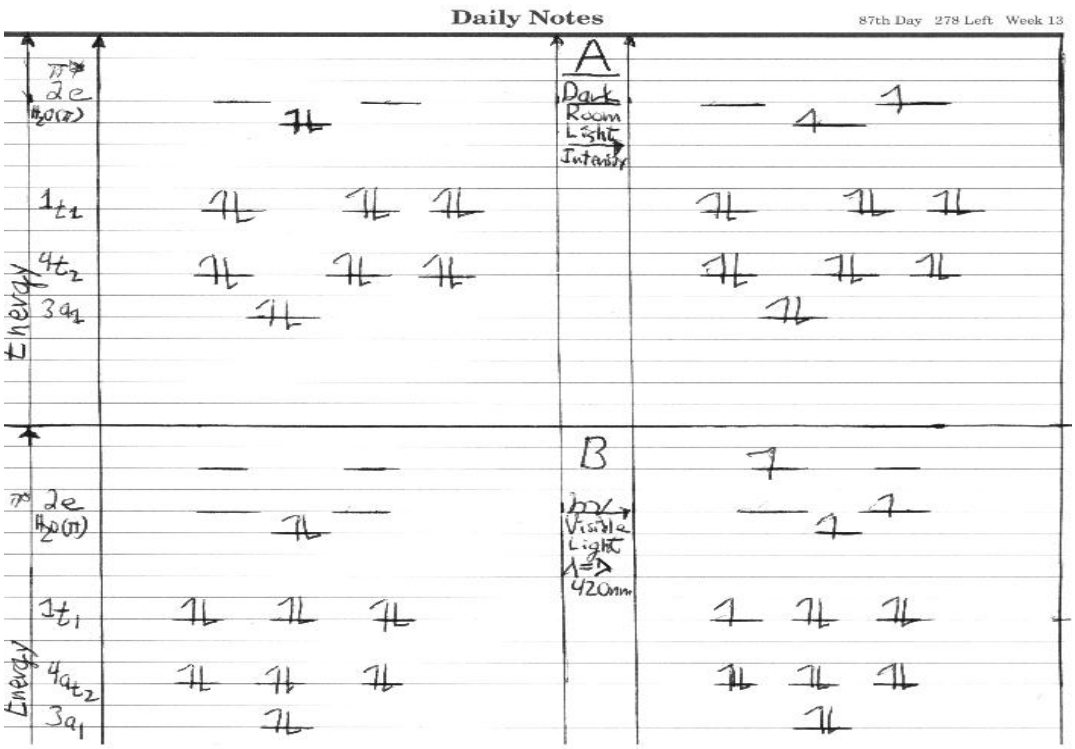


**Figure C:2 Molecular Orbital Diagram with Aqua Donation into the Tetrahedral Framework $V^{5+}$ Centers.**

**Supplemental text for Appendix C-C:2**-In molecular orbital diagram in part A electron density from oxygen aqua ligand donates into the empty metal 2e orbital in the dark. In part B, visible-light initiates promotion of an electron from the $1_{t1}$ framework ligand orbital into a higher energy orbital above metal 2e one. The above molecular orbital diagrams would be consistent with Tran *et al.* work with $V^{5+}$ in silica xerogel matrix. [1,2]


1. Tran, K. *et al.*, *Journal of the American Chemical Society* **1995**, *117*, 2618-2626
2. Tran, K. *et al.*, *Inorganica Chimica Acta* **1996**, *243*, 185-191

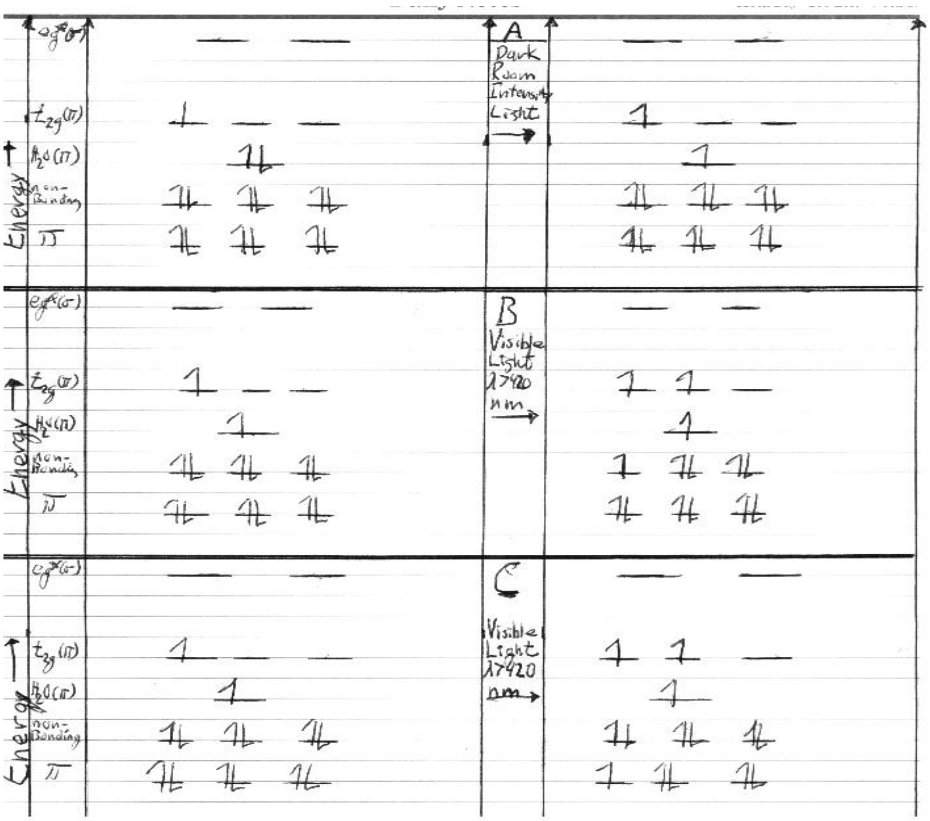


**Figure C:3 Octahedral $V^{5+}$ Coordination Molecular Orbital Diagram with Aqua Electron Donation.**

**Supplemental text for Appendix C-C:3**-In contrast to C:1 and C:2 with aqua donation into tetrahedral/distorted tetrahedral coordination geometry, the coordination geometry with two aqua ligands would be distorted octahedral, which could be approximated with octahedral molecular orbital diagram. In part A, electron density from aqua oxygen donates into the the empty $t_{2g}$ metal orbital under dark condition. In part B, an electron from non-bonding framework oxygen orbital donates into the $t_{2g}$ orbital with one aqua electron under visible-light ($\lambda > 420$ nm). In part C, an electron could promote from the framework oxygen $\pi$ energy level to the partially occupied $t_{2g}$ metal orbital. The above molecular orbital drawing would be consistent with literature. [1]

1. Miessler, G. L.; Tarr, D. A. "*Inorganic Chemistry*," **2004**, *Third Edition*, Chapter 10, pages 337-378

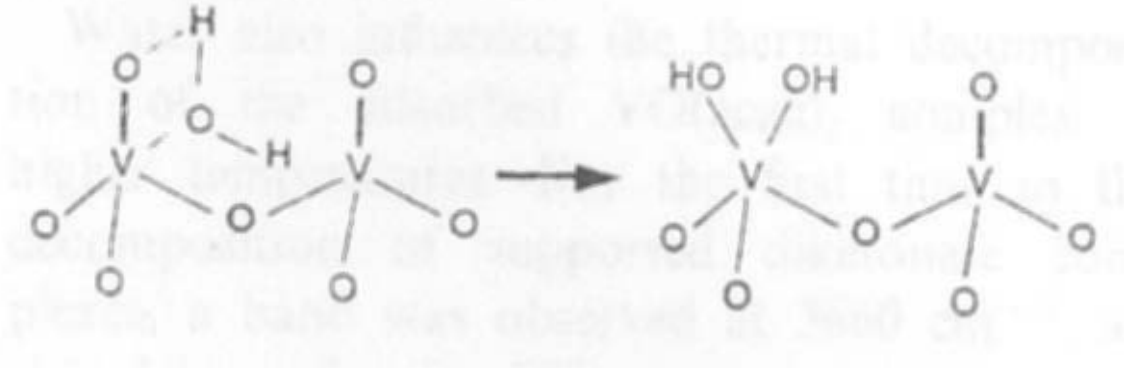


**Figure C:4 Schematic Illustration of Two Hydroxyls Coordinated to $V^{5+}$ Center on Silica.**

**Supplemental text for Appendix C-C:4**-The above image shows the effect of hydration on the vanadium centers on silica at high vanadium loading. The formation of geminal hydroxyls was elucidated with UV-Raman spectroscopy by Vansant and co-workers. [1]

1. Van Der Voort, P. *et al.*, *Spectrochimica Acta Part A: Molecular and Biomolecular Spectroscopy* **1997**, *53*, 2181-2187; **DOI:** 10.1016/S1386-1425(97)00145-5 Permission granted by Elesiver Scientific Publishing, Inc. Copyright 1997 ©

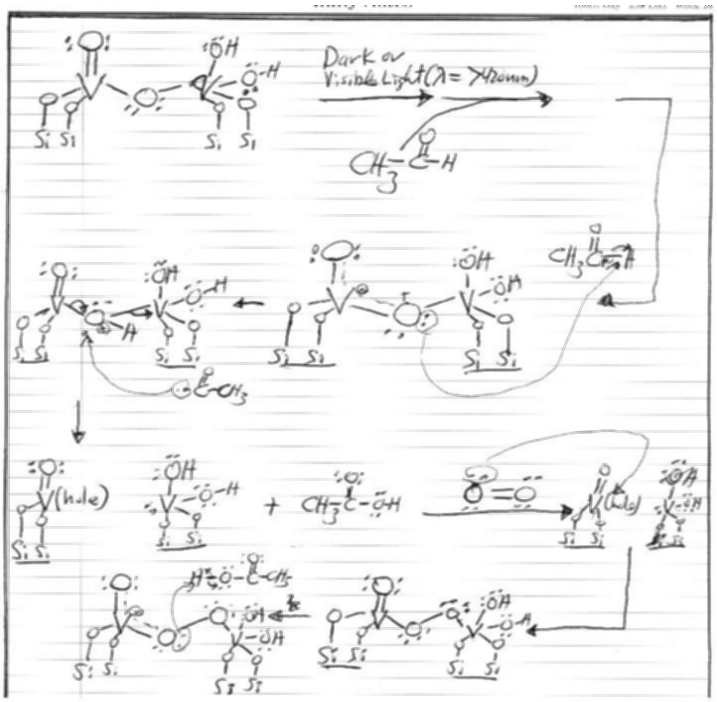


**Figure C:5 Part I-Dark-Visible-Light Acetaldehyde Degradation Mechanism over V(x)-MCM-48.**

**Supplemental text for Appendix C-C:5**-This above proposed mechanism would be consistent previous literature on $TiO_2$ and vanadium oxide on silica. [1-6] Previously, three vanadium species were proposed from DR-UV-vis spectroscopy analysis present in V(x)-MCM-48. One of those structures would be wall bonded pseudotetrahedral $VO_4^{3-}$ upon hydration at higher $V^{5+}$ loading leads to the dimeric species in the upper left-hand corner of mechanism. Support would come from Vansant and co-workers UV-Raman study with vanadium oxide on silica, where they found the aqua ligand caused formation of structure in C:4 with geminal hydroxyls not isolated hydroxyls. [4] Consistent with Tran *et al.* research on $V^{5+}$ on silica xerogel matrix, the introduction of light causes an non-bonding electron from the bridging oxygen to pass into the empty 3d orbital. [2,3] Tran *et al.* found that the basal oxygen non-bonding electron in $VO_4^{3-}$ pseudotetrahedral structure proceeds in under UV-light. Irusta *et al.* note that the bridging oxygen between two $VO_4^{3-}$ species would be involved in formation of $CO_2$ due to relatively long metal-oxygen-metal bonds that could break easily. [5] In research on diesel soot particles oxidized over $K^+$ modified $VO_x/SiO_2$, Wachs and co-workers note bridging oxygen between $V^{5+}$ centers would be involved in complete oxidation product formation. [6] The formation of geminal hydroxyls on one $V^{5+}$ species could donate electron density to the $V^{5+}$ empty 3d orbital, which could be donated to the bridging oxygen, thereby increasing the basicity of the oxygen atom. This might accout for the novel behavior seen for V(x)-MCM-48 in dark degradation reaction of acetaldehyde. Finally, C:6 and C:7 show addition reaction steps involved with radicals, which would be consistent with acetaldehyde photodegradation over $TiO_2$. [1]


1. Fujishima, A. *et al.*, *Journal of Photochemistry and Photobiology C: Photochemistry Reviews* **2000**, *1*, 1-21
2. Tran, K. *et al.*, *Journal of the American Chemical Society* **1995**, *117*, 2618-2626
3. Tran, K. *et al.*, *Inorganica Chimica Acta* **1996**, *243*, 185-191
4. Van Der Voort, P. *et al*., *Spectrochimica Acta Part A: Molecular and Biomolecular Spectroscopy* **1997**, *53*, 2181-2187
5. Irusta, S. *et al.*, *Catalysis Letters* **1996**, *40*, 9-16
6. Zhao, Z. *et al.*, *Topics in Catalysis* **2006**, *38*, 309-325

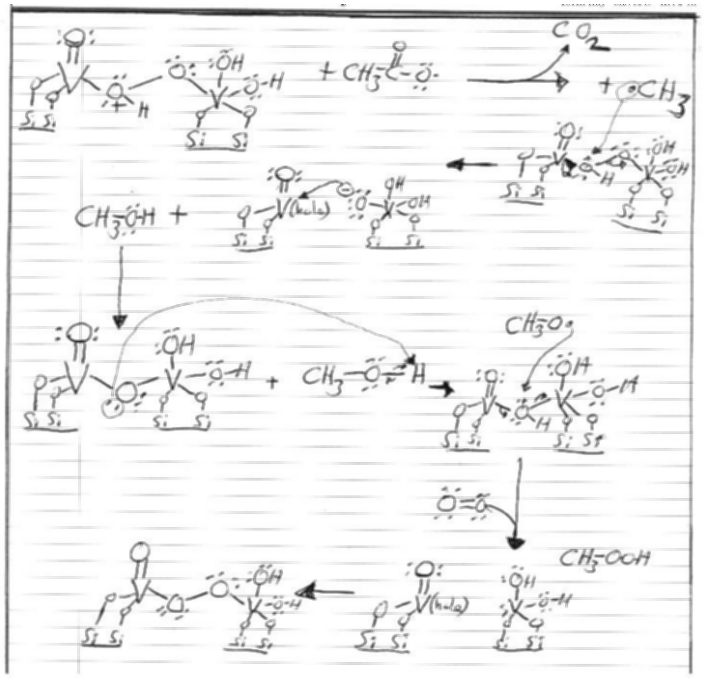

**Figure C:6 Part-II Dark-Visible-Light Acetaldehyde Degradation Mechanism over V(x)-MCM-48.**

**Supplemental text for Appendix C-C:6**-The key components would be the acetate radical ($CH_3COO\cdot$) converts through molecular rearrangement to form $CO_2$ and methyl radical ($\cdot CH_3$), according to mechanism proposed by Fujishima *et al.* in $TiO_2$. [1] Similar to previous reaction steps, the methyl radical bonds to the bridging oxygen radical that has a hydrogen attached to form methanol. As noted with other steps, the molecular oxygen bonds between the $V^{5+}$ centers with the enhanced basicity from the geminal hydroxyls abstracts a hydrogen atom from the methanol molecule, which continues to form a methyl peroxide species.

1. Fujishima, A. *et al.*, *Journal of Photochemistry and Photobiology C: Photochemistry Reviews* **2000**, *1*, 1-21

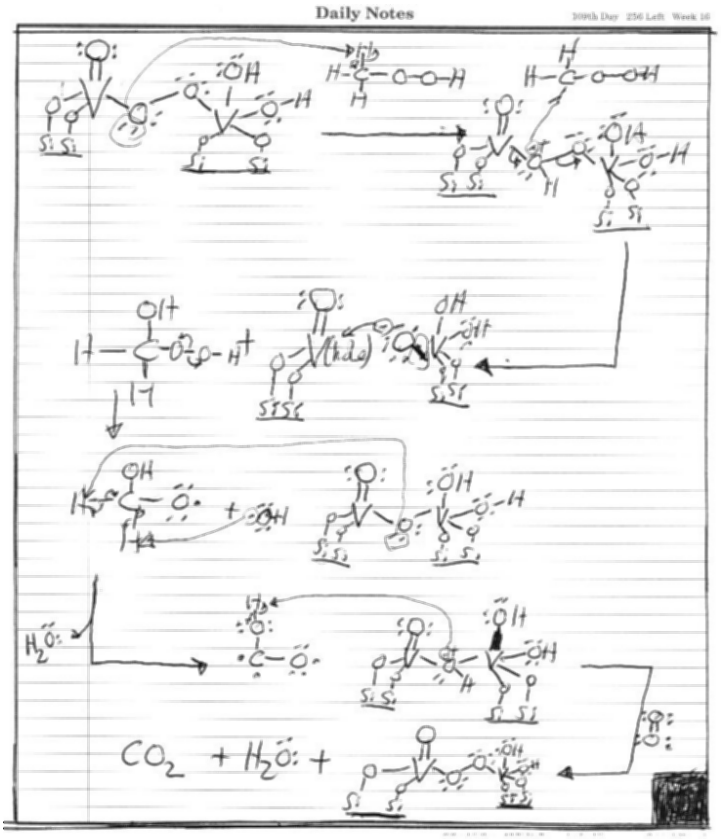


**Figure C:7 Part III Dark-Visible-Light Acetaldehyde Degradation Mechanism over V(x)-MCM-48.**

**Supplemental text for Appendix C-C:7**-In these final degradation reaction steps, the methyl peroxide would be attacked by the bridging oxygens between the $V^{5+}$ centers coupled with molecular reorganization would lead to final oxidation products: $CO_2 + H_2O$. In conclusion, this proposed degradation mechanism could be applied to other organic molecules with few modifications: for this mechanism to be valid, the bridging oxygen needs to receive additional electron density from the geminal hydroxyls, thereby would increase the basicity (ability to abstract an hydrogen atom) of the oxygen atom.

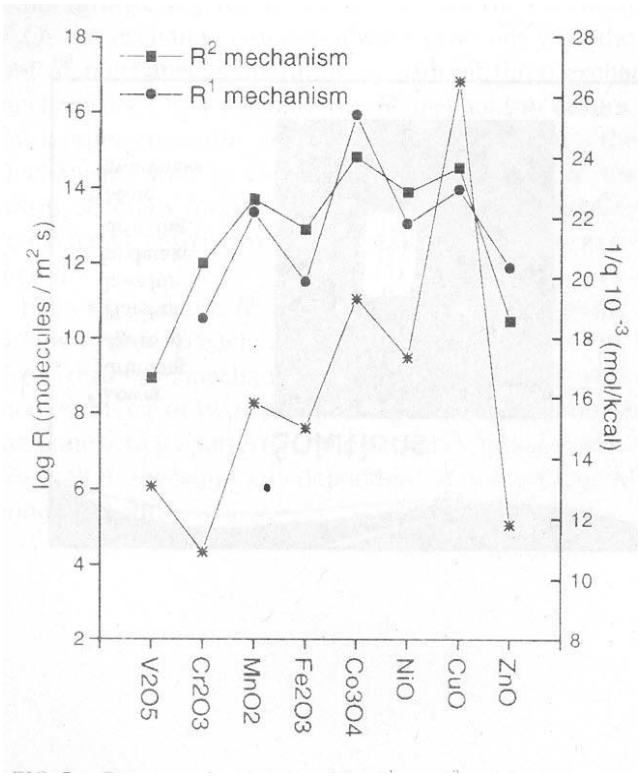


**Figure C:8 Oxygen Exchange as a function Bond Strength for Various Metal Oxides.**

**Supplemental text for Appendix C-C:8**-This plot shows the lattice oxygen exchange rate of various metal oxides as function of metal-oxygen (M-O) bond strength. [1] Using $^{18}O_2$ isotopic reaction conditions, Doornkamp *et al.* found two lattice oxygen exchange mechanisms predominate: $R^1$, and $R^2$. $R^1$ lattice oxygen exchange mechanism involves on lattice $^{16}O$ exchanging with one $^{18}O$ from $^{18}O_2$. $R^2$ lattice exchange oxygen mechanism involves two $^{16}O$ atoms exchanging with $^{18}O_2$. The rate of these two mechanisms was determined to be related to the M-O value: q = M-O value. Refering to the right y-axis above with 1/q, the smaller q-value led to larger lattice oxygen reaction for both $R^1$ and $R^2$ mechanisms. Further Doornkamp and Ponec indicate that the increased lattice oxygen exchange reaction favors deep oxidation: $CO_2$. [2] $V_2O_5$ has one of the lowest M-O values and has a large oxygen exchange mechanism with only $R^2$ occuring. The reason would be that all lattice oxygen atoms in $V_2O_5$ would be able to exhange. Doornkamp, C. *et al*., *Journal of Catalysis* **1999**, *182*, 390-399; **DOI:**10.1006/jcat.1998.2377 Permission granted by Elesiver Scientific Publishing, Inc. Copyright 1999 ©


**1.** Doornkamp, C. *et al*., *Journal of Catalysis* **1999**, *182*, 390-399

**2.** Doornkamp, C.; Ponec, V., *Journal of Molecular Catalysis A: Chemical* **2000**, *162*, 19-32


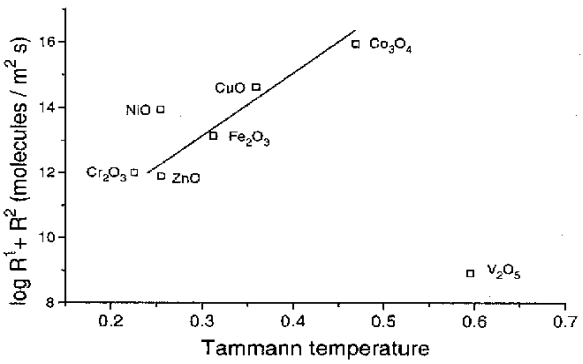


**Figure C:9 Lattice Oxygen Exchange Rate as a Function Tammann Temperature for Several Metal Oxides.**

**Supplemental text for Appendix C-C:9**-The above plot shows that $V_2O_5$ has the highest Tammann temperature (Reaction temperature-in this case 573 K-/+melting temperature of metal oxide). This means that bulk diffusion of lattice oxygen occurs with $V_2O_5$ in addition to surface diffusion, as would be the case with the other metal oxides presented in the above plot. Doornkamp, C. *et al*., *Journal of Catalysis* **1999**, *182*, 390-399; **DOI:**10.1006/jcat.1998.2377 Permission granted by Elesiver Scientific Publishing, Inc. Copyright 1999 ©

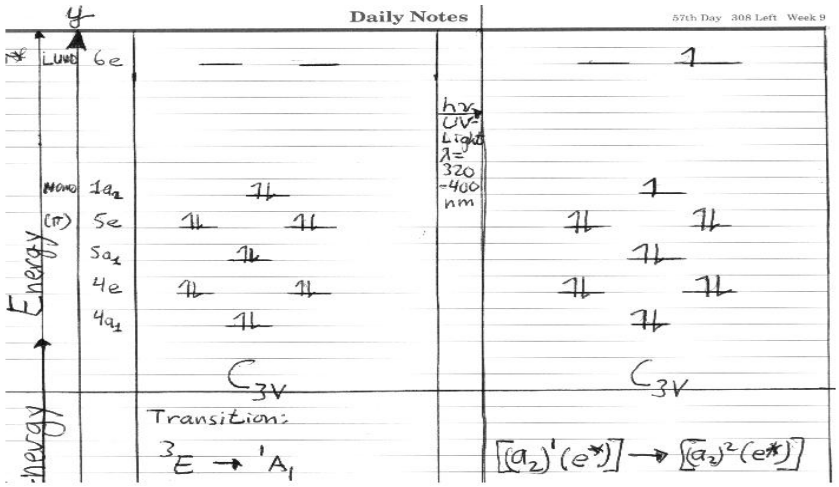


**Figure C:10 Lowest Energy Triplet State for $VO_4^{3-}/SiO_2$.**

**Supplemental text for Appendix C-C:10**-The above molecular orbital diagram shows the promotion of a non-bonding electron from $1a_2$ orbital to 6e state with change of spin to triplet state. This transition has been proposed to occur with pseudotetrahedral $VO_4^{3-}$ species on silica xerogel by *Tran et al.* under UV-light irradiation. [1,2]


3. Tran *et al.*, *Journal of the American Chemical Society* **1995**, *117*, 2618-2626
4. Tran *et al.*, *Inorganica Chimica Acta* **1996**, *243*, 185-191


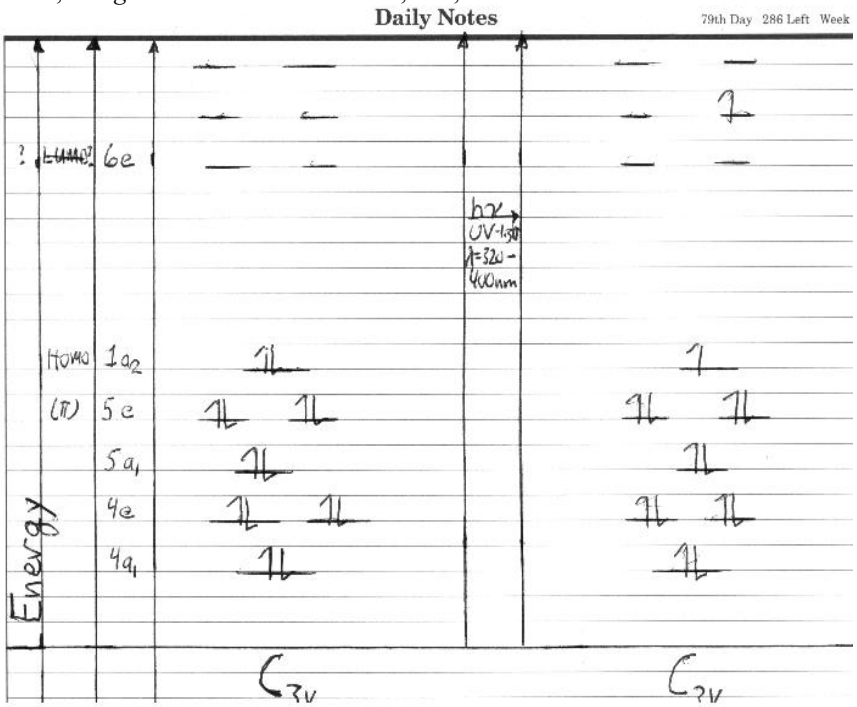


**Figure C:11 Promotion of Non-Bonding Oxygen Electron into Higher Anti-Bonding in $V^{5+}$-$VO_4^{3-}/SiO_2$.**

**Supplemental text for Appendix C-C:11**-Similar to C:7 above, a non-bonding electron from $1a_2$ orbital from oxide ligands promotes into a higher energy anti-bonding orbital above 6e mainly comprised of empty 3d $V^{5+}$ orbital under

UV-light irradiation. This proposed n→ π* electron transition into the metal anti-bonding orbital would be consistent with Tran et al. research with $VO_4^{3-}/SiO_2$ xeregel silica matrix. [1,2] The above electron transition singlet to triplet transition would be one of several possible under UV-light irradiation.


1. Tran *et al.*, *Journal of the American Chemical Society* **1995**, *117*, 2618-2626
2. Tran *et al.*, *Inorganica Chimica Acta* **1996**, *243*, 185-191


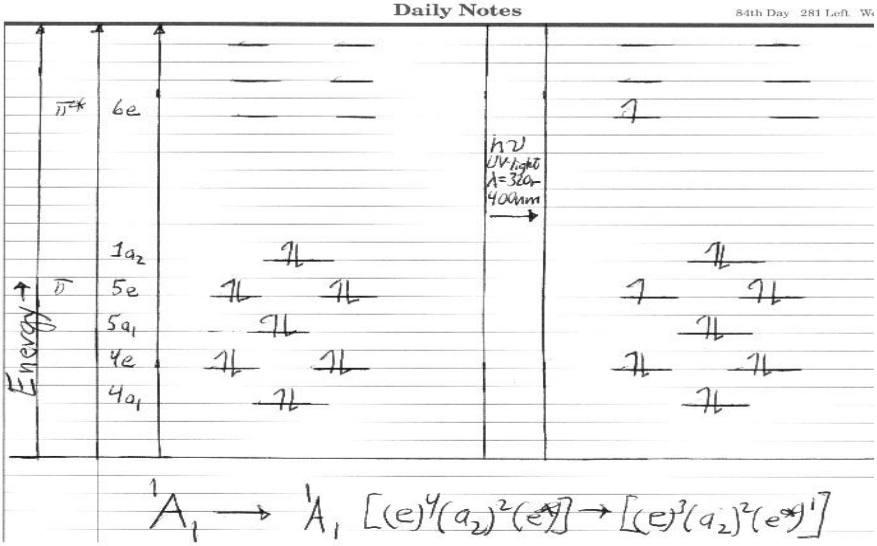


**Figure C:12 Singlet-to-Singlet Transition from 5e Oxide Ligand $V^{5+}$ 6e Orbitals in $VO_4^{3-}/SiO_2$.**

**Supplemental text for Appendix C-C:12**-In contrast to C:8 above, this electronic transition occurs deeper in the oxide ligand 5e molecular orbital of π→π* would require greater energy for electron promotion to occur as singlet-to-singlet transition. This transition could occur with $VO_4^{3-}/SiO_2$ under UV-light irradiation, according to Tran et al. [1,2]


1. Tran *et al.*, *Journal of the American Chemical Society* **1995**, *117*, 2618-2626
2. Tran *et al.*, *Inorganica Chimica Acta* **1996**, *243*, 185-191


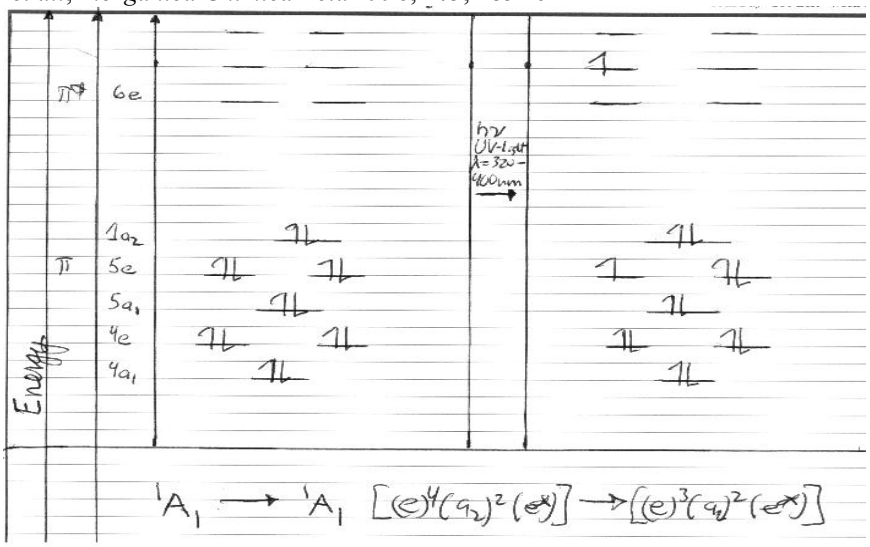


**Figure C:13 Higher Energy Singlet-to-Singlet Transition in $VO_4^{3-}/SiO_2$.**

**Supplemental text for Appendix C-C:13**-Similar to C:9 above, the UV-light initiated electronic transition would occur in $VO_4^{3-}/SiO_2$ silica xerogel matrix as π→π* transition. This would be another possible higher energy singlet-to-singlet transition in vanadium oxide on silica, as proposed by Tran et al. [1,2]


1. Tran *et al.*, *Journal of the American Chemical Society* **1995**, *117*, 2618-2626
2. Tran *et al.*, *Inorganica Chimica Acta* **1996**, *243*, 185-191

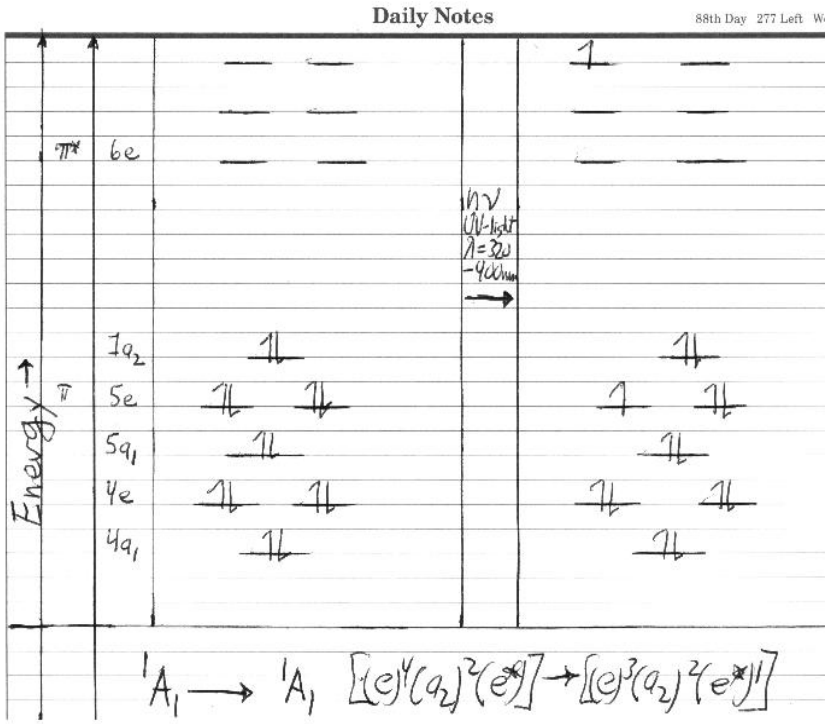


**Figure C:14 Highest Energy Singlet-to-Singlet Electronic Transition in $VO_4^{3-}/SiO_2$.**

**Supplemental text for Appendix C-C:14**-This would be the highest possible electronic transition with $VO_4^{3-}/SiO_2$ under UV-light irradiation, according to Tran et al. [1,2]


1. Tran *et al.*, *Journal of the American Chemical Society* **1995**, *117*, 2618-2626
2. Tran *et al.*, *Inorganica Chimica Acta* **1996**, *243*, 185-191


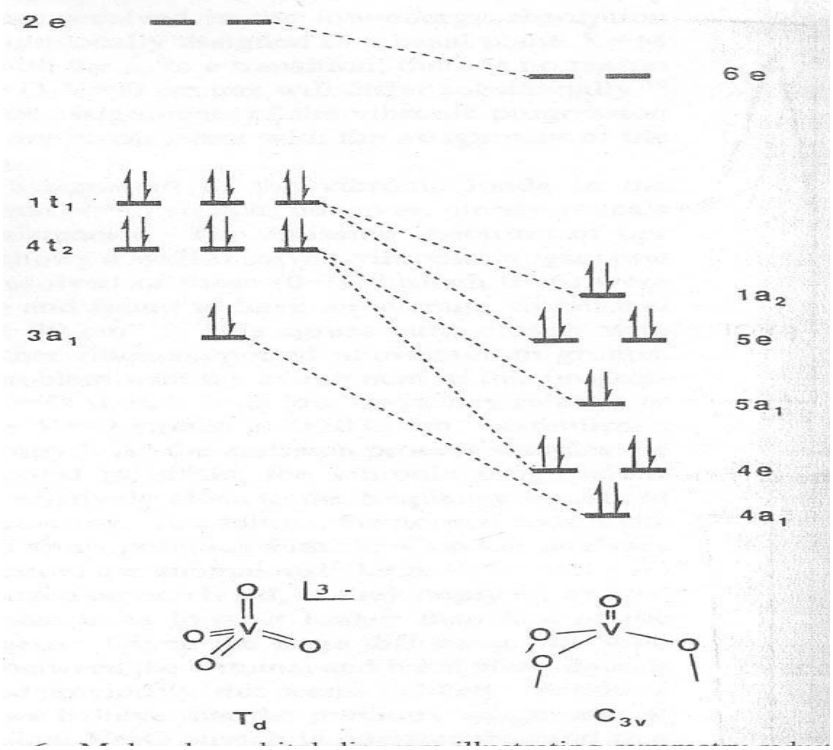


**Figure C:15 Lowest Singlet-to-Triplet Energy Electronic Transition in $VO_4^{3-}/SiO_2$ Xerogel.**

**Supplemental text for Appendix C-C:15**-The above molecular orbital diagram shows how the energy separation increases from tetredral to pseudotetrahedral $C_{3v}$ symmetry: This diagram was used to derive molecular orbital diagrams C:1-C:3 and C:7-C:11. The lowest singlet-to-triplet ($n \rightarrow \pi^*$) transition could occur in V-MCM-48; since, $VO_4^{3-}$ species would be throughout the MCM-48 silica structure similar to $VO_4^{3-}/SiO_2$ xerogel in Tran *et al.* research. [1,2] Tran *et al*, *Journal of the American Chemical Society* **1995**, *117*, 2618-2626; **DOI:** 10.1021/ja00114a026 Permission granted by American Chemical Society Copyright 1995 ©


1. Tran *et al.*, *Journal of the American Chemical Society* **1995**, *117*, 2618-2626
2. Tran *et al.*, *Inorganica Chimica Acta* **1996**, *243*, 185-191


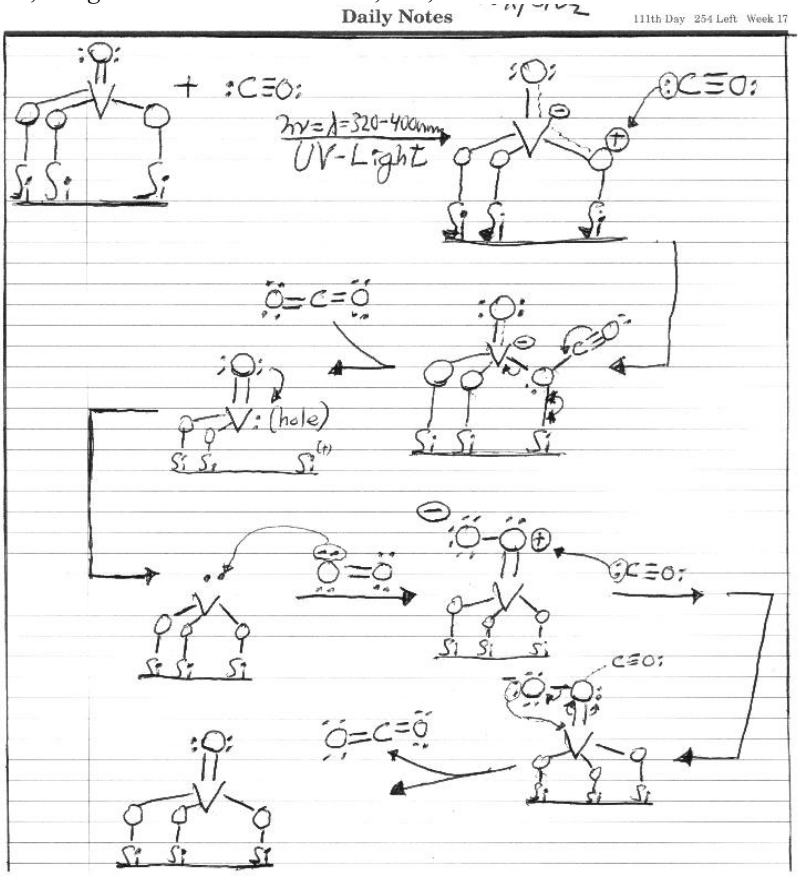


**Figure C:16 UV-Light Activated CO Photooxidation over V(x)-MCM-48.**

**Supplemental text for Appendix C:16**-The initial step in the photooxidation of carbon monoxide involves pseudotetrahedral $VO_4^{3-}$ species on the silica MCM-48 pore walls bonded through silanol groups (Si-OH) activated through UV-light. The promotion of a non-bonding electron from the basal oxygen into the empty 3d $V^{5+}$ orbital destabilizes the double bond, V=O, as noted in Tran *et al.* research on $VO_4^{3-}/SiO_2$ xerogel matrix. [1,2] CO donates electron density through sigma bond from lone pair of electron on carbon to the electrophilic oxygen. The next step would occur quickly with the oxo bond transforming into a V-O-Si bond with $V^{5+}$ reduces to $V^{3+}$. This would be consistent with Jonson *et al.* findings with $VO_4^{3-}$ species on silica converting from $V^{5+}$ to $V^{3+}$ upon oxidation of CO. [3] The next step with $O_2$ reoxidizing $V^{3+}$ back to $V^{5+}$ would be critical and intuitively one might conclude as the rate determining step for $V^{3+}$ to return to $V^{5+}$.


1. Tran *et al.*, *Journal of the American Chemical Society* **1995**, *117*, 2618-2626
2. Tran *et al.*, *Inorganica Chimica Acta* **1996**, *243*, 185-191
3. Jonson, B. *et al.*, *Journal of the Chemical Society, Faraday Transactions I* **1998**, *84*, 1897-1910

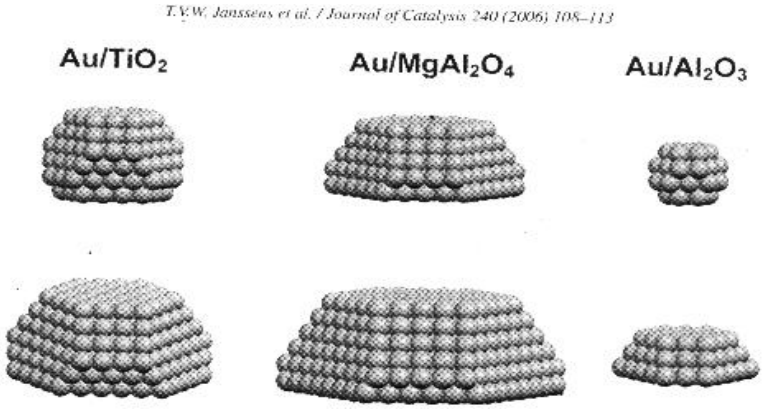


**Figure C:17 Coordination Number as a Function Au Particle Size on Various Supports.**

**Supplemental text for Appendix C-C:17**-The key variables would be the coordination number and support effects, according to Janssens *et al*. [1] These researchers note the coordination number of $Au/Al_2O_3$ would be less than $Au/TiO_2$ but 4-5 times lower turn-over-frequency (TOF) per corner Au atom. The reason would be related to the inert $Al_2O_3$ support vs. active $TiO_2$ support, which liberates lattice oxygen in the CO oxidation reaction. However, when comparing $Au/TiO_2$ (active support) with $Au/MgAl_2O_4$ (inert support) the TOF values would be close, which infers that reducibility of the support would play a minor role. Finally, the major influence with various supports would be the particle shape taken. Janssens, T. V. W. *et al*., *Journal of Catalysis* **2006**, *240*, 108-113; **DOI:** 10.1016/j.jcat.2006.03.008 Permission granted by Elsevier Scientific Publishing, Inc. Copyright 2006 ©

1. Janssens, T. V. W. *et al*., *Journal of Catalysis* **2006**, *240*, 108-113

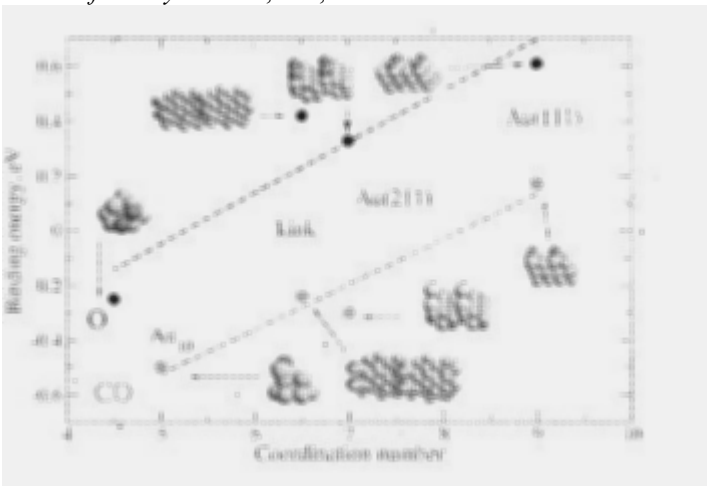


**Figure C:18 Coordination Number as a Function of Different Au Cluster Shapes.**

**Supplemental text for Appendix C-C:18**-The major point with the above plot would be that particle and coordination number do not scale linearly due to particle shape, which would be determined by gold atom placement to the support. Lopez, N. *et al*., *Journal of Catalysis* **2004**, *223*, 232-235; **DOI:** 10.1016/j.jcat.2004.01.001 Permission granted by Elsevier Scientific Publishing, Inc. Copyright 2004 ©

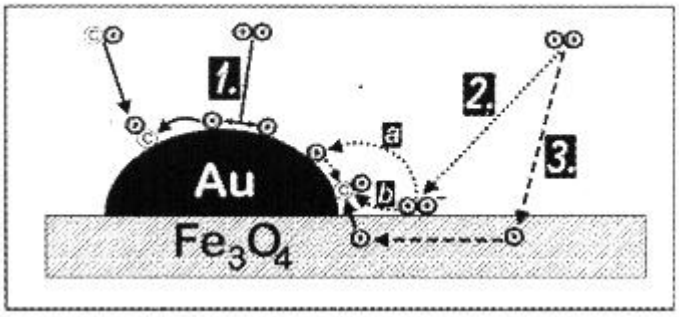


**Figure C:19 Pictorial Illustration of Gold Cluster on Active $Fe_3O_4$ Support and How CO/$O_2$ Coordinates.**

**Supplemental text for Appendix C-C:19**-The first $O_2$ absorption model (labeled 1) has molecular oxygen absorbing directly on the gold nanoparticle; then, it dissociates into oxygen atoms that travel across the small gold cluster to CO. [1] This model would only work on tiny gold clusters with needed reactive sites, such as: surface defects on the metal particle, and/or gold particle with flat shape that has different electronic state. The second $O_2$ model (labeled 2 a & b) involves the molecular oxygen absorbing on the edge of gold particle interface with the support. This would be possible with semiconductor supports that have oxygen vacancies. The molecular oxygen could dissociate to form oxygen-adsorbed species or could react directly with CO at the gold-support interface as superoxide ($O_2^-$). Finally, the third $O_2$ absorption model (labeled 3) has molecular oxygen absorb on the support to immediately form lattice oxygen to react at the gold-support interface with CO or oxygen spillover onto the gold particle surface. Schubert, M. M. *et al.*, *Journal of Catalysis* **2001**, *197*, 113-122; **DOI:** 10.1006/jcat.2000.3069 Permission granted by Elesiver Scientific Publishing, Inc. Copyright 2001 ©

1. Schubert, M. M. *et al.*, *Journal of Catalysis* **2001**, *197*, 113-122

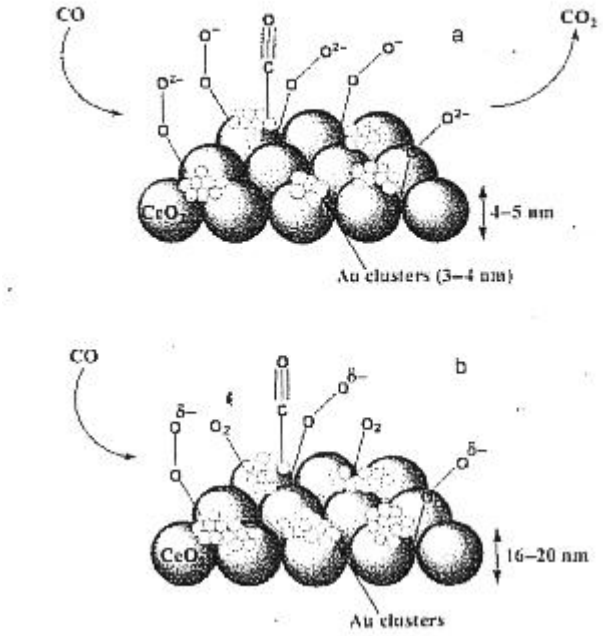


**Figure C:20 CO Oxidation as a Function of Au Clusters on Active High Surface Area $CeO_{2-x}$ Support.**

**Supplemental text for Appendix C-C:20**-The pictoral representation of gold clusters on nanocrystalline (part a) and conventional $CeO_2$ (part b) would be the two CO oxidation mechanisms that could occur, respectively. In parts (a & b), the CO absorbs on the gold nanocluster. [1] However, with nanocrystalline $CeO_{2-x}$ support, the oxygen would

be suppled by the support at one-electron defect sites on the support to produce $\eta^1$-superoxide and peroxide species. In contrast, conventional $CeO_2$ does not provide reactive oxygen and $O_2 + O_2^{\delta-}$ absorbs directly on gold clusters with CO, as shown in part (b). Guzman, J. *et al*., *Angewandte Chemie International Edition* **2005**, *44*, 4778-4781; **DOI:** 10.1002/anie.200500659 Permission granted by Wiley VCH Verlag GmbH &Co. KGaA, Weinheim Copyright 2005 ©

1. Guzman, J. *et al*., *Angewandte Chemie International Edition* **2005**, *44*, 4778-4781

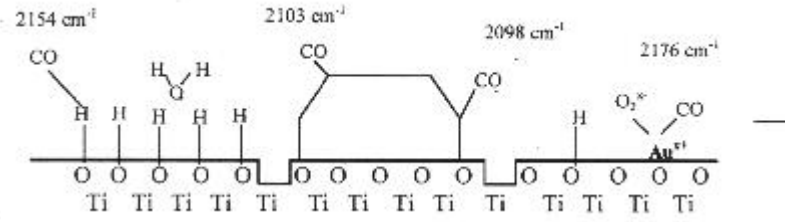


**Figure C:21 Effect of Water and Step Corner Sites on Au/$TiO_2$ at 90 K.**

**Supplemental text for Appendix C-C:21**-The above model of water and CO interactions on Au/$TiO_2$ by Boccuzzi *et al.* employed to explain the IR absorption peaks. [1] The absorption of water on the $TiO_2$ surface has been proposed to reactive with superoxide species to form $OOH^-$ on the gold particle surface. The gold nanoparticle depicted above on $TiO_2$ with absorption at 2103 $cm^{-1}$ and 2098 $cm^{-1}$ would be step and corner gold sites. Isolated carbonyl peroxide species would also occur at 2176 $cm^{-1}$ at the expensive of step and corner sites, when Au/$TiO_2$ made at 873 K vs. 573 K. Boccuzzi, F. *et al.*, *Journal of Catalysis* **2001**, *202*, 256-267; **DOI:** 10.1006/jcat.2001.3290 Permission granted by Elesiver Scientific Publishing, Inc. Copyright 2001 ©

1. Boccuzzi, F. *et al.*, *Journal of Catalysis* **2001**, *202*, 256-267

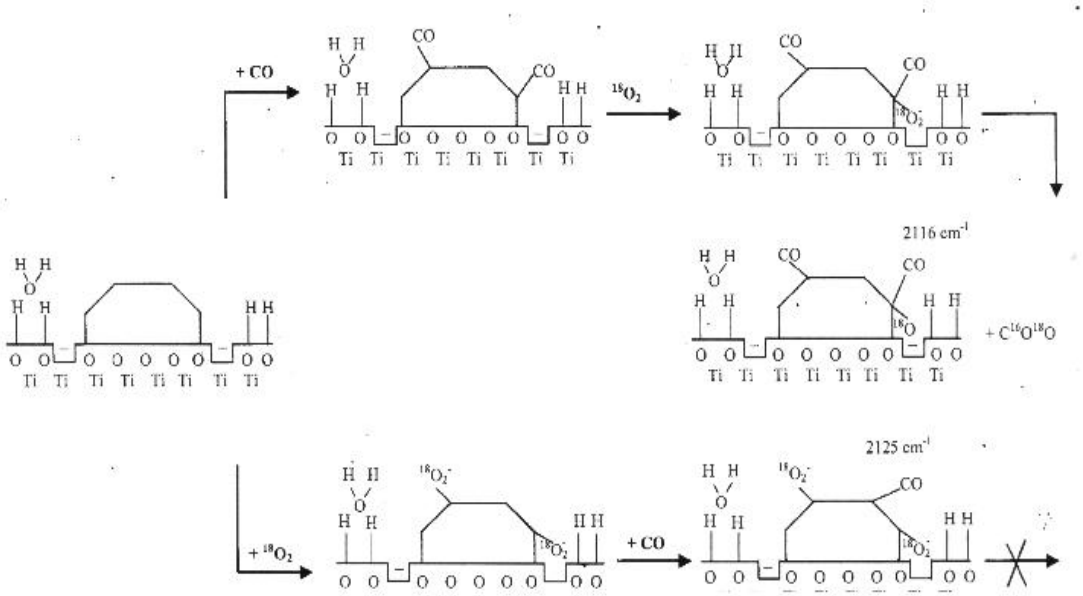


**Figure C:22 How $O_2$ needs to Bind to Au Cluster on $TiO_2$ in addition to CO.**

**Supplemental text for Appendix C-C:22**-As seen in the above schematic depiction, CO absorbs on the step/corner gold cluster sites; then, $^{18}O_2^-$ binds to the corner site with CO and proposed to be activated by absorbed water to form $C^{16}O^{18}O$. [1] In the lower drawing with $^{18}O_2^-$ absorbing on the step and corner sites on gold nanoclusters, the CO binds to gold nanocluster sites away from the gold-support interface with water, thereby preventing $CO_2$ formation from occurring. Boccuzzi, F. *et al.*, *Journal of Catalysis* **2001**, *202*, 256-267; **DOI:** 10.1006/jcat.2001.3290 Permission granted by Elesiver Scientific Publishing, Inc. Copyright 2001 ©

1. Boccuzzi, F. *et al.*, *Journal of Catalysis* **2001**, *202*, 256-267

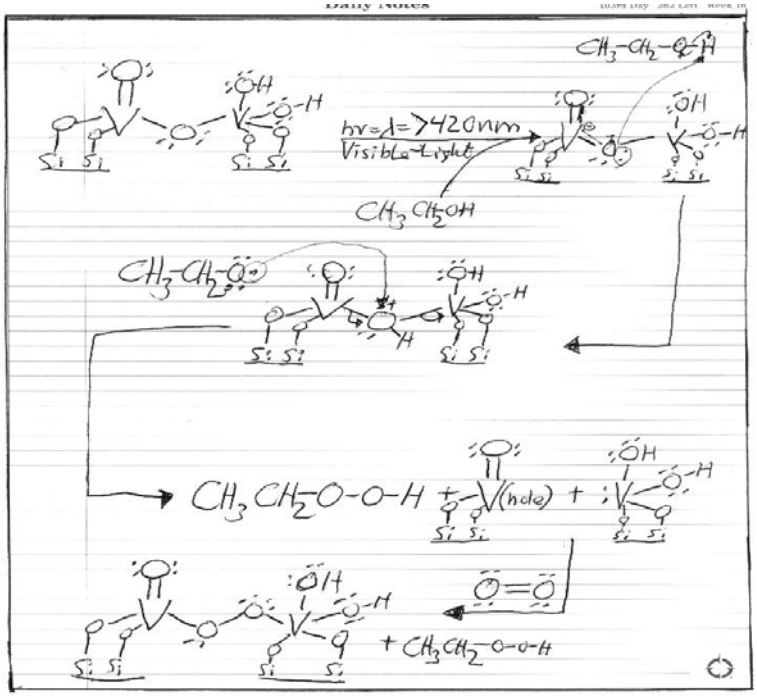


**Figure C:23 Part I-Visible-Light Initiated Ethanol Photodegradation Mechanism over V(x)-MCM-48.**

**Supplemental text for Appendix C-C:23**-The above visible-light photodegradation proposed ethanol mechanism operates in a similar fashion as visible-light acetaldehyde photodegradation mechanism presented in C:5-C:7. The major difference between ethanol and acetaldehyde visible-light photodegradation over V(x)-MCM-48 would be the number of reaction steps needed to completely oxidize ethanol to $CO_2$ vs. acetaldehyde.

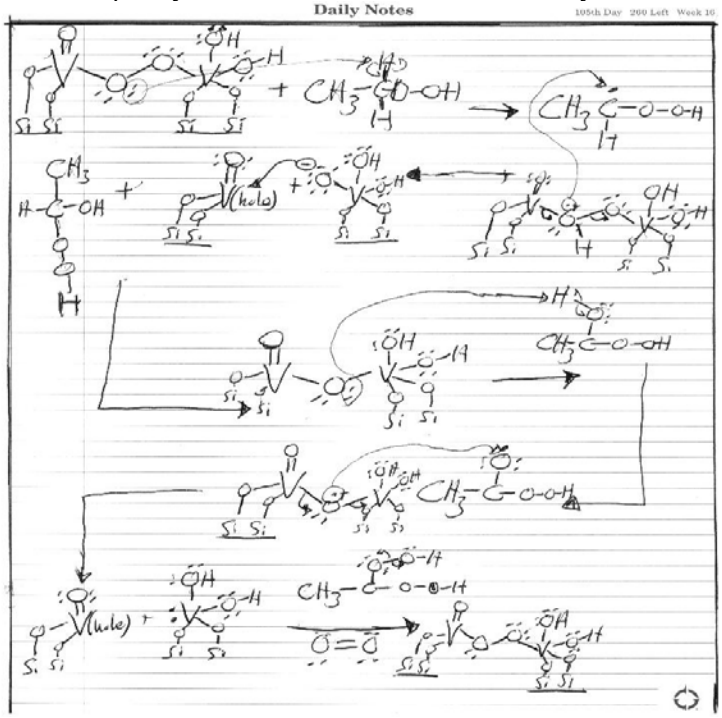


**Figure C:24 Part II-Visible-Light Initiated Ethanol Photodegradation Mechanism over V(x)-MCM-48.**

**Supplemental text for Appendix C-C:24**-As mention in the visible-light acetaldehyde photodegradation earlier in C:5-C:7, the insertion of molecular oxygen between the $V^{5+}$ centers as bridging oxygens and related radical abstrac-

tion of electrophilic species (commonly hydrogen atom) would be needed for the ethanol molecule to convert completely to $CO_2$.

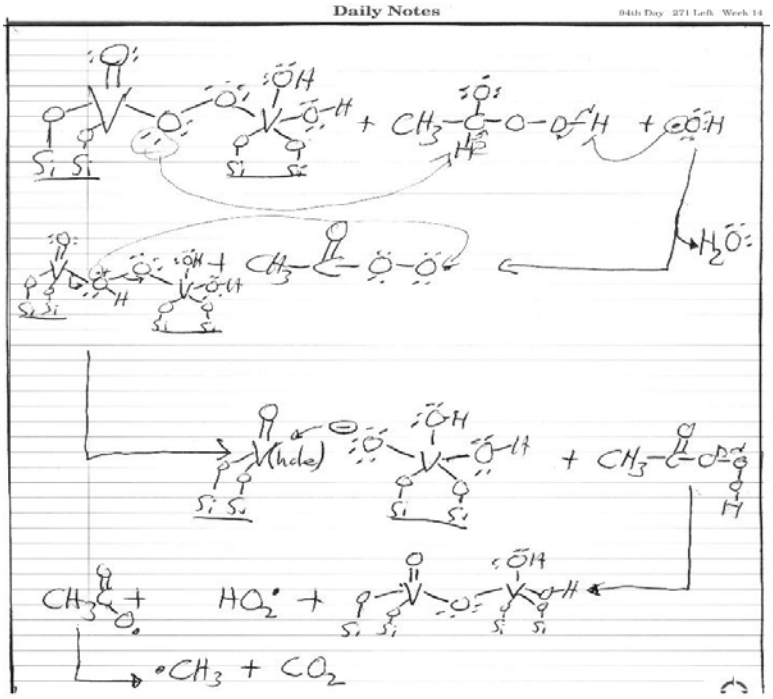


**Figure C:25 Part III-Visible-Light Initiated Ethanol Photodegradation Mechanism over V(x)-MCM-48.**

**Supplemental text for Appendix C-C:25**-In this section of ethanol visible-light photodegradation mechanism over V(x)-MCM-48 formation of hydroxyl radical (OH) and hydroperoxide radical ($HO_2\cdot$) species would be critical in addition to the basicity of the bridging oxygen species between the $V^{5+}$ centers.

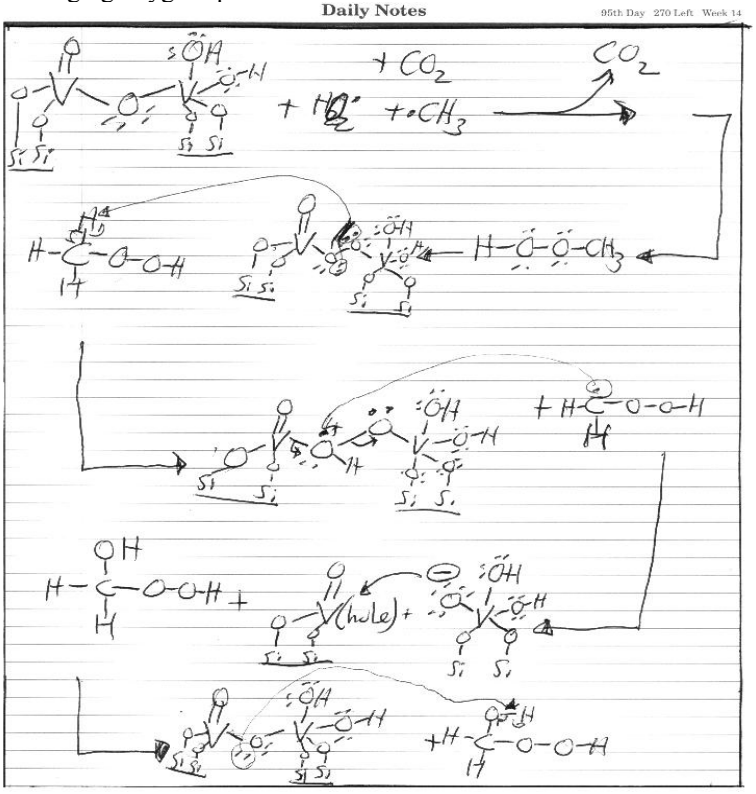

**Figure C:26 Part IV-Visible-Light Initiated Ethanol Photodegradation Mechanism over V(x)-MCM-48.**

**Supplemental text for Appendix C-C:26**-The major visible-light photodegradation steps would involve abstraction electrophilic hydrogen atom one carbon species. The ability to continue abstracting hydrogen species placing oxygen species on the one carbon species would be critical for increasing instability in remaining probe molecule segment, thereby causing molecular reorganization to stable $CO_2$.

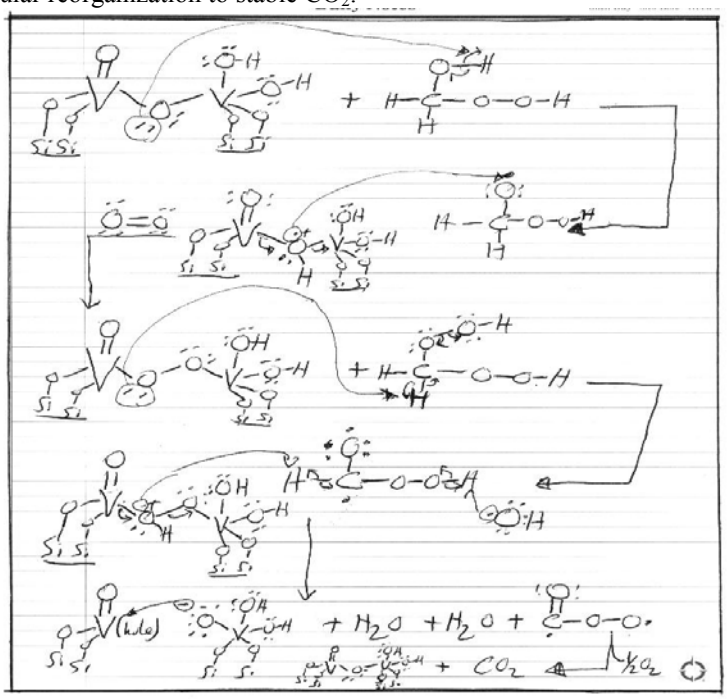

**Figure C:27 Part IIV-Visible-Light Initiated Ethanol Photodegradation over V(x)-MCM-48.**

**Supplemental text for Appendix C-C:27**-In these final photodegradation steps, hydroxyl radical would be critical in addition to bridging oxygens between the $V^{5+}$ centers for complete oxidation of ethanol to occur.

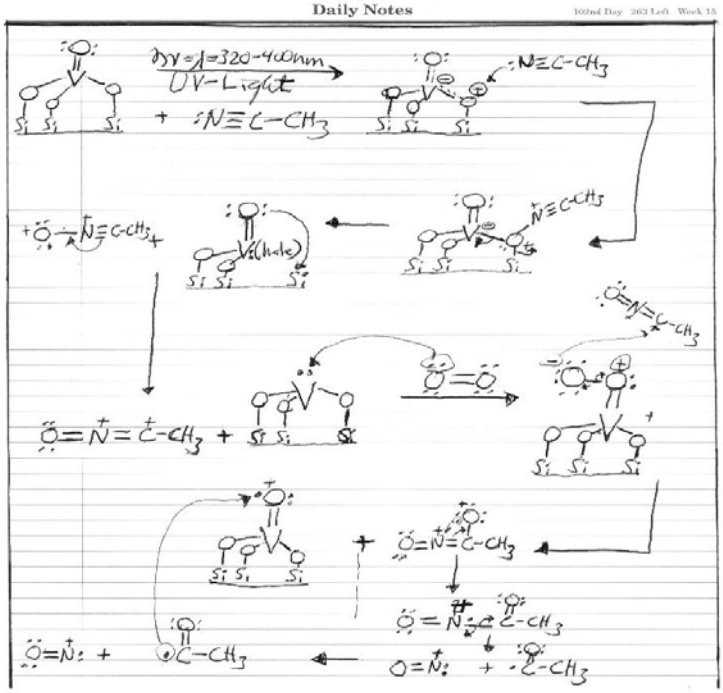


**Figure C:28 Part I-UV-Light Initiated Acetonitrile Photodegradation Mechanism over V(x)-MCM-48.**

**Supplemental text for Appendix C-C:28**-Similar to the proposed CO UV-light photooxidation presented in C.16 earlier, the acetonitrile photooxidation mechanism involves pseudotetrahedral $VO_4^{3-}$ members on the pore walls of MCM-48 activated by UV-light with non-bonding electron from basal oxygen to empty 3d $V^{5+}$ orbital. Then, the nitrogen atom from acetonitrile donates electron pair to the electrophilic oxygen. Subsequent reaction steps involve $V^{5+}$ reduced to $V^{3+}$ and reoxidized to $V^{5+}$ with $O_2$ similar to CO UV-light photooxidation mechanism. Finally, more reaction steps would be needed to fully oxidize acetonitrile to $CO_2 + H_2O$ due to more carbons in $CH_3CN$.

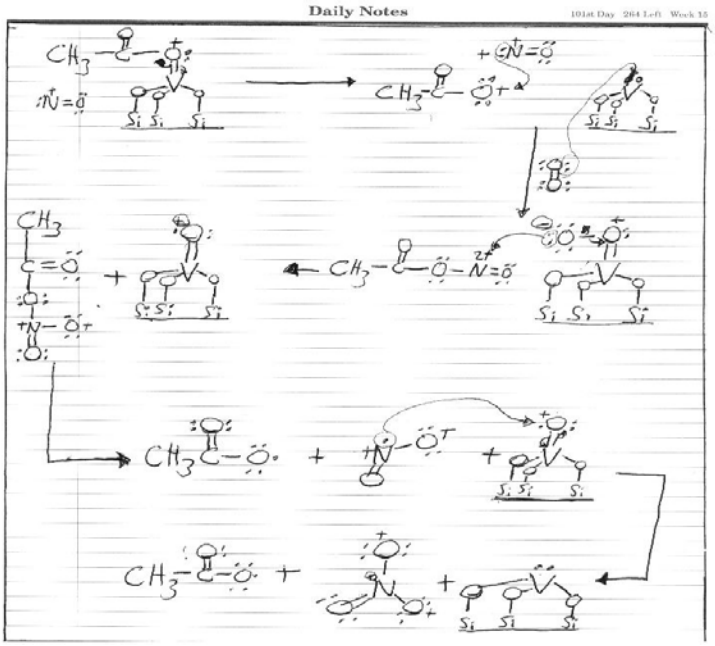


**Figure C:29 Part II-UV-Light Initiated Acetonitrile Photodegradation Mechanism over V(x)-MCM-48.**

**Supplemental text for Appendix C-C:29**-The key for the above UV-light photooxidation reactions to occur over V(x)-MCM-48 would require the continual reoxidation of $V^{3+}$ back to $V^{5+}$. Radical abstraction would also be pivotal in conversion of probe molecule to final oxidation products: $CO_2 + H_2O$.

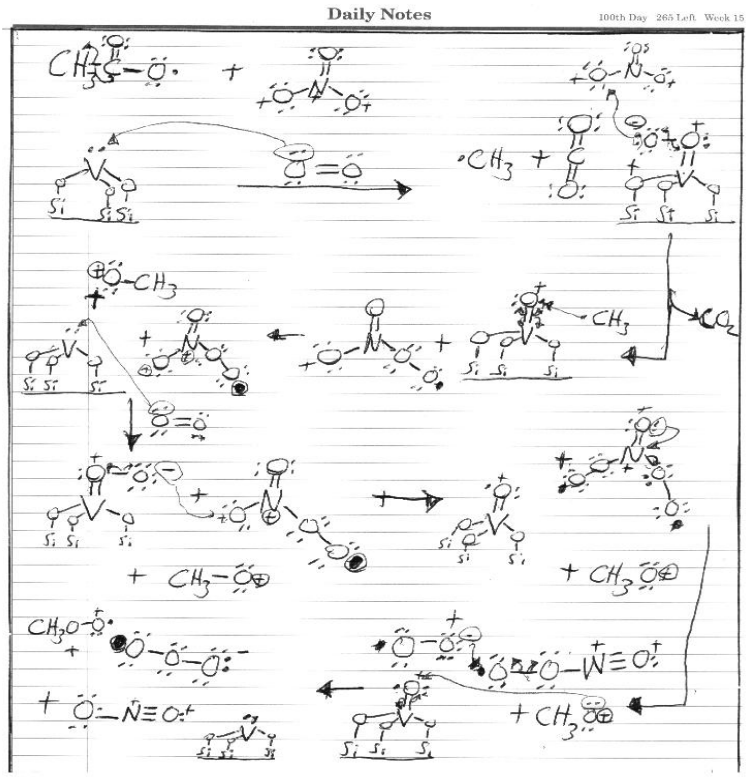


**Figure C:30 Part III-UV-Light Initiated Acetonitrile Photodegradation Mechanism over V(x)-MCM-48.**

**Supplemental text for Appendix C-C:30**-In the above reaction steps the methyl fragment from $CH_3CN$ has more oxygen atoms added to form unstable peroxide species and nitrogen atom from acetonitrile addition oxygen atoms.

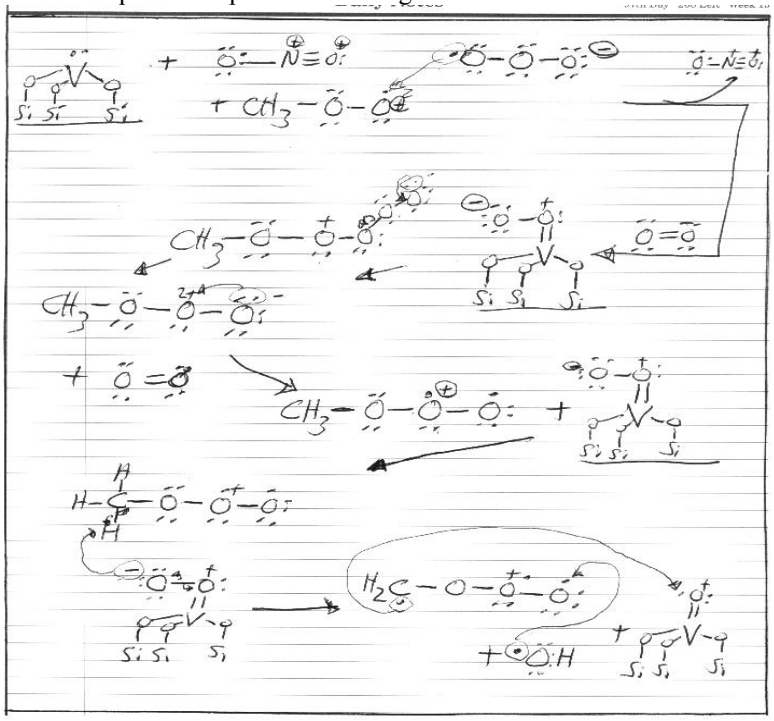

**Figure C:31 Part IV-UV-Light Initiated Acetonitrile Photodegradation Mechanism over V(x)-MCM-48.**

**Supplemental text for Appendix C-C:31**-The methyl fragment from $CH_3CN$ continues to acquire oxygen atoms and $N_2O$ spins off from the reaction. The continue addition of oxygen-oxygen species to the methyl fragment would increase instability of the methyl peroxide species.

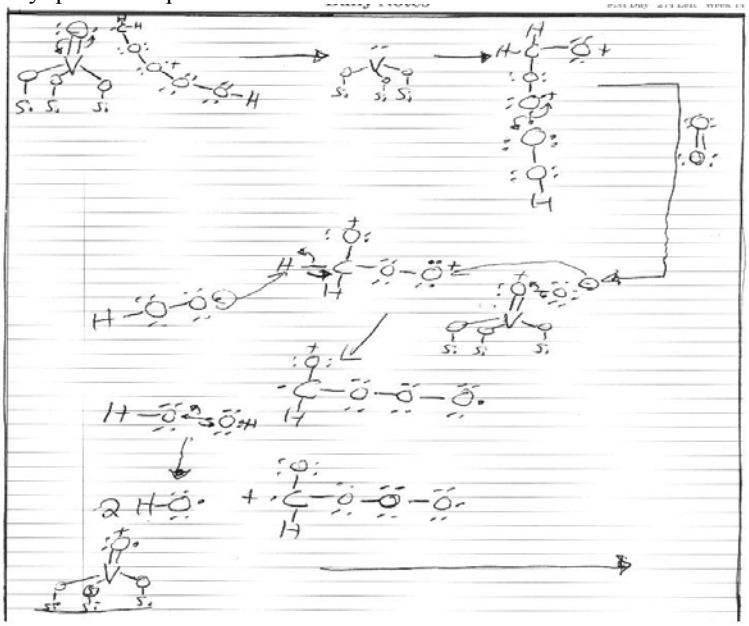

**Figure C:32 Part IIV-UV-Light Initiated Acetonitrile Photodegradation Mechanism over V(x)-MCM-48.**

**Supplemental text for Appendix C-C:32**-Hydrogen atom abstraction coupled with formation of two hydroxyl radicals with carbon peroxy radical species continues to lead to final oxidation product: $CO_2$.

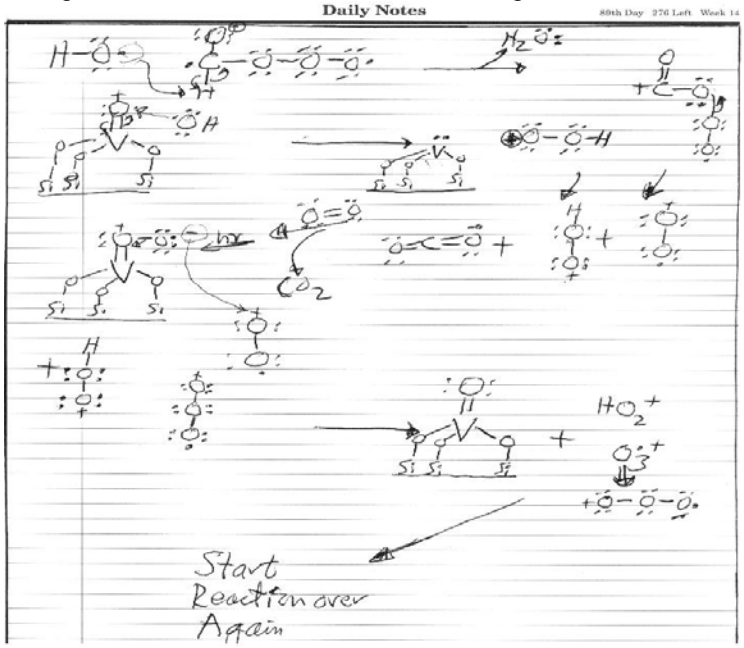


**Figure C:33 Part VI-UV-Light Initiated Acetonitrile Photodegradation Mechanism over V(x)-MCM-48.**

**Supplemental text for Appendix C-C:33**-In these last reaction steps $H_2O$ and $CO_2$ spin off hydroproxyl and $O_3^{\cdot+}$ radical species formed. The $VO_4^{3-}$ species would be in the original state to begin the acetonitrile UV-light initiated photooxidation process over again.

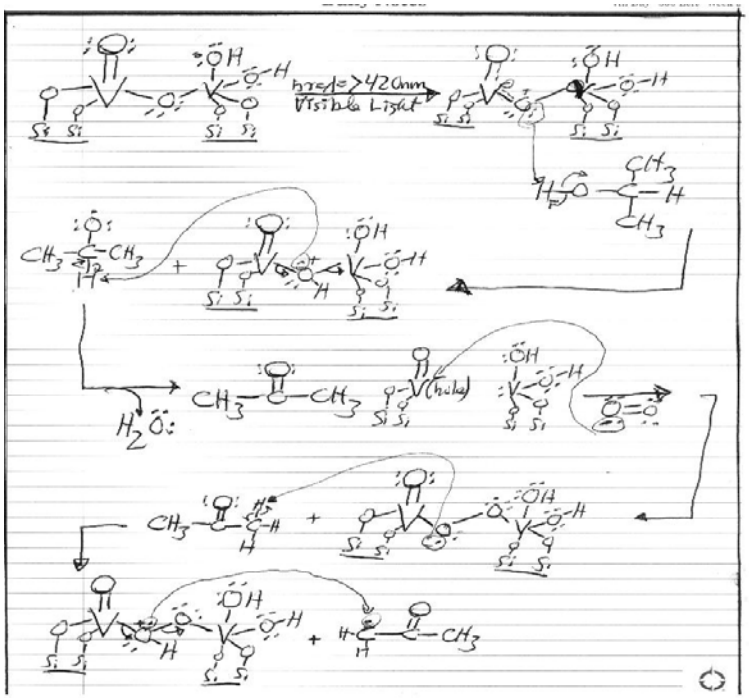


**Figure C:34 Part I-Visible-Light 2-Propanol/Acetone Photodegradation Mechansim over V(x)-MCM-48.**

**Supplemental text for Appendix C-C:34**-The above 2-propanol/acetone visible light photodegradation mechanism over V(x)-MCM-48 would involve bridging oxygen atom between the $V^{5+}$ centers abstracting a hydrogen atom from 2-propanol. The reaction steps following formation of acetone would be rate determined by the basicity of the oxygen bridging atoms between the $V^{5+}$ centers. Similar to other proposed photodegradation mechanisms over V(x)-MCM-48, the abstraction of a hydrogen off of the probe molecule followed by addition of a oxygen atom probe molecule sequence.

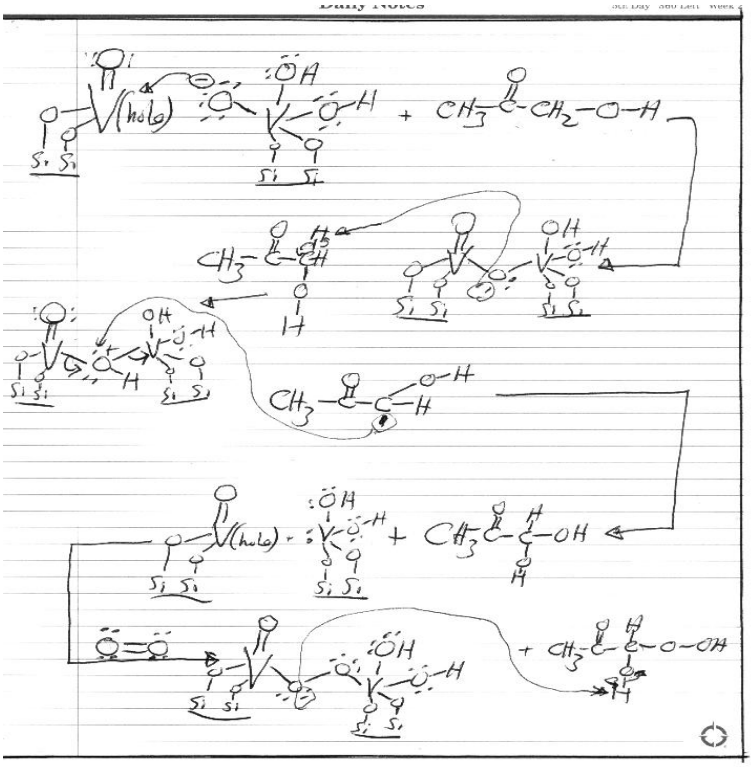

**Figure C:35 Part II-Visible-Light 2-Propanol/Acetone Photodegradation Mechanism over V(x)-MCM-48.**

**Supplemental text for Appendix C-C:35**-As noted in C:5-C:7, the continued addition of oxygen atoms and abstraction of hydrogen atoms would decrease stability of the probe molecule, thereby causing molecular reorganization.

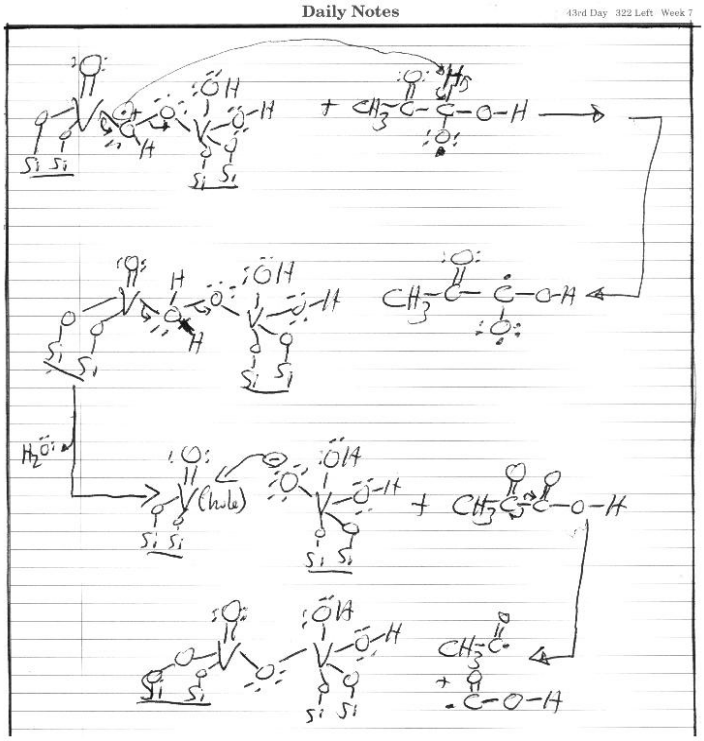


**Figure C:36 Part III-Visible-Light 2-Propanol/Acetone Photodegradation Mechanism over V(x)-MCM-48.**

**Supplemental text for Appendix C-C:36**-In the above photodegradation steps the probe molecule splits in half recembling acetaldehyde species.

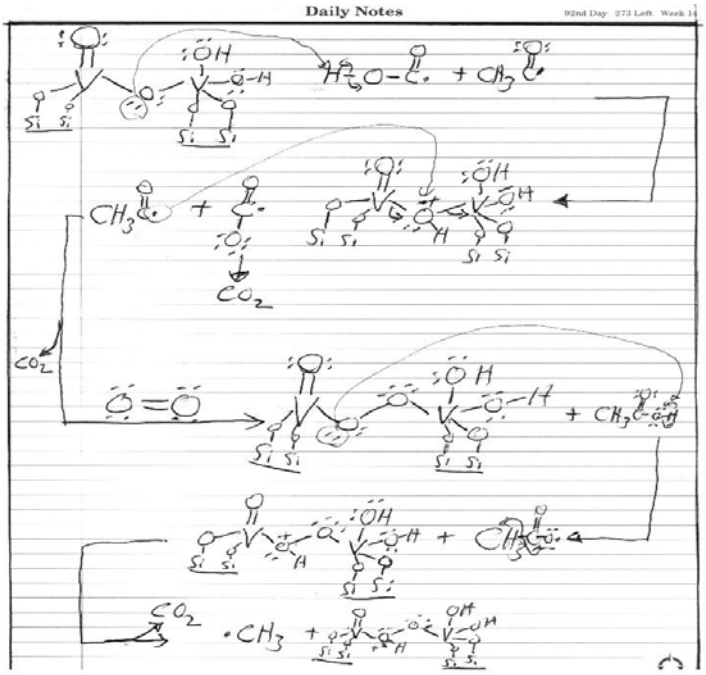


**Figure C:37 Part IV-Visible-Light 2-Propanol/Acetone Photodegradation Mechanism over V(x)-MCM-48.**

**Supplemental text for Appendix C-C:37**-Bridging oxygen between the $V^{5+}$ centers continues to abstract hydrogen atoms from the probe molecule and adds to the probe molecule fragments with $CO_2$ forming.

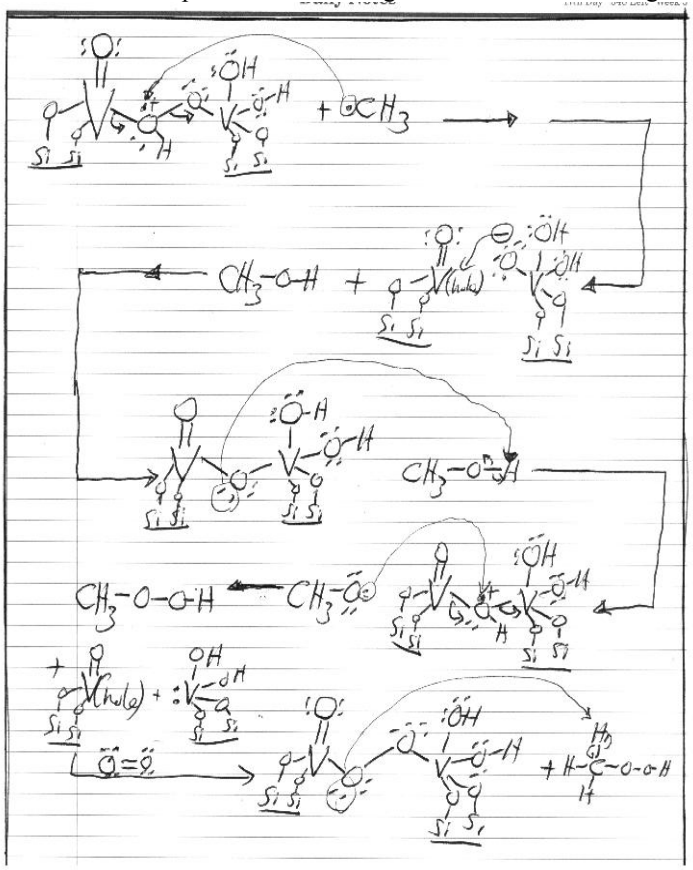

**Figure C:38 Part IIV-Visible-Light 2-Propanol/Acetone Photodegradation Mechanism over V(x)-MCM-48.**

**Supplemental text for Appendix C-C:38**-The methyl fragment continues to gain addition oxygen atoms to form methyl peroxide species. Similar to the other photodegradation mechanisms over V(x)-MCM-48, the abstraction of methyl hydrogen atoms followed by addition of oxygen atoms would continue to destabilize the resulting molecule.

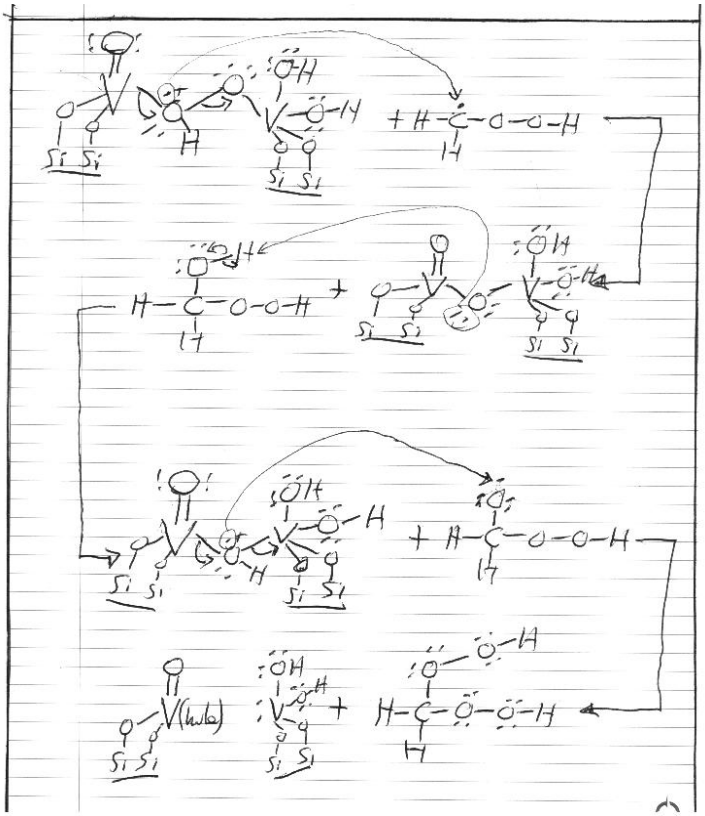

**Figure C:39 Part VI-Visible-Light 2-Propanol/Acetone Photodegradation Mechanism over V(x)-MCM-48.**

**Supplemental text for Appendix C-C:39**-The molecular bonding continues to be strained with uneven distribution of electron density.

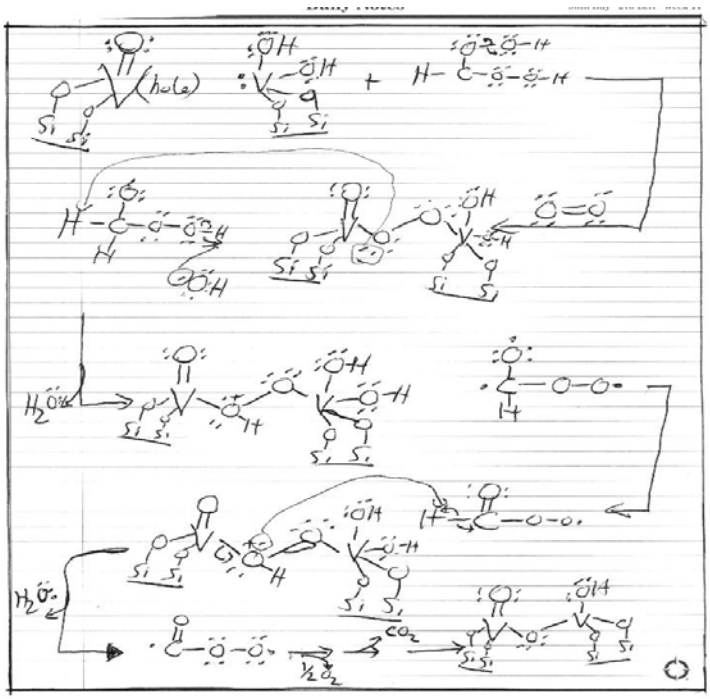

**Figure C:40 Part VII-Visible-Light 2-Propanol/Acetone Photodegradation Mechanism over V(x)-MCM-48.**

**Supplemental text for Appendix C-C:40**-In these final photodegradation steps abstraction hydrogen atoms continues probe molecule molecular rearrangement occurring. The continued molecular transformation leads to final oxidation product: $CO_2$.

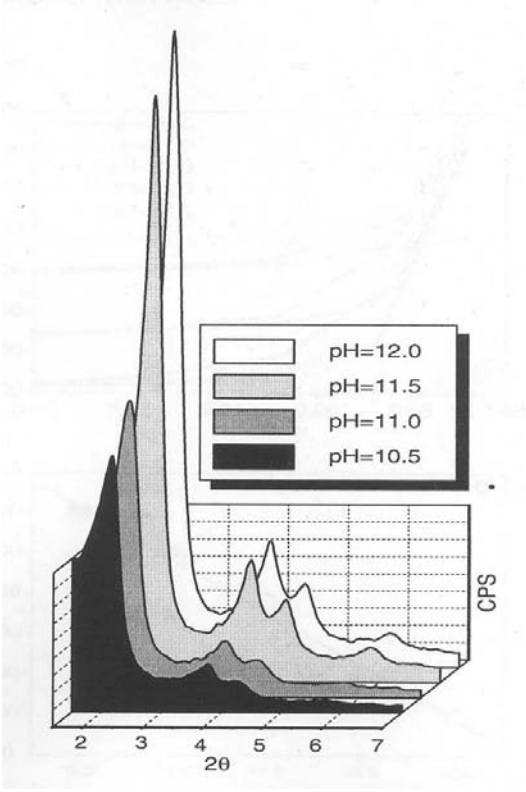


**Figure C:41 Powder XRD Peak Intensity and 2-Theta *d*-spacing as a Function of pH value in Co-MCM-41.**

**Supplemental text for Appendix C-C:41**-The above powder XRD of 1wt% Co ion in MCM-41 intensity increased dramatically up to pH of 12. The Co-MCM-41 sample made at pH of 12 had approximately three times the peak intensity of Co-MCM-41 made at pH of 10.5. As noted in discussion chapter part II, the size of the powder XRD intensity provides level of long-range order in a given structure; therefore, the higher pH value means the formed Co-MCM-41 sample would exhibit greater structural long-range order. Lim, S. *et al.*, *Microporous and Mesoporous Materials* **2007**, *101*, 200-206; **DOI:** 10.1016/j.micromeso.2006.11.002 Permission granted by Elesiver Scientific Publishing, Inc. Copyright 2006 ©

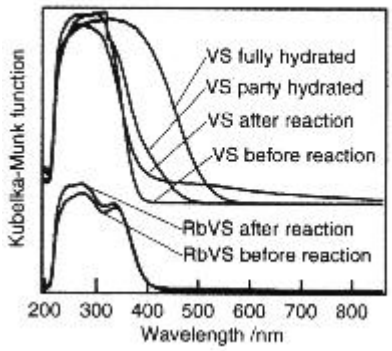


**Figure C:42 Hydration Effect on $VO_x$ with and without Alkali-metal-ions over Silica support.**

**Supplemental text for Appendix C-C:42**-The above DR-UV-vis spectra of $VO_4^{3-}/SiO_2$ (VS) with hydration and without coordination of aqua ligands to $V^{5+}$ center shows that water extends the absorption range of VS species and VS has little visible-light absorption. $Rb^+$ ion modified VS has little change before and after reaction, according to

the above DR-UV-vis spectra. The use of $Rb^+$ ion leads to visible-light absorption of VS without aqua ligands. Finally, the yellow-organge color of fully hydrated $VO_4^{3-}$ would be due to coordination of aqua ligands. Tanaka, T. *et al.*, *Catalysis Today* **2000**, *61*, 109-115; **DOI:** 10.1016/S0920-5861(00)00371-0 Permission granted by Elsevier Scientific Publishing, Inc. Copyright 2000 ©



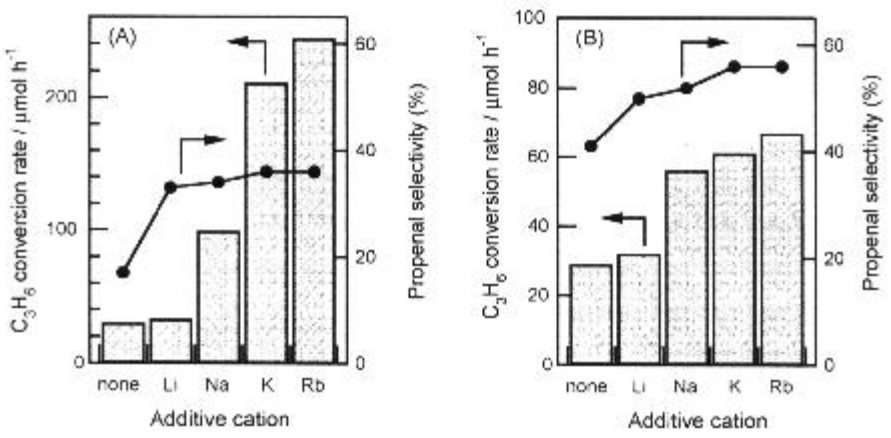


**Figure C:43 Effects of Alkali-Metal-Ions on Vanadium Oxide on Silica or $Al_2O_3$ with and without.**

**Supplemental text for Appendix C-C.43**-Refering to plot (A), the $Rb^+$ ion modified $VO_4^{3-}/SiO_2$ (Rb-VS) had the largest propenal selectivity with greatest propylene conversion rate. $Rb^+$ ion over $VO_4^{3-}/Al_2O_3$ (Rb-VA) showed the largest propylene conversion rate and selectivity. Althought not shown in these above plots, the $CO_2$ production from propylene increases dramatically in Table C:1 table of values. Finally, the most important results of application of $Rb^+$ ions over VS would be the eight-fold propylene conversion rate. The alkali-metal-ion to vanadium ion ratio was 1.5. Amano, F. *et al*., *Catalysis Today* **2007**, *120*, 126-132; **DOI:** 10.1016/j.cattod.2006.07.041 Permission granted by Elsevier Scientific Publishing, Inc. Copyright 2006 ©

Table 1
Results of photocatalytic oxidation of propylene with molecular oxygen at 373 K

| Sample | $V_2O_5$ loading (wt%) | $Rb_2O$ loading (wt%) | $A_{BET}$[a] ($m^2 g^{-1}$) | $C_3H_6$ conversion rate (μmol $h^{-1}$) | Selectivity (%) | | | | Acrolein formation rate (μmol $h^{-1}$) |
|---|---|---|---|---|---|---|---|---|---|
| | | | | | Propenal | $C_3$[b] | Ethanal | $CO_2$ | |
| 0.1VS | 0.1 | 0.0 | 590 | 52 | 15 | 42 (38)[c] | 32 | 11 | 8 |
| 2.5VS | 2.5 | 0.0 | 588 | 30 | 17 | 25 (14)[c] | 46 | 12 | 5 |
| Rb-2.5VS | 2.5 | 3.8[d] | 179 | 244 | 36 | 6 | 7 | 51 | 88 |
| $Al_2O_3$ | 0.0 | 0.0 | 154 | 7 | n.d. | 13 | 6 | 81 | n.d. |
| 2.5VA | 2.5 | 0.0 | 152 | 29 | 41 | 6 | 23 | 30 | 12 |
| Rb-2.5VA | 2.5 | 3.8[d] | 154 | 67 | 56 | 5 | 8 | 31 | 38 |
| $Rb_2O/Al_2O_3$ | 0.0 | 2.5 | 152 | 15 | 11 | 14 | 12 | 63 | 2 |
| $RbVO_3$ | 49.3 | 50.7 | – | 3 | 92 | 8 | n.d. | n.d. | 3 |

The data were obtained at 300 min on stream.
[a] BET specific surface area.
[b] The $C_3$ oxygenated products except propenal: propanal, propylene oxide, and acetone.
[c] The selectivity to propylene oxide are shown in the parenthesis.
[d] The molar ratio of rubidium to vanadium (Rb/V) was adjusted to 1.5.

**Table C:1 Propylene Conversion and Selectivity as Function of $Rb^+$ ion over VS and VA.**

**Supplemental text for Appendix C-C:1**-As seen in the above table of values for propylene photooxidation at 373 K with $O_2$ over Rb-2.5VS (2.5 wt% $V_2O_5$) has conversion rate increase of 244 vs. 52 with VS. From an environmental point of view, $CO_2$ production increases from 11 to 51 of product selectivity. This clearly shows that $Rb^+$ ion modified VS produces greater amounts of $CO_2$ with a higher conversion rate. Amano, F. *et al*., *Catalysis Today* **2007**, *120*, 126-132; **DOI:** 10.1016/j.cattod.2006.07.041 Permission granted by Elsevier Scientific Publishing, Inc. Copyright 2006 ©

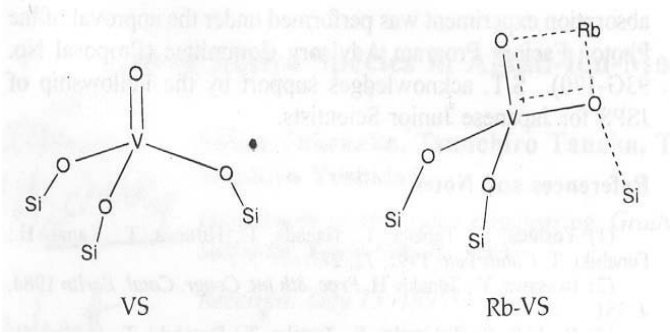


**Figure C:44 Proposed Structure for $Rb^{+}$ ion Modified $VO_4^{3-}/SiO_2$.**

**Supplemental text for Appendix C-C:44**-The above two structures proposed by Tanaka and co-workers from DR-UV-vis spectroscopy, Raman spectroscopy, X-ray absorption spectroscopy (XANES + EXAFS), and XPS analysis. In addition, ab initio molecular orbital calculations were completed, which support the $Rb^{+}$ ion adjactent to the $VO_4^{3-}$ cluster. [1] The lengthening and shortening of V-O bonds with double bond character spread over the Rb-VS structure was suggested to be the reason for enhanced selectivity due to change of triplet energy state. Takenaka, S. *et al.*, *Journal of Physical Chemistry B* **1997**, *101*, 9035-9040; **DOI:** 10.1021/jp9716086 Permission granted by American Chemical Society Copyright 1997 ©

1. Takenaka, S. *et al.*, *Journal of Physical Chemistry B* **1997**, *101*, 9035-9040

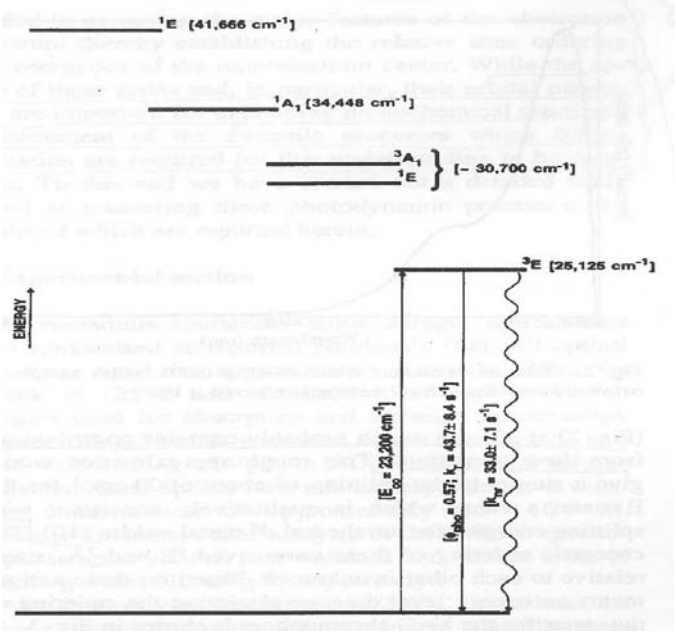


**Figure C:45 Energy Level Digram for Electronic Transitions in $VO_4^{3-}$ on Silica Support.**

**Supplemental text for Appendix C-C:45**-The above energy level diagram would be $VO_4^{3-}$ pseudotetrahedral species on silica, shown in C.44. The top energy transitions in brackets would be estimated values with ordering unkrown between these two states. The completely elucidated energy transitions would be at wavelength maximum ($\lambda_{maximum}$) determined at 14 K for absorption, quantum yield, and decay rate values. The key point in this diagram would be that there would be several energy states about the lowest triplet state that could occur with appropriate wavelength of light. Tran, K. *et al.*, *Inorganica Chimica Acta* **1996**, *243*, 185-191; **DOI:** 10.1016/0020-1693(95)04906-1 Permission granted by Elsevier Scientific Publishing, Inc. Copyright 1996 ©

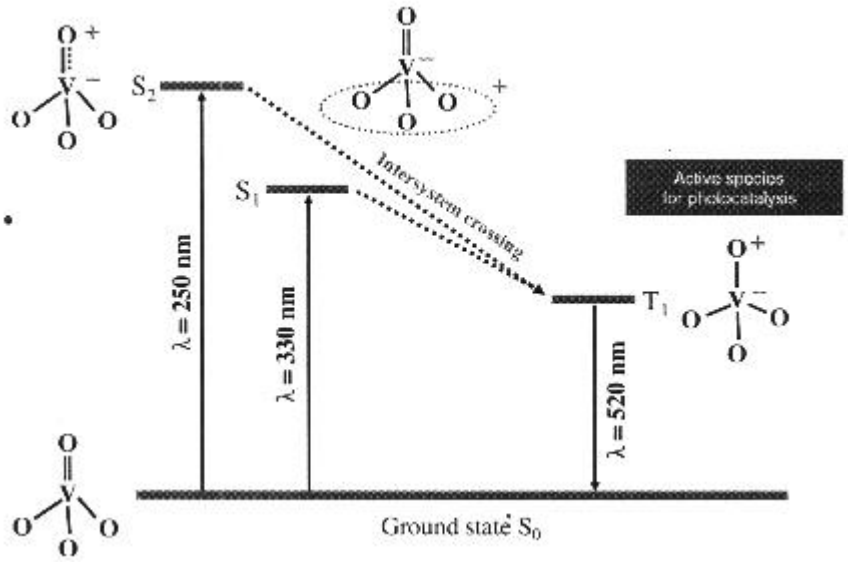


**Figure C:46 Pictorial Illustrations of $VO_4^{3-}/Al_2O_3$ Singlet-to-Tripet Transitions.**

**Supplemental text for Appendix C-C:46**-The above pictorial energy level diagram for $VO_4^{3-}/Al_2O_3$ shows that two unstable singlet states exist ($S_2$, $S_1$); then, they convert to the more stable electronic lower energy triplet state ($T_1$) through intersystem crossing. This representation of the energy states by Tanaka and co-workers [1] would be similar to Tran *et al.* [2,3] research with $VO_4^{3-}$ pseudotetrahedral species in silica xerogel matrix with the exception of the oxo oxygen being electrophilic instead of basal support oxygen to silica support. Finally, this latest research shows that the triplet state would be the one active in photocatalysis. Teramura, K. *et al.*, *Chemical Physics Letters* **2008**, *460*, 478-481; **DOI:** 10.1016/j.cplett.2008.06.025 Permission granted by Elsevier Scientific Publishing, Inc. Copyright 2008 ©


1. Teramura, K. *et al.*, *Chemical Physics Letters* **2008**, *460*, 478-481
2. Tran *et al.*, *Journal of the American Chemical Society* **1995**, *117*, 2618-2626
3. Tran *et al.*, *Inorganica Chimica Acta* **1996**, *243*, 185-191


**Photooxidation of Propane over $V_2O_5/SiO_2$ and Alkali-Ion-Modified $V_2O_5/SiO_2$ Catalysts under Irradiation by the Light of Wavelengths $\lambda > 310$ nm[a]**

| Catalyst | Conv.[b] (%) | Selectivity[c] (%) | | | | | | |
|---|---|---|---|---|---|---|---|---|
| | | $C_3H_6$ | $C_2H_5CHO$ | $(CH_3)_2CO$ | $C_2H_3CHO$ | $C_3H_4$ | $CH_3CHO$ | $CO_x$ |
| VS | 63.4 | 10 | 12 | 16 | 1 | 2 | 17 | 42 |
| Na–VS | 83.8 | 4 | 1 | 33 | 0 | 4 | 2 | 56 |
| K–VS | 85.2 | 2 | 1 | 37 | 0 | 1 | 1 | 57 |
| Rb–VS | 88.5 | 1 | 0 | 33 | 0 | 1 | 1 | 63 |

[a] Catalyst 0.5 g, propane 70 μmol, $O_2$ 140 μmol, reaction time 1 h.
[b] Based on propane.
[c] Based on converted propane. $CO_x$ stands for CO and $CO_2$. The other products were propene oxide, butanone, and hexanes of trace amounts.

**Table C:2 Effects of Various Alkali-Metal-Ions with $VO_4^{3-}/SiO_2$ Conversion and Selectivity Rates under UV.**

**Supplemental text for Appendix C-Table C:2**-The major aspects to consider in the above data table would be the conversion rate and selectivity of various products. Clearly, with application of alkali-metal-ions over $VO_4^{3-}/SiO_2$ (VS), the conversion rate of propane was 63.4% with VS vs. 88.5% with Rb-VS. $CO_x$ ($CO/CO_2$) production increased from 42% vs. 63% with Rb-VS selectivity under UV-light ($\lambda > 310$ nm). Takenaka, S. *et al.*, *Journal of Catalysis* **1995**, *155*, 196-203; **DOI:** 10.1006/jcat.1995.1203 Permission granted by Elesvier Scientific Publishing, Inc. Copyright 1995 ©

Photooxidation of Propane over $V_2O_5/SiO_2$ and Alkali-Ion-Modified $V_2O_5/SiO_2$ Catalysts under Irradiation by the Light of Wavelengths $\lambda > 390$ nm[a]

| Catalyst | Conv.[b] (%) | Selectivity[c] (%) | | | | | | |
|---|---|---|---|---|---|---|---|---|
| | | $C_3H_6$ | $C_2H_5CHO$ | $(CH_3)_2CO$ | $C_2H_3CHO$ | $C_2H_4$ | $CH_3CHO$ | $CO_x$ |
| VS | 5.0 | 43 | 19 | 15 | 0 | tr | 13 | 9 |
| Na–VS | 60.3 | 8 | 7 | 52 | 0 | 1 | 7 | 25 |
| K–VS | 67.0 | 4 | 2 | 51 | 0 | 1 | 3 | 39 |
| Rb–VS | 67.1 | 3 | 1 | 60 | 0 | 1 | 1 | 34 |

[a] Catalyst 0.5 g, propane 70 μmol, $O_2$ 140 μmol, reaction time 1 h.
[b] Based on propane.
[c] Based on converted propane. $CO_x$ stands for CO and $CO_2$. The other products were propene oxide, butanone, and hexanes of trace amounts.

**Table C:3 Effects of Alkali-Metal-Ions over $VO_4^{3-}/SiO_2$ Conversion and Selectivity Rates $\lambda > 390$ nm.**

**Supplemental text for Appendix C-Table C:3**-Similar to Table C:2 above of values with alkali-metal-ions over VS under UV-light, the alkali-metal-ion modified VS has less activity under visible light; whereas, VS essentially has little propane conversion rate. This result supports C.42 DR-UV-vis spectra with VS having little visible light absorption, thereby essentially no visible light photocatalytic activity. Also, the $CO_x$ production increases with alkali-metal-ion use, although K-VS had the most $CO_x$ selectivity percent for propane photooxidation. Takenaka, S. *et al.*, *Journal of Catalysis* **1995**, *155*, 196-203; **DOI:** 10.1006/jcat.1995.1203 Permission granted by Elesvier Scientific Publishing, Inc. Copyright 1995 ©

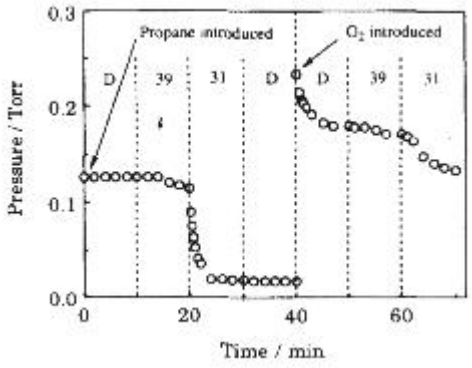


**Figure C:47 Propane Conversion Rate under UV and Visible-Light Unmodified $VO_4^{3-}/SiO_2$ (VS).**

**Supplemental text for Appendix C-C:47**-The above pressure diagram of propane and $O_2$ vs reaction time over VS under dark (D), visible-light (39), and UV-light (31) shows little propane consumption under dark and visible-light ($\lambda > 390$ nm-label in above diagram 39). Under UV-light ($\lambda > 310$ nm), the propane pressure decreases dramatically with $O_2$ pressure decreasing steadily. The $O_2$ consumption was larger under the dark vs. light conditions, which might be due to replenishment of the consumed lattice oxygen in propane photooxidation over VS. Clearly, the above pressure diagram shows that VS would be essentially inactive under dark and visible-light conditions, which supports proposed photodegradation mechanisms with V(x)-MCM-48 presented earlier in Appendix C. Takenaka, S. *et al.*, *Journal of Catalysis* **1995**, *155*, 196-203; **DOI:** 10.1006/jcat.1995.1203 Permission granted by Elesvier Scientific Publishing, Inc. Copyright 1995 ©

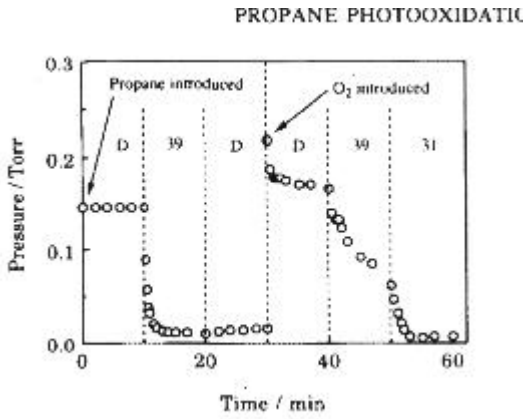


**Figure C:48 $Rb^+$ Ion Effect over $VO_4^{3-}/SiO_2$ (VS) on Propane Conversion Rate under UV and Visible-Light.**

**Supplemental text for Appendix C-C:48**-Similar to C:49 the propane pressure remains steady under dark (D) conditions with Rb-VS; however, with use of visible-light ($\lambda > 390$ nm-labeled above 39), the propane pressure drops quickly. Rb-VS in the dark $O_2$ consumption were similar to UV-light activated VS. The introduction of visible and UV-light led to dramatic reduction in $O_2$ pressure. This indicates that Rb-VS would be visible and UV-light active photocatalytically. Clearly, the above plot supports the dark-visible light activated V(x)-MCM-48 photodegradation mechanism; since, aqua ligand does not bind to the $VO_4^{3-}$ species on silica as noted before and after reaction over Rb-VS with propane in C:42. Takenaka, S. *et al.*, *Journal of Catalysis* **1995**, *155*, 196-203; **DOI:** 10.1006/jcat.1995.1203 Permission granted by Elesvier Scientific Publishing, Inc. Copyright 1995 ©

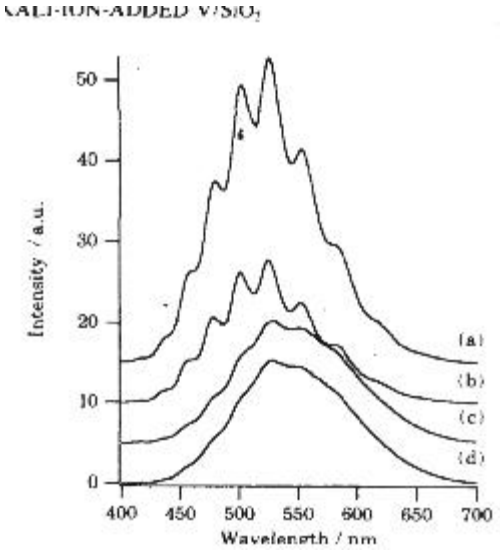


**Figure C:49 Photoluminesence Spectra of $VO_4^{3-}/SiO_2$ (VS) as a Function of Alkali-Metal-Ion Size.**

**Supplemental text for Appendix C-C:49**-In the photoluminescent emission spectra above under 310 nm light at 77 K shows greater electronic modification with larger size alkali-metal-ion, as trend noted in spectrum (a-d): (a) VS; Na-VS; K-VS; and Rb-VS. Spectrum (a) shows the fine-structure for $VO_4^{3-}$ (VS); however, as the alkali-metal-ion size increases, the double-bond V=O character of VS diluted with electron density spread between adjacent alkali-metal-ion and two oxygen atoms, as proposed in C.45 with Rb-VS. Takenaka, S. *et al.*, *Journal of Catalysis* **1995**, *155*, 196-203; **DOI:** 10.1006/jcat.1995.1203 Permission granted by Elesvier Scientific Publishing, Inc. Copyright 1995 ©

ited by 400 nm light at 77 K. Phosphorescent emissior

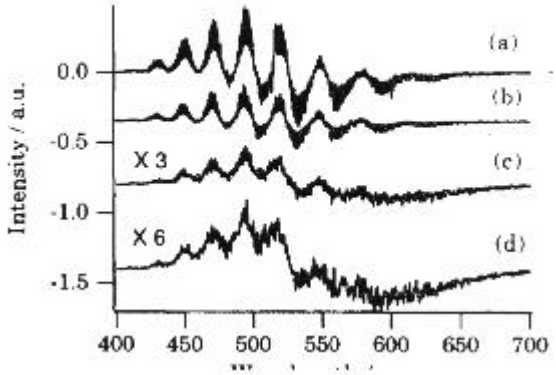


**Figure C:50 First Derivatives of Photoluminesence Spectra with Alkali-Metal-Ions.**

**Supplemental text for Appendix C-C:50**-Futher analysis of photoluminescent emission spectra under 310 nm at 77 K with first derivative analysis shows VS fine-structure decreases substantially with increased alkali-metal-ion, as shown in the above spectra: (a) VS; (b) Na-VS; (c) K-VS; and (d) Rb-VS. This reinforces the above conclusions in C.52. Takenaka, S. *et al.*, *Journal of Catalysis* **1995**, *155*, 196-203; **DOI:** 10.1006/jcat.1995.1203 Permission granted by Elesvier Scientific Publishing, Inc. Copyright 1995 ©

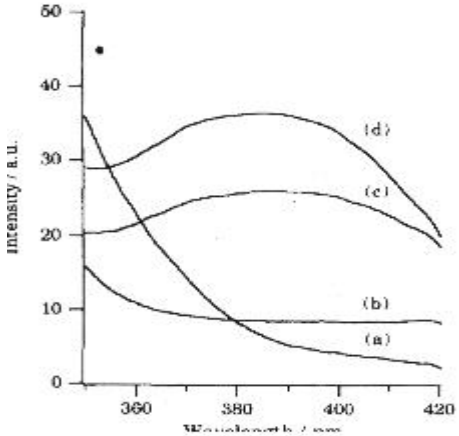


**Figure C:51 Photoluminescence Absorption Spectra for Alkali-Metal-Ion Modified $VO_4^{3-}/SiO_2$.**

**Supplemental text for Appendix C-C:51**-The above photoluminescent excitation spectra shows that the larger the alkali-metal-ion applied over VS led to broad excitation absorption with increased intensity, as shown in above spectra: (a) VS; (b) Na-VS; (c) K-VS; and (d) Rb-VS. The emission from the excitation from the above VS, and alkali-metal-ion modified VS was checked at 530 nm at room temperature. Takenaka, S. *et al.*, *Journal of Catalysis* **1995**, *155*, 196-203; **DOI:** 10.1006/jcat.1995.1203 Permission granted by Elesvier Scientific Publishing, Inc. Copyright 1995 ©

o vibrational fine structure (21). They showed that

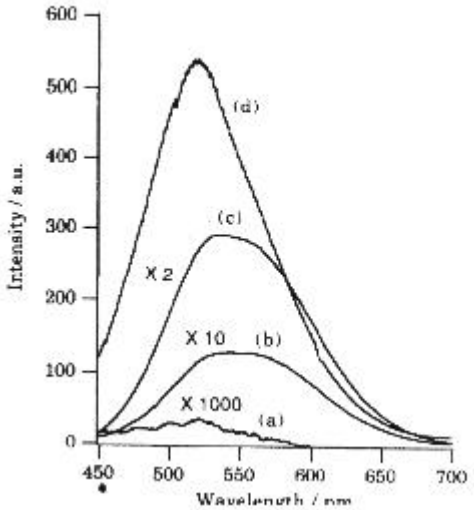


**Figure C:52 Photoluminescene Spectra Excitation Peak Intensity as a Function of Alkali-Metal-Ion Size.**

**Supplemental text for Appendix C-C:52**-The above photoluminescent emission spectra of VS + alkali-metal-ion modified VS with 400 nm light at 77 K: (a) VS; (b) Na-VS; (c) K-VS; and (d) Rb-VS. Clearly, the Rb-VS have the largest emission in comparison to the other spectra, which shows that the $Rb^{+}$ ion has greater control over the electronic states and causes visible-light $VO_4^{3-}$ photocatalytic center. Takenaka, S. *et al.*, *Journal of Catalysis* **1995**, *155*, 196-203; **DOI:** 10.1006/jcat.1995.1203 Permission granted by Elesvier Scientific Publishing, Inc. Copyright 1995 ©

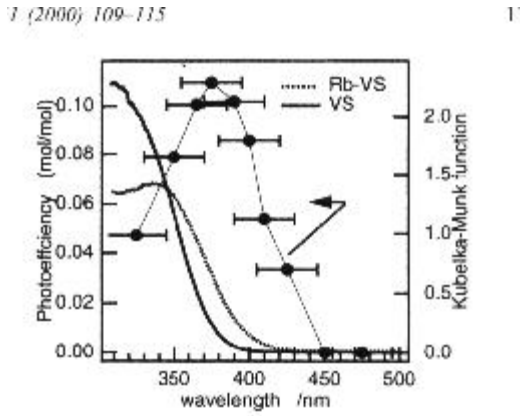


**Figure C:53 $Rb^{+}$ Ion Addition to $VO_4^{3-}/SiO_2$ as a Function of Visible Light Absorption.**

**Supplemental text for Appendix C-C:53**-The Rb-VS photoefficiency would be approximately the highest at 390 nm and decreases increasing wavelength of light to 450 nm. VS had a greater DR-UV-vis absorption under UV-light conditions but decreases to essentially zero in visible light range. Clearly, the introduction of visible-light center with $Rb^{+}$ ion modified $VO_4^{3-}$ on silica has a relatively high even without aqua ligands. Tanaka, T. *et al.*, *Catalysis Today* **2000**, *61*, 109-115; **DOI:** 10.1016/S0920-5861(00)00371-0 Permission granted by Elsevier Scientific Publishing, Inc. Copyright 2000 ©

Conversion and selectivity in percent for photo-oxidation of propane over various photocatalysts (λ>310)[a]

| Catalyst | Conversion (%) | $C_3H_6$ | $CH_3CHO$ | $C_2H_5CHO$ | $(CH_3)_2CO$ | $Co_x$ |
|---|---|---|---|---|---|---|
| VS | 0.11 | 9 | 36 | 27 | 287 | Trace |
| Rb-VS | 0.47 | Trace | 8 | 6 | 43 | 42 |
| K-VS | 0.31 | Trace | 6 | 5 | 45 | 43 |
| Na-VS | 0.24 | Trace | 11 | 12 | 44 | 33 |
| $Mo/SiO_2$ | 0.01 | 42 | 29 | 11 | 17 | Trace |
| $RbMo/SiO_2$ | 0.02 | Trace | Trace | 11 | 88 | Trace |
| $TiO_2$ | 0.42 | 0 | Trace | Trace | 31 | 68 |

[a] The data were obtained at 60 min time on stream.

**Table C:4 Photooxidation Conversion Rate of Propane as Function Alkali-Metal-Ion Used.**

**Supplemental text for Appendix C-Table C:4**-The major aspects to review would be the UV-light activated (λ > 310 nm) photooxidation of propane percent conversion and percent selectivity. Rb-VS had the highest percent conversion of propane with $TiO_2$ close and VS much less. $CO_x$ production was slightly higher for K-VS at 43% selectivity vs. 68% for $TiO_2$. This shows that the increased alkali-metal-ion size leads to greater probe molecule conversion with formation of much greater amounts of $CO_2$ vs. VS. Tanaka, T. *et al.*, *Catalysis Today* **2000**, *61*, 109-115; **DOI:** 10.1016/S0920-5861(00)00371-0 Permission granted by Elsevier Scientific Publishing, Inc. Copyright 2000 ©

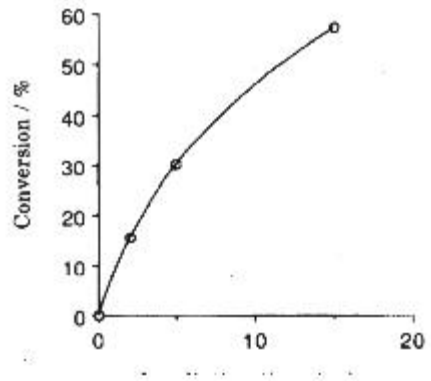


**Figure C:54 Conversion Rate of Propane over $Rb^+$ Ion Modified $VO_4^{3-}/SiO_2$ as Function of Reaction Time.**

**Supplemental text for Appendix C-C:58**-As seen in the above percent visible-light (λ > 390 nm) photooxidation of propane with $^{18}O_2$ + Rb-VS vs. irradiation time in minutes on x-axis. The initial few minute of visible-light irradiation led to increased propane conversion; however, as irradiation time continues to increase, propane conversion decreases, which infers that lattice oxygen ($^{16}O$) first would be consumed and replenished with $^{18}O$. Support for this conclusion would come from no activity under dark conditions, as presented in C.50 and C.51. Takenaka, S. *et al.*, *Journal of Catalysis* **1995**, *155*, 196-203; **DOI:** 10.1006/jcat.1995.1203 Permission granted by Elesvier Scientific Publishing, Inc. Copyright 1995 ©

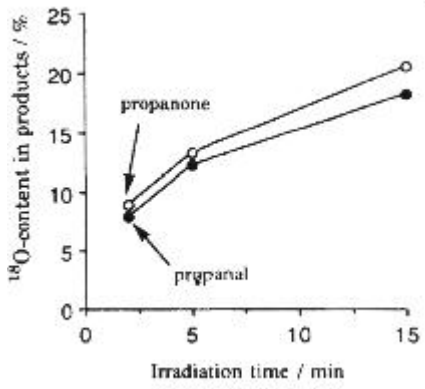


**Figure C:55 Oxygen-18 Content in Propane Photooxidation Products as Function of Irradiation Time.**

**Supplemental text for Appendix C-C:55**-With increased visible-light ($\lambda > 390$ nm), the $^{18}O$ content in propanone and propanal increases due to consumption of lattice oxygen ($^{16}O$) followed by replacement with $^{18}O$. Simple exchange of $^{16}O$ atom for $^{18}O$ atom from $^{18}O_2$ would be slow, so this infers that $^{18}O_2$ acts as a reagent to replace consumed $^{16}O$ lattice atoms. Takenaka, S. *et al.*, *Journal of Catalysis* **1995**, *155*, 196-203; **DOI:** 10.1006/jcat.1995.1203 Permission granted by Elesvier Scientific Publishing, Inc. Copyright 1995 ©

TAKENAK

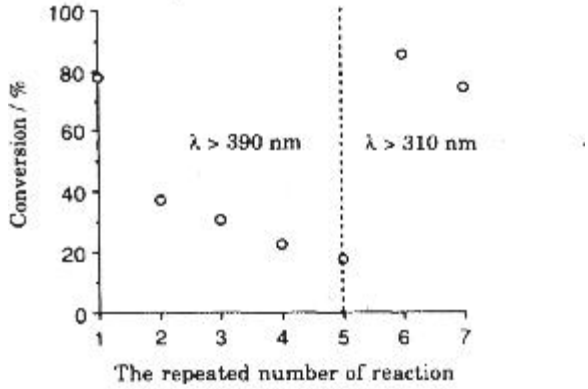


**Figure C:56 Conversion (%) of 2-methylpropane as a Function of the Number of Reaction Cycles over Rb-VS.**

**Supplemental text for Appendix C-C:56**-The two aspects to consider in the above plot would be decreased 2-methylpropane percent conversion with repeated reactions without molecular oxygen and fact of two types of light centers in Rb-VS. For each of the reactions, the duration was 20 minutes. Conversion percent steadily decreases with repeated use without $O_2$, which infers that molecular oxygen would be needed to replace lattice oxygen under visible light. However, the introduction of UV-light leads to increased 2-methylpropane conversion percent with steadily decline with repeated use. Therefore, $O_2$ would be needed to act as a reagent for replacement of lattice oxygen and use of $Rb^+$ leads to visible-light active metal center. Takenaka, S. *et al.*, *Journal of Catalysis* **1995**, *155*, 196-203; **DOI:** 10.1006/jcat.1995.1203 Permission granted by Elesvier Scientific Publishing, Inc. Copyright 1995 ©

TABLE 2

Photoassisted Reaction of Propane in the Absence of Gaseous Oxygen over $V_2O_5/SiO_2$ and Alkali-Ion-Modified $V_2O_5/SiO_2$ Catalysts under Irradiation by the Light of Wavelengths $\lambda > 310$ nm[a]

| Catalyst | Conv.[b] (%) | Selectivity[c] (%) | | | | | | |
|---|---|---|---|---|---|---|---|---|
| | | $C_3H_6$ | $C_2H_5CHO$ | $(CH_3)_2CO$ | $C_2H_3CHO$ | $C_2H_4$ | $CH_3CHO$ | $CO_x$ |
| VS | 11.6 | 80 | 0 | 4 | 0 | 6 | 5 | 5 |
| Na–VS | 15.9 | 80 | tr | 4 | 0 | 3 | 0 | 13 |
| K–VS | 15.9 | 91 | 0 | 2 | 0 | 1 | 0 | 0 |
| Rb–VS | 17.8 | 82 | 0 | 1 | 0 | 1 | 0 | 16 |

[a] Catalyst 0.5 g, propane 70 $\mu$mol, reaction time 1 h.
[b] Based on propane.
[c] Based on converted propane. $CO_x$ stands for CO and $CO_2$.

**Table C:5 Conversion (%) of Propane in Absence $O_2$ under UV with VS and Alkali-Metal-Ion Modified VS.**

**Supplemental text for Appendix C- Table C:5**-As would be expected, the propane percent conversion rate was much lower for VS and alkali-metal-ion modified VS under UV-light noted earlier in C.48. Propylene selectivity was high for all of the catalysts, which could be due to less oxygen available for successive deep oxidation reaction to occur. Takenaka, S. *et al.*, *Journal of Catalysis* **1995**, *155*, 196-203; **DOI:** 10.1006/jcat.1995.1203 Permission granted by Elesvier Scientific Publishing, Inc. Copyright 1995 ©

Table 1

Results of photo-oxidation of propylene over Rb–VS samples[a]

| Sample | Rb/V | $S_{BET}$[b] ($m^2 g^{-1}$) | TOS (min)[c] | $C_3H_6$ conversion (%) | Selectivity (%) | | | |
|---|---|---|---|---|---|---|---|---|
| | | | | | PO | $C_3$[d] | Ethanal | CO |
| VS | 0 | 588 | 180 | 0.38 | 13.7 | 19.4 | 52.4 | 14. |
| Rb–VS | 0.5 | 510 | 60 | 0.59 | 27.6 | 7.7 | 31.2 | 33. |
| | 1 | 485 | 60 | 1.40 | 31.3 | 6.2 | 15.8 | 46. |
| | 1.5 | 348 | 60 | 1.56 | 30.7 | 6.8 | 15.3 | 47. |
| | | | 600 | 1.39 | 28.1 | 8.1 | 15.0 | 48 |
| | 3 | 296 | 60 | 1.50 | 19.3 | 4.6 | 10.2 | 65 |
| | 6 | 191 | 60 | 1.02 | 8.9 | 4.8 | 6.2 | 80 |
| $SiO_2$ | | 650 | 180 | 0.01 | 72.3 | 0.0 | Trace | 27 |

[a] $V_2O_5$ loading 0.5 wt%.
[b] BET specific surface area.
[c] Time on stream.
[d] Oxygenated $C_3$ products: acrolein, acetone, and propanal.

**Table C:6 Photooxidation of Propylene Results over VS, Rb-VS, and Rb-VA.**

**Supplemental text for Appendix C-Table C:6**-Although propylene percent conversion would be substantially less than propane, larger Rb/V loading ratio led to increased propylene percent conversion to $CO_2$ with 80.1% selectivity. This occurred even with a significant reduction in surface area from 588 $m^2/g$ for VS to 191 $m^2/g$ with a Rb/V ratio of 6. Clearly, this shows that large loading of $Rb^+$ ion leads to increase probe molecule conversion to $CO_2$. Amano, F.; Tanaka, T. *Catalysis Communications* **2005**, *6*, 269-273; **DOI:** 10.1016/j.catcom.2005.01.007 Permission granted by Elsevier Scientific Publishing, Inc. Copyright 2005 ©

TABLE 3

Oxidative Dehydrogenation of *n*-Butane on Supported Vanadium Catalysts

| Sample | W/F[a] | T (°C) | Conversion (%) | Catalytic activity (mol $C_4$ $h^{-1}$ $g_{cat}^{-1}$) | TOF (mol $C_4$ $h^{-1}$ mol-$V^{-1}$) | Selectivity (%) ODH[b] | CO | $CO_2$ | Others[c] |
|---|---|---|---|---|---|---|---|---|---|
| V/MG | 4.1 | 500 | 11.2 | 2.73 | 12.4 | 58.6 | 9.7 | 29.4 | 2.3 |
| | | 525 | 17.6 | 4.29 | 19.5 | 62.0 | 9.9 | 26.1 | 2.0 |
| | | 550 | 25.7 | 6.27 | 28.5 | 61.2 | 10.7 | 26.2 | 1.9 |
| V/HTH | 10 | 500 | 10.9 | 1.09 | 3.63 | 50.4 | 12.8 | 33.2 | 3.6 |
| | | 525 | 16.6 | 1.66 | 5.53 | 53.5 | 13.0 | 29.8 | 3.7 |
| | | 550 | 22.7 | 2.27 | 7.57 | 54.9 | 12.7 | 29.1 | 3.3 |
| V/SEP | 20 | 500 | 10.6 | 0.53 | 14.3 | 49.1 | 22.1 | 26.0 | 2.9 |
| | | 525 | 14.0 | 0.70 | 18.9 | 52.3 | 20.9 | 24.1 | 2.7 |
| | | 550 | 19.0 | 0.95 | 25.7 | 48.5 | 23.9 | 24.6 | 2.9 |
| V/AL | 2.3 | 500 | 9.9 | 4.30 | 113 | 53.7 | 21.8 | 21.8 | 2.7 |
| | | 525 | 16.1 | 7.00 | 184 | 45.2 | 28.6 | 24.0 | 2.2 |
| | | 550 | 26.0 | 11.3 | 297 | 34.9 | 36.4 | 26.6 | 2.1 |

[a] Contact time, W/F in $g_{cat}$ h (mol $C_4$)$^{-1}$.
[b] Selectivity to $C_4$-olefins (1-butene, 2-butenes, and butadiene).
[c] $C_2$ and $C_1$-hydrocarbons.

**Table C:7 Conversion Rate of *n*-Butane over Modified $VO_x$ in Oxidative Dehydrogenation.**

**Supplemental text for Appendix C-Table C:7**-The key aspects to review in the above table of values for oxidative dehydrogenation of *n*-butane would be the contact time (W/F), percent conversion, catalytic activity, and selectivity of products. Focusing on the $CO_2$ production, V/HTH had largest $CO_2$ selectivity of 33.2% with conversion *n*-butane rate of 10.9%. Second, V/MG had 29.4% selectivity and 11.2 percent n-butane conversion. V/SEP was third largest $CO_2$ selectivity of 26.0% with conversion of 10.6%. V/AL had the lowest $CO_2$ selectivity of 21.8% with conversion of *n*-butane of 9.9%. The trend would be higher basicity leads to greater $CO_2$ production. This could be due to larger $V^{5+}$ loading coupled with basic support would lead to increased basicity, thereby causing increased $CO_2$ production. However, the $V^{5+}$ loading was not the same over the four supports, as shown in C.64 below; therefore, the *n*-butane conversion rate would be largest for V/AL with acidic $Al_2O_3$ support. Blasco, T. *et al.*, *Journal of Catalysis* **1995**, *157*, 271-282; **DOI:** 10.1006/jcat.1995.1291 Permission granted by Elsevier Scientific Publishing, Inc. Copyright 1995 ©

TABLE 1

Characteristics of Supports and Supported Vanadium Catalysts

| Sample | $S_{BET}$ ($m^2$ $g^{-1}$) | $V_2O_5$ (wt%) | Atomic ratio (%)[c] V | Mg | Al | Si |
|---|---|---|---|---|---|---|
| MgO | 140 | 0 | — | 100 | — | — |
| V/MG | 108 | 20.0 | 10.0 | 90.0 | — | — |
| HTH[a] | 196 | 0 | — | 73.0 | 27.0 | — |
| V/HTH | 166 | 27.0 | 8.5 | 67.0 | 24.5 | — |
| Sepiolite[b] | 139 | 0 | — | 38.3 | 1.1 | 60.6 |
| V/SEP | 82.4 | 6.7 | 4.1 | 36.8 | 1.0 | 58.1 |
| $Al_2O_3$ | 188 | 0 | — | — | 100 | — |
| V/AL | 160 | 7.0 | 4.4 | — | 95.6 | — |

[a] Heat-treated hydrotalcite type.
[b] Natural Sepiolite. Chemical composition as in Ref. (12).
[c] Chemical analysis of the elements was done by atomic absorption spectrometry.

**Table C:8 Bulk Properties of Various Modified $VO_x$ Catalysts.**

**Supplemental text for Appendix C-Table C:8**-As noted in Table C:7, the $V_2O_5$ loading was highest on basic MgO and HTH supports in comparison to acidic SEP and $Al_2O_3$ supports. From comparing the $V_2O_5$ loading and $CO_2$ production in Table C:7, a trend of higher $V^{5+}$ loading on basic support leads to more $CO_2$ production. Blasco, T. *et al.*, *Journal of Catalysis* **1995**, *157*, 271-282; **DOI:** 10.1006/jcat.1995.1291 Permission granted by Elsevier Scientific Publishing, Inc. Copyright 1995 ©

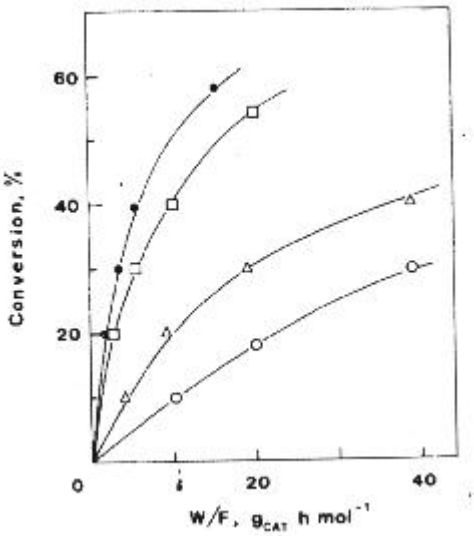


**Figure C:57 Conversion *n*-Butane Rate as Function of Reaction Time over Modified $VO_x$ Catalysts.**

**Supplemental text for Appendix C-C:57**-The *n*-butane percent conversion rate vs. contact time (W/F) shows at 550°C following trend: (●) V/AL; (□) V/MG; (Δ) V/SEP; and (○) V/HTH. Blasco, T. *et al.*, *Journal of Catalysis* **1995**, *157*, 271-282; **DOI:** 10.1006/jcat.1995.1291 Permission granted by Elsevier Scientific Publishing, Inc. Copyright 1995 ©

Table 1
Photooxidation of 2-methylpropane over VS and alkali-ion-modified VS catalysts by irradiation by light of wavelengths $\lambda > 310$ nm [a]

| Catalysts [b] | Conv. [c] (%) | Selectivity [d] (%) | | | | | | | |
|---|---|---|---|---|---|---|---|---|---|
| | | IB | PR | AA | AC | TB | BA | ML | COx |
| VS [e] | 58.4 | 8 | 6 | 10 | 36 | 0 | 9 | 1 | 29 |
| Na-VS | 84.6 | 7 | 1 | 2 | 41 | 1 | 3 | 1 | 39 |
| K-VS | 90.7 | 6 | 1 | 2 | 51 | 5 | 2 | 1 | 31 |
| Rb-VS [e] | 94.3 | 6 | 1 | 1 | 51 | 5 | 3 | 1 | 31 |

[a] Catalyst 0.5 g, 2-methylpropane 70 μmol, $O_2$ 140 μmol, irradiation time 60 min.
[b] The contents of alkali-ion are 1, 2, or 4 wt% as $Na_2O$, $K_2O$, or $Rb_2O$, respectively.
[c] Based on introduced 2-methylpropane.
[d] Based on converted 2-methylpropane. IB 2-methylpropene, PR propene, AA ethanal, AC propanone, TB 2-methylpropan-2-ol, BA 2-methylpropanal, ML methacrolein, COx CO and $CO_2$. Trace amounts of methanol, ethene, propene oxide, propanal, propan-2-ol, and 2-methylpropanol were formed.
[e] Taken from ref. [13].

**Table C:9 Photooxidation Conversion Rate of 2-methylpropane over VS and Alkali-Metal-Ion VS.**

**Supplemental text for Appendix C-Table C:9**-The above data table of 2-methylpropane photooxidation under UV-light ($\lambda > 310$ nm) clearly shows that percent conversion dramatically increases from VS to Rb-VS. The $CO_x$ production was the largest for Na-VS in contrast to Rb-VS with propane, which might be due to the size of the alkali-metal-ion hindering the larger 2-methylpropane molecule from fully interacting with metal center. Takenaka, S. *et al.*, *Catalysis Letters* **1997**, *44*, 67-74; **DOI:** 10.1023/A:1018944118203 Permission granted by J.C. Baltzer, Science Publishers Copyright 1997 ©

10.0 wt % (d) under irradiation; catalyst $V_2O_5/SiO_2$ (0.3 g); total fl
He.

**Table 1. Results of Photooxidation of Propene over Various Catalysts under Irradiation[a]**

| catalyst | conversion rate ($\mu$mol min$^{-1}$) | selectivity[b] (C%) | | | | | |
|---|---|---|---|---|---|---|---|
| | | PO | PA | AC | AL | AA | $CO_2$ |
| $TiO_2$ | 1.11 | 0 | 0 | 6 | 0 | 13 | 80 |
| $SiO_2$ | 0.01 | 100 | 0 | 0 | 0 | 0 | 0 |
| 0.18 VS | 0.71 | 43 | 2 | 7 | 6 | 33 | 7 |
| 0.18 VS[c] | 0.00 | 0 | 0 | 0 | 0 | 0 | 0 |
| 0.5 VS | 0.72 | 30 | 5 | 5 | 8 | 43 | 9 |
| 2.5 VS | 0.65 | 23 | 14 | 2 | 20 | 33 | 7 |
| 10.0 VS | 0.65 | 9 | 34 | 5 | 10 | 36 | 5 |

[a] The data were obtained at 5 h on stream. Conditions: $TiO_2$ (0.6 g), $x$ VS = $x$ wt % $V_2O_5/SiO_2$ (0.3 g), $SiO_2$ (0.4 g); total flow rate 100 mL min$^{-1}$; reactants 20% $C_3H_6$, 10% $O_2$, and 70% He. [b] PO = propene oxide, PA = propanal, AC = acetone, AL = acrylaldehyde, and AA = ethanol. [c] Reaction in the dark at 373 K.

**Table C:10 Propene Conversion Rate over Various $V^{5+}$ loadings over Silica.**

**Supplemetal text for Appendix C-Table C:10**-As seen in the above data table of propene photooxidation under UV-light, the conversion rate was 0.72 µmole/minute at 0.5wt% $V_2O_5$ loading on VS with little $CO_2$ production. [1] Whereas, application of Rb ion of Rb/V ratio of 1.5 over VS (0.5 wt% $V_2O_5$ loading) led to 186 µmole/hour rate (3.1 µmole/minute). [2] This clearly shows alkali-metal-ion use enhances conversion rate and $CO_2$ production, as shown in C.62 earlier. Amano, F. *et al.*, *Langmuir* **2004**, *20*, 4236-4240; **DOI:** 10.1021/la0359981 Permission granted by American Chemical Society Copyright 2004 ©


1. Amano, F. *et al.*, *Langmuir* **2004**, *20*, 4236-4240
2. Amano, F.; Tanaka, T. *Catalysis Communications* **2005**, *6*, 269-273


Table 4

Photooxidation of 2-methylpropane over $V_2O_5/SiO_2$ modified by KOH, $KNO_3$ or $NH_3$ by irradiation by light of wavelengths $\lambda > 390$ nm [a]

| Catalyst [b] | Conv. [c] (%) | Selectivity [d] (%) | | | | | | |
|---|---|---|---|---|---|---|---|---|
| | | IB | PR | AA | AC | TB | BA | COx |
| VS | 1.7 | 42 | 6 | 0 | 23 | 0 | 18 | tr [e] |
| $NH_3$-VS | 2.4 | 31 | 8 | 3 | 28 | 1 | 18 | tr [e] |
| K-VS | 38.4 | 10 | 1 | tr [e] | 51 | 13 | 12 | 3 |
| Kn-VS | 19.9 | 13 | 1 | tr [e] | 52 | 7 | 13 | 3 |

[a] Catalyst 0.5 g, 2-methylpropane 70 µmol, $O_2$ 140 µmol, irradiation time 15 min.
[b] The contents of alkali-ion are 2 wt% as $K_2O$.
[c] Based on introduced 2-methylpropane.
[d] Based on converted 2-methylpropane. IB 2-methylpropene, PR propene, AA ethanal, AC propanone, TB 2-methylpropan-2-ol, BA 2-methylpropanal, COx CO and $CO_2$. Trace amounts of methanol, ethene, propene oxide, propanal, propan-2-ol, methacrolein and 2-methylpropanol were formed.
[e] tr trace amount.

**Table C:11 Photooxidation Conversion 2-methylpropane Rate over Modified $VO_4^{3-}/SiO_2$.**

**Supplemental text for Appendix C-Table C:11**-Reviewing the percent conversion of 2-methylpropane over modified VS with $NH_3$, KOH, or $KNO_3$, the KOH prepared VS ($VO_4^{3-}/SiO_2$) had the largest converstion rate with small amount of $CO_2$ made. Takenaka, S. *et al*., *Catalysis Letters* **1997**, *44*, 67-74; **DOI:** 10.1023/A:1018944118203 Permission granted by J.C. Baltzer, Science Publishers Copyright 1997 ©

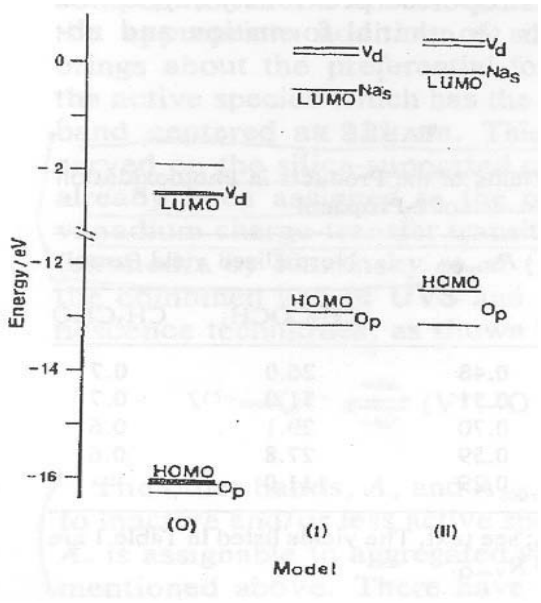


**Figure C:58 Molecular Orbital Digram with use of Sodium Ion over Model $VO_4^{3-}$.**

**Supplemental text for Appendix C-C:58**-The above molecular orbital diagram with sodium ion over model $VO_4^{3-}$ on silica shows that energy separation between LUMO and HUMO orbitals decreases and shift of potential to more basic values. In model (l) and (ll) the LUMO would be primarily on the $Na^+$ ion. Tanaka, T. *et al*., *Journal of Catalysis* **1989**, *118*, 327-338; **DOI:** 10.1016/0021-9517(89)90321-7 Permission granted by Elsevier Scientific Publishing, Inc. Copyright 1989 ©

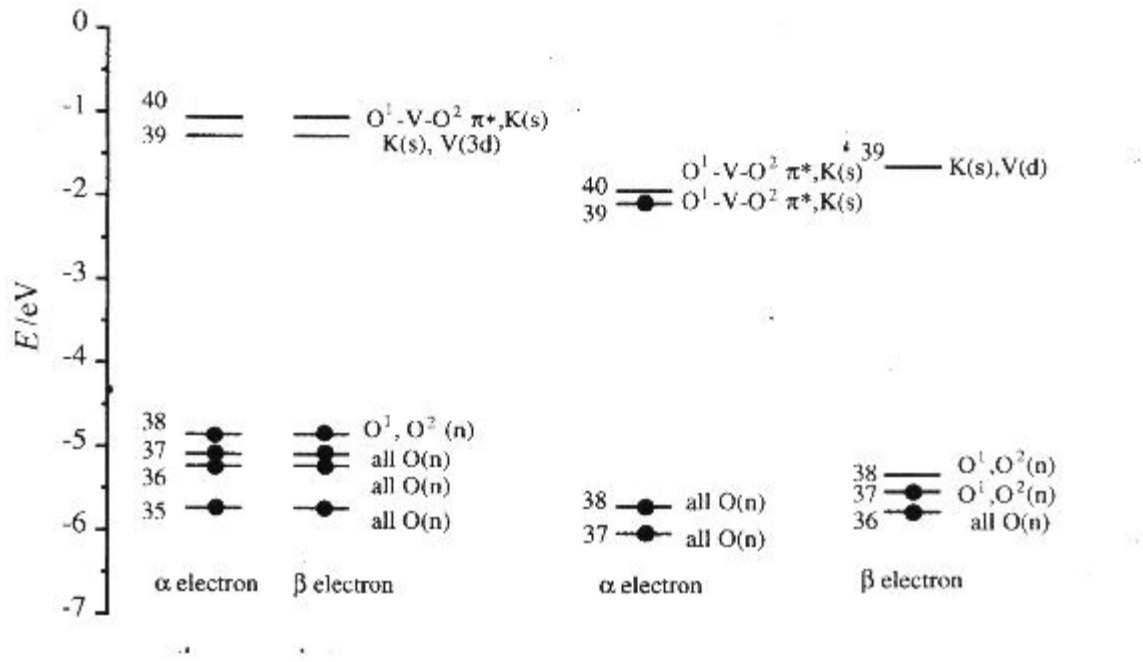


**Figure C:59 Molecular Orbital Diagram with $K^+$ ion over $VO_4^{3-}/SiO_2$.**

**Supplemental text for Appendix C-C:59**-The above molecular orbital diagram shows the promotion 38β electron to 39 $O^1$-V-$O^2$ π*, K(s) triplet energy state under visible-light. The $K^+$ ion converts the V=O and one V-O-Si support bond to elongated $O^1$-V-$O^2$ species with $K^+$ ion adjacent. As seen above, this changes the triplet energy state, which permits more probe molecule interaction leading to more product production. Takenaka, S. *et al*., *Journal of*

*Chemical Society, Faraday Transactions* **1997**, *93*, 4151-4158; **DOI:** 10.1039/a704794k Permission granted by Royal Society of Chemistry Copyright 1997 ©

electrons in the triplet state) of the non-bonding orbitals

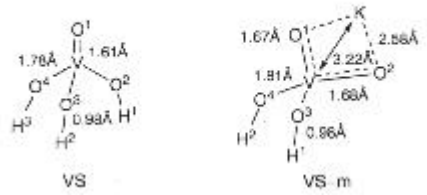


**Figure C:60 Pictorial Representations of VS and K-VS.**

**Supplemental text for Appendix C-C:60**-The proposed model of K-VS shows that the V=O lengthens and V-O bond shortens with $K^+$ ion adjacent to $V^{5+}$ metal center. This spread out double bond character over several atoms enhances the triplet state leading to more probe molecule interactions. Takenaka, S. *et al*., *Journal of Chemical Society, Faraday Transactions* **1997**, *93*, 4151-4158; **DOI:** 10.1039/a704794k Permission granted by Royal Society of Chemistry Copyright 1997 ©

Ground State and Lowest Triplet St

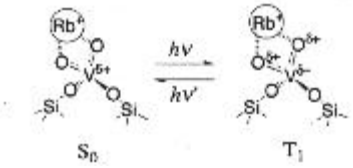


**Figure C:61 $Rb^+$ Ion with $VO_4^{3-}/SiO_2$ in Singlet and Triplet Electronic States.**

**Supplemental text for Appendix C-C:61**-The above pictorial representation of Rb-VS in ground singlet state ($S_0$) and excited triplet state ($T_1$) shows that the two oxygen atoms close to $Rb^+$ ion become electrophilic in $T_1$ state under UV-vis light with $V^{5+}$ gaining electron density. This electrophilic nature of oxygen species might explain increased $CO_2$ production with alkali-metal-ions over VS. Amano, F. *et al*., *Journal of Physical Chemistry B* **2005**, *109*, 10973-10977; **DOI:** 10.1021/jp0507871 Permission granted by American Chemical Society Copyright 2005 ©

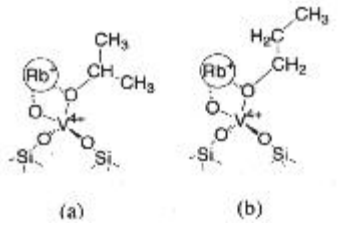


**Figure C:62 $Rb^+$ Ion with $VO_4^{3-}/SiO_2$ Interactions Primary and Secondary Hydrogens in Propane.**

**Supplemental text for Appendix C-C:62**-The above model shows that $V^{5+}$ reduce to $V^{4+}$ with propane molecule attached in Rb-VS. Using model calculation between 2-propanol and 1-propanol, 3.4 kcalorie/mole differences in stability of the secondary carbon favored over primary carbon. This might explain why 2-propanol forms with propane photooxidation vs. 1-propanol. Amano, F. *et al*., *Journal of Physical Chemistry B* **2005**, *109*, 10973-10977; **DOI:** 10.1021/jp0507871 Permission granted by American Chemical Society Copyright 2005 ©

# Appendix D - Copyright Page-Permission to Reproduce Material in Thesis

## Note of appreciation to Authors and Publishers:

I would like to express deep graditude to all of the authors' and publishers for granting their permission to use the various images and data tables to illustrate certain points throughout the master's thesis.

### Journal Publishers Key:

| Journal Publisher | Journal Publisher's Web-Site | Journal Titles |
|---|---|---|
| American Chemical Society | www.pubs.acs.org | *Journal of Physical Chemistry B; Langmuir; Chemical Reviews; Chemistry of Materials; Journal of the American Chemical Society* |
| Elsevier Scientific Publishing, Inc.-Now-Elsevier, Inc. | www.sciencedirect.com | *Journal of Catalysis; Catalysis Communications; Chemical Physics Letters; Inorganica Chimica Acta; Catalysis Today; Microporous and Mesoporous Materials; Spectrochimica Acta Part A: Molecular and Biomolecular Spectroscopy; Solid State Sciences; Journal of Physics and Chemistry of Solids; Zeolites* |
| Royal Society of Chemistry | www.rsc.org/Pubishing/Journals/Index.asp | *Journal of the Chemical Society, Faraday Transactions; Journal of Materials Chemistry; Chemical Communications* |
| Spinger Netherlands | www.springerlink.com/content/101742/ | *Catalysis Letters* |
| John Wiley & Sons, Inc-Wiley InterScience | www3.interscience.wiley.com/browse/?subject=CHEM | *Angewandte Chemie International Edition* |
| American Association for the Advancement of Science | www.sciencemag.org/ | *Science* |

## Chapter-1-Introduction

1. Schumacher, K.; Ravikovitch, P. I.; Du Chesne, A.; Neimark, A. V.; Unger, K. K.. *Langmuir* **2000**, *16*, 4648-4654; **DOI:** 10.1021/la991595i Permission granted by American Chemical Society Copyright 2000 ©

## Chapter-2-Literature Review of M41S Mesoporous Silica Materials

1. Collart, O.; Cool, P.; Voort, P.V.D.; Meynen, V.; Vansant, E. F.; Houthoofd., K.; Grobet, P.J.; Lebedev, O.I.;; Tendeloo, G. V. *Journal of Physical Chemistry B* **2004**, *108*, 13905-13912; **DOI:** 10.1021/jp049837x Permission granted by American Chemical Society Copyright 2004 ©

2. Moore, J. W.; Stanitski, C. L.; Jurs, P. C. "*Chemistry The Molecular Science*," **First Edition**, Chapter 11, pages 500-501 Permission granted by Thomson Learning Brooks/Cole Publishing Company, a part of Cengage Learning, Inc. (www.cengage.com/permissions) Copyright 2002 ©

3. Brus, L., *Journal of Physical Chemistry* **1986**, *90*, 2555-2560; **DOI:** 10.1021/j100403a003 Permission granted by the American Chemical Society Copyright 1986 ©

4. Fyfe, C. A.; Fu, G., *Journal of the American Chemical Society* **1995**, *117*, 9709-9714; **DOI:** 10.1021/ja00143a014 Permission granted by American Chemical Society Copyright 1995 ©

5. Raman, N. K.; Anderson, M. T.; Brinker, C. J. *Chemistry of Materials* **1996**, *8*, 1682-1701; **DOI:** 10.1021/cm960138+ Permission granted by the American Chemical Society Copyright 1996 ©

6. Anderson, M. W. *Zeolites* **1997**, *19*, 220-227; **DOI:** 10.1016/S0144-2449(97)00061-4 Permission granted by Elsevier Scientific Publishing, Inc. Copyright 1997 ©

7. Shao, Y.; Wang, L.; Zhang, J.; Anpo, M. *Journal of Physical Chemistry B* **2005**, *109*, 20835-20841; **DOI:** 10.1021/jp054024+ Permission granted by American Chemical Society Copyright 2005 ©

8. Cheng, C-F.; Zhou, W.; Park, D. H.; Klinowski, J.; Hargreaves, M.; Gladden, L. F. *Journal of the Chemical Society, Faraday Transactions* **1997**, *93*, 359-363; **DOI:** 10.1039/a605136g Permission granted by Royal Society of Chemistry Copyright 1997 ©

9. Taralkar, U. S.; Kasture, M. W.; Joshi, P. N. *Journal of Physics and Chemistry of Solids* **2008**, *69*, 2075-2081; **DOI:** 10.1016/j.jpcs.2008.03.004 Permission granted by Elsevier Scientific Publishing, Inc. Copyright 2008 ©

10. Monnier, A.; Schuth, F.; Huo, Q.; Kumar, D.; Margolese, D.; Maxwell, R. S.; Stucky, G. D.; Krishnamurty, M.; Petroff, P.; Firouzi, A.; Janicke, M.; Chmelka, B. F. *Science* **1993**, *261*, 1299-1303; **DOI:** 10.1126/science.261.5126.1299 Permission granted by the American Association Advancement of Science Copyright 1993 ©

11. Zhao, W.; Kong, L.; Luo, Y.; Li, Q. *Microporous and Mesoporous Materials* **2007**, *100*, 111-117; **DOI:** 10.1016/j.micromeso.2006.10.020 Permission granted by Elsevier Scientific Publishing, Inc. Copyright 2006 ©

12. Firouzi, A.; Kumar, D.; Bull, L. M.; Besier, T.; Sieger, P.; Huo, Q.; Walker, S. A.; Zasadzinski, J. A.; Glinka, C.; Nicol, J.; Margolese, D.; Stucky, G. D.; Chmelka, B. F. *Science* **1995**, *267*, 1138-1143; **DOI:** 10.1126/science.7855591 Permission granted by American Association Advancement of Science Copyright 1995 ©

13. Tolbert, S. H.; Landry, C. C.; Stucky, G. D.; Chmelka, B. F.; Norby, P.; Hanson, J. C.; Monnier, A. *Chemistry of Materials* **2001**, *13*, 2247-2256; **DOI:** 10.1021/cm0003727 Permission granted by American Chemical Society Copyright 2001 ©

14. Landry, C. C.; Tolbert, S. H.; Gallis, K. W.; Monnier, A.; Stucky, G. D.; Norby, P.; Hanson, J. C. *Chemistry of Materials* **2001**, *13*, 1600-1608; **DOI:** 10.1021/cm000373z Permission granted by American Chemical Society Copyright 2001 ©

15. Echchahed, B.; Morin, M.; Blais, S.; Badiei, A-R.; Berhault, G.; Bonneviot, L. *Microporous and Mesoporous Materials* **2001**, *44-45*, 53-63; **DOI:** 10.1016/S1387-1811(01)00168-8 Permission granted by Elsevier Scientific Publishing, Inc. Copyright 2001 ©

16. Yu, C.; Fan, J.; Tian, B.; Zhao, D. *Chemistry of Materials* **2004**, *16*, 889-898; **DOI:** 10.1021/cm035011g Permission granted by American Chemical Society Copyright 2004 ©

17. Lebedev, O. I.; Tendeloo, G. V.; Collart, O.; Cool, P.; Vansant, E. F. *Solid State Sciences* **2004**, *6*, 489-498; **DOI:** 10.1016/j.solidstatesciences.2004.01.013 Permission granted by Elsevier Scientific Publishing, Inc. Copyright 2004 ©

18. Kim, J. M.; Kim, S. K.; Ryoo, R. *Chemical Communications* **1998**, 259-260; **DOI:** 10.1039/a707677k Permission granted by the Royal Society of Chemistry Copyright 1998 ©

19. Corma, A.; Kan, Q.; Rey, F. *Chemical Communications* **1998**, 579-580; **DOI:** 10.1039/a709093e Permission granted by Royal Society of Chemistry Copyright 1998 ©

20. Galarneau, A.; Driole, M-F.; Petitto, C.; Chiche, B.; Bonelli, B.; Armandi, M.; Onida, B.; Garrone, E.; Di Renzo, F.; Fajula, F. *Microporous and Mesoporous Materials* **2005**, *83*, 172-180; **DOI:** 10.1016/j.micromeso.2005.03.020 Permission granted by Elsevier Scientific Publishing, Inc. Copyright 2005 ©

21. Coasne, B.; Galarneau, A.; Di Renzo, F.; Pellenq, R. J. M. *Langmuir* **2006**, *22*, 11097-11105; **DOI:** 10.1021/la0611728h Permission granted by American Chemical Society Copyright 2006 ©

22. Kleitz, F.; Schmidt, W.; Schuth, F. *Microporous and Mesoporous Materials* **2003**, *65*, 1-29; **DOI:** 10.1016/S1387-1811(03)00506-7 Permission granted by Elsevier Scientific Publishing, Inc. Copyright 2003 ©

23. Chen, L.; Horiuchi, T.; Mori, T.; Maeda, K. *Journal of Physical Chemistry B* **1999**, *103*, 1216-1222; **DOI:** 10.1021/jp983100o Permission granted by American Chemical Society Copyright 1999 ©

24. Keene, M. T. J.; Gougeon, R. D. M.; Denoyel, R.; Harris, R. K.; Rouquerol, J.; Llewellyn, P. L. *Journal of Materials Chemistry* **1999**, *9*, 2843-2850; **DOI:** 10.1039/a904937a Permission granted by Royal Society of Chemistry Copyright 1999 ©

25. Vralstad, T. "Synthesis and characterization of cobalt-containing mesoporous model catalysts," Ph.D. Thesis, December, 2005 Norwegian University of Science and Technology http://www.chemeng.ntnu.no/research/polymer/ugelstadlab/thesis/tyralstad.pdf (accessed 12/12/08)

26. Lin, H-P.; Mou, C-Y., *Microporous and Mesoporous Materials* **2002**, *55*, 69-80; **DOI:** 10.1016/S1387-1811(02)00407-9 Permission granted by Elsevier Scientific Publishing, Inc. Copyright 2002 ©

27. Cheng, C-F.; Park, D. H.; Klinowski, J. *Journal of the Chemical Society, Faraday Transactions* **1997**, *93*, 193-197; **DOI:** 10.1039/a605100f Permission granted by Royal Society of Chemistry Copyright 1997 ©

28. Di Renzo, F.; Testa, F.; Chen, J. D.; Cambon, H.; Galarneau, A.; Plee, D.; Fajula, F. *Microporous and Mesoporous Materials* **1999**, *28*, 437-446; **DOI:** 10.1016/S1387-1811(98)00315-1 Permission granted by Elsevier Scientific Publishing, Inc. Copyright 1999 ©

29. Wang, L.; Shao, Y.; Zhang, J.; Anpo, M. *Microporous and Mesoporous Materials* **2006**, *95*, 17-25; **DOI:** 10.1016/j.micromeso.2006.04.016 Permission granted by Elsevier Scientific Publishing, Inc. Copyright 2006 ©

30. Vralstad, T.; Oye, G.; Stocker, M.; Sjoblom, J. *Microporous and Mesoporous Materials* **2007**, *104*, 10-17; **DOI:** 10.1016/j.micromeso.2006.06.006 Permission granted by Elsevier Scientific Publishing, Inc. Copyright 2006 ©

31. Chen, D.; Li, Z.; Yu, C.; Shi, Y.; Zhang, Z.; Tu, B.; Zhao, D. *Chemistry of Materials* **2005**, *17*, 3228-3234; **DOI:** 10.1021/cm50209h Permission granted by American Chemical Society Copyright 2005 ©

32. Voort, P. V. D.; Baltes, M.; Vansant, E. F. *Catalysis Today* **2001**, *68*, 119-128; **DOI:** 10.1016/S0920-5861(01)00273-3 Permission granted by Elsevier Scientific Publishing, Inc. Copyright 2001 ©

33. Huo, Q.; Margolese, D. I.; Ciesla, U.; Demuth, D. G.; Feng, P.; Gier, T. E.; Sieger, P.; Firouzi, A.; Chmelka, B. F.; Schuth, F.; Stucky, G. D. *Chemistry of Materials* **1994**, *6*, 1176-1191; **DOI:** 10.1021/cm00044a016 Permission granted by American Chemical Society Copyright 1994 ©

34. Kong, L.; Liu, S.; Yan, X.; Li, Q.; He, H. *Microporous and Mesoporous Materials* **2005**, *81*, 251-257; **DOI:** 10.1016/j.micromeso.2005.02.011 Permission granted by Elsevier Scientific Publishing, Inc. Copyright 2005 ©

35. Kim, W. J.; Yoo, J. C.; Hayhurst, D. T. *Microporous and Mesoporous Materials* **2002**, *49*, 125-137; **DOI:** 10.1016/S1387-1811(01)00410-3 Permission granted by Elsevier Scientific Publishing, Inc. Copyright 2001 ©

36. Van Der Voort, P.; Mathieu, M.; Mees, F.; Vansant, E. F. *Journal of Physical Chemistry B* **1998**, *102*, 8847-8851; **DOI:** 10.1021/jp982653w Permission granted by American Chemical Society Copyright 1998 ©

37. Ryoo, R.; Joo, S. H.; Kim, J. M. *Journal of Physical Chemistry B* **1999**, *103*, 7435-7440; **DOI:** 10.1021/jp9911649 Permission granted by American Chemical Society Copyright 1999 ©

38. Gomez, S.; Garces, L. J.; Villegas, J.; Ghosh, R.; Giraldo, O.; Suib, S. L. *Journal of Catalysis* **2005**, *233*, 60-67; **DOI:** 10.1016/j.cat2005.04.015 Permission granted by Elsevier Scientific Publishing, Inc. Copyright 2005 ©

39. Morey, M.; Davidson, A.; Eckert, H.; Stucky, G. *Chemistry of Materials* **1996**, *8*, 486-492; **DOI:** 10.1021/cm950397j Permission granted by American Chemical Society Copyright 1996 ©

40. Van Der Voort, P.; Morey, M.; Stucky, G. D.; Mathieu, M.; Vansant, E. F. *Journal of Physical Chemistry B* **1998**, *102*, 585-590; **DOI:** 10.1021/jp9727761 Permission granted by American Chemical Society Copyright 1998 ©

41. Gomez, S.; Giraldo, O.; Garces, L. J.; Villegas, J.; Suib, S. L. *Chemistry of Materials* **2004**, *16*, 2411-2417; **DOI:** 10.1021/cm040018z Permission granted by American Chemical Society Copyright 2004 ©

42. Hartmann, M.; Bischof, C. *Journal of Physical Chemistry B* **1999**, *103*, 6230-6235; **DOI:** 10.1021/jp991103a Permission granted by American Chemical Society Copyright 1999 ©

## Appendix B Copyright Materials

1. Linsebigler, A. L.; Lu, G.; Yates, J. T. Jr. *Chemical Reviews* **1995**, *95*, 735-758 **DOI:** 10.1021/cr00035a13; Permission granted by American Chemical Society Copyright 1995 ©

## Appendix C Copyright Materials

1. Van Der Voort, P.; White, M. G.; Mitchell, M. B.; Verberckmoes, A. A.; Vansant, E. F. *Spectrochimica Acta Part A: Molecular and Biomolecular Spectroscopy* **1997**, *53*, 2181-2187; **DOI:** 10.1016/S1386-1425(97)00145-5 Permission granted by Elesiver Scientific Publishing, Inc. Copyright 1997 ©

2. Doornkamp, C.; Clement, M.; Ponec, V. *Journal of Catalysis* **1999**, *182*, 390-399; **DOI:**10.1006/jcat.1998.2377 Permission granted by Elesiver Scientific Publishing, Inc. Copyright 1999 ©

3. Tran, K.; Hanning-Lee, M. A.; Biswas, A.; Stiegman, A. E.; Scott, G. W. *Journal of the American Chemical Society* **1995**, *117*, 2618-2626; **DOI:** 10.1021/ja00114a026 Permission granted by American Chemical Society Copyright 1995 ©

4. Janssens, T. V. W.; Carlsson, A.; Puig-Molina, A.; Clausen, B. S. *Journal of Catalysis* **2006**, *240*, 108-113; **DOI:** 10.1016/j.jcat.2006.03.008 Permission granted by Elsevier Scientific Publishing, Inc. Copyright 2006 ©

5. Lopez, N.; Janssens, T. V. W.; Clausen, B. S.; Xu, Y.; Mavrikakis, M.; Bligaard, T.; Norskov, J. K. *Journal of Catalysis* **2004**, *223*, 232-235; **DOI:** 10.1016/j.jcat.2004.01.001 Permission granted by Elsevier Scientific Publishing, Inc. Copyright 2004 ©

6. Schubert, M. M.; Hackenberg, S.; van Veen, A. C.; Muhler, M.; Plzak, V.; Behm, R. J. *Journal of Catalysis* **2001**, *197*, 113-122; **DOI:** 10.1006/jcat.2000.3069 Permission granted by Elesiver Scientific Publishing, Inc. Copyright 2001 ©

7. Guzman, J.; Carrettin, S.; Fierro-Gonzalez, J. C.; Hao, Y.; Gates, B. C.; Corma, A. *Angewandte Chemie International Edition* **2005**, *44*, 4778-4781; **DOI:** 10.1002/anie.200500659 Permission granted by Wiley VCH Verlag GmbH &Co. KGaA, Weinheim Copyright 2005 ©

8. Boccuzzi, F.; Chiorino, A.; Manzoli, M.; Lu, P.; Akita, T.; Ichikawa, S.; Haruta, M. *Journal of Catalysis* **2001**, *202*, 256-267; **DOI:** 10.1006/jcat.2001.3290 Permission granted by Elesiver Scientific Publishing, Inc. Copyright 2001 ©

9. Lim, S.; Ciuparu, D.; Yang, Y.; Du, G.; Pfefferle, L. D.; Haller, G. L. *Microporous and Mesoporous Materials* **2007**, *101*, 200-206; **DOI:** 10.1016/j.micromeso.2006.11.002 Permission granted by Elesiver Scientific Publishing, Inc. Copyright 2006 ©

10. Tanaka, T.; Ito, T.; Takenaka, S.; Funabiki, T.; Yoshida, S. *Catalysis Today* **2000**, *61*, 109-115; **DOI:** 10.1016/S0920-5861(00)00371-0 Permission granted by Elsevier Scientific Publishing, Inc. Copyright 2000 ©

11. Amano, F.; Yamaguchi, T.; Tanaka, T. *Catalysis Today* **2007**, *120*, 126-132; **DOI:** 10.1016/j.cattod.2006.07.041 Permission granted by Elsevier Scientific Publishing, Inc. Copyright 2006 ©

12. Takenaka, S.; Tanaka, T.; Yamazaki, T.; Funabiki, T.; Yoshida, S. *Journal of Physical Chemistry B* **1997**, *101*, 9035-9040; **DOI:** 10.1021/jp9716086 Permission granted by American Chemical Society Copyright 1997 ©

13. Tran, K.; Stiegman, A. E.; Scott, G. W. *Inorganica Chimica Acta* **1996**, *243*, 185-191; **DOI:** 10.1016/0020-1693(95)04906-1 Permission granted by Elsevier Scientific Publishing, Inc. Copyright 1996 ©

14. Teramura, K.; Hosokawa, T.; Ohuchi, T.; Shishido, T.; Tanaka, T. *Chemical Physics Letters* **2008**, *460*, 478-481; **DOI:** 10.1016/j.cplett.2008.06.025 Permission granted by Elsevier Scientific Publishing, Inc. Copyright 2008 ©

15. Tanenaka, S.; Kuriyama, T.; Tanaka, T.; Funabiki, T.; Yoshida, S. *Journal of Catalysis* **1995**, *155*, 196-203; **DOI:** 10.1006/jcat.1995.1203 Permission granted by Elesvier Scientific Publishing, Inc. Copyright 1995 ©

16. Amano, F.; Tanaka, T. *Catalysis Communications* **2005**, *6*, 269-273; **DOI:** 10.1016/j.catcom.2005.01.007 Permission granted by Elsevier Scientific Publishing, Inc. Copyright 2005 ©

17. Blasco, T.; Lopez Nieto, J. M.; Dejoz, A.; Vazquer, M. I. *Journal of Catalysis* **1995**, *157*, 271-282; **DOI:** 10.1006/jcat.1995.1291 Permission granted by Elsevier Scientific Publishing, Inc. Copyright 1995 ©

18. Takenaka, S.; Tanaka, T.; Funabiki, T.; Yoshida, S. *Catalysis Letters* **1997**, *44*, 67-74; **DOI:** 10.1023/A:1018944118203 Permission granted by J.C. Baltzer, Science Publishers Copyright 1997 ©

19. Amano, F.; Tanaka, T.; Funabiki, T. *Langmuir* **2004**, *20*, 4236-4240; **DOI:** 10.1021/la0359981 Permission granted by American Chemical Society Copyright 2004 ©

20. Tanaka, T.; Nishimura, Y.; Kawasaki, S-C.; Ooe, M.; Funabiki, T.; Yoshida, S. *Journal of Catalysis* **1989**, *118*, 327-338; **DOI:** 10.1016/0021-9517(89)90321-7 Permission granted by Elsevier Scientific Publishing, Inc. Copyright 1989 ©

21. Takenaka, S.; Tanaka, T.; Funabiki, T.; Yoshida, S. *Journal of Chemical Society, Faraday Transactions* **1997**, *93*, 4151-4158; **DOI:** 10.1039/a704794k Permission granted by Royal Society of Chemistry Copyright 1997 ©

22. Amano, F.; Ito, T.; Takenaka, S.; Tanaka, T. *Journal of Physical Chemistry B* **2005**, *109*, 10973-10977; **DOI:** 10.1021/jp0507871 Permission granted by American Chemical Society Copyright 2005 ©